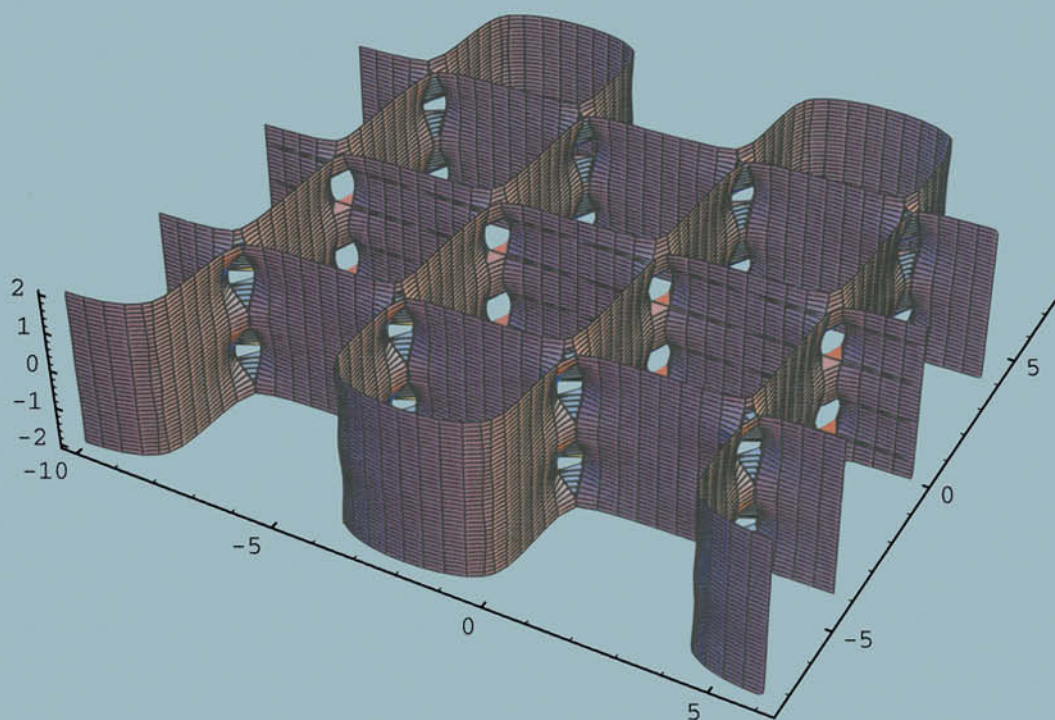


BIOMATHEMATICS

Mathematics of Biostructures and Biodynamics



Sten Andersson
Kåre Larsson
Marcus Larsson
Michael Jacob

Elsevier

BIOMATHEMATICS

**Mathematics of Biostructures
and Biodynamics**

This Page Intentionally Left Blank

BIOMATHEMATICS

Mathematics of Biostructures and Biodynamics

Sten Andersson

Sandviks Forskningsinstitut, S-380 74 Löttorp, Sweden

Kåre Larsson

KL Chem AB, S-237 34 Bjärred and Camurus Lipid Research, S-223 70 Lund, Sweden

Marcus Larsson

Lund University, Department of Clinical Physiology, S-214 01 Malmö, Sweden

Michael Jacob

Department of Inorganic Chemistry, Arrhenius Laboratory, University of Stockholm, S-106 91 Stockholm, Sweden



1999

Elsevier

Amsterdam – Lausanne – New York – Oxford – Shannon – Singapore – Tokyo

ELSEVIER SCIENCE B.V.
Sara Burgerhartstraat 25
P.O. Box 211, 1000 AE Amsterdam, The Netherlands

© 1999 Elsevier Science B.V. All rights reserved.

This work and the individual contributions contained in it are protected under copyright by Elsevier Science, and the following terms and conditions apply to its use:

Photocopying

Single photocopies of single chapters may be made for personal use as allowed by national copyright laws. Permission of the Publisher and payment of a fee is required for all other photocopying, including multiple or systematic copying, copying for advertising or promotional purposes, resale, and all forms of document delivery. Special rates are available for educational institutions that wish to make photocopies for non-profit educational classroom use.

Permissions may be sought directly from Elsevier Science Rights & Permissions Department, PO Box 800, Oxford OX5 1DX, UK; phone: (+44) 1865 843830, fax: (+44) 1865 853333, e-mail: permissions@elsevier.co.uk. You may also contact Rights & Permissions directly through Elsevier's home page (<http://www.elsevier.nl>), selecting first 'Customer Support', then 'General Information', then 'Permissions Query Form'.

In the USA, users may clear permissions and make payments through the Copyright Clearance Center, Inc., 222 Rosewood Drive, Danvers, MA 01923, USA; phone: (978) 7508400, fax: (978) 7504744, and in the UK through the Copyright Licensing Agency Rapid Clearance Service (CLARCS), 90 Tottenham Court Road, London W1P 0LP, UK; phone: (+44) 171 631 5555; fax: (+44) 171 631 5500. Other countries may have a local reprographic rights agency for payments.

Derivative Works

Tables of contents may be reproduced for internal circulation, but permission of Elsevier Science is required for external resale or distribution of such material. Permission of the Publisher is required for all other derivative works, including compilations and translations.

Electronic Storage or Usage

Permission of the Publisher is required to store or use electronically any material contained in this work, including any chapter or part of a chapter.

Except as outlined above, no part of this work may be reproduced, stored in a retrieval system or transmitted in any form or by any means, electronic, mechanical, photocopying, recording or otherwise, without prior written permission of the Publisher.

Address permissions requests to: Elsevier Science Rights & Permissions Department, at the mail, fax and e-mail addresses noted above.

Notice

No responsibility is assumed by the Publisher for any injury and/or damage to persons or property as a matter of products liability, negligence or otherwise, or from any use or operation of any methods, products, instructions or ideas contained in the material herein. Because of rapid advances in the medical sciences, in particular, independent verification of diagnoses and drug dosages should be made.

First edition 1999

Library of Congress Cataloging in Publication Data

A catalog record from the Library of Congress has been applied for.

ISBN: 0 444 50273 4

⊗The paper used in this publication meets the requirements of ANSI/NISO Z39.48-1992 (Permanence of Paper).
Printed in The Netherlands.

Contents

Chapter 1

1 Introduction	1
References 1	4

Chapter 2

2 Counting, Algebra and Periodicity - the Roots of Mathematics are the Roots of Life	7
2.1 Counting and Sine	7
2.2 Three Dimensions; Planes and Surfaces, and Surface Growth	9
2.3 The Growth of Nodal Surfaces - Molecules and Cubosomes	16
References 2	26

Chapter 3

3 Nodal Surfaces of Tetragonal and Hexagonal Symmetry, and Rods	27
3.1 Non Cubic Surfaces	27
3.2 Tetragonal Nodal Surfaces and their Rod Structures	27
3.3 Hexagonal Nodal Surfaces and their Rod Structures	36
References 3	45

Chapter 4

4 Nodal Surfaces, Planes, Rods and Transformations	47
4.1 Cubic Nodal Surfaces	47
4.2 Nodal Surfaces and Planes	50
4.3 Cubic Nodal Surfaces and Parallel Rods	56
4.4 Transformations of Nodal Surfaces	68
References 4	72

Chapter 5

5 Motion in Biology	73
5.1 Background and Essential Functions	73
5.2 The Control of Shape - the Natural Exponential or cosh in 3D	76
5.3 The Gauss Distribution (GD) Function and Simple Motion	81
5.4 More Motion in 3D	93
References 5	102

Chapter 6

6 Periodicity in Biology - Periodic Motion	105
6.1 The Hermite Function	105
6.2 Flagella - Snake and Screw Motion	111

6.3 Periodic Motion with Particles in 2D or 3D	116
6.4 Periodic Motion with Rotation of Particles in 2D	127
References 6	130
 Chapter 7	
7 Finite Periodicity and the Cubosomes	131
7.1 Periodicity and the Hermite Function	131
7.2 Cubosomes and the Circular Functions	133
7.3 Cubosomes and the GD-Function - Finite Periodicity and Symmetry P	139
7.4 Cubosomes and the GD-Function - Symmetry G	143
7.5 Cubosomes and the GD Function - Symmetry D	147
7.6 Cubosomes and the Handmade Function	152
References 7	162
 Chapter 8	
8 Cubic Cell Membrane Systems/Cell Organelles and Periodically Curved Single Membranes	163
8.0 Introduction	163
8.1 Cubic Membranes	163
8.2 The Endoplasmatic Reticulum	169
8.3 Protein Crystallisation in Cubic Lipid Bilayer Phases and Cubosomes - Colloidal Dispersions of Cubic Phases	175
8.4 From a Minimal Surface Description to a Standing Wave Dynamic Model of Cubic Membranes	177
8.5 Periodical Curvature in Single Membranes	183
References 8	190
 Chapter 9	
9 Cells and their Division - Motion in Muscles and in DNA	193
9.1 The Roots and Simple Cell Division	193
9.2 Cell Division with Double Membranes	201
9.3 Motion in Muscle Cells	206
9.4 RNA and DNA Modelling	213
References 9	220
 Chapter 10	
10 Concentration Gradients, Filaments, Motor Proteins and again - Flagella	223
10.1 Background and Essential Functions	223
10.2 Filaments	227
10.3 Microtubulus and Axonemes	235
10.4 Motor Proteins and the Power Stroke	244
10.5 Algebraic Roots Give Curvature to Flagella	247
References 10	255

Chapter 11

11 Transportation	257
11.1 Background - Examples of Docking and Budding with Single Plane Layers, and Other Simple Examples	257
11.2 Docking and Budding with Curved Single Layers	265
11.3 Transport Through Double Layers	273
References 11	284

Chapter 12

12 Icosahedral Symmetry, Clathrin Structures, Spikes, Axons, the Tree, and Solitary Waves	285
12.1 The icosahedral symmetry	285
12.2 Hyperbolic Polyhedra, Long Cones, Cylinders and Catenoids	294
12.3 Cylinder Division and Cylinder Fusion - Cylinder Growth	299
12.4 Solitary Waves, Solitons and Finite Periodicity	305
References 12	311

Chapter 13

13 Axon Membranes and Synapses - A Role of Lipid Bilayer Structure in Nerve Signals	313
13.1 The Nerve Impulse	313
13.2 At the Action Potential Region of the Membrane there is a Phase Transition in the Lipid Bilayer	315
13.3 A Model of a Phase-Transition/Electric Signal Coupling at Depolarisation and its Physiological Significance	317
13.4 Transmission of the Nerve Signal at the Terminal Membrane of the Neurons - Synaptic Transmission	327
13.5 Synchronisation of Muscle Cell Activation	333
13.6 The General Anaesthetic Effect	335
13.7 Physiological Significance of Involvement of a Lipid Bilayer Phase Transition in Nerve Signal Conduction	337
References 13	338

Chapter 14

14 The Lung Surface Structure and Respiration	341
14.1 The Alveolar Surface	341
14.2 Lung Surfactant	342
14.3 Structure of Tubular Myelin - A Bilayer arranged as the Classical CLP-Surface	344
14.4 The Existence of a Coherent <i>Surface Phase</i> Lining the Alveoli	349
14.5 Respiration	357
14.6 Physiological Significance of the Existence of an Organised Surface Phase at the Alveolar Surface	359
References 14	361

Chapter 15	
15 Epilogue	363
Acknowledgement	372
References 15	372
Appendix 1	
The Plane, the Cylinder and the Sphere	375
Appendix 2	
Periodicity	385
Appendix 3	
The Exponential Scale, the GD function, Cylinder and Sphere Fusion	399
Appendix 4	
The Exponential Scale, the Planes and the Natural Function, Addition and Subtraction	409
Appendix 5	
Multiplication of Planes, Saddles and Spirals	419
Appendix 6	
Symmetry	431
Appendix 7	
The Complex Exponential, the Natural Exponential and the GD-Exponential - General Examples and Finite Periodicity	447
Appendix 8	
Classical Differential Geometry and the Exponential Scale	463
Appendix 9	
Mathematica (Contains the Mathematica scripts used for calculating the equations for the figures in this book.)	477

1 Introduction

There is no permanent place in the world for ugly mathematics [Hardy,1].

This book deals with the shape of cells and cell organelles in plants and animals, and changes of shape associated with various life processes. The cell membranes and cytoskeleton proteins build these shapes based on physical forces. A mathematical/geometrical description of cellular and molecular shapes is presented in this book, and the biological relevance is discussed in the epilogue. We demonstrate here new mathematics for cellular and molecular structures and dynamic processes.

Life began in water, and every single function of life takes place in an aqueous environment. A profound way of classification in chemistry is the relation and interaction between molecules, or groups within molecules, and water. Molecules (or parts of molecules) can attract water in which case they are called *hydrophilic*. As the opposite extreme they can strive to avoid water; these molecules or molecular parts are termed *hydrophobic*. Most biomolecules possess both these properties; they are *amphiphilic*. This is a fundamental principle which determines the organisation of biomolecules - from the folding of peptide chains into native structures of proteins, to self-assembly of lipid and protein molecules into membranes. One consequence of the existence of these two media is that the interface between them define surfaces that tend to be closed. The lipid bilayer of membranes, for example, always form closed surfaces; the hydrocarbon chain core is never exposed to water. The curvature of these surfaces is an important concept in order to understand structural features above the molecular level. Surface and colloid science deals with forces involved in formation of such organisations. The behaviour of the colloidal state of matter involves van der Waals interaction, electrostatic forces, so-called hydration forces and hydrophobic forces. The colloidal level of structure extended towards curvature of surfaces and finite periodicity is a main theme in our book. These concepts are seldom considered in molecular biology.

Our present understanding of the cell membrane dates back to Luzzati's classical work from 1960 [2], where the liquid character of the hydrocarbon chains in liquid-crystalline lipid-water phases with the combination of long-range order with short-range disorder first were revealed. Another important aspect was introduced by Helfrich [3]; the curvature elastic energy. Long time ago, two of us [4] proposed the idea that a bilayer

conformation analogous to that of cubic phases might occur in cell membranes. Phase transitions in three dimensions, obtained by exposure of membrane lipids to general anaesthetic agents, for example, were interpreted as experimental evidence [5]. These aspects were summarised in a monograph - *The Language of Shape* [6] - focusing on the role of curvature in membranes. Cubic lipid-water phases and cubic cell membrane assemblies were described as infinite periodic minimal surfaces (IPMS). Some thousand examples where the membrane is folded into a three-dimensional aggregate were shown to be cubic structures consistent with the three fundamental IPMS (the P-, D- and G-surface). Here we propose that the occurrence of perfect cubic symmetry of membrane assemblies reflects a vegetative state with lack of concentration gradients, resulting in an equilibrium-like situation. We conclude that active states of membrane systems, such as the endoplasmatic reticulum, are far from a compositional equilibrium, and therefore exhibit systematic variations of curvature. Such active states of membrane organisations are characterised based on the new mathematics introduced here.

The IPMS description reflects a static structure and might be regarded as a time-averaged conformation of the bilayer. Recently we introduced a description of the lipid bilayer of membranes based on nodal surfaces of standing wave conformations [7,8]. We consider this description to be significant to cellular phenomena, providing a true description of the dynamic character of cell membranes. The mathematical basis of the wave dynamics is extended in this book. We consider this feature to be of utmost importance in cell membrane physiology, providing space-time relations.

Cell membranes exhibit lipid bilayer states on the border towards a transition into a reverse type of structure (in three dimensions corresponding to phase transitions from lamellar to cubic or reverse hexagonal lipid-water phases). This tendency results in a high inner packing pressure of the bilayer, and therefore increases the elastic rigidity of the lipid bilayer. The wave motions of the bilayer are related to this elastic rigidity. Membrane-embedded enzymes responsible for lipid synthesis/modification can utilise the inner packing pressure as an on/off switch to control membrane lipid composition. This is an example of shape control *via* physical properties. The mathematical wave description reflects the dynamics of shape.

Another important feature of the cell membranes is their control of topology in the cell - separation of the inside and the outside. Considering any cell in our body and moving backwards in time via the embryo and through earlier generations down the evolution, the DNA has never been exposed to the outside world. There is always a membrane enveloping DNA in all forms of life, as we know them. A closed membrane providing shape

and topology is thus a necessity for life. Its implicit expression in DNA is a challenging question, which we will consider in the epilogue.

There are hundreds of journals in molecular biology today dealing with structure and function. In our interdisciplinary approach we can only deal with some basic principles behind shape and shape changes. In our description of vesicle traffic between cellular compartments, for example, we apply only mathematics of lipid bilayers with varying curvature. We are aware of the numerous studies which have demonstrated involvement of for example kinesin in the endoplasmatic reticulum and of dynein in the Golgi structure. Our model of cell membrane dynamics and morphology, although ignoring the role of microtubuli, still gives a description consistent with reality. This might be due to the redundancy in biology; systems working in parallel to guarantee functional safety. Evidence is also given for the occurrence of mechanical waves at the axon membrane, with a conformational transition accompanying the electrical pulse. Finally by applying these new mathematics it has been possible to derive the structure of the surface film lining the lung alveoli.

We describe the lipid bilayer of cell membranes by surfaces located at the middle of the bilayer. The liquid-like hydrocarbon chains extend about 15 - 20 Å from this surface, and they might be compared with the delocalised electrons forming molecular surfaces. It is in this context tempting to go further in this analogy, perhaps to speculate on the possibility of quantum phenomena with phonons involved in the lipid bilayer motions.

In order to derive the various cell structures discussed in this book the following new tools/concepts have been used:

The *exponential scale* [9], which was developed to describe shapes of bodies like polyhedra, crystals, or anything that may be described with faces. Structures, crystal structures, symmetries, rod structures and molecules are also conveniently described.

The symmetry and structure of lipid membranes in confined space, like a cubosome, follow the electron densities of smaller molecules, like B_4H_4 and $B_{12}H_{12}$. We propose such lipid structures also have a standing wave behaviour - quantized or not. We describe this analogy of the quantized space and the lipid space with the exponential scale. We find great parts of these mathematics to be closely related to shapes in biology.

The *Gaussian distribution function* (GD) - a special case of the exponential scale - which is also known as the error function. It is used to describe diffusion, and it is also the ground state solution for the Schrödinger harmonic oscillator. We use the GD function to generate finite periodicity

to describe structures like the cubosomes. We use the GD function to describe *biological motion* and we use the related Hermite operator to describe periodic biological motion. Examples are the flagella motion, the motor proteins and cell division. The fractal growth of a tree and the formation of icosahedral symmetry of virus are other examples.

We describe transportation with exponential functions. We describe budding and docking of vesicles, the endoplasmatic reticulum and the Golgi machine, holes in double membranes, the nuclear pore complex, and much more.

The GD-function is used here to define surfaces of the condensed state of cellular biomolecules. To illustrate this approach let us again consider a lipid bilayer with water on each side. Most of the lipid constituents have very low solubility (down to 10^{-12} M), which varies with environmental factors, such as pH and present ions. We are dealing with non-equilibrium conditions, with lipid molecules either moving inwards to condensate at the surface, or moving out into the water phase from the surface. The molecular distribution at the surface follows the GD function. Such concentration changes may even result in transient shape changes of cell membranes.

The *standing wave dynamic conformation of membranes* is a third new concept we apply in order to describe membrane shape. As mentioned earlier the membrane assemblies exhibiting cubic symmetry can be described as IPMS when the conformation is averaged over time but the wave character provides information on dynamic membrane processes.

Readers who directly want to see the biological relevance of this approach can start with chapters 8, 13 and 14 and later read the earlier chapters focusing on the mathematics. For readers who lack a mathematical background, the basic concepts we are using are introduced in the appendices. The use of Mathematica in the calculations is shown with examples in appendix 9.

References 1

1. G.H. Hardy; *A MATHEMATICIAN'S APOLOGY*, Cambridge University press, 1976, page 85.
2. V. Luzzati, H. Mustacchi, A. Skoulios, and F. Husson, *Acta Cryst.* **13** (1960) 660.

-
3. W. Helfrich, *Z. Naturforsch.* **A28** (1973) 693.
 4. K. Larsson and S. Andersson, *Acta Chem Scand.* **B40** (1986) 1.
 5. K. Larsson, *Langmuir* **4** (1988) 215.
 6. S. Hyde, S. Andersson, K. Larsson, Z. Blum, T. Landh, S. Lidin and B. Ninham; *THE LANGUAGE OF SHAPE*, Elsevier, Amsterdam, 1997.
 7. M. Jacob, K. Larsson and S. Andersson, *Z. Kristallogr.* **212** (1997) 5.
 8. K. Larsson, M. Jacob and S. Andersson, *Z. Kristallogr.* **211** (1996) 875.
 9. M. Jacob and S. Andersson; *THE NATURE OF MATHEMATICS AND THE MATHEMATICS OF NATURE*, Elsevier, Amsterdam, 1998.

This Page Intentionally Left Blank

2 Counting, Algebra and Periodicity - the Roots of Mathematics are the Roots of Life

All things are numbers [Pythagoras,1].

Using simple counting, or algebra, we show the principles of periodicity, which is just using roots, number, or planes in space. We also show you what sine is.

With counting we make saddles move in bilateral or screw repetition. We continue in that way and show that fundamental mathematics is built of planes, and go from a molecule to a cubosome, which is an example of how symmetry shows up in a 3D space of just numbers.

We show how cubic surfaces nucleate from the simplest of saddles and planes.

We show how to move a surface or a cubosome in space.

We show how to derive the nodal surface geometry from algebra - or just by counting.

2.1 Counting and Sine

We assume mathematics used by Nature may be described in simple terms.

We start from the beginning;

$x=1$ is a plane in space, and so is $x=2$. With such planes we formulate our first equation, which also is an example of the fundamental theorem of algebra.

$$(x-1)(x-2)(x-3)(x-4) = 0 \qquad 2.1.1$$

This operation we call *counting* and we want to see what it means in 3D. The roots are 1, 2, 3 and 4. We see in figure 2.1.1 the planes, and we discover that counting - put together in form of multiplication into a product - is a beautiful way to get periodicity. Which so far is finite.

We presume Nature may be described by counting positive numbers.

For reasons of convenience we shall sometimes in the description below use zero and negative numbers, but in every case it is possible to make a parallel transformation to the positive part of space as shown below with examples.

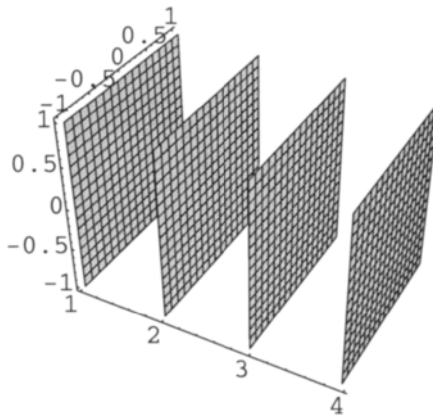


Figure 2.1.1 Periodicity from the fundamental theorem of algebra.

Equation 2.1.1 is the fundamental theorem of algebra, and Euler realised that this is really the same as sine - using an infinite product. 1, 2, 3 and 4 are the roots of the equation, and also the origin to periodicity. For comparison we give $\sin\pi x=0$ in figure 2.1.2.

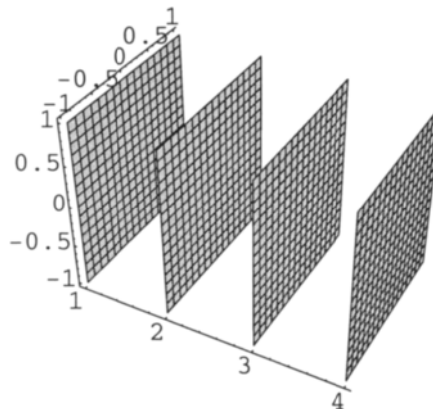


Figure 2.1.2 Periodicity from sine.

Below we give the formula in equation 2.1.2, from Euler for the infinite products, which he showed was identical with the power expansion of $\sin(x)$ (an alternative definition). This definition of the circular functions which uses infinite products is attractive since it brings in the translation.

$$\sin x = x \left(1 - \frac{x^2}{\pi^2}\right) \left(1 - \frac{x^2}{2^2 \pi^2}\right) \left(1 - \frac{x^2}{3^2 \pi^2}\right) \dots \quad 2.1.2$$

Rearranging formula 2.1.2 into 2.1.3 it becomes clear that sine is identical to the fundamental theorem of algebra of an infinite number of terms [2]. The roots of algebra are the nodes of periodicity - or the wave functions.

$$\sin \pi x = \frac{\pi}{(n!)^2} x(x^2 - 1)(x^2 - 4)(x^2 - 9) \dots (x^2 - n^2) \quad 2.1.3$$

2.2 Three Dimensions; Planes and Surfaces, and Surface Growth

From equation 2.1.3 we take two of the roots and extend them to three dimensions in the following equations.

$$x^2 - 1 = 0 \quad 2.2.1$$

$$y^2 - 1 = 0 \quad 2.2.2$$

$$z^2 - 1 = 0 \quad 2.2.3$$

The planes are found in the corresponding figures 2.2.1-3.

If we, in equation 2.2.4 add two of the equations, the planes collaborate to form a cylinder, see figure 2.2.4.

$$x^2 + y^2 - 1 = 0 \quad 2.2.4$$

And if we add all three equations, six planes collaborate to form the sphere in figure 2.2.5.

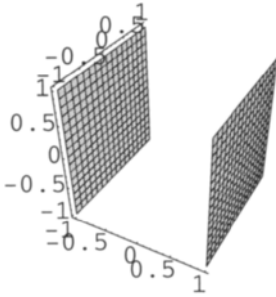


Figure 2.2.1 The simplest roots of x in space.

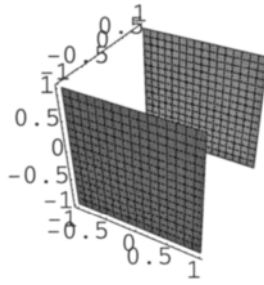


Figure 2.2.2 The simplest roots of y in space.

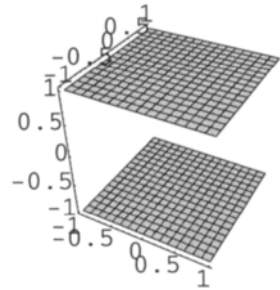


Figure 2.2.3 The simplest roots of z in space.

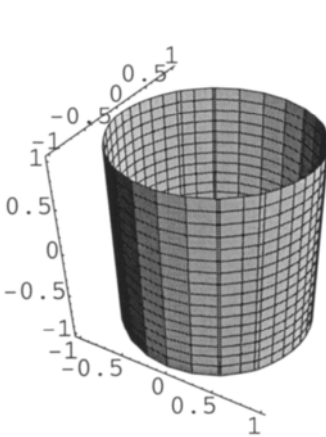


Figure 2.2.4 Four planes form a cylinder.

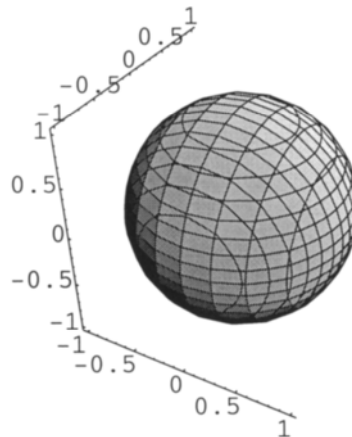


Figure 2.2.5 Six planes form a sphere.

Going up in exponent, still using the algebra, brings out the planes as in equations 2.2.5-6 and figures 2.2.5-7.

$$x^4 + y^4 = 1 \tag{2.2.5}$$

$$x^4 + y^4 + z^4 = 1 \tag{2.2.6}$$

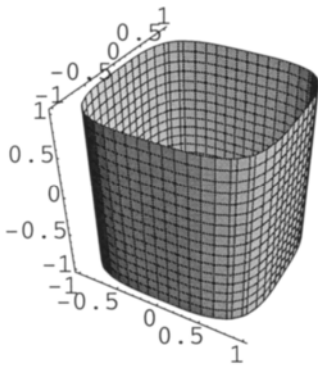


Figure 2.2.6 Four planes form a square cylinder.

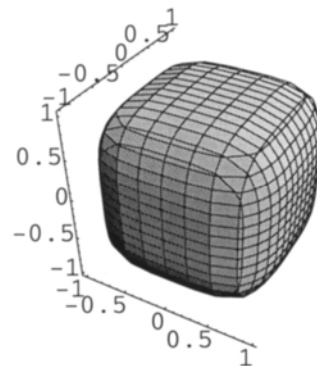


Figure 2.2.7 Six planes form a "cube".

Above was shown simple examples of elliptic geometry, which has positive gaussian curvature. We now move on to hyperbolic geometry with negative gaussian curvature. For a definition of curvature see appendix 8.

The function $xy=0$ is two intersecting planes, and in equation 2.2.7 a z -plane is added.

$$xy - z = 0 \tag{2.2.7}$$

This simple product - so important in algebra - gives the famous saddle as shown in figures 2.2.8-9, the last one in projection with huge boundaries to show that it is built of planes.

We bring in roots in one dimension and start the counting, or translation of z -planes, which are finite periodic in that direction. Corresponding figures are 2.2.10-13.

$$xy + z(z - 0.5) = 0 \tag{2.2.8}$$

$$xy + z(z - 0.5)(z - 1) = 0 \tag{2.2.9}$$

$$xy + z(z - 0.5)(z - 1)(z - 1.5) = 0 \tag{2.2.10}$$

$$xy + z(z - 0.5)(z - 1)(z - 1.5)(z - 2)(z - 2.5)(z - 3) = 0 \tag{2.2.11}$$

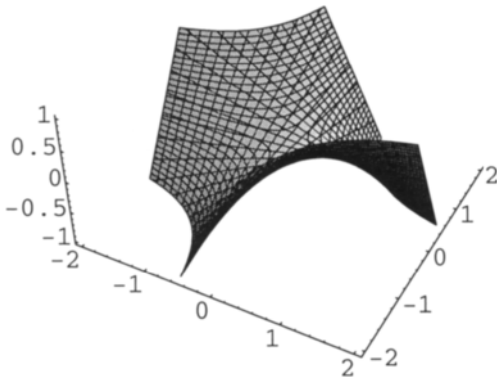


Figure 2.2.8 A saddle.

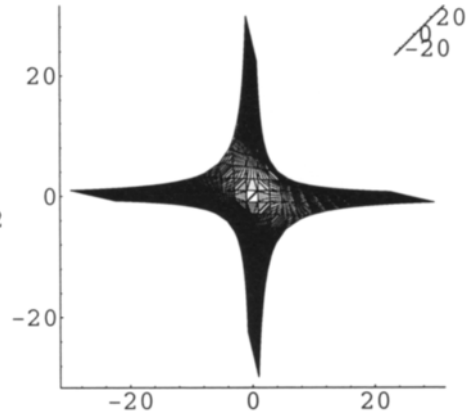


Figure 2.2.9 Increased boundaries show that the saddle is built of planes.

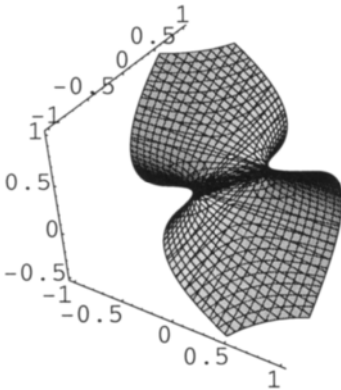


Figure 2.2.10 One more z-plane and the saddle.

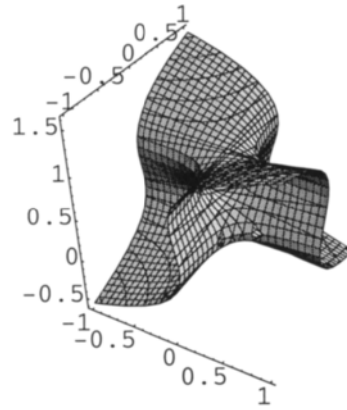


Figure 2.2.11 Two more z-planes and the saddle.

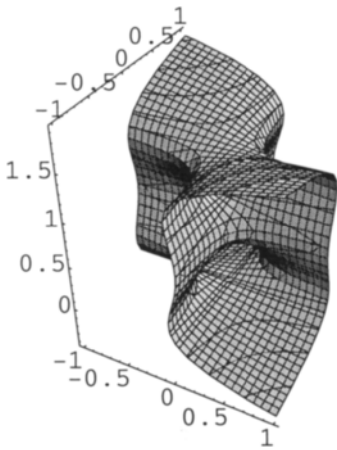


Figure 2.2.12 Three more z-planes and the saddle.

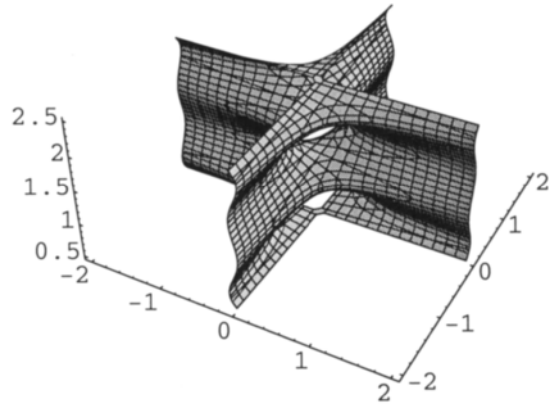


Figure 2.2.13 Six more z-planes and the saddle give a tower surface.

The original saddle is repeated and makes the surface grow to form a so called tower surface, topologically the same as Scherk's fifth minimal surface [see appendix 5]. This is shown in figure 2.2.13 with proper boundaries. Planes meet and go through each other in space without intersections, which is the simplest possible periodic saddle surface.

The double products give the intersecting planes as shown in figure 2.2.14.

$$xz + yz = 0 \tag{2.2.12}$$

Doing a translation, or starting the counting as in equation 2.2.13, makes the planes join via a saddle in figure 2.2.15.

$$xz + y(z - 0.5) = 0 \tag{2.2.13}$$

By adding z-planes, as in equations 2.2.14-15, a screw surface starts to grow, as shown in figures 2.2.16-17.

$$xz(z - 1) + y(z - 0.5) = 0 \tag{2.2.14}$$

$$xz(z - 1) + y(z - 0.5)(z - 1.5) = 0 \tag{2.2.15}$$

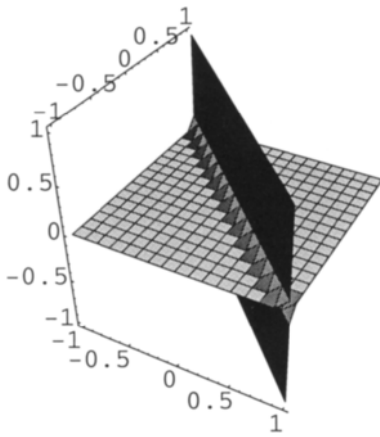


Figure 2.2.14 Intersecting planes.

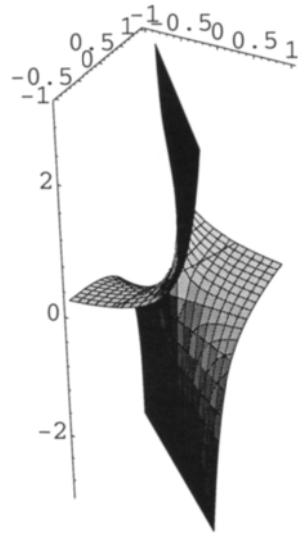


Figure 2.2.15 Translation in z , and the intersecting planes become a saddle.

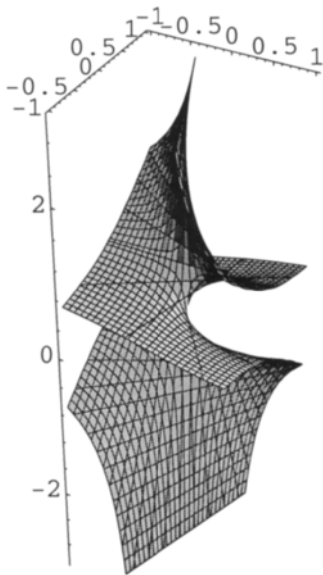


Figure 2.2.16 Two translations in z .

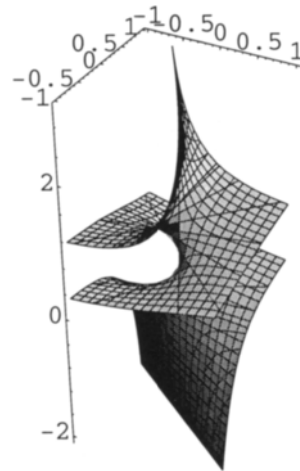


Figure 2.2.17 Three translations in z and a screw surface is growing.

We continue counting after equation 2.2.16 and obtain the famous helicoid in figures 2.2.18-19, as grown from planes.

These two surfaces, the tower surface and helicoid, are the building block units of many biological structures. They are formed by the 3D periodic nodal surfaces that will be discussed extensively in this book.

$$xz(z-1)(z-2)(z-3)(z-4)(z-5)(z-6)(z-7) + y(z-.5)(z-1.5)(z-2.5)(z-3.5)(z-4.5)(z-5.5)(z-6.5) = 0 \tag{2.2.16}$$

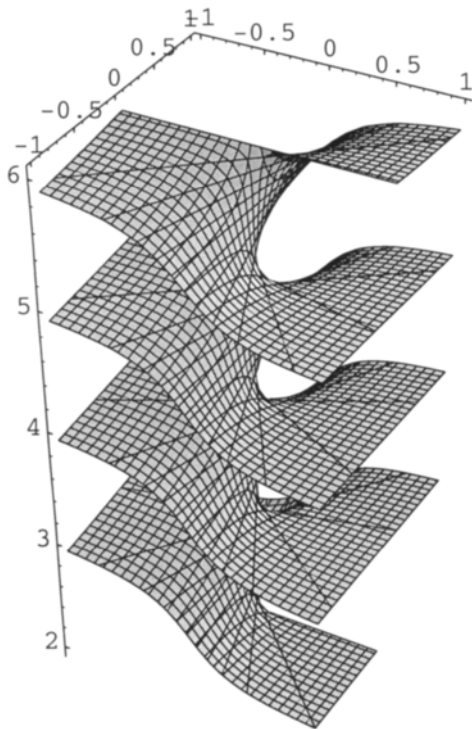


Figure 2.2.18 The helicoid surface as obtained from pure counting, or algebra.

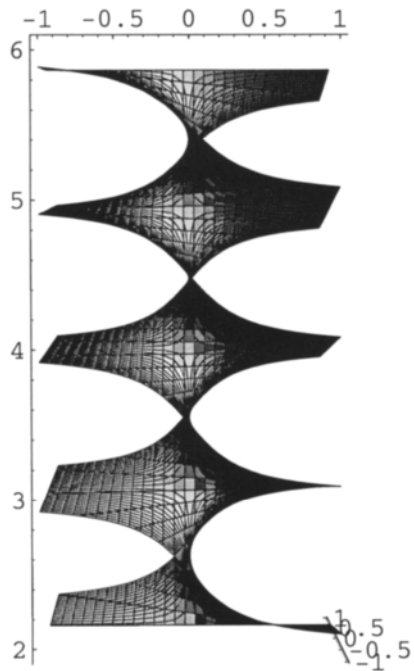


Figure 2.2.19 Different projection of the helicoid.

We will now show how to move a surface with this algebra, doing a translation operation of the helicoid as shown in equations 2.2.17 and 2.2.18, and figures 2.2.20 and 21.

$$(x-2)(z-1)(z-2)(z-3)(z-4)(z-5)(z-6) + (y-2)(z-0.5)(z-1.5)(z-2.5)(z-3.5)(z-4.5)(z-5.5) = 0 \quad 2.2.17$$

$$(x-4)(z-5)(z-6)(z-7)(z-8)(z-9)(z-10) + (y-4)(z-4.5)(z-5.5)(z-6.5)(z-7.5)(z-8.5)(z-9.5) = 0 \quad 2.2.18$$

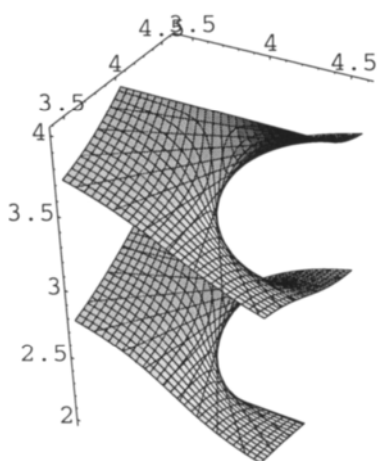


Figure 2.2.20 Translation of the helicoid.

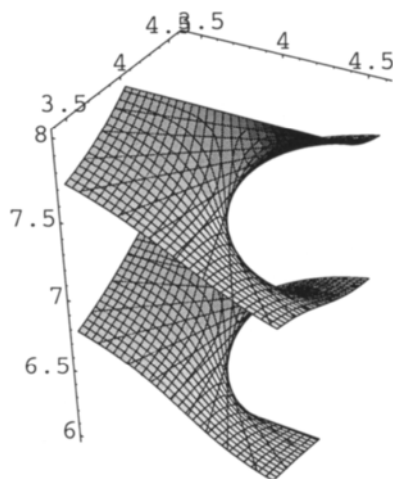


Figure 2.2.21 Further translation of the helicoid.

2.3 The Growth of Nodal Surfaces - Molecules and Cubosomes

Periodical nodal surfaces, or the topologically identical minimal surfaces, are used to describe such phenomena in Nature as membranes and cubosomes in biology, crystal structures and reactivity like catalysis in chemistry, and membrane wave mechanics and the Fermi surfaces in physics. We will show below that in the mathematical description of such surfaces there is no need for circular functions or their power expansions. All needed is counting.

So we do the counting and add polynomina from the fundamental theorem of algebra in three directions, and show first the planes as in figures 2.3.1-3.

$$\begin{aligned}
 x(x-1)(x-2)(x-3) &= 0 \\
 y(y-1)(y-2)(y-3) &= 0 \\
 z(z-1)(z-2)(z-3) &= 0
 \end{aligned}
 \tag{2.3.1}$$

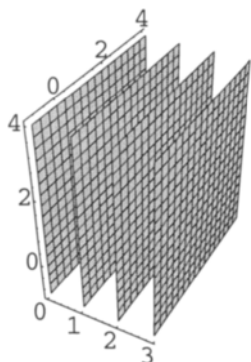


Figure 2.3.1 Four planes and counting in x.

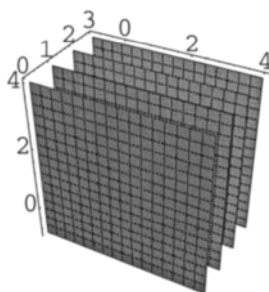


Figure 2.3.2 Four planes and counting in y.

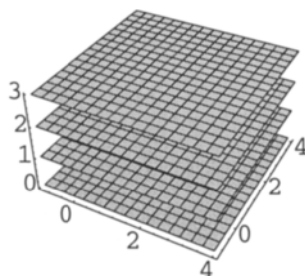


Figure 2.3.3 Four planes and counting in z.

We add the three systems into one equation, 2.3.2, and the planes collaborate in space to give figure 2.3.4.

$$\begin{aligned}
 &x(x-1)(x-2)(x-3) \\
 &+y(y-1)(y-2)(y-3) \\
 &+z(z-1)(z-2)(z-3) = -1
 \end{aligned}
 \tag{2.3.2}$$

We can do the counting elsewhere in space, which means translating the structure as in figure 2.3.5, after equation 2.3.3.

$$\begin{aligned}
 &(x-6)(x-7)(x-8)(x-9) \\
 &+(y-6)(y-7)(y-8)(y-9) \\
 &+(z-6)(z-7)(z-8)(z-9) = -1
 \end{aligned}
 \tag{2.3.3}$$

The structure is a piece of the symmetry created by this way of counting. It can be considered as a piece of a primitive cubic structure, the ELF structure (Electron Localisation Function) of the B_6H_6 molecule [3], the smallest possible closed piece of the P-surface, or the smallest possible cubosome. Cubosomes are important structures of biomembranes, which we focus on in chapter 8. We shall below make bigger parts and it is then easier to explain these concepts. Here we just mention the boron octahedron in

figure 2.3.6, which is calculated from zero constant in equation 2.3.4. The electrons are distributed to the cubic structure in figure 2.3.5, which is the dual of the octahedron.

$$\begin{aligned}
 &x(x-1)(x-2)(x-3) \\
 &+y(y-1)(y-2)(y-3) \\
 &+z(z-1)(z-2)(z-3)=0
 \end{aligned}
 \tag{2.3.4}$$

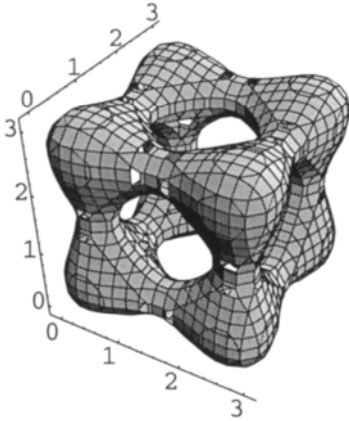


Figure 2.3.4 Counting to four in 3D gives a hollow cube, which can be considered as a small part of the P-surface.

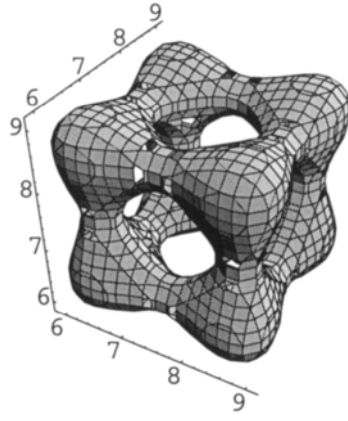


Figure 2.3.5 The structure from figure 2.3.4 translated in space.

We add more planes as in figure 2.3.7 after equation 2.3.5, and now have a bigger part of the P-surface. The periodicity is finite, so this is a cubosome.

$$\begin{aligned}
 &x(x-1)(x+1)(x-2)(x+2)(x-3)(x+3) \\
 &\cdot (x-4)(x+4)(x-5)(x+5)(x-6) \\
 &+y(y-1)(y+1)(y-2)(y+2)(y-3)(y+3) \\
 &\cdot (y-4)(y+4)(y-5)(y+5)(y-6) \\
 &+z(z-1)(z+1)(z-2)(z+2)(z-3)(z+3) \\
 &\cdot (z-4)(z+4)(z-5)(z+5)(z-6)=20000
 \end{aligned}
 \tag{2.3.5}$$

For an infinite product this becomes $\cos x + \cos y + \cos z = 0$, which is the nodal P-surface equation as described in appendix 2.

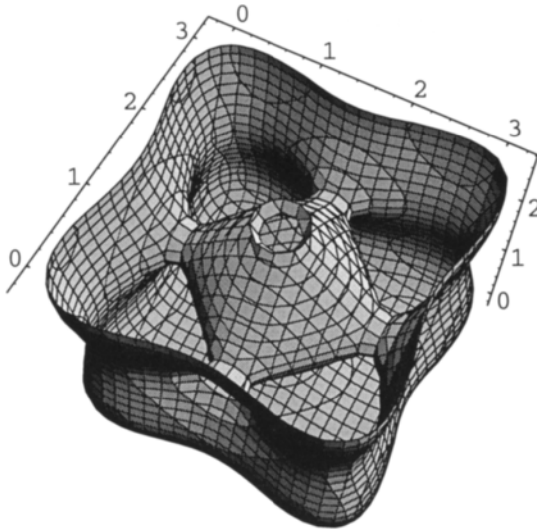


Figure 2.3.6 The hollow cube and its dual.

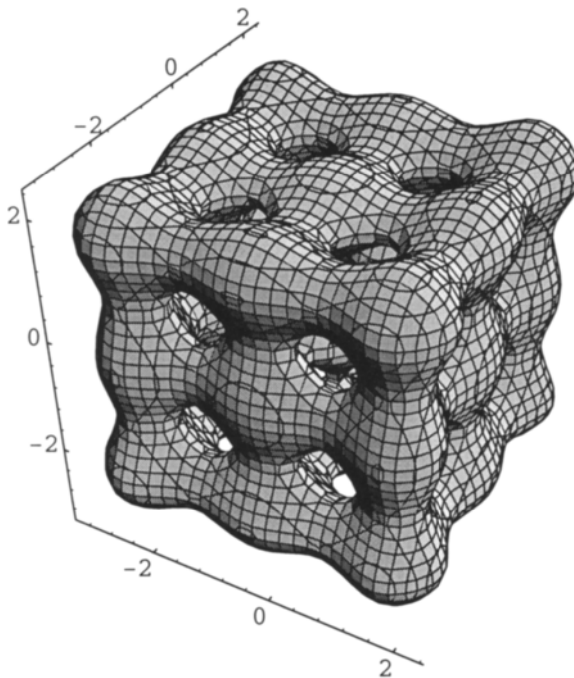


Figure 2.3.7 More counting gives bigger part of the P-surface.

The 3D function in 2.3.6 gives a 'three dimensional saddle' - a catenoid - with its axes along the cube diagonal as in figures 2.3.8-9.

$$xy + xz + yz + 1 = 0$$

2.3.6

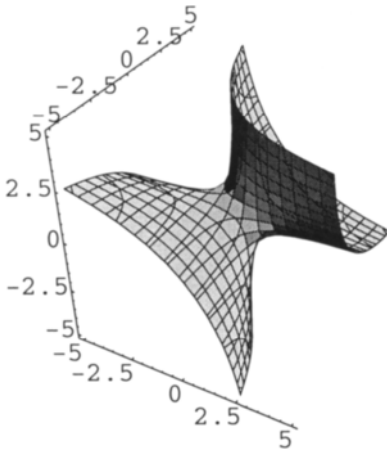


Figure 2.3.8 Three dimensional saddle.

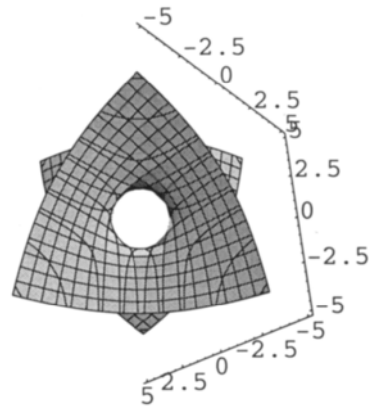


Figure 2.3.9 Different projection.

The complete multiplication xyz gives three planes intersecting after equation 2.3.7, and is shown in 2.3.10. Adding a constant gives four cube corners that meet after tetrahedral symmetry, as in figure 2.3.11. This is the commencement of periodicity and symmetry - the three planes collaborate in space to form four identical units. We continue with one more plane after equation 2.3.9, which is shown in figure 2.3.12.

$$xyz = 0 \tag{2.3.7}$$

$$xyz = 1 \tag{2.3.8}$$

$$xyz(x - 0.5)(y - 0.5)(z - 0.5) = 0 \tag{2.3.9}$$

Using this simple algebra we derive some more very fundamental surfaces, which also appear with different and more familiar derivations in appendix 2.

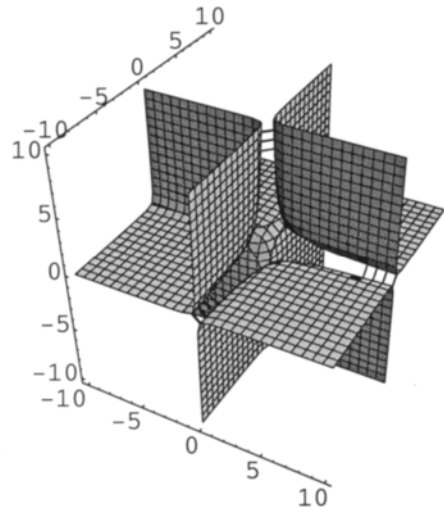
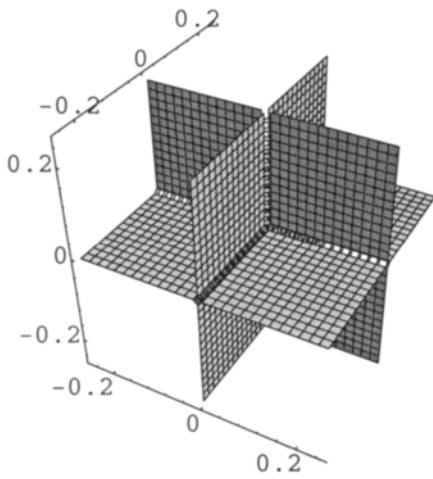


Figure 2.3.10 Three intersecting planes.

Figure 2.3.11 Four cube corners in space.

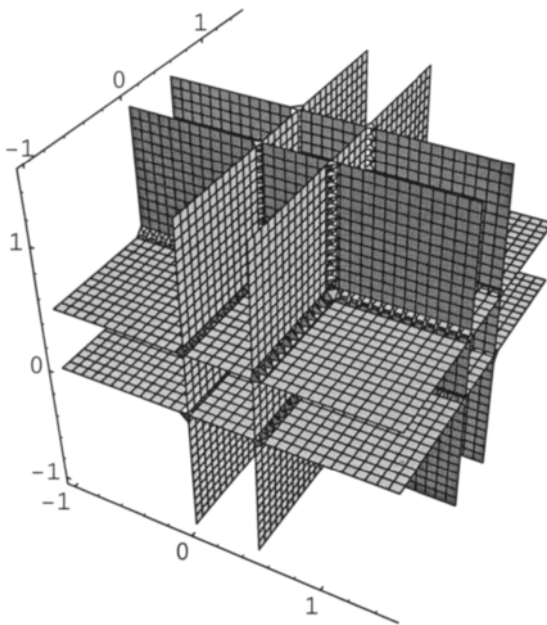


Figure 2.3.12 Counting gives more periodicity.

We do the experiment by continuing with periodicity, adding an identical unit by translation after equation 2.3.10.

$$xyz + (x - 0.5)(y - 0.5)(z - 0.5) = 0 \quad 2.3.10$$

The result is a monkey saddle as in figure 2.2.13 - the arch symbol for symmetry and periodicity!

We make the surface grow according to equation 2.3.11 and get figure 2.3.14. The continuation after 2.3.12 gives a piece of the D surface as shown in figure 2.3.15. Figure 2.3.16 shows the same thing, but with larger boundaries.

$$xyz(x - 1)(y - 1)(z - 1) + (x - 0.5)(y - 0.5)(z - 0.5) = 0 \quad 2.3.11$$

$$xyz(x - 1)(y - 1)(z - 1) + (x - 0.5)(y - 0.5) \cdot (z - 0.5)(x - 1.5)(y - 1.5)(z - 1.5) = 0 \quad 2.3.12$$

Alternatively we could continue with the complete permutation of variables in space as above, when the P-surface was obtained to give the other cubic symmetries. We have done that elsewhere [2] and here we just say that this is the way to obtain the other fundamental surfaces called G and IWP, by using simple counting.

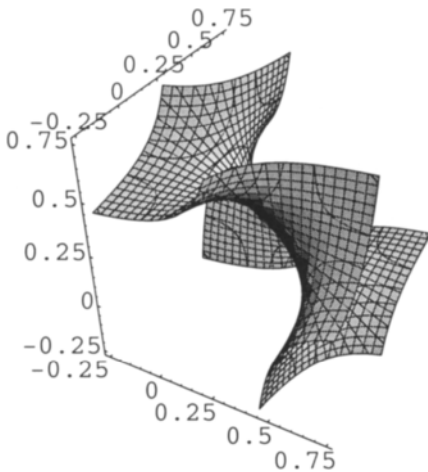


Figure 2.3.13 Translation and counting gives a monkey saddle.

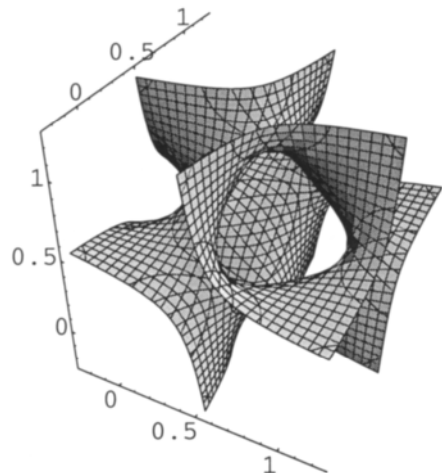


Figure 2.3.14 More counting and a surface starts to form.

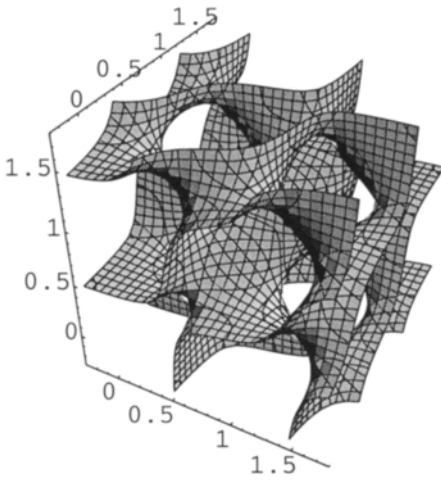


Figure 2.3.15 A piece of the D surface.

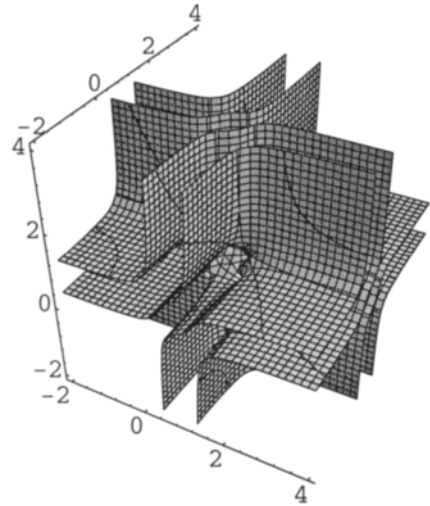


Figure 2.3.16 The same structure as in figure 2.3.15, but with larger boundaries.

The translation above corresponds to a phase shift from sine to cosine in the circular functions. We do the simplest, and most important, of the surfaces here. Instead of the infinite products in the algebra we use circular functions and go cosine with equation 2.3.10 in equation 2.3.13 below, which is identical to equation 2.3.14.

$$\cos \pi x \cos \pi y \cos \pi z + \cos \pi(x - 0.5) \cos \pi(y - 0.5) \cos \pi(z - 0.5) = 0 \quad 2.3.13$$

$$\cos \pi x \cos \pi y \cos \pi z + \sin \pi x \sin \pi y \sin \pi z = 0 \quad 2.3.14$$

This gives the famous D surface, which is just the periodic repetition of the monkey saddle from equation 2.3.10, shown figure 2.3.17.

We do the same with the saddle from equation 2.3.6, and the equations 2.3.15 and 2.3.16 give the surfaces of IWP and G in figures 2.3.18 and 19.

$$\cos \pi x \cos \pi y + \cos \pi x \cos \pi z + \cos \pi y \cos \pi z = 0 \quad 2.3.15$$

$$\sin \pi x \cos \pi y + \cos \pi x \sin \pi z + \sin \pi y \cos \pi z = 0 \quad 2.3.16$$

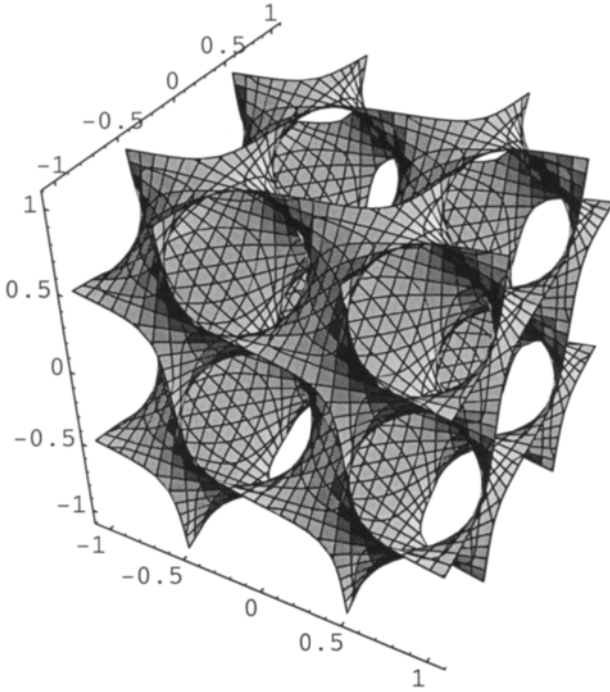


Figure 2.3.17 D surface from circular functions.

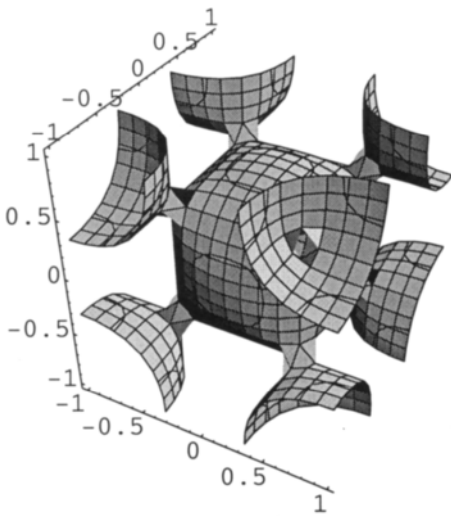


Figure 2.3.18 The IWP surface.

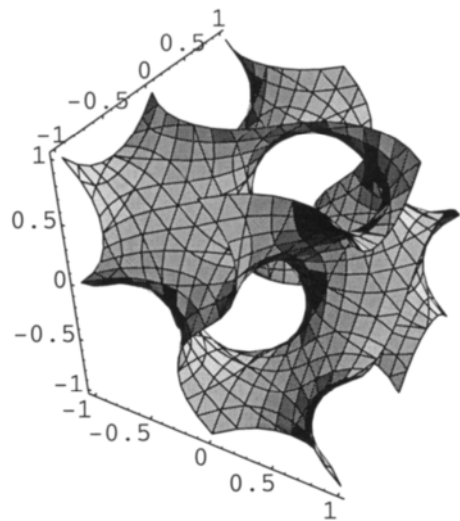


Figure 2.3.19 The gyroid surface.

The complete multiplication and addition is done in equation 2.3.17.

$$xyz + x + y + z = 0 \tag{2.3.17}$$

The result is a monkey saddle in figure 2.3.20, which build the periodic Neovius surface [4]. We show how it consists of planes using much larger boundaries in 2.3.21. We see that this is really four cube corners that meet in a non-intersecting figure. Going to infinite products we obtain equation 2.3.18 which gives the classic Neovius surface in figure 2.3.22.

$$2 \cos \pi x \cos \pi y \cos \pi z + \cos \pi x + \cos \pi y + \cos \pi z = 0 \tag{2.3.18}$$

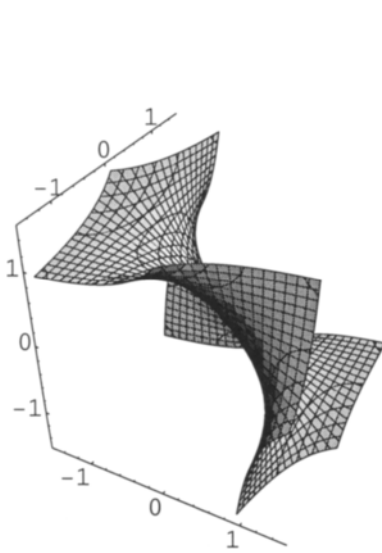


Figure 2.3.20 Simple multiplication and addition of variables gives a saddle.

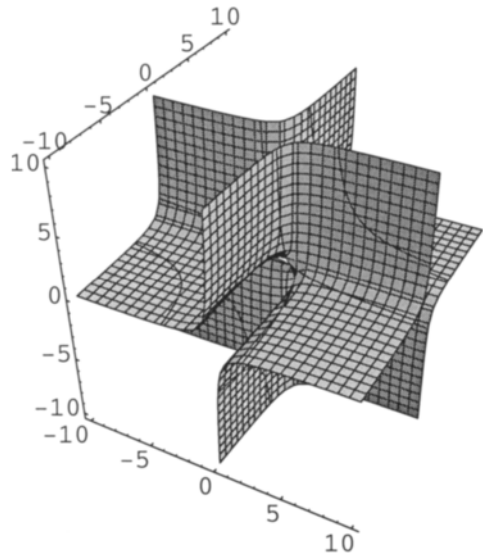


Figure 2.3.21 Same surface as in figure 2.3.20 but with larger boundaries.

Equation 2.3.18 adds the planes of the D surface with those of the surface of P. These trigonometric equations are the same as those originally derived by von Schnering and Nesper [4].

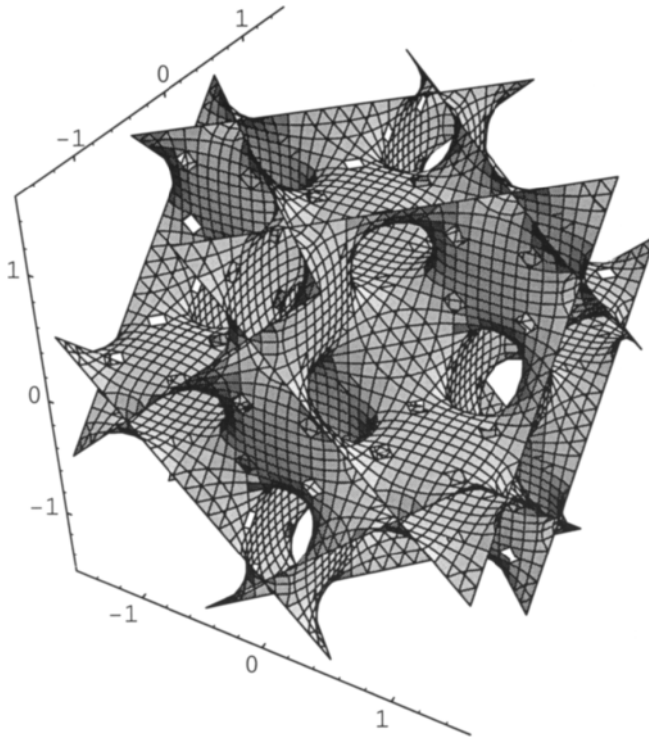


Figure 2.3.22 Going circular with the monkey saddle gives the Neovius surface.

References 2

- 1 *Pythagoras* from Georg D. Birkhoff, *Century Mag.* June 1929, 118, pp 156-160.
- 2 M. Jacob and S. Andersson, *THE NATURE OF MATHEMATICS AND THE MATHEMATICS OF NATURE*, Elsevier, 1998.
- 3 A. Burkhardt, U. Wedig, H.G. von Schnering and A. Savin, *Z. anorg. allg. Chem.* **619** (1993) 437.
- 4 H.G. von Schnering and R. Nesper, *Z. Phys. B - Condensed Matter* **83**, 407 (1991).

3 Nodal Surfaces of Tetragonal and Hexagonal Symmetry, and Rods

There are many ways to skin a cat.

We have shown that the circular functions, or periodicity, is obtained by counting positive numbers from the algebra.

We use the saddle mathematics from chapter 2 and describe hexagonal and tetragonal surfaces, and how they are formed from their rod packings.

We can do it all by counting, but as a short-cut we use the trigonometry for the circular functions.

For a description of symmetries we refer to appendix 6.

3.1 Non Cubic Surfaces

In biology it is important to realise that cubic symmetry is by no means common.

The DNA structure is one case, the apatite structure that is the inorganic part of bones and teeth is another. The filaments do also represent very important examples. Motion is to its nature anisotropic. The structure of the sacromere is hexagonal.

A saddle is by itself non-cubic and a good starting point. We will describe a way to derive tetragonal and hexagonal surfaces.

3.2 Tetragonal Nodal Surfaces and their Rod Structures

We have shown before that there is no obvious link or path between 3D non-intersecting rod systems and the fundamental surfaces [2]. However there is a link between *one* parallel rod system and the surfaces, and we shall in the next chapter show simple transformations. Here we show how such rod systems may be used in the derivation of surfaces of lower symmetry.

An obvious path to derive surfaces of lower symmetry than cubic is via the saddles.

We start with the saddle equation 2.2.7 from chapter 2,

$$xy - z = 0$$

and go periodic in equation 3.2.1.

$$\cos \pi x \cos \pi y = C \tag{3.2.1}$$

This gives intersecting planes in figure 3.2.1 for zero constant. For a constant of 0.2 we get the parallel rods shown in figure 3.2.2.

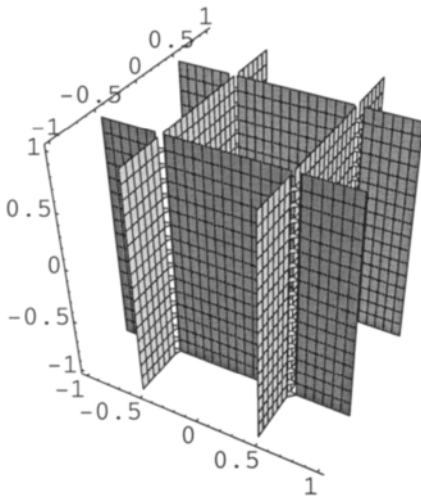


Figure 3.2.1 Intersecting planes.

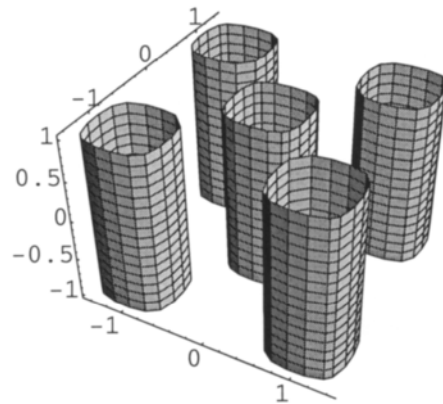


Figure 3.2.2 Tetragonal rod packing.

With a z-term and constant as in equation 3.2.2, the rods are joined by catenoids to form a beautiful tetragonal structure in figure 3.2.3.

$$\cos \pi x \cos \pi y - \frac{1}{10} \cos 2\pi z = 0.05 \tag{3.2.2}$$

In equation 3.2.3 the surface is calculated with different constants, and shown in figure 3.2.4. This surface is topologically right between the P-surface and the hexagonal H-surface (shown below). A projection is shown in figure 3.2.5, and the surface calculated after equation 3.2.4 is shown in figure 3.2.6.

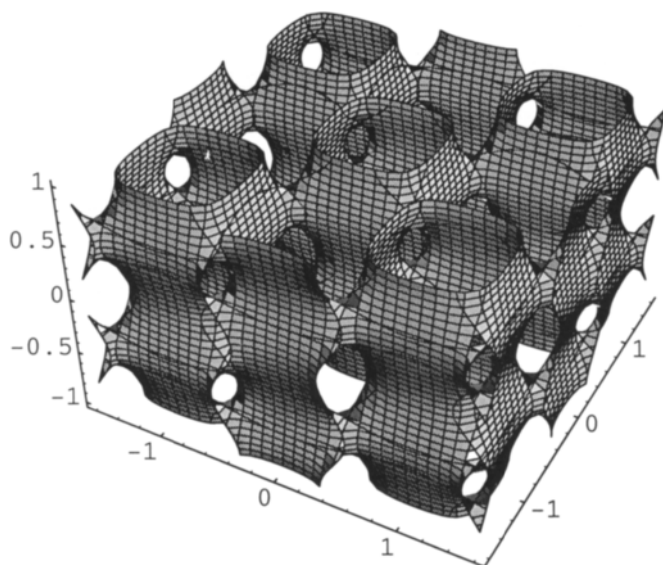


Figure 3.2.3 Simple tetragonal surface.

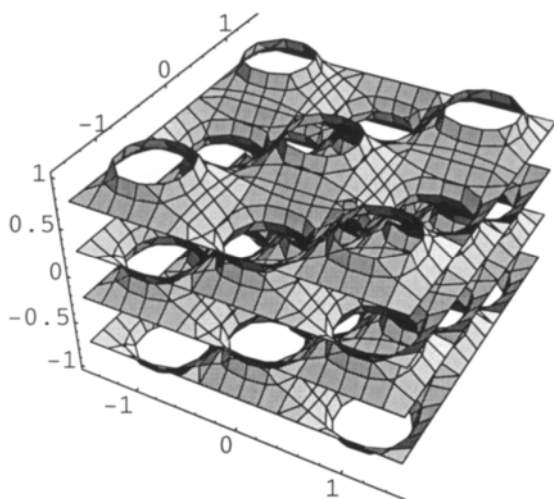


Figure 3.2.4 The simple tetragonal surface chosen to show relationships with the P- surface.

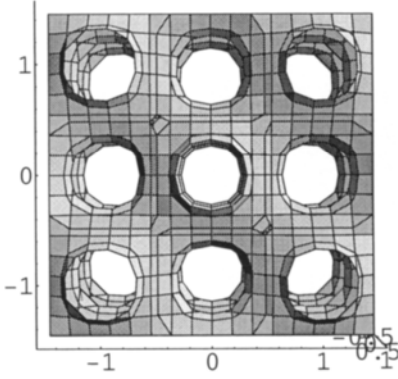


Figure 3.2.5 Different projection of the tetragonal surface.

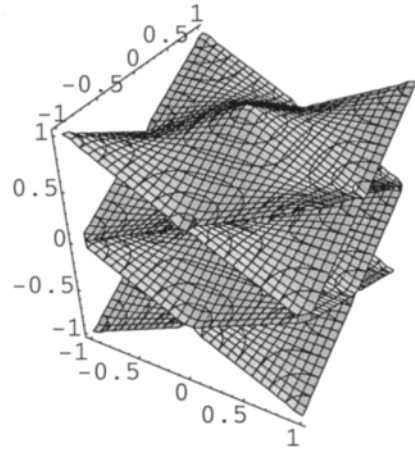


Figure 3.2.6 The simple tetragonal surface for zero constant.

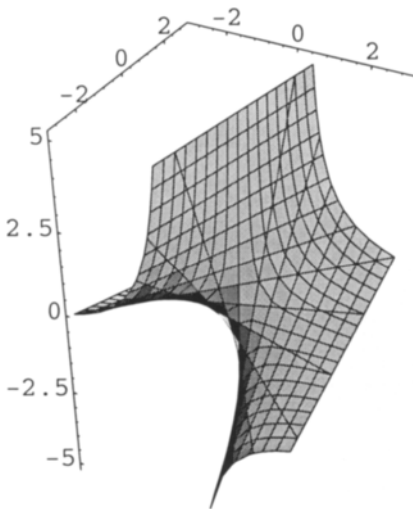


Figure 3.2.7 CLP saddle.

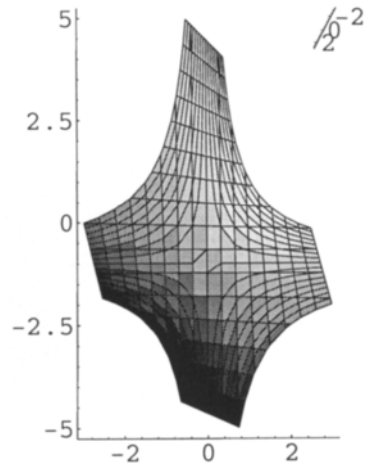


Figure 3.2.8 Different projection of the CLP saddle.

$$\cos \pi x \cos \pi y - \frac{1}{2} \cos 2\pi z = 0 \quad 3.2.3$$

$$\cos \pi x \cos \pi y - \cos 2\pi z = 0 \quad 3.2.4$$

A saddle that gives a surface of the same topology as the important tetragonal CLP minimal surface is found in equation 3.2.5. The Weierstrass parametrisation of this minimal surface was first derived by Lidin and Hyde [4].

$$x - y + xz = 0 \quad 3.2.5$$

The saddle is shown in figure 3.2.7, a projection along one of the tetragonal axes is added in figure 3.2.8.

Going circular everywhere we have the equation 3.2.6, and the corresponding surface is shown in figure 3.2.9.

$$\cos \pi x - \cos \pi y + \cos \pi x \cos \pi z = 0 \quad 3.2.6$$

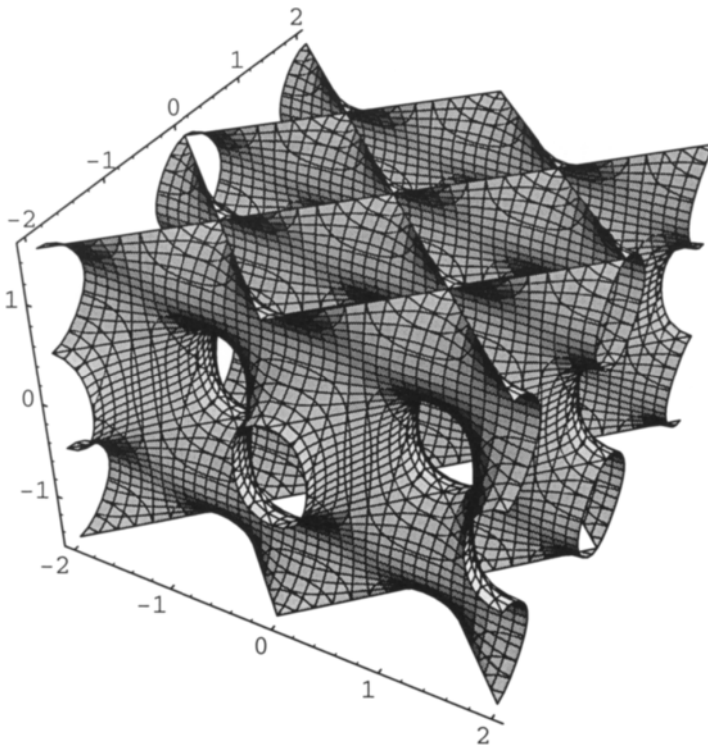


Figure 3.2.9 Surface with the topology of the tetragonal CLP minimal surface.

Equation 3.2.7 brings out the planar character of this surface as seen in figure 3.2.10.

$$\cos \pi x - \cos \pi y + \frac{1}{10} \cos \pi x \cos \pi z = 0 \quad 3.2.7$$

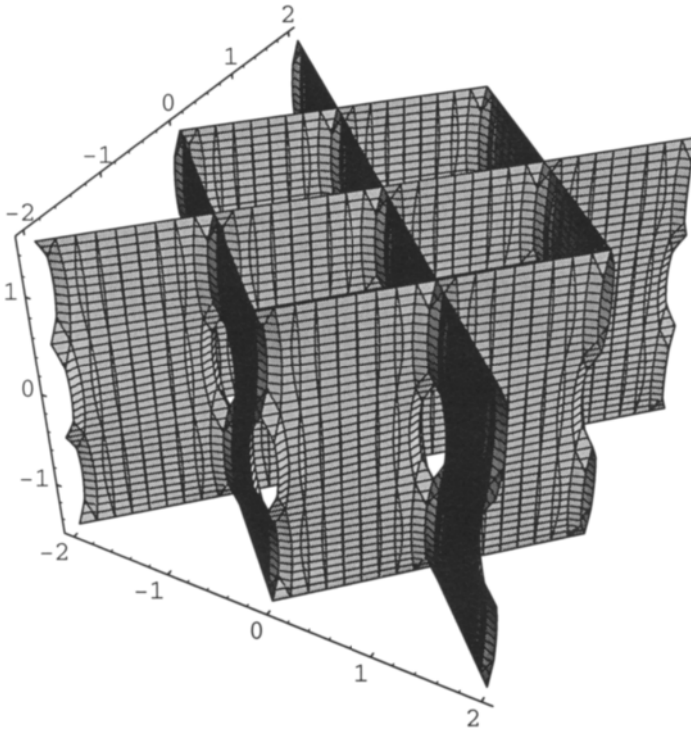


Figure 3.2.10 Planar character of the CLP type surface.

The rods come out with a constant of 0.5 in 3.2.8, which is shown in figure 3.2.11.

$$\cos \pi x - \cos \pi y + \frac{1}{10} \cos \pi x \cos \pi z + \frac{1}{2} = 0 \quad 3.2.8$$

These two seem to be the most fundamental tetragonal surfaces, and we shall return to a more general derivation of the CLP nodal surface later on. The CLP-surface is the physiological basis for the lung function, as treated

in chapter 14. But we shall do just one more tetragonal and use the saddle concept again.

Instead of two, there are four intersecting planes in equation 3.2.9 and figure 3.2.12.

$$xy(x-y)(x+y) = 0 \tag{3.2.9}$$

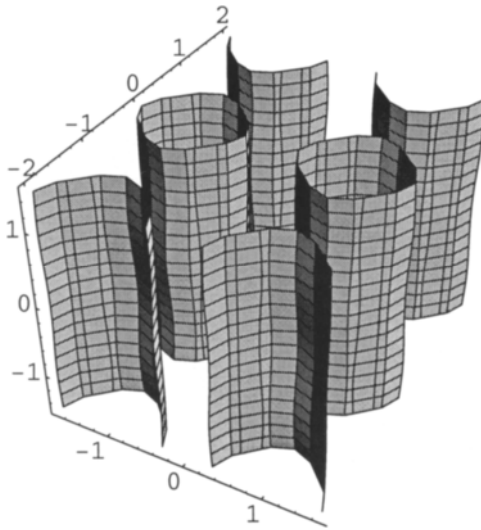


Figure 3.2.11 The rods of CLP.

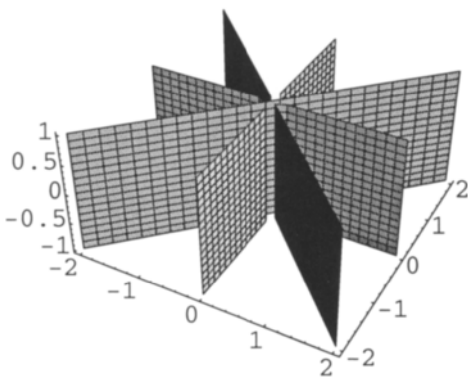


Figure 3.2.12 Four intersecting planes.

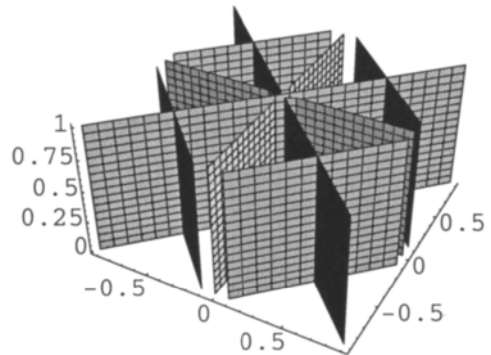


Figure 3.2.13 Periodicity also gives two intersecting planes.

The periodicity is given in equation 3.2.10 and shown in figure 3.2.13.

$$\sin \pi x \sin \pi y \sin \pi(x-y) \sin \pi(x+y) = 0 \quad 3.2.10$$

The four fold saddle is found in equation 3.2.11 and figure 3.2.14.

$$xy(x-y)(x+y) = z \quad 3.2.11$$

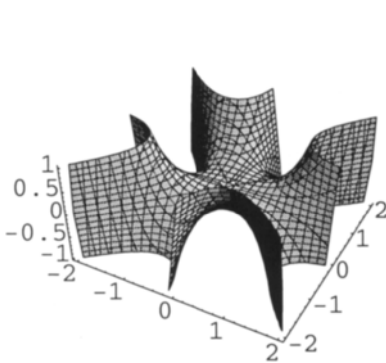


Figure 3.2.14 The saddle from four intersecting planes.

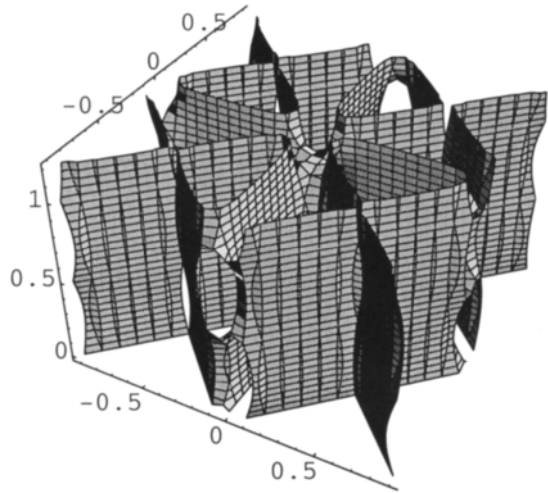


Figure 3.2.15 Periodicity shows the rod structure.

The rods are liberated with a constant, as before, and we continue to make them connect by catenoids with a z term as in equation. 3.2.12. This is shown in figure 3.2.15.

$$6 \sin \pi x \sin \pi y \sin \pi(x-y) \sin \pi(x+y) + \frac{1}{10} \sin 2\pi z = 0 \quad 3.2.12$$

Careful inspection of this surface reveals that it is really composed of units of the first tetragonal surface, twinned in a cyclic way. The twin operation creates the four-saddle.

The surface after equation 3.2.13 is shown in figure 3.2.16, and in projection along the tetragonal axes in 3.2.17.

$$6 \sin \pi x \sin \pi y \sin \pi(x-y) \sin \pi(x+y) + \sin 2\pi z = 0 \quad 3.2.13$$

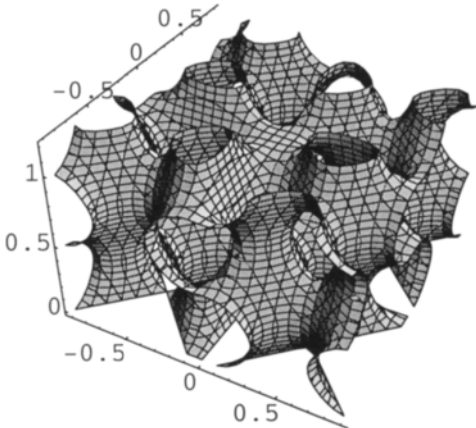


Figure 3.2.16 Periodic surface from four planes.

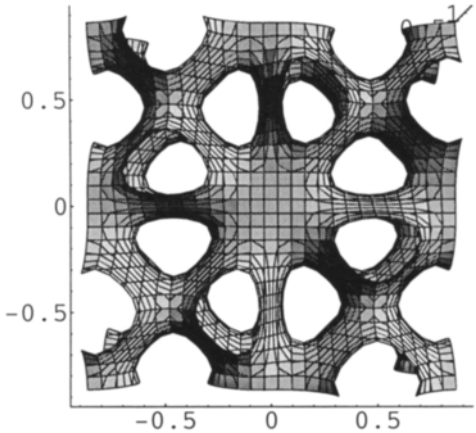


Figure 3.2.17 Different projection reveals the twin character of the structure.

3.3 Hexagonal Nodal Surfaces and their Rod Structures

The hexagonal symmetry is common in life as the building principle for apatite, in rod systems, and in the arrangements of giant molecules. It is also essential for the description of muscle contraction which we will show below. The best packing for rods is the hexagonal and we derive this again from parallel planes. For the simplest forms of cubic or tetragonal structures we had three intersecting planes after the Cartesian coordinate system. A corresponding hexagonal coordinate system would need four planes. In crystallography such a system is used for this type of symmetry.

Since we here have the Cartesian, we bring in the $\sqrt{3}$ and start again from the saddle mathematics in equations 3.3.1-2 which give the intersecting planes in figure 3.3.1, and the monkey saddle in 3.3.2. Figures 3.3.3 and 4 show the same monkey saddle but with larger boundaries.

$$x[x+y\sqrt{3}][x-y\sqrt{3}] = 0 \quad 3.3.1$$

$$x[x+y\sqrt{3}][x-y\sqrt{3}] - z = 0 \quad 3.3.2$$

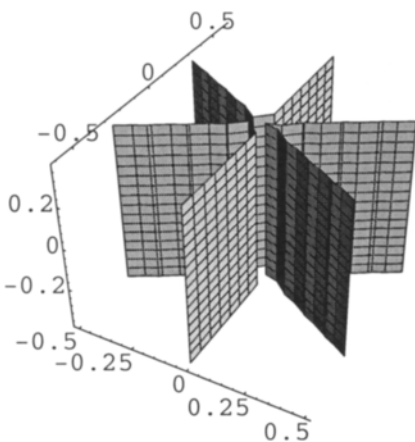


Figure 3.3.1 Three intersecting planes.

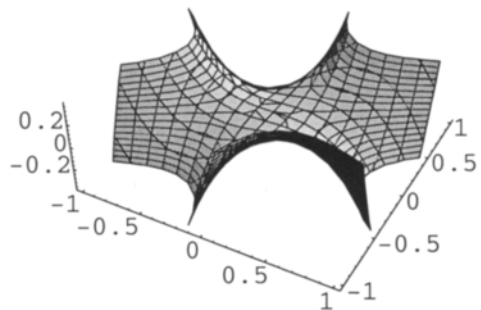


Figure 3.3.2 Monkey saddle.

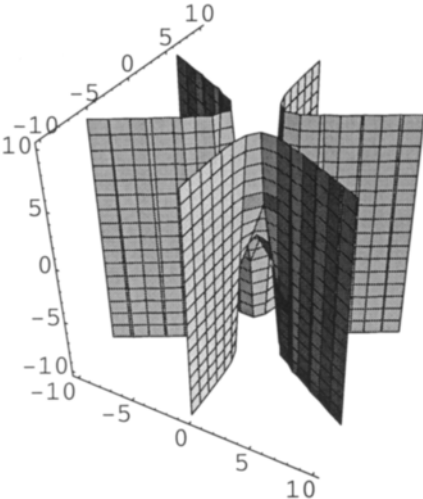


Figure 3.3.3 The monkey saddle with larger boundaries.

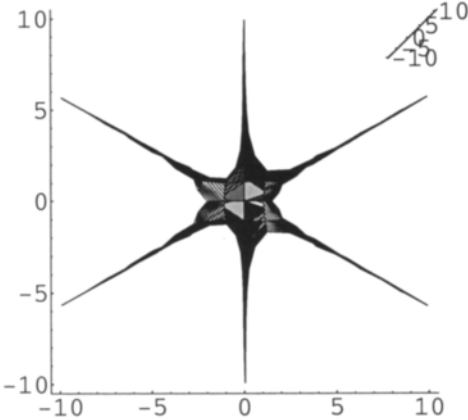


Figure 3.3.4 Different projection of the monkey saddle.

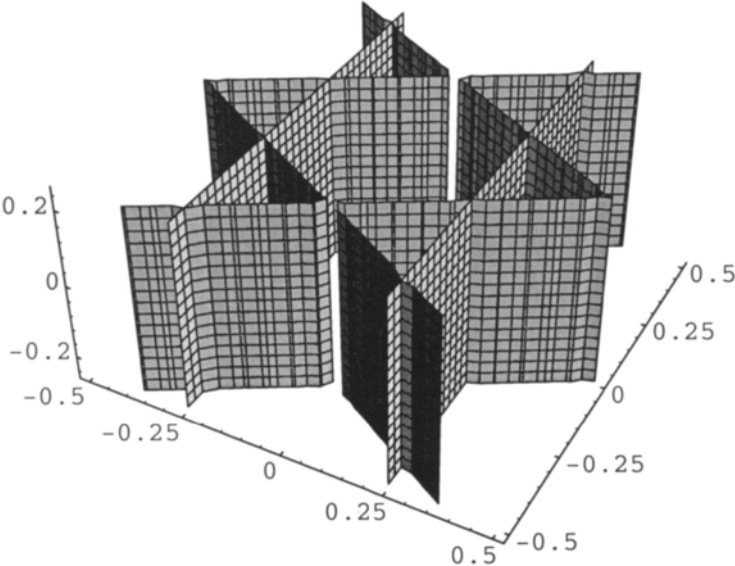


Figure 3.3.5 Periodic hexagonal planes with cosine.

We introduce periodicity by using cosine in equation 3.3.3 and get the intersecting planes in figure 3.3.5.

$$\cos 2\pi x \cos 2\pi \left(\frac{x}{2} + \frac{\sqrt{3}}{2} y \right) \cos 2\pi \left(-\frac{x}{2} + \frac{\sqrt{3}}{2} y \right) = 0 \quad 3.3.3$$

Subtracting or adding a constant give the two kinds of hexagonal cylinder packings after equations 3.3.4 and 3.3.5 and shown in figures 3.3.6 and 3.3.7, where the latter is the honeycomb packing.

$$\cos 2\pi x \cos 2\pi \left(\frac{x}{2} + \frac{\sqrt{3}}{2} y \right) \cos 2\pi \left(-\frac{x}{2} + \frac{\sqrt{3}}{2} y \right) - 0.1 = 0 \quad 3.3.4$$

$$\cos 2\pi x \cos 2\pi \left(\frac{x}{2} + \frac{\sqrt{3}}{2} y \right) \cos 2\pi \left(-\frac{x}{2} + \frac{\sqrt{3}}{2} y \right) + 0.03 = 0 \quad 3.3.5$$

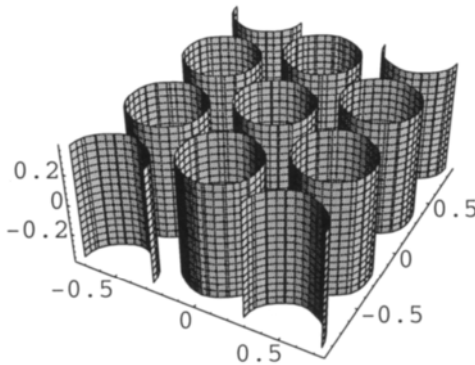


Figure 3.3.6 Cosine and subtracting a constant gives hexagonal packing of cylinders.

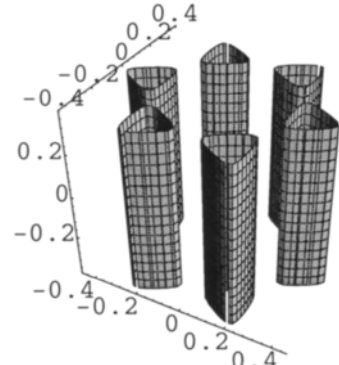


Figure 3.3.7 Cosine and adding a constant gives honeycomb packing of cylinders.

The addition of a z-term as in equation 3.3.6 makes catenoids contact between the rods as in figure 3.3.8. Finally equation 3.3.7 gives the beautiful honey comb surface in figure 3.3.9.

$$\cos 2\pi x \cos 2\pi \left(\frac{x}{2} + \frac{\sqrt{3}}{2} y \right) \cos 2\pi \left(-\frac{x}{2} + \frac{\sqrt{3}}{2} y \right) + 0.02 \cos 4\pi z = 0 \quad 3.3.6$$

$$\cos 2\pi x \cos 2\pi \left(\frac{x}{2} + \frac{\sqrt{3}}{2} y \right) \cos 2\pi \left(-\frac{x}{2} + \frac{\sqrt{3}}{2} y \right) + 0.1 \cos 4\pi z = 0 \quad 3.3.7$$

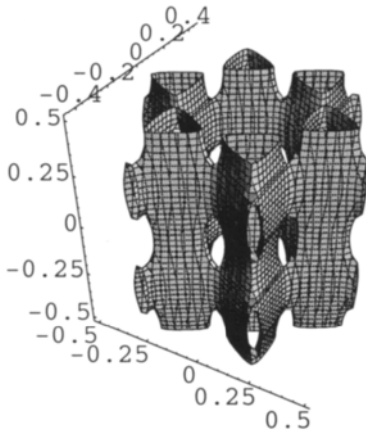


Figure 3.3.8 Addition of a z-term gives catenoids between rods.

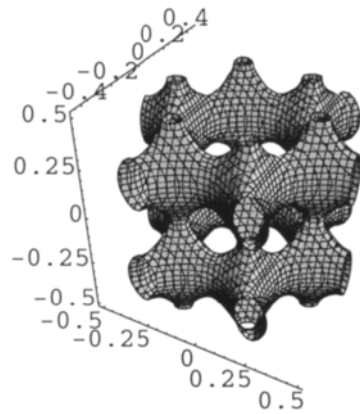


Figure 3.3.9 The honeycomb surface.

With the same saddle, and sine, the intersecting planes are shown after equation 3.3.8 in figure 3.3.10.

$$\sin 2\pi x \sin 2\pi \left(\frac{x}{2} + \frac{\sqrt{3}}{2} y \right) \sin 2\pi \left(-\frac{x}{2} + \frac{\sqrt{3}}{2} y \right) = 0 \quad 3.3.8$$

Adding a constant after equation 3.3.9 liberates the rods as in figure 3.3.11.

$$\sin 2\pi x \sin 2\pi \left(\frac{x}{2} + \frac{\sqrt{3}}{2} y \right) \sin 2\pi \left(-\frac{x}{2} + \frac{\sqrt{3}}{2} y \right) - 0.1 = 0 \quad 3.3.9$$

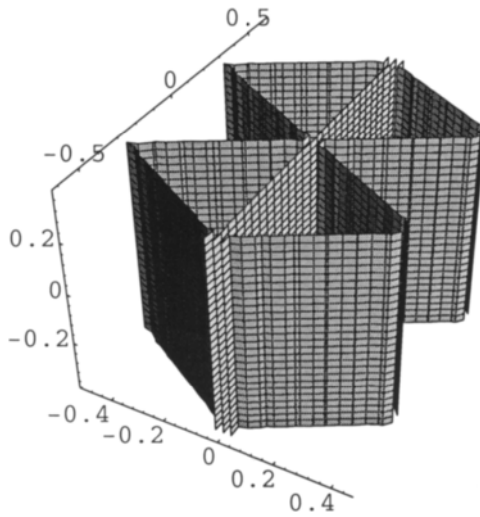


Figure 3.3.10 Hexagonal sine gives intersecting planes.

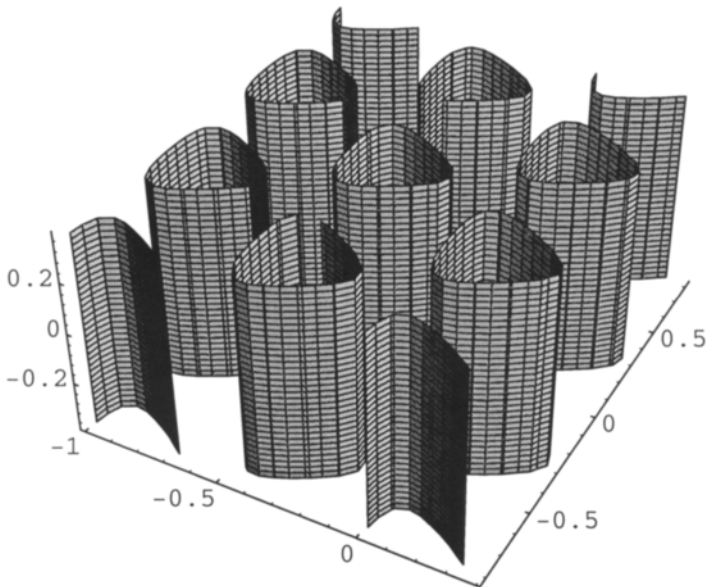


Figure 3.3.11 Sine and the rods.

With equation 3.3.10 we get catenoids between the rods as seen in figure 3.3.12a.

$$\sin 2\pi x \sin 2\pi \left(\frac{x}{2} + \frac{\sqrt{3}}{2} y \right) \sin 2\pi \left(-\frac{x}{2} + \frac{\sqrt{3}}{2} y \right) + 0.025 \sin 4\pi z = 0 \quad 3.3.10$$

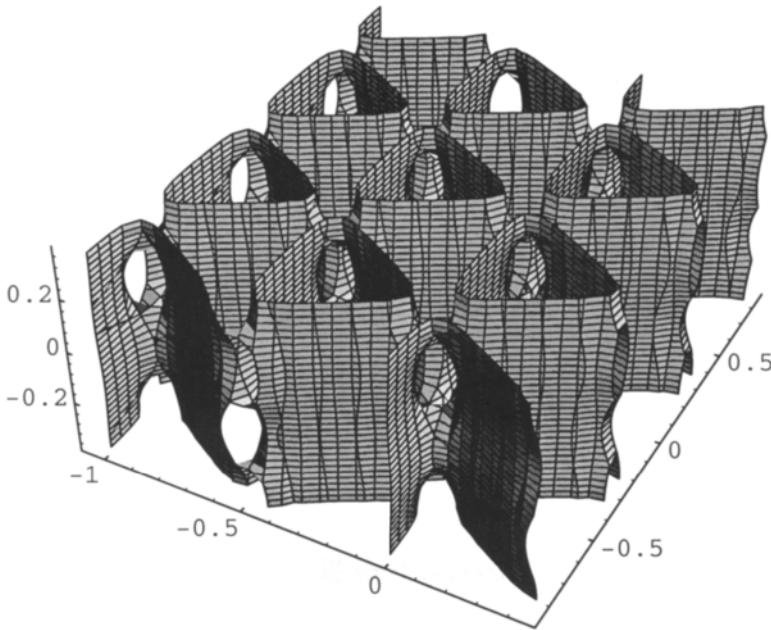


Figure 3.3.12a With a z-term there are catenoids between rods.

This surface, and the next one shown below, are of interest in consideration of hexagonal structures of membrane lipids and cell membranes. The common liquid-crystalline phase is termed reverse hexagonal (HII). It is two-dimensional and the lipid bilayer centre has a honeycomb structure. However, the possibility of the occurrence of hexagonal structures free from self-intersections, so that one bilayer can form the whole phase, should be kept in mind. A projection of this structure as in figure 3.3.12b will show (hk0) reflections as if it were two-dimensional, but it is uncertain whether (hkl)-reflections will be observed experimentally. The projection of this structure along the c-axis will contain two water cylinders in the unit cell.

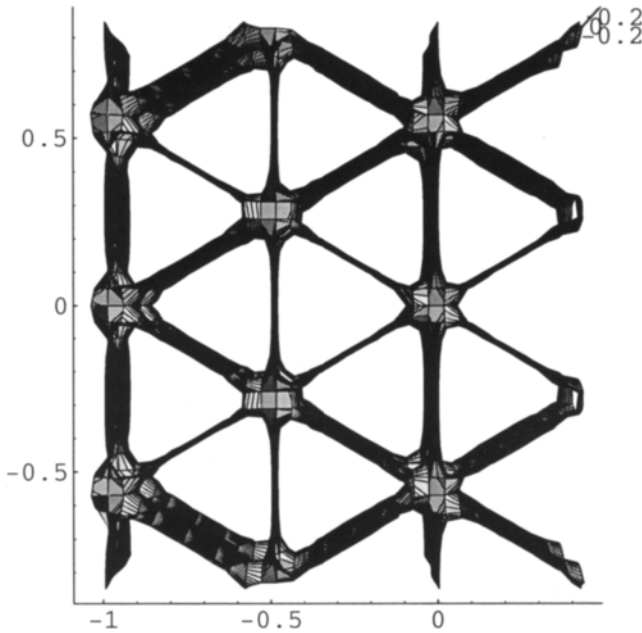


Figure 3.3.12b Projection along the hexagonal axis.

With equation 3.3.11 we get the famous H-surface, as shown in figure 3.3.13. The Weierstrass representation of this surface was found by Lidin [5]. The H-surface is projected along the c -axis in figure 3.3.14.

$$4 \sin 2\pi x \sin 2\pi \left(\frac{x}{2} + \frac{\sqrt{3}}{2} y \right) \sin 2\pi \left(-\frac{x}{2} + \frac{\sqrt{3}}{2} y \right) + \sin 4\pi z = 0 \quad 3.3.11$$

The H structure, as well as the hexagonal honey comb structure, can be turned into an elongated structure with the property of a rod structure by changing the periodicity along z . This is in crystallography called change of c/a , and shown in figure 3.3.15 after equation 3.3.12. The H-surface character is maintained as obvious from the projection along c in figure 3.3.16.

$$6 \sin 2\pi x \sin 2\pi \left(\frac{x}{2} + \frac{\sqrt{3}}{2} y \right) \sin 2\pi \left(-\frac{x}{2} + \frac{\sqrt{3}}{2} y \right) + \sin \pi z = 0 \quad 3.3.12$$

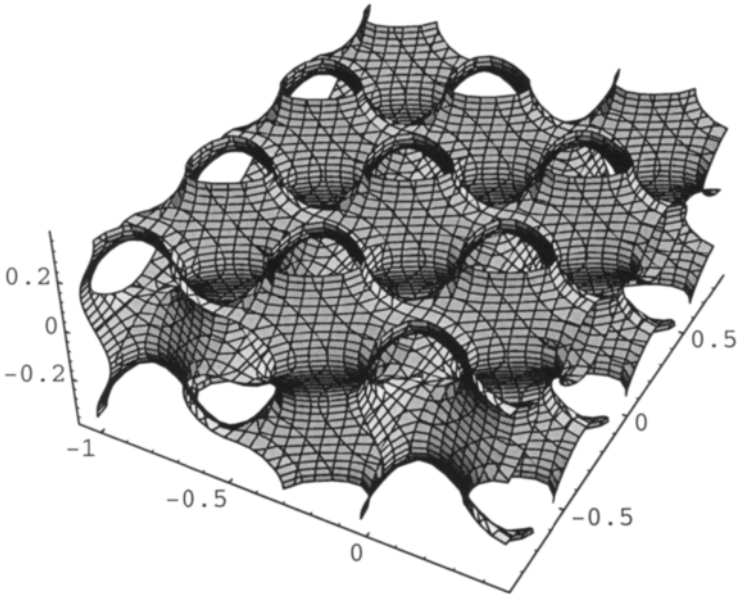


Figure 3.3.13 The H surface.

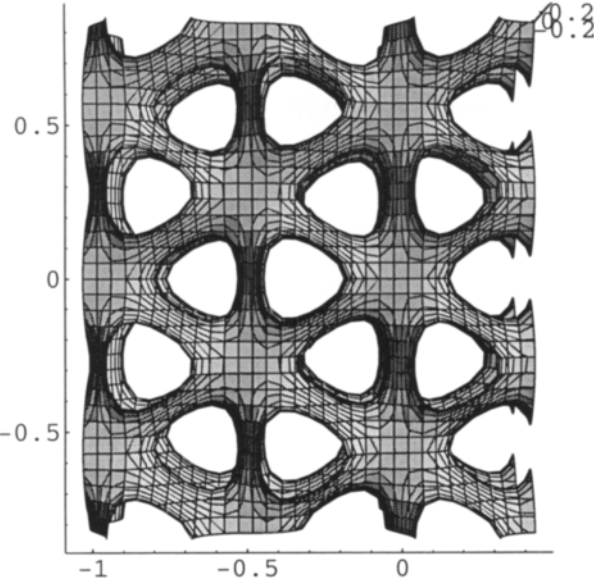


Figure 3.3.14 Projection of the H surface along c.

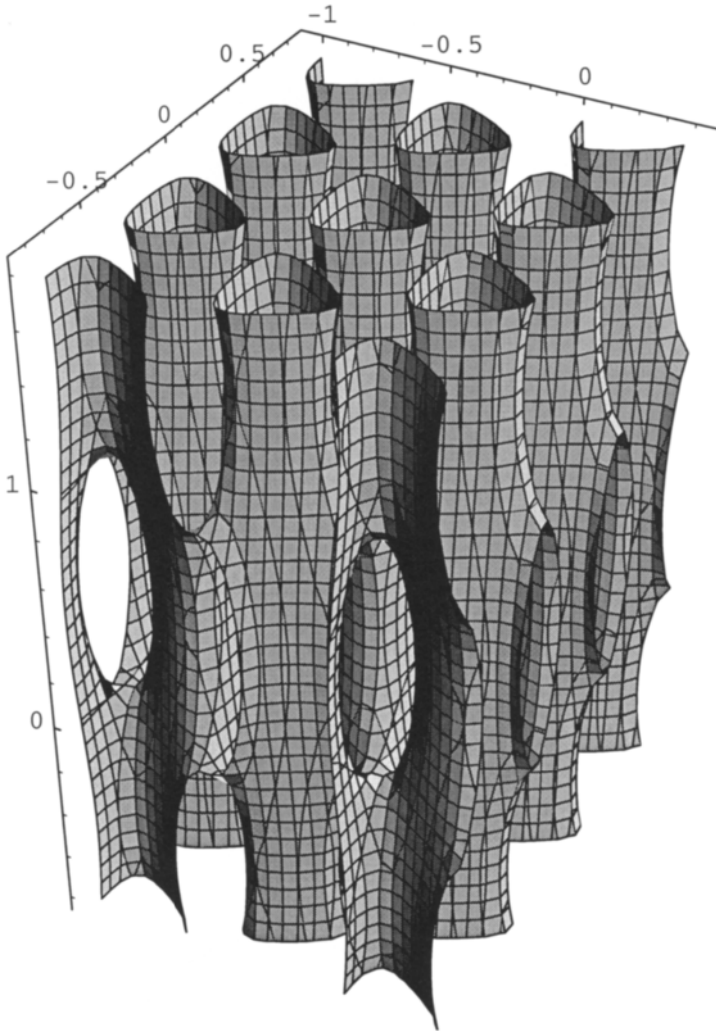


Figure 3.3.15 The H surface at different of c/a .

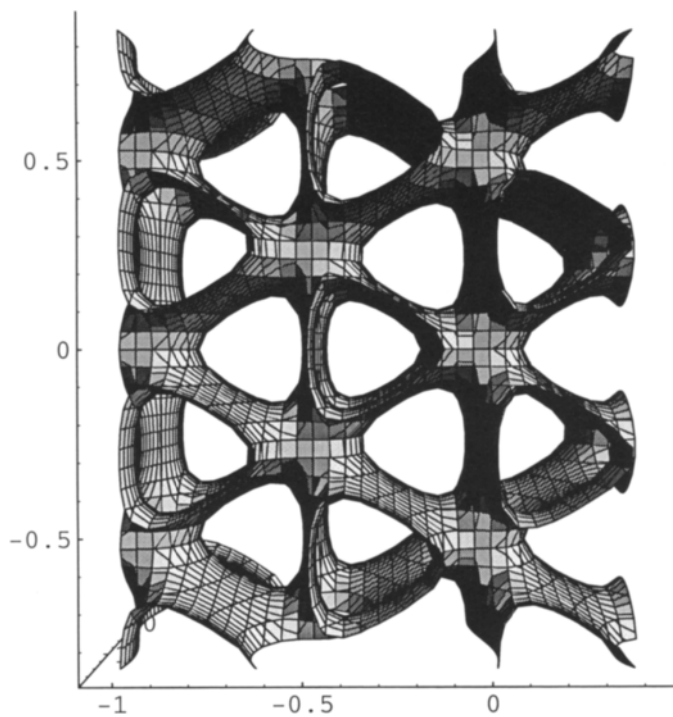


Figure 3.3.16 Projection along c of figure 3.3.15.

References 3

- 1 H.G. von Schnering and R. Nesper, *Z. Phys. B - Condensed Matter* **83**, 407 (1991).
- 2 M. Jacob and S. Andersson, *THE NATURE OF MATHEMATICS AND THE MATHEMATICS OF NATURE*, Elsevier, 1998.
- 3 A. Burkhardt, U. Wedig, H.G. von Schnering and A. Savin, *Z. anorg. allg. Chem.* **619** (1993) 437.
- 4 S. Lidin, and S. T. Hyde, *J. Phys. France* **48**, 15 (1987).
- 5 S. Lidin, *J. Phys. France* **49**, 421 (1988).

This Page Intentionally Left Blank

4 Nodal Surfaces, Planes, Rods and Transformations

In the actual three-dimensional case we have nodal surfaces, nodal planes and spheres, instead of nodal lines [Born,1].

We show how the cubic nodal surfaces are derived from the permutation of variables in space.

We study how parallel planes transform into surfaces.

We study how parallel cylinders transform into surfaces. We notice that the tetragonal CLP shows up as an important intermediate in transformations.

We also describe the transformation between the D, G and P surfaces as an alternative to the isometric Bonnet transformation.

All transformations have catenoid opening or closing as a mechanism.

4.1 Cubic Nodal Surfaces

In chapter 2 we used counting and finite products to derive the circular functions, and in the simplest case in 3D the P surface. The same can be done for the permutations $\cos(x+y)$ and $\cos(x+y+z)$ in space, and below we give the complete equations for the nodal surfaces created.

The P surface

$$\cos \pi x + \cos \pi y + \cos \pi z = 0 \quad 4.1.1$$

The gyroid surface

$$\begin{aligned} \sin \pi(x+y) + \sin \pi(x-y) + \sin \pi(x+z) \\ + \sin \pi(z-x) + \sin \pi(y+z) + \sin \pi(y-z) = 0 \end{aligned} \quad 4.1.2$$

The IWP surfaces

$$\begin{aligned} \cos \pi(x+y) + \cos \pi(x-y) + \cos \pi(x+z) \\ + \cos \pi(z-x) + \cos \pi(y+z) + \cos \pi(y-z) = 0 \end{aligned} \quad 4.1.3$$

$$\begin{aligned} &\cos \pi(x+y) + \cos \pi(x-y) + \cos \pi(x+z) \\ &+ \cos \pi(z-x) + \cos \pi(y+z) + \cos \pi(y-z) + 1 = 0 \end{aligned} \quad 4.1.4$$

The D surface

$$\begin{aligned} &\cos \pi(x+y+z) + \cos \pi(x-y-z) + \cos \pi(-x-y+z) \\ &+ \cos \pi(-x+y-z) + \sin \pi(x+y+z) + \sin \pi(x-y-z) \\ &+ \sin \pi(-x-y+z) + \sin \pi(-x+y-z) = 0 \end{aligned} \quad 4.1.5$$

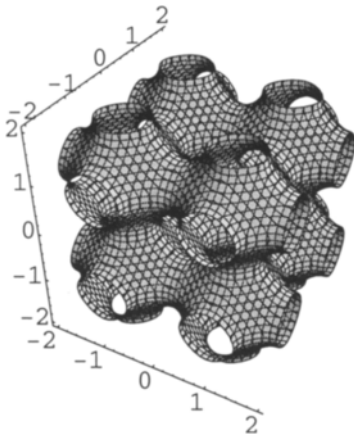


Figure 4.1.1 The P surface.

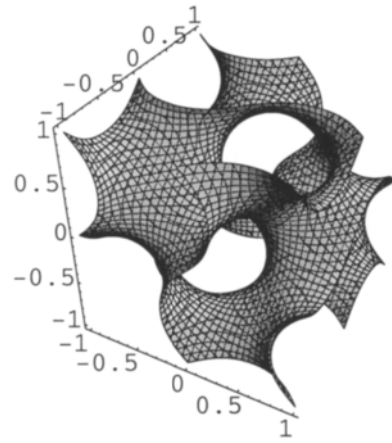


Figure 4.1.2 The gyroid surface.

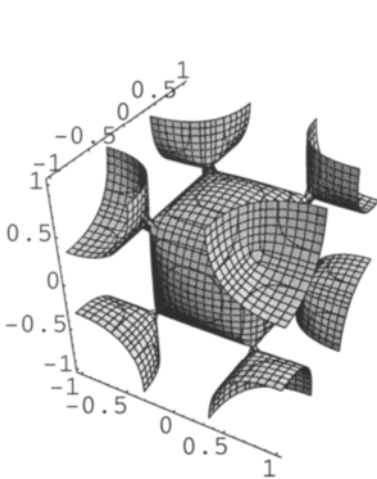


Figure 4.1.3 The IWP surface.

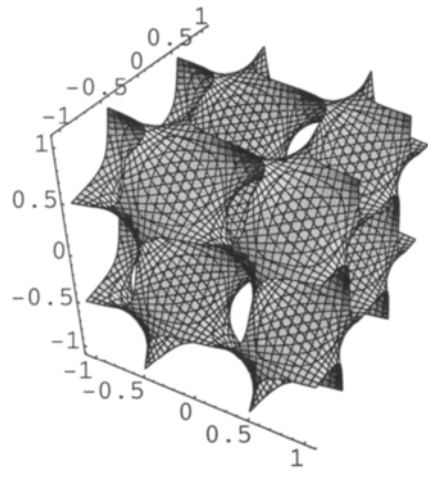


Figure 4.1.4 The D surface.

These equations are mathematically the same as the equations given in chapter 2, which are identical with those originally, but differently, derived by von Schnering and Nesper [2]. The names of the surfaces come from the corresponding minimal surfaces as given in appendix 2.

In figures 4.1.1-10 we show representative parts of each surface.

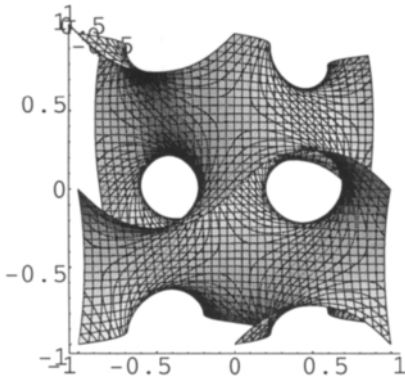


Figure 4.1.5 Projection of the gyroid along the a-axis.

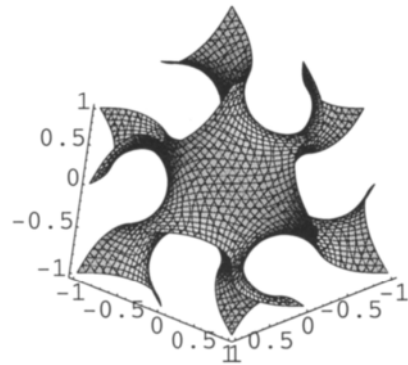


Figure 4.1.6 Projection of the gyroid along a space diagonal.

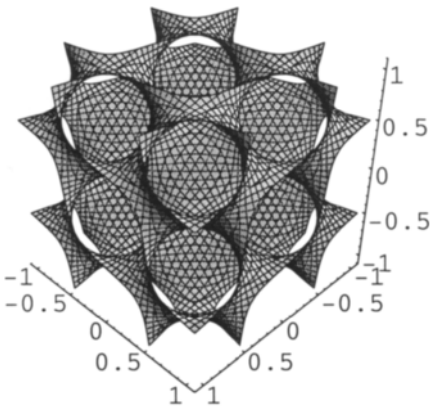


Figure 4.1.7 Projection of D along a cubic space diagonal.

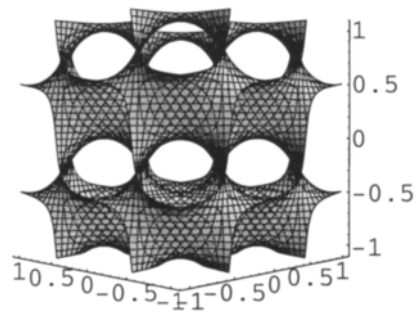


Figure 4.1.8 Projection of D along a cubic face diagonal.

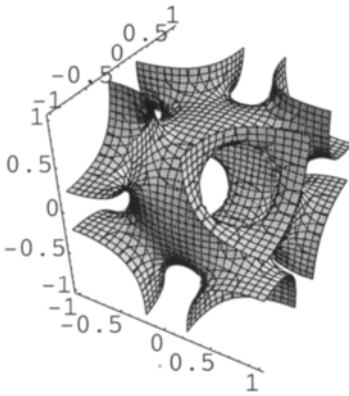


Figure 4.1.9 IWP from equation 4.1.4.

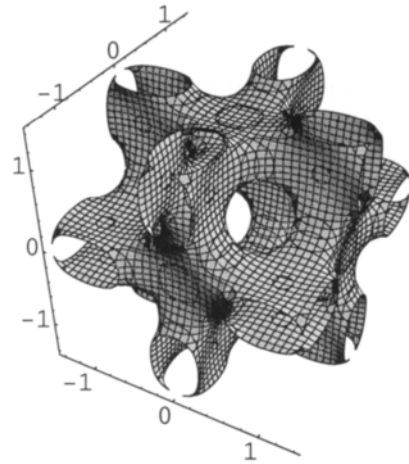


Figure 4.1.10 IWP as in 4.1.9 but with larger boundaries.

4.2 Nodal Surfaces and Planes

The way we describe the nodal surfaces is particularly useful to study some of their properties.

We assume that in an expression for a surface

$$\cos A + \cos B + \cos C + \cos E + \cos D \dots = 0, \quad 4.2.1$$

one term, $\cos A$, is an infinite number of parallel planes.

We want to study how such planes are transformed into the surface and formulate the equation 4.2.2.

$$\cos A + N(\cos B + \cos C + \cos E + \cos D \dots) = 0 \quad 4.2.2$$

Similarly the terms $\cos A + \cos B$, or $\cos A + \cos B + \cos C$, are two sets of intersecting planes that via the addition of a constant become parallel rod systems.

We want to study how such rods are transformed into a surface and formulate the equations

$$\cos A + \cos B + N(\cos C + \cos E + \cos D \dots) = 0 \quad 4.2.3$$

or

$$\cos A + \cos B + \cos C + N(\cos E + \cos D\dots) = 0. \tag{4.2.4}$$

To transform a plane or rod system into a surface, N starts as a small number.

We illustrate this with examples, and start with the P-surface. The function $\cos x$ is implicitly an infinite number of planes, and we derive a transformation of these planes into the P-surface by weighted addition after equation 4.2.5.

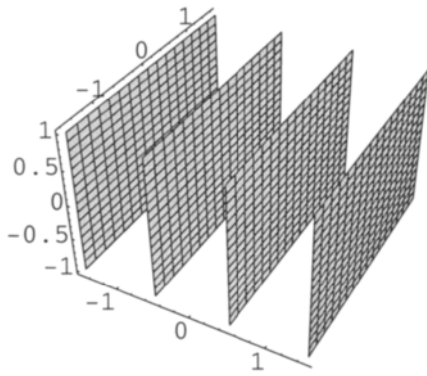


Figure 4.2.1 A=0 in equation 4.2.5.

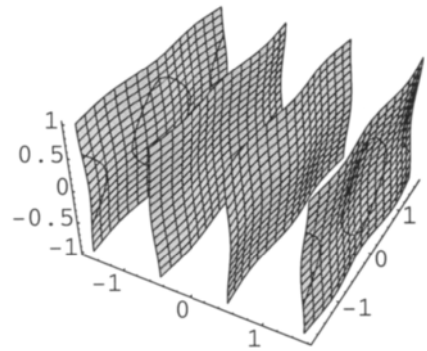


Figure 4.2.2 A=0.1 in equation 4.2.5.

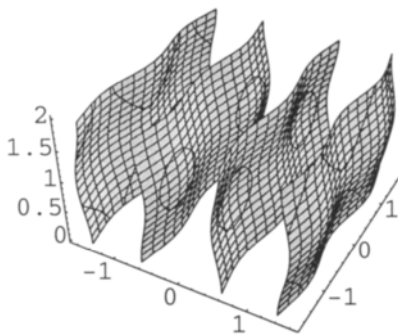


Figure 4.2.3 A=0.2 in equation 4.2.5

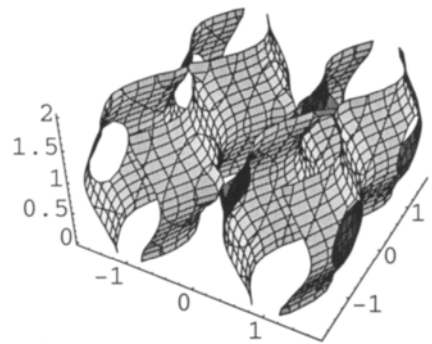


Figure 4.2.4 A=0.5 in equation 4.2.5.

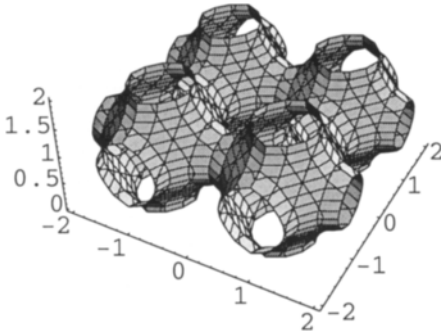


Figure 4.2.5 $A=0.8$ in equation 4.2.5.

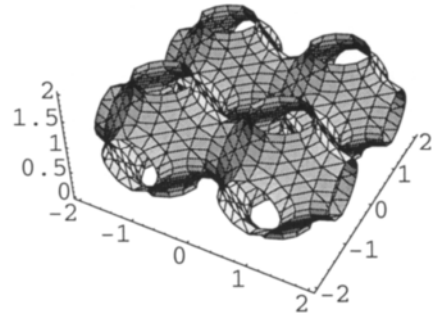


Figure 4.2.6 $A=1$ in equation 4.2.5.

$$\cos \pi x + A[\cos \pi y + \cos \pi z] = 0 \quad 4.2.5$$

In figures 4.2.1-6, A takes the values 0, 0.1, 0.2, 0.5, 0.8, and 1. $A=1$ is of course the P-surface. For lower A 's, curvature is given to the plane and gradually, as A increases, the planes are joined via catenoids and the transformation to the P-surface is obvious.

Next, we do a similar sequential transformation with the gyroid, where the plane system is $\sin(x+y)$, and let A take the values 0, 0.1, 0.3, and 0.8 in figures 4.2.7-10 and equation 4.2.6.

$$\begin{aligned} \sin \pi(x+y) + A[\sin \pi(x-y) + \sin \pi(x+z) \\ + \sin \pi(z-x) + \sin \pi(y+z) + \sin \pi(y-z)] = 0 \end{aligned} \quad 4.2.6$$

With equation 4.2.7 we demonstrate that it is possible to use a plane that does not belong to the surface. These mathematics are used to describe the structural changes in the Endoplasmic Reticulum in chapter 8.

$$\begin{aligned} \sin \pi x + A[\sin \pi(x+y) + \sin \pi(x-y) + \sin \pi(x+z) \\ + \sin \pi(z-x) + \sin \pi(y+z) + \sin \pi(y-z)] = 0 \end{aligned} \quad 4.2.7$$

The figures 4.2.11-14 below are calculated with A equal to 0.1, 0.3, 0.37, and 0.6.

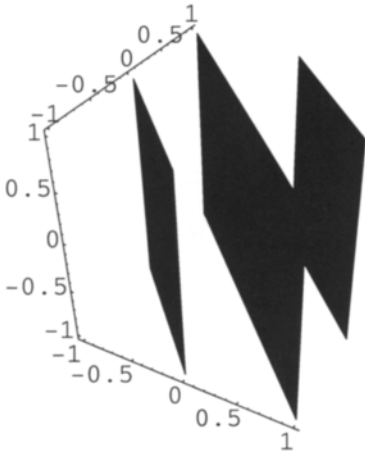


Figure 4.2.7 $A=0$ in equation 4.2.6.

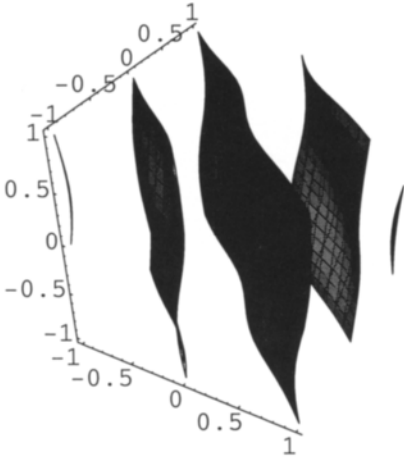


Figure 4.2.8 $A=0.1$ in equation 4.2.6.

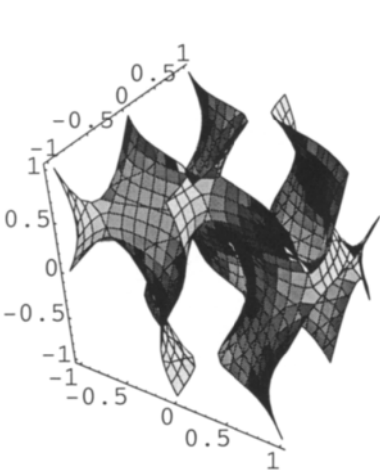


Figure 4.2.9 $A=0.3$ in equation 4.2.6.

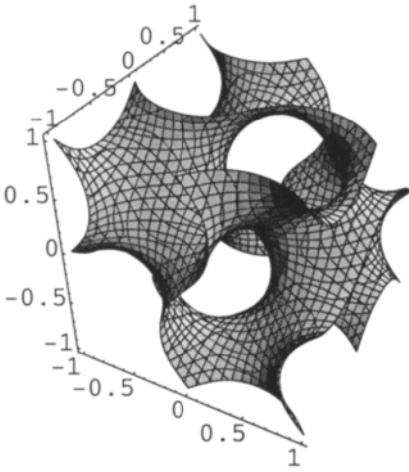


Figure 4.2.10 $A=0.8$ in equation 4.2.6.

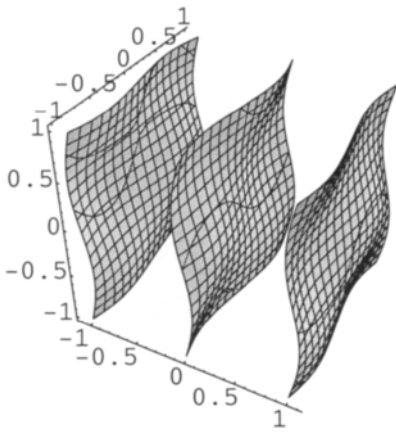


Figure 4.2.11 $A=0.1$ in equation 4.2.7.

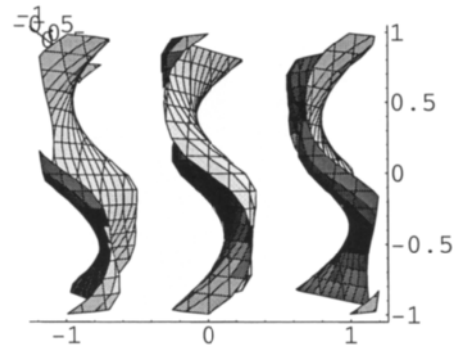


Figure 4.2.12 $A=0.3$ in equation 4.2.7.

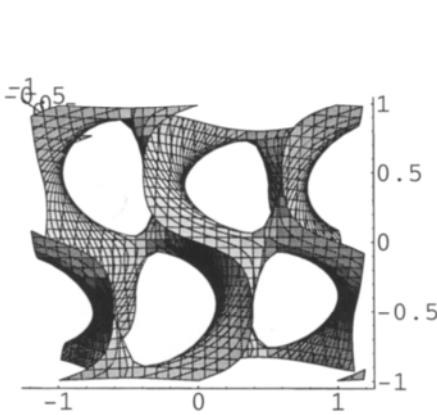


Figure 4.2.13 $A=0.37$ in equation 4.2.7.

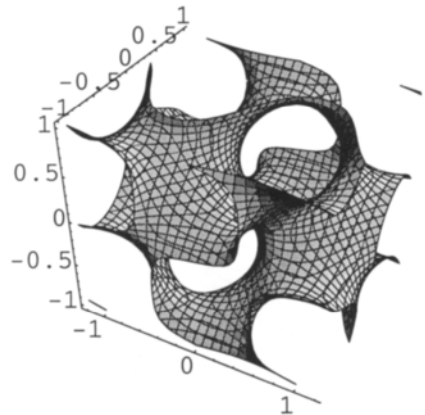


Figure 4.2.14 $A=0.6$ in equation 4.2.7.

We redo the calculations with the D-surface and the plane, $\cos(x+y+z)$. We let A vary between 0.2 equation 4.2.8, and get figures 4.2.15-19.

$$\begin{aligned}
 &\cos \pi(x+y+z) + A[\cos \pi(x-y-z) + \cos \pi(-x-y+z) \\
 &+ \cos \pi(-x+y-z) + \sin \pi(x+y+z) \\
 &+ \sin \pi(x-y-z) + \sin \pi(-x-y+z) + \sin \pi(-x+y-z)] = 0
 \end{aligned}
 \tag{4.2.8}$$

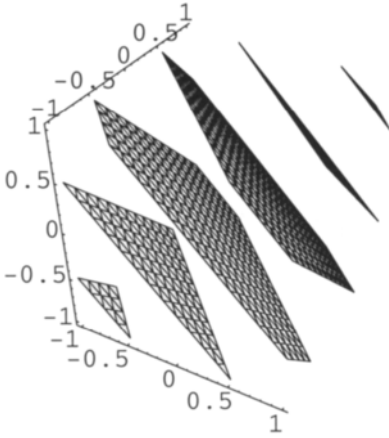


Figure 4.2.15 $A=0$ in equation 4.2.8.

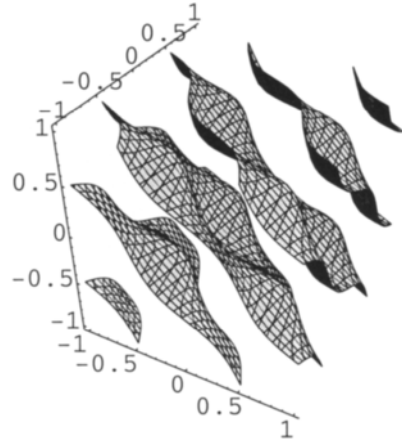


Figure 4.2.16 $A=0.2$ in equation 4.2.8.

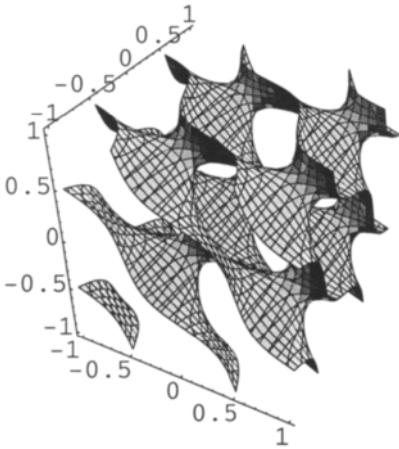


Figure 4.2.17 $A=0.3$ in equation 4.2.8.

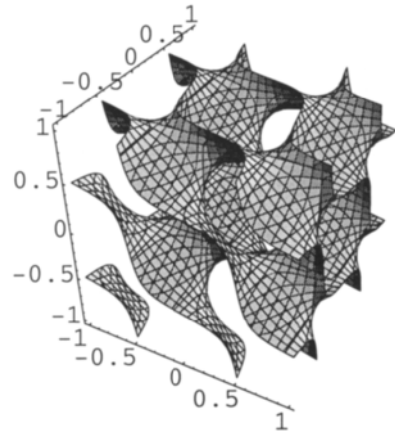


Figure 4.12.18 $A=0.5$ in equation 4.2.8.

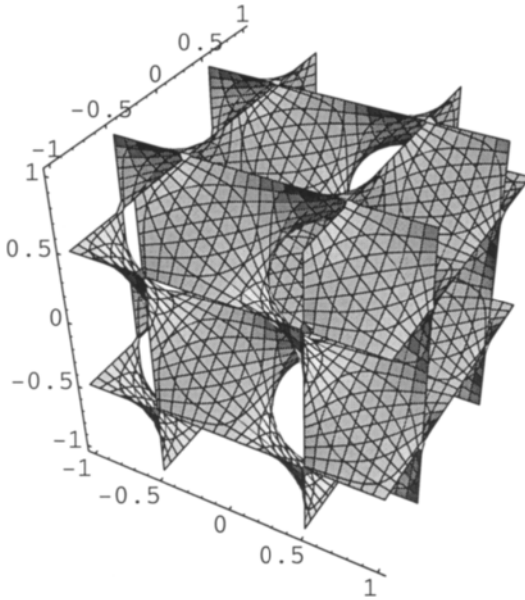


Figure 4.12.19 $A=1$ in equation 4.2.8.

4.3 Cubic Nodal Surfaces and Parallel Rods

For symmetry reasons we start with hexagonally parallel rods for an orientation of the cubic space diagonal, which is a three fold axis. The equation for such rods is given in 4.3.1. This is illustrated in figure 4.3.1, with the rods projected in 4.3.2.

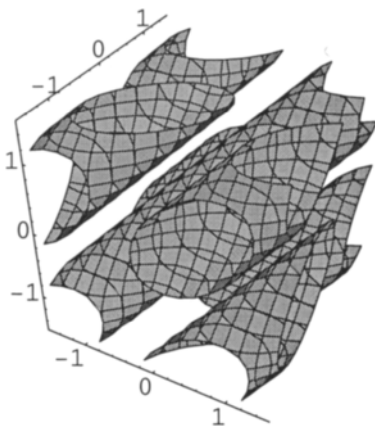


Figure 4.3.1 Hexagonally parallel rods along a cubic space diagonal.

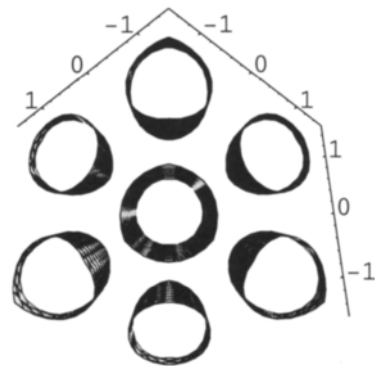


Figure 4.3.2 Projection along the cubic space diagonal.

$$\cos \pi(x - y) + \cos \pi(-x + z) + \cos \pi(y - z) = 0 \tag{4.3.1}$$

$$\begin{aligned} \cos \pi(x - y) + \cos \pi(-x + z) + \cos \pi(y - z) \\ + A[\cos \pi x + \cos \pi y + \cos \pi z] = 0 \end{aligned} \tag{4.3.2}$$

The equation for the transformation to a P-surface is formulated in 4.3.2, and in figures 4.3.3-6 we let A be 0.8, 1.2, 1.8, and 2.4. The rod structure becomes a P-surface via the opening of catenoids.

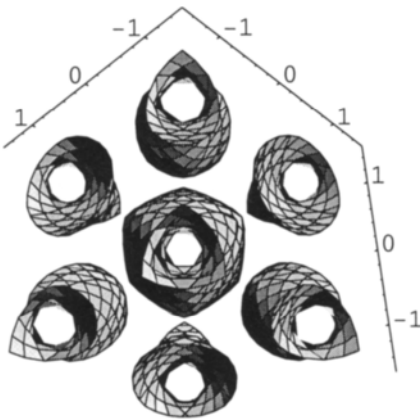


Figure 4.3.3 A=0.8 in equation 4.3.2.

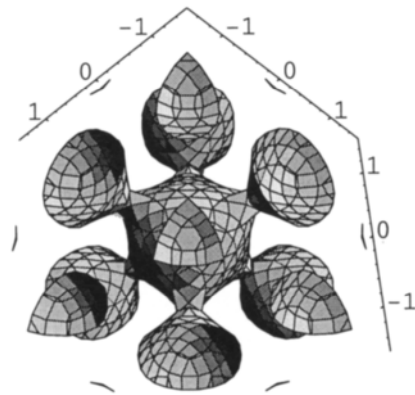


Figure 4.3.4 A=1.2 in equation 4.3.2.

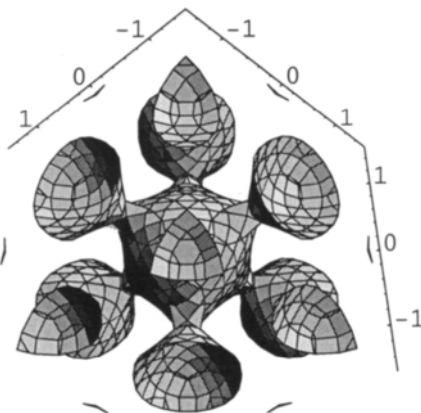


Figure 4.3.5 A=1.8 in equation 4.3.2

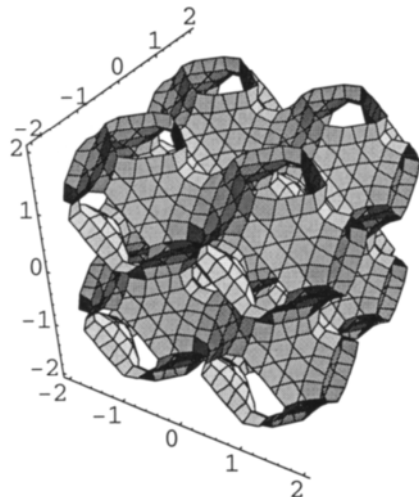


Figure 4.3.6 A=2.4 in equation 4.3.2.

The formation of the gyroid from hexagonal rods is very simple, and we show this in equation 4.3.3.

$$\sin \pi(x - y) + \sin \pi(z - x) + \sin \pi(y - z) + A[\sin \pi(x + y) + \sin \pi(x + z) + \sin \pi(y + z)] - 0.5 = 0 \tag{4.3.3}$$

For figures 4.3.7-14 A takes the values 0, 0.15, 0.2, 0.3, and 0.6. Figures 4.3.11 and 12 show how three catenoids meet to form a monkey saddle. As indicated in the figure texts, some of the figures are just different projections of others.

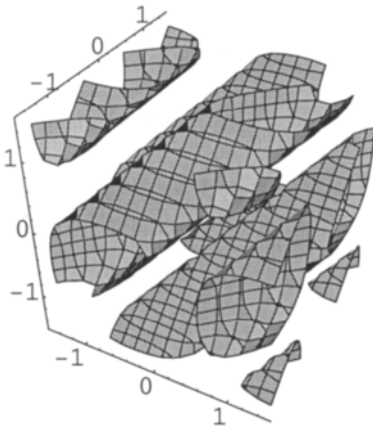


Figure 4.3.7 Hexagonally parallel rods along a cubic space diagonal.

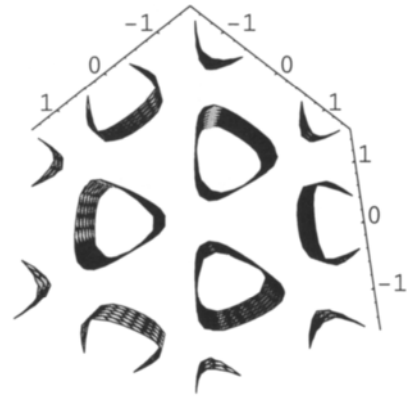


Figure 4.3.8 Projection along the cubic space diagonal.

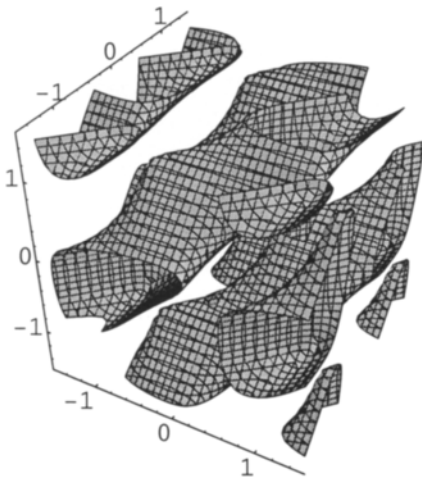


Figure 4.3.9 A=0.15 in equation 4.3.3.

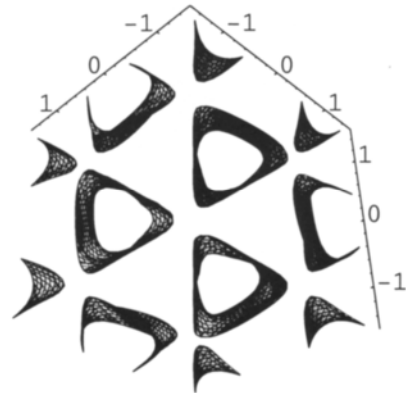


Figure 4.3.10 A=0.15 in equation 4.3.3, projection of 4.3.9.

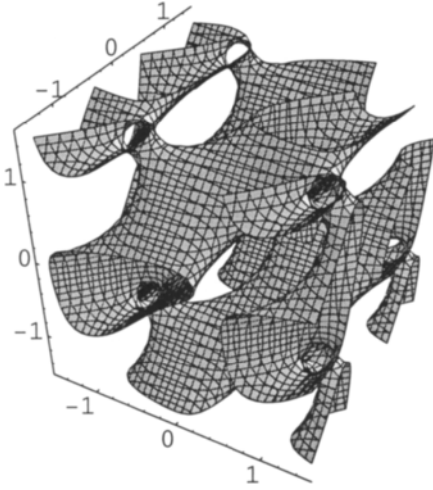


Figure 4.3.11 $A=0.2$ in equation 4.3.3.

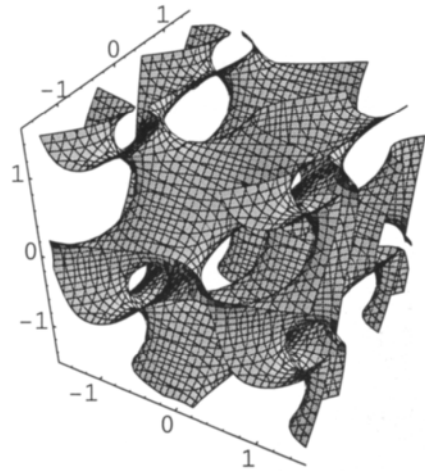


Figure 4.3.12 $A=0.3$ in equation 4.3.3.

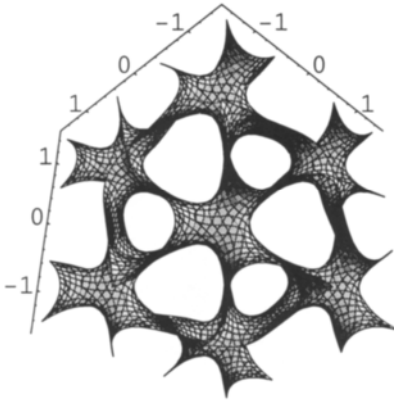


Figure 4.3.13 $A=0.3$ in equation 4.3.3, different projection of 4.3.12.

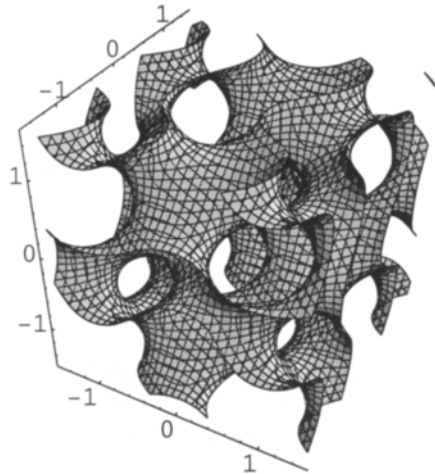


Figure 4.3.14 $A=0.6$ in equation 4.3.3.

The D-surface can also be easily obtained with a similar mechanism. The equation is in 4.3.4.

$$\begin{aligned} &\sin \pi(x - y) + \sin \pi(-x + z) + \sin \pi(y - z) + \\ &+ A[\cos \pi(x + y + z) + \cos \pi(x - y - z) + \cos \pi(-x - y + z) \\ &+ \cos \pi(-x + y - z) + \sin \pi(x + y + z) + \sin \pi(x - y - z) \\ &+ \sin \pi(-x - y + z) + \sin \pi(-x + y - z)] - 0.5 = 0 \end{aligned} \tag{4.3.4}$$

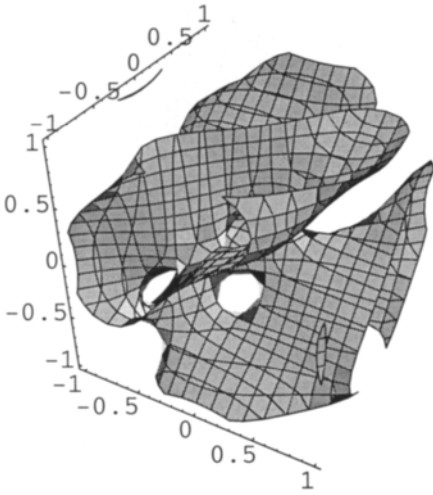


Figure 4.3.15 A=0.2 in equation 4.3.4.

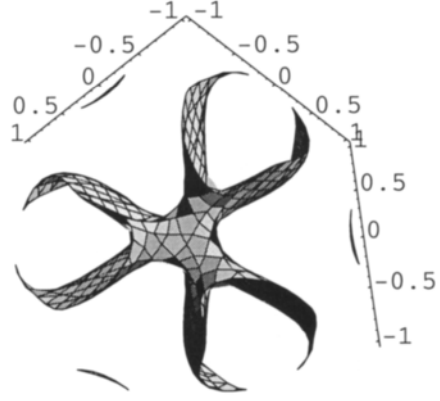


Figure 4.3.16 A=0.2 in equation 4.3.4.

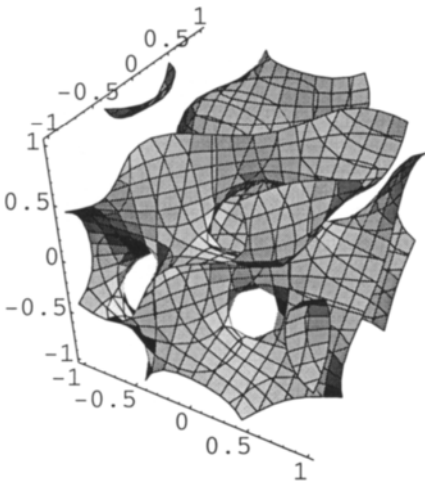


Figure 4.3.17 A=0.6 in equation 4.3.4.

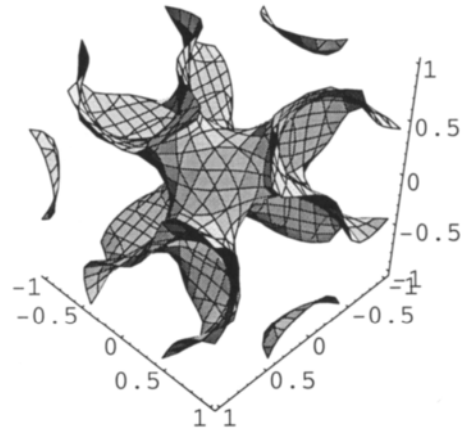


Figure 4.3.18 A=0.6 in equation 4.3.4.

The A takes the values 0.2, 0.6, and 2 for the figures 4.3.15-20. The figures to the right are projected along the three fold axes in the figures to the left.

Again we see that the catenoids coming out from a rod meet to form a monkey saddle.

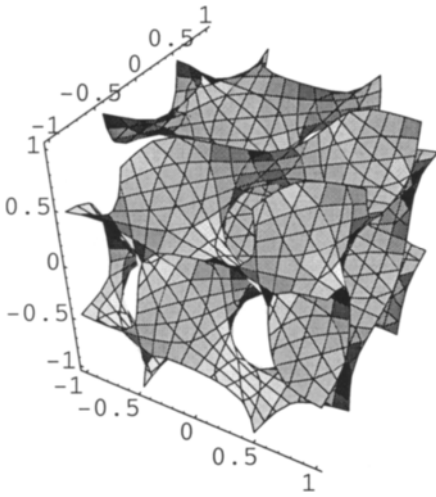


Figure 4.3.19 $A=2$ in equation 4.3.4.

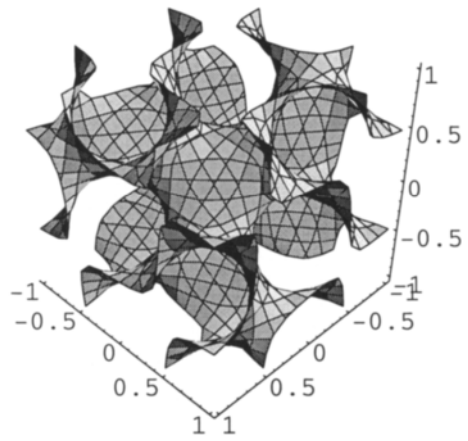


Figure 4.3.20 $A=2$ in equation 4.3.4.

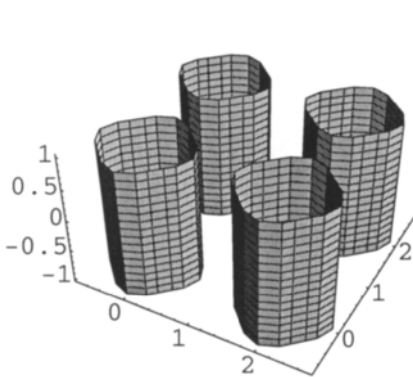


Figure 4.3.21 Simple tetragonal rods, from equation 4.3.5.

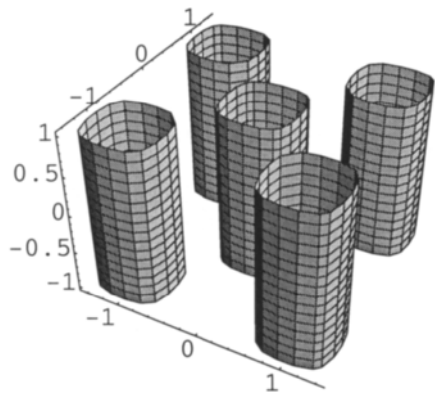


Figure 4.3.22 Simple tetragonal rods, from equation 4.3.6.

Just as the hexagonal, the parallel tetragonal cylinders make a simple rod system. We have produced it in two different orientations in equations 4.3.5 and 4.3.6, which is illustrated in figures 4.3.21-22. We shall make them form surfaces via catenoids.

$$\cos \pi x + \cos \pi y = 0 \quad 4.3.5$$

$$\cos \pi(x+y) + \cos \pi(x-y) = 0 \quad 4.3.6$$

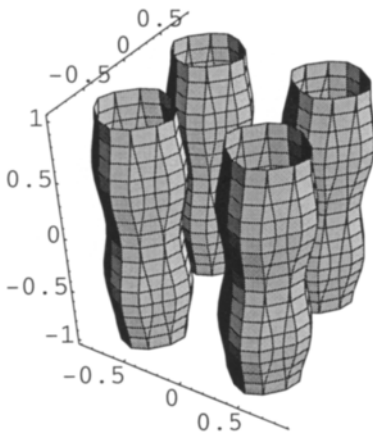


Figure 4.3.23 $A=0.2$ in equation 4.3.7.

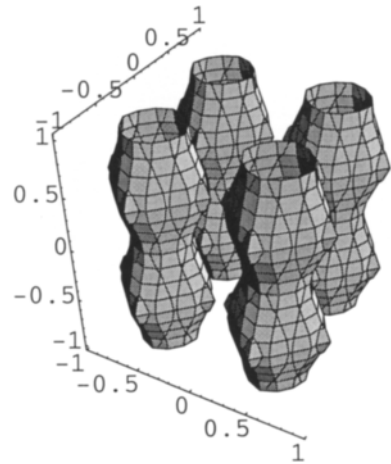


Figure 4.3.24 $A=0.4$ in equation 4.3.7.

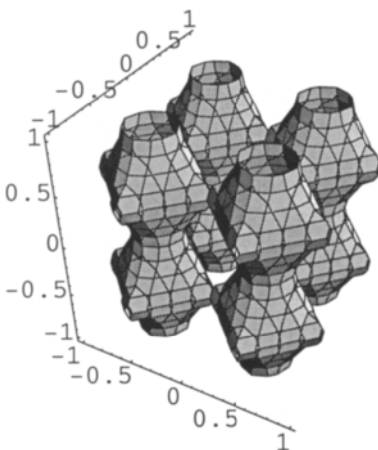


Figure 4.3.25 $A=0.6$ in equation 4.3.7.

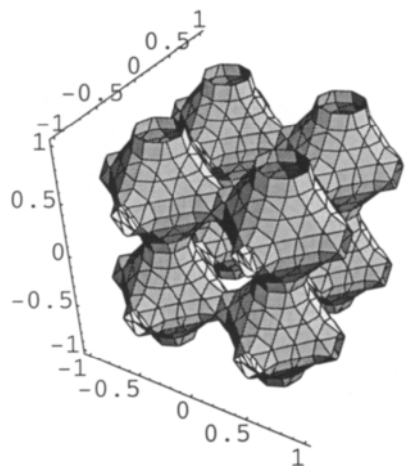


Figure 4.3.26 $A=0.8$ in equation 4.3.7.

Using equation 4.3.7 we start to make the P-surface from the rods of figure 4.3.21.

$$\cos 2\pi x + \cos 2\pi y + A \cos 2\pi z + 0.5 = 0 \tag{4.3.7}$$

A varies between 0.2, 0.4, 0.6 and 0.8 in figures 4.3.23-26.

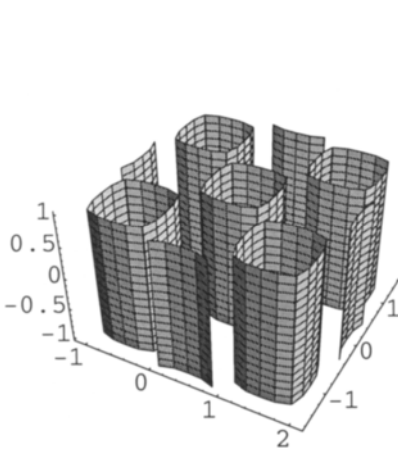


Figure 4.3.27 A=0 in equation 4.3.8.

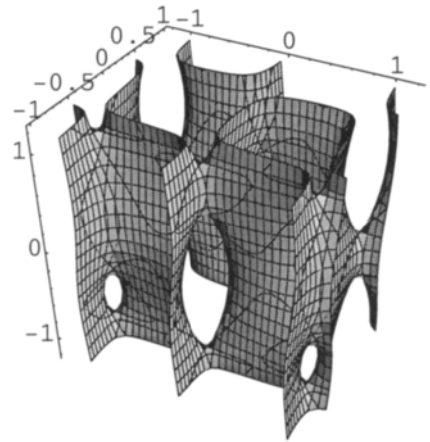


Figure 4.3.28 A=0.1 in equation 4.3.8.

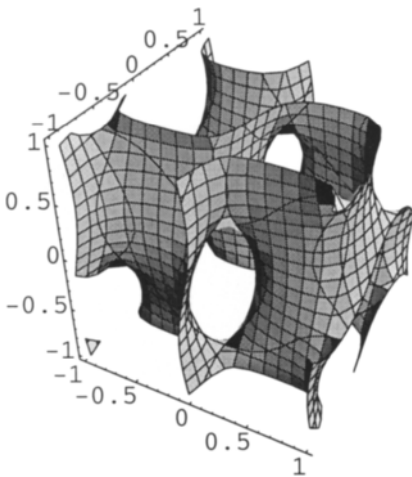


Figure 4.3.29 A=0.2 in equation 4.3.8.

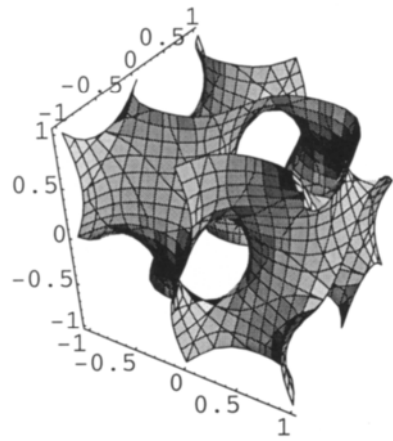


Figure 4.3.30 A=0.4 in equation 4.3.8.

With this tetragonal rod system we can make a transformation to the gyroid with the very simple equation 4.3.8. A takes the values 0, 0.1, 0.2, and 0.4 in figures 4.3.27-30.

$$\begin{aligned} &\sin \pi(x+y) + \sin \pi(x-y) \\ &+ A[\sin \pi(x+z) + \sin \pi(-x+z) + \sin \pi(y+z) + \sin \pi(y-z)] - 0.2 = 0 \end{aligned} \quad 4.3.8$$

Using the same rod system but with the first orientation from 4.3.5, we formulate equation 4.3.9.

$$\begin{aligned} &\cos \pi x + \cos \pi y \\ &+ A[\sin \pi(x+y) + \sin \pi(x-y) + \sin \pi(x+z) \\ &+ \sin \pi(-x+z) + \sin \pi(y+z) + \sin \pi(y-z)] = 0 \end{aligned} \quad 4.3.9$$

A has been given the values 0.02, 0.08, 0.4, 0.8, and 2 for the figures 4.3.31-36.

The gyroid is not formed directly from this simple tetragonal rod system - first the fundamental tetragonal CLP surface is formed, which is clear for $A=0.08$ in figure 4.3.32. The CLP surface is of great biological relevance, and we have recently shown that this surface forms a separate phase at the air/water interface in the lung alveoli, which we return to in chapter 14. Via catenoid formation between parts of the distorted CLP surface at an A of 0.5, there is a continuous transformation of the CLP to the gyroid.

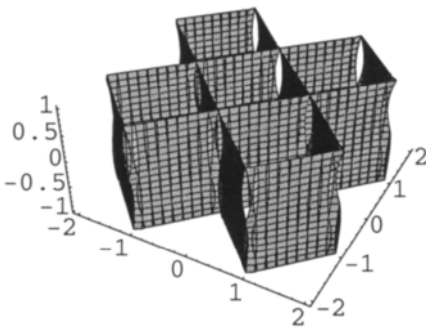


Figure 4.3.31 $A=0.02$ in equation 4.3.9.

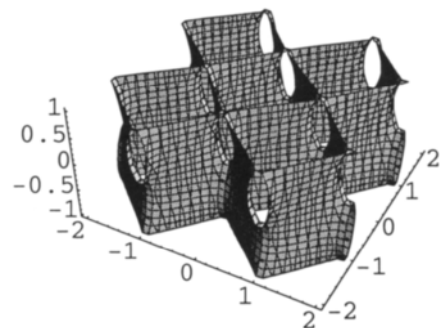


Figure 4.3.32 $A=0.08$ in equation 4.3.9 (CLP).

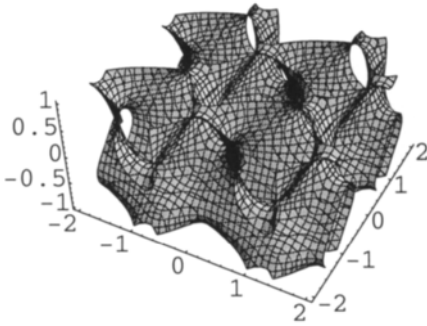


Figure 4.3.33 $A=0.4$ in equation 4.3.9.

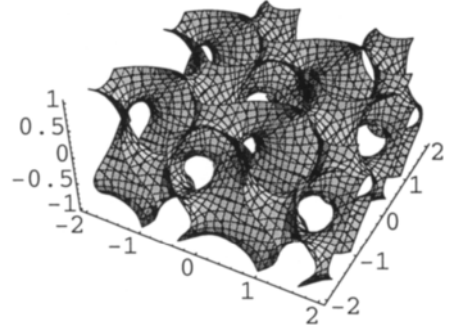


Figure 4.3.34 $A=0.8$ in equation 4.3.9.

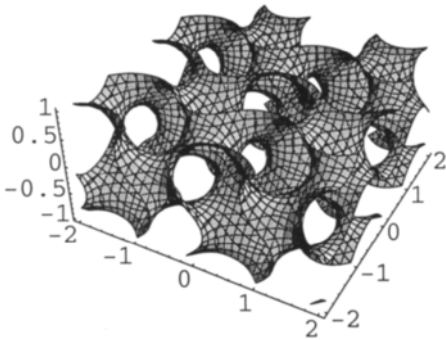


Figure 4.3.35 $A=2$ in equation 4.3.9.

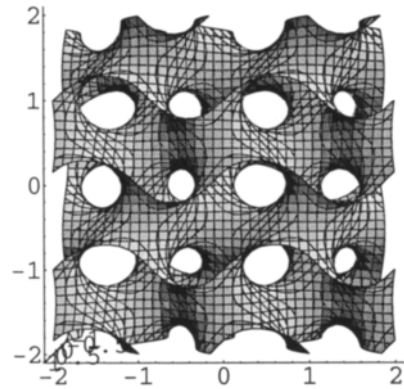


Figure 4.3.36 Different projection of 4.3.35.

Using the same rod system, but with the first orientation and the D surface, we formulate equation 4.3.10. We show only two figures here, for $A=0.02$ and 0.2 respectively for figures. 4.3.37 and 4.3.38.

Again the tetragonal CLP shows up, and at higher A there are heavy intersections before going to the D surface.

$$\begin{aligned} &\cos \pi(x+y) + \cos \pi(x-y) \\ &+ A[\cos \pi(x+y+z) + \cos \pi(x-y-z) + \cos \pi(-x-y+z) + \cos \pi(-x+y-z) \\ &+ \sin \pi(x+y+z) + \sin \pi(x-y-z) + \sin \pi(-x-y+z) + \sin \pi(-x+y-z)] = 0 \end{aligned} \tag{4.3.10}$$

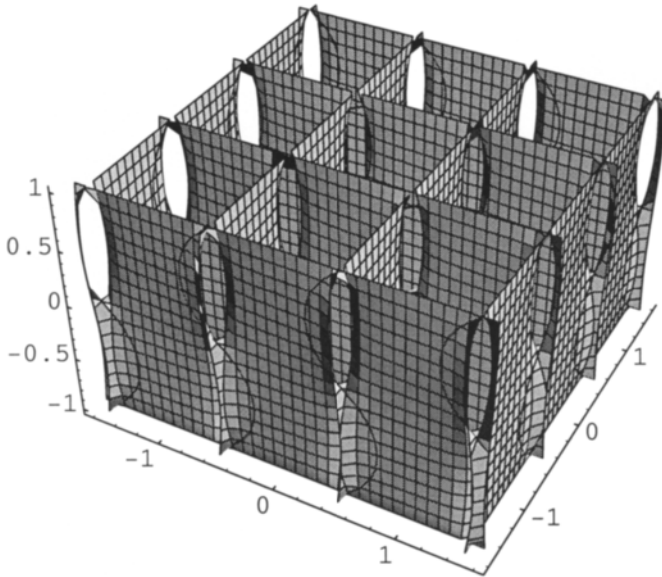


Figure 4.3.37 $A=0.02$ in equation 4.3.10.

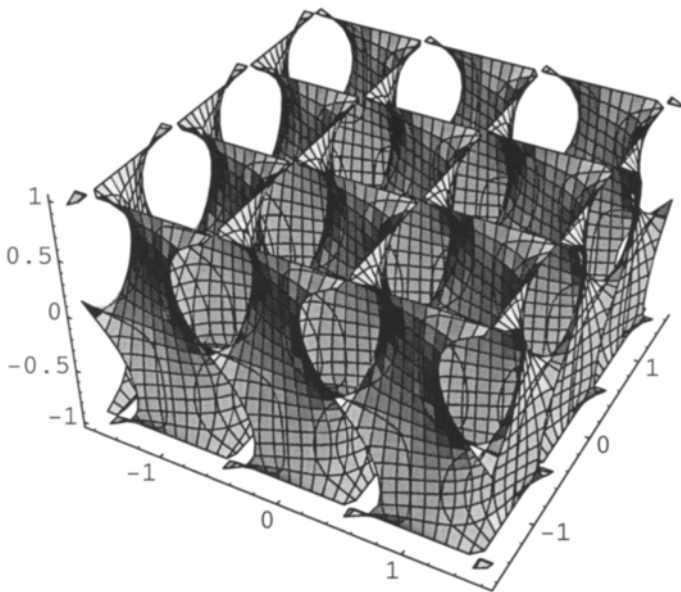


Figure 4.3.38 $A=0.2$ in equation 4.3.10.

From the equation for the D-surface we can extract a rod system, which is tetragonally distorted. We show it with the equation we use to study how such rods are transformed into the D-surface (4.3.11).

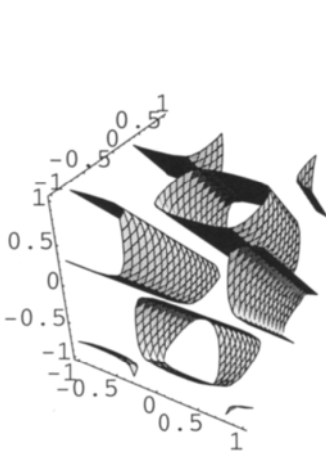


Figure 4.3.39 $A=0$ in equation 4.3.11.

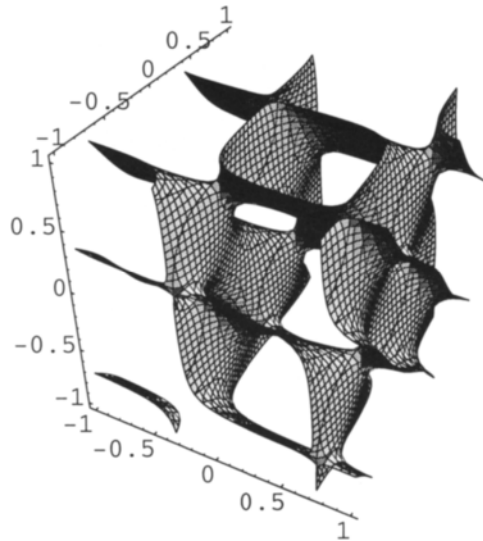


Figure 4.3.40 $A=0.1$ in equation 4.3.11.

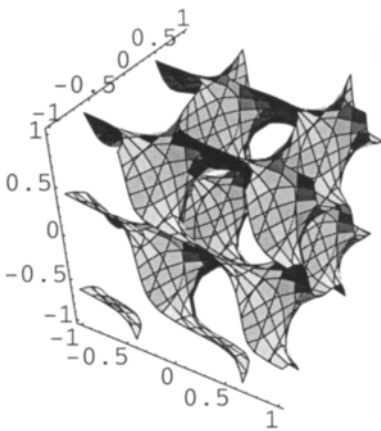


Figure 4.3.41 $A=0.3$ in equation 4.3.11.

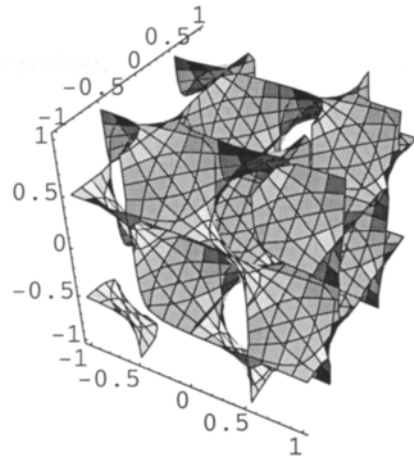


Figure 4.3.42 $A=0.8$ in equation 4.3.11.

$$\begin{aligned} & \cos\pi(x+y+z) + \sin\pi(x-y-z) \\ & + A[\cos\pi(x-y-z) + \cos\pi(-x-y+z) + \cos\pi(-x+y-z) \\ & + \sin\pi(x+y+z) + \sin\pi(-x-y+z) + \sin\pi(-x+y-z)] + 0.2 = 0 \end{aligned} \quad 4.3.11$$

Here A takes the values 0, 0.1, 0.3 and 0.8 in figures 4.3.39-42.

4.4 Transformations of Nodal Surfaces

Transformation of one surface into another is of great importance in membrane science. We have earlier proposed the isometric Bonnet transformation as a guide for a mechanism for such a transformation [3]. The advantage is that the curvature at each point is constant during the action - it costs no energy. The disadvantage is the heavy intersecting that occurs during the transformation. We will now propose a mechanism that means no intersection, instead there is closing or openings of catenoids, a phenomenon common in biology. There are local changes in curvature, but the start and end products must be very close to being isometric, so there is no or very little energy exchange with the surroundings.

The celebrated transformation path in Bonnet [4] is

$$D \rightarrow G \rightarrow P,$$

and we shall here have this as the simplest path. Our mathematics involves only the weighted addition of the corresponding nodal equations as in 4.4.1. We show this first with $G \rightarrow D$. The mechanism is opening of catenoids as is obvious from figures 4.4.3-4.

A and B take the pairwise values 0, 1; 0.5, 1; 1, 1; 1, 0.75; 1, 0.5; and 1, 0.25 for figures 4.4.1-6 respectively.

$$\begin{aligned} & A[\cos\pi(x+y+z) + \cos\pi(x-y-z) + \cos\pi(-x-y+z) \\ & + \cos\pi(-x+y-z) + \sin\pi(x+y+z) + \sin\pi(x-y-z) \\ & + \sin\pi(-x-y+z) + \sin\pi(-x+y-z)] \\ & + B[\sin\pi(x+y) + \sin\pi(x-y) + \sin\pi(x+z) \\ & + \sin\pi(z-x) + \sin\pi(y+z) + \sin\pi(y-z)] = 0 \end{aligned} \quad 4.4.1$$

We show below in equation 4.4.2 the transformation of G into P, and start with a picture of G and its projection along its cubic axes. The mechanism is closing of catenoids as is obvious from the figures. A takes the values 0, 0, 1, 1.7, 2.2 and 3 for the figures 4.4.7-12.

$$\begin{aligned} &\sin \pi(x + y) + \sin \pi(x - y) + \sin \pi(x + z) + \sin \pi(z - x) \\ &+ \sin \pi(y + z) + \sin \pi(y - z) + A[\cos \pi x + \cos \pi y + \cos \pi z] = 0 \end{aligned} \tag{4.4.2}$$

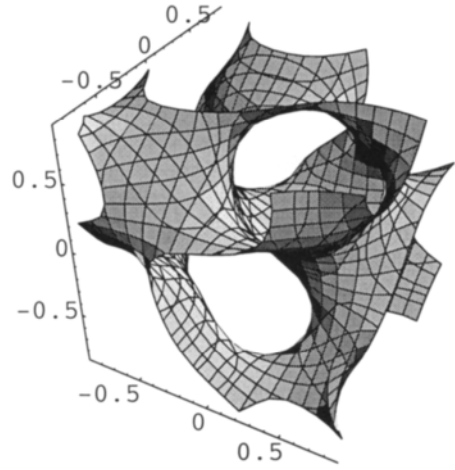
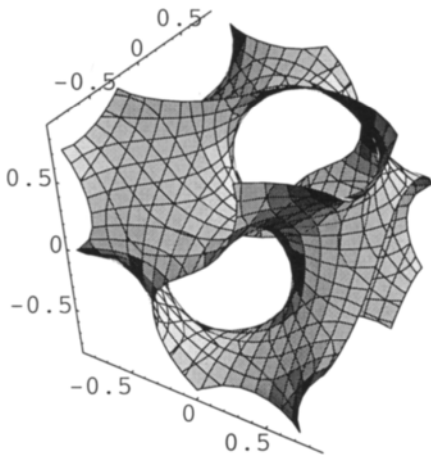


Figure 4.4.1 Transformation G→D. A=0, B=1 in equation 4.4.1.

Figure 4.4.2 A=0.5, B=1 in equation 4.4.1.

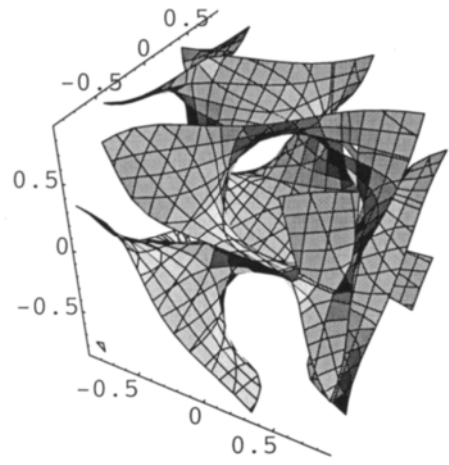
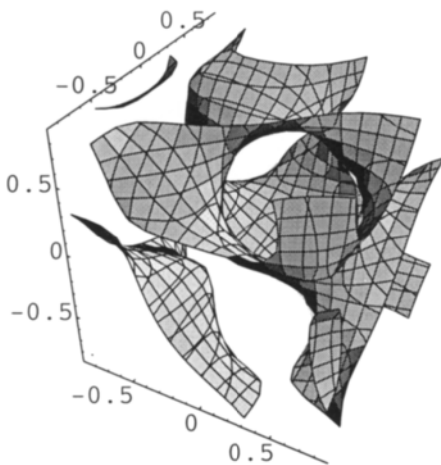


Figure 4.4.3 A=1, B=1 in equation 4.4.1.

Figure 4.4.4 A=1, B=0.75 in equation 4.4.1.

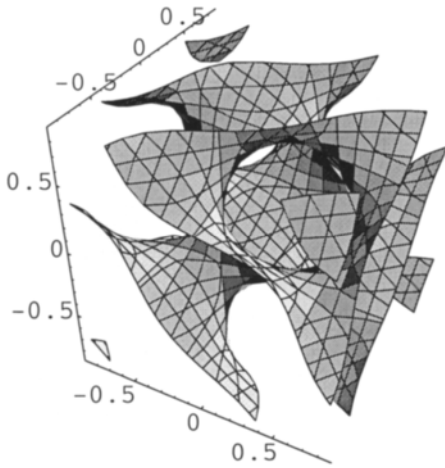


Figure 4.4.5 $A=1, B=0.5$ in equation 4.4.1.

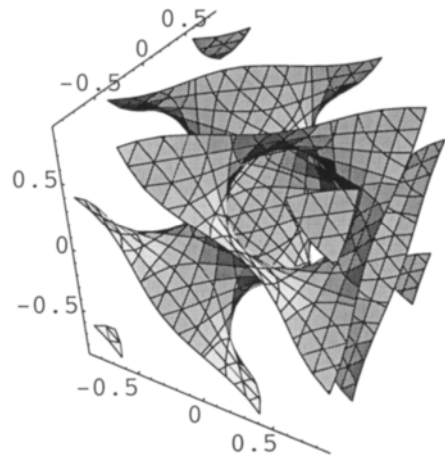


Figure 4.4.6 $A=1, B=0.25$ in equation 4.4.1.

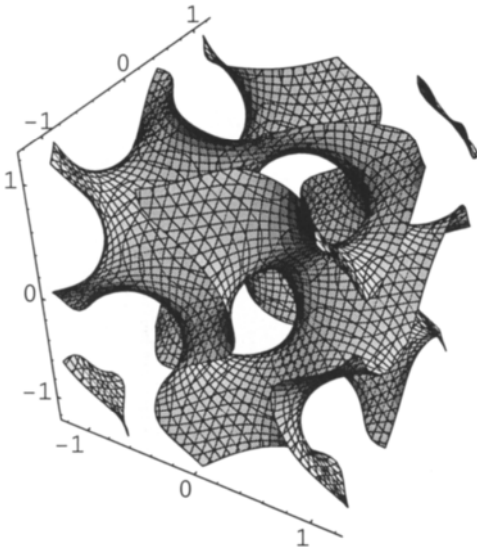


Figure 4.4.7 Transformation $G \rightarrow P$. $A=0$ in equation 4.4.2.

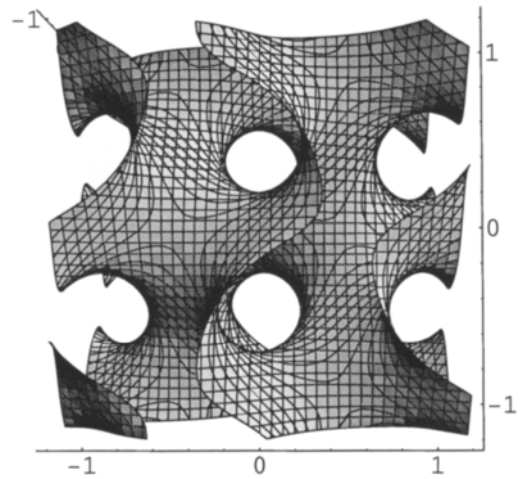


Figure 4.4.8 $A=0$ in equation 4.4.2. Projection.

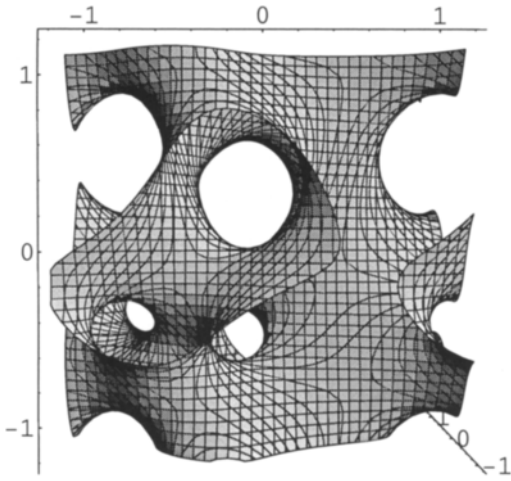


Figure 4.4.9 $A=1$ in equation 4.4.2.

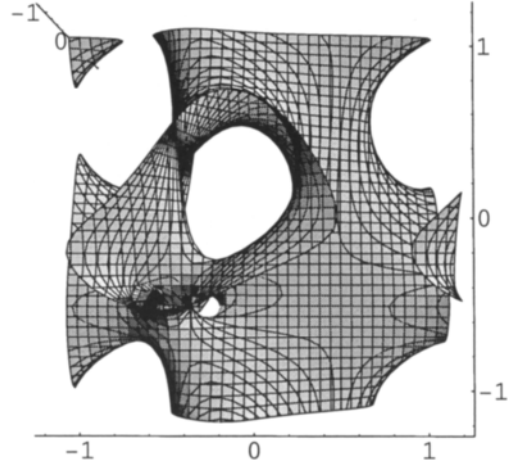


Figure 4.4.10 $A=1.7$ in equation 4.4.2.

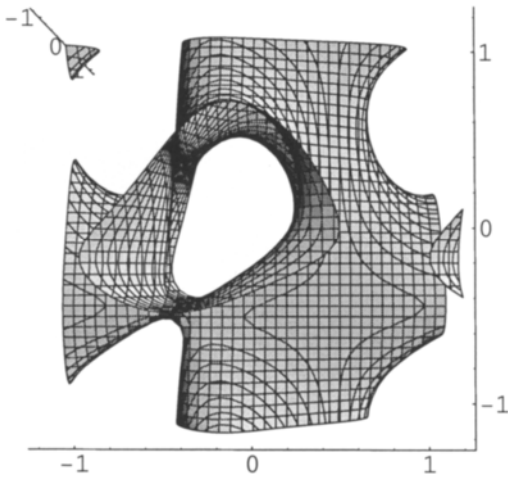


Figure 4.4.11 $A=2.2$ in equation 4.4.2.

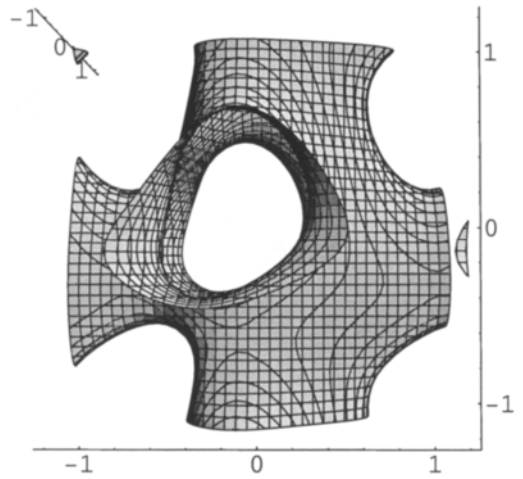


Figure 4.4.12 $A=3$ in equation 4.4.2.

References 4

1. Max Born, Wave Mechanics of the hydrogen atom in 'The restless universe'.
2. H. G. von Schnering and R. Nesper, *Z. Phys. B - Condensed Matter* **83**, 407 (1991).
3. S. T. Hyde, S. Andersson, B. Ericsson and K. Larsson, *Z. Kristallogr.* **168**, 213 (1984).
4. S. T. Hyde, S. Andersson, *Z. Kristallogr.* **174**, 225 (1986).

5 Motion in Biology

What harm a wind too strong at sea might do [Shakespeare,1].

We describe dynamics in biology as change of site, shape, and size.

We describe how to control the shape of bodies using the exponential shape.

We propose here that the GD function is used to describe biological bodies such as vesicles or cells, how they move, and how they interact with other bodies (attraction or repulsion).

We describe how bodies of different shapes move through planes, catenoids, or lenses shaped like rings.

5.1 Background and Essential Functions

We shall not review the history of dynamics, we shall just give a pure mathematical description of motion and interactions, and apply it to biology.

Examples of classic motion, very well described in reference [2], are free particle motion, particle motion under central forces, the standing wave motion, the travelling wave motion, and solitary wave motion. References [3] and [4] are also excellent reading for the motion of electrons.

The picture of motion we shall develop is not based on speed, acceleration, momentum, quantisation or minimisation. We shall use special functions for the mathematical motion of a molecule or particle. For the interactions with surroundings, the shape, size and site of the molecule or particle will be important. Interactions in biology occur with other particles, small or large, with cell membranes of various shapes. Interactions may also occur with different concentrations of the solutes in the aqueous medium, or gradients of concentrations. A biological molecule or particle is moving in a surrounding of interactions.

We shall develop two new concepts, finite motion and finite periodicity, which are particularly important for the description of motion of biological molecules or particles.

It must be said that the mathematical functions we shall use to describe shape, size, and motion are solutions to some very basic differential equations. We deal with this first.

Many physical phenomena are described with second order partial differential equations, and we give three important ones below in 5.1.1-3.

Wave equation:

$$\frac{\partial^2 u}{\partial x^2} - \frac{\partial^2 u}{\partial t^2} = 0 \quad 5.1.1$$

Diffusion equation:

$$\frac{\partial^2 u}{\partial x^2} - \frac{\partial u}{\partial t} = 0 \quad 5.1.2$$

Laplace equation:

$$\frac{\partial^2 u}{\partial x^2} - \frac{\partial^2 u}{\partial y^2} = 0 \quad 5.1.3$$

We see below first two simple equations as variations of the wave equation, in equations 5.1.4-5. A solution to the first one is *cosh*, a function that can be used to describe the outer shapes of solids like polyhedra, crystals, houses, or virtually anything [5]. A solution to the second is *cos*, and stands for infinite periodicity, which is useful for describing inner structures of a solid or membrane. These two simple and almost identical differential equations have entirely different solutions, each one giving rise to two completely different branches of mathematics. Both with great applications in life, as we shall see in this book. Why are the differential equations so similar? Just a mathematical accident, or of course a property of the derivatives.

$$\frac{d^2 y}{dx^2} - y = 0 \quad 5.1.4$$

Solution: $e^x + e^{-x} = 2 \cosh x$

$$\frac{d^2y}{dx^2} + y = 0 \quad 5.1.5$$

Solution: $\cos x$

The initial solution to the diffusion equation in 5.1.2 is the error function, or the Gauss distribution function (GD) in equation 5.1.6.

$$y = e^{-x^2} \quad 5.1.6$$

The mathematics that this simple function offers will also be of great use in this book.

We also say here that the square of *sech* is an initial solution to a more complicated differential equation - the Korteweg-de Vries (KdV) equation for travelling waves in equation 5.1.7.

$$\frac{\partial u}{\partial t} = 6u \frac{\partial u}{\partial x} - \frac{\partial^3 u}{\partial x^3} \quad 5.1.7$$

The function *sech* is defined by the relation in 5.1.8.

$$\operatorname{sech} x = 1/\cosh x \quad 5.1.8$$

The *sech* function is very similar to the GD function, and as such also useful in our description of solitons in chapter 12.

So we shall describe biological dynamics as the *change* of *size*, *site* and, when needed, *shape*.

We need a collective description of forces, and shall use *curvature* for this.

Motion, we start with two dimensions, can be described with the two position parameters *x* and *y*, and with the two dependent parameters, time, *t*, and speed, *v*, as in equation 5.1.6.

$$y = f(x - vt) \quad 5.1.6$$

We shall use the kind of mathematics that allows us to move a particle as we like.

Speed *v* is meters per second, and with *t* in seconds we can write equation 5.1.6 as in 5.1.7.

$$y=f(x-\Delta x) \quad 5.1.7$$

$x-\Delta x$ is now the *site* which is changed with Δx .

If we add, or multiply, a constant to equation 5.1.7, we frequently find that the function in its graphical representation changes *size*. So the equations we shall use to describe biological dynamics will be of the type:

$$y=f(x-\Delta x) + \text{constant} \quad 5.1.8$$

By changing size via the constant we have seen spheres via catenoids form 3D surfaces. We have also seen planes or rods turn into surfaces via catenoids. This means change of curvature, and bonding.

Examples of this biological motion start below with equations 5.3.4 and 5.3.6.

5.2 The Control of Shape - the Natural Exponential or cosh in 3D

The change of site describes the motion itself and will be dealt with in figure 5.3. For the description of shape, which is important for interactions and curvature, we have developed the method of the exponential scale [5,6], which we shortly describe below.

The function

$$y = e^x \quad 5.2.1$$

is $y=e \cdot e \cdot e \dots$ multiplied x times. This is called the natural exponential, which will be of great use in this book.

The natural number e was invented by Euler who realised it to be so important that he named it after himself. Some properties of the natural number is found below.

$$e=2.718281828459045\dots$$

$$\ln e = 1 \quad 5.2.2$$

$$y = e^x, \text{ if } x = \ln y$$

We start again the counting, and find that

$$e^x = 100 \tag{5.2.3}$$

is a plane in space, as shown in figure 5.2.1. And we find that

$$e^x + e^{-x} = 100, \tag{5.2.4}$$

which is the famous *coshx*, has two planes as shown in figure 5.2.2. Cosh is the solution to one of the fundamental differential equations above.

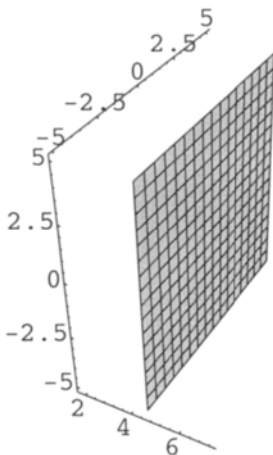


Figure 5.2.1 An “exponential” plane.

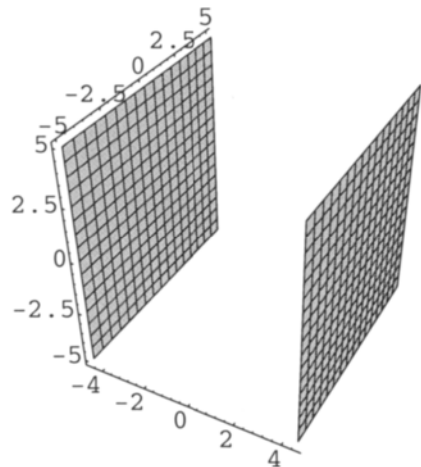


Figure 5.2.2 Two exponential planes.

Now we come to a very important property of the Euler function in the equations 5.2.5 and 5.2.6, as shown in figures 5.2.3 and 5.2.4. It is obvious from figure 5.2.3 and equation 5.2.5, that when y becomes very small, e^y approaches one and x becomes $\ln 99$, which is 4.6 and is the limit for x as shown in the figure. And vice versa for e^x . If x and y simultaneously take the same value we may write $2e^x=100$, and x becomes $\ln 50$, which is 3.9. Or for equation 5.2.6 x becomes $\ln 500$, which is 6.2. This is located right in the bend. The size of the surface for the function, or $x+y$, is controlled by the constant, and the two variables x and y cannot simultaneously grow unlimited, they cannot intersect, they must go continuously over into each other. The curvature of the outer tip of the bend is constant and independent of its size [5]. In figure 5.2.4 the bend is sharper, which is only due to the larger size.

We can now make the natural exponential in 3D, which is a cube corner, in equation 5.2.7 and figure 5.2.5, and the cube in 5.2.6 and equation 5.2.8.

$$e^x + e^y = 100 \tag{5.2.5}$$

$$e^x + e^y = 1000 \tag{5.2.6}$$

$$e^x + e^y + e^z = 100 \tag{5.2.7}$$

$$e^x + e^y + e^z + e^{-x} + e^{-y} + e^{-z} = 100 \tag{5.2.8}$$

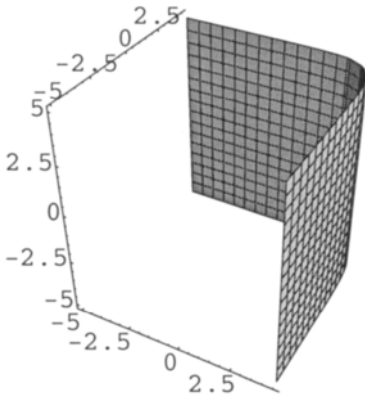


Figure 5.2.3 Two exponential planes that meet.

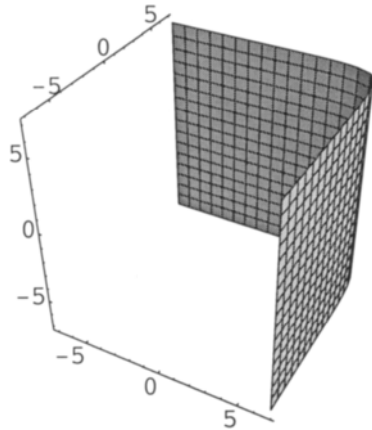


Figure 5.2.4 Larger size after equation 5.2.6.

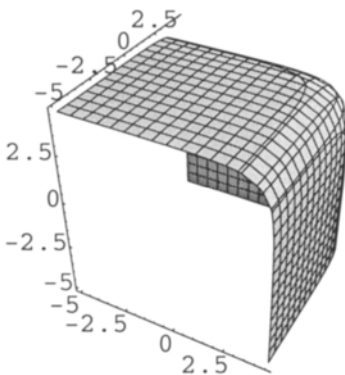


Figure 5.2.5 The Euler function, the natural exponential, in 3D.

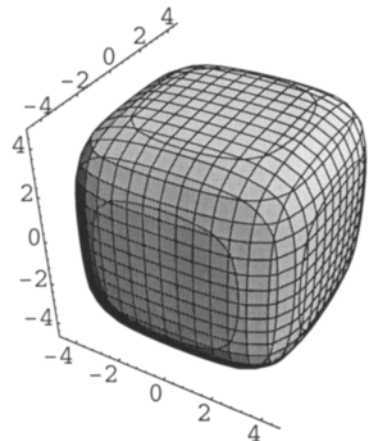


Figure 5.2.6 The exponential cube.

The cube may be shifted to positive numbers as with equation 5.2.9, which is shown in figure 5.2.7.

We can make the cube grow and become sharper with a constant of 1000, as shown in figure 5.2.8.

$$e^{x-6} + e^y + e^z + e^{-(x-6)} + e^{-y} + e^{-z} = 100 \tag{5.2.9}$$

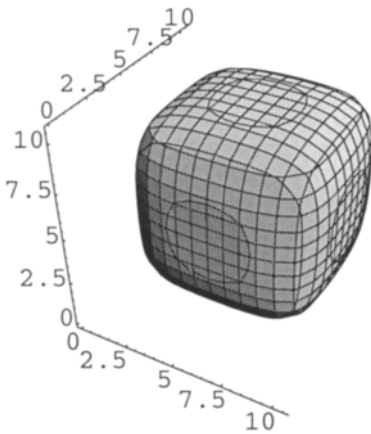


Figure 5.2.7 The cube is translated.

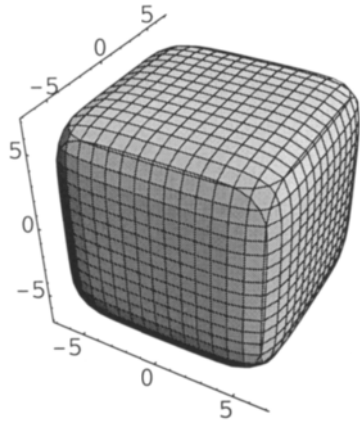


Figure 5.2.8 The cube is made bigger with higher constant.

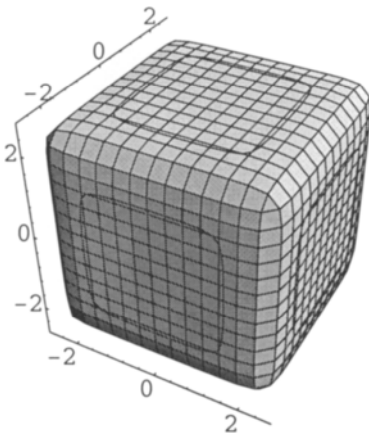


Figure 5.2.9 Higher exponentials give sharper cube.

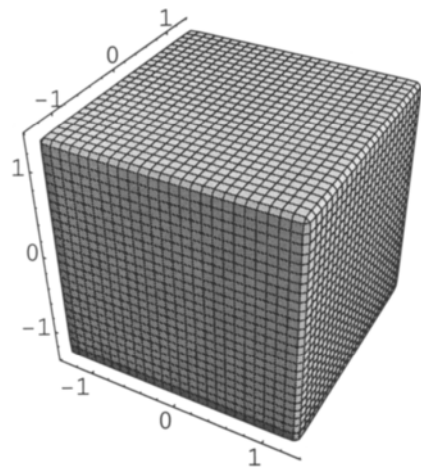


Figure 5.2.10 Still higher exponentials give still higher curvature on the corners and edges.

$$e^{x^2} + e^{y^2} + e^{z^2} = 1000 \quad 5.2.10$$

$$e^{x^6} + e^{y^6} + e^{z^6} = 1000 \quad 5.2.11$$

For polyhedra with parallel faces it is good to use higher exponentials, as shown in equations 5.2.10 and 5.2.11, and figures 5.2.9 and 5.2.10.

The tetrahedron and the octahedron have the same sets of planes, eight pairwise parallel in the octahedron and four in the tetrahedron, so we use the equations 5.2.12 and 5.2.13 which are plotted in figures 5.2.11-12. The sets of planes are the same as the ones used to make the D-surface in chapter 4.

$$e^{(x+y+z)^3} + e^{(x-y-z)^3} + e^{(-x-y+z)^3} + e^{(-x+y-z)^3} = 4 \cdot 10^4 \quad 5.2.12$$

$$e^{(x+y+z)^4} + e^{(x-y-z)^4} + e^{(-x-y+z)^4} + e^{(-x+y-z)^4} = 4 \cdot 10^4 \quad 5.2.13$$

Other polyhedra will be constructed when needed later.

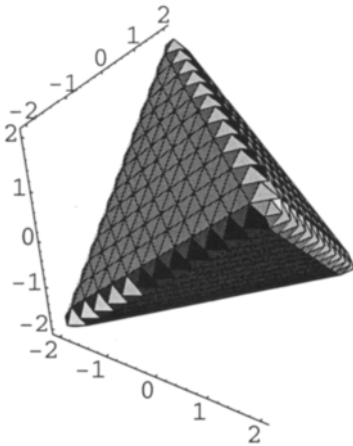


Figure 5.2.11 Exponential tetrahedron.

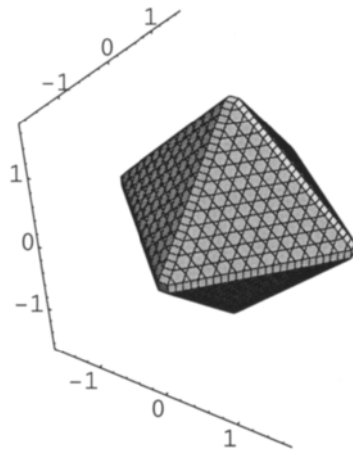


Figure 5.2.12 Exponential octahedron.

5.3 The Gauss Distribution (GD) Function and Simple Motion

When functions are very similar, concentric or parallel, we use the negative scale. We have plotted the two functions in equations 5.3.0a and b below in figures 5.3.0a and b, and the difference is dramatic.

$$e^{x^2+y^2+z^2} + e^{x^2+y^2+(z-2)^2} = 20 \tag{5.3.0a}$$

$$e^{-(x^2+y^2+z^2)} + e^{-(x^2+y^2+(z-2)^2)} = 0.8 \tag{5.3.0b}$$

The exponential equation with negative terms have the two spheres resolved, which we discuss to some length below.

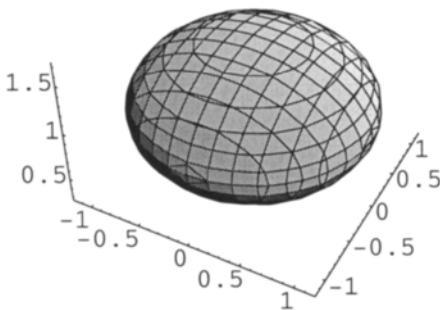


Figure 5.3.0a Two spheres after ordinary exponentials.

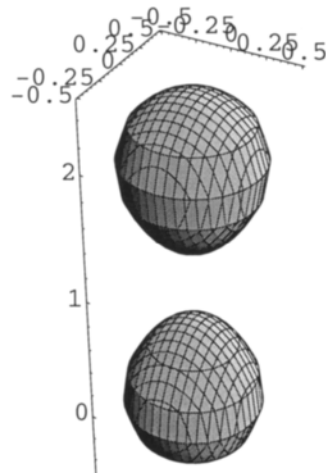


Figure 5.3.0b The same spheres after the GD function.

Next we turn to the Gauss distribution function, or the GD function, which in one dimension is e^{-x^2} .

We plot first the equation

$$e^{-x^2} = C, \tag{5.3.1}$$

which has two planes in 3D that go apart for smaller $C=0.1$ in figure 5.3.1, and come together for increasing $C=0.9$ in figure 5.3.2, to one plane $x=0$ for $C=1$.

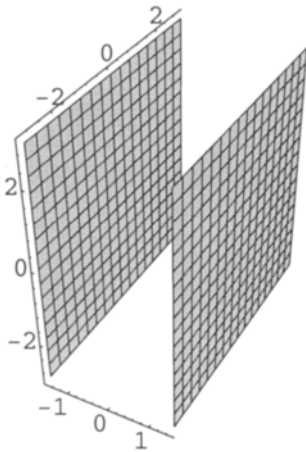


Figure 5.3.1 Two planes after GD function $e^{-x^2} = 0.1$.

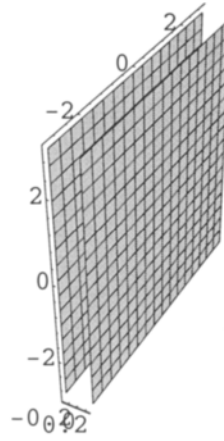


Figure 5.3.2 Two planes after GD function $e^{-x^2} = 0.9$.

The fundamental solution to the diffusion equation at $t=0$ is the GD distribution as in equation 5.3.2.

$$u = e^{-x^2}$$

5.3.2

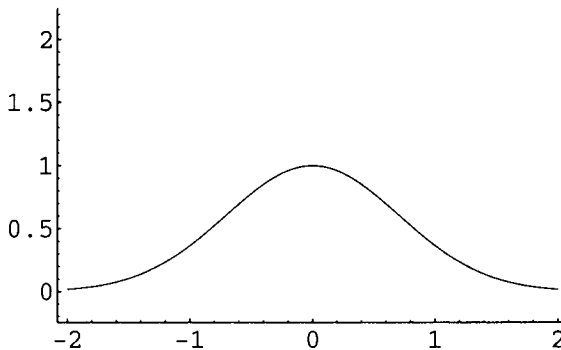


Figure 5.3.3 The GD function $y = e^{-x^2}$.

Changing to Cartesian, the concentration u can be expressed as in equation 5.3.3.

$$y = e^{-x^2} \quad 5.3.3$$

This is also called a GD profile, or a GD function of a concentration gradient, or the error function, and shown in figure 5.3.3.

We have found that this function can be moved and made bigger given proper coordinates, as in the explicit equation 5.3.4 and figure 5.3.4.

$$y = e^{-(x)^2} + 2e^{-(x-8)^2} \quad 5.3.4$$

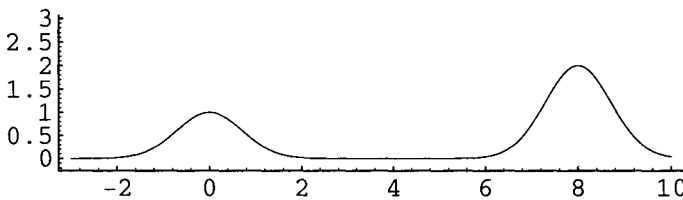


Figure 5.3.4 Two GD exponentials in one function.

For $x=0$, y is very close to 1, and for $x=8$, y is close to 2. For x -values around 4, y is close to e^{-16} , which is a very small number. This is the nature of the GD function, and it is used to describe finite periodicity below. Functions with very similar behaviour are the square of sech (solitary wave function), the sech itself and a Hermite function like xe^{-x^2} .

We multiply the GD functions in 3D,

$$e^{-x^2} e^{-y^2} e^{-z^2} = C$$

which is

$$e^{-(x^2+y^2+z^2)} = C. \quad 5.3.5$$

Plotted, this is a sphere, and the size of it may be changed using one of the constants in equation 5.3.6.

$$Ae^{-B(x^2+y^2+z^2+r)} = C \tag{5.3.6}$$

This sphere can be moved as an ordinary sphere, but we can also put two spheres next to each other by giving them different coordinates as in equation 5.3.7, which is shown in figure 5.3.5. Similar was done in the explicit example above in equation 5.3.4, and in equations 5.3.0a and 5.3.0b. The two spheres are described by one mathematical function, which causes a geometrical distortion appearing as if there was a physical attraction between the two. They can be moved to meet each other and we give an example of that below. Here they come closer by growing, from the change of constant.

$$e^{-(x^2+y^2+z^2)} + e^{-(x^2+y^2+(z-3)^2)} = 0.3 \tag{5.3.7}$$

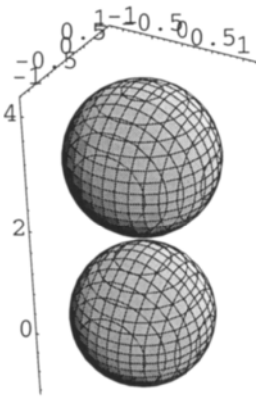


Figure 5.3.5 Two GD spheres after equation 5.3.7.

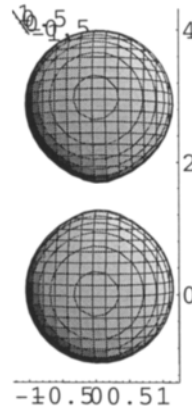


Figure 5.3.6 Different projection of figure 5.3.5.

We can precast when the two bodies meet, a catenoid starts to form which is at a constant of $2e^{-1.5^2} \approx 0.2108$. This is when the function exist for a value of $z=1.5$, $x=0$ and $y=0$, which is right between the two bodies, and shown after equation 5.3.8 in figure 5.3.7.

$$e^{-(x^2+y^2+z^2)} + e^{-(x^2+y^2+(z-3)^2)} = 0.2108 \tag{5.3.8}$$

For a higher constant the two bodies are isolated, and for a smaller constant the catenoid has developed, which is shown in figure 5.3.8, calculated with a constant of 0.18.

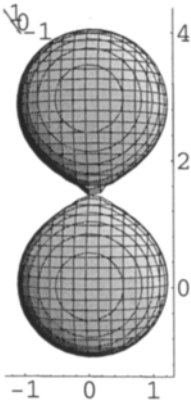


Figure 5.3.7 Two GD spheres meet after equation 5.3.8.

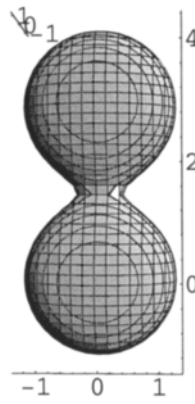


Figure 5.3.8 The two GD spheres meet after equation 5.3.8.

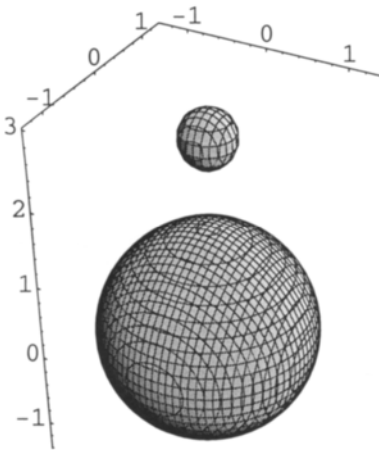


Figure 5.3.9 Small sphere/vesicle moves after equation 5.3.9. $\Delta z=0$.

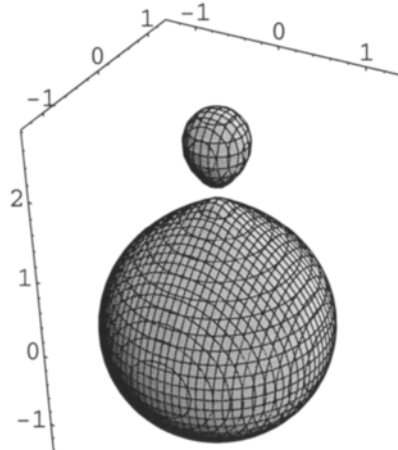


Figure 5.3.10 $\Delta z=0.2$.

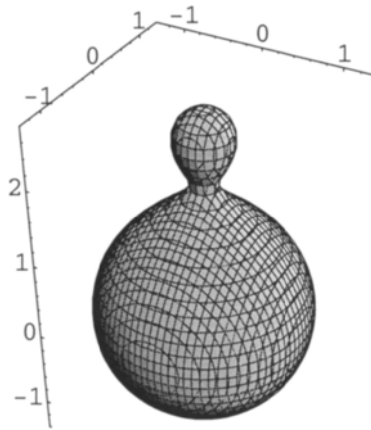


Figure 5.3.11 $\Delta z=0.22$.

We also wish to model how a very small vesicle interacts with a much larger one. We formulate equation 5.3.9, and with a small weight on one of the spheres/vesicles, its size is reduced as shown in figure 5.3.9. Now we move the small one by changing the distance from 2.6 to 2.4, and also to 2.36 via Δz in figures 5.3.10 and 5.3.11.

$$e^{-(x^2+y^2+z^2)} + \frac{1}{5}e^{-(x^2+y^2+(z-(2.6-\Delta z))^2)} = 0.18 \quad 5.3.9$$

The mathematical picture of attraction is an overlap of two functions, and we shall do an experiment to enlighten this description.

In figure 5.3.7 a very thin catenoid had formed at a constant of 0.2108. An extra particle, weighted to be very small, is added in equation 5.3.10. The effect is dramatic, the small particle/vesicle is fused into a well developed catenoid as shown in figure 5.3.12.

We may also subtract the same particle in the neighbourhood, and this is done in equation 5.3.11, and shown in figure 5.3.13, as a projection. The distortion of the spheres indicates repulsion.

We have seen typical pictures of physical attraction and repulsion with the origin in simple variations of one mathematical function. Attraction is due to the addition of a particle, and the repulsion is due to the loss of one.

$$e^{-(x^2+y^2+z^2)} + e^{-(x^2+y^2+(z-3)^2)} + \frac{1}{10}e^{-(x^2+y^2+(z-1.5)^2)} = 0.2108 \tag{5.3.10}$$

$$e^{-(x^2+y^2+z^2)} + e^{-(x^2+y^2+(z-3)^2)} - \frac{1}{10}e^{-(x^2+y^2+(z-1.5)^2)} = 0.2108 \tag{5.3.11}$$

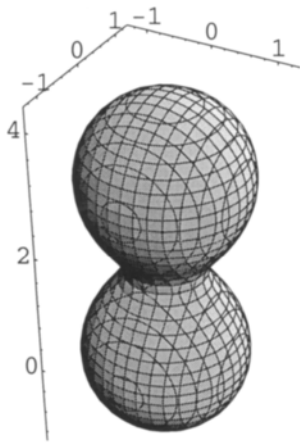


Figure 5.3.12 A very small particle/vesicle is added to two spheres/vesicles just in contact as in figure 5.3.7, and transforms to a well developed catenoid.

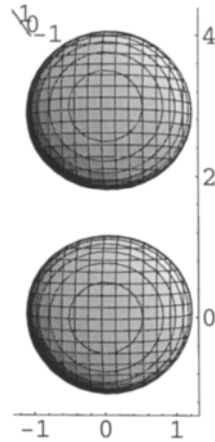


Figure 5.3.13 A very small sphere/vesicle is subtracted.

This is also shown in two dimensions. Equation 5.3.12 expresses attraction as a particle is added.

$$e^{-(x^2+(y-1.7)^2)} + 0.4e^{-((x-\Delta x)^2+y^2)} + e^{-(x^2+(y+1.7)^2)} = 0.4 \tag{5.3.12}$$

Δx takes the values of 2, 1.5, 1, 0, -1.5 in figures 5.3.14 a-e. The Δx corresponds to the motion of the small particle.

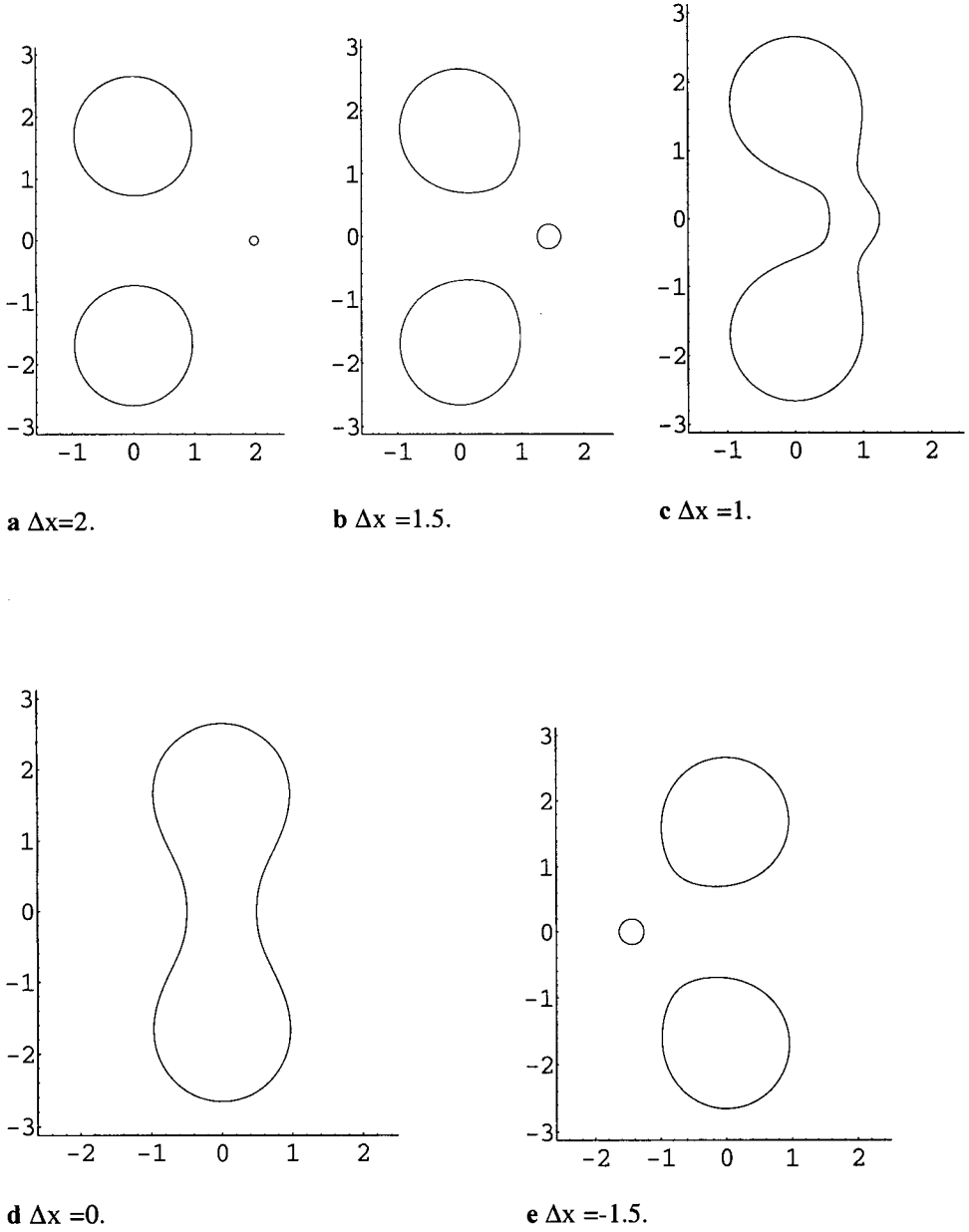


Figure 5.3.14 A small particle/vesicle is passing between two bigger under interactions.

Equations 5.3.13-14 demonstrate the repulsion as a particle/vesicle is subtracted in figures 5.3.15 a-b.

$$e^{-(x^2+(y-1.25)^2)} + e^{-(x^2+(y+1.25)^2)} = 0.4 \tag{5.3.13}$$

$$e^{-(x^2+(y-1.25)^2)} - 0.4e^{-((x)^2+y^2)} + e^{-(x^2+(y+1.25)^2)} = 0.4 \tag{5.3.14}$$

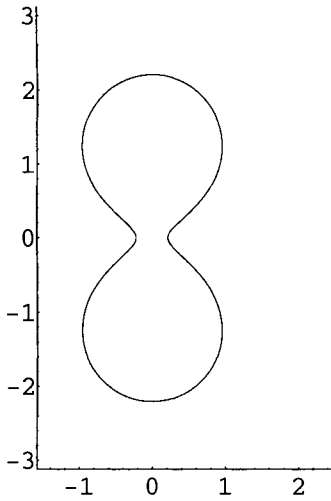


Figure 5.3.15a Two particles/vesicles.

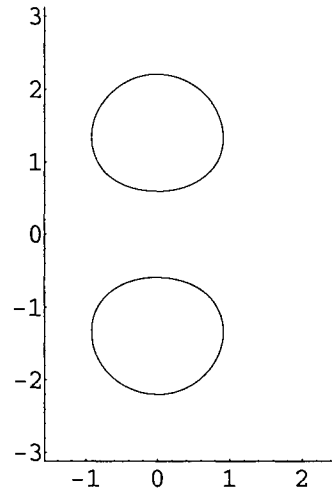


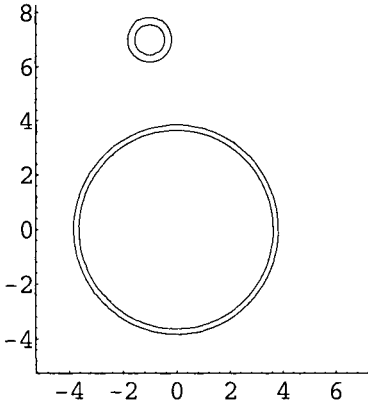
Figure 5.3.15b A small particle/vesicle is subtracted.

We have found it useful to square a function. As $x^2=1$ has two roots and forms two planes, the square of the equation of a circle becomes two circles. This can be regarded as a more complete structure description of the plasma membrane around a cell or a vesicle, showing the outer surfaces of the lipid bilayer. If we use the squares as in equation 5.3.14, we see in figure 5.3.16 how a small vesicle can go right through a bigger one. We will below relate this mechanism to pinocytosis, *i.e.* a flow of vesicles through a cell.

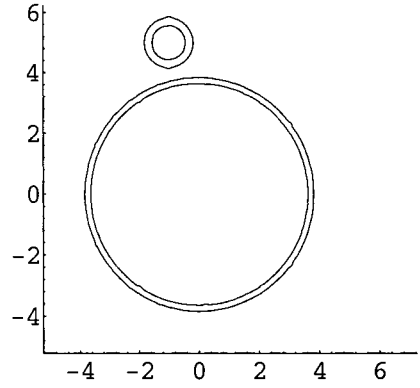
$$e^{-(x^2+y^2-14)^2} + e^{-4[(x+\Delta x)^2+(y-\Delta y)^2-0.5]^2} = 0.6 \tag{5.3.14}$$

For the figures 5.3.16 a-1 the Δx and Δy take the pairwise values below.

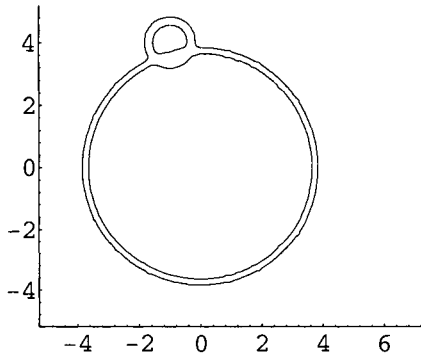
- 1,-7; 1,-5; 1,-4; 1,-3.2; 1,-2.8; .5,-2; -.5,-1; -2,-.5; -3,0; -4.1,0; -5,.5; -7,1;



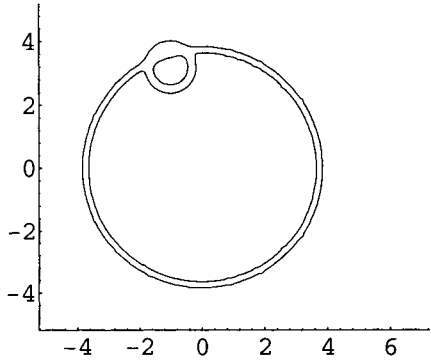
a



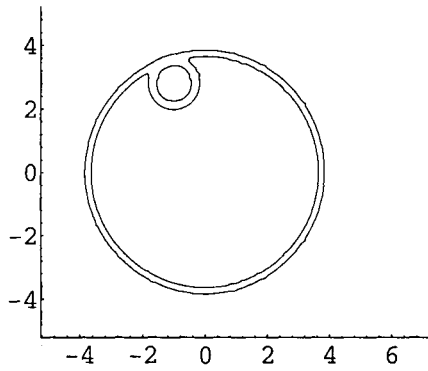
b



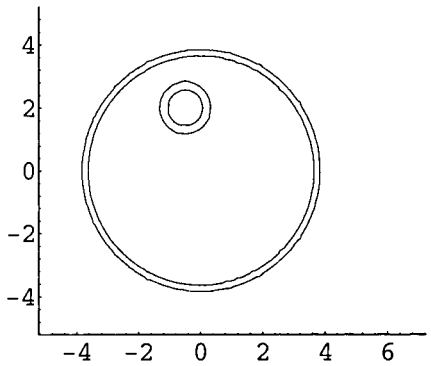
c



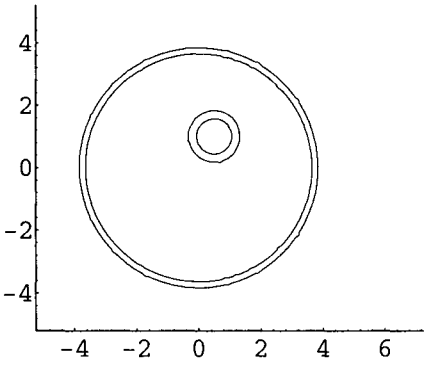
d



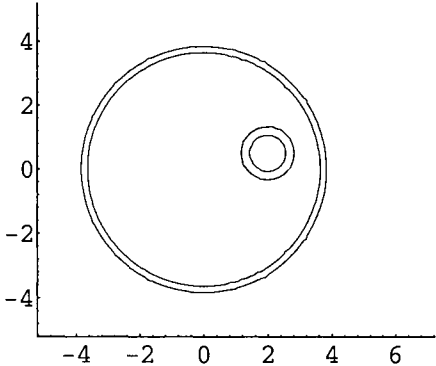
e



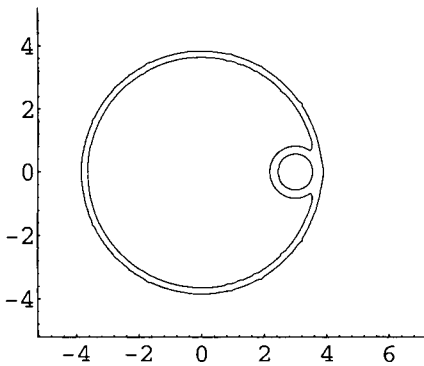
f



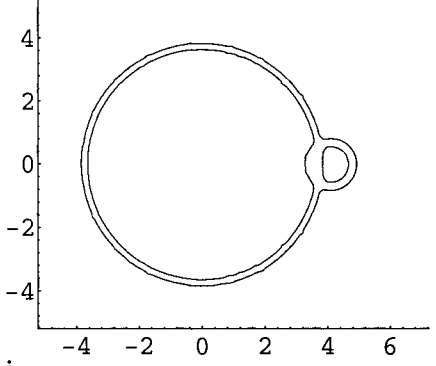
g



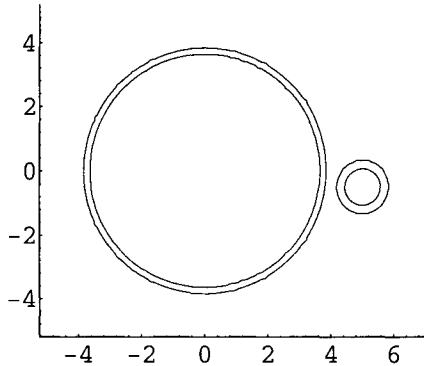
h



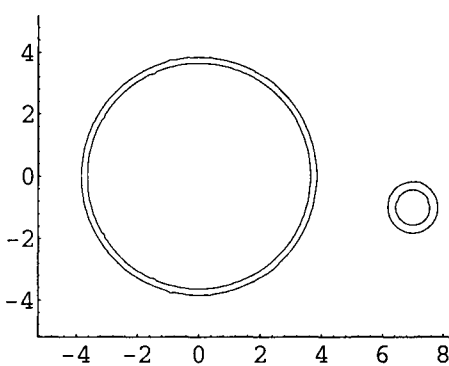
i



j



k



l

Figure 5.3.16 A small particle/vesicle going through a bigger. Δx and Δy from above.

Vesicles control the transport in and out from cells by processes called endocytosis and exocytosis respectively. Endocytosis is usually achieved via coat-proteins in the plasma membrane, such as clathrin. A kind of cage is formed by clathrin, and with the lipid bilayer a vesicle is successively formed (coated vesicle).

Pinocytosis is endocytosis taking place by small vesicles (radius below 100 nm), and often this transport goes through the whole cell (transcytosis). One example is the efficient flow of macromolecules through the endothelial cells lining blood vessels. These vesicles are not coated by clathrin. Another example is the flow through the tubule cell of the kidney, as shown in figure 5.3.17 [9].

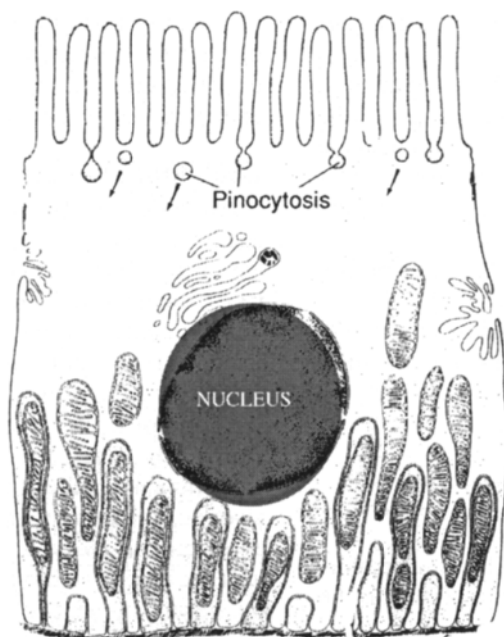


Figure 5.3.17 Illustration of transcytosis via flow of pinocytic vesicles through kidney tubuli cells. The protein molecules from the lumen side are digested by lysosomes during the passage. Modified after [9].

There is no physical explanation of this efficient flow through cells in the literature. The model shown above seems relevant in order to understand the bilayer mechanisms. See further chapter 8.

5.4 More Motion in 3D

We show three vesicles and two sets of GD-planes in a number of pictures after equation 5.4.1. We make only one of the vesicles move, and Δx describes this in equation 5.4.1 and takes the values 3, 2, 1, 0, -1 and -2. In figures 5.4.1a-e this is shown, and we see that a vesicle fuses with the plane/membrane. At the other side a new vesicle is formed and the operation continues.

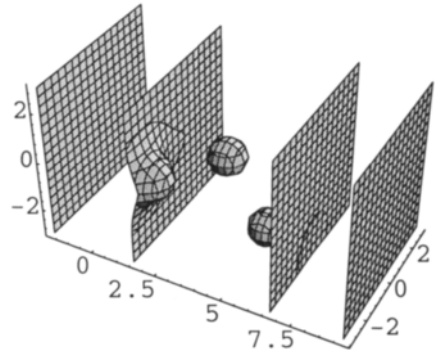
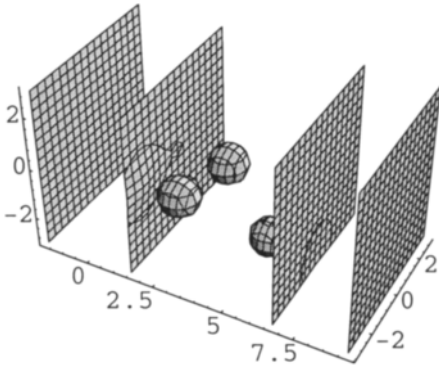
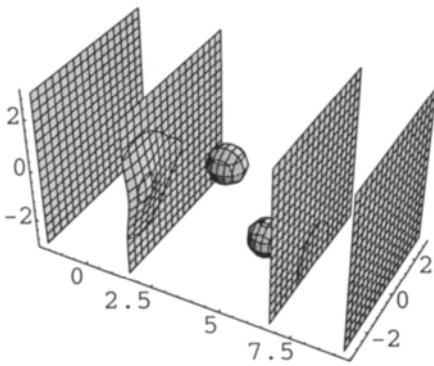
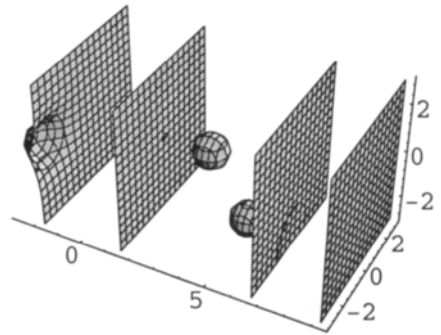


Figure 5.4.1 Only one of several vesicles move with Δx . **a** $\Delta x = 3$.

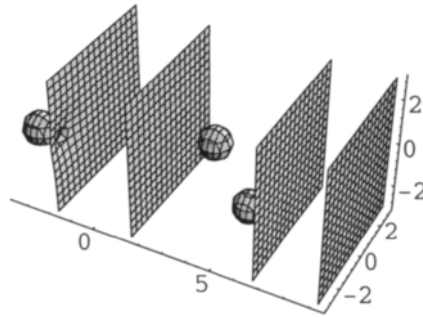
b $\Delta x = 2$.



c $\Delta x = 1$.



d $\Delta x = 0$.



$$e \Delta x = -1.$$

$$\begin{aligned} & \frac{1}{4}e^{-[(x-3.5)^2+y^2+z^2-\frac{1}{4}]} + \frac{1}{4}e^{-[(x-\Delta x)^2+(y+2.3)^2+z^2-\frac{1}{4}]} \\ & + \frac{1}{4}e^{-[(x-5)^2+y^2+(z+2.5)^2-\frac{1}{4}]} + e^{-(x^2-1)} + e^{-(x-8)^2} = 0.2 \end{aligned} \tag{5.4.1}$$

Catenoids are very commonly formed in structures occurring in nature, for example at liquid interfaces.

First a simple catenoid is made from a double cone after equations 5.4.2-3, and shown in figures 5.4.2-3.

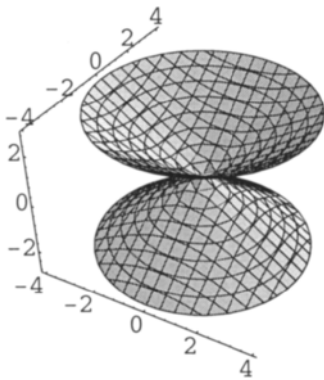


Figure 5.4.2 Catenoid from 5.4.2.

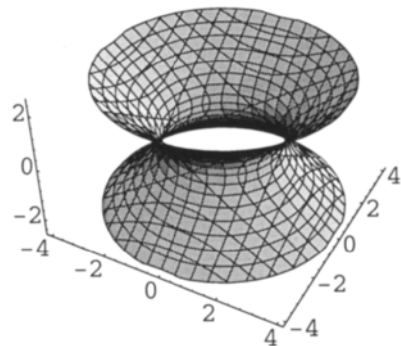


Figure 5.4.3 Different constant.

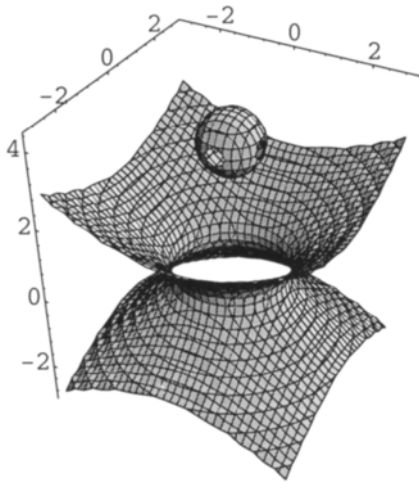
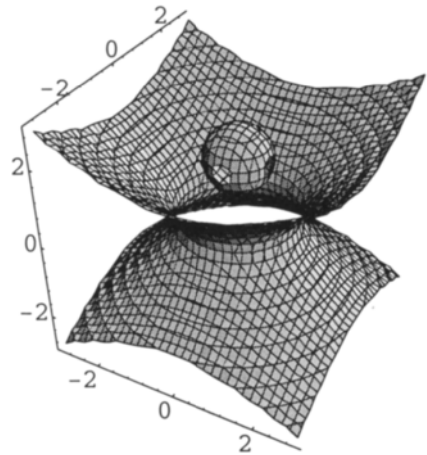
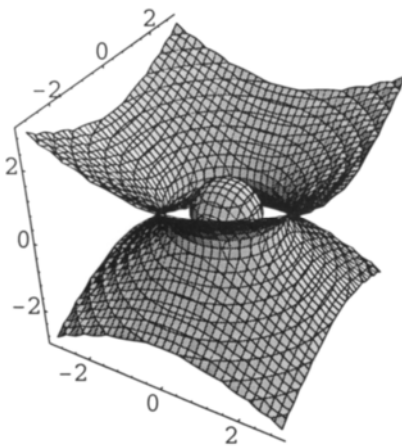


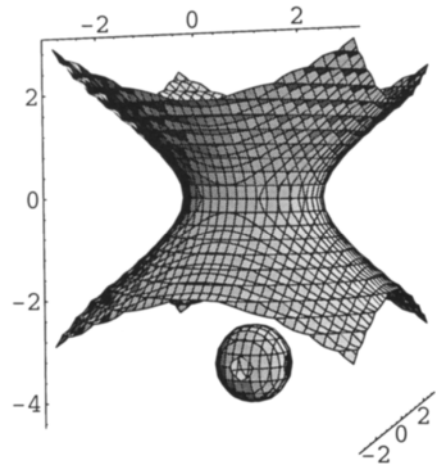
Figure 5.4.4 A particle moves through a catenoid after 5.4.4.
a $\Delta z = 3.5$.



b $\Delta z = 1.5$.



c $\Delta z = 0$.



d $\Delta z = -3.5$.

$$x^2 + y^2 - 2z^2 = 0 \tag{5.4.2}$$

$$x^2 + y^2 - 2z^2 - 4 = 0 \tag{5.4.3}$$

A spherical body, which may be a protein molecule or a vesicle, goes through the catenoid under interactions, if modelled by these mathematics. We go exponential to keep the two geometries apart. The equation is 5.4.4.

$$e^{x^2+y^2-2z^2-4} + e^{-3[x^2+y^2+(z-\Delta z)^2]} = 0.15 \quad 5.4.4$$

Δz describes the motion of the particle, and takes the values 3.5, 1.5, 0, and -3.5 for the figures 5.4.4a-d.

Interaction is studied with a bigger sphere with equation 5.4.5.

$$e^{x^2+y^2-2z^2-4} + e^{-1.6[x^2+y^2+(z)^2]} = 0.15 \quad 5.4.5$$

Reaction between the particle and the catenoid under these conditions gives high curvature which cracks the particle, as seen in figure 5.4.5.

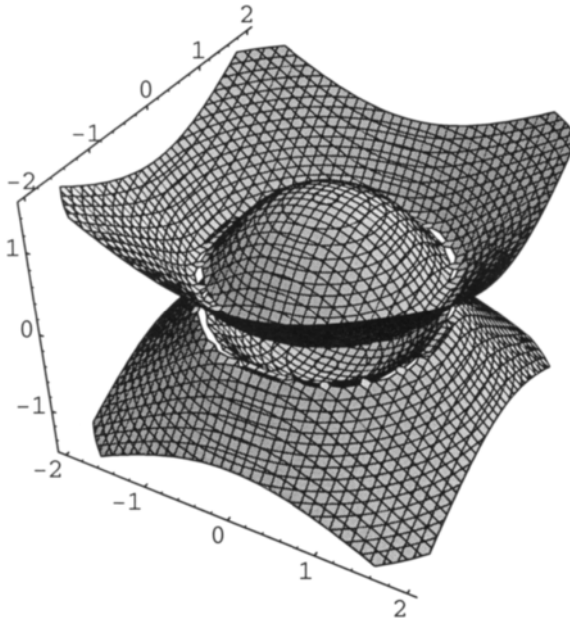


Figure 5.4.5 A particle and the catenoid are reacting.

Figure 5.4.6a-d shows the passage of a body shaped as a cube through the catenoid, and the corresponding equation is in 5.4.6.

$$e^{x^2+y^2-2z^2-4} + e^{-2[x^6+y^6+(z-\Delta z)^6]} = 0.15 \tag{5.4.6}$$

Δz describes the motion of the particle and takes the values 3, 0, -3, for the figures 5.4.6a-d. Figure 5.4.6c is the projection of b.

The interaction occurs via opening of catenoids from the cube edges as seen in 5.4.6c.

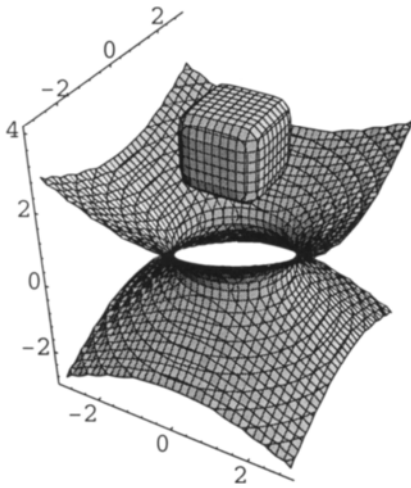


Figure 5.4.6a A cube is going through a catenoid. a $\Delta z=3$.

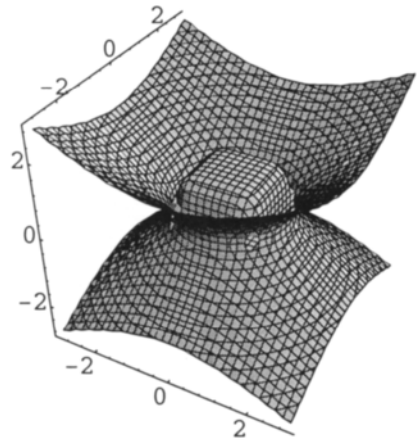


Figure 5.4.6b $\Delta z=0$.

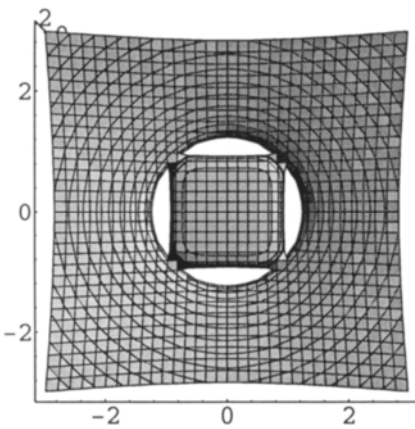


Figure 5.4.6c projection of b.

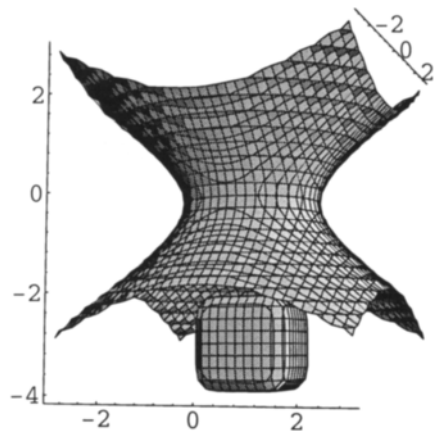


Figure 5.4.6d $\Delta z=-3$.

We want to make a tetrahedron go through, and therefore formulate equation 5.4.7.

$$e^{(x^2+y^2-2z^2-4)} + e^{-0.4[e^{x+y+z-\Delta z} + e^{x-y-z+\Delta z} + e^{-x-y+z-\Delta z} + e^{-x+y-z+\Delta z}]} = 0.15 \quad 5.4.7$$

Δz varies as 3, 0, -3 for figures 5.4.7a-c.

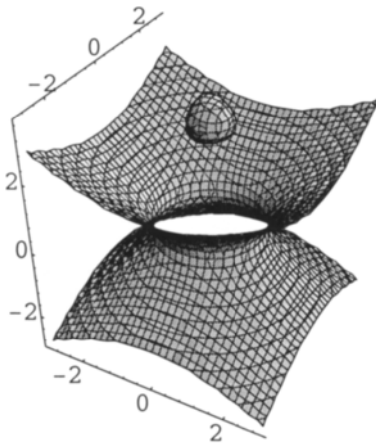


Figure 5.4.7a A tetrahedron is approaching a catenoid.

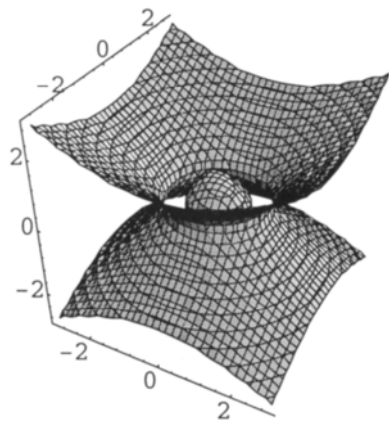


Figure 5.4.7b The tetrahedron has reached the centre of the catenoid.

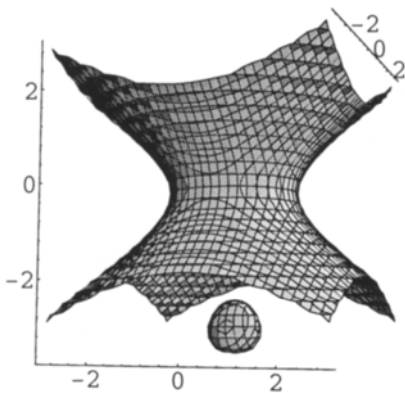


Figure 5.4.7c The tetrahedron has gone through the catenoid.

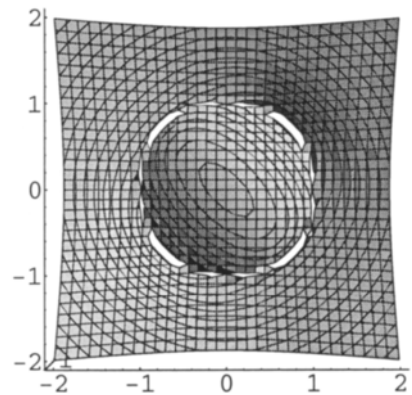


Figure 5.4.8 A bigger tetrahedron is reacting.

For figure 5.4.8 and equation 5.4.8, the tetrahedron is larger, and again the edges make interactions in form of catenoids.

$$e^{(x^2+y^2-2z^2-4)} + e^{-0.362[e^{x+y+z} + e^{x-y-z} + e^{-x-y+z} + e^{-x+y-z}]} = 0.15 \tag{5.4.8}$$

A sphere goes through a torus, and the equation is in 5.4.9, with the figures 5.4.9a-e. The Δz :s are 4, 2, 0, -2, -4.

$$e^{-(((x^2+y^2)^{0.5}-4)^2+z^2)} + e^{-(x^2+y^2+(z-\Delta z)^2)} = 0.2 \tag{5.4.9}$$

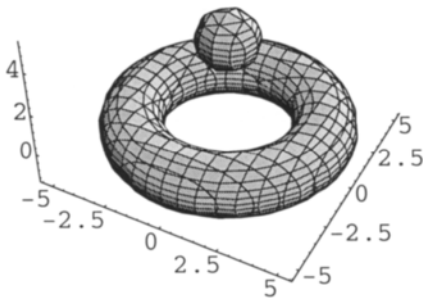


Figure 5.4.9a A sphere goes through a torus. a $\Delta z=4$.

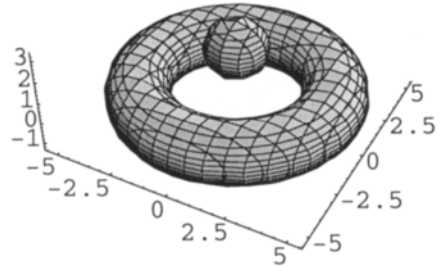


Figure 5.4.9b $\Delta z=2$.

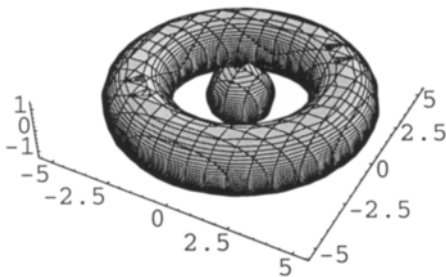


Figure 5.4.9c $\Delta z=0$.

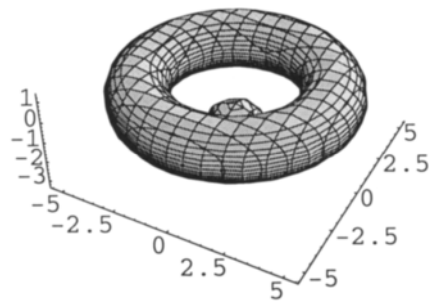


Figure 5.4.9d $\Delta z=-2$.

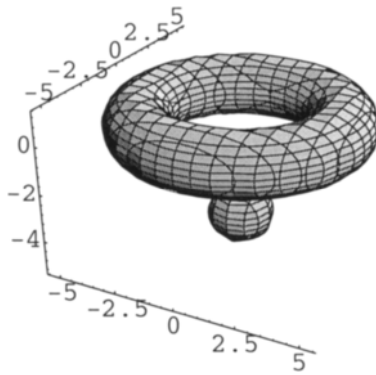


Figure 5.4.9e $\Delta z = -4$.



Figure 5.4.10 Polymerase and DNA. Reproduced with permission from ref. [7].

By making the sphere bigger, interaction occurs with the torus, of the same circular kind as in figure 5.4.5.

We wish to show an example in molecular biology of the dynamics above. In figure 5.4.10, from x-ray crystallography [7], there are two sub-units of the enzyme polymerase III that form a doughnut, or torus, around DNA, which permits the enzyme to synthesise long stretches of DNA. The polymerase ring may also slide along the DNA. We have formulated an equation for this motion. First we show the DNA molecule of different groves after equation 5.4.10 and ref. [8].

$$\begin{aligned}
 & e^{\frac{1}{5}(x^2+y^2)} + e^{(y \cos \frac{\pi}{2} z + x \sin \frac{\pi}{2} z)} \\
 & + \frac{1}{2} e^{(y \cos \frac{\pi}{2}(z+2) + x \sin \frac{\pi}{2}(z+2))} = 3.5
 \end{aligned}
 \tag{5.4.10}$$

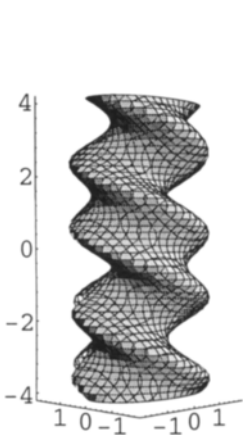


Figure 5.4.11 DNA from ref. [8].

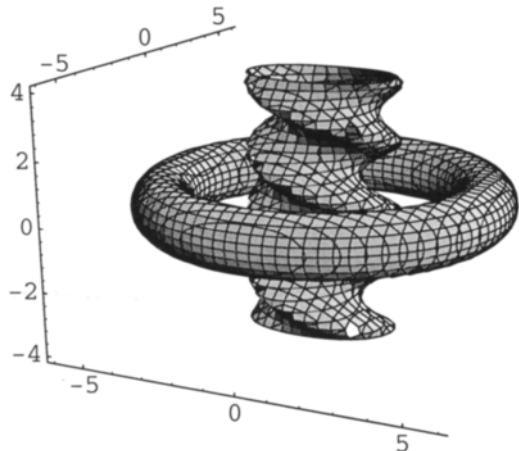


Figure 5.4.12 DNA goes through a torus.

Now we formulate equation 5.4.11, to make this DNA molecule go through a torus.

Above in figure 5.4.12, Δ is zero, but below Δ is 4, making the torus slide on the DNA molecule in the job of replication, or proof reading.

$$4e^{-\frac{1}{2}\left[e^{\frac{1}{5}(x^2+y^2)} + e^{(y \cos \frac{\pi}{2} z + x \sin \frac{\pi}{2} z)} + \frac{1}{2}e^{(y \cos \frac{\pi}{2}(z+2) + x \sin \frac{\pi}{2}(z+2))}\right]} + e^{-\left(\left((x^2+y^2)^{0.5}-5\right)^2 + (z+\Delta)^2\right)} = 0.4 \quad 5.4.11$$

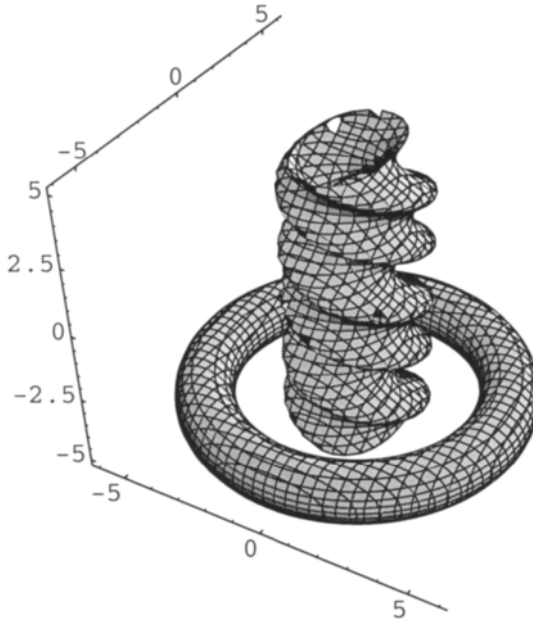


Figure 5.4.13 DNA continues sliding through a torus.

References 5

- 1 Shakespeare, *The Merchant of Venice*.
- 2 J. B. Marion and S. T. Thornton. *Classic Dynamics*, third edition, HB, 1988.
- 3 R. Hoffmann, *SOLIDS and SURFACES, A Chemist's View of Bonding in Extended Structures*. VCH, 1988.
- 4 D. A. Davies, *Waves, Atoms and Solids*. Longman 1978.

-
- 5 S. Andersson and M. Jacob, *THE MATHEMATICS OF STRUCTURES, THE EXPONENTIAL SCALE*, Oldenbourg, München, 1997.
 - 6 Andersson, S., Jacob, M., Lidin, S.: On the Shape of Crystals. *Z. Kristallogr.* **210**, 3-4 (1995).
 - 7 A.L. Lehninger, D.L. Nelson, M.M. Cox, *PRINCIPLES OF BIOCHEMISTRY*, page 788, Second edition, Worth Publishers, 1993.
 - 8 M. Jacob and S. Andersson, *THE NATURE OF MATHEMATICS AND THE MATHEMATICS OF NATURE*, page 152, Elsevier, 1998.
 - 9 L.C. Junqueira, J. Carnerio and R.O. Kelly, *BASIC HISTOLOGY*, page 42, Printice Hall, Norfolk, Connecticut, Int. Inc. 1992.

This Page Intentionally Left Blank

6 Periodicity in Biology - Periodic Motion

The scene is Hollywood; Archimedes is meeting Newton to shoot the Millenniums in the year 1999.

Archimedes: Euclid started his geometry with a point; what do you start dynamics with?

I start with a body, replied Newton.

Archimedes cried: ... I am eaten with impatience, how is this body defined? What is its size? What is its shape?... perhaps it is just a mathematical point in motion?

Newton blushed slightly [Synge,1].

Periodic translation motion is described with damped circular functions, equivalent with the Hermite function.

In this way the flagella movements are described as snake and screw motions.

During a damped periodic particle motion the particle/object changes shape.

Rotation in biology is described as a double translation operation. Circular and elliptical orbits are described.

6.1 The Hermite Function

The basics of periodicity was given in chapter 2 with the link between the fundamental theorem of algebra and the circular functions. Finite periodicity is described as finite products of roots.

The GD-function is in statistics called the error function, and was discussed in chapter 5. In chemistry it is used to describe concentration gradients, and as such, a solution to the diffusion equation. In physics the equivalent is valid for heat.

The GD-function is unique as there exist no anti-derivative expression, which means it must be evaluated numerically.

Some simple and fundamental mathematics of the GD-function lead us over to the foundation of finite and infinite periodicity. Nature has also examples of almost periodic phenomena, where the DNA molecule is one example which has stimulated the study below.

The Hermite polynomials build some of the most famous nearly periodic functions.

We give the derivatives of the GD-function, starting with the GD-function with each successive derivative below.

$$\begin{aligned}
 &e^{-x^2} \\
 &-2xe^{-x^2} \\
 &(-2 + 4x^2)e^{-x^2} \\
 &(12x - 8x^3)e^{-x^2} \\
 &(12 - 48x^2 + 16x^4)e^{-x^2} \\
 &(-120x + 160x^3 - 32x^5)e^{-x^2} \\
 &(-120 + 720x^2 - 480x^4 + 64x^6)e^{-x^2}
 \end{aligned} \tag{6.1.1}$$

These derivatives, also called Hermite functions, consist of the Hermite polynomials multiplied with the GD-function itself. So the GD-function is an essential part of the Hermite function, and is often called a weight or damping function.

With the proper physical constants, these are the Schrödinger wave functions of the harmonic oscillator, with the GD-function itself as the ground state.

We shall show that these polynomials are very similar to the polynomials that build the roots of the fundamental theorem of algebra. We start by using the polynomial from the fourth derivative of the GD-function,

$$x^4 - 3x^2 + y^4 - 3y^2 + z^4 - 3z^2 + 2.25 = 0 \tag{6.1.2}$$

and show it in figure 6.1.1.

$$x(x-1)(x+1)(x-2) + y(y-1)(y+1)(y-2) + z(z-1)(z+1)(z-2) = 0 \tag{6.1.3}$$

The corresponding root function from the fundamental theorem of algebra, equation 6.1.3, is shown in figure 6.1.2, and the two structures are almost identical. Changing the constant in the Hermite polynomial, as in 6.1.4, gives figure 6.1.3, which is similar to the electron distribution of a B_6H_6 molecule

from Schrödinger calculations. The B_6H_6 octahedron has a similar shape as in figure 6.1.1, where only half of it is shown, while the electron distribution describes the dual form, which is a cube. This is the beginning of the description of molecules, small or big, with finite periodicity.

$$x^4 - 3x^2 + y^4 - 3y^2 + z^4 - 3z^2 + 3.5 = 0 \tag{6.1.4}$$

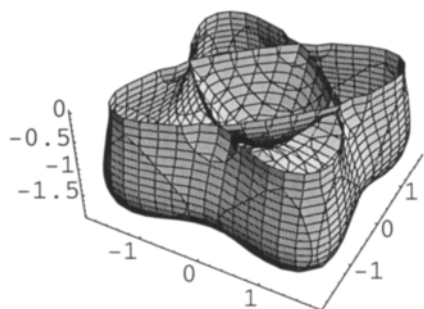


Figure 6.1.1 P-surface cubosome after a Hermite polynomial.

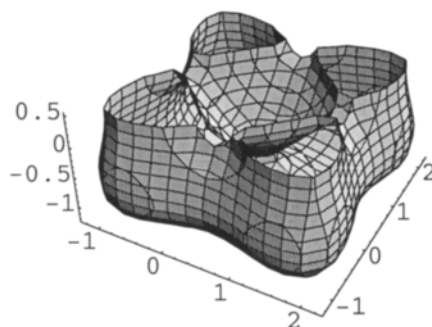


Figure 6.1.2 P-surface cubosome after the fundamental theorem of the algebra.

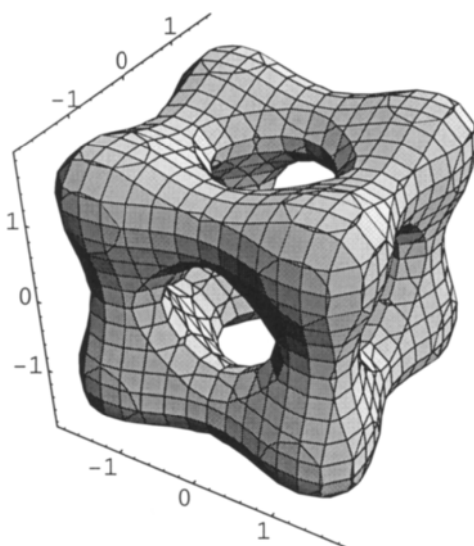


Figure 6.1.3 The B_6H_6 molecule from the Hermite polynomial of equation 6.1.4.

We also show the power expansions of sine and cosine, to point out the similarity with the Hermite polynomials. The odd polynomials are similar to sine, and the even are similar to cos.

$$\begin{aligned} \sin x &= x - \frac{x^3}{6} + \frac{x^5}{120} - \frac{x^7}{5040} + \dots \\ \cos x &= 1 - \frac{x^2}{2} + \frac{x^4}{24} - \frac{x^6}{720} + \dots \end{aligned} \tag{6.1.5}$$

We shall now compare the Hermite functions directly with cosine to study this similarity. We take advantage of the power of the computer program Mathematica in a case like this and use the routine

`HermiteH[n,x],`

where `n` stands for the order of the derivative, and the output is just the Hermite polynomials. While the Hermite polynomials oscillate violently, the functions do not, since they contain a damping term. We plot the equation 6.1.6 in figure 6.1.4, which simply is the derivative number eight of the GD-function.

$$e^{-x^2} \text{hermite}[8x] = y \tag{6.1.6}$$

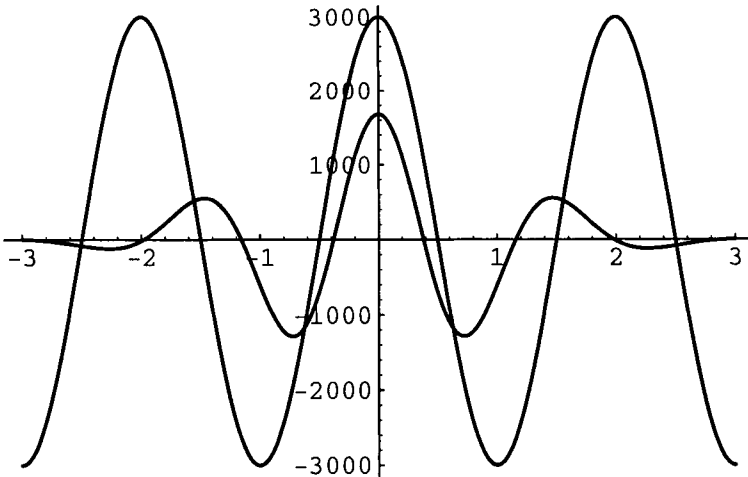


Figure 6.1.4 Hermite function of degree 8 as compared with cosine.

Next, we make the cosine function overlap as a separate function in form of equation 6.1.7, which is plotted in figure 6.1.4.

$$3000 \cos \pi x = y \quad 6.1.7$$

We shall show that the Hermite functions are very similar to the circular functions by reducing the power of the damping term, using $e^{-\frac{1}{2}x^2}$. So in equation 6.1.8 we calculate for various n the shapes, and compare corresponding cosine functions after 6.1.9, which is illustrated in figures 6.1.5-8.

$$e^{-\frac{1}{2}x^2} \text{hermite}[nx] = y \quad 6.1.8$$

$$n = 10$$

$$3 \cdot 10^4 \cos 1.5\pi x = y$$

$$n = 20$$

$$6.7 \cdot 10^{11} \cos 2\pi x = y \quad 6.1.9$$

$$n = 30$$

$$2 \cdot 10^{20} \cos 2.48\pi x = y$$

$$n = 40$$

$$3.4 \cdot 10^{29} \cos 2.84\pi x = y$$

We observe that with increasing n, the Hermite function is becoming very similar to cosine.

So we formulate the equation 6.1.10, when n is very high. In textbooks of quantum physics this is said to represent the wave function of a particle, and there called a wavelet or wave packet.

$$y = e^{-x^2} \cos 2\pi x \quad 6.1.10$$

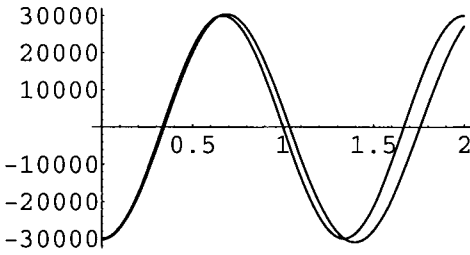


Figure 6.1.5 Hermite function of degree 10 as compared with cosine.

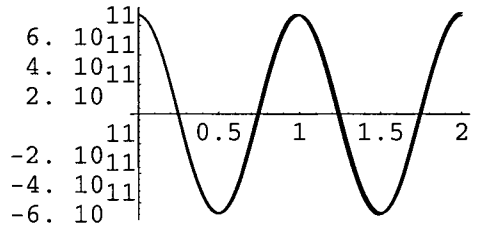


Figure 6.1.6 Hermite function of degree 20 as compared with cosine.

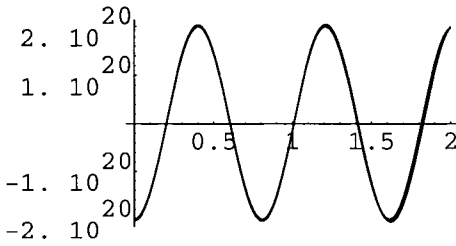


Figure 6.1.7 Hermite function of degree 30 as compared with cosine.

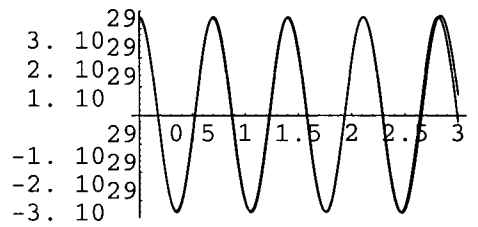


Figure 6.1.8 Hermite function of degree 40 as compared with cosine.

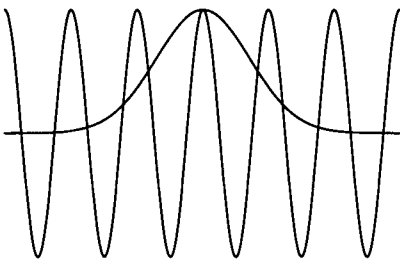


Figure 6.1.9 The GD-function compared with cosine.

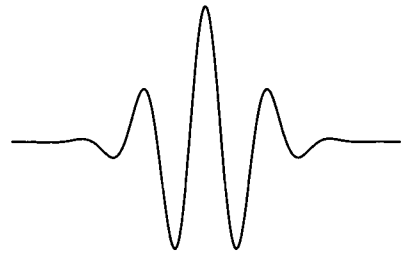


Figure 6.1.10 Cosine damped with the GD-function to become a wave packet.

In figure 6.1.9 we compare the GD-function with $\cos x$, plotted as two different functions. And in figure 6.1.10 we have multiplied the two terms after equation 6.1.10 to show the effect of damping. From figure 6.1.4 we see that the Hermite functions very early become similar to the damped cos function in equation 6.1.10.

For us this is indeed a very important function. Earlier we have shown that it can be used to describe the translation of structures of dilatation symmetries, which gives the mathematics to describe many structures in solid state science [2]. We shall use this application later in biology, but first we describe its use for motion, and in particular periodic motion.

6.2 Flagella - Snake and Screw Motion

In chapter 5 we showed that we could move things with a GD-function. We go back to the simple Hermite damping function used to describe a particle wave.

$$y = e^{-(x-\Delta x)^2} \cos 2\pi x \tag{6.2.1}$$

When Δx takes the values 0; 0.2; 0.4;...1, the curve moves as seen in figure 6.2.1a-f. This is periodic motion, or damped sinusoidal, in one plane, resembling the characteristic snake motion, which of course is similar to the movement of the paddle wheel, or to the way birds fly. And you can make a wave packet move - via the Hermite functions and their relations to the algebra, we understand that this is nothing but counting.

This is the way the flagella of sperms make these cells swim. In figures 6.2.2a-e we have used a piece of the function of equation 6.2.2, and let Δx takes the values 0; -0.4; -0.8;...-1.6. The pictures we obtain are similar to the pictures of the flagella sperms occurring in common textbooks [3]. As the sperm swims to the left, the head is also to the left.

$$y = e^{-\frac{1}{2}(x-\Delta x)^2} \cos \pi x \tag{6.2.2}$$

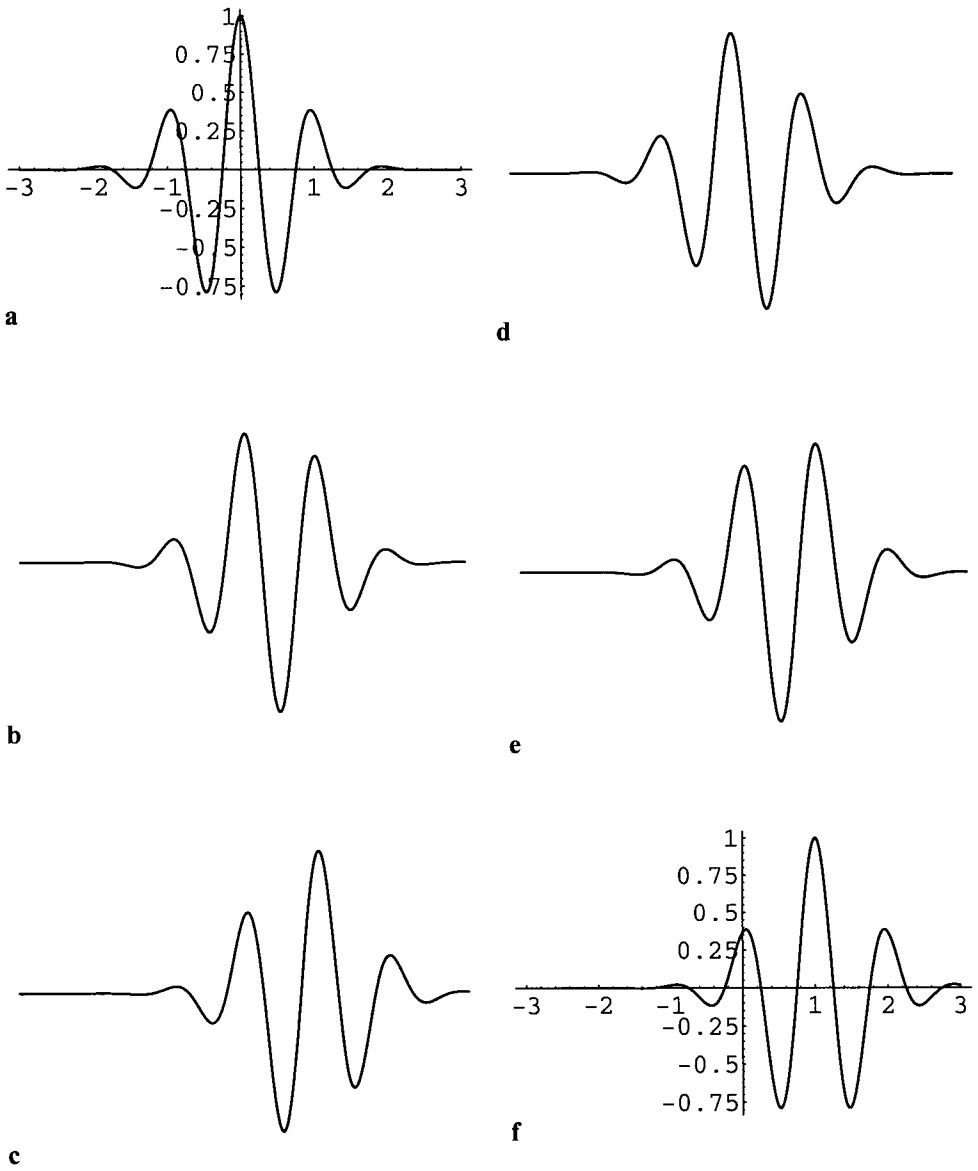


Figure 6.2.1a-f Biological motion modelled by a wavepacket after equation 6.2.1.

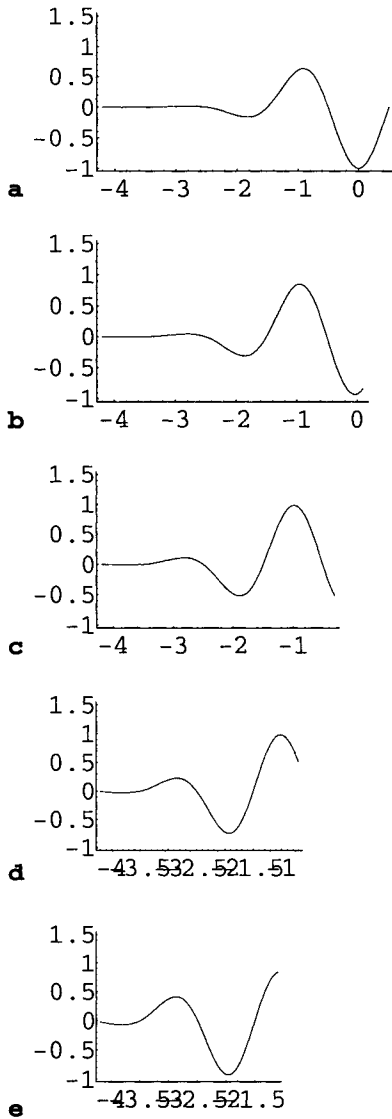


Figure 6.2.2a-e The flagellum of a sperm with movement modelled by equation 6.2.2.

There is an entirely different motion for the flagella of bacteria, an example is the *E. coli* bacteria, which swims with a helical tube or spiral movement. This is attached via an axis of rotation, an elongation of the spiral, to a motor built of ring-forming proteins, sitting in the outer and inner membrane of the bacteria. The ‘ship’ is driven by a propeller instead of a paddle wheel.

We now show how to derive the mathematics for this motion. We start by making a helicoid as in figure 6.2.3, with the classic equation in 6.2.3.

$$z \cos 2\pi x - y \sin 2\pi x = 0 \tag{6.2.3}$$

By enveloping a cylinder in equation 6.2.4, we get a helical tube in figure 6.2.4.

$$z \cos 2\pi x - y \sin 2\pi x + 4(x^2 + y^2) = 0 \tag{6.2.4}$$

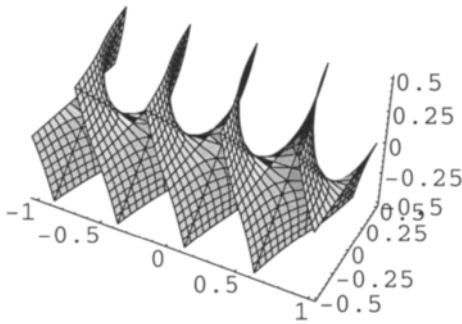


Figure 6.2.3 The helicoid.

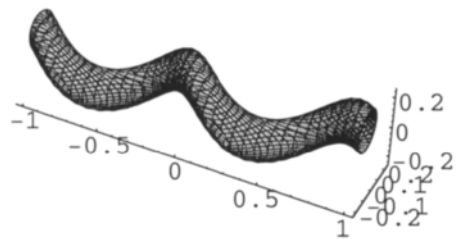


Figure 6.2.4 A spiral tube.

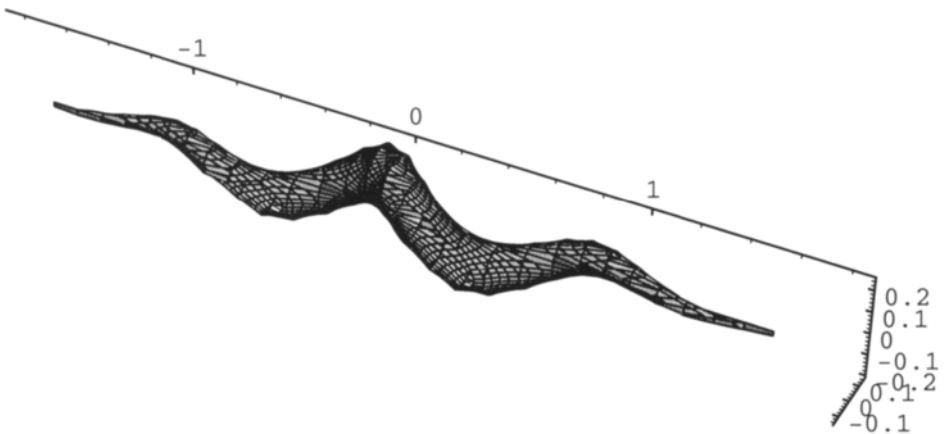


Figure 6.2.5 GD-damping of spiral tube gives a worm like screw.

We now do the damping as we did in the Hermite function, and as in the last example of moving the flagella sperm. The equation will simply be as in 6.2.5.

$$e^{-x^2} (z \cos 2\pi x - y \sin 2\pi x) + 4(x^2 + y^2) = 0 \tag{6.2.5}$$

This equation gives the beautiful worm in figure 6.2.5.

Now we make this worm or spiral move in the same way as we did with the flagellum of sperm, using the GD-function in equation 6.2.6.

$$e^{-(x-\Delta x)^2} (z \cos 2\pi x - y \sin 2\pi x) + 4(x^2 + y^2) = 0 \tag{6.2.6}$$

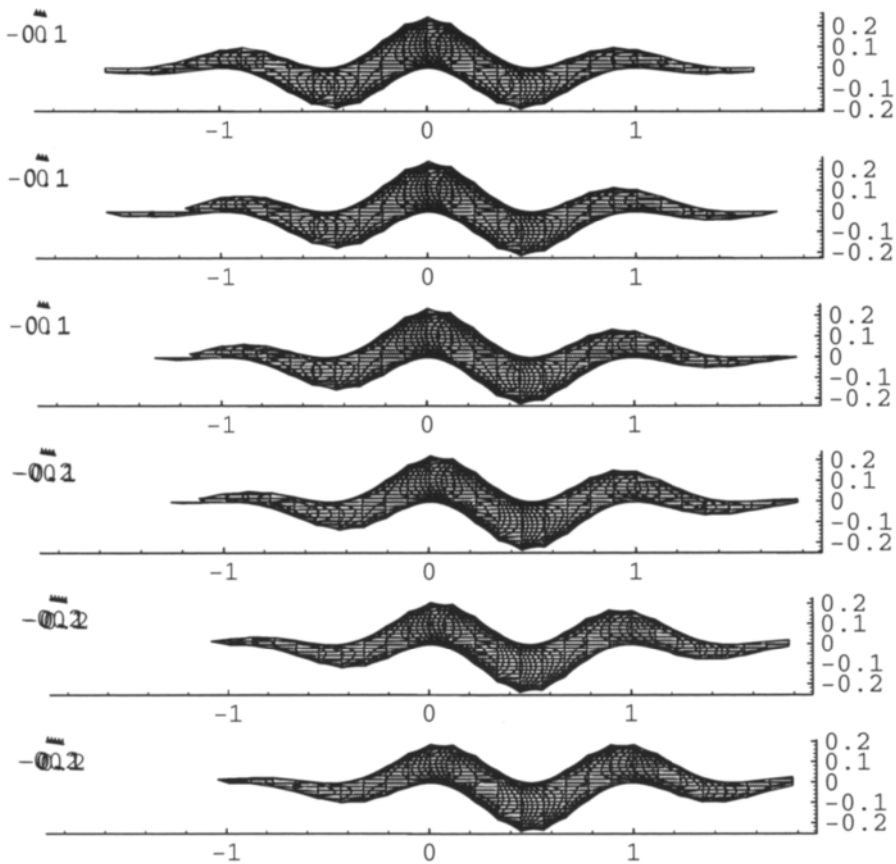


Figure 6.2.6 The motion of a screw or flagellum of bacteria.

Δx takes the values 0; 0.1; 0.2; 0.3; 0.4; and 0.5; in the figures 6.2.6, which simply are projections of 6.2.5. We clearly see that the GD-function is pushing the screw along x, making the screw rotate. It must do this, since the spiral function is changing all the time with Δx . Indeed we have a complete mathematical model for the topological motion of a screw and thereby of the E. coli bacteria movement as well.

6.3 Periodic Motion with Particles in 2D or 3D

We know that motion in biology is not only change of site, or size, it is also change of shape. We saw that on the study of flagella. Here we extend the analysis and extend to 3D. Equation 6.3.1 expresses a simple spherical damping of the simplest cosine function. For the given constant this is a sphere. In figure 6.3.1 we can move this body with Δx taking values 0; 0.4; 0.8; ... to 4.

$$e^{-[(x-\Delta x)^2+y^2+z^2]}[\cos \pi x + \cos \pi y + \cos \pi z] = \frac{1}{2} \quad 6.3.1$$

The 'structure' moves, and changes shape periodically in a continuous way. Just like a walking human being. The x-coordinate shows where the 'structure' is.

We may of course easily make the 'structure' move in different directions. This is a true, and very simple, 3D periodic motion.

This was crawling, and the periodic motion is also well described with equation 6.3.1b and shown in figure 6.3.2a. This agrees very well with the current pictures of cyclic crawling of cells [4], which we reproduce in figure 6.3.2b. Two mechanisms driving this kind of motion have been described. One is just changes in the membrane, involving endocytosis in the back and exocytosis in the front. This means that the membrane will move and force its inside content to follow this motion. The other mechanism is a force on the membrane from the inside, provided by actin, as shown in figure 6.3.2b.

$$e^{-[(x-\Delta x)^2+y^2+5z^2]}[\cos \frac{1}{2} \pi x + \cos \pi y + \cos \pi z] = \frac{1}{2} \quad 6.3.1b$$

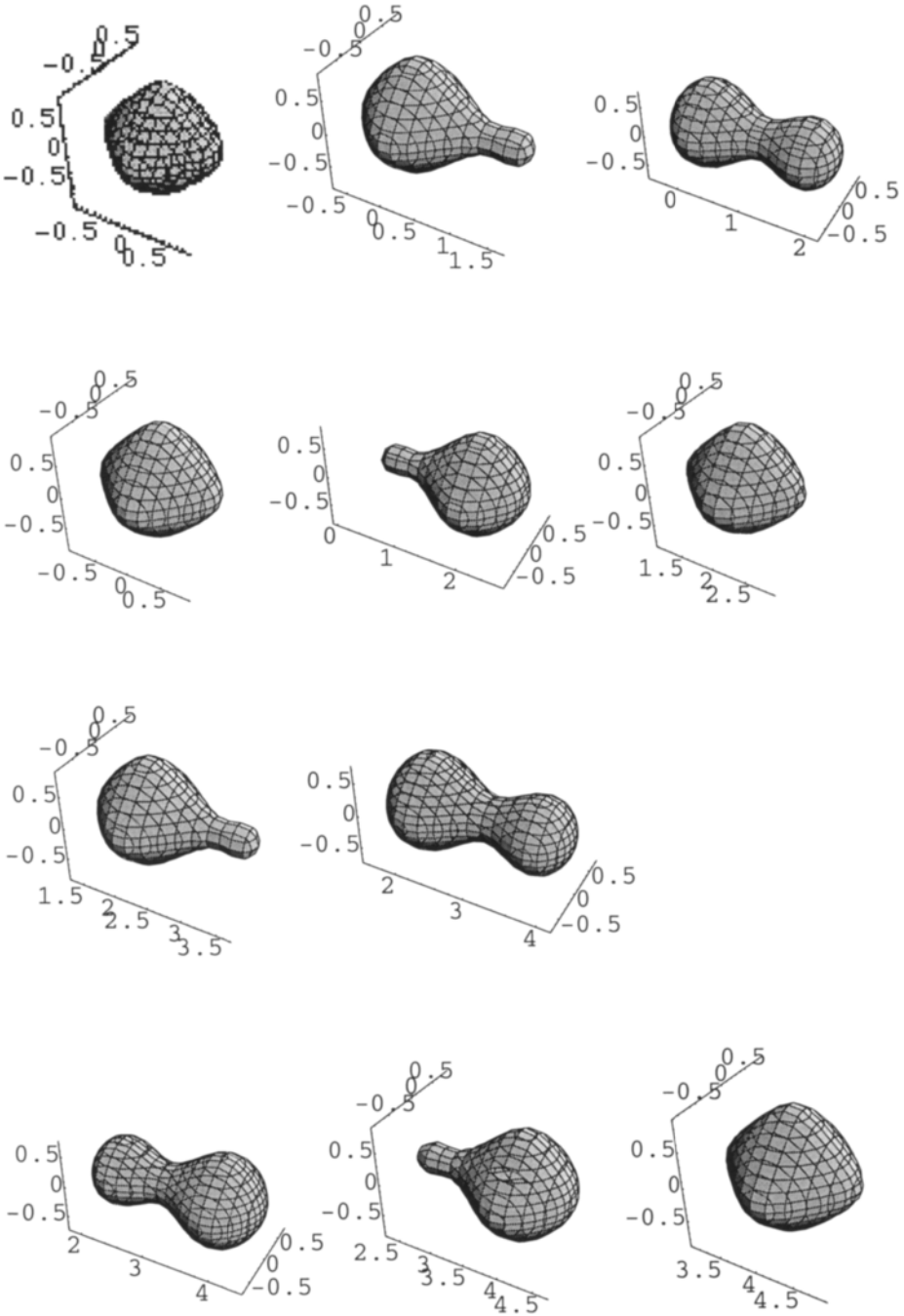


Figure 6.3.1 Periodic motion in 3D.

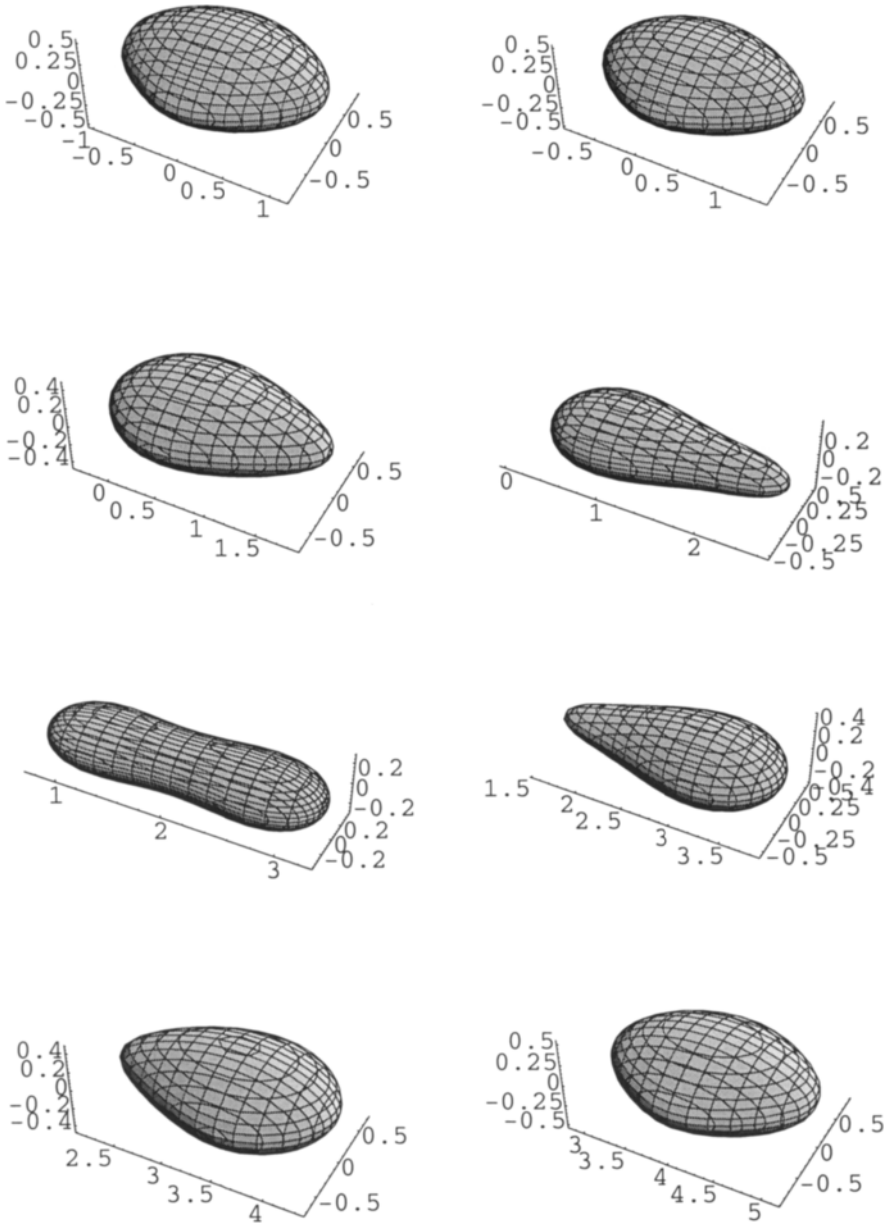


Figure 6.3.2a More periodic motion.

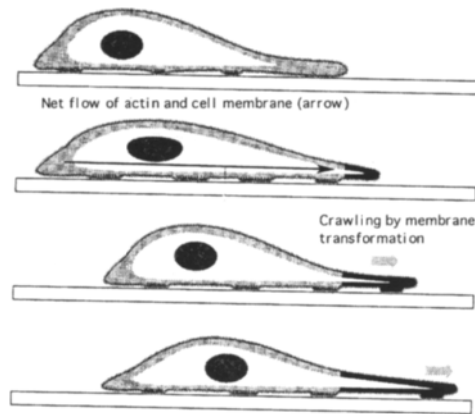


Figure 6.3.2b Crawling motion of a cell, modified after [4].

We will now do the experiment with two particles meeting each other. To make it simple they have the same structure but different sizes.

We take the simplest circular or nodal function of all, and damp it with a GD-function like we did above. We start in two dimensions after equations 6.3.2 - 6.3.4.

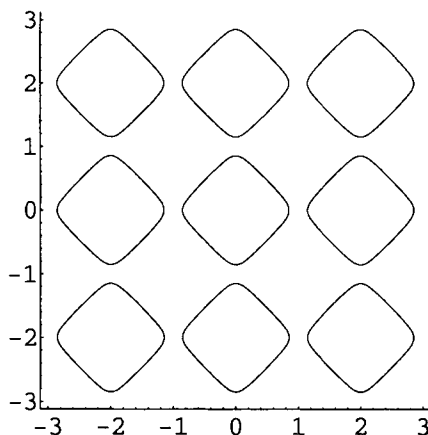


Figure 6.3.3 Nodal structure.

$$\cos \pi x + \cos \pi y = 0.1 \quad 6.3.2$$

$$e^{-\frac{1}{2}(x^2+y^2)} [\cos x + \cos y] = 0.1 \quad 6.3.3$$

$$e^{-\frac{1}{4}(x^2+y^2)} [\cos \pi x + \cos \pi y] = 0.1 \quad 6.3.4$$

First we show the nodal structure after equation 6.3.2 in figure 6.3.3.

With the damping we cut two different sizes of the nodal surface after equation 6.3.3 and 6.3.4 in figures 6.3.4a and 6.3.4b.

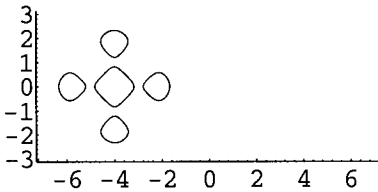


Figure 6.3.4a Damped nodal structure.

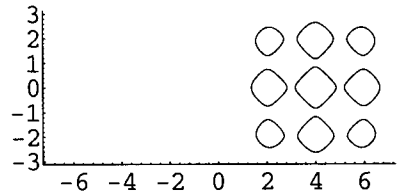


Figure 6.3.4b Less damped nodal structure.

$$e^{-\frac{1}{2}[(x-\Delta x)^2+y^2]} [\cos \pi x + \cos \pi y] + e^{-\frac{1}{4}[(x+\Delta x)^2+y^2]} [\cos \pi x + \cos \pi y] = 0.1 \quad 6.3.5$$

Due to the nature of the GD-function we can put equations on different places in space by addition, and keep their original shape. This is done in one function with 6.3.3 and 6.3.4, together with separation in the x-dimension, in equation 6.3.5. In figures 6.3.5a-i Δx takes the values 4, 3, 2, 1, 0, -1, -2, -3, -4, after equation 6.3.5. When the particles move towards each other, they change in shape due to the periodic motion. They go right through each other and regain their original shapes. This is a mathematical mechanism for how a particle (of some structure, in this case periodic) goes through another particle (also of some structure, in this case also periodic), or how a small crystal is added to a bigger one.

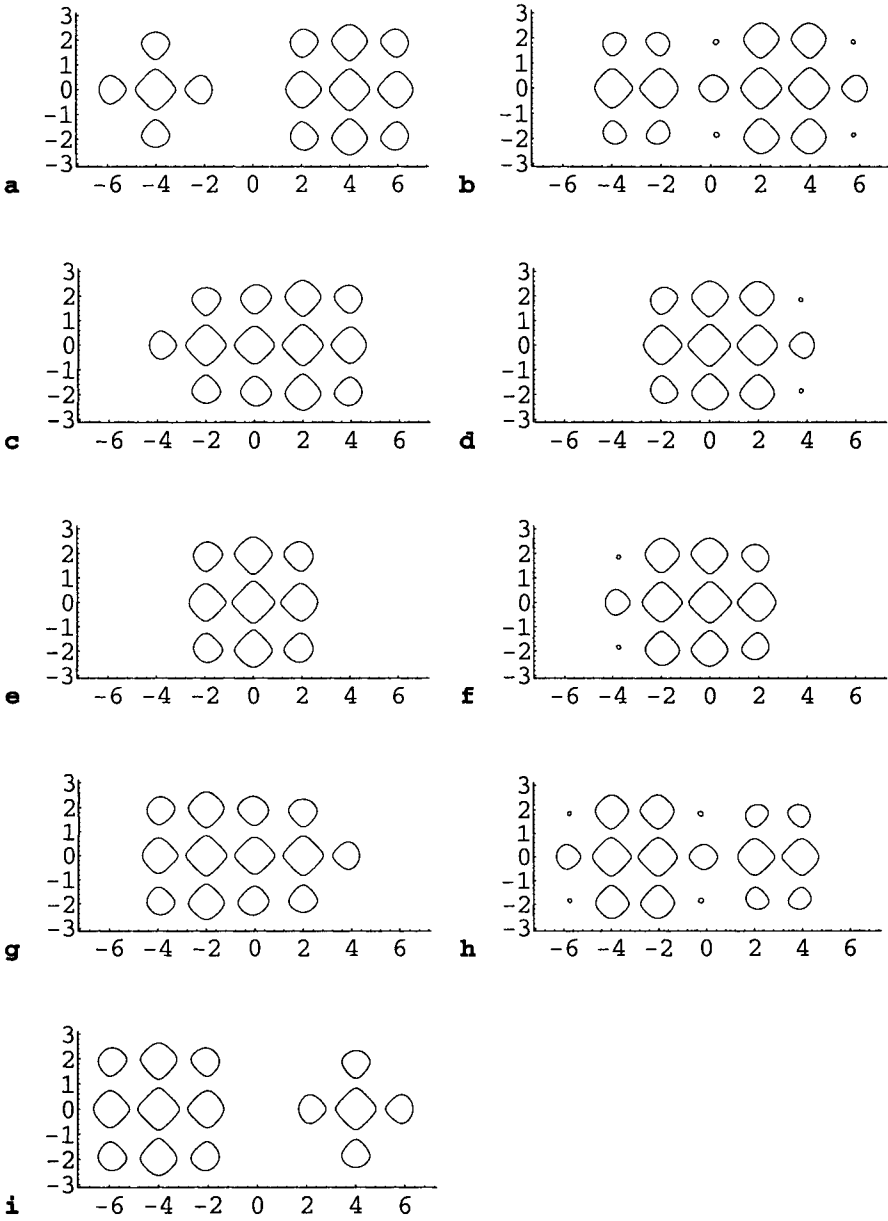


Figure 6.3.5a-i Two nodal structures go through each others.

In equation 6.3.6 we do this in three dimensions to show that the functions are continuous.

$$\begin{aligned}
 & e^{-\frac{1}{2}[(x-\Delta x)^2+y^2+z^2]} [\cos \pi x + \cos \pi y + \cos \pi z] \\
 & + e^{-\frac{1}{4}[(x+\Delta x)^2+y^2+z^2]} [\cos \pi x + \cos \pi y + \cos \pi z] = 0.1
 \end{aligned}
 \tag{6.3.6}$$

With the variation of Δx from -4; -3;...0 the particles continuously fuse as in figures 6.3.6a-e, and separate again, or go through each other if the motion is continued.

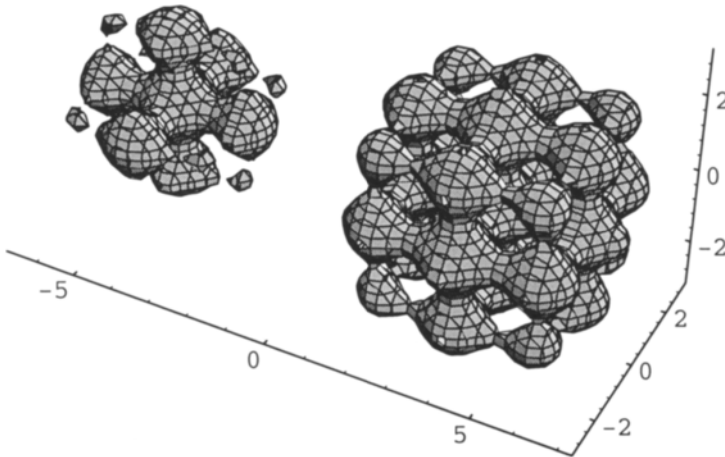


Figure 6.3.6a Two cubosome like structures belonging to equation 6.3.6 damped to different sizes. The two structures are made to go through each other via “biological motion” in the figures below.

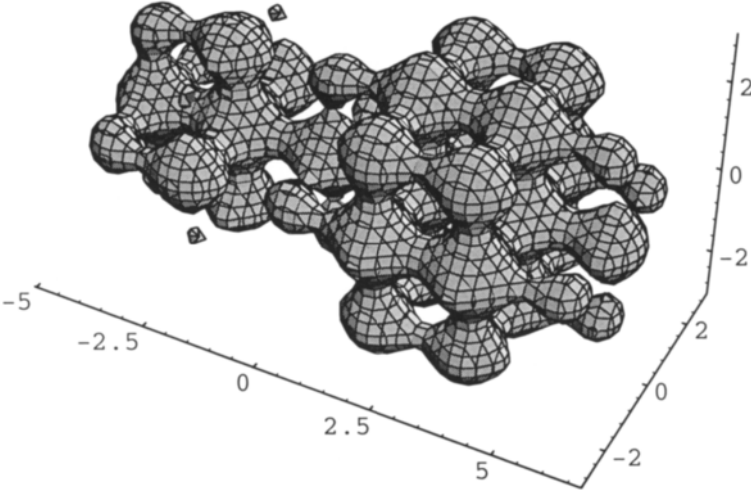


Figure 6.3.6b

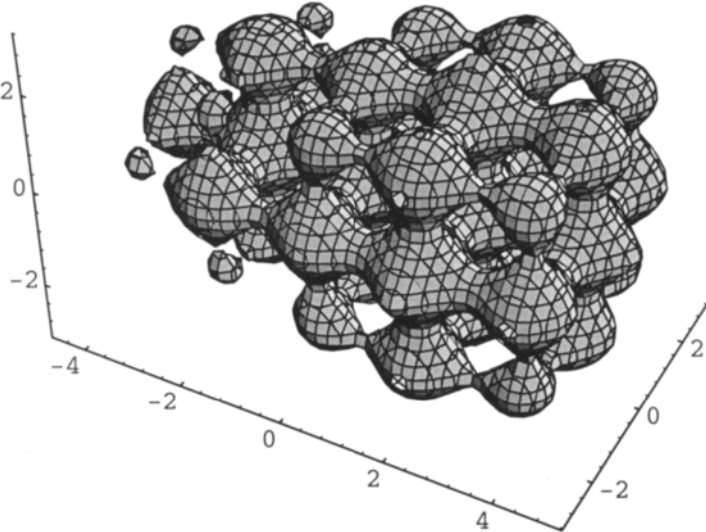


Figure 6.3.6c

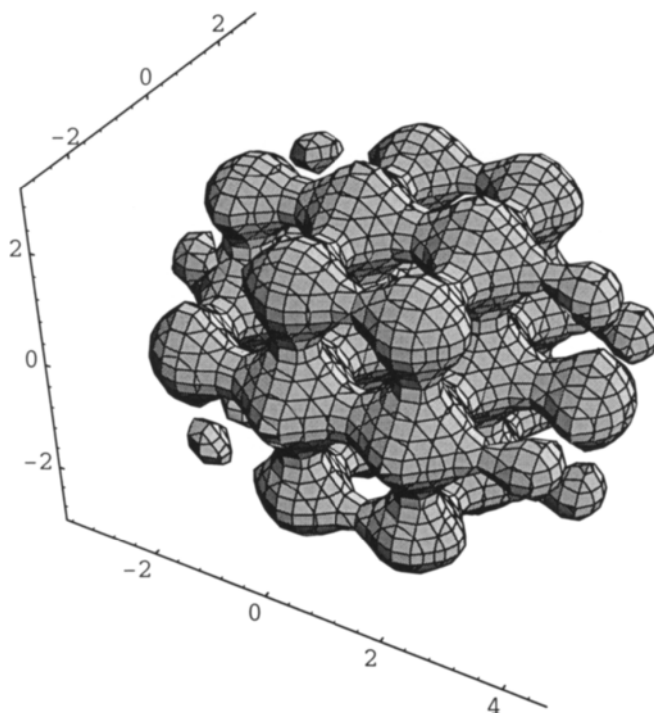


Figure 6.3.6d

We shall also move a tetrahedron along the Cartesian space diagonal. The equation is in 6.3.7, which is partly recognised from 5.2.12.

$$\begin{aligned}
 & e^{-2[(x+\Delta x)^2+(y+\Delta y)^2+(z+\Delta z)^2]}[\sin \pi(x+y+z)+\sin \pi(-x+y-z) \\
 & +\sin \pi(-x-y+z)+\sin \pi(x-y-z)+\cos \pi(x+y+z) \qquad 6.3.7 \\
 & +\cos \pi(-x+y-z)+\cos \pi(-x-y+z)+\cos \pi(x-y-z)]-0.4=0
 \end{aligned}$$

The Δ :s take the values 0.50, 0.50, 0.50; 0.25, 0.25, 0.25; 0, 0, 0; -0.2, -0.2, -0.2; -0.5, -0.5, -0.5;

In figures 6.3.7a-e we see first a beautiful inversion of this damped part of the D-surface, a tetrahedron of four spheres, over a transition state. Then there is a transition to a bigger piece of diamond, or a molecule called adamantane.

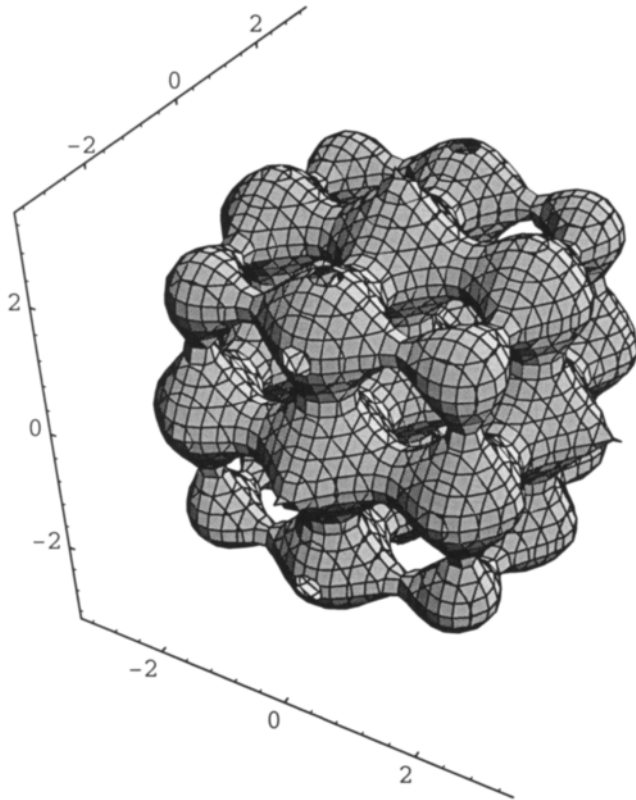


Figure 6.3.6e Continuing the motion means complete separation with the smaller part coming out to right.

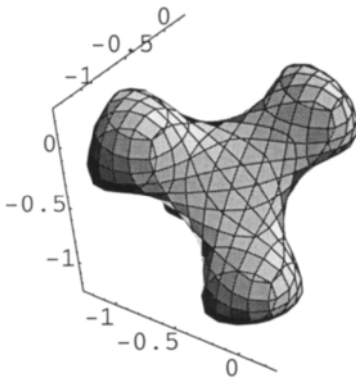


Figure 6.3.7a A body of tetrahedral symmetry moves along the Cartesian space diagonal.

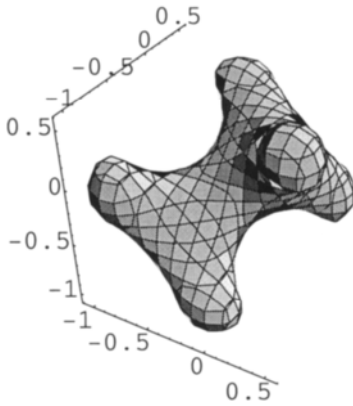


Figure 6.3.7b

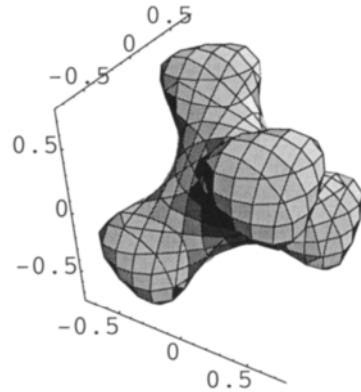


Figure 6.3.7c

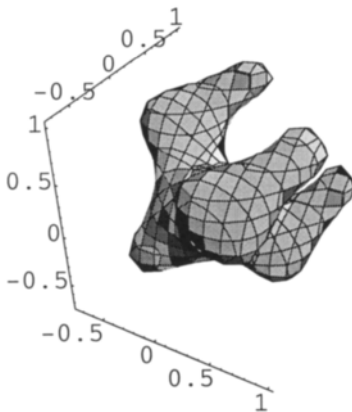


Figure 6.3.7d

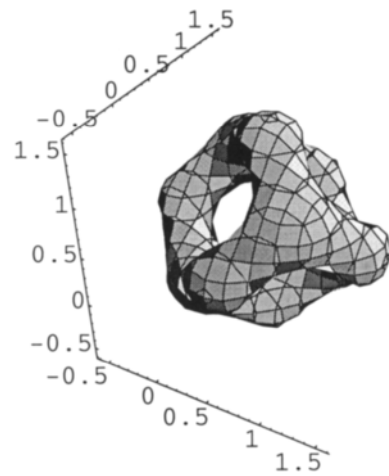


Figure 6.3.7e Continuing the climbing means a return to the tetrahedron as the motion is periodic.

This motion with dramatic changes of shape may be induced by a locomote like in chapter 5, but is of course periodic. Crawling, walking, swimming, or the flagella motions are tied up to geometry, and it is only natural to describe them with periodic mathematics, as we have done. The jelly fish for example has movements that are periodic, and the simple topology in 6.3.7c-d may serve as a model for that.

6.4 Periodic Motion with Rotation of Particles in 2D

So far we have described motion via translation. Rotation is the other fundamental operation and we shall shortly describe it here, as it can also be said to be periodic.

We start to rotate a square with the simple equation in 6.4.1. We vary A between 0, 0.2, 0.4, 0.6, 0.8, and 1. In figure 6.4.1 we plot one square on the top of another, and see the squares rotate beautifully.

$$(Ax + y)^4 + (x - Ay)^4 = 1 \tag{6.4.1}$$

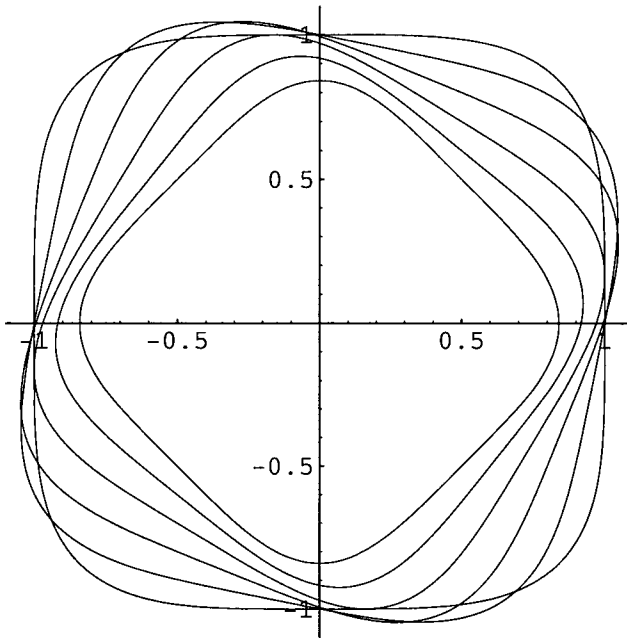


Figure 6.4.1 Different functions plotted on top of each others.

Next is to put a particle into an orbit. We start with a small circle after equation 6.4.2.

$$x^2 + y^2 = r^2$$

and

$$y = \sqrt{r^2 - x^2}$$

and

$$\Delta y = \sqrt{r^2 - \Delta x^2} \quad 6.4.2$$

Below is an equation describing a small circle that is translated a distance, r , along the x -axis.

$$(x-r)^2 + y^2 = \frac{5}{1000}$$

We let $r=1$ and we want to make the small circle rotate in an orbit of the bigger circle of radii $=1$. The centre for this orbit will be the centre of the coordinate system.

$$(x-1)^2 + y^2 = \frac{5}{1000}$$

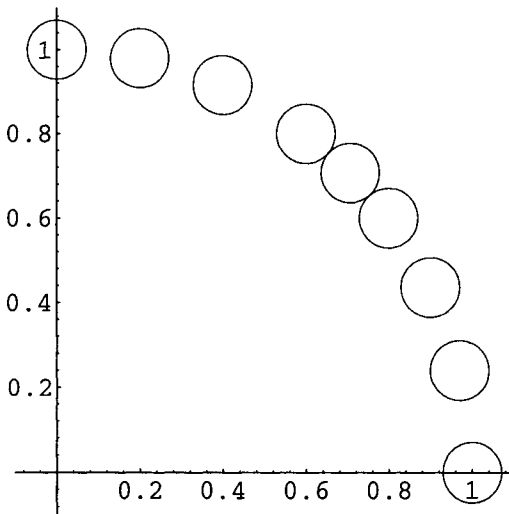


Figure 6.4.2 Rotation described as double translation after equation 6.4.3.

And the equation of motion will be 6.4.3.

$$(x-1+\Delta x)^2 + (y-1+\Delta y)^2 = \frac{5}{1000} \tag{6.4.3}$$

This description of the rotation operation as a double translation operation is simple and useful, and fits into our way to describe biological motion. We do believe that the mechanism of the motor proteins when they make things rotate, is more like double translation than anything else.

For various Δx we calculate Δy and for some of the circles we give the pairs 0.2, 0.4; 0.29, 0.29; 0.4, 0.2; 0.6, 0.08; and 0.8, 0.02; The plot is found in figure 6.4.2.

We make the orbit elliptical as plotted in figure 6.4.3, after equation 6.4.4.

$$(x-1+\Delta x)^2 + (2y-1+\Delta y)^2 = \frac{5}{1000} \tag{6.4.4}$$

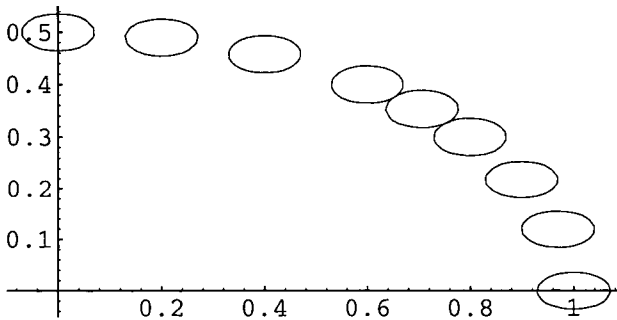


Figure 6.4.3 Elliptical orbit after equation 6.4.4.

The ellipses are made circles by the equation 6.4.5 as in the plot of figure 6.4.4.

$$4(x-1+\Delta x)^2 + (2y-1+\Delta y)^2 = \frac{5}{1000} \tag{6.4.5}$$

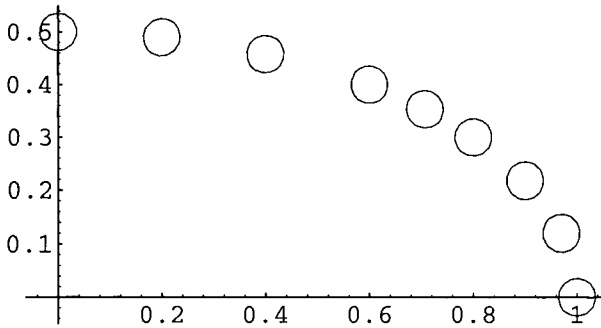


Figure 6.4.4 Elliptical orbit after equation 6.4.5.

References 6

- 1 J. L. Synge, *SCIENCE: SENSE AND NONSENSE*, Books for Libraries Press, New York, 1972, page 91.
- 2 M. Jacob and S. Andersson, *THE NATURE OF MATHEMATICS AND THE MATHEMATICS OF NATURE*, Elsevier, 1998.
- 3 B. Alberts, D. Bray, J. Lewis, M. Raff, K. Roberts, and J. D. Watson, *Molecular Biology of THE CELL*, Garland Publishing, Third Edition, 1994, page 816.
- 4 B. Alberts, D. Bray, J. Lewis, M. Raff, K. Roberts, and J. D. Watson, *Molecular Biology of THE CELL*, Garland Publishing, Third Edition, 1994, page 846.
- 5 G. M. Cooper, *THE CELL A Molecular Approach*, ASM Press, 1997, page 442.

7 Finite Periodicity and the Cubosomes

*And thick and fast they came at last,
And more, and more, and more.*

In his description of isometry and symmetry, Coxeter quotes Lewis Carroll, [1]

The cubosomes constitute formidable examples of the occurrence of symmetry in soft matter in Nature.

Finite periodicity with circular functions, the GD-function, or the Hermite functions are used to describe the giant cubosome lipid bilayer assemblies.

The structures of the three different kinds of cubosomes - the G, D and P - are also discussed using connectivity 3, 4, and 6.

Connectivity 2 is used to describe topology of twisted ropes, or proteins.

7.1 Periodicity and the Hermite Function

The cubosome colloidal particle was first identified in *in vitro* lipid systems and described by one of us [2]. The possibility of periodic curvature along the lipid bilayer of cell membranes was introduced when the triply-periodic character of cubic lipid-water phases was revealed [3]. In thousands of cases such cubic structures have since then been clearly demonstrated to exist in cell membrane assemblies [4,5]. This is further described in chapter 8.

In a wave mechanical description of a molecule, the molecule itself and its outer forces of attraction constitute the boundaries for a standing wave. In our descriptions of the structure of the cubosome, using the circular function, we have added a function like a sphere, or a cube, as boundaries, giving the structure a shape of finite periodicity [6,9].

We have described the cubosome as a standing wave, a giant aggregate formed by self-assembly of lipid molecules. We postulated this property with the boundaries we used [7,8]. We shall here give a more complete mathematical description of the cubosome.

Furthermore, we shall describe hexagonal structures related to cubosomes, like the muscle cells in chapter 9, and the tubular arrangement between cells in chapter 11.

We shall first use the Hermite function, which is the Schrödinger solution to the harmonic oscillator, as discussed in chapter 6. The equations are in 7.1.1 and 7.1.2, and the figures in 7.1.1 and 7.1.2. The period is doubled in 7.1.2 which gives the double molecule, which is an example how a finite part of a crystal structure, or molecule, is derived. In this case it is a cubic close packed arrangement of bodies, and in figure 7.1.1 the bodies form the corners of a cube octahedron.

$$e^{-x^2} e^{-y^2} e^{-z^2} \cos \pi x \cos \pi y \cos \pi z - 0.05 = 0 \quad 7.1.1$$

$$e^{-x^2} e^{-y^2} e^{-z^2} \cos 2\pi x \cos 2\pi y \cos 2\pi z - 0.05 = 0 \quad 7.1.2$$

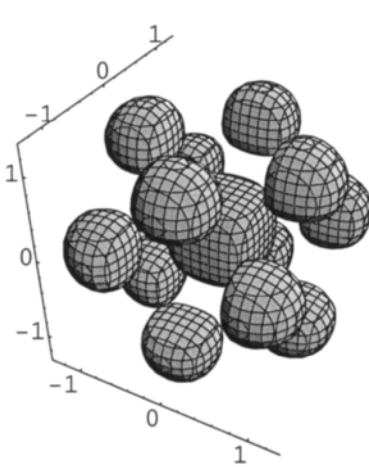


Figure 7.1.1 Cube octahedron of bodies.

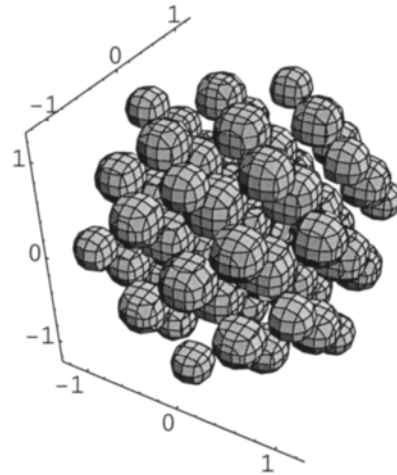


Figure 7.1.2 Bigger part of cubic close packed arrangement of bodies

The damping property of the Hermite function gives the type of structures we want, and we feel there is reason to use similar boundary constructions to make giant molecular aggregates, the cubosomes.

We have no simple analytic function for periodicity when it stands for translation in one dimension. Cosine is by definition an infinite product, which means that the periodicity is really hand-made, like the periodicity we made with the roots. We can only handle periodicity well in dimensions higher than one, as we showed in chapter 2, and as we will show in further detail below.

In this description of the cubosomes we shall use three different branches of periodicity;

- I The circular functions
- II The GD-type functions.
- III Hand-made functions.

7.2 Cubosomes and the Circular Functions

The essential property of periodicity is easily understood from the figures below. The first three equations of 7.2.1 are the infinitely repeated planes in space as shown in figure 7.2.1. If we add them together pair-wise as in 7.2.2, they collaborate in space to form cylinders as in figure 7.2.2. If all three sets of planes, or cylinders, are added together after equation 7.2.3, they collaborate to give the infinitely periodic P-surface, as in figure 7.2.3. A good example is if all the planes are multiplied with each other after equation 7.2.4, and shown in figure 7.2.4. In figure 7.2.5 we have added a constant of 0.2 as in equation 7.2.5, and as a result we have ‘bodies’. We now realise that periodicity is a mathematical machine which is formidable for duplication. If we in this machine add a number of bodies, n , after each axis, the machine produces at least n^3 new bodies altogether.

$$\cos \pi x = 0$$

$$\cos \pi y = 0$$

$$\cos \pi z = 0$$

7.2.1

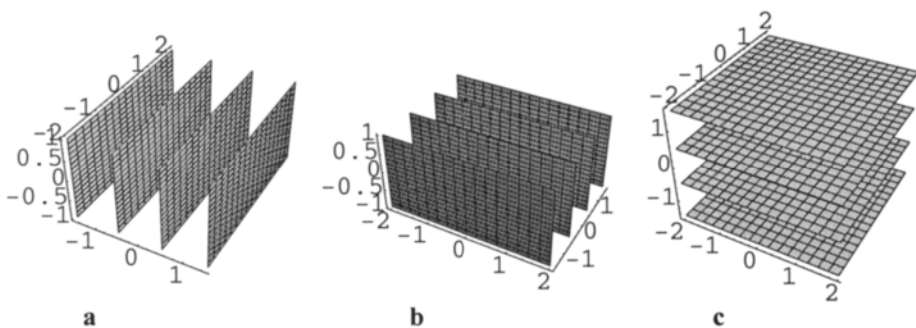


Figure 7.2.1 The planes in space from cosine

$$\cos \pi x + \cos \pi y = 0$$

$$\cos \pi x + \cos \pi z = 0$$

$$\cos \pi y + \cos \pi z = 0$$

7.2.2

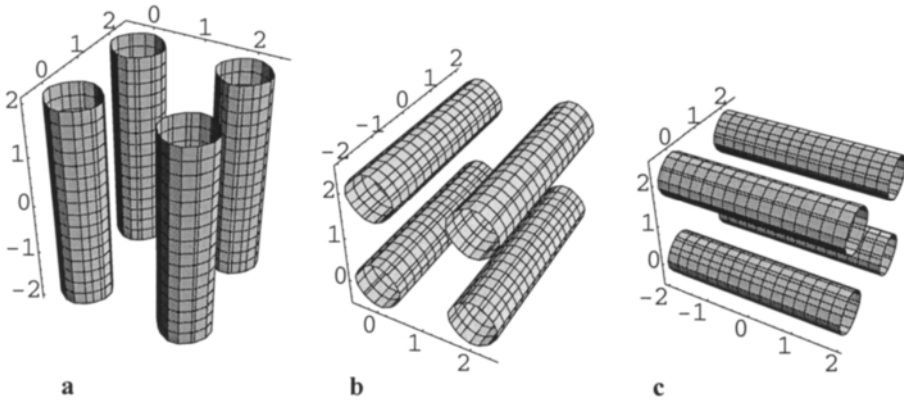


Figure 7.2.2 The cylinders in space after cosine

$$\cos \pi x + \cos \pi y + \cos \pi z = 0$$

7.2.3

$$\cos \pi x \cos \pi y \cos \pi z = 0$$

7.2.4

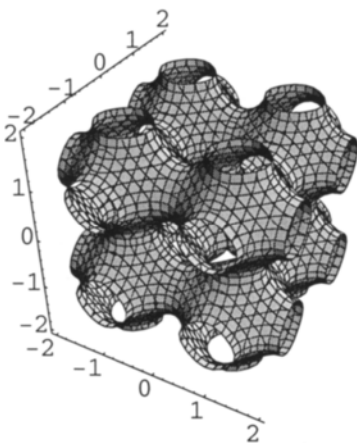


Figure 7.2.3 P-surface after addition of cosine.

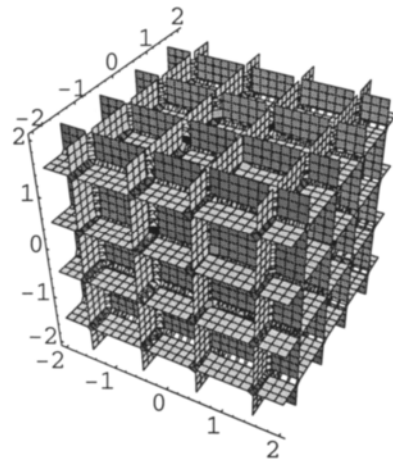


Figure 7.2.4 Intersecting planes after product of cosine.

$$\cos \pi x \cos \pi y \cos \pi z = 0.2$$

7.2.5

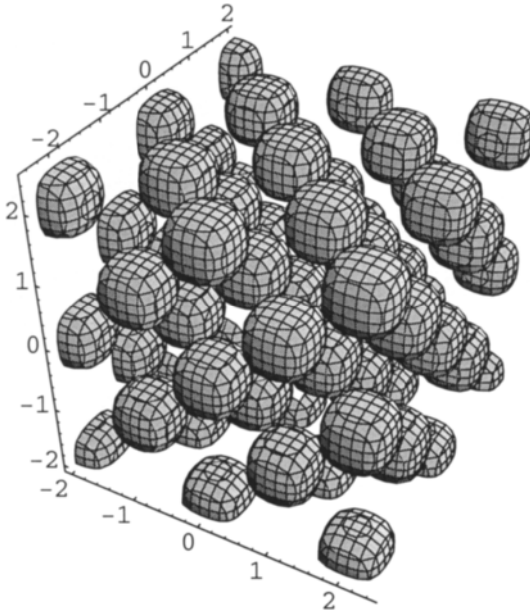


Figure 7.2.5 By adding a constant the intersecting planes become bodies.

In order to make cubosomes, the periodic functions need to be damped in a simple way, depending on what shape we want. The simplest is a sphere, which really is a set of planes as in equation 7.2.6, and this cubosome is illustrated in figure 7.2.6.

$$\cos 2\pi x + \cos 2\pi y + \cos 2\pi z + x^2 + y^2 + z^2 = 2 \quad 7.2.6$$

Using four planes, or a cylinder, as in 7.2.7, and we get the column structure in figure 7.2.7.

$$\cos \pi x + \cos \pi y + \cos \pi z + x^2 + y^2 = 1 \quad 7.2.7$$

A double plane as in 7.2.8 gives a beautiful layer structure as in figure 7.2.8.

$$\cos \pi x + \cos \pi y + \cos \pi z + x^2 = 0.5 \quad 7.2.8$$

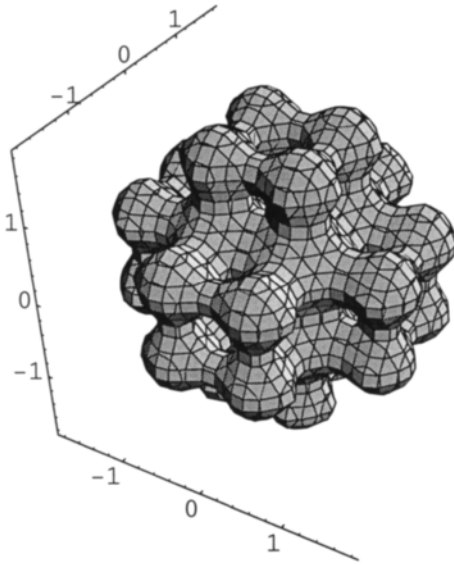


Figure 7.2.6 Cubosome of the P-surface with spherical boundaries.

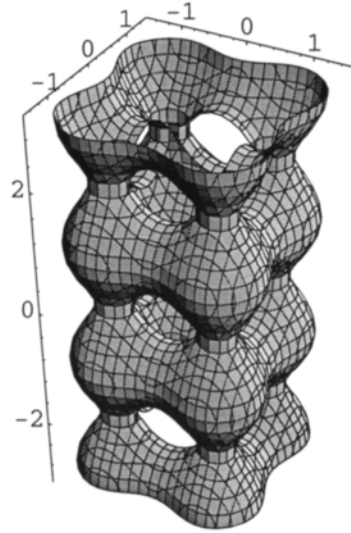


Figure 7.2.7 Column structure of the P-surface with cylindrical boundaries.

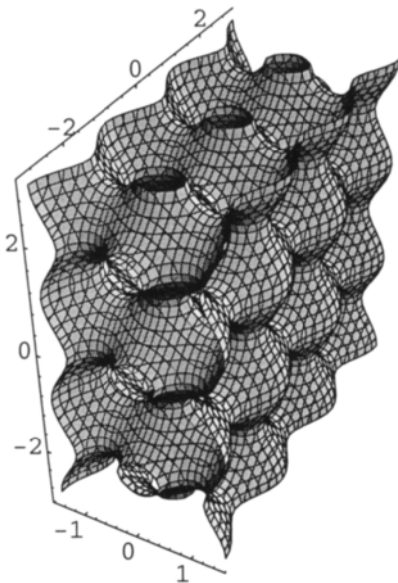


Figure 7.2.8 Layer structure of the P-surface with planar boundaries.

In equation 7.2.9 we have used a cube as boundary which gives the beautiful cubosome in figure 7.2.9.

$$e^{\cos 3\pi x + \cos 3\pi y + \cos 3\pi z} + e^{x^2} + e^{y^2} + e^{z^2} = 8.7 \tag{7.2.9}$$

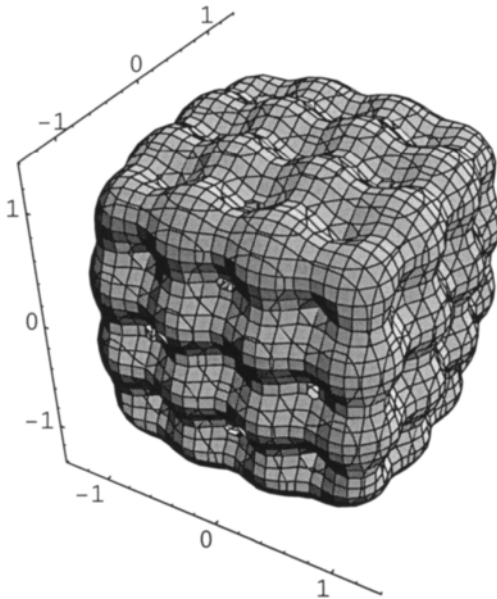


Figure 7.2.9 Cubosome of the P-surface with cubic boundaries.

The D-surface has tetrahedral symmetry, which makes it natural to use a tetrahedron as boundary. This is shown in figure 7.2.10, after equation 7.2.10.

$$e^{\cos \pi(x+y+z) + \cos \pi(x-y-z) + \cos \pi(-x-y+z) + \cos \pi(-x+y-z)} + e^{\sin \pi(x+y+z) + \sin \pi(x-y-z) + \sin \pi(-x-y+z) + \sin \pi(-x+y-z)} + e^{x+y+z} + e^{x-y-z} + e^{-x-y+z} + e^{-x+y-z} = 11 \tag{7.2.10}$$

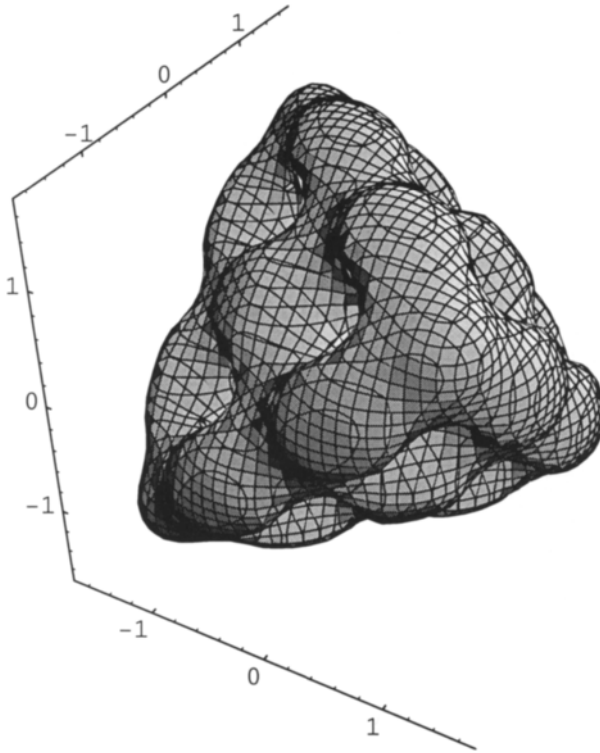


Figure 7.2.10 Cubosome of the D-surface with tetrahedral boundaries.

The polyhedron created by the symmetry of the gyroid is the rhombic dodecahedron, but we have given cubic boundaries to the cubosome in figure 7.2.11 after 7.2.11.

$$e^{\sin 4\pi(x+y)+\sin 4\pi(x-y)+\sin 4\pi(x+z)+\sin 4\pi(z-x)+\sin 4\pi(y+z)+\sin 4\pi(y-z)} + e^{x^2} + e^{y^2} + e^{z^2} = 5.5$$

7.2.11

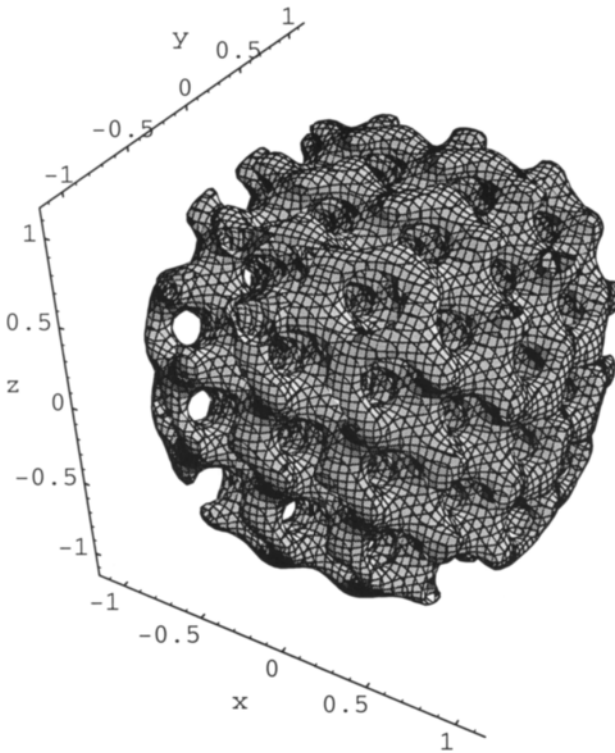


Figure 7.2.11 Cubosome of the gyroid surface with cubic boundaries.

7.3 Cubosomes and the GD-Function - Finite Periodicity and Symmetry P

The properties of the GD-function were used to develop biological motion as we saw in chapter 5, and will now be applied to periodicity.

Using the polynomials, we found in chapter 2 that it was the cooperation of planes, the roots, in space that generates periodicity. This was also shown for the circular functions above. Similar planes are found in the GD-mathematics, which has 'built in' boundaries like a molecule or cubosome, so there is no need for damping.

In the equations in 7.3.1 we do the counting as before, and get the planes in space as in figures 7.3.1a-c.

$$e^{-x^2} = 0.5$$

$$e^{-y^2} = 0.5$$

$$e^{-z^2} = 0.5$$

7.3.1

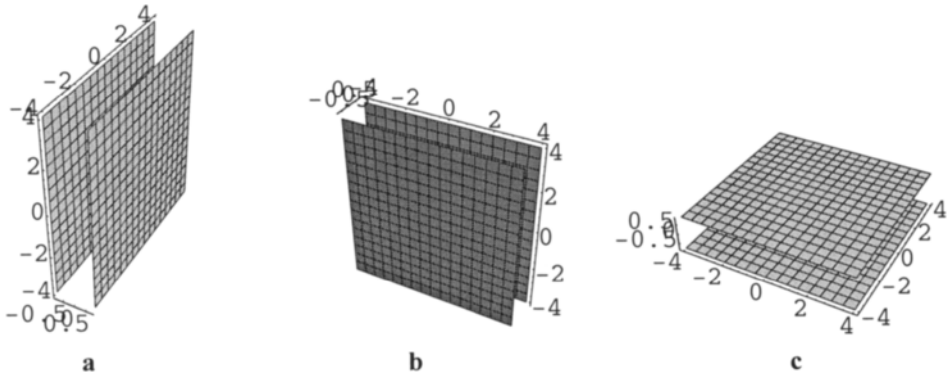


Figure 7.3.1 GD-planes that give periodicity.

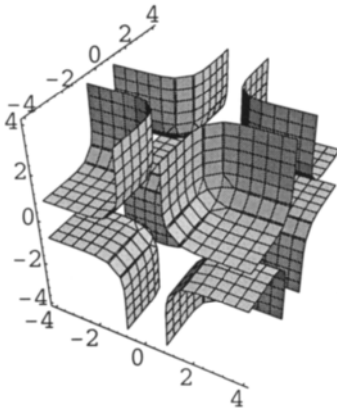


Figure 7.3.2 Six GD-planes give eight cube corners.

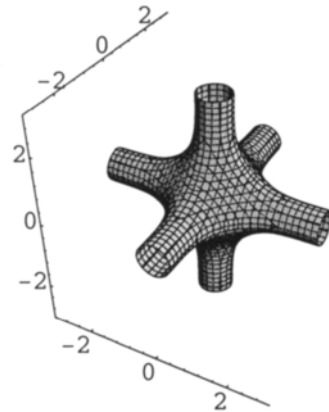


Figure 7.3.3 The six GD-planes have formed three cylinders that meet.

$$e^{-x^2} + e^{-y^2} + e^{-z^2} = 0.5$$

7.3.2

Adding the planes together, as in equation 7.3.2, we make them cooperate and the first periodic picture is found in figure 7.3.2. The three terms in the equation give eight cube corners.

$$e^{-x^2} + e^{-y^2} + e^{-z^2} = 1.8 \quad 7.3.3$$

Changing the constant to 1.8, as in equation 7.3.3 gives the beautiful polyhedron in figure 7.3.3, obviously ready for periodicity.

$$e^{-x^2} + e^{-y^2} + e^{-z^2} = 2.5 \quad 7.3.4$$

$$e^{-x^2} + e^{-y^2} + e^{-z^2} + e^{-(x-2)^2} + e^{-(y-2)^2} + e^{-(z-2)^2} = 2.7 \quad 7.3.5$$

Increasing the constant further, the GD-cylinders close up and give a body, as in figure 7.3.4. And by adding terms with new coordinates as in 7.3.5, the periodicity starts giving the picture of the molecule B_6H_6 . A change of constant brings out the bodies as in figure 7.3.6. More finite periodicity is shown in 7.3.7 after equation 7.3.7.

$$e^{-x^2} + e^{-y^2} + e^{-z^2} + e^{-(x-2)^2} + e^{-(y-2)^2} + e^{-(z-2)^2} = 2.9 \quad 7.3.6$$

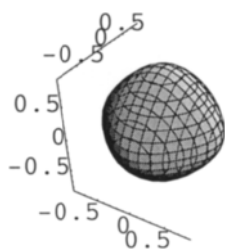


Figure 7.3.4 Change of constant makes the GD-cylinders close up.

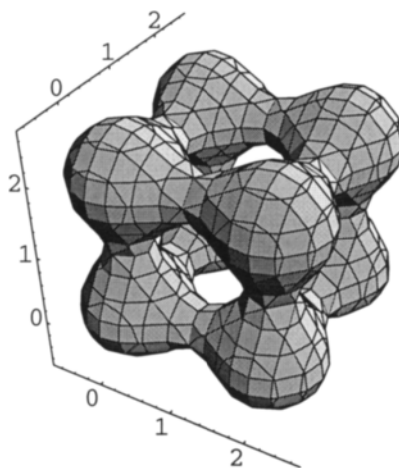


Figure 7.3.5 Two bodies along the Cartesian space diagonal give periodicity to six more bodies, joined by catenoids to form a B_6H_6 molecule.

$$\begin{aligned}
 &e^{-x^2} + e^{-y^2} + e^{-z^2} + e^{-(x-2)^2} + e^{-(y-2)^2} + e^{-(z-2)^2} \\
 &+ e^{-(x-4)^2} + e^{-(y-4)^2} + e^{-(z-4)^2} = 2.85
 \end{aligned}
 \tag{7.3.7}$$

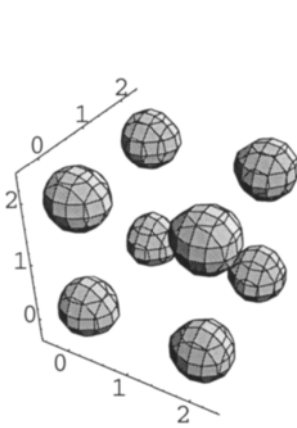


Figure 7.3.6 Bodies liberated.

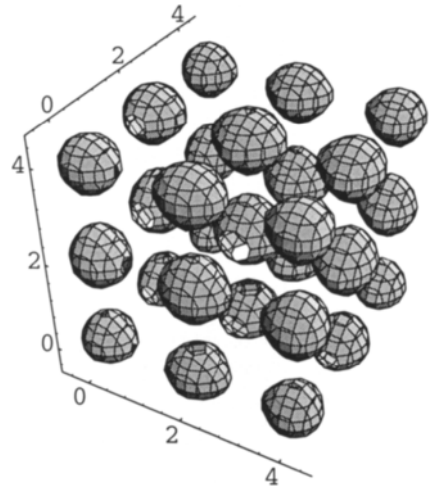


Figure 7.3.7 Three bodies along the diagonal give a 27 body periodic structure.

After equation 7.3.8 we get the formidable cubosome in figure 7.3.8.

$$\begin{aligned}
 &e^{-x^2} + e^{-y^2} + e^{-z^2} + e^{-(x-2)^2} + e^{-(y-2)^2} + e^{-(z-2)^2} \\
 &+ e^{-(x-4)^2} + e^{-(y-4)^2} + e^{-(z-4)^2} + e^{-(x-6)^2} + e^{-(y-6)^2} + e^{-(z-6)^2} \\
 &+ e^{-(x-8)^2} + e^{-(y-8)^2} + e^{-(z-8)^2} \\
 &+ e^{-(x-10)^2} + e^{-(y-10)^2} + e^{-(z-10)^2} = 2.65
 \end{aligned}
 \tag{7.3.8}$$

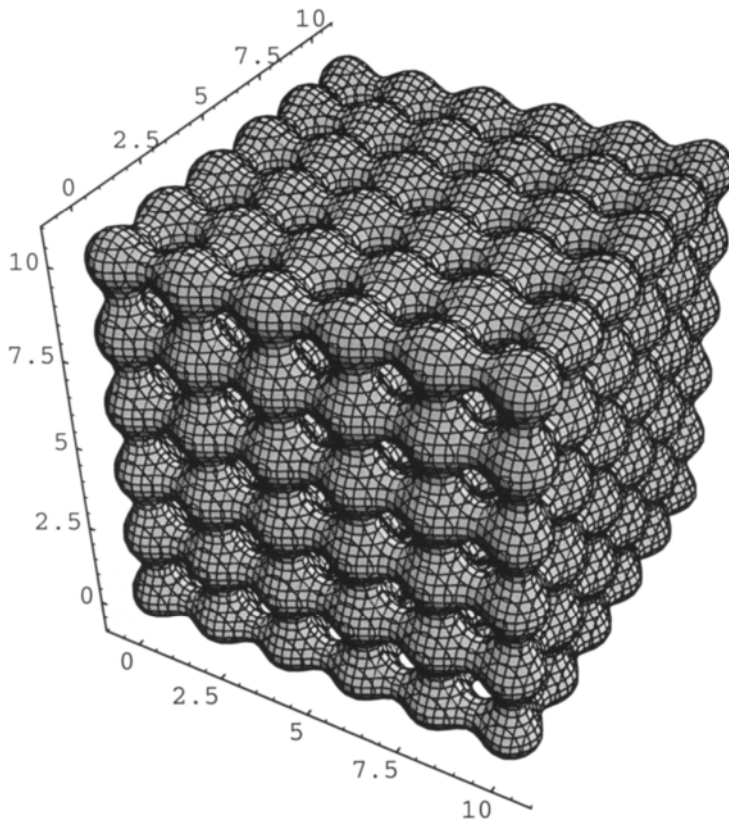


Figure 7.3.8 Six bodies along the space diagonal multiply to a formidable cubosome of 216 bodies.

7.4 Cubosomes and the GD-Function - Symmetry G

Cubosomes of the gyroid symmetry are derived from the $(x+y)$ permutations in space which generate planes, like in figure 7.4.1 after equation 7.4.1.

$$e^{-(x+y)^2} = 0.8 \quad 7.4.1$$

With all the six permutations of planes in space, and with the proper translations to give more terms after equation 7.4.2, there is now a small cubosome, shown in figure 7.4.2.

$$\begin{aligned}
 & e^{-(x+y-0.5)^2} + e^{-(x-y-0.5)^2} + e^{-(x+z-0.5)^2} + e^{-(y+z-0.5)^2} + \\
 & + e^{-(-x+z-0.5)^2} + e^{-(y-z-0.5)^2} + e^{-(x+y-2.5)^2} + e^{-(x-y-2.5)^2} + \\
 & + e^{-(x+z-2.5)^2} + e^{-(y+z-2.5)^2} + e^{-(-x+z-2.5)^2} + e^{-(y-z-2.5)^2} + \\
 & + e^{-(x+y+1.5)^2} + e^{-(x-y+1.5)^2} + e^{-(x+z+1.5)^2} + e^{-(y+z+1.5)^2} + \\
 & + e^{-(-x+z+1.5)^2} + e^{-(y-z+1.5)^2} = 5.3
 \end{aligned}
 \tag{7.4.2}$$

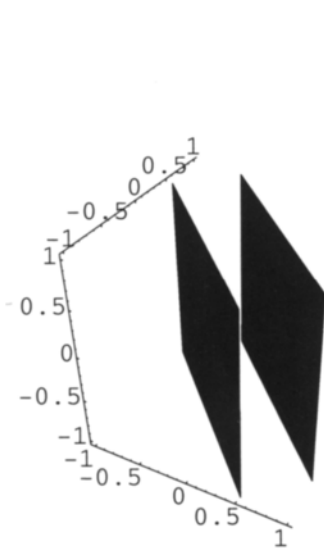


Figure 7.4.1 The gyroid symmetry give diagonal double planes of GD-type.

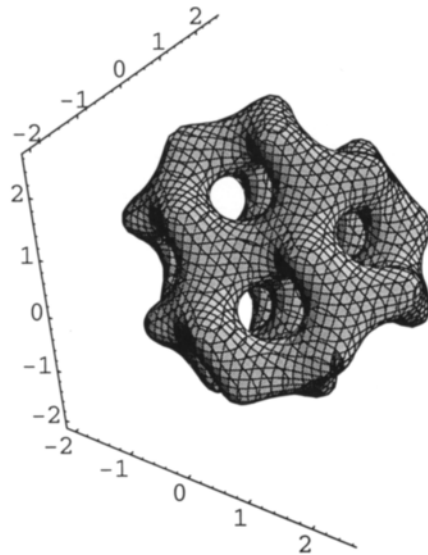


Figure 7.4.2 Three bodies after equation 7.4.2 give a small cubosome.

A bigger cubosome is obtained using still more terms after equation 7.4.3, which is illustrated in figure 7.4.3. The cubosome has the shape of a rhombic dodecahedron, and the structure is projected after its three fold axis in the figure.

$$\begin{aligned}
 & e^{-(x+y-0.5)^2} + e^{-(x-y-0.5)^2} + e^{-(x+z-0.5)^2} + e^{-(y+z-0.5)^2} \\
 & + e^{-(x+z-0.5)^2} + e^{-(y-z-0.5)^2} + e^{-(x+y-2.5)^2} + e^{-(x-y-2.5)^2} \\
 & + e^{-(x+z-2.5)^2} + e^{-(y+z-2.5)^2} + e^{-(x+z-2.5)^2} + e^{-(y-z-2.5)^2} \\
 & + e^{-(x+y-4.5)^2} + e^{-(x-y-4.5)^2} + e^{-(x+z-4.5)^2} + e^{-(y+z-4.5)^2} \\
 & + e^{-(x+z-4.5)^2} + e^{-(y-z-4.5)^2} + e^{-(x+y+1.5)^2} + e^{-(x-y+1.5)^2} \\
 & + e^{-(x+z+1.5)^2} + e^{-(y+z+1.5)^2} + e^{-(x+z+1.5)^2} + e^{-(y-z+1.5)^2} \\
 & + e^{-(x+y+3.5)^2} + e^{-(x-y+3.5)^2} + e^{-(x+z+3.5)^2} + e^{-(y+z+3.5)^2} \\
 & + e^{-(x+z+3.5)^2} + e^{-(y-z+3.5)^2} + e^{-(x+y+5.5)^2} + e^{-(x-y+5.5)^2} \\
 & + e^{-(x+z+5.5)^2} + e^{-(y+z+5.5)^2} + e^{-(x+z+5.5)^2} + e^{-(y-z+5.5)^2} = 5.3
 \end{aligned}
 \tag{7.4.3}$$

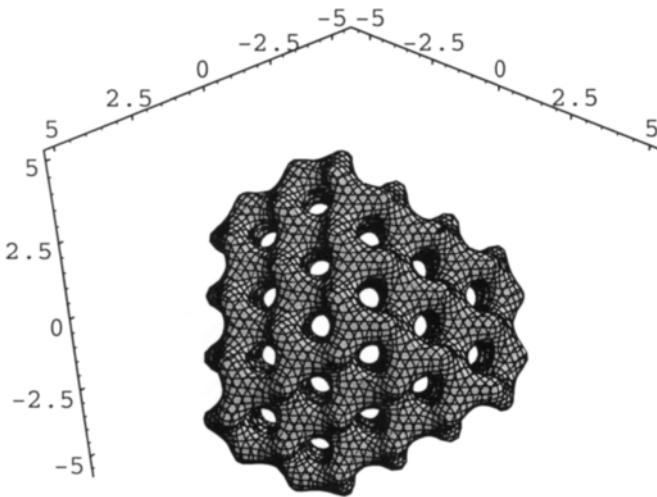


Figure 7.4.3 Six bodies give a beautiful gyroid cubosome. The shape is rhombic dodecahedral and the projection is along a space diagonal, which is a three fold axis.

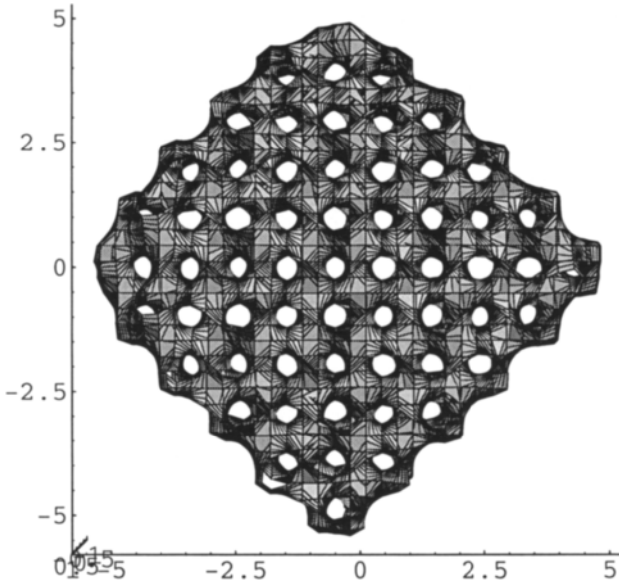


Figure 7.4.4 Bounded projection of the cubosome from figure 7.4.3 along the a-axis. **a** Thickness of 2 unit cells.

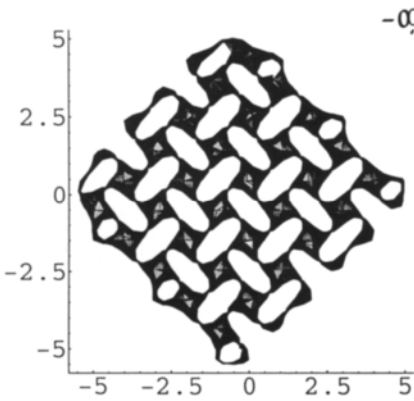


Figure 7.4.4b Thickness of 1/4 of a unit cell.

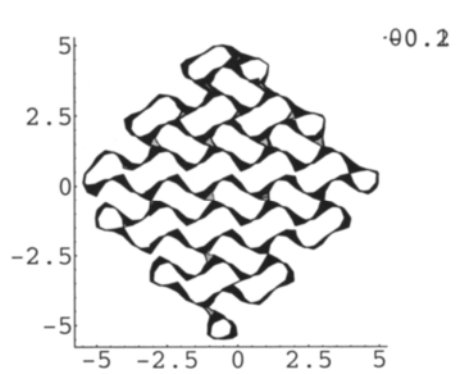


Figure 7.4.4c Thickness of 1/8 of a unit cell.

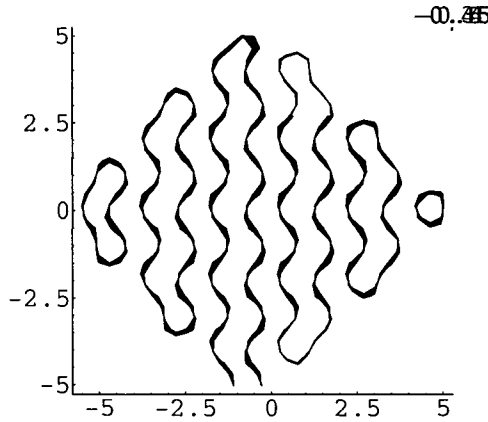


Figure 7.4.4d Thickness of 1/12 of a unit cell.

From equation 7.4.3 and figure 7.4.3, we have calculated slices of various thickness in projection after a cubic axis. Figure 7.4.4a corresponds to a thickness of 2 unit cells and b to 1/4, c to 1/8 and finally d to 1/12 of the cubic unit cell projection axis. Bounded projections like these from fractions of unit cell dimensions make the picture of the structure vary. We show such slices here, because cubosomes can be very large, and electron microscopy pictures may have been taken on thin slices of objects. This is a background for identifications of cubosomes [5] described in chapter 8.

7.5 Cubosomes and the GD Function - Symmetry D

We show the planes, or roots, in figure 7.5.1 to the first general permutation of the variables in space after equation 7.5.1.

$$e^{-(x+y+z)^2} = 0.8 \tag{7.5.1}$$

With all the permutations and proper phase shifts there is tetrahedral symmetry in figure 7.5.2, after equation 7.5.2.

$$e^{-(x+y+z+0.5)^2} + e^{-(x-y+z+0.5)^2} + e^{-(x+y-z+0.5)^2} + e^{-(x-y-z+0.5)^2} = 2.3 \tag{7.5.2}$$

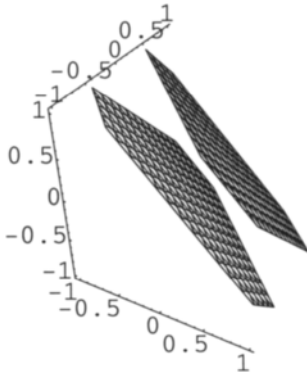


Figure 7.5.1 GD planes corresponding to tetrahedral symmetry.

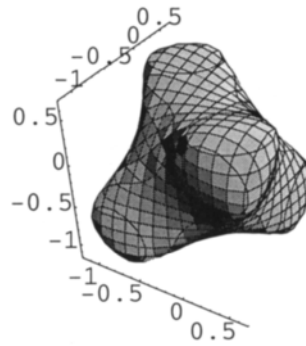


Figure 7.5.2 Tetrahedral body from GD exponentials.

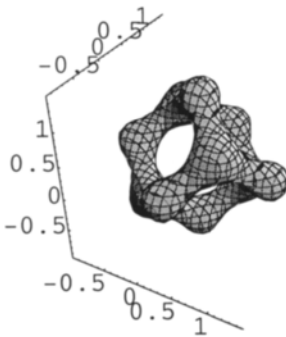


Figure 7.5.3 Two bodies give the adamantane molecule.

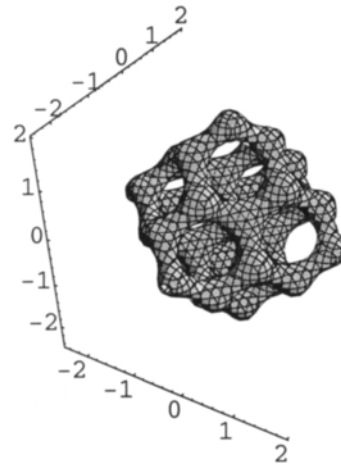


Figure 7.5.4 Three bodies give a small piece of the diamond structure - or a small cubosome.

With increased number of terms of translation, there is the beautiful structure of adamantane in figure 7.5.3 after equation 7.5.3, and a piece of diamond in figure 7.5.4 after equation 7.5.4.

$$\begin{aligned}
& e^{-(x+y+z+0.5)^2} + e^{-(x-y+z+0.5)^2} + e^{-(x+y-z+0.5)^2} \\
& + e^{-(x+y+z-1.5)^2} + e^{-(x-y+z-1.5)^2} + e^{-(x+y-z-1.5)^2} \\
& + e^{-(x+y-z-1.5)^2} + e^{-(x+y-z-1.5)^2} = 3.7
\end{aligned}
\tag{7.5.3}$$

$$\begin{aligned}
& e^{-(x+y+z+0.5)^2} + e^{-(x-y+z+0.5)^2} + e^{-(x+y-z+0.5)^2} \\
& + e^{-(x+y+z-1.5)^2} + e^{-(x-y+z-1.5)^2} + e^{-(x+y-z-1.5)^2} \\
& + e^{-(x+y-z-1.5)^2} + e^{-(x+y-z-1.5)^2} + e^{-(x+y+z+2.5)^2} \\
& + e^{-(x-y+z+2.5)^2} + e^{-(x+y-z+2.5)^2} + e^{-(x+y+z+2.5)^2} = 3.7
\end{aligned}
\tag{7.5.4}$$

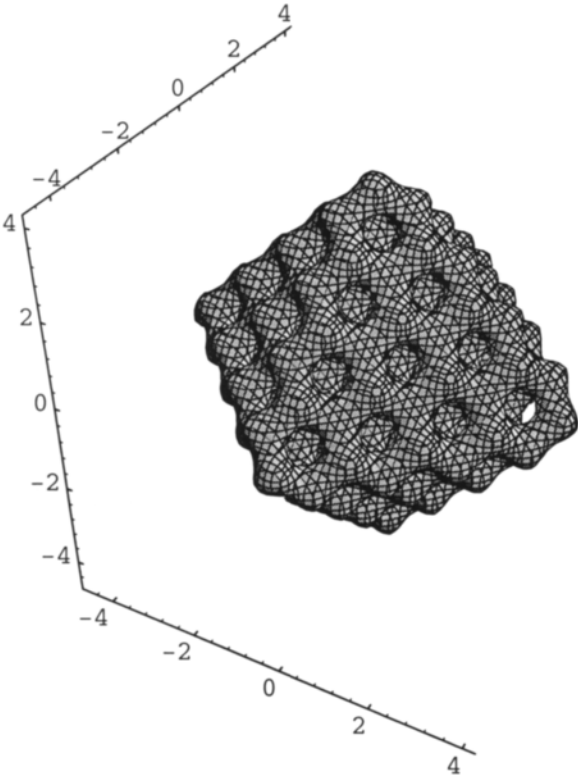


Figure 7.5.5 Six bodies give a bigger cubosome of the D type. The outer shape is an octahedron.

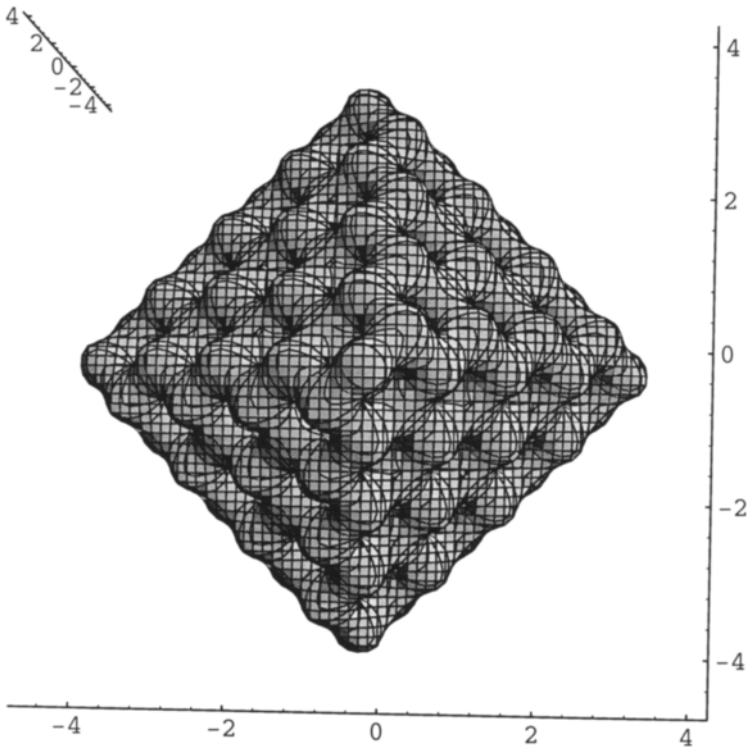


Figure 7.5.6 Different projection.

Finally we show a D-cubosome in figure 7.5.5, after equation 7.5.5. The shape is octahedral, and we also show a projection in figure 7.5.6.

$$\begin{aligned}
 & e^{-(x+y+z+0.5)^2} + e^{-(x-y+z+0.5)^2} + e^{-(x+y-z+0.5)^2} \\
 & + e^{-(x+y+z-1.5)^2} + e^{-(x-y+z-1.5)^2} + e^{-(x+y-z-1.5)^2} \\
 & + e^{-(x+y+z-3.5)^2} + e^{-(x-y+z-3.5)^2} + e^{-(x+y-z-3.5)^2} \\
 & + e^{-(x+y+z+2.5)^2} + e^{-(x-y+z+2.5)^2} + e^{-(x+y-z+2.5)^2} \\
 & + e^{-(x+y+z+4.5)^2} + e^{-(x-y+z+4.5)^2} + e^{-(x+y-z+4.5)^2} \\
 & + e^{-(x+y+z+0.5)^2} + e^{-(x-y+z+0.5)^2} + e^{-(x+y-z+0.5)^2} = 3.5
 \end{aligned} \tag{7.5.5}$$

Another advantage with finite periodicity is the possibility to bring in defects, or disorder, by just adding or omitting a term corresponding to the growth. This is of course important in biology.

Also, there needs not be any translation at all between the terms in the equation input - as long as these terms can be described as planes, periodicity will be present in space.

An obvious application is found in functions of dilatation symmetry. In equation 7.5.6 we have formulated a function which indeed gives the remarkable structure of a 3D Fibonacci periodicity, illustrated in figure 7.5.7. The structure is a dilated P-surface, or dilated primitive packing of bodies. In figure 7.5.8 we give a larger region of this beautiful symmetry as the corresponding 2D plot, at a constant of 1.9.

$$\begin{aligned}
 & e^{-(x-3)^2} + e^{-(y-3)^2} + e^{-(z-3)^2} + e^{-(x-5)^2} + e^{-(y-5)^2} + e^{-(z-5)^2} \\
 & + e^{-(x-8)^2} + e^{-(y-8)^2} + e^{-(z-8)^2} + e^{-(x-13)^2} + e^{-(y-13)^2} + e^{-(z-13)^2} \\
 & + e^{-(x-21)^2} + e^{-(y-21)^2} + e^{-(z-21)^2} \\
 & + e^{-(x-34)^2} + e^{-(y-34)^2} + e^{-(z-34)^2} = 2.5
 \end{aligned}$$

7.5.6

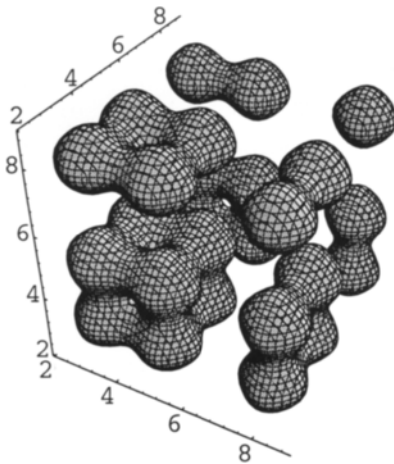


Figure 7.5.7 3D Fibonacci periodicity.

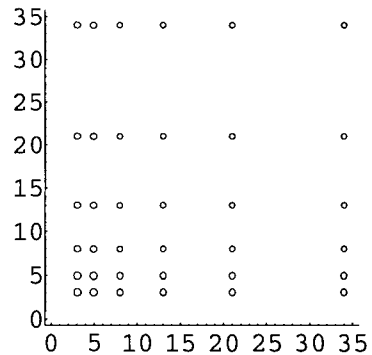


Figure 7.5.8 2D Fibonacci periodicity.

We know that the Fibonacci periodicity gives a sharp Fourier transform (=sharp diffraction pattern), which is evidence of long range order. We conjecture that this will also be the case when there is no regular connection at all between the terms in the equations of finite periodicity as in equation 7.5.7, which is plotted in figure 7.5.9. And the terms represent planes and give repetition in space, but there is no translation vector. Complete disorder in one dimension becomes repetition in two dimensions. This is one of the lowest degrees of order ever - only irregular spaced planes - and might be relevant in biology.

$$e^{-(x-2)^2} + e^{-(y-3)^2} + e^{-(x-4)^2} + e^{-(y-5)^2} + e^{-(x-7)^2} + e^{-(y-9)^2} + e^{-(x-10)^2} + e^{-(y-12)^2} + e^{-(x-12)^2} + e^{-(y-15)^2} = 1.85 \tag{7.5.7}$$

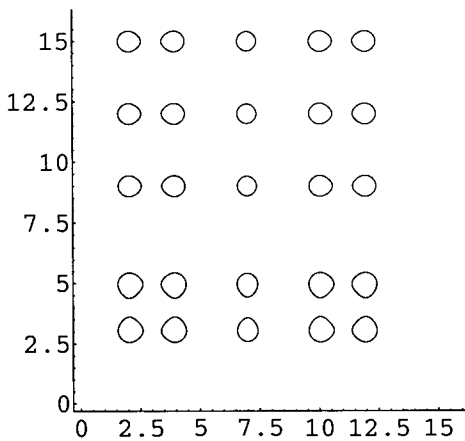


Figure 7.5.9 Low degree of order according to equation 7.5.7.

7.6 Cubosomes and the Handmade Function

We now study functions of the type

$$e^{-(x^2+y^2+z^2)} = C.$$

The function disappears at $C=1$ ($e^0=1$), and with decreasing C there is a growing sphere.

As there are no planes, the function cannot be used to generate periodicity. But the sphere is protected by the exponential, and may be moved and repeated manually to a periodic structure, as has been shown earlier in this book.

With this function we may now put out spheres in space and make them approach each other. We use the concept of connectivity: If one vesicle is surrounded by six other vesicles, and they approach each other so that catenoids are formed, we have the commencement of the formation of the P surface. This is shown in figure 7.6.1a and b, after equation 7.6.1 and clearly demonstrates connectivity 6.

$$\begin{aligned}
 &e^{-(x^2+y^2+z^2)} + e^{-((x-2)^2+y^2+z^2)} + e^{-(x^2+(y-2)^2+z^2)} \\
 &+ e^{-(x^2+y^2+(z+2)^2)} + e^{-((x+2)^2+y^2+(z)^2)} \\
 &+ e^{-(x^2+(y-2)^2+(z)^2)} + e^{-((x)^2+(y+2)^2+z^2)} = C
 \end{aligned}
 \tag{7.6.1}$$

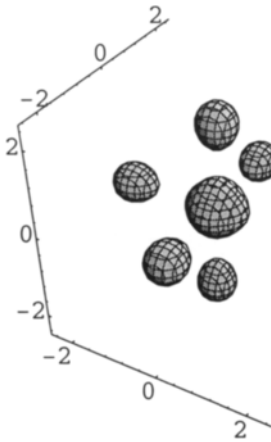


Figure 7.6.1a Six bodies approaching a central one.

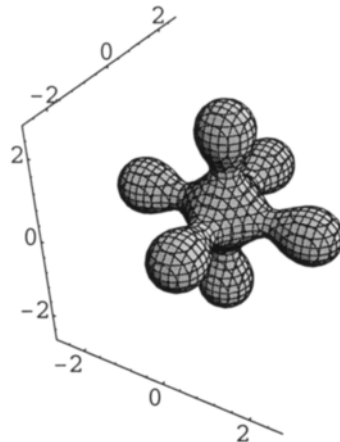


Figure 7.6.1b Six-connectivity.

We increase the number of bodies in equation 7.6.2, and get a cubosome as we show in a split picture in figure 7.6.2.

$$\begin{aligned}
& e^{-(x^2+y^2+z^2)} + e^{-((x-2)^2+y^2+z^2)} + e^{-(x^2+(y-2)^2+z^2)} \\
& + e^{-(x^2+y^2+(z-2)^2)} + e^{-((x-2)^2+y^2+(z-2)^2)} \\
& + e^{-(x^2+(y-2)^2+(z-2)^2)} + e^{-((x-2)^2+(y-2)^2+z^2)} \\
& + e^{-((x-2)^2+(y-2)^2+(z-2)^2)} + e^{-((x-4)^2+y^2+z^2)} + \\
& + e^{-(x^2+(y-4)^2+z^2)} + e^{-(x^2+y^2+(z-4)^2)} + e^{-((x-4)^2+y^2+(z-2)^2)} \\
& + e^{-(x^2+(y-2)^2+(z-4)^2)} + e^{-((x-4)^2+(y-2)^2+z^2)} \\
& + e^{-((x-2)^2+y^2+(z-4)^2)} + e^{-(x^2+(y-4)^2+(z-2)^2)} \qquad 7.6.2 \\
& + e^{-((x-2)^2+(y-4)^2+z^2)} + e^{-((x-4)^2+(y-2)^2+(z-2)^2)} \\
& + e^{-((x-2)^2+(y-2)^2+(z-4)^2)} + e^{-((x-2)^2+(y-4)^2+(z-2)^2)} \\
& + e^{-((x-4)^2+(y-2)^2+(z-4)^2)} + e^{-((x-4)^2+(y-4)^2+(z-2)^2)} \\
& + e^{-((x-2)^2+(y-4)^2+(z-4)^2)} + e^{-((x-4)^2+y^2+(z-4)^2)} \\
& + e^{-(x^2+(y-4)^2+(z-4)^2)} + e^{-((x-4)^2+(y-4)^2+z^2)} \\
& + e^{-((x-4)^2+(y-4)^2+(z-4)^2)} = 0.68
\end{aligned}$$

Next is connectivity four of tetrahedral symmetry which gives the commencement of the D surface, as shown in figure 7.6.3a and b, and equation 7.6.3. More bodies are added in figure 7.6.4 which is a small cubosome, or a piece of diamond. The cubic diamond structure has a hexagonal version (hexagonal diamonds have been found in meteorites from outer space, and their mineral name is Lonsdaleite), and as we have no nodal surface equation for this, we build one with these mathematics. The cubosome is derived from a number of hexagonal coordinates and shown in figure 7.6.5a, with a projection in b. We point out that this is of course also connectivity four, and the density of this hexagonal form is identical with the cubic. The equation for this cubosome may be found in reference [10].

$$\begin{aligned}
& e^{-(x-1)^2+(y-1)^2+(z-1)^2} + e^{-(x+1)^2+(y+1)^2+(z+1)^2} \\
& + e^{-(x+1)^2+(y-3)^2+(z-3)^2} + e^{-(x-3)^2+(y+1)^2+(z-3)^2} \qquad 7.6.3 \\
& + e^{-(x-3)^2+(y-3)^2+(z+1)^2} = 0.08
\end{aligned}$$

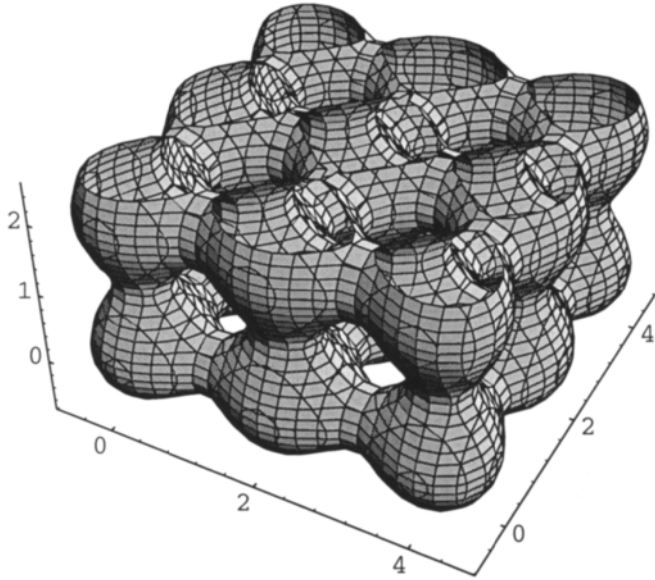


Figure 7.6.2 Split of a handmade cubosome.

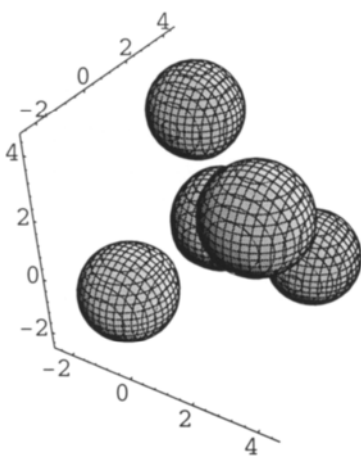


Figure 7.6.3a Four bodies approach a fifth in a tetrahedral manner.

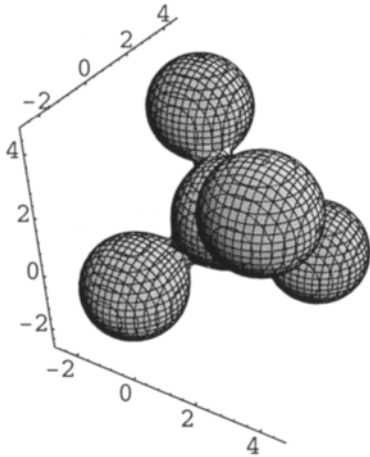


Figure 7.6.3b Four-connectivity.

$$\begin{aligned}
& e^{-(x-1)^2+(y-1)^2+(z-1)^2} + e^{-(x+1)^2+(y+1)^2+(z+1)^2} \\
& + e^{-(x+1)^2+(y-3)^2+(z-3)^2} + e^{-(x-3)^2+(y+1)^2+(z-3)^2} \\
& + e^{-(x-3)^2+(y-3)^2+(z+1)^2} + e^{-(x-1)^2+(y-5)^2+(z-5)^2} \\
& + e^{-(x-5)^2+(y-1)^2+(z-5)^2} + e^{-(x+3)^2+(y-1)^2+(z-5)^2} \\
& + e^{-(x-1)^2+(y+3)^2+(z-5)^2} = 0.08
\end{aligned} \tag{7.6.4}$$

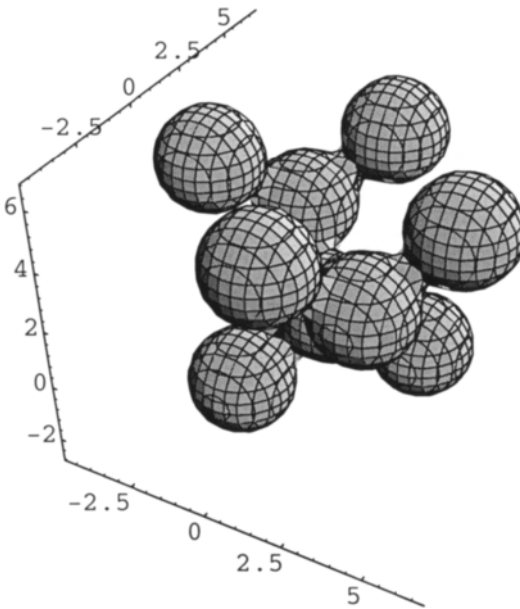


Figure 7.6.4 A piece of diamond.

Connectivity three is the lowest possible for the hyperbolic nodal surface types we deal with here, and we have it in the important gyroid surface. So we put out spheres after this symmetry as in equation 7.6.5, and the structure is plotted in two different projections in figures 7.6.6 a-b to make the connectivity clear.

$$\begin{aligned}
& e^{-(x+1)^2+(y-1)^2+(z-1)^2} + e^{-(x-1)^2+(y-1)^2+(z-3)^2} \\
& + e^{-(x-3)^2+(y-3)^2+(z-3)^2} + e^{-(x-1)^2+(y+1)^2+(z-5)^2} \\
& + e^{-(x-3)^2+(y-5)^2+(z-5)^2} + e^{-(x-5)^2+(y-3)^2+(z-1)^2} = 0.25
\end{aligned} \tag{7.6.5}$$

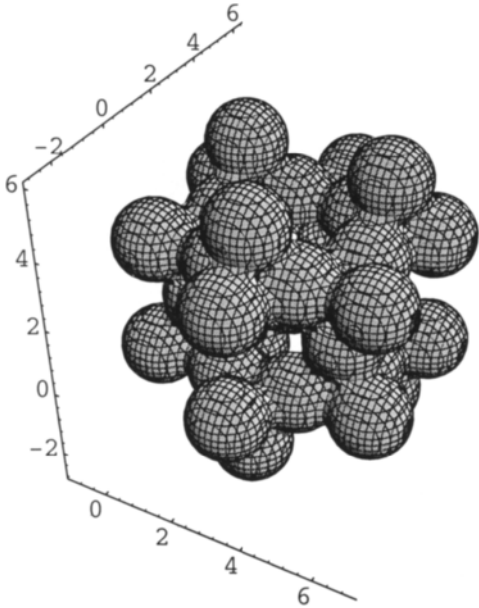


Figure 7.6.5a Hexagonal correspondence of the D surface in finite form.

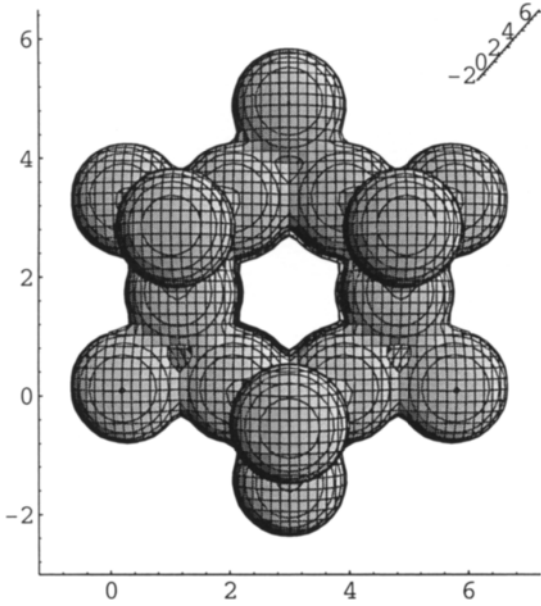


Figure 7.6.5b Different projection.

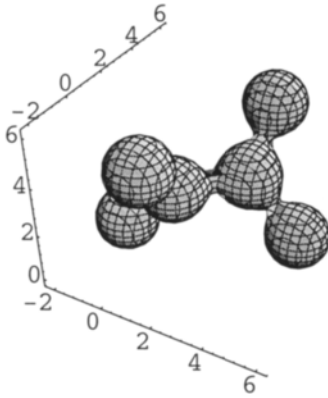


Figure 7.6.6a Three connectivity from the gyroid symmetry.

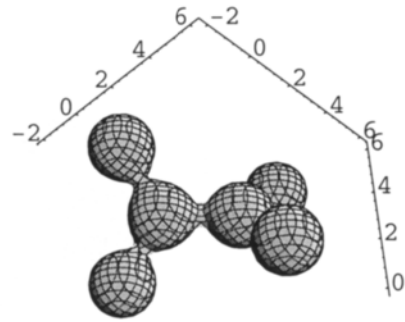


Figure 7.6.6b Different projection.

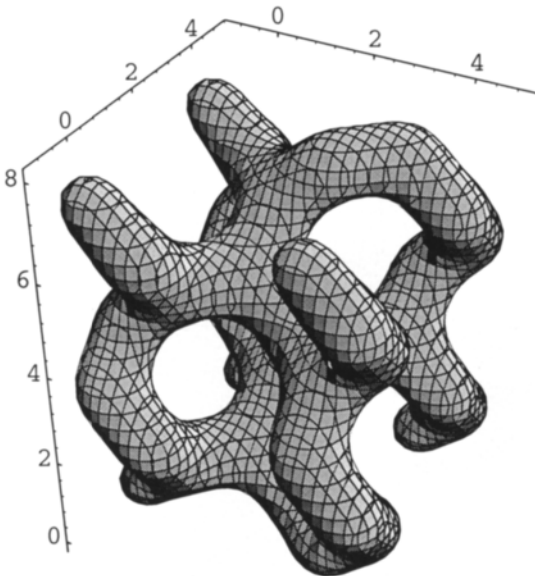


Figure 7.6.7 A handmade gyroid cubosome.

Many more vesicles can be organised after this symmetry to give the gyroid cubosome structure in figure 7.6.7. The equation for this cubosome may be found in reference [10].

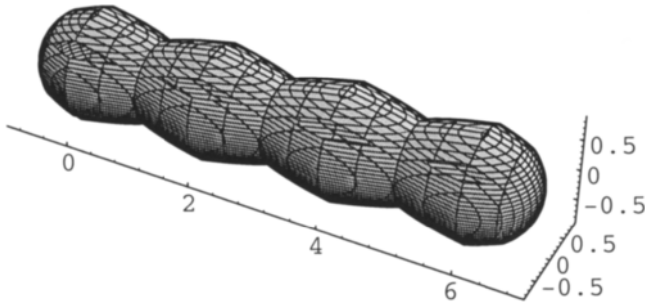


Figure 7.6.8a Linear conformation of two-connectivity.

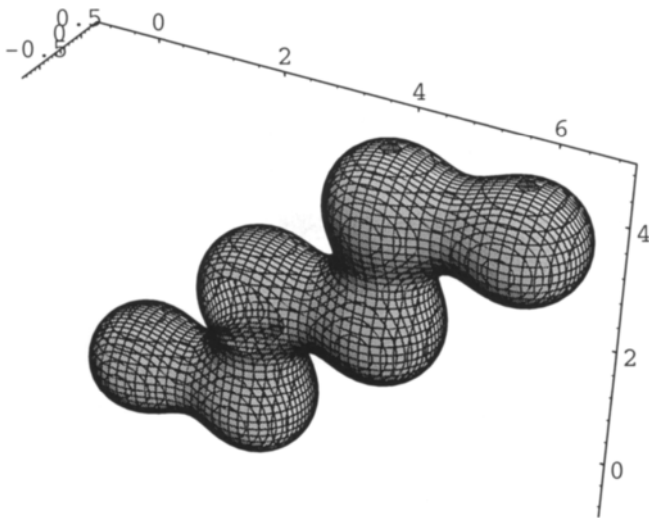


Figure 7.6.8b Two-connectivity with zigzag conformation.

It is clear that connectivity two cannot form hyperbolic periodic surfaces, but we shall deal with it as it is a way to describe the protein structures. There are two methods to describe this connectivity using units of three amino acid residues, the linear and the zigzag ways which are given in figures 7.6.8a-b, and equations 7.6.6 and 7.6.7.

$$e^{-(x)^2+(y)^2+(z)^2} + e^{-(x-2)^2+(y)^2+(z)^2} + e^{-(x-4)^2+(y)^2+(z)^2} + e^{-(x-6)^2+(y)^2+(z)^2} = 0.5 \quad 7.6.6$$

$$e^{-(x)^2+(y)^2+(z)^2} + e^{-(x-2)^2+(y)^2+(z)^2} + e^{-(x-2)^2+(y)^2+(z-2)^2} + e^{-(x-4)^2+(y)^2+(z-2)^2} + e^{-(x-4)^2+(y)^2+(z-4)^2} + e^{-(x-6)^2+(y)^2+(z-4)^2} = 0.5 \quad 7.6.7$$

Two-connectivity does not give simple periodicity, but offers instead a formidable topology. It can form long chains which may be twisted, or turned to form any type of protein structure.

We have chosen the zigzag topology to describe a simple model of sheets distributed in space in a tetragonal manner as present in the catenoid or barrel proteins. The equation is in 7.6.8 and the figures are in two different projections in 7.6.9a-b. The connection between the sheets may be constructed with the linear connectivity, or a mixture of the two. The connection may be made 'thinner' by proper weighting of the terms.

$$e^{-(x)^2+(y)^2+(z)^2} + e^{-(x)^2+(y)^2+(z-2)^2} + e^{-(x-2)^2+(y)^2+(z)^2} + e^{-(x+2)^2+(y)^2+(z-2)^2} + e^{-(x-2)^2+(y)^2+(z+2)^2} + e^{-(x+2)^2+(y-2)^2+(z+2)^2} + e^{-(x+2)^2+(y-2)^2+(z)^2} + e^{-(x+2)^2+(y-4)^2+(z)^2} + e^{-(x+2)^2+(y-4)^2+(z-2)^2} + e^{-(x+2)^2+(y-6)^2+(z-2)^2} + e^{-(x)^2+(y-6)^2+(z+2)^2} + e^{-(x)^2+(y-6)^2+(z)^2} + e^{-(x-2)^2+(y-6)^2+(z)^2} + e^{-(x-2)^2+(y-6)^2+(z-2)^2} + e^{-(x-4)^2+(y-6)^2+(z-2)^2} + e^{-(x-4)^2+(y-4)^2+(z+2)^2} + e^{-(x-4)^2+(y-4)^2+(z)^2} + e^{-(x-4)^2+(y-2)^2+(z)^2} + e^{-(x-4)^2+(y-2)^2+(z-2)^2} + e^{-(x-4)^2+(y)^2+(z-2)^2} = 0.5 \quad 7.6.8$$

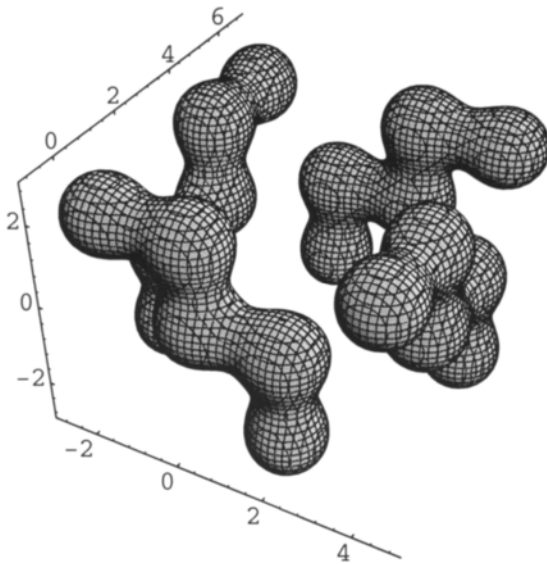


Figure 7.6.9a Two-connectivity in space in a tetragonal manner to give a catenoid or barrel.

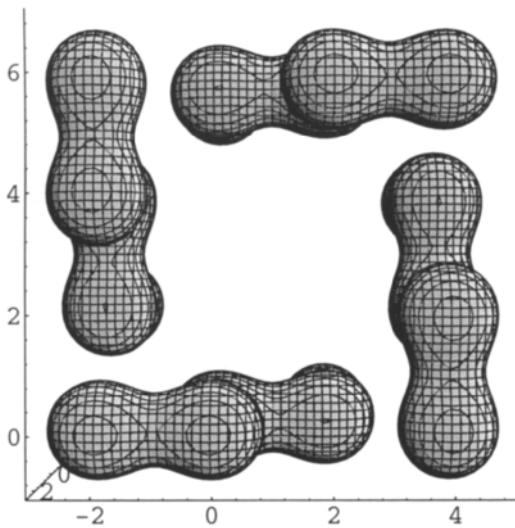


Figure 7.6.9b Different projection.

References 7

- 1 H.S.M. Coxeter, INTRODUCTION TO GEOMETRY, Wiley, New York, 1969.
- 2 K. Larsson, Cubic Lipid-Water Phases: Structure and Biomembrane Aspects, J. Phys. Chem. **93** (1989) 7304 - 7314.
- 3 K. Larsson, S. Andersson, A Phase Transition Model of Co-operative Phenomena in Membranes, Acta Chem Scand. **B40** (1986) 1-5.
- 4 S.T. Hyde, S. Andersson, K. Larsson, Z. Blum, T. Landh, S. Lidin and B. Ninham; THE LANGUAGE OF SHAPE, The Role of Curvature in Physical and Biological Sciences, Elsevier, Amsterdam, 1997.
5. T. Landh CUBIC CELL MEMBRANE ARCHITECTURES, Thesis, University of Lund, 1994.
- 6 S. Andersson, M. Jacob, K. Larsson, S. Lidin, Structure of the Cubosome - a closed Lipid Bilayer Aggregate, Z. Kristallogr. **210** (1995) 315-318.
- 7 K. Larsson, M. Jacob, S. Andersson, Lipid bilayer standing waves in cell membranes, Z. Kristallogr. **211** (1996) 875-878.
- 8 M. Jacob, K. Larsson and S. Andersson, Lipid Bilayer Standing Wave Conformations in Aqueous Cubic Phases. Z. Kristallogr. **212**, 5 (1997)
- 9 M. Jacob, S. Andersson, Finite Periodicity and Crystal Structures, Z. Kristallogr. **212** (1997) 486-492.
- 10 M. Jacob and S. Andersson, *THE NATURE OF MATHEMATICS AND THE MATHEMATICS OF NATURE*, Elsevier, 1998.

8 Cubic Cell Membrane Systems/Cell Organelles and Periodically Curved Single Membranes

'Gentlemen, the views of space and time which I wish to lay before you have sprung from the soil of experimental physics, and therein lies their strength.'

[Minkowski presenting his very famous equation for the amalgamation of time and space introducing four-dimensional space for the first time: Lecture in Köln 1908].

Cell membranes forming cubic symmetry, cubosomes, are described. The time-averaged conformation of the lipid bilayer corresponds to nodal surfaces, reflecting the standing wave dynamics of these membranes. Cubosomes can be produced *in vitro* using well-defined lipids, and the experimental knowledge on these colloidal particles are derived from such lipid systems. *In vivo* cubosomes seem to be formed under some kind of equilibrium condition in the cell. Other three-dimensional cell membrane systems are related to cubosomes, and an example described mathematically here is the endoplasmatic reticulum. Periodic curvature along single membranes is analysed, and the bilayer conformational changes involved in vesicle transport processes are derived based on standing wave dynamics.

8.0 Introduction

Membranes formed by lipid bilayers with embedded proteins envelope all kinds of living cells, from microorganisms to the cell organisation in mammals, and the organelles in the cells. The shape of the cell membranes and structural changes involved in biological processes therefore tell us a lot about basic biological structures.

8.1 Cubic Membranes

For a long time the structure and functionality of the lipid bilayer of cell membranes have been related to the lamellar liquid-crystalline phase. Later segregating regions with solid-like hydrocarbon chains of the lipid

molecules (the gel-state in lipid-water bulk phases) have been introduced in the description.

New aspects on cell membrane structure and function are based on our recent understanding of the bilayer character of cubic lipid-water phases. The most obvious proof of the biological significance of cubic lipid bilayers was the observation that cell membranes can form three-dimensional aggregates with the same cubic symmetry. It seemed natural to term these colloidal particles *cubosomes* [1]. A description of these structural features of cell membranes will be presented below.

The structure determination of the complex cubic lipid-water phases has been complicated due to the limited number of X-ray diffraction lines from the different phases, which is related to the high degree of disorder and a strong temperature fall-off of the intensities. A milestone was the introduction of infinite periodic minimal surfaces, cf. [1]. It is now generally accepted that cubic lipid-water phases, which are lipid and water continuous, have structures consistent with the three fundamental types of minimal surfaces D, G and P. We will first demonstrate the biological occurrence of these structure types. Later, in paragraph 8.4, we will go one step further, from the minimal surface structure representing a time-averaged conformation to what we consider to be the true dynamic conformation of the lipid bilayer.

The early identification of the fundamental minimal surface structures in cell membrane assemblies [1] has been extended to involve thousands of reported electron micrographs of cell membranes [5,6]. Thus membrane textures were analysed in relation to periodicity and curvature of different fracture planes of the three surfaces D, G, and P.

The endoplasmatic reticulum and mitochondria are the membrane assemblies which most commonly (under conditions discussed below) exhibit cubic textures, cf. figure 8.1.1.

The experimental basis behind the identification of these membrane structures is studies during the last decade of cubic phases in well defined lipid-water systems. Such phases occur in aqueous environments of polar lipids, for example certain membrane lipids, which tend to form reverse structures in water. The binary system which has been best characterised is the monooleylglycerol-water system, exhibiting two cubic phases in the temperature range from about 10 °C to about 90 °C. This polar lipid, although not a membrane lipid, is a good model lipid in order to study the reverse types of structures. The introduction of periodic minimal surfaces in order to understand the structures of these cubic phases proved to be very fruitful, and it was demonstrated that the two cubic phases give X-ray

diffraction data consistent with the minimal surfaces known as the gyroid surface, G, and the diamond surface, D [2]. Furthermore the dimensions at the phase transitions shows a relation in agreement with a Bonnet relation between the two forms (involving a transformation without change of curvature). By this result it was obvious that curvature of the lipid bilayer is a significant factor in lipid bilayer behaviour. The conclusion was that these phases are formed by infinite and intersection-free lipid bilayers curved in three dimensions so as to correspond to the D-surface and G-surface, representing the mid-surface of the bilayer. These are two of the three fundamental cubic periodic minimal surfaces. The third, the P (primitive) surface, can be formed if proteins or polymers are added to this lipid-water mixture, cf. [3]. Later these phases/surface types have also been observed in aqueous systems of true membrane lipids. The three surfaces are shown in chapter 3 and in appendix 2.

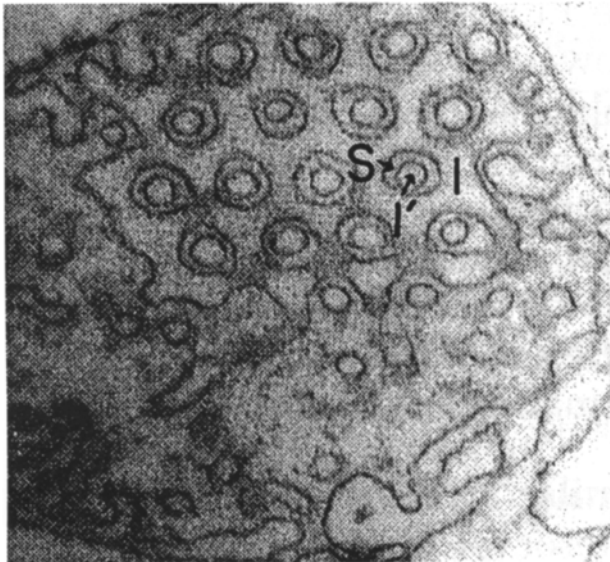


Figure 8.1.1 A mitochondrial membrane from *Pelomyxa carolinensis* after [6]. This texture was earlier interpreted as tubular but examinations by Landh of different projections shows that it is a continuous membrane with conformation according to the P-surface. This section is a projection cut perpendicular to the (111)-direction.

Why are only these minimal surface types observed, and no others, and why does a particular surface occur under certain conditions? Hyde has reported extensive theoretical studies in order to explain the fundamental

relations between these structures, cf. [4]. An important factor is the Gaussian curvature (K) inhomogeneity over the whole structure, expressed as $\langle K^2 \rangle / \langle K \rangle^2$.

Among the ordered surfaces, the genus 3 surfaces P, D, and G are the most homogeneous. The value is 1.218755 (the same value due to the Bonnet relation). They compare with other surfaces (for example the genus 4 surface IW-P with value 1.483759, and conclude that the P, D and G surfaces are the “least frustrated” immersions of a minimal surface sponge in three-dimensional space.

Let us now return to biological tissues. Cubic membranes with extended periodicities have been observed in catfish. This membrane system correspond to the D-surface, and occur in glandular cells of the dendritic organ [6]. The t-tubuli system of muscle cell have also been observed to sometimes exhibit cubic membranes [5,6]. Such a structure is shown in figure 8.1.2.

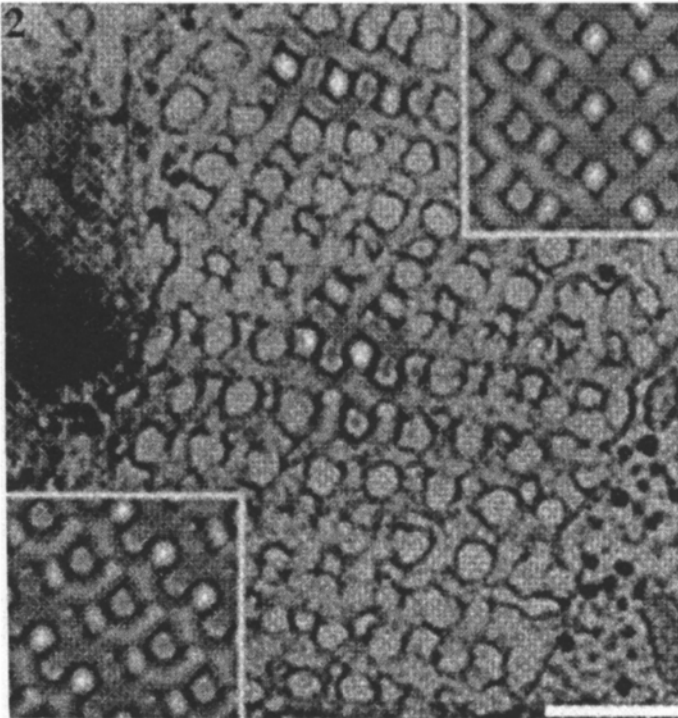


Figure 8.1.2 Cubic membrane system formed by the t-tubuli system of cultured skeletal muscle cells from embryos, courtesy of Tomas Landh [7]. The upper inserted pattern was calculated from the G-surface projected along the [320] direction and the lower pattern along [331]. The bar is 200 nm.

What are the physiological functions of cubic membranes? Landh observed that cubic membrane symmetry is often seen under pathological conditions, cf. [5]. An example of such a cubic cell membrane structure is shown in figure 8.1.3.

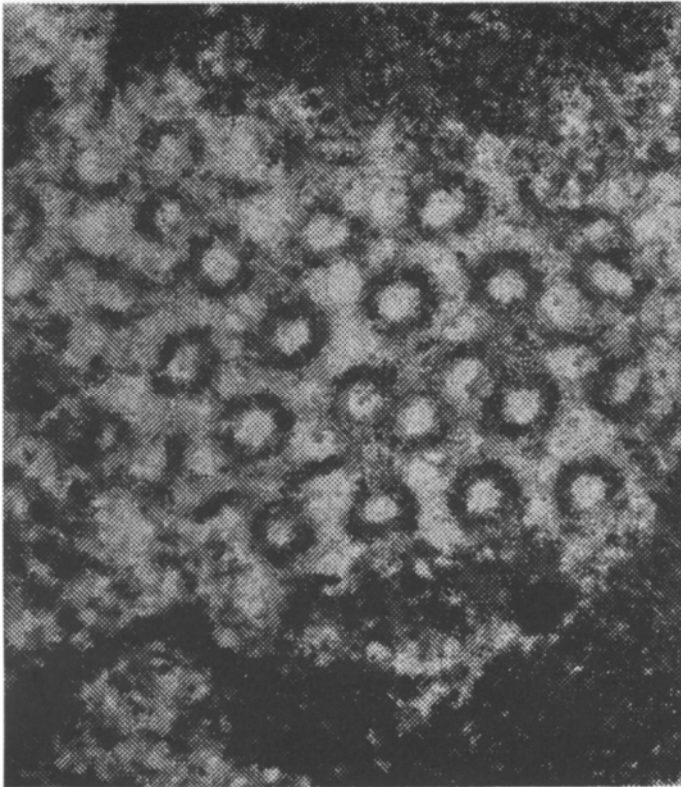


Figure 8.1.3 Intranuclear cubic membrane of cells of a human bone tumour, from [6]. The symmetry indicates that the membrane forms a P-surface.

Landh proposed that cubic arrangements of cell membranes is a way of providing space control in the cell [5]. Formation of parallel surfaces in cubic membrane assemblies makes possible creation of new compartments, not just the separation of an inside from the outside which characterises the classical membrane structure. Usually two parallel surfaces are seen in the ER, for example, providing three closed compartments.

A recent report by Deng and Mieczkowski [8] of reversible formation of cubic membranes in mitochondria is most interesting in this context. They followed the ultrastructure of the mitochondria membrane structure of the giant amoeba *Chaos carolinensis*. The cubic membrane formed in the absence of food and disappeared in the presence of food as in figure 8.1.4. They were able to identify the periodic structures induced when starving, as double membranes of the cubic D- or P-surface, see [8].

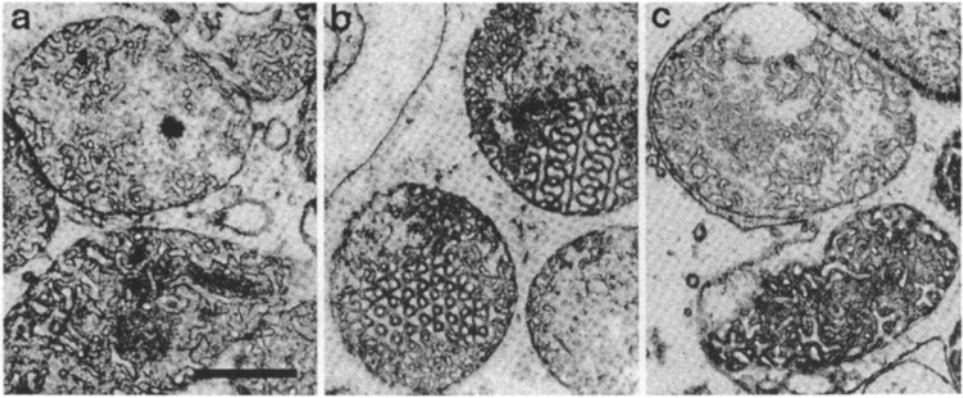


Figure 8.1.4 TEM mitochondrial images of amoeba *Chaos carolinensis* under three conditions: a) fed, b) unfed, c) refed. With permission from [8].

It is interesting in this connection to consider the phenomenon of programmed cell death; apoptosis. It has been proposed that the symbiotic origin of mitochondria in eukaryotic cells leads to the evolution of apoptosis. By binding of certain proteins (Bax-proteins) to the bilayer surface, a permeability transition pore in the mitochondrial membrane is opened [9]. Cytochrome, c, is then released, which activates the caspase family of proteases, responsible for the biochemical breakdown of the cell. The first permeability changes also results in inactivation of the mitochondria itself [9], with loss of volume homeostasis and dissipation of inner transmembrane potential. In other words an equilibrium situation.

These aspects of mitochondria are somewhat similar to the transition between thylakoid membranes of chloroplasts and the cubic membrane forming the so-called prolamellar body. The prolamellar body in plants is a storage form of membranes, for example in pine trees during the winter season in arctic climates when there is no photosynthesis. In the spring season when the photosynthesis starts the prolamellar body is transformed into a new membrane morphology building chloroplasts. As far as we know, this was the first report relating a cell membrane system to cubic lipid-

water phases [10]. It was then interpreted as a P-surface, according to the ultrastructure observed by Gunning. Landh later showed that the membrane in prolamellar bodies is a D-surface [5].

If we consider these features of cubic membranes in mitochondria, in the prolamellar bodies in plants, and Landh's observation that cubic membranes seem to occur frequently in connection with pathological conditions, it seems likely to us that cubic membranes reflect a vegetative state when compositional equilibrium has been reached. The lipid bilayer can hardly vary in composition within a cubosome, as the periodicity then will be destroyed. In a dynamic situation characteristic for life processes, a membrane assembly cannot be perfectly periodic due to gradients in lipid composition along the bilayer and variations in water space composition in the three dimensions. A general property of cell membranes is an asymmetry in lipid species between the two sides of the bilayer. The observed cubic membranes are all symmetric in relation to the mid-surface of the membrane. This is an additional argument for an equilibrium structure.

On this basis we propose that the explanation for the occurrence of the cubic membranes is a state of compositional equilibrium. This does not make them less interesting. Their crystallographic character opens the possibility to study structures of such an enormous complexity by X-ray diffraction and electron crystallography methods. Particularly the discovery of methods to produce cubic symmetry of mitochondria mentioned above will probably be of great importance in the future.

Provided that cubosomes represent an equilibrium state (a vegetative state), the non-equilibrium state of membrane assemblies will involve variations in curvature and periodicity. An important membrane system which is known to occasionally exhibit cubosome structure is analysed below.

8.2 The Endoplasmatic Reticulum

The endoplasmatic reticulum is the dominating membrane system in eukaryotic cells. The common textbook description is a network of interpenetrating tubuli in the centre, smooth ER (SER), which outwards continuously folds into oriented stacks of flattened cisternae; the rough ER (RER). Landh [5] observed that the most common structure of SER is a double membrane forming the G-type of cubic structure. He also observed the connection between the cubic morphology of SER and the lamellar RER, see figure 8.2.1.

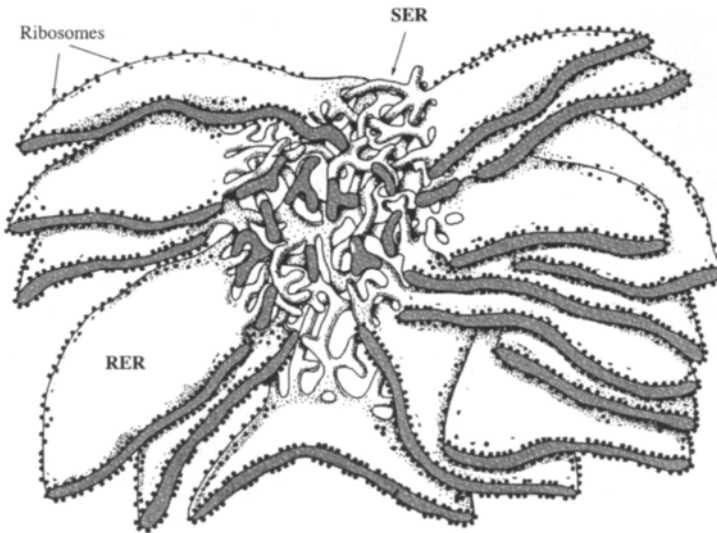


Figure 8.2.1. ER according to a three-dimensional reconstruction, modified after [11].

According to our discussion above about cubic membranes representing a kind of equilibrium state, we assume that a fully active ER is formed by a lipid bilayer with curvature that changes from a tubular network with G-type of structure towards planar lamellae forming the outer RER cisternae. We apply the mathematics from chapter 4 to build this ER-structure.

From figure 4.1.12 and its equation 4.1.3 we make the strategy to formulate the mathematics needed. There we make an arbitrary orientation of parallel planes react with the gyroid. By weighted addition the planes are gradually transformed into the gyroid surface.

We start with the equation of the double gyroid in equation 8.2.1.

$$e^{\cos \pi x \sin \pi z + \cos \pi y \sin \pi x + \cos \pi z \sin \pi y} + e^{-(\cos \pi x \sin \pi z + \cos \pi y \sin \pi x + \cos \pi z \sin \pi y)} = 3,9 \quad 8.2.1$$

We add a cube to this equation to make a cubosome and get 8.2.2.

$$e^{\cos \pi x \sin \pi z + \cos \pi y \sin \pi x + \cos \pi z \sin \pi y} + e^{-(\cos \pi x \sin \pi z + \cos \pi y \sin \pi x + \cos \pi z \sin \pi y)} + x^2 + y^2 + z^2 = 3.9 \quad 8.2.2$$

We will now add parallel planes as the original ER, in form of the double exponential of cosine. We have to do that to keep the identity of each function in the final grand equation.

$$e^{-e^{\cos \pi x}} = 0.2$$

The planes come out pair-wise with interplanar distances which may be changed with the constant. The pairing is important for the transformation mechanism given below.

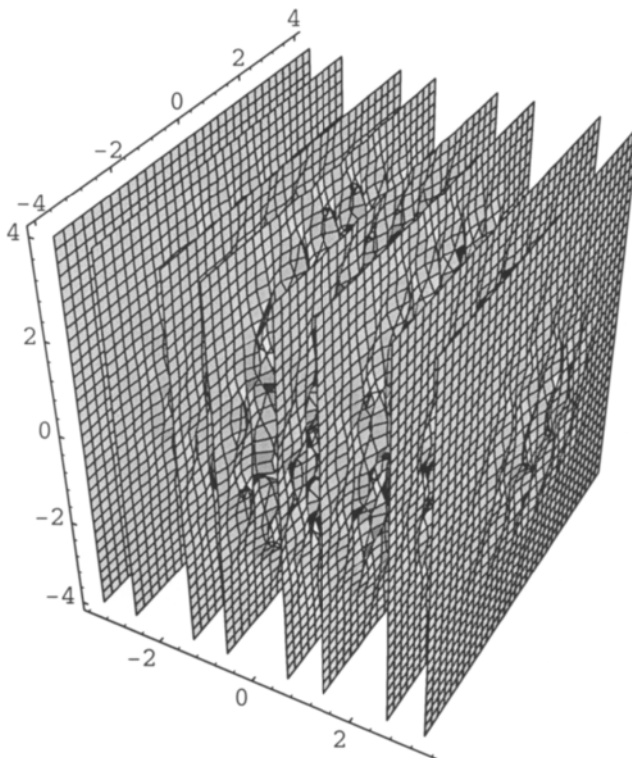


Figure 8.2.2 General projection of equation 8.2.3.

After some trying, we can now formulate the grand equation 8.2.3.

$$e^{-[e^{\cos \pi x \sin \pi z + \cos \pi y \sin \pi x + \cos \pi z \sin \pi y} + e^{-(\cos \pi x \sin \pi z + \cos \pi y \sin \pi x + \cos \pi z \sin \pi y)} + \frac{1}{5}(x^2 + y^2 + z^2) - 1]} + \frac{1}{5}e^{-e^{\cos \pi x}} = \frac{1}{10}$$

8.2.3

With this formula we calculate how an ER has been transformed in the centre to a cubosome structure related to the double gyroid type as shown in a number of different pictures of different projections and borders in figure 8.2.2-6.

In a different projection from figure 8.2.2, it is easily seen in figure 8.2.3 that tubes are formed via pair-wise layers. The whole structure is a layer structure.

In figure 8.2.4 there is a split to show the formation of the cubosome structure in the centre.

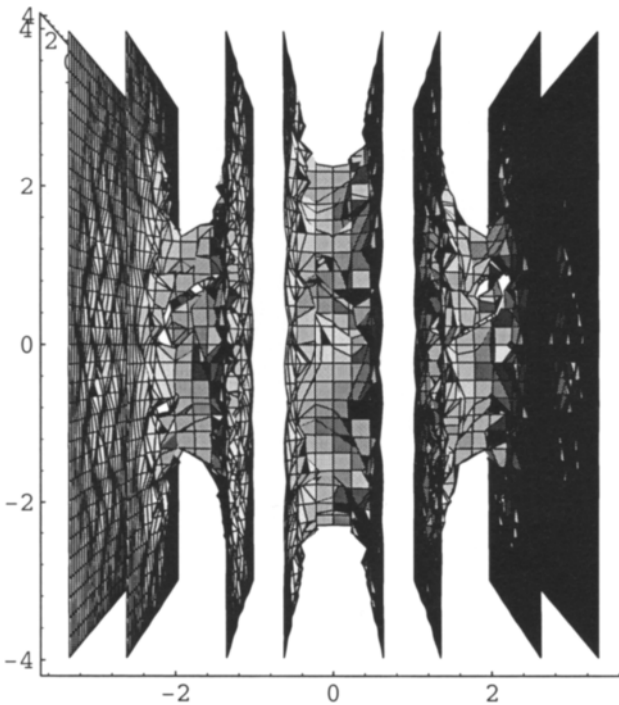


Figure 8.2.3 Tubes are formed via pair-wise layers.

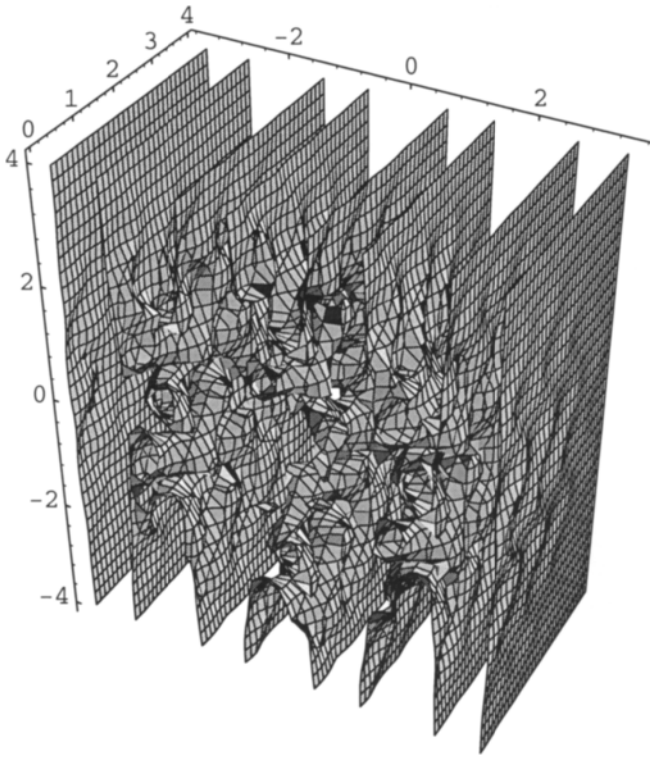


Figure 8.2.4 Split to show cubosome formation.

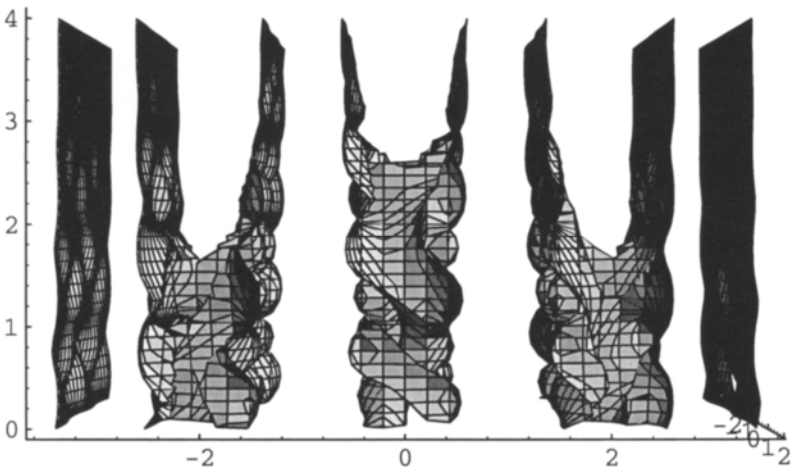


Figure 8.2.5 Detail to show layer and tubular structure.

We go into more detail to show the tubular structure from the double layers in figure 8.2.5.

We select a new projection and new borders to show how planes transform to tubes in figure 8.2.6.

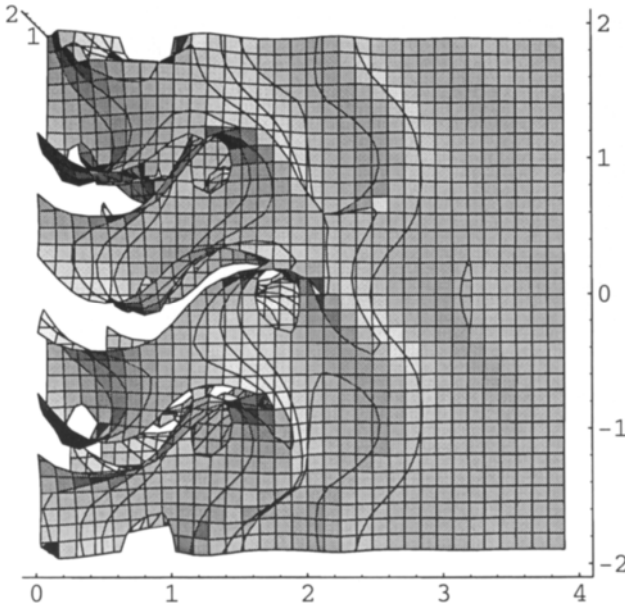


Figure 8.2.6 Plane transformation to tubes.

Different borders give a detailed picture of the double gyroid, and we also see how the planes surround and transform into a tubular structure in figure 8.2.7.

If we change the equation 8.2.3 by weighting down the constant for the exponential $\cos(x)$ term the whole structure is transformed to a structure topologically identical with a double gyroid structure. This structure is consistent with ultrastructural descriptions of ER, cf. figure 8.2.1.

It is thus proposed that ER under normal functional conditions is a complex lipid bilayer structure with compositional gradients, resulting in varying curvature. The bilayer system is described by equation 8.2.3, and it is closed at the outer regions of the planar RER bilayers.

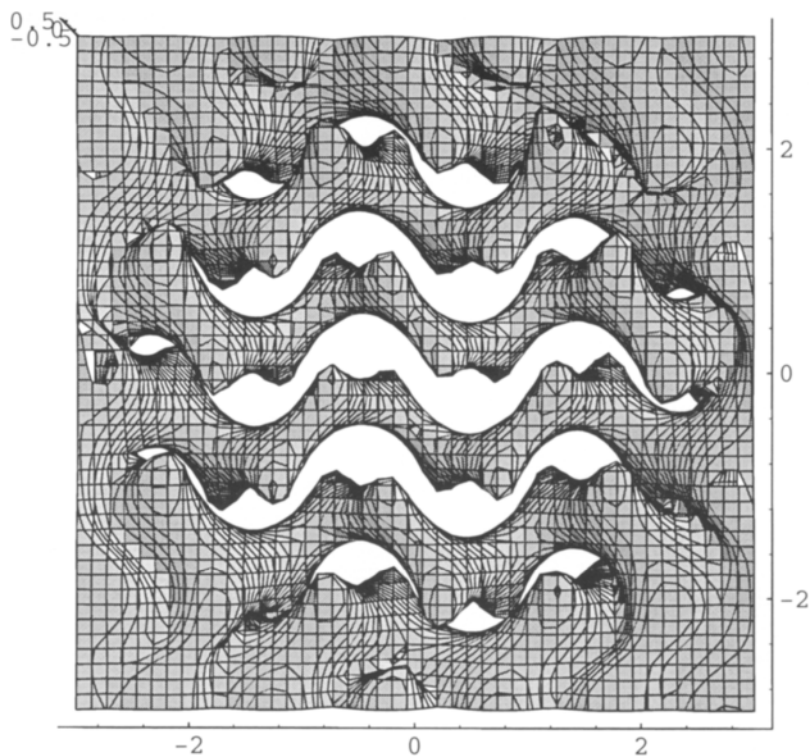


Figure 8.2.7 Double tubular gyroid-like structure.

8.3 Protein Crystallisation in Cubic Lipid Bilayer Phases and Cubosomes - Colloidal Dispersions of Cubic Phases

Landau and Rosenbusch have found that bacteriorhodopsin crystals can be grown from monoolein-water cubic phase where the protein is solubilised [28]. The crystals obtained were hexagonal, and of such good quality that the structure could be studied by X-ray diffraction. Their work provides a promising approach to crystallise membrane proteins, which are unable to aqueous solution. Beside providing a medium where such protein molecules can be solubilised, the lipid molecules of the bilayer can also co-crystallise in order to fill space of this would be needed.

Cubic phases can be dispersed into colloidal particles which closely resembles the cubic structures identified in biological samples [1]. The dispersion can be obtained in regions of ternary phase diagrams, where the cubic phase coexists in equilibrium with a lamellar liquid-crystalline phase and water. This can be observed in lipid systems where one lipid component tends to be cubic whereas the other tends to be lamellar; a situation which often can be expected in membrane lipid systems. A cryo transmission electron microscopy study has shown the morphology and lattice of all three types of surfaces [12]. And an example of this is shown in figure 8.3.1.

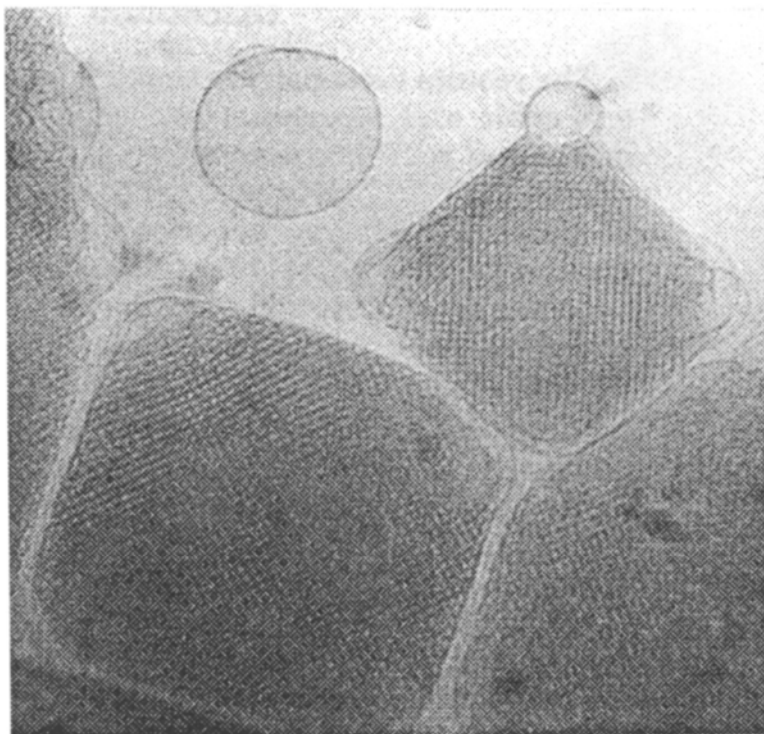


Figure 8.3.1. A cryo -TEM micrograph of colloidal particles with the cubic P-surface type of structure obtained from 1-monooleylglycerol: poloxamer in weight ratio 92.6:7.3, with permission from [12]. The repetition distance observed here is about 10 nm.

8.4 From a Minimal Surface Description to a Standing Wave Dynamic Model of Cubic Membranes

The background to our changed view from that expressed in LANGUAGE OF SHAPE [6] on cubic lipid-water phases and cubic membrane systems will first be summarised. A few years ago von Schnering and Nesper [13] found that the Fourier series which were used to calculate the electron density, involving only one, or in some cases two, low-index structure factors, could give surfaces very close to those of minimal surface when the sum was set to zero (therefore they used the term nodal surface). In the case of the P-surface the nodal surface is found in equation 8.4.1.

$$\cos x + \cos y + \cos z = 0 \quad 8.4.1$$

This surface was observed to agree with the P-type minimal surface within 0.5 %. In this paper they pointed out that they saw no direct physical meaning of their calculated nodal surfaces.

Inspired by their work we started to reconsider the minimal surface model of cubic lipid bilayers, and came to the conclusion that the nodal surface description reflects the true *dynamic* character of the cubic lipid bilayer phases [14]. In other words, the lipid bilayer conformation oscillates as standing waves in relation to the nodal surfaces D, G and P respectively. Driven by thermal excitations, the lipid bilayer is known to exhibit wave motions with amplitudes related to the elastic rigidity. Considering a lipid-water nanocrystal, a cubosome, with perfect crystallographic periodicity, these motions must be in phase along the lattice; the bilayer exhibits standing wave oscillations. The higher the elastic rigidity, the smaller the amplitudes will be.

A lipid bilayer in a cubosome with the cubic P-surface type of structure follows a standing wave conformation which can be expressed by the equation (bilayer centre):

$$\cos x + \cos y + \cos z = p \quad 8.4.2$$

where p will oscillate with time between the maximal amplitudes. The nodal surface of these standing wave motions corresponds to $p=0$. The equation 8.4.2 is a wave equation describing the centre of the bilayer, and different values of p represents isosurfaces frozen in time. A breathing mode of motions is illustrated in figure 8.4.1.

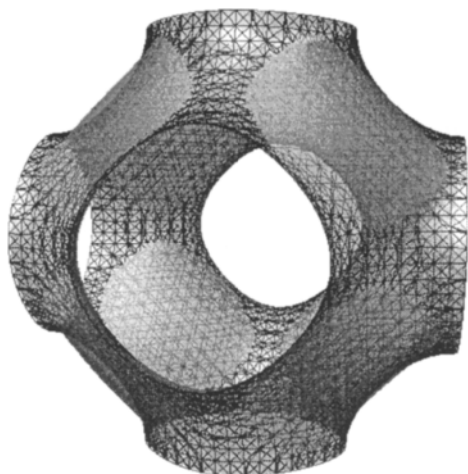


Figure 8.4.1 The P-nodal surface illustrated as a net surrounded by the breathing vibration as transparent layers, from ref. [14].

It is shown in chapter 3 that in the same way as the P-surface represents permutation of $\cos x$, the simple permutations of $\cos(x+y)$ gives the G- and IWP-surfaces, and the permutations of $\cos(x+y+z)$ gives the D-surface. Here we will only show the formulas as illustrations of the simple mathematical equations which describes the most complex of all known lipid structures; molecular organisations which until recently were unknown in spite of extensive studies.

We give first the von Schnering-Nesper formulas in equations 8.4.1, 8.4.3, and 8.4.4.

The P-surface

$$\cos \pi x + \cos \pi y + \cos \pi z = 0 \quad 8.4.1$$

The G-surface

$$\cos \pi x \sin \pi y + \sin \pi x \cos \pi z + \cos \pi y \sin \pi z = 0 \quad 8.4.3$$

The D-surface

$$\cos \pi x \cos \pi y \cos \pi z + \sin \pi x \sin \pi y \sin \pi z = 0 \quad 8.4.4$$

And below we give the equations we get with our mathematics, which are identical to the von Schnering-Nesper equations.

The P-surface

$$\cos \pi x + \cos \pi y + \cos \pi z = 0$$

The G-surface

$$\sin \pi(x+y) + \sin \pi(x-y) + \sin \pi(x+z) + \sin \pi(z-x) + \sin \pi(y+z) + \sin \pi(y-z) = 0$$

The D-surface

$$\begin{aligned} &\cos \pi(x+y+z) + \cos \pi(x-y-z) + \cos \pi(-x-y+z) + \cos \pi(-x+y-z) + \\ &\sin \pi(x+y+z) + \sin \pi(x-y-z) + \sin \pi(-x-y+z) + \sin \pi(-x+y-z) = 0 \end{aligned}$$

Representative parts of each surface are shown in figures 4.1.1-10.

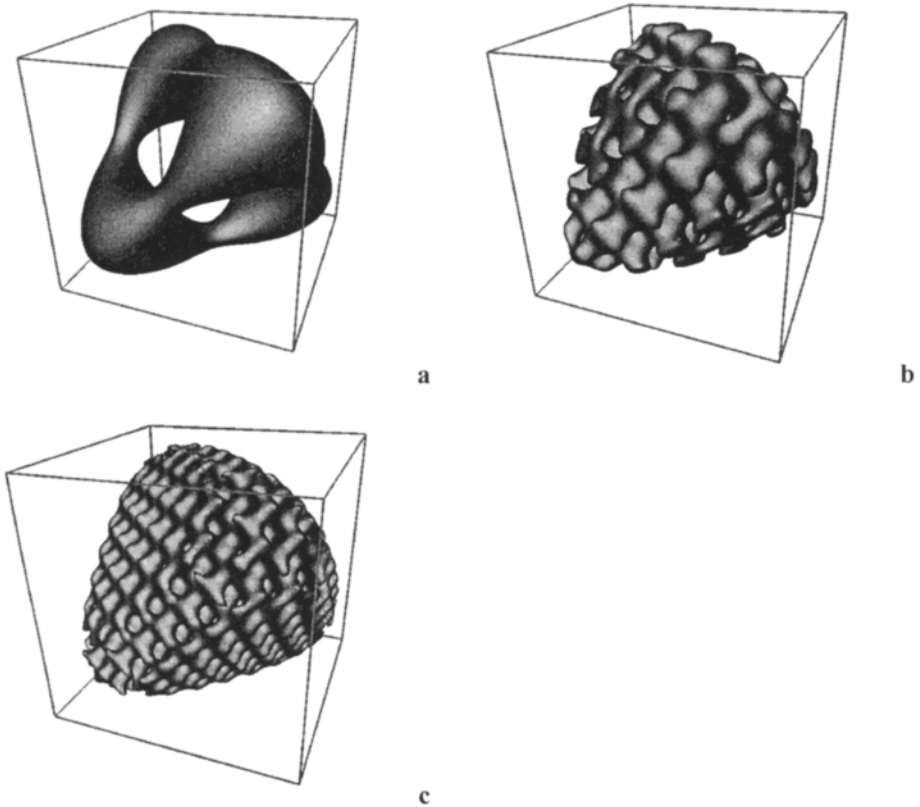


Figure 8.4.2. D-surface cubosomes with tetrahedral boundaries and periodicity n equal to 1, 6 and 10 in **a**, **b** and **c** respectively, after [14].

To describe these standing wave conformations in cubosomes of different sizes, the exponential scale description can be used. An example is shown in figure 8.4.2.

We will now return to the question why the lipid bilayers adopt the different surfaces P, D, and G. In simple binary systems the unit axis of the cubic phases is short, and the different surfaces therefore result in different average molecular shape, and it has been possible to explain the transitions between the three cubic phases in this way. In cubic symmetry occurring in cell membranes, however, the unit cell length is much longer and therefore the shape factor is always like that of lamellar phases (close to 1).

Cubic membrane systems will be formed when single membranes associate into three-dimensional assemblies, and when there is no directional preference. This might occur by fusion of vesicles or by excess membrane material starting to invaginate surrounding tissues and forming isotropic aggregates. We assume that the possibility of transport and motion of solutes in the water medium is important, and therefore the structure should be as open as the bilayer organisation can allow. If vesicles are considered, which fuse by catenoid formation, the most open structure is that with the lowest possible number of connections per vesicle (connectivity). The lowest is 3-coordination of vesicles, which after fusion corresponds to the G-surface. Next comes the D-surface with connectivity 4, and finally the P-surface with connectivity 6.

The wave motions of the bilayer is related to the elastic energy of curvature, cf. [15]. Considering now the picture of the G-, D-, and P-surfaces formed from vesicle fusion, with the wave shape following the bilayer shape, the simplest cubic wave geometry will correspond to the lowest connectivity, which is the G-surface. Then follows with increasing complexity the 4-connected units (D-surface) and connectivity 6 (P-surface). Still higher connectivity has not been observed. The IWP-surface has not been found experimentally in lipid-water systems or in cubic membrane textures. The reason is probably the complex standing wave motions which would be required by such a high connectivity (8).

This, in addition to the Gaussian curvature homogeneity discussed in section 8.1, indicates that cubic lipid bilayer membrane assemblies will show D-, G-, and P-nodal surface conformations of standing wave motions and no other conformations.

The local conformational changes of the bilayer involved in the standing wave oscillations will now be discussed. The transverse motions of the bilayer means that the surface area will expand and contract. These motions will be related both to the bilayer compressibility and the curvature

elasticity. Contrary to standing wave vibrations in an ordinary crystal, the space changes on each side of the bilayer must be taken into account. Minor oscillations may reflect density fluctuations in the water channel system. The standing waves are described by oscillations with time of p in equation 8.4.2, (analogously in the equations of the D- or the G-surface). The wave shape defines the mid-surface of the lipid bilayer. If the amplitudes, *i.e.* the variations of the water compartment size, are larger than the density fluctuation in the water compartments, there will be a net movement of water molecules between the globular units coupled to the wave frequency, as it seems reasonable to assume that there is no water transport over the bilayer.

Let us consider one alternative of motion of water in the P-surface structure. We start from the globular bilayer structure unit around origin, which, at a certain time, is assumed to oscillate inwards in relation to the nodal surface conformation. This means that the adjacent units in x-, y-, and z-direction will oscillate in phase, but outwards. The next units in the three directions will oscillate inwards, and so on.

An alternative would be that the bilayer in every globular unit moves through the nodal surface, with the same kind of alternations inwards/outwards as described before. This intuitively appears more attractive. The time-averaged conformation of the centre of the bilayer in both these alternatives is equal to the nodal surface.

We can illustrate the extremes of these conformations by calculations of the P-surface, allowing p in equation 8.4.2 to alternate between the positive and a negative extreme values of p when going from one unit to the next. This corresponds to motions according to the second alternative described above.

There are other alternatives of bilayer motion. In figure 8.4.3 it can be seen that half of each globular unit moves inwards as the other half moves outwards.

The wave motion amplitude varies with Gaussian curvature of the time-averaged conformation, exhibiting a maximum at flatpoints and changing to zero at the middle of the catenoids (with the smallest negative value of the Gaussian curvature). This appears logical from a molecular packing point of view. The freedom of lipid molecules to move in a transverse direction must be highest at the flatpoints. The conclusion from this discussion is that the requirement of a coherent bilayer and constant total volumes on each side leaves only a few wave motion alternatives.

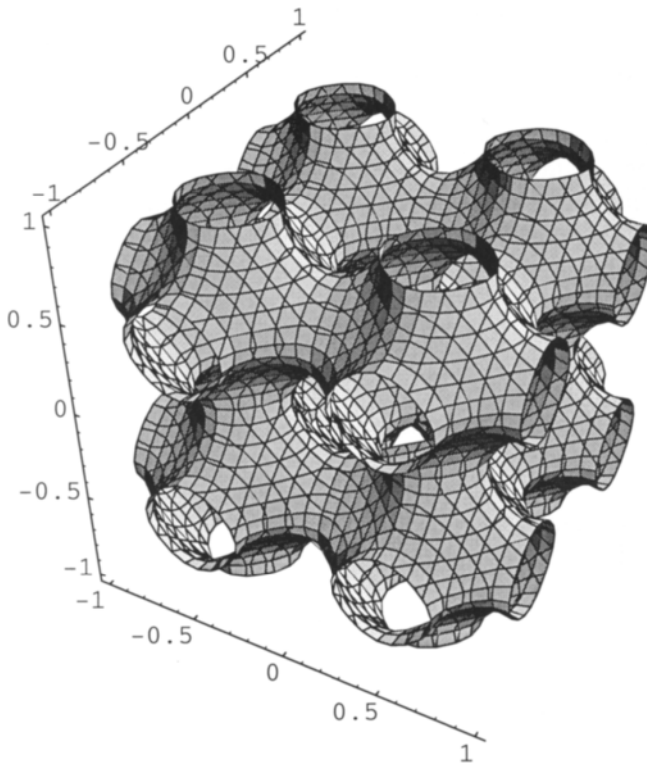


Figure 8.4.3 Illustration of alternation of conformation within each unit of the P-surface according to the equation: $\cos x + \cos y + \cos z - 0.6 \sin x \sin y \sin z = 0$.

Going from the perfect cubic symmetry of lipid-water cubosomes discussed above to cubic membranes, the situation must be the same even if the unit cell of the membrane assemblies is much longer, and therefore the periodicity less perfect. Standing wave motions of the membranes are thus assumed to take place in all cell organelles exhibiting cubic symmetry. Even surface membranes like the plasma membrane may sometimes form periodically curved bilayers. Considering such periodicity along a closed surface, standing wave oscillations should occur, as described in the last paragraph. A general feature of biomembranes is that the bilayer seem to exist on the border between an ordinary planar conformation, corresponding to the lamellar phase in lipid-water systems, and reverse phases (such as the cubic or reverse hexagonal phases in lipid-water systems). This means that the bilayer has a high inner packing pressure, which results in elastic rigidity. And we repeat; with elastic rigidity and periodicity of the bilayer the thermal motions must form standing waves.

8.5 Periodical Curvature in Single Membranes

When the bilayer character of cubic lipid-water phases and their existence in biology had been revealed, as described above, it was natural to consider the possibility of a similar periodic curvature along the surface of single membranes [16]. We proposed that the periodically curved conformation represents a functional state. Experimental evidence were later reported, such as effects of anaesthetic agents, cf. [1]. Helfrich has independently proposed a similar periodicity (“highly localised saddles of very high curvature”) along membrane surfaces [17].

Meyer et al [18] observed periodically curved membranes in L-form cells of *Streptomyces hygrosopicus* and also in vesicles prepared from their lipids, see figure 8.5.1.

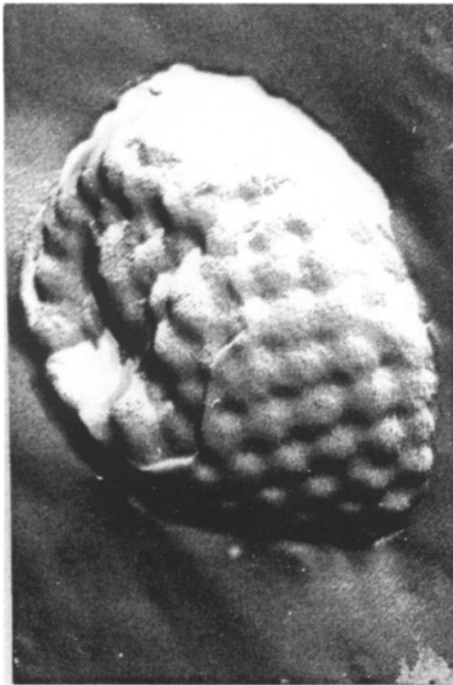


Figure 8.5.1 Periodically curved membrane observed in the L-form of membranes of *Streptomyces hygrosopicus*, after [18].

In an analysis of the mechanical properties of the bilayer in simple lipid phases, Seddon [19] concluded from the stress profile that non-planar spontaneous curvatures should occur frequently. This tendency should be more pronounced in cell membranes, with an asymmetric lipid distribution over the bilayer.

The membrane lipid composition of membranes is regulated to induce a structure very close to the transition into a reversed phase, either a cubic or reverse hexagonal [20,21]. Detailed analysis of environmental influence on membrane lipids of *E. coli* shows that they regulate membrane composition to correspond to the three-dimensional transition region “between the gel-state and non-lamellar structures” [22]. Diacylglycerols added to membrane lipids tend to induce a phase transition into cubic phases. From a study in yeast, this molecule has been proposed to give “non-bilayer” structures in Golgi, and by this mechanism induce vesicle formation [23]. Phase changes of the lipid bilayer induced by anaesthetic agents is a striking demonstration of the intricate balance between bilayer/nonbilayer conformations, and provides strong evidence for the significance of periodic curvature. This is not discussed further here as it is covered in connection with nerve signal propagation in chapter 13.

Our interpretation of these data is that membrane lipid composition is controlled by the physical state in the bilayer; the lateral packing pressure [1]. Membrane embedded enzymes for lipid synthesis/modification can provide these mechanisms, with the inner pressure working as an on/off switch. The inner pressure reflects the balance between a lamellar (α -type) and a periodically curved conformation, which in turn determines elastic rigidity and periodic curvature of the bilayer structure.

If there is crystallographically perfect periodicity along the surface, the thermal motions, which in a bilayer are wave oscillations, must form standing waves.

A calculation modelling an oscillating periodic membrane is shown in figure 8.5.2. These calculations should only be regarded as indications of possible standing wave conformations. The smallest vesicles observed have diameters in the size range a few hundred Å. There is some information on wave geometry from undulation studies of lamellar liquid-crystalline phases, which indicate that such small vesicles will exhibit maximal wave-length, which means that the shape will oscillate between an oblate and prolate ellipsoid. With larger vesicles other wave conformations will be possible. Positions along the spherical surface with largest amplitudes must form networks fitting the surface area. The simplest wave conformation with a triangular network is shown in figure 8.5.2 and equation 8.5.1. The amplitude maxima are located at the six points of intersection between the

coordinate axes and the sphere, and the wave-length is a quarter of the radius. The simplest case (longest possible wave-length) with a square network is obtained when the surface is divided into six equal squares (by intersections between two circles perpendicular to each of the three coordinate axes, giving eight points of amplitude maxima). The waves in this simplified description will sweep through the spherical surface. In the last case, the three circles through the origin perpendicular to the three axes will form nodal lines at their intersection with the sphere.

$$x^2 + y^2 + z^2 + \omega(\cos 2\pi x + \cos 2\pi y + \cos 2\pi z) = 1 \quad 8.5.1$$

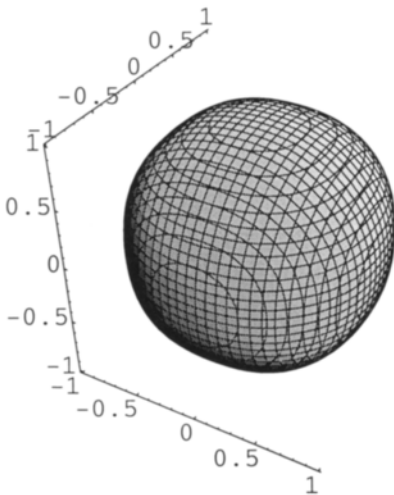


Figure 8.5.2a $\omega=0.02$.

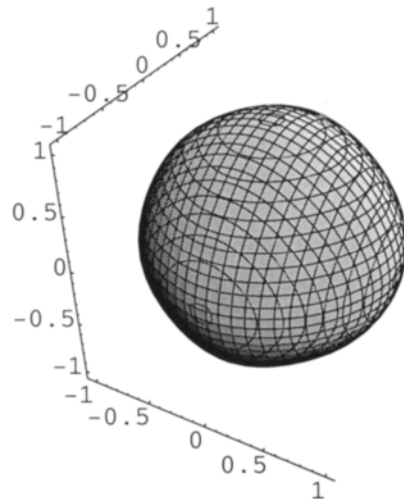


Figure 8.5.2b $\omega=-0.02$. (the dual of a).

In a true membrane the spontaneous curvature is likely to deviate from that of a spherical shape, as pointed out early by Helfrich, cf. [15], and the time-averaged equilibrium shape will therefore exhibit periodic curvature. When the structure is periodic, involving elastic rigidity, the motions will be restricted to standing waves. These motions may therefore be limited to oscillations between the equilibrium position. An example, which we consider relevant to a true membrane in the micron size range, is illustrated in figure 8.5.3 as spherical cuts and equation 8.5.2.

$$x^2 + y^2 + z^2 + \omega(\cos 2\pi x \sin 2\pi z + \cos 2\pi y \sin 2\pi x + \cos 2\pi z \sin 2\pi y) = 12 \quad 8.5.2$$

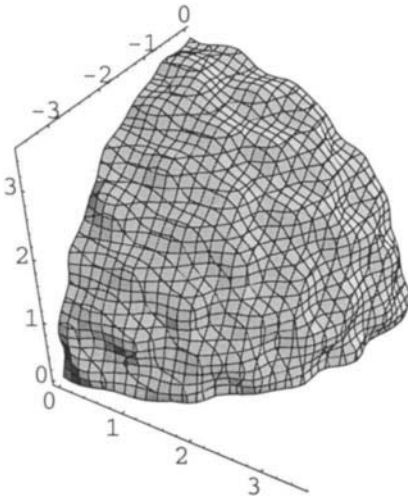


Figure 8.5.3a $\omega=0.4$.

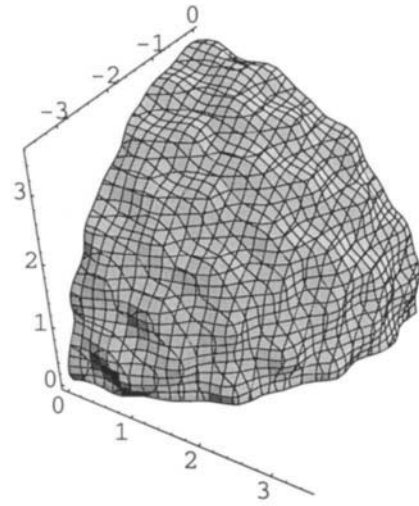


Figure 8.5.3b $\omega=-0.4$ (the dual of a).

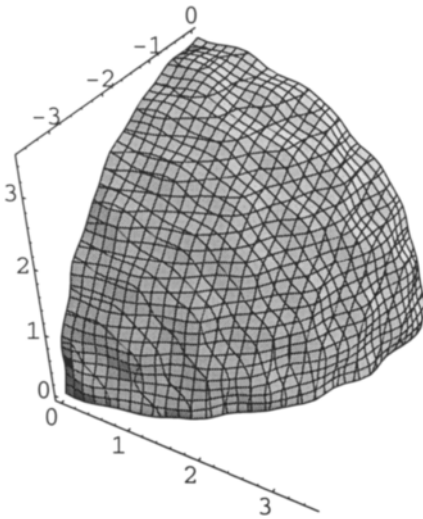


Figure 8.5.3c $\omega=0.25$.

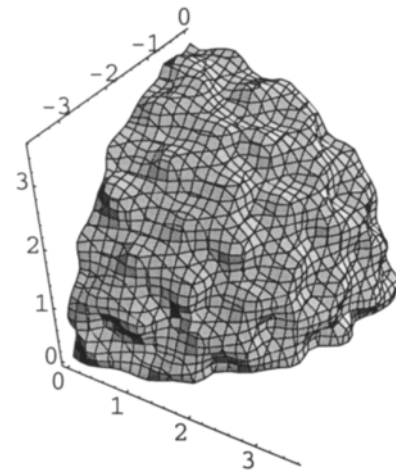


Figure 8.5.3d $\omega=0.6$.

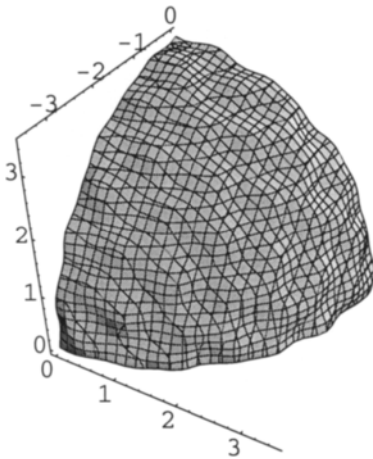


Figure 8.5.3e $\omega=0.3$

In order to get a uniform wave conformation in this way, the outer shape will follow the $C_P(100)$ -, $C_D(111)$ - or $C_G(111)$ -surface structure (giving square or hexagon repetition units) in all directions. It can also be mentioned that the C_G -surface can provide chirality to the membrane curvature, see figure 8.5.4.

$$x^2 + y^2 + z^2 + 0.4[\cos 2\pi x \sin 2\pi z + \cos 2\pi y \sin 2\pi x + \cos 2\pi z \sin 2\pi y] = 12 \quad 8.5.3$$

As discussed above in connection with cubosomes, it is assumed that there is one dominating mode of wave oscillations, which is directly related to the periodicity of the curvature. The oscillations represents contraction and expansion of the bilayer in relation to the time-averaged conformation. This average conformation is assumed to be of the same order of magnitude as observed in erythrocyte membranes [24] with a wave-length of about 100 nm and an amplitude of about 10 nm. The frequency of this kind of bilayer motions is considered to be about 10 Hz [25]. There are less information available on probable size of the standing wave conformational variations, which is related to the elastic rigidity of the bilayer. They can be expressed as variations in average cross-section area per lipid molecule, and there are some data on this from X-ray studies of bilayer dimensions of cubic phases with different curvatures, cf. [6].

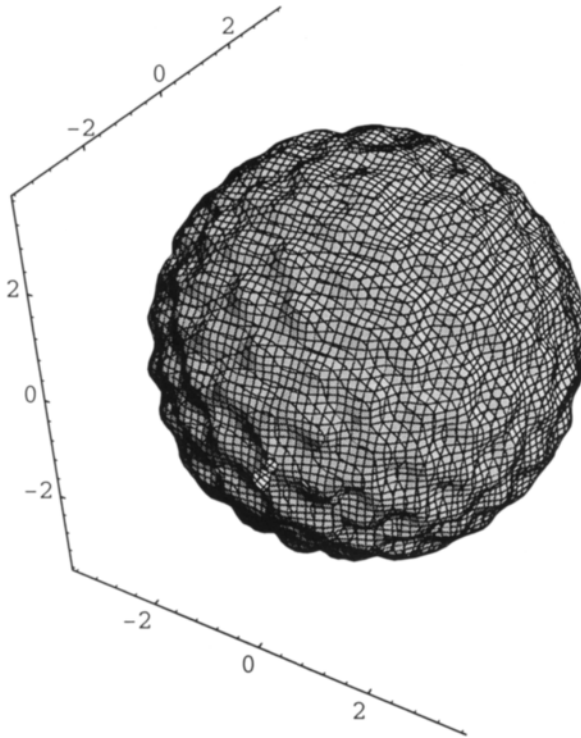


Figure 8.5.4. Illustration of a time-averaged conformation of a membrane of spherical shape oscillating as a standing wave according to equation 8.5.3.

Wave-like motions of lipid bilayers in vesicles and membranes have earlier been frequently discussed, cf. [25,26]. These undulations/fluctuations have been assumed to occur statistically along the bilayer, and the bilayer units moving in and out have been modelled as a two-dimensional gas. It seems natural to assume this kind of wave movements when the bilayer lacks lateral periodicity. With periodic curvature occurring in the membrane, the bilayer will exhibit standing waves, providing an organisation of the membrane in time and space (membrane functions requires control in time and space).

Finally we will consider the budding off processes of vesicles from membranes and membrane assemblies, and the reverse processes, both of which are involved in cellular transport phenomena. An intensive vesicle traffic occur constantly between ER, where proteins and lipids are produced, the Golgi apparatus, and the plasma membrane. Some vesicle

formation takes place through cage-forming proteins like clathrin, but there are also vesicle formation/transportation phenomena which do not involve such skeleton forming molecules. Transport via pinocytosis is one example.

In any periodic cell membrane assembly, the bilayer will exhibit wave motions. A change in packing within the bilayer, for example a pH-shift leading to change of a membrane protein conformation or a membrane lipid ionic charge, must be expected to influence the wave length of these wave motions. We show below in figure 8.5.5, in the case of a curved membrane system how such wave structure variations can lead to vesicle budding off. If we reverse the process it corresponds to membrane fusion.

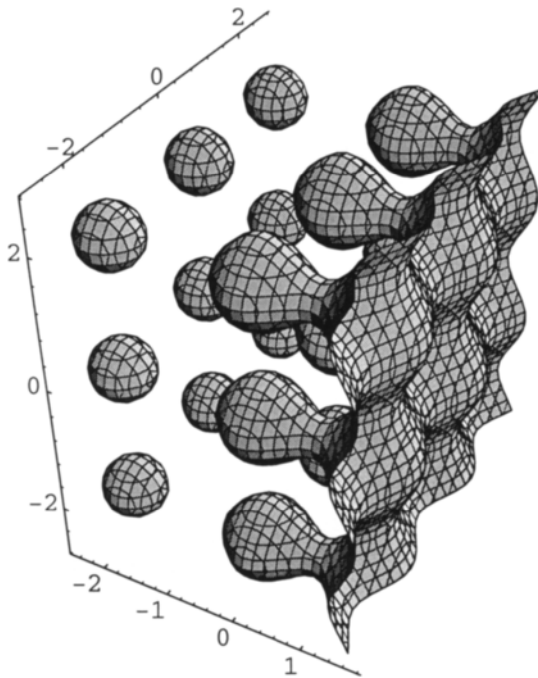


Figure 8.5.5 Vesicle formation, as defined by
 $\cos \pi x + \cos \pi y + \cos \pi z + e^{(x-0.5)} - 2.2 = 0.$

These vesicle transport phenomena, particularly the ones involving the Golgi apparatus, are further described in chapter 11.

The standing wave view on membrane structure has fundamental implications. A membrane with periodic curvature, which therefore shows standing wave motions, represents a mechanical equilibrium along the whole membrane surface. A mechanical disturbance, the fusion of a vesicle, or a conformational change inside the bilayer of a membrane protein, will be sensed over the whole membrane within the time of the standing wave frequency (neglecting damping effects).

Assuming that this dynamic model of control of membrane structure via its physical properties is correct, many questions remain to be answered. How common is the occurrence of periodic curvature along a bilayer? If it only occurs as a transient state, what are the conditions that will switch the conformation from non-periodic (with thermal mobility taking place as “undulations”) to a periodic structure and a standing wave state?

References 8

- 1 K. Larsson, *J. Phys. Chem.* **93**, 7304 (1989).
- 2 S. Hyde, S. Andersson, B. Ericsson and K. Larsson, *Z. Kristallogr.* **168**, 213 (1984).
- 3 T. Landh, *J. Phys. Chem.* **98**, 8453 (1994).
- 4 S. Hyde and A. Fogden, *Progr. Colloid Polym. Sci.* **108**, 139 (1998).
- 5 T. Landh CUBIC CELL MEMBRANE ARCHITECTURES, Thesis, University of Lund, 1994.
- 6 S. Hyde, S. Andersson, K. Larsson, Z. Blum, T. Landh, S. Lidin and B. Ninham; *THE LANGUAGE OF SHAPE*, Elsevier, Amsterdam, 1997.
- 7 T. Landh, *Zoological Studies*, **34** suppl 1, 241 (1995).
- 8 Y. Deng and M. Mieczkowski, *PROTOPLASMA* **203**, 16 (1998).
- 9 I. Marzo, C. Brenner, N. Zamzami, J. M. Jurgensmeier, S. A. Susin, H. L. A. Vieira, M.-C. Prevost, Z. Xie, S. Matsuyama, J. Reed and G. Kroemer, *Science* **281**, 2027 (1998).
- 10 K. Larsson, K. Fontell and N. Krog, *Chem Phys. Lipids* **27**, 321 (1980).

- 11 B. Alberts, D. Bray, J. Lewis, M. Raff, K. Roberts, and J.D. Watson, *Molecular Biology of THE CELL*, page 580, Garland Publishing, Third Edition, 1994.
- 12 J. Gustavsson, H. Ljusberg-Wahren, M. Almgren and K. Larsson, *Langmuir* **26** 6964 (1997).
- 13 H. G. von Schnering and R. Nesper, *J. Phys. B- Cond. Matter* **85**, 407 (1991).
- 14 M. Jacob, K. Larsson and S. Andersson, *Z. Kristallogr.* **212**, 5 (1997).
- 15 W. Helfrich, *Z. Naturforsch.* **A28**, 693 (1973).
- 16 K. Larsson and S. Andersson, *Acta Chem Scand.* **B40**, 1 (1986).
- 17 W. Helfrich, *Liq. Crystals* **5**, 1647 (1989).
- 18 H. W. Meyer, W. Richter and J. Gumpert, *Biochim. Biophys. Acta* **1026**, 171 (1990).
- 19 J. Seddon, *Biochim Biophys. Acta* **1031**, 1 (1990).
- 20 G. Lindblom and L. Rilfors, *Biochem. Biophys. Acta* **988**, 221 (1989).
- 21 B. de Kruijff, *Nature* **366**, 129 and 587 (1997).
- 22 S. Morein, A. Andersson, L. Rilfors and G. Lindblom, *J. Biol. Chem.* **271**, 6801 (1996).
- 23 T. F. J. Martin, *Nature* **387**, 21 (1997).
- 24 K. Zeeman, H. Engelhart and E. Sackmann, *Eur. J. Biophys.* **18**, 203 (1990).
- 25 E. Sackmann, *Science* **271**, 43 (1996).
- 26 R. Lipovsky, *Nature* **349**, 475 (1991).
- 27 K. Larsson, M. Jacob and S. Andersson, *Z. Kristallogr.* **211** (1996) 875.

This Page Intentionally Left Blank

9 Cells and their Division - Motion in Muscles and in DNA

Un homme qui y consacrerait son existence arriverait peut-être à se peindre la quatrième dimension [Poincaré,1].

A mathematical model of membranes in cell division is given. Such divisions are carried out with the two kinds of lipid bilayer membranes, the single plasma membrane and the double nuclear membrane and of mitochondria.

The Hermite operator is used to transfer cell content through the transformation.

With mathematics for “handmade” periodicity, a mitochondrion cell is divided.

The motion in a muscle cell is described mathematically.

A translation operation on two single spirals gives a double of DNA-type.

Mathematical mechanisms are given to form the DNA-structures of the Holliday junction, and the cruciform.

9.1 The Roots and Simple Cell Division

This section is partly an example of periodic growth, and we shall use a mathematical machinery similar to that of the periodic motion. We will treat two cases, the single plasma lipid bilayer-membrane as in division of animal cells, and the double membrane as in division of mitochondria. The plant cell with the plasma membrane and the cell wall are topologically similar to the mitochondrion case.

We begin with some basic functions. In the first two equations we use the square roots and see periodicity, and after this variants of the GD-function are used. We do also notice that squares give double roots. The equations are in order in 9.11 for figures 9.1.1a-f.

We are now ready to derive the division of cells with a single plasma bilayer membrane, and an organelle with a double membrane. We do it first in the simplest possible way.

$$x^{-2} = 4$$

$$x^{-2} + (x-4)^{-2} = 4$$

$$e^{-x^2} + e^{(x-4)^2} = 0.8$$

$$e^{-(x^2+y^2-1)} = 0.5 \tag{9.1.1}$$

$$e^{-(x^2+y^2-5)} = 0.5$$

$$e^{-(x^2+y^2-5)^2} = 0.5$$

We put two cells together with $\Delta x=0$ in equation 9.1.2a, in which the cells overlap completely mathematically. The motion starts when we increase Δx in equation 9.1.2a, splitting the cells as in figures 9.1.2a-d where Δx takes the values 0, 2, 3, and 4.

$$e^{-((x-\Delta x)^2+y^2-5)} + e^{-(x^2+y^2-5)} = 0.5 \tag{9.1.2a}$$

In figures 9.1.2e-f there are quadruple division and motion after formula 9.1.2b below. Δx and Δy take the values 4 and 3 for figure e, and 4 and 4 for figure f.

$$e^{-((x-\Delta x)^2+y^2-5)} + e^{-(x^2+y^2-5)} \tag{9.1.2b}$$

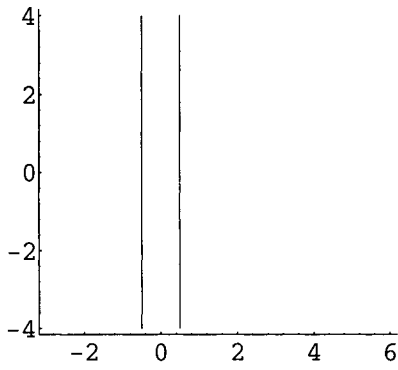
$$+ e^{-((x-\Delta x)^2+(y-\Delta y)^2-5)} + e^{-(x^2+(y-\Delta y)^2-5)} = 0.5$$

In pictures in ref. [12] of about eight new cells it is clear that the spherical cells have been heavily distorted in order to fill space. Primitive packing of spheres, as it is from the beginning, fill space badly. Cubes in primitive packing fill space to 100%, so we distort the spheres towards cubes and repeat the division procedure.

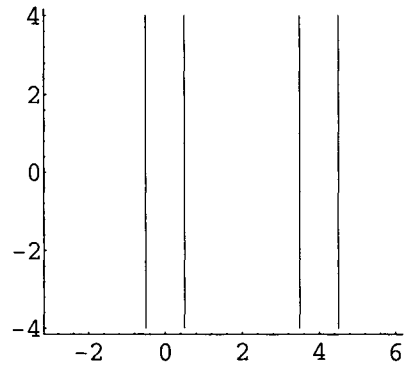
Δx takes the values 0, 2, 3.1, and 3.2 in figure 9.1.3a-d.

$$e^{-((x-\Delta x)^4+y^4-5)} + e^{-(x^4+y^4-5)} = 0.5 \tag{9.1.3}$$

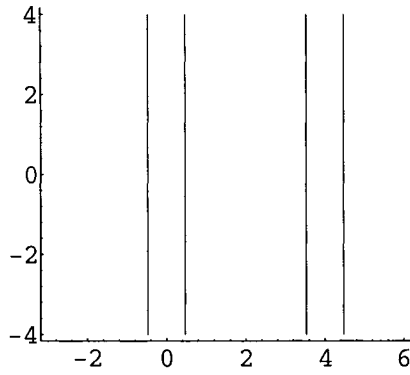
We have continued the cell division after equation 9.1.4 to show the packing of cuboid cells as in figure 9.1.3e.



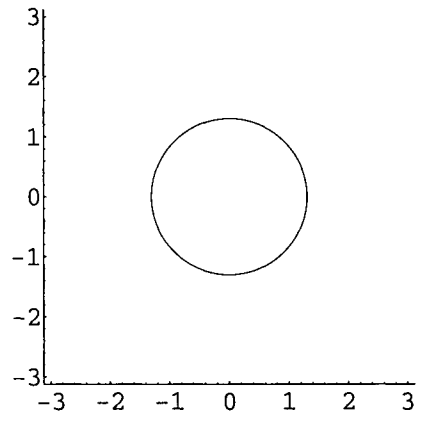
a



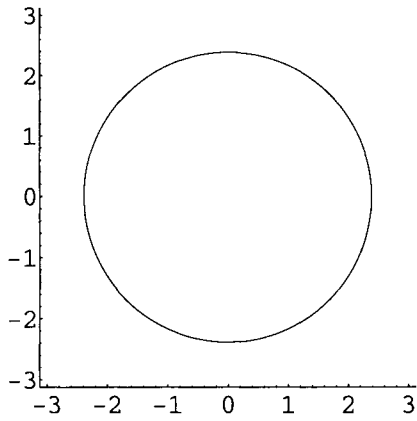
b



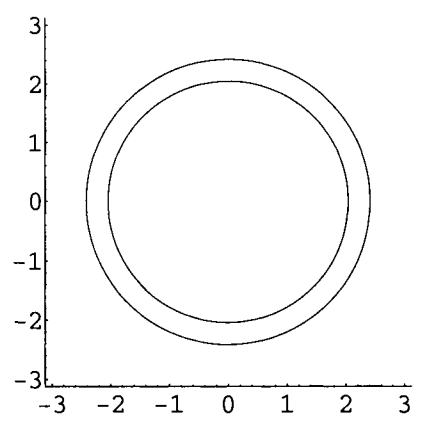
c



d

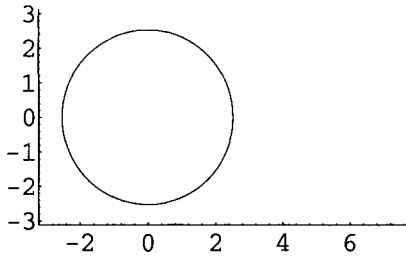
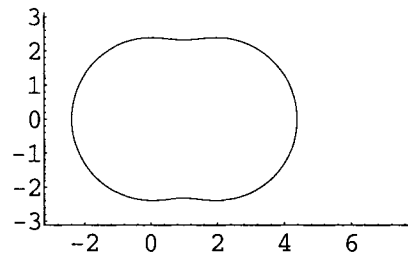
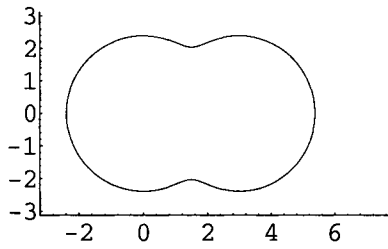
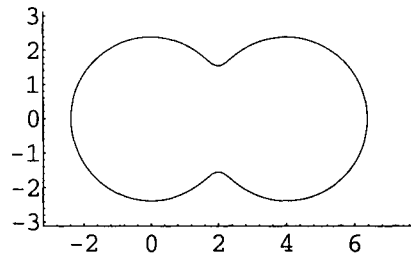
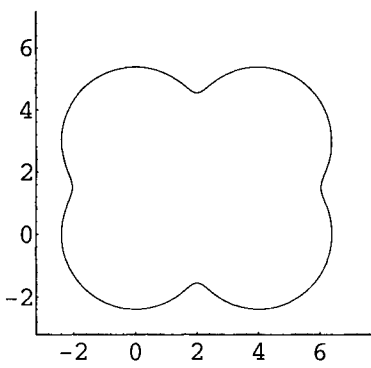
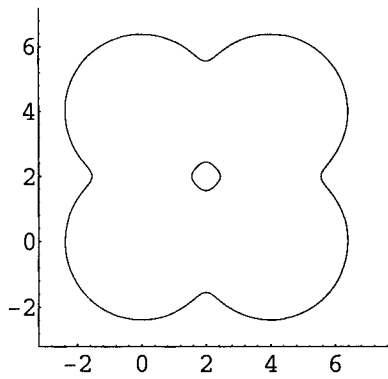


e



f

Figure 9.1.1a-f Plots from equation 9.1.1.

**a****b****c****d****e****f****Figure 9.1.2** Simple cell division after equation 9.1.2

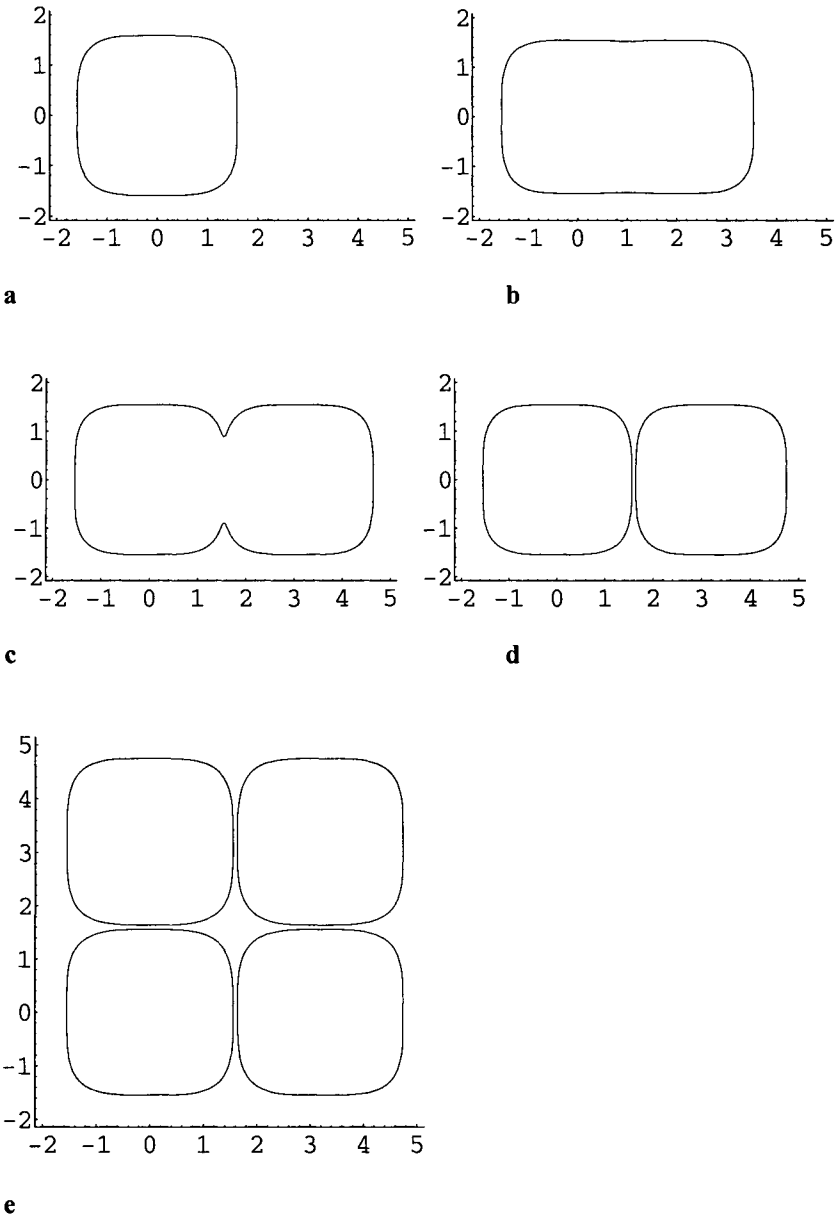
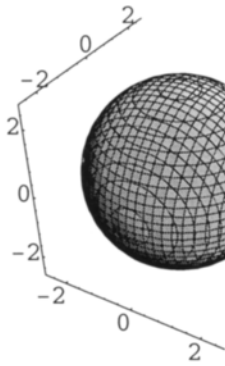
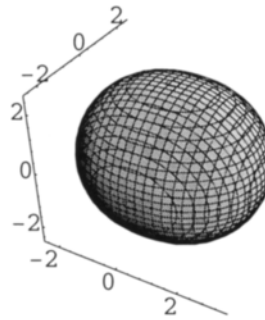


Figure 9.1.3 Cell division after equations 9.1.3-4.

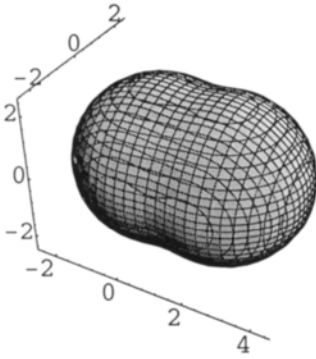
$$\begin{aligned}
 &e^{-((x-3.2)^4+y^4-5)} + e^{-(x^4+y^4-5)} \\
 &+ e^{-(x^4+(y-3.2)^4-5)} + e^{-((x-3.2)^4+(y-3.2)^4-5)} = 0.5
 \end{aligned}
 \tag{9.1.4}$$



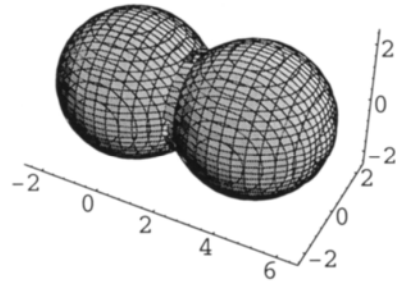
a



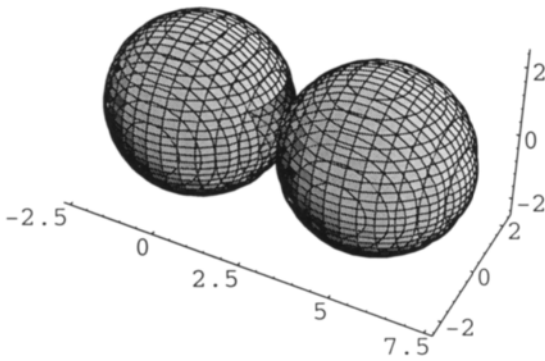
b



c



d



e

Figure 9.1.4 First cell division after equation 9.1.5.

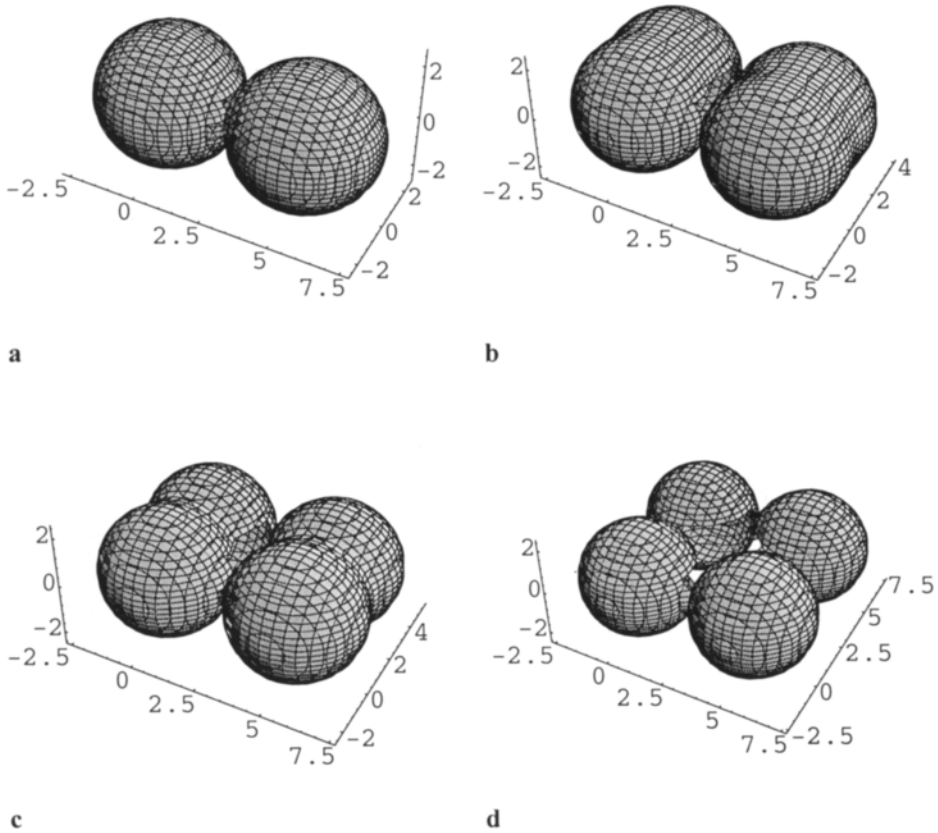


Figure 9.1.5 Second cell division after equation 9.1.5.

We do the same in 3D, and with our experience we can formulate an equation for the first three divisions.

$$\begin{aligned}
 &N_1 e^{-(x^2+y^2+z^2-5)} + e^{-((x-\Delta x)^2+y^2+z^2-5)} \\
 &+ N_2 e^{-(x^2+(y-\Delta y)^2+z^2-5)} + e^{-((x-5)^2+(y-\Delta y)^2+z^2-5)} \\
 &+ N_3 e^{-(x^2+y^2+(z-\Delta z)^2-5)} + e^{-((x-5)^2+y^2+(z-\Delta z)^2-5)} \\
 &+ N_4 e^{-(x^2+(y-5)^2+(z-\Delta z)^2-5)} + e^{-((x-5)^2+(y-5)^2+(z-\Delta z)^2-5)} \\
 &-\frac{1}{2} = 0
 \end{aligned}
 \tag{9.1.5}$$

For the first division $N_1=1$, $N_2=N_3=N_4=0$, and Δx varies between 0, 1, 2, 4, and 5. This is shown in figure 9.1.4a-e.

For the second division $N_1=1$, $\Delta x=5$, $N_2=1$, $N_3=N_4=0$ and Δy varies between 0, 2, 3, and 5. This is shown in figure 9.1.5a-d.

For the third division $N_1=1$, $\Delta x=5$, $N_2=1$, $\Delta y=5$, $N_3=N_4=1$ and Δz varies between 0, 1, 3.5, and 5. This is shown in figure 9.1.6a-d.

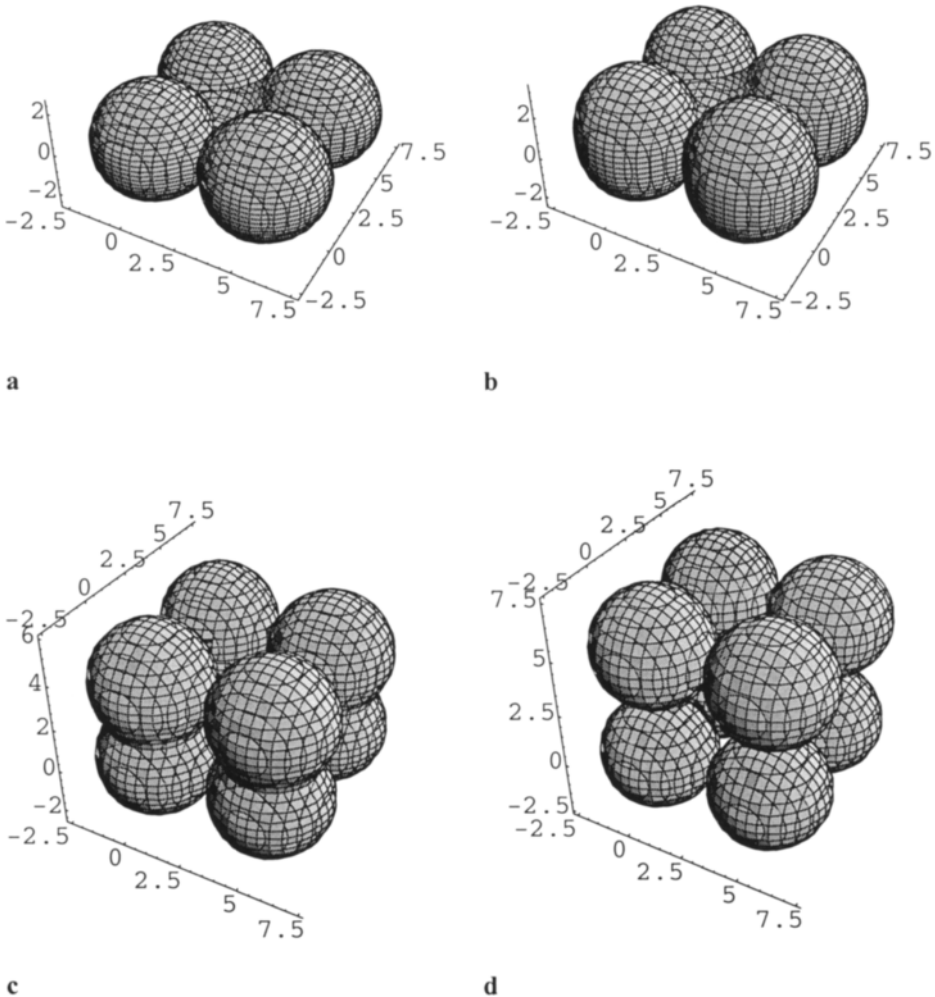


Figure 9.1.6 Third cell division after equation 9.1.5

Using this method we may formulate one equation that gives any number of cell divisions.

There are numerous examples in the literature showing the cell division process as in these calculations. See for example the beautiful micrographs showing fertilisation and division of the sand dollar in ref. [2].

9.2 Cell Division with Double Membranes

Next, we will use the double root functions in a simple form to describe the division with double membranes, which must take place in the nuclear envelope and in the mitochondrion. The equations start with 9.2.1 with $\Delta x=0$ and 1, and are shown in figures 9.2.1a-b. Figure 9.2.1b is not quite what we want, so we reformulate the equation in 9.2.2. In figures 9.2.1c-h we obtain a typical cell division, and we notice in figures f and g that one double membrane is in common for two cells.

$$e^{-(x^2+y^2-5)^2} + e^{-(x-\Delta x)^2+y^2-5)^2} = 0.5 \quad 9.2.1$$

In equation 9.2.2 Δx takes the values 1, 3, 4, 4.7, 5, and 5.4.

$$[e^{-(x^2+y^2-5)} + e^{-((x-\Delta x)^2+y^2-5)}]^2 = 0.5 \quad 9.2.2$$

Cell division is of course more complicated than this, but our intention is just to derive a mathematical machinery that works for the topological transformation of the plasma membrane. For the complete motion it is important to derive a machinery that carries the internal structure of the cell through the transformation. We shall model that in two different ways.

The first is to use the Hermite operator after equation 9.2.3. The damping is reinforced by adding a GD like term, which gives the plasma membrane boundary. The structure is really a cubosome.

$$e^{-(x^2+y^2-6)}[\cos 2\pi x + \cos 2\pi y] + e^{-(x^4+y^4-6)} - 24 = 0 \quad 9.2.3$$

The motion of the cell division is in the equation 9.2.4. The content gives curvature to the membrane and the structure changes shape during the motion. The last connection is a catenoid, or the umbilical cord, as seen in figure 9.2.2e.

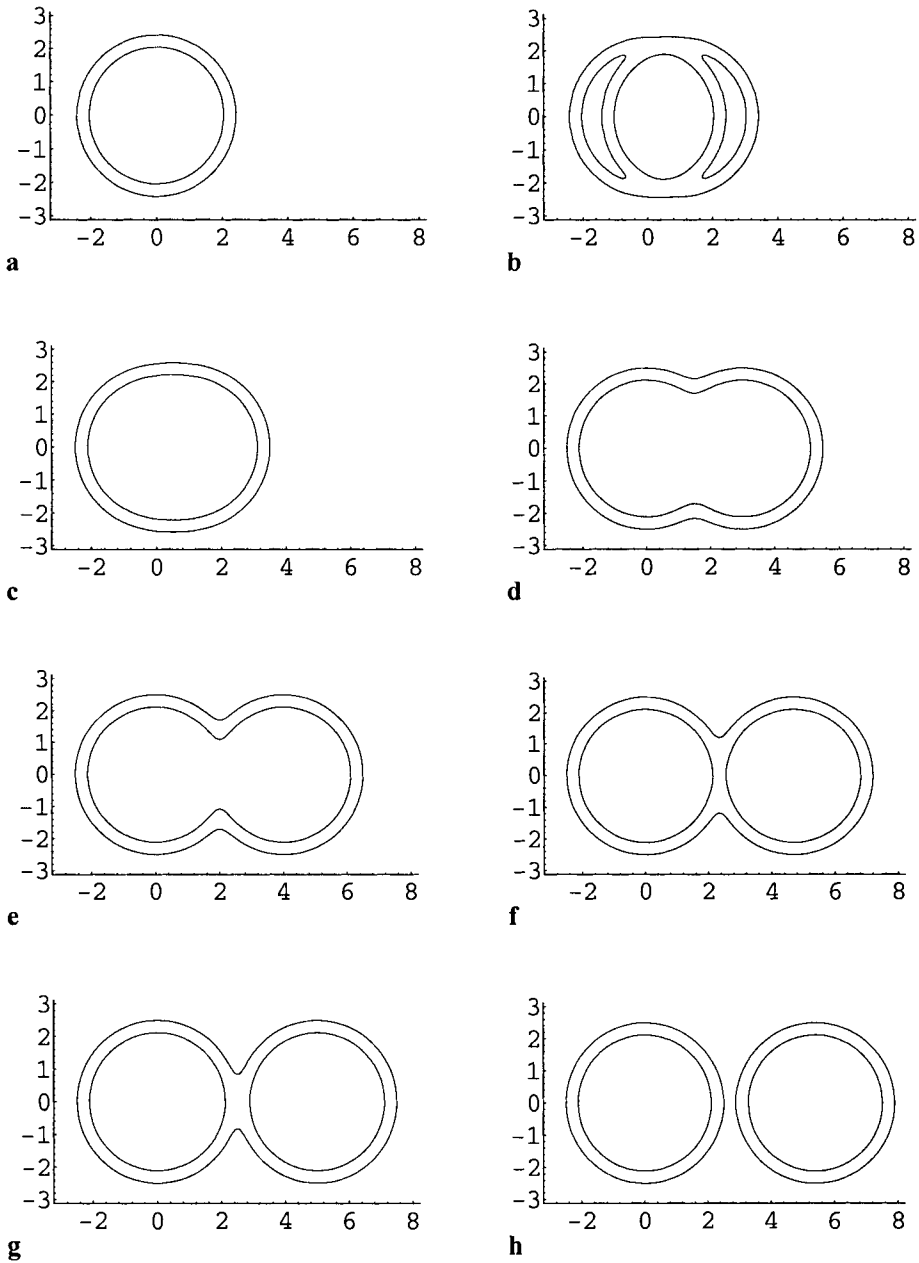
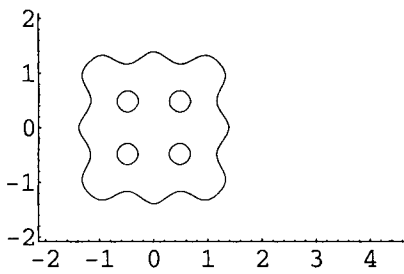


Figure 9.2.1 Double cell membrane division.

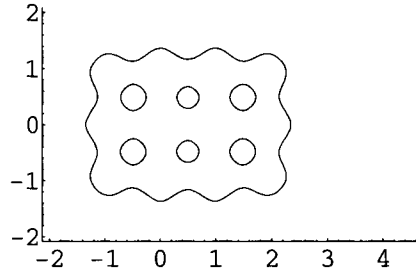
Δx takes the values 0, 1, 2, 2.5, 2.7, and 3 in figures 9.2.2a-f respectively.

$$e^{-(x^2+y^2-6)}[\cos 2\pi x + \cos 2\pi y] + e^{-(x^4+y^4-6)} \tag{9.2.4}$$

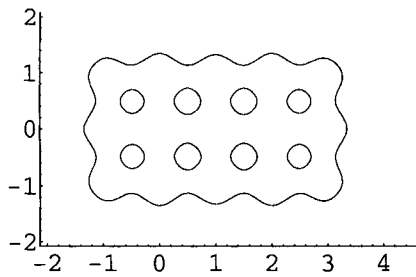
$$+ e^{-((x-\Delta x)^2+y^2-6)}[\cos 2\pi x + \cos 2\pi y] + e^{-((x-\Delta x)^4+y^4-6)} - 44 = 0$$



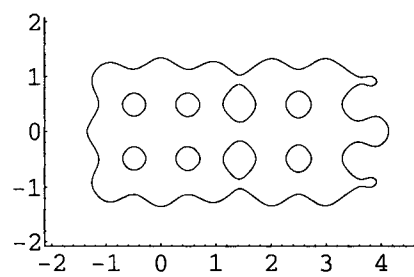
a



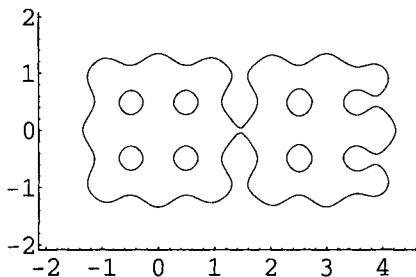
b



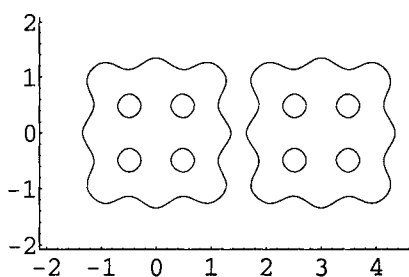
c



d



e



f

Figure 9.2.2 Cell division with Hermite operator after equation 9.2.4.

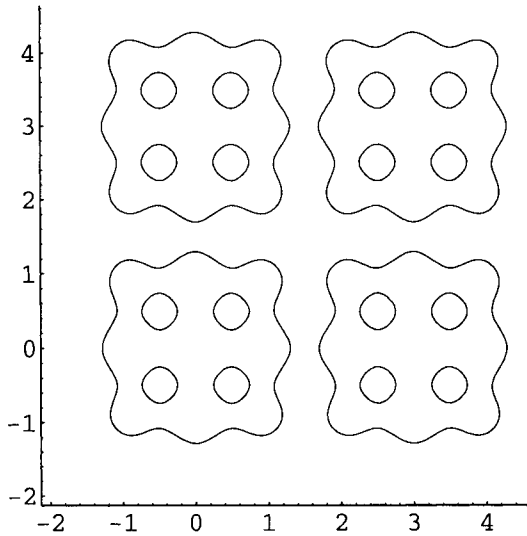


Figure 9.2.2g After equation 9.2.5.

Finally we show the packing of four cells with equation 9.2.5, which is illustrated in figure 9.2.2g.

$$\begin{aligned}
 & e^{-(x^2+y^2-6)}[\cos 2\pi x + \cos 2\pi y] + e^{-(x^4+y^4-6)} \\
 & + e^{-((x-3)^2+y^2-6)}[\cos 2\pi x + \cos 2\pi y] + e^{-((x-3)^4+y^4-6)} \\
 & + e^{-((x-3)^2+(y-3)^2-6)}[\cos 2\pi x + \cos 2\pi y] + e^{-((x-3)^4+(y-3)^4-6)} \\
 & + e^{-(x^2+(y-3)^2-6)}[\cos 2\pi x + \cos 2\pi y] + e^{-(x^4+(y-3)^4-6)} - 88 = 0
 \end{aligned}
 \tag{9.2.5}$$

We realise now that this mathematical description of cell division was founded earlier in chapter 5, where we showed the property of the GD-function which made it possible for functions, and structures, to go through each other and yet keep their identities.

The other method involves using a handmade construction with a function similar to the GD-function. We use this to build a model of a mitochondrion as in [3]. The equation is derived below in 9.2.4, and the figures are in 9.2.3a-d. We note that just before separation, the two “individvs” have one double membrane in common as we expect. This is shown in 9.2.3c. The result is similar to ultrastructural observations of mitochondria divisions, and an example is shown in ref. [4] (figure 23-5).

We give the equation for **9.2.3c** in 9.2.5. The final separation is shown in figure **9.2.3d**.

$$\begin{aligned}
 &10^{-[(x-3)^2+10^{-(y-10)}+10^{(y-33)}]} + 10^{-[(x-8)^2+10^{-(y-10)}+10^{(y-33)}]} \\
 &+ 10^{-[(x+3)^2+10^{-(y+15)}+10^{(y-33)}]} + 10^{-[(x)^2+10^{(y-8)}+10^{-(y+15)}]} \\
 &+ 10^{-[(x-5)^2+10^{(y-8)}+10^{-(y+15)}]} + 10^{-[(x-15)^2+10^{(y-8)}+10^{-(y+15)}]} \\
 &+ 10^{-[(x-17)^2+10^{(y-28)}+10^{-(y-15)}]} + 10^{-[(x-11)^2+10^{(y-18)}+10^{-(y+10)}]} \\
 &+ 10^{-[(x-20)^2+10^{-(y+15)}+10^{(y-33)}]} + 10^{-[(y-33)^2+10^{(x-21)}+10^{-(x+4)}]} \\
 &+ 10^{-[(y+15)^2+10^{(x-21)}+10^{-(x+4)}]} = 0.6
 \end{aligned}
 \tag{9.2.4}$$

$$\begin{aligned}
 &10^{-[(x-3)^2+10^{-(y-10)}+10^{(y-33)}]} + 10^{-[(x-8)^2+10^{-(y-10)}+10^{(y-33)}]} \\
 &+ 10^{-[(x+3)^2+10^{-(y+15)}+10^{(y-33)}]} + 10^{-[(x)^2+10^{(y-8)}+10^{-(y+15)}]} \\
 &+ 10^{-[(x-5)^2+10^{(y-8)}+10^{-(y+15)}]} + 10^{-[(x-15)^2+10^{(y-8)}+10^{-(y+15)}]} \\
 &+ 10^{-[(x-17)^2+10^{(y-28)}+10^{-(y-15)}]} + 10^{-[(x-11)^2+10^{(y-18)}+10^{-(y+10)}]} \\
 &+ 10^{-[(x-20)^2+10^{-(y+15)}+10^{(y-33)}]} + 10^{-[(y-33)^2+10^{(x-21)}+10^{-(x+4)}]} \\
 &+ 10^{-[(y+15)^2+10^{(x-21)}+10^{-(x+4)}]} \\
 &+ 10^{-[(x-26)^2+10^{-(y-10)}+10^{(y-33)}]} + 10^{-[(x-31)^2+10^{-(y-10)}+10^{(y-33)}]} \\
 &+ 10^{-[(x-20)^2+10^{-(y+15)}+10^{(y-33)}]} + 10^{-[(x-23)^2+10^{(y-8)}+10^{-(y+15)}]} \\
 &+ 10^{-[(x-28)^2+10^{(y-8)}+10^{-(y+15)}]} + 10^{-[(x-38)^2+10^{(y-8)}+10^{-(y+15)}]} \\
 &+ 10^{-[(x-40)^2+10^{(y-28)}+10^{-(y-15)}]} + 10^{-[(x-34)^2+10^{(y-18)}+10^{-(y+10)}]} \\
 &+ 10^{-[(x-43)^2+10^{-(y+15)}+10^{(y-33)}]} + 10^{-[(y-33)^2+10^{(x-44)}+10^{-(x-19)}]} \\
 &+ 10^{-[(y+15)^2+10^{(x-44)}+10^{-(x-19)}]} = 0.6
 \end{aligned}
 \tag{9.2.5}$$

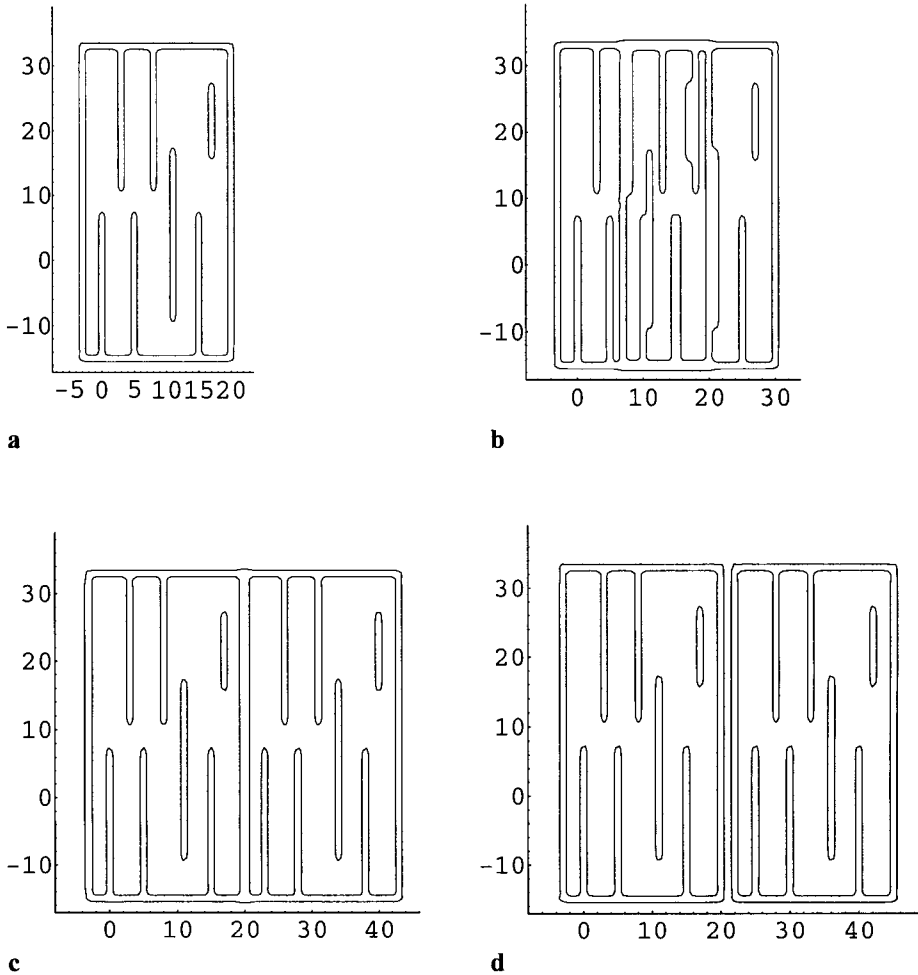


Figure 9.2.3 Model of mitochondrion and its division from equations 9.2.4-5.

9.3 Motion in Muscle Cells

That 'function presupposes structure' has been declared an accepted axiom of biology ... the cell histologists have ever since been trying to comply [5].

The actin/myosin complex in skeletal muscle cells exhibit perfect periodicity in three dimensions, as is evident from the sharp X-ray diffraction characteristics and the electron microscopy textures, cf. figure 9.3.1 from [6]. The thick elements are myosin molecules, whereas the thin ones are actin, and we see a cross-section of the helical association

complexes. These contractile elements, being surrounded by water in a hexagonal organisation, allow some disorder at atomic distances, like the liquid-crystalline phases of lipids that we have discussed in some detail above. A remarkable feature is the movement of the myosin heads in relation to the associated actin about 10 nm to give the power stroke within the ordered lattice. The perfect crystalline periodicity means that molecular motions will be accurately controlled, and should be expected to form standing waves like motion in other crystals. We think that this aspect of muscle contraction is relevant to coordination of motions of each contractile element. The motion of an individual myosin molecule in relation to an actin helix is described in chapter 10. Here we will deal with the overall motion and the cooperativity.

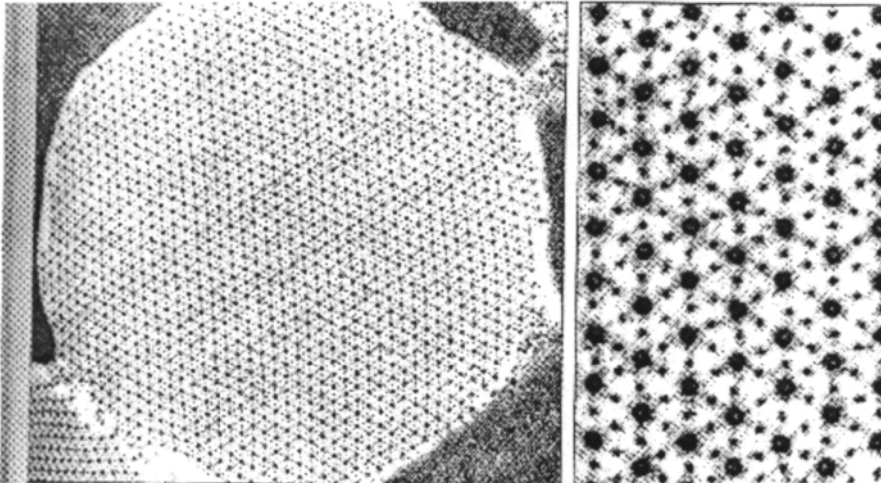


Figure 9.3.1 Electron micrographs of a muscle revealing excellent crystallinity, from the classical work by Auber, cf. ref [6]. Enlargement to the right.

Let us now consider two major motion geometries of the hexagonal organisation.

The first type is the motions in the (ab)-plane; standing wave oscillations of the long molecules perpendicular to their axes. The association/dissociation of actin and myosin heads localised in the same (ab)-plane (involving calcium ions and the ATP-binding) will therefore take place in phase. It is known that the movements of different myosin heads along a myosin thread, fuelled by the ATP-cycle, occur asynchronously, and the generated force is therefore constant with time. With the standing wave model of motion, only the myosin heads separated by the whole pitch

(about 145 Å) will move at the same time. The other five heads along the pitch will move at successively later times during the cycle, related to wave oscillations along the myosin rod.

The second type of motion takes place along the *c*-axis. The myosin heads form a helical surface. These helices should be expected to exhibit standing wave motions corresponding to movement forward and backwards in relation to the myosin molecule endings at the core of the rods. When the myosin heads change their conformation driven by the ATP \rightarrow ADP reaction, it seems likely that the motion of the heads will be coupled with this second type of standing wave motion, so that the conformational induced lateral movement of myosin in relation to actin does not counteract, but amplifies the standing wave movement. Such coordination requires that there is a coupling between all the actin and all the myosin movements.

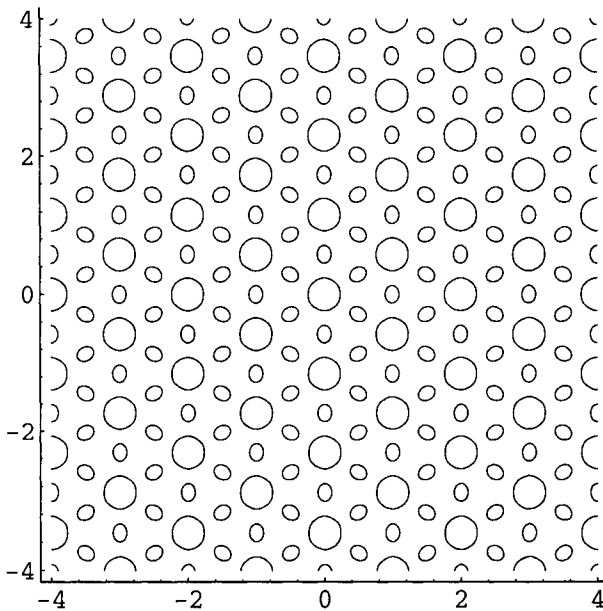


Figure 9.3.2 Equation in 9.3.1 gives 2D projection of the hexagonal picture in figure 9.3.1.

We give the mathematical equation for the projection in figure 9.3.1 in equation 9.3.1, and show it in figure 9.3.2.

$$\begin{aligned} & \cos \pi x \cos \pi \left(\frac{x}{2} + \frac{\sqrt{3}}{2} y \right) \cos \pi \left(-\frac{x}{2} + \frac{\sqrt{3}}{2} y \right) \\ & + \cos 2\pi x \cos 2\pi \left(\frac{x}{2} + \frac{\sqrt{3}}{2} y \right) \cos 2\pi \left(-\frac{x}{2} + \frac{\sqrt{3}}{2} y \right) = 0.5 \end{aligned} \quad 9.3.1$$

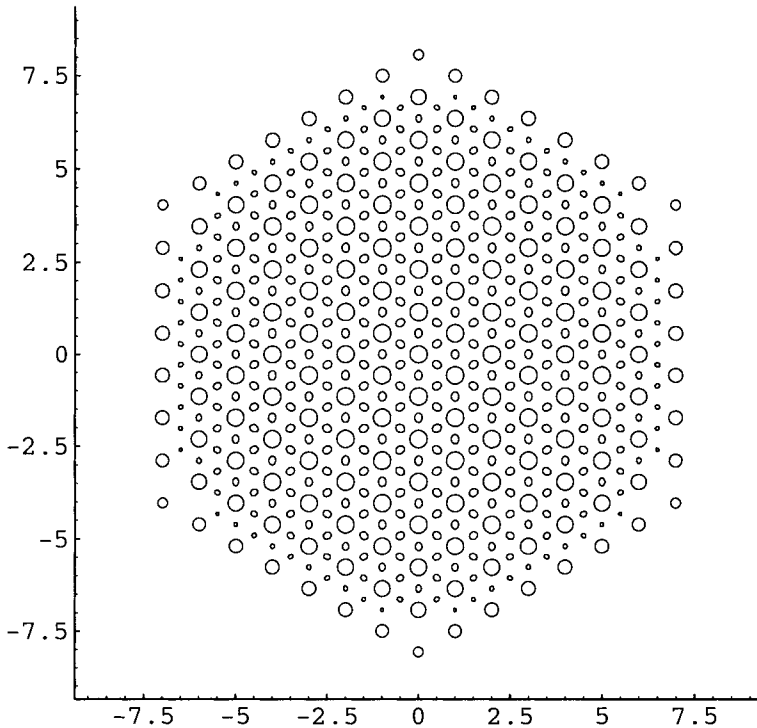


Figure 9.3.3 Equation 9.3.2 combines external boundaries with the structure in figure 9.3.1.

As is obvious from figure 9.3.1, the structure unit, the sarcomere, consists of hexagonal rods, so we design an equation by combining a periodic structure with outer boundaries, using a hexagon equation to give the sarcomere borders in equation 9.3.2, the result is shown in figure 9.3.3.

$$\begin{aligned}
 & 1.2 \times 10^{-4} [e^{(x \cos(\pi/3) + y \sin(\pi/3))} + e^{(x \cos(2\pi/3) + y \sin(2\pi/3))} \\
 & + e^{(x \cos(3\pi/3) + y \sin(3\pi/3))} + e^{-(x \cos(\pi/3) + y \sin(\pi/3))} \\
 & + e^{-(x \cos(2\pi/3) + y \sin(2\pi/3))} + e^{-(x \cos(3\pi/3) + y \sin(3\pi/3))}] \\
 & - [\cos \pi x \cos \pi \left(\frac{x}{2} + \frac{\sqrt{3}}{2} y\right) \cos \pi \left(-\frac{x}{2} + \frac{\sqrt{3}}{2} y\right) + \cos 2\pi x \cos 2\pi \left(\frac{x}{2} + \frac{\sqrt{3}}{2} y\right) \cos 2\pi \left(-\frac{x}{2} + \frac{\sqrt{3}}{2} y\right)] = \frac{1}{2}
 \end{aligned}$$

9.3.2

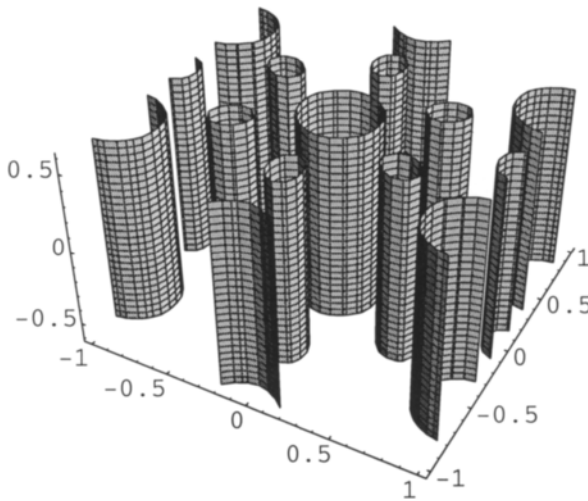


Figure 9.3.4 Corresponding 3D-structure.

In figure 9.3.4 we extend it to 3D.

Changing equation 9.3.1, after the principles described in chapter 3, to bring in the z dimension we get equation 9.3.3.

$$\begin{aligned}
 & \cos \pi x \cos \pi \left(\frac{x}{2} + \frac{\sqrt{3}}{2} y\right) \cos \pi \left(-\frac{x}{2} + \frac{\sqrt{3}}{2} y\right) \\
 & + \cos 2\pi x \cos 2\pi \left(\frac{x}{2} + \frac{\sqrt{3}}{2} y\right) \cos 2\pi \left(-\frac{x}{2} + \frac{\sqrt{3}}{2} y\right) \\
 & + 0.075 \cos 4\pi z = 0.5
 \end{aligned}$$

9.3.3

This brings in small catenoids between the actin and myosin filaments, which may represent the myosin II motor proteins which perform the sliding work. The figures are in 9.3.5 and 9.3.6, the latter being the projection.

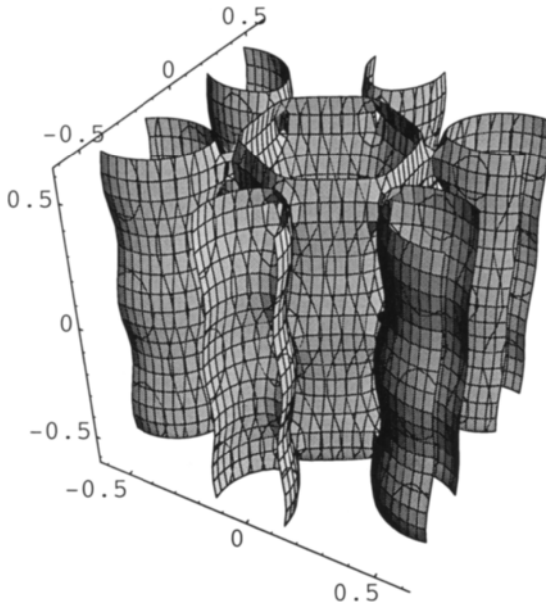


Figure 9.3.5 Catenoids between the actin and myosin filaments after 9.3.3.

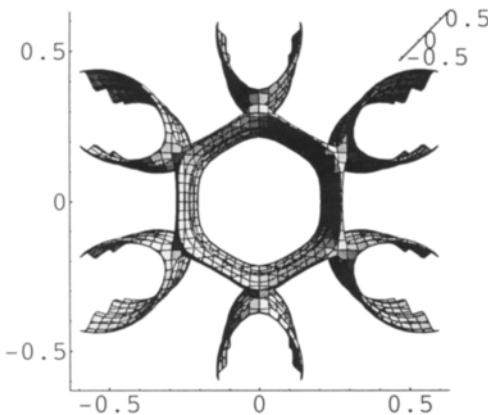


Figure 9.3.6 Projection of figure 9.3.5.

It should be pointed out that this shows the total association over the whole crystallographic repetition period. As mentioned above, only one of the six heads is associated at a particular time.

Shown above in 3D is only a piece of the sarcomere, and here we derive a complete model in 2D.

The equations are 9.3.4 and 9.3.5, and the biological motion is obtained by changing some of the y-coordinates. This is a good example of handling the exponential scale, and the muscle work is shown in figures 9.3.7 and 9.3.8 for sarcomere units.

$$\begin{aligned}
 &10^{-[(x-4)^2+10^{(y-22)}+10^{-(y+4)}]} + 10^{-[(x)^2+10^{(y-22)}+10^{-(y+4)}]} \\
 &+ 10^{-[(x-8)^2+10^{(y-22)}+10^{-(y+4)}]} + 0.15 \cdot 10^{-[(x-2)^2+10^{-(y-15)}]} \\
 &+ 0.15 \cdot 10^{-[(x-6)^2+10^{-(y-15)}]} + 0.15 \cdot 10^{-[(x+2)^2+10^{-(y-15)}]} \\
 &+ 0.15 \cdot 10^{-[(x-10)^2+10^{-(y-15)}]} + 0.15 \cdot 10^{-[(x-2)^2+10^{(y-3)}]} \qquad 9.3.4 \\
 &+ 0.15 \cdot 10^{-[(x-6)^2+10^{(y-3)}]} + 0.15 \cdot 10^{-[(x+2)^2+10^{(y-3)}]} \\
 &+ 0.15 \cdot 10^{-[(x-10)^2+10^{(y-3)}]} + 0.2 \cdot 10^{-[(y-38)^2+10^{(x-11)}+10^{-(x+2)}]} \\
 &+ 0.2 \cdot 10^{-[(y+19)^2+10^{(x-11)}+10^{-(x+2)}]} = 0.1
 \end{aligned}$$

$$\begin{aligned}
 &10^{-[(x-4)^2+10^{(y-22)}+10^{-(y+4)}]} + 10^{-[(x)^2+10^{(y-22)}+10^{-(y+4)}]} \\
 &+ 10^{-[(x-8)^2+10^{(y-22)}+10^{-(y+4)}]} + 0.15 \cdot 10^{-[(x-2)^2+10^{-(y-10)}]} \\
 &+ 0.15 \cdot 10^{-[(x-6)^2+10^{-(y-10)}]} + 0.15 \cdot 10^{-[(x+2)^2+10^{-(y-10)}]} \\
 &+ 0.15 \cdot 10^{-[(x-10)^2+10^{-(y-10)}]} + 0.15 \cdot 10^{-[(x-2)^2+10^{(y-8)}]} \qquad 9.3.5 \\
 &+ 0.15 \cdot 10^{-[(x-6)^2+10^{(y-8)}]} + 0.15 \cdot 10^{-[(x+2)^2+10^{(y-8)}]} \\
 &+ 0.15 \cdot 10^{-[(x-10)^2+10^{(y-8)}]} + 0.2 \cdot 10^{-[(y-33)^2+10^{(x-11)}+10^{-(x+2)}]} \\
 &+ 0.2 \cdot 10^{-[(y+15)^2+10^{(x-11)}+10^{-(x+2)}]} = 0.1
 \end{aligned}$$

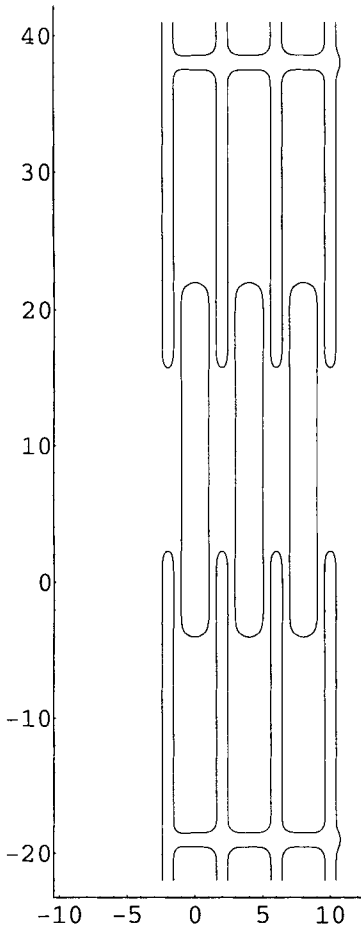


Figure 9.3.7 Sarcomere units.

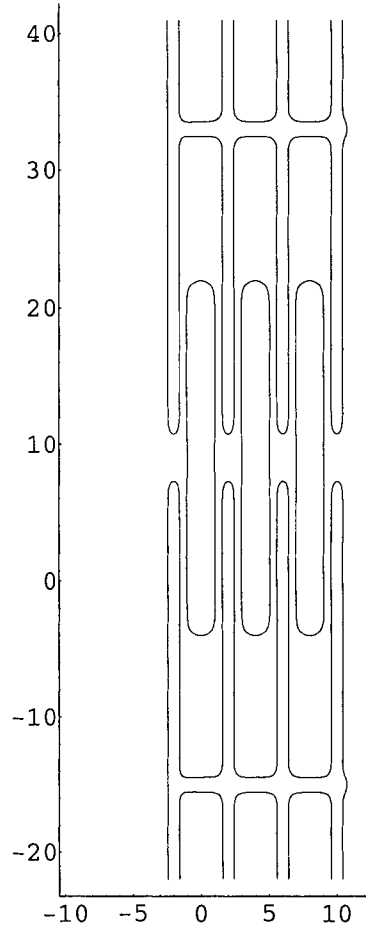


Figure 9.3.8 The muscle work.

9.4 RNA and DNA Modelling

Self-replicating RNA molecules were supposed to exist in the first membrane bounded cells in the prebiotic soup (cf. chapter 15). Such molecules could carry genetic information as well as being catalytic.

As a starting point we make two spirals after equation 9.4.1. For $\Delta=0$ the two are identical, and overlapping as in figure 9.4.1.a.

$$e^{-e^{(x^2+y^2)}+e^{y\cos\pi z+x\sin\pi z-\frac{1}{8}}}] \quad 9.4.1$$

$$+e^{-e^{((x+\Delta)^2+(y+\Delta)^2)}+e^{(y+\Delta)\cos\pi z+(x+\Delta)\sin\pi z-\frac{1}{8}}}] - \frac{1}{8} = 0$$

“Mathematical self replication” is obtained by giving Δ the values 1, 1.1, and 1.25, and the result is two parallel RNA strands in figures 9.4.1b-d.

If we for $\Delta=1$ above, introduce a phase shift of 1 in z for one of the strands, the total structure transforms via interactions between the two strands to a double spiral of DNA type. We shall do this stepwise and first we formulate equation 9.4.2.

$$e^{-e^{(x^2+y^2)}+e^{y\cos\pi z+x\sin\pi z-\frac{1}{8}}}] \quad 9.4.2$$

$$+e^{-e^{((x+\Delta)^2+(y+\Delta)^2)}+e^{(y+\Delta)\cos\pi(z+1)+(x+\Delta)\sin\pi(z+1)-\frac{1}{8}}}] - \frac{1}{8} = 0$$

Then, having the two strands separated, we bring them together with $\Delta=1.5, 1.25, 1, 0.8,$ and $0.5,$ as shown in figure 9.4.2a-d. The two strands approaching each other form a double helix via cross bonding.

This mathematical transformation, applied locally at one helix turn, offers a model similar to the cleavage and rejoining mechanism of a phosphodiester bond, as done by DNA-polymerase during the DNA-replication [8].

We shall also show the topology when two spirals in a double-helix meet another identical double-helix of a different orientation. The double spirals unify after some translation as in equation 9.4.3. As one strand of one double spiral proceeds into another strand of another double spiral, we generate a topology similar to a so called Holliday junction. We show this in figure 9.4.3a-b.

$$e^{-[\frac{1}{5}e^{x^2+(y-3)^2}+2x(y-3)\cos\pi z-(x^2-(y-3)^2)\sin\pi z]} \quad 9.4.3$$

$$+e^{-[\frac{1}{5}e^{z^2+y^2}+2zy\cos\pi x+(z^2-y^2)\sin\pi x]} - 1 = 0$$

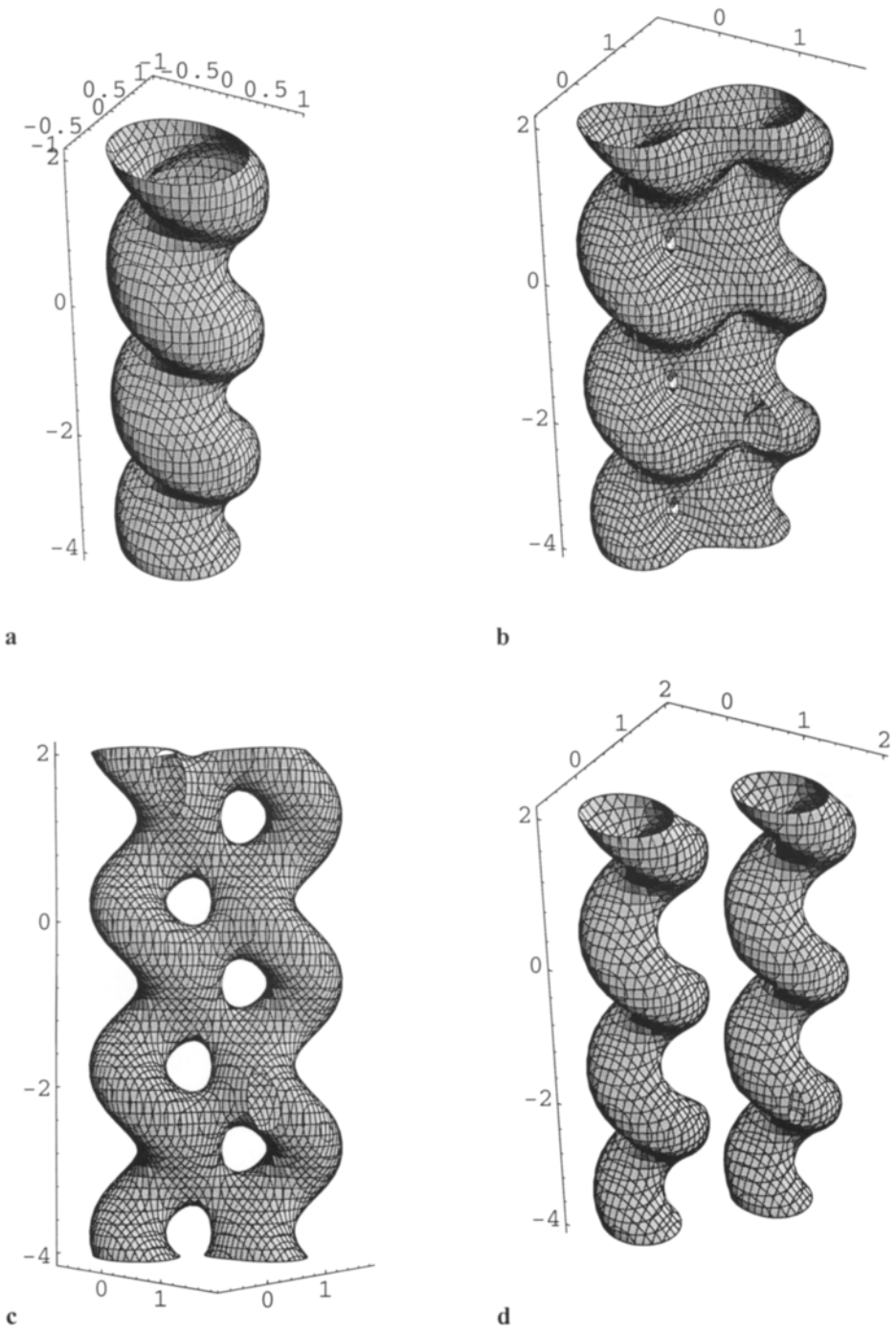
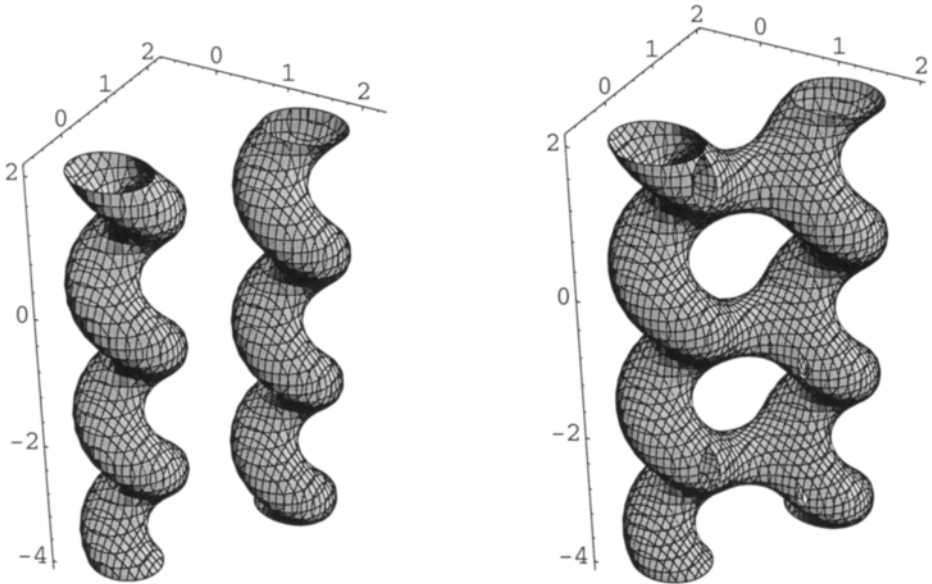
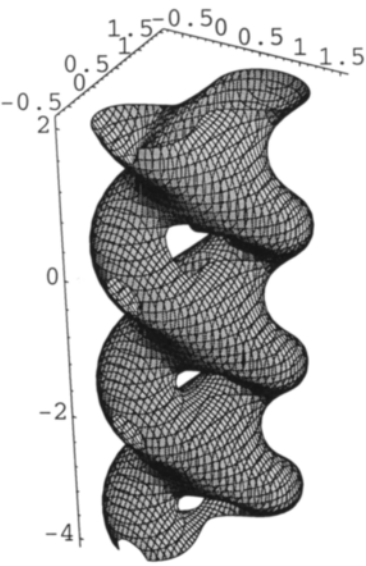
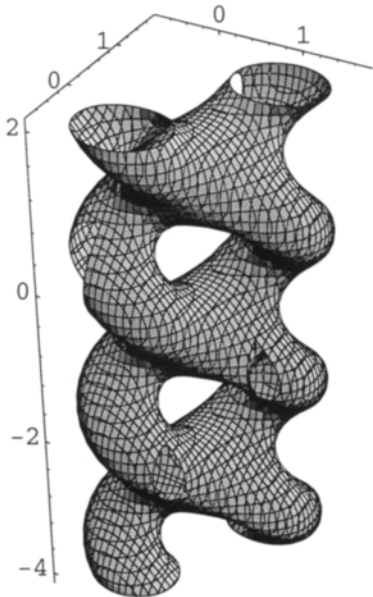


Figure 9.4.1 Two spiral units show mathematical self-replication.



a

b



c

d

Figure 9.4.2 Two spirals form a double helix under a phase shift.

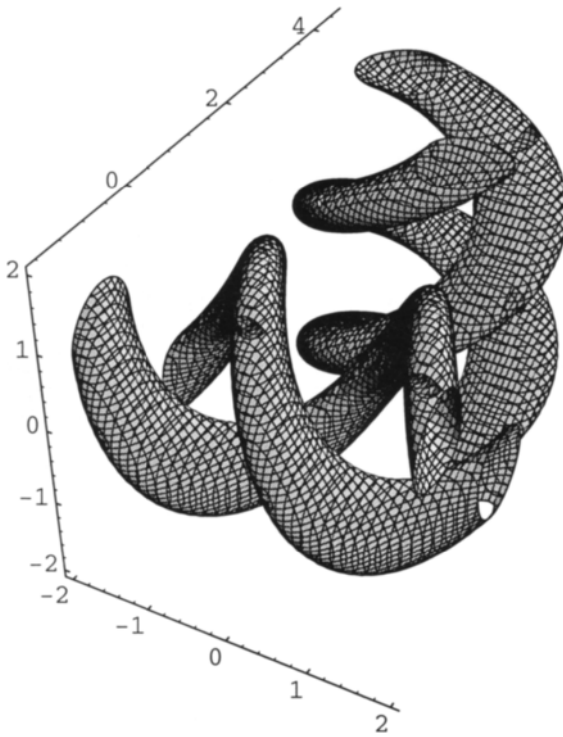


Figure 9.4.3a Two spirals in a double-helix meet another identical double-helix of a different orientation.

We make the two spirals interpenetrate even more in equation 9.4.4, and see in figures 9.4.4a-b that the topology now resembles cruciform DNA in figure 9.4.5 (from ref. [10]). The cruciform conformation is visible in electron micrographs of circular DNA, cf. [11]. These models of DNA interactions does of course leave out the enzyme wrestling and the specific base pair interactions. Furthermore, we simplify the double helix by making both helices identical with a translation of half a pitch in relation to one another. Never-the-less, the mathematical handling of DNA and RNA elements may reveal relevant interaction mechanisms.

A more complete mathematical description of DNA and other multi-spirals is given in appendix 5.

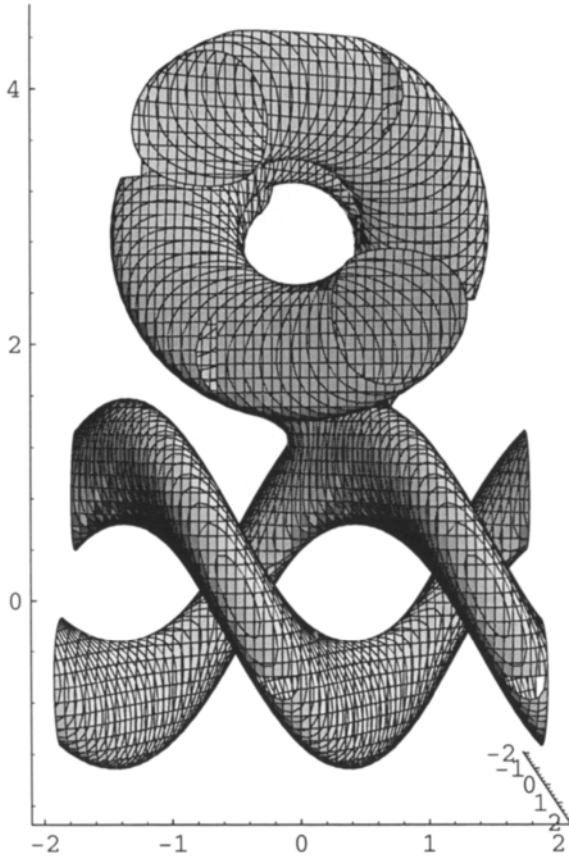


Figure 9.4.3b Projection of a.

$$\begin{aligned}
 &e^{-[\frac{1}{5}e^{x^2+(y-1.5)^2} + 2x(y-1.5)\cos \pi z - (x^2 - (y-1.5)^2)\sin \pi z]} \\
 &+ e^{-[\frac{1}{5}e^{z^2+y^2} + 2zy \cos \pi x + (z^2 - y^2)\sin \pi x]} - 1 = 0
 \end{aligned}$$

9.4.4

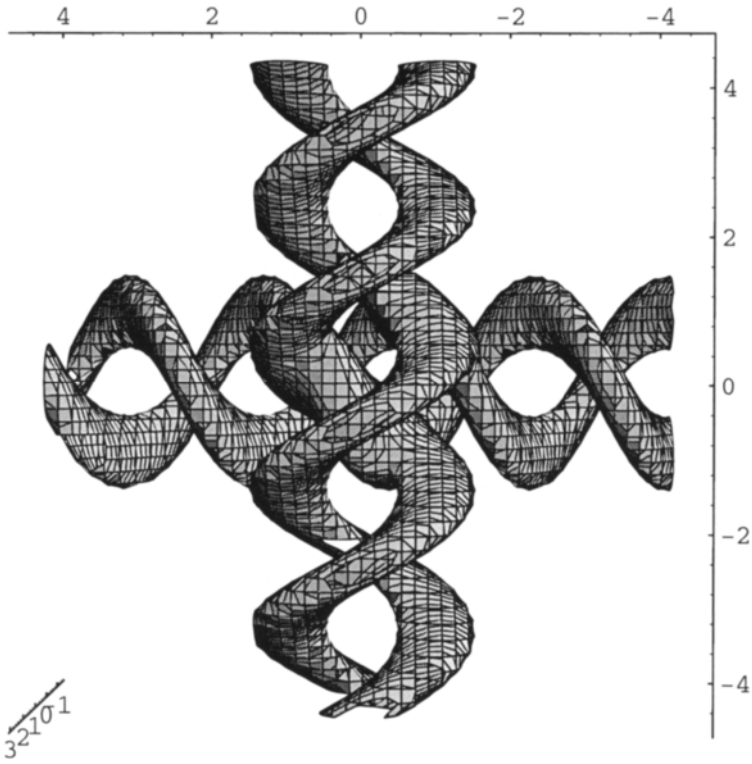


Figure 9.4.4a Topology of cruciform DNA.

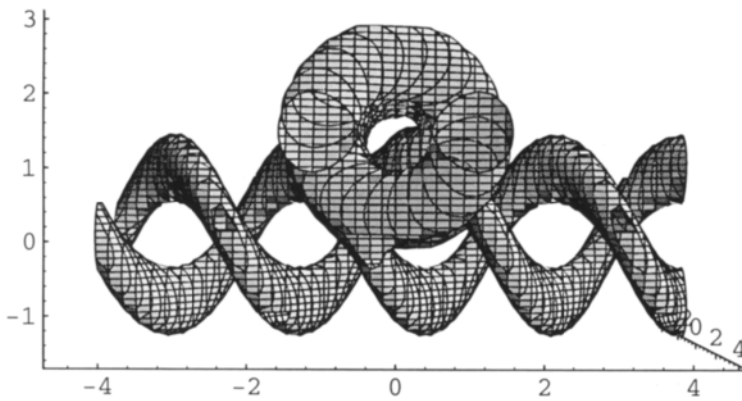


Figure 9.4.4b Different projection of a.

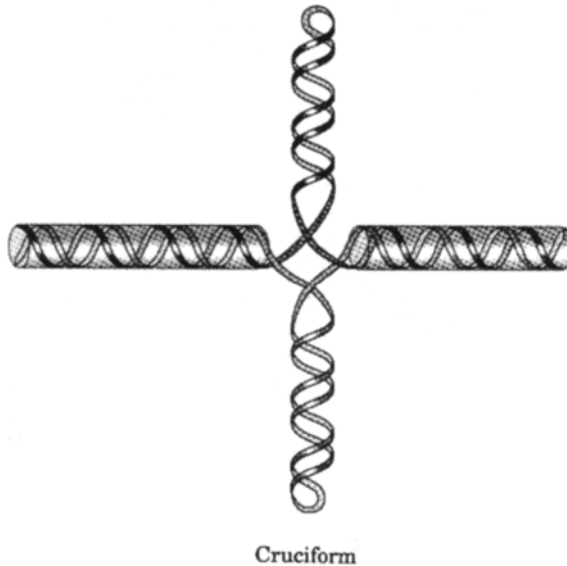


Figure 9.4.5 Cruciform DNA from ref. [10].

References 9

- 1 H.S.M. Coxeter, *Regular Polytopes*. Dover 1973. Page 118.
- 2 J. Darnell, H. Lodish, D. Baltimore. *Molecular Cell Biology*. Scientific American Books 1986 page 996.
- 3 B. Alberts, D. Bray, J. Lewis, M. Raff, K. Roberts, and J.D. Watson, *Molecular Biology of THE CELL*, page 657, Garland Publishing, Third Edition, 1994.
- 4 A.L. Lehninger, D.L. Nelson, M.M. Cox, *Principles of Biochemistry*, page 795, Second edition, Worth Publishers, 1993.
- 5 D'Arcy Wentworth Thompson, *ON GROWTH AND FORM*, Cambridge University press, 1942, page 290.

-
- 6 B. Alberts, D. Bray, J. Lewis, M. Raff, K. Roberts, and J.D. Watson, *Molecular Biology of THE CELL*, page 849, Garland Publishing, Third Edition, 1994.
 - 7 S. Hyde, S. Andersson, K. Larsson, Z. Blum, T. Landh, S. Lidin and B. Ninham; *THE LANGUAGE OF SHAPE*, Elsevier, Amsterdam, 1997.
 - 8 B. Alberts, D. Bray, J. Lewis, M. Raff, K. Roberts, and J.D. Watson, *Molecular Biology of THE CELL*, page 260, Garland Publishing, Third Edition, 1994.
 - 9 B. Alberts, D. Bray, J. Lewis, M. Raff, K. Roberts, and J.D. Watson, *Molecular Biology of THE CELL*, page 263, Garland Publishing, Third Edition, 1994.
 - 10 A.L. Lehninger, D.L. Nelson, M.M. Cox, *Principles of Biochemistry*, page 804, Second edition, Worth Publishers, 1993.
 - 11 S.L. Wolfe, *Molecular and Cellular Biology*, page 536, Wadsworth Publishing, 1993.
 - 12 G.M. Cooper. *THE CELL A Molecular Approach*, ASM Press, 1997, page 563.

This Page Intentionally Left Blank

10 Concentration Gradients, Filaments, Motor Proteins and again - Flagella

Thermodynamics is mainly concerned with the transformations of heat into mechanical work and the opposite transformations of mechanical work into heat [Fermi,1].

We describe the formation of catenoids between vesicles.

We build actin filaments and show how they move, grow or shrink, or pack in bundles or networks.

We describe the dilatation symmetry of the axoneme, and cog-wheels.

We describe the power stroke of the myosin head.

We describe how algebraic roots, or counting, give curvature to flagella, and how a twin operation (crystallographic) on the dynamic structure of flagella gives the breast stroke swim motion of cilia.

All with mathematical functions.

10.1 Background and Essential Functions

So far we have described how cell, organelles and vesicles change shape, size and site during biological motion, and also how they interact with other bodies. This was done mathematically and topologically. We shall now show how building by filaments of the cyto skeleton can be described, and then model the function of motor proteins. In order to do that we need to analyse the physical picture that can be pulled out from the mathematics we use.

Membranes and vesicles are formed by self-assembly of lipid and protein molecules in water, which means that there is a distribution of the molecules out in the water medium. Close to the surface, the concentration will be higher than the equilibrium concentration out in the bulk water environment (the solubility). This is due to the constant motion of molecules in and out from their sites of their associated state in the surface layer. The variation of the concentration $u(x)$ at a distance x from the body, will follow the GD-function in 10.1.1, which is shown in figure 10.1.1. This means that if some of the molecules which are outside the surface are removed, some molecules in the surface layer will move into the water to make up for the loss. On the contrary, if some molecules are added to the water, or if the solubility is reduced, for example by a pH shift, some

molecules must be precipitated at the surface. With these processes, the membrane changes shape and obtains a dynamic behaviour. There are other reasons for changes of shape, such as protein conformation transitions, but now we will focus on the lipid bilayer only.

The fundamental solution to the diffusion equation at $t=0$ is the GD-distribution *10.1.1a*.

$$u(x) = e^{-x^2} \quad 10.1.1a$$

In a Cartesian system this will be as in equation *10.1.1b*.

$$y = e^{-x^2} \quad 10.1.1b$$

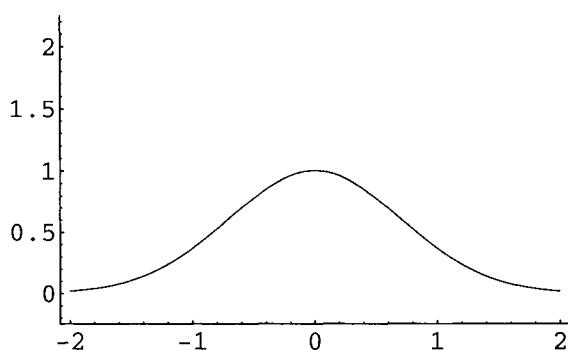


Figure 10.1.1 The GD-function.

The addition of a larger peak via a coordinate shift as in equation *10.1.2*, and figure **10.1.2**, make the two GD-functions exist next to each other. This property of the GD-function was used in chap 5 to describe motion. Here we consider the overlap of two functions, generating excess concentration ($C > 0$) between the two. This is even more evident in equation *10.1.3* and figure **10.1.3**, where two identical GD-functions are used.

$$y = e^{-(x)^2} + 2e^{-(x-3)^2} \quad 10.1.2$$

$$y = e^{-x^2} + e^{-(x-2.5)^2} \quad 10.1.3$$

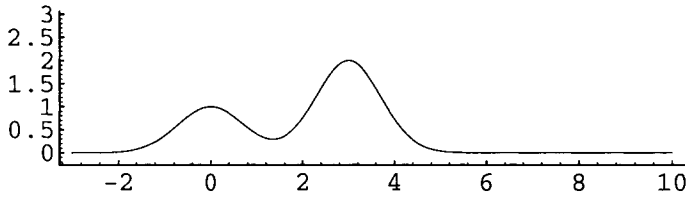


Figure 10.1.2 Two GD-functions.

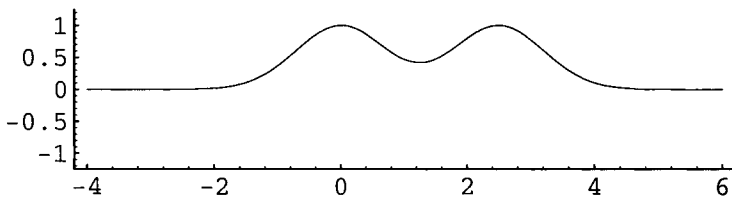


Figure 10.1.3 Two overlapping GD-functions.

This means that if a body like a vesicle which exists in a lipid solution, and has its own GD-profile, approaches another similar vesicle, there is an increase in lipid concentration between the two, due to the overlap. The lipid molecules constituting the surface membranes of all organelles and vesicles have different specific solubilities (sometime this is forgotten as they are just regarded as insoluble). In the case of phosphatidylcholine, for example, the value is about 10^{-12} M. Thus, very few molecules need to be added or removed to change the structure at the surface. When the solubility (molecular solution) is reached, precipitation occurs with a topology dictated by concentration gradients, a neck or a catenoid.

Spherical vesicles will now be considered. In three dimensions the formulas corresponding to 10.1.1a-b is found in 10.1.4 or 10.1.5 respectively.

$$u(x, y, z) = e^{-(x^2 + y^2 + z^2)} \quad 10.1.4$$

or

$$e^{-(x^2 + y^2 + z^2)} = C \quad 10.1.5$$

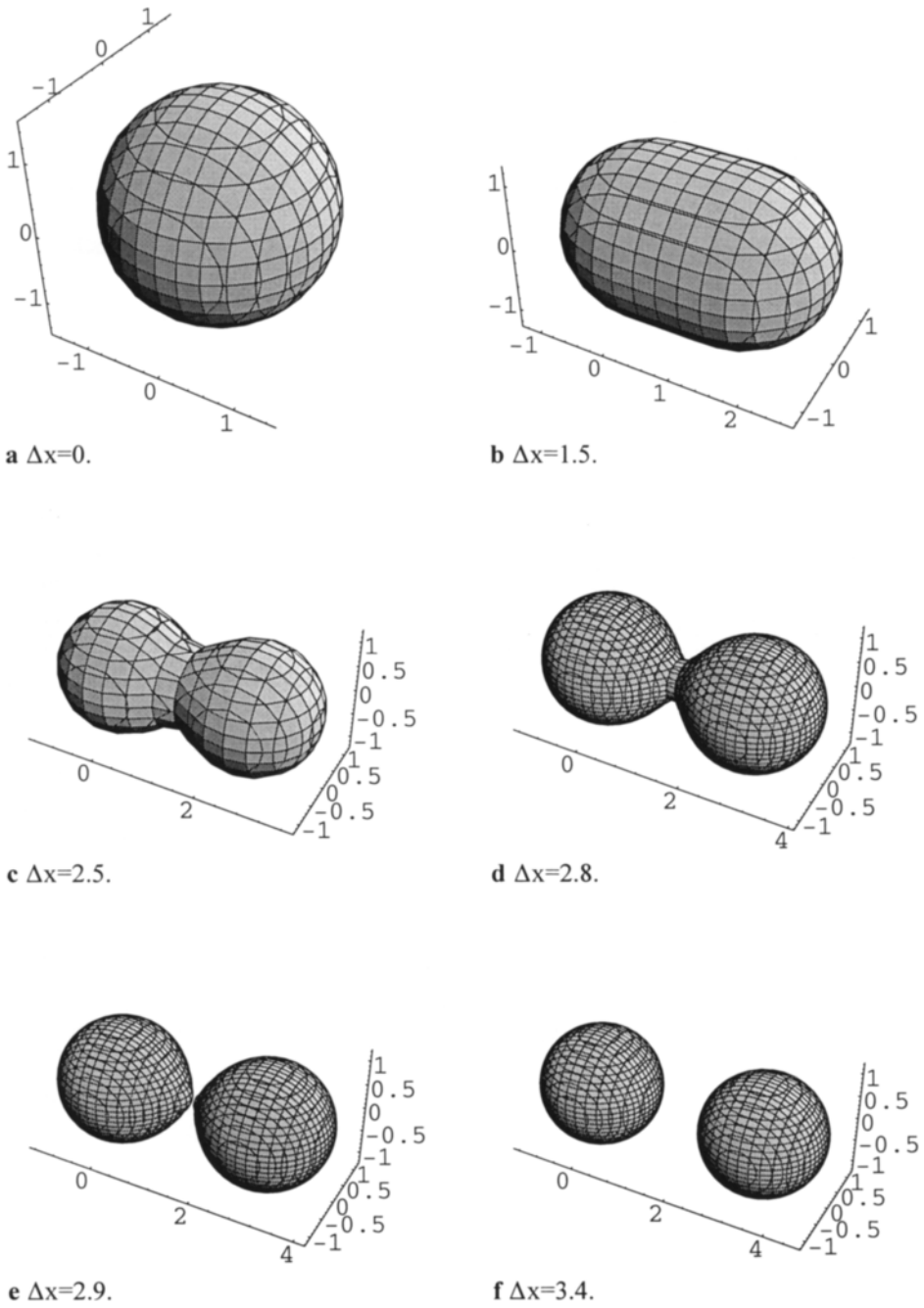


Figure 10.1.4 Two spheres are separated after equation 10.1.6.

There is no need to worry about a complete picture of the equations. It is sufficient to say that with concentration, the implicit function in 10.1.5 is a sphere, and the smaller the concentration, the bigger sphere. The sphere is then also a picture of the body that sets up the concentration. With the GD-function it is possible to put two such spheres next to each other, and make them move. We did that to study motion in section 5.3. We shall do something similar here, but from a different angle, which indicates how it is constructed mathematically. We start by making a complete overlap, as if we had a cell division in equation 10.1.6. We then move the two spheres apart, and Δx varies with 0, 1.5, 2.5, 2.8, 2.9, and 3.4, which is shown in figures 10.1.4a-e.

$$e^{-(x^2+y^2+z^2)} + e^{-((x-\Delta x)^2+y^2+z^2)} = 1/4 \quad 10.1.6$$

Mathematically there is interaction between the constant and the x-parameters. In reality the two functions can, when separated, be said to represent two different concentrations. When we put together one function, under a common constant, we conjecture that this is also a picture of reality. These mathematical interactions describes the mixing of concentration gradients in space. What we do with these implicit functions is to stay in 3D, and just vary the metric parameters and keep the concentration $u(x,y,z)$ constant for each experiment.

The reverse process can take place when two vesicles made of lipids happen to be close. We have discussed elsewhere how the lipid bilayer exists in equilibrium with monomers at saturated concentration in solution. Their respective concentration gradients overlap, and precipitation occurs in the form of catenoids.

So we have a good tool, adding or subtracting GD-functions give changes in concentrations and dynamics of shape. We shall now build structures like filaments which form the frames of the cells. We shall also build structures to describe the motor proteins.

10.2 Filaments

Actin and microtubules are two important filaments which are essential for cell division. They give the stability and flexibility to the skeleton of the cell, they form parts of muscles, they make the flagella swim, they shape the axons, *etc.*

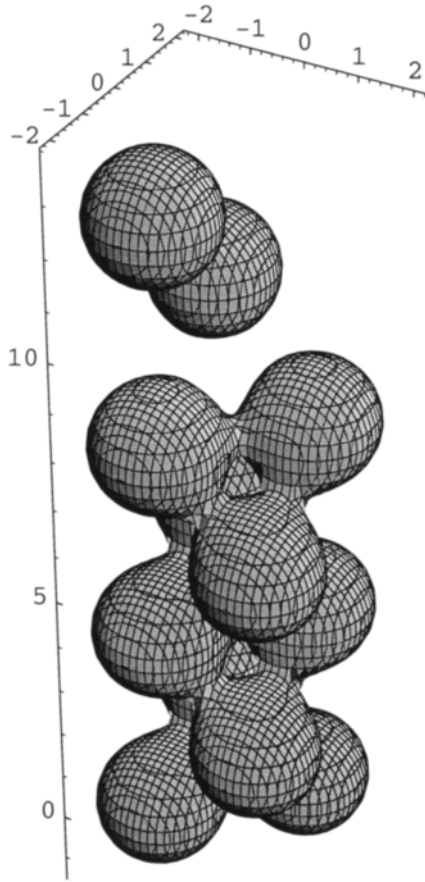


Figure 10.2.1 Actin rod with two “free” actin molecules.

Actin protein molecules polymerise to give rod filaments in a helical arrangement. This occurs from actin in solution when the concentration is high enough. The interactions between molecules become strong (and frequent) and precipitation begins. The helical shape of the precipitation has its origin in the shape of the molecule that also gives the rod a polar character.

In figure 10.2.1 we have used catenoids between spheres to show interactions between molecules in an actin rod after equation 10.2.1. Two molecules are just about to land (or have just left), demonstrating the dynamic behaviour of the filament, as depending on variations of the GD-concentration gradients outside the tip of the filament.

$$\begin{aligned}
 & e^{-[(x-1)^2+(y-1)^2+z^2]} + e^{-[(x+1)^2+(y+1)^2+z^2]} + \\
 & + e^{-[(x-1)^2+(y+1)^2+(z-2)^2]} + e^{-[(x+1)^2+(y-1)^2+(z-2)^2]} + \\
 & + e^{-[(x-1)^2+(y-1)^2+(z-4)^2]} + e^{-[(x+1)^2+(y+1)^2+(z-4)^2]} + \\
 & + e^{-[(x-1)^2+(y+1)^2+(z-6)^2]} + e^{-[(x+1)^2+(y-1)^2+(z-6)^2]} + \\
 & + e^{-[(x-1)^2+(y-1)^2+(z-8)^2]} + e^{-[(x+1)^2+(y+1)^2+(z-8)^2]} + \\
 & + e^{-[(x+1)^2+(y-1)^2+(z-10.5)^2]} + e^{-[(x+1)^2+(y+1)^2+(z-12.5)^2]} = 1/4
 \end{aligned}
 \tag{10.2.1}$$

The actin filaments are most important for the stability and flexibility of most mammalian cells. The molecules polymerise to networks of non-intersecting rods, and the rods are held together with special proteins. Non-intersecting rods occur frequently in biology, and we have done the mathematics of such structures elsewhere [2], and in this book we will only repeat a couple of essential parts. We described the parallel rod systems in chapters 3-4, and we shall put three such systems together. The systems are identical but with different orientations in space, and they are always non-intersecting. We have to go exponential, otherwise they would all fuse together. The first equation is after equations used earlier in chapters 3-4. There is an intimate relation between the circular and the GD equations, as discussed earlier [3].

The rod system in figures 10.2.2-3, made from cosine and GD respectively (equations 10.2.2 and 10.2.3), is the simplest packing of rods. We continue with the GD-types, as they are easier to handle

$$e^{\cos\frac{\pi}{2}x+\cos\frac{\pi}{2}(z+2)} + e^{\cos\frac{\pi}{2}z+\cos\frac{\pi}{2}(y+2)} + e^{\cos\frac{\pi}{2}y+\cos\frac{\pi}{2}(x+2)} = 6
 \tag{10.2.2}$$

$$\begin{aligned}
 & e^{-(x^2+(y+2)^2)^2} + e^{-(y^2+(z+2)^2)^2} + e^{-(z^2+(x+2)^2)^2} \\
 & + e^{-(x^2+(y-2)^2)^2} + e^{-(y^2+(z-2)^2)^2} + e^{-(z^2+(x-2)^2)^2} = 0.65
 \end{aligned}
 \tag{10.2.3}$$

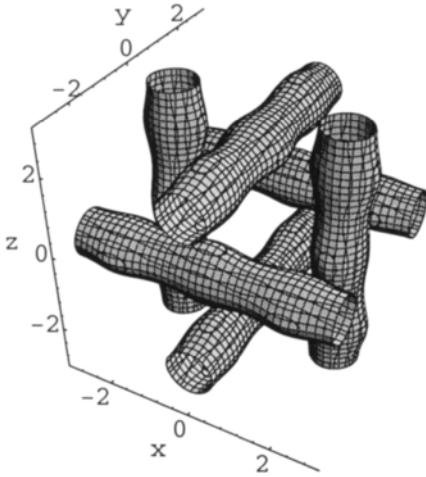


Figure 10.2.2 Fence packing of rods with cosine.

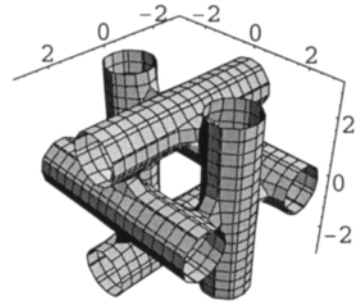


Figure 10.2.3 Fence packing of rods with GD-function.

We take a more general rod packing, of the same symmetry as the gyroid surface, and give the equations in 10.2.4-5. The cos version is shown in figure 10.2.4.

$$\begin{aligned}
 & e^{\cos\frac{\pi}{2}(x-y)+\cos\frac{\pi}{2}(y+z)+\cos\frac{\pi}{2}(x+z)} \\
 & + e^{\cos\frac{\pi}{2}(x+y+2)+\cos\frac{\pi}{2}(y-z)+\cos\frac{\pi}{2}(x+z+2)} \\
 & + e^{\cos\frac{\pi}{2}(x+y)+\cos\frac{\pi}{2}(y+z+2)+\cos\frac{\pi}{2}(x-z-2)} \\
 & + e^{\cos\frac{\pi}{2}(x-y+2)+\cos\frac{\pi}{2}(y-z-2)+\cos\frac{\pi}{2}(x-z)} = 15
 \end{aligned}
 \tag{10.2.4}$$

Now we use the GD-function, to make the rods separate, we also change the constant to make them thinner. The result in figure 10.2.5 reminds us very much of an actin bundle.

$$\begin{aligned}
 & e^{-((x-y)^2+(y+z)^2+(x+z)^2)} + e^{-((x+y)^2+(y+z+4)^2+(x-z-4)^2)} \\
 & + e^{-((x-y+4)^2+(y-z-4)^2+(x-z)^2)} + e^{-((x+y-4)^2+(y-z)^2+(x+z-4)^2)} = 0.95
 \end{aligned}
 \tag{10.2.5}$$

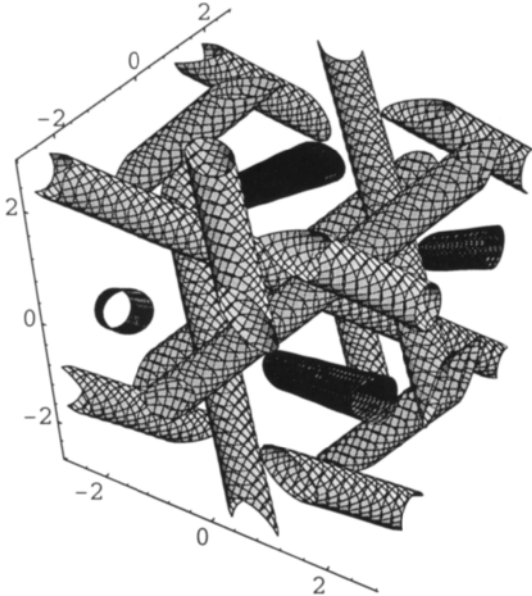


Figure 10.2.4 Rod packing of garnet or gyroid symmetry.

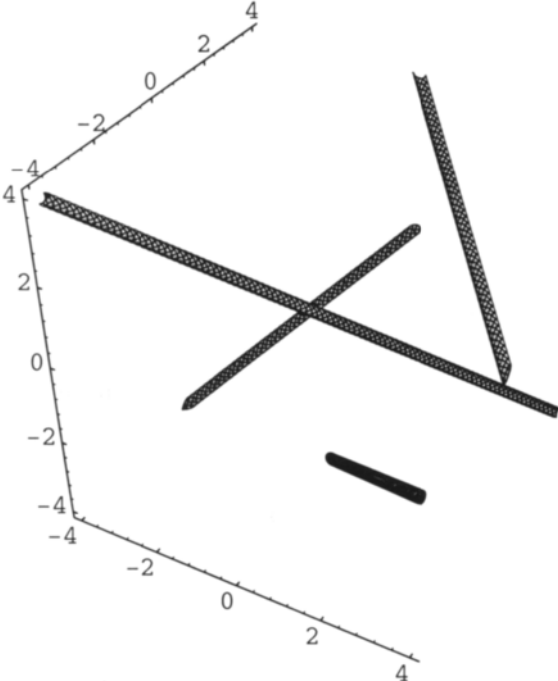


Figure 10.2.5 Filament of GD-mathematics and gyroid symmetry.

We demonstrate the dynamics of filaments, important for cell motion, cell growth, cell division, and cell stability, with the use of these rod mathematics. For this purpose we select a cylinder, shown in figure 10.2.6, with the equation in 10.2.6, and with $\Delta_1=\Delta_2=6$.

$$e^{-[10(y^2+z^2)+e^{x-\Delta_1}+e^{-(x+\Delta_2)}]} = 1/2 \tag{10.2.6}$$

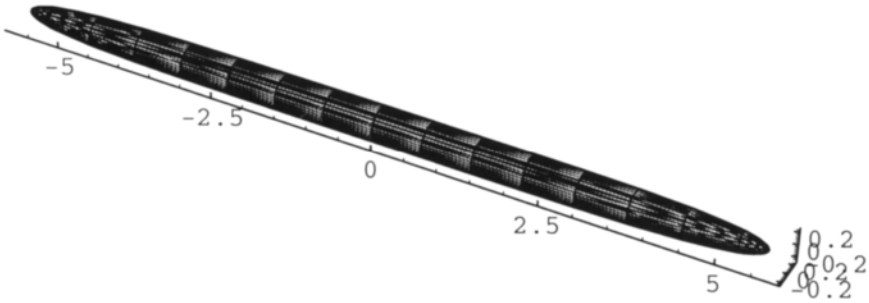


Figure 10.2.6 Rod of certain extension and size.

We make it thinner and vary its length with equation 10.2.6, and we give all equations for the changes of size below. The series of figures shown, reveals that mathematics easily may change the speed of growth in both the ends of the filament, and also move the filament itself. In two cases there are no scale since the sizes are clear from the equations given. Each figure has its corresponding equation number.

$$e^{-[100(y^2+z^2)+e^{x-10}+e^{-(x+10)}]} = 1/2 \tag{10.2.7}$$

$$e^{-[100(y^2+z^2)+e^{x-10}+e^{-(x+10)}]} = 1/2 \tag{10.2.8}$$

$$e^{-[100(y^2+z^2)+e^{x-8}+e^{-(x+14)}]} = 1/2 \tag{10.2.9}$$

$$e^{-[100(y^2+z^2)+e^{x-15}+e^{-(x+15)}]} = 1/2 \tag{10.2.10}$$

$$e^{-[100(y^2+z^2)+e^{x-15}+e^{-(x+15)}]} = 1/2 \tag{10.2.11}$$

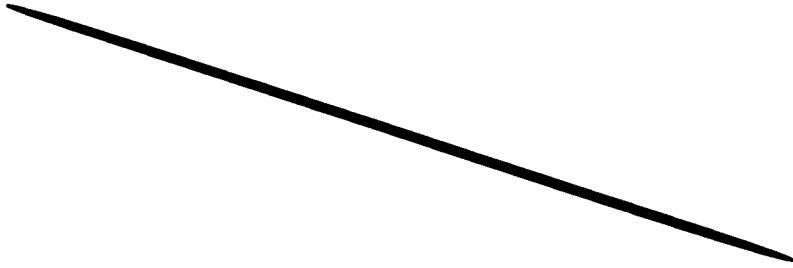


Figure 10.2.7 Thinner and longer rod.

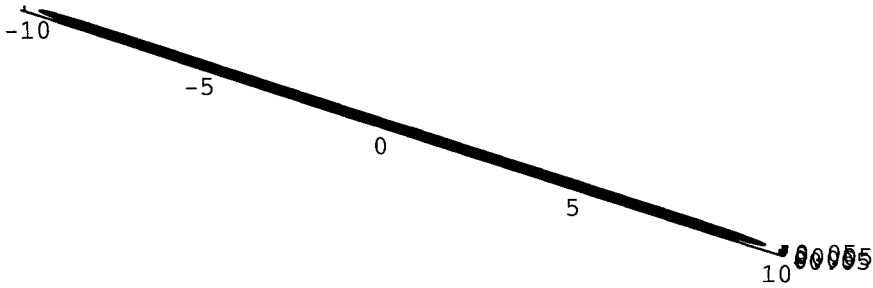


Figure 10.2.8 Same rod but with scale.

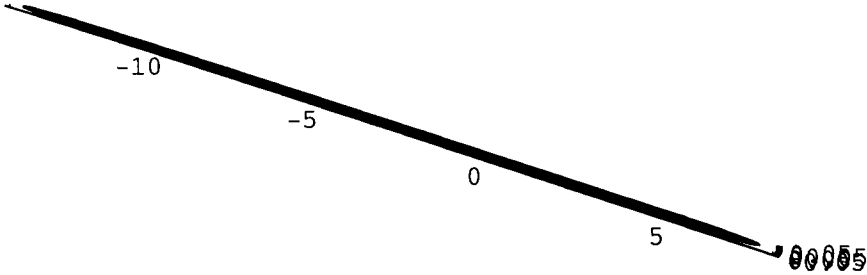


Figure 10.2.9 The rod moved towards left.

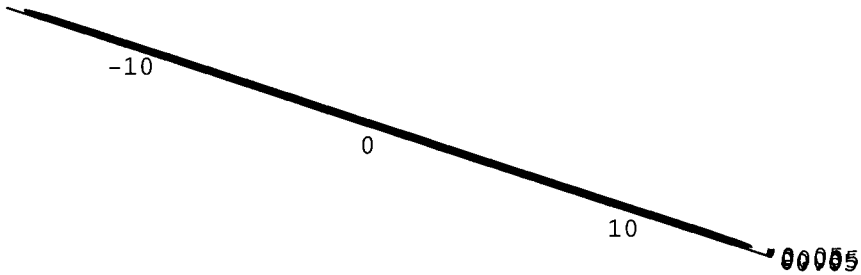


Figure 10.2.10 Still longer rod.

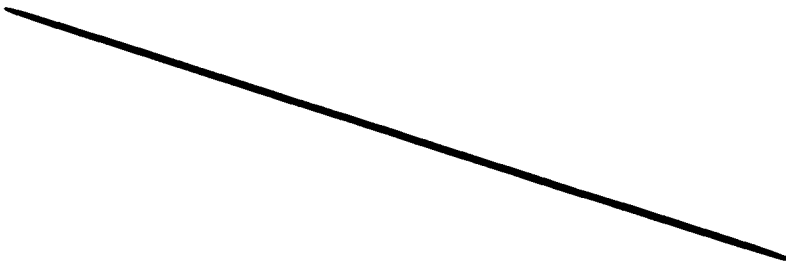


Figure 10.2.11 Same rod but without scale.

We shall end with a simple filament construction using these mathematics. In figure **10.2.12** there are thin filaments anchored to planes via catenoids, in reality there are special proteins that serve as glue. There is also a filament going perpendicular, non intersecting, but joined to the others via catenoids, which again substitute for proteins. The equation is in *10.2.12*.

$$e^{-5[x^2+(y+2)^2]} + e^{-5[x^2+(y-3)^2]} + e^{-5[(x-0.5)^2+z^2]} + e^{z-12} + e^{-(z+12)} = 1/2 \quad 10.2.12$$

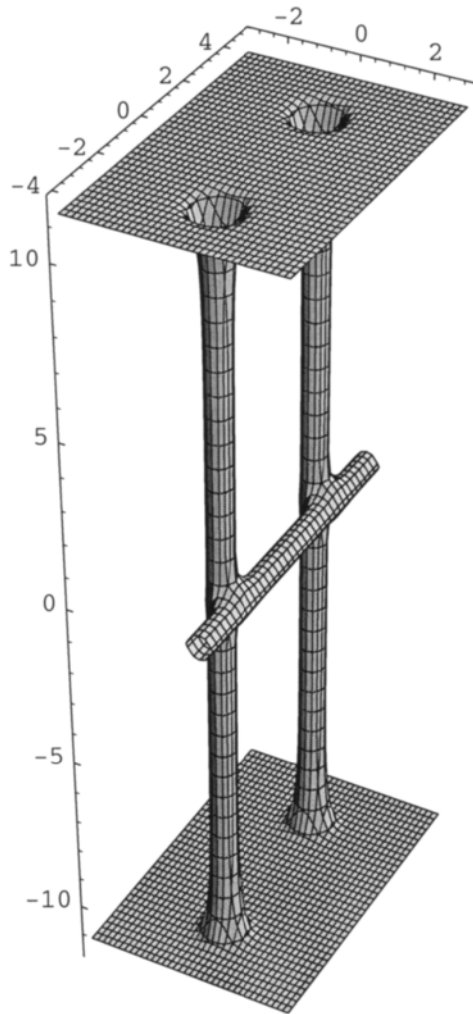


Figure 10.2.12 Filament construction.

10.3 Microtubulus and Axonemes

Tubulin protein dimers polymerise to form hollow microtubulus in a helical arrangement, giving a polar structure. The dimers can polymerise, and later depolymerise, which generates dynamic instability as a result of GTP-hydrolysis, analogously to the actin filaments.

Nine triplets of microtubulus organise themselves to a centriole, and to the similar structure of a basal body. Such bodies anchor cilia and flagella to the surface of the cell. They also initiate the growth of the most important axonemes, the fundamental structure of both flagella and cilia. The microtubules in axonemes are arranged in a 9+2 pattern, in which a central pair of microtubulus are surrounded by nine doublets.

Symmetry nine is important here, and we shall in our mathematical description of this symmetry use a structure of one central microtubulus surrounded by nine others, something between a centriole, or a basal body, and the axoneme.

Nine-fold symmetry cannot give regular translation periodicity. So why does Nature choose nine-fold symmetry? A guess would be that the sliding motion, giving the bending to flagella, requires a certain number and space, and nine would then be the lower limit. The central one or two would serve to help the extra filaments or proteins between these units of microtubulin to build a structure strong enough. Much like a so-called goke which is needed in a rope with four or more strands.

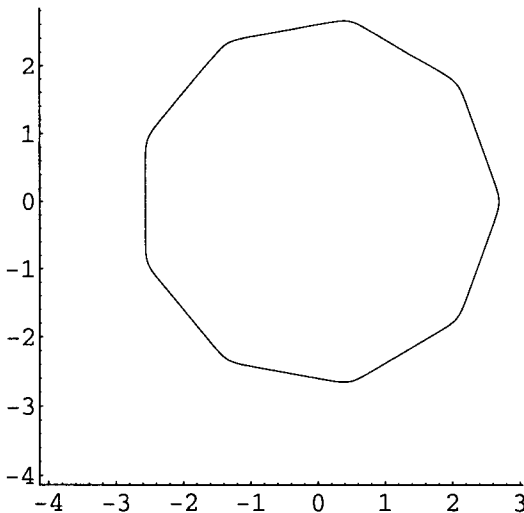


Figure 10.3.1 Polygon with 9 edges - a nonagon.

But we like to demonstrate this symmetry as derived from a mathematical discussion. We start by showing the nine polygon, the nonagon, taken from the mathematics we have derived earlier [4]. Equation 10.3.1 below gives

exponential scale, do not intersect but bend over to the polygon in figure 10.3.1.

$$\begin{aligned}
 & e^{(x \cos(\pi/9) + y \sin(\pi/9))^3} + e^{(-x \cos(2\pi/9) - y \sin(2\pi/9))^3} \\
 & + e^{(x \cos(3\pi/9) + y \sin(3\pi/9))^3} + e^{(-x \cos(4\pi/9) - y \sin(4\pi/9))^3} \\
 & + e^{(x \cos(5\pi/9) + y \sin(5\pi/9))^3} + e^{(-x \cos(6\pi/9) - y \sin(6\pi/9))^3} \\
 & + e^{(x \cos(7\pi/9) + y \sin(7\pi/9))^3} + e^{(x \cos(8\pi/9) + y \sin(8\pi/9))^3} + \\
 & + e^{(x \cos(9\pi/9) + y \sin(9\pi/9))^3} = 2 \cdot 10^7
 \end{aligned}
 \tag{10.3.1}$$

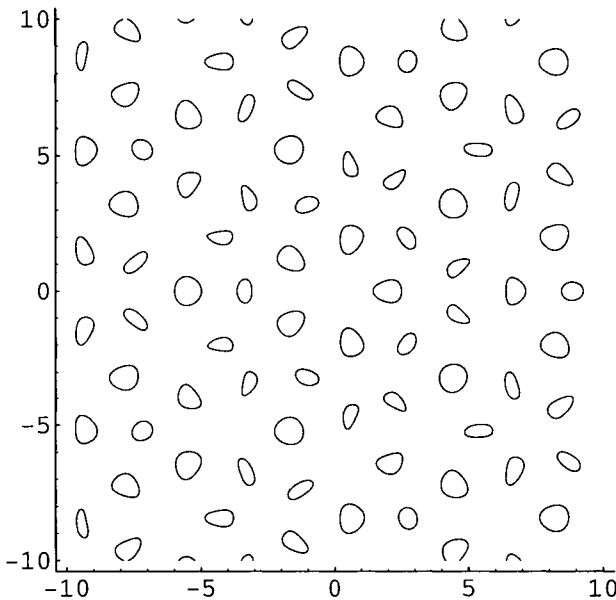


Figure 10.3.2 Five fold symmetry.

We shall go circular with this kind of mathematics to give the kind of repetition this quasi symmetry gives. And we start with celebrated five-fold symmetry in figure 10.3.2 from equation 10.3.2. The repetition is of dilatation nature, a symmetry one of us has described in 3D in detail before [5,6,7]. In the origin there is a five-ring, which in various shapes is repeated in a radial manner. The distances between the five-rings follow the famous Fibonacci numbers 1,1,2,3,5,8,13,21... Fibonacci (son of good

nature) had the name Leonardo of Pisa, and lived between 1175-1250. His sequence is indeed one of the early applications of mathematics to biology. There are many examples of biological growth involving this sequence: the reproduction of rats and bees, the branching of trees, the patterns of petals on many flowers, and much more.

$$\begin{aligned} & \sin \pi x - \sin \pi \left(x \cos \frac{\pi}{5} + y \sin \frac{\pi}{5} \right) + \sin \pi \left(x \cos \frac{2\pi}{5} + y \sin \frac{2\pi}{5} \right) \\ & - \sin \pi \left(x \cos \frac{3\pi}{5} + y \sin \frac{3\pi}{5} \right) + \sin \pi \left(x \cos \frac{4\pi}{5} + y \sin \frac{4\pi}{5} \right) = 2 \end{aligned} \quad 10.3.2$$

From the exponential equation 10.3.1 we design equation 10.3.3 to show the 9-fold symmetry in figure 10.3.3.

$$\begin{aligned} & \sin \pi x - \sin \pi \left(x \cos \frac{\pi}{9} + y \sin \frac{\pi}{9} \right) + \sin \pi \left(x \cos \frac{2\pi}{9} + y \sin \frac{2\pi}{9} \right) \\ & - \sin \pi \left(x \cos \frac{3\pi}{9} + y \sin \frac{3\pi}{9} \right) + \sin \pi \left(x \cos \frac{4\pi}{9} + y \sin \frac{4\pi}{9} \right) \\ & - \sin \pi \left(x \cos \frac{5\pi}{9} + y \sin \frac{5\pi}{9} \right) + \sin \pi \left(x \cos \frac{6\pi}{9} + y \sin \frac{6\pi}{9} \right) \\ & - \sin \pi \left(x \cos \frac{7\pi}{9} + y \sin \frac{7\pi}{9} \right) + \sin \pi \left(x \cos \frac{8\pi}{9} + y \sin \frac{8\pi}{9} \right) = 3 \end{aligned} \quad 10.3.3$$

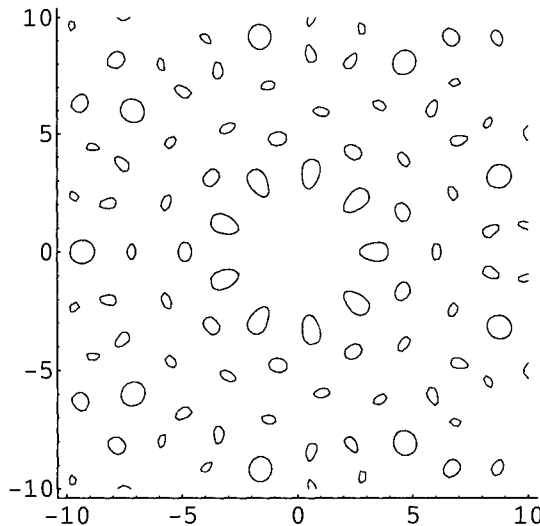


Figure 10.3.3 9-fold symmetry.

The axonemes have nine doublets of microtubulus, and the individuals in each doublet have different sizes, which means we need to square. We also need to damp in order to cut off the outer terms, this is done using the Hermite operator in equation 10.3.4.

$$\begin{aligned}
 & e^{-\frac{1}{4}(x^2+y^2)} \left[\sin \pi x - \sin \pi \left(x \cos \frac{\pi}{9} + y \sin \frac{\pi}{9} \right) + \sin \pi \left(x \cos \frac{2\pi}{9} + y \sin \frac{2\pi}{9} \right) \right. \\
 & - \sin \pi \left(x \cos \frac{3\pi}{9} + y \sin \frac{3\pi}{9} \right) + \sin \pi \left(x \cos \frac{4\pi}{9} + y \sin \frac{4\pi}{9} \right) \\
 & - \sin \pi \left(x \cos \frac{5\pi}{9} + y \sin \frac{5\pi}{9} \right) + \sin \pi \left(x \cos \frac{6\pi}{9} + y \sin \frac{6\pi}{9} \right) \\
 & \left. - \sin \pi \left(x \cos \frac{7\pi}{9} + y \sin \frac{7\pi}{9} \right) + \sin \pi \left(x \cos \frac{8\pi}{9} + y \sin \frac{8\pi}{9} \right) - 0.5 \right]^2 = 1
 \end{aligned}$$

10.3.4

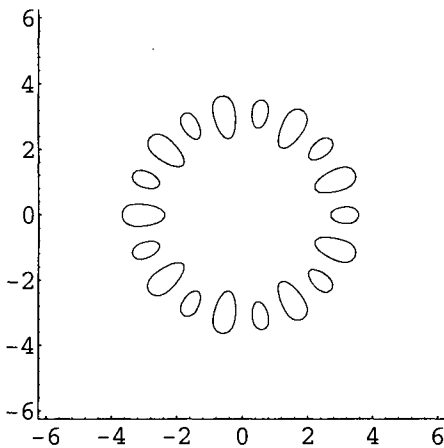


Figure 10.3.4 Square of function give doublets.

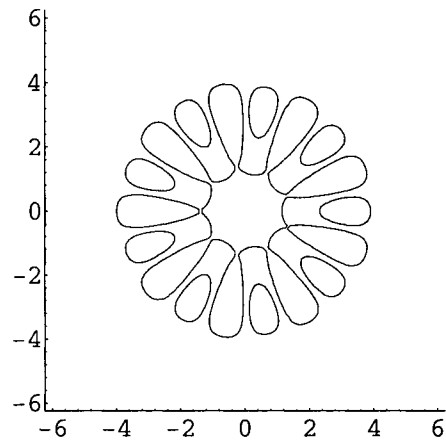


Figure 10.3.5 Interaction with central circle.

In figure 10.3.4 we have the doublets, and by changing constant, as in equation 10.3.5, we get a structure in the centre that interacts with the doublets in figure 10.3.5.

$$\begin{aligned}
& e^{-\frac{1}{4}(x^2+y^2)} \left[\sin \pi x - \sin \pi \left(x \cos \frac{\pi}{9} + y \sin \frac{\pi}{9} \right) + \sin \pi \left(x \cos \frac{2\pi}{9} + y \sin \frac{2\pi}{9} \right) \right. \\
& - \sin \pi \left(x \cos \frac{3\pi}{9} + y \sin \frac{3\pi}{9} \right) + \sin \pi \left(x \cos \frac{4\pi}{9} + y \sin \frac{4\pi}{9} \right) \\
& - \sin \pi \left(x \cos \frac{5\pi}{9} + y \sin \frac{5\pi}{9} \right) + \sin \pi \left(x \cos \frac{6\pi}{9} + y \sin \frac{6\pi}{9} \right) \\
& \left. - \sin \pi \left(x \cos \frac{7\pi}{9} + y \sin \frac{7\pi}{9} \right) + \sin \pi \left(x \cos \frac{8\pi}{9} + y \sin \frac{8\pi}{9} \right) - 0.5 \right]^2 = 0.175
\end{aligned} \tag{10.3.5}$$

In equation 10.3.6 we have added a circle and changed some of the constants. In figure 10.3.6 we show the plasma membrane, slightly curved, to complete the axoneme structure.

$$\begin{aligned}
& e^{-\frac{1}{10}(x^2+y^2)} \left[\sin \pi x - \sin \pi \left(x \cos \frac{\pi}{9} + y \sin \frac{\pi}{9} \right) + \sin \pi \left(x \cos \frac{2\pi}{9} + y \sin \frac{2\pi}{9} \right) \right. \\
& - \sin \pi \left(x \cos \frac{3\pi}{9} + y \sin \frac{3\pi}{9} \right) + \sin \pi \left(x \cos \frac{4\pi}{9} + y \sin \frac{4\pi}{9} \right) \\
& - \sin \pi \left(x \cos \frac{5\pi}{9} + y \sin \frac{5\pi}{9} \right) + \sin \pi \left(x \cos \frac{6\pi}{9} + y \sin \frac{6\pi}{9} \right) \\
& - \sin \pi \left(x \cos \frac{7\pi}{9} + y \sin \frac{7\pi}{9} \right) + \sin \pi \left(x \cos \frac{8\pi}{9} + y \sin \frac{8\pi}{9} \right) - 0.5 \right]^2 \\
& + \frac{1}{10} e^{\frac{1}{10}(x^2+y^2)} = 3.2
\end{aligned} \tag{10.3.6}$$

$$\begin{aligned}
& e^{-\frac{1}{10}(x^2+y^2)} \left[\sin \pi x - \sin \pi \left(x \cos \frac{\pi}{9} + y \sin \frac{\pi}{9} \right) + \sin \pi \left(x \cos \frac{2\pi}{9} + y \sin \frac{2\pi}{9} \right) \right. \\
& - \sin \pi \left(x \cos \frac{3\pi}{9} + y \sin \frac{3\pi}{9} \right) + \sin \pi \left(x \cos \frac{4\pi}{9} + y \sin \frac{4\pi}{9} \right) \\
& - \sin \pi \left(x \cos \frac{5\pi}{9} + y \sin \frac{5\pi}{9} \right) + \sin \pi \left(x \cos \frac{6\pi}{9} + y \sin \frac{6\pi}{9} \right) \\
& - \sin \pi \left(x \cos \frac{7\pi}{9} + y \sin \frac{7\pi}{9} \right) + \sin \pi \left(x \cos \frac{8\pi}{9} + y \sin \frac{8\pi}{9} \right) - 1 \left. \right]^2 \\
& + \frac{1}{10} e^{\frac{1}{10}(x^2+y^2-1)} = 2
\end{aligned} \tag{10.3.7}$$

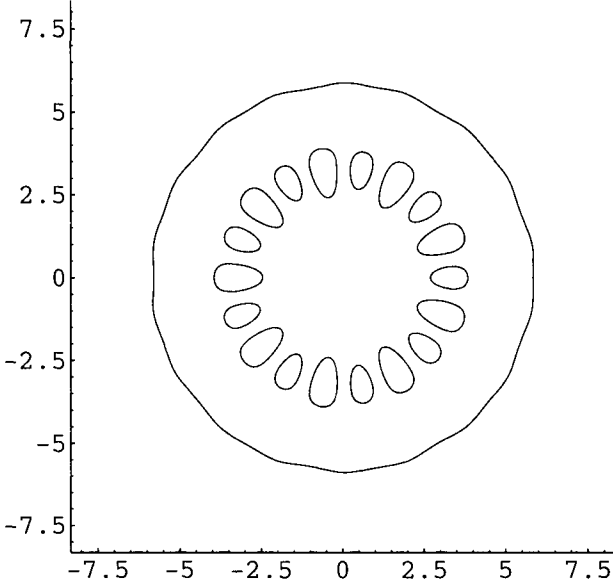


Figure 10.3.6 Plasma membrane added.

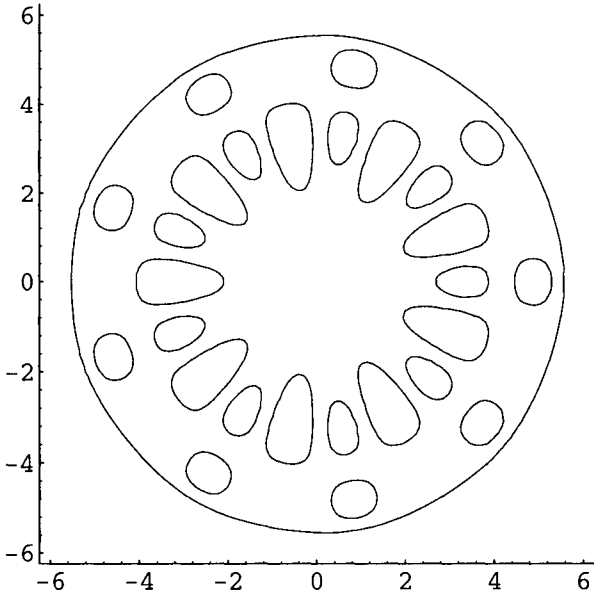


Figure 10.3.7 Nine more fibres.

The advantage with this quasi-, or dilatation-, symmetry is that it can expand, similar to ordinary translation. In the mammalian sperm there are nine more outer denser fibres, which we can get just by changing weights as in figure 10.3.3. The equation is in 10.3.7 and the figure in 10.3.7.

We have also made a 3D calculation after equation 10.3.4, and show this in figure 10.3.8.

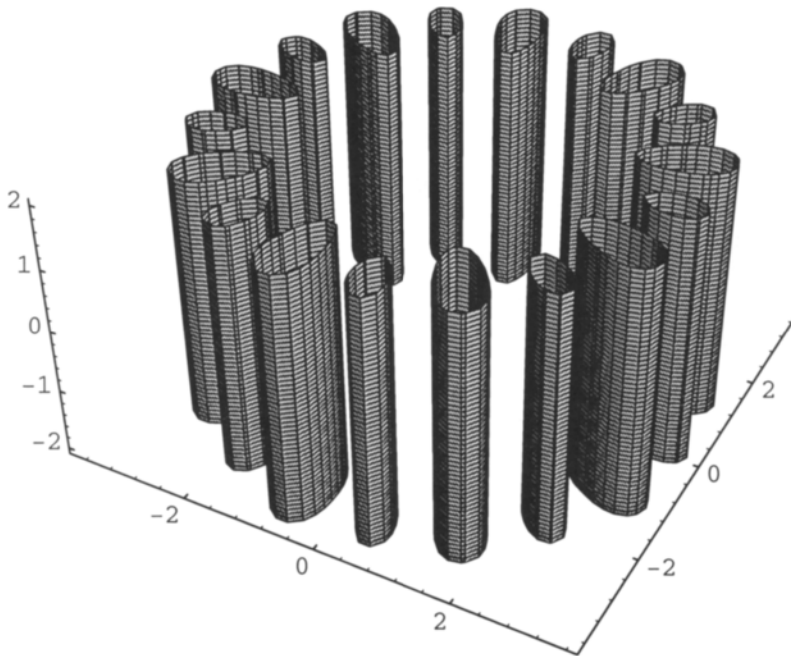


Figure 10.3.8 Three dimensional model of the axoneme.

We also like to demonstrate the possibility of using these polygonal mathematics for making cog-wheels. We use nine-fold symmetry, as we have it above (any symmetry can be used of course), the equation is found in 10.3.8 and the figure in 10.3.9.

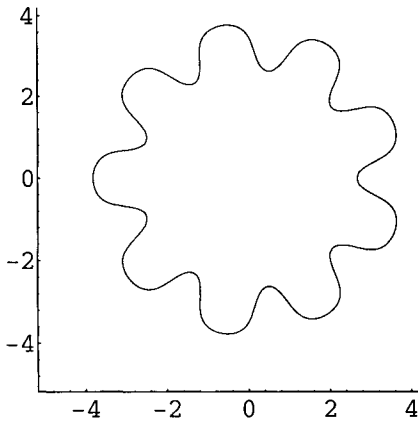


Figure 10.3.9 Cog wheel.

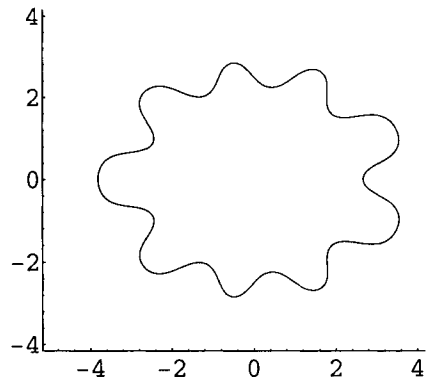


Figure 10.3.10 Eccentric cog wheel.

$$\begin{aligned}
 & e^{-\frac{1}{10}(x^2+y^2)} \left[\sin \pi x - \sin \pi \left(x \cos \frac{\pi}{9} + y \sin \frac{\pi}{9} \right) + \sin \pi \left(x \cos \frac{2\pi}{9} + y \sin \frac{2\pi}{9} \right) \right. \\
 & - \sin \pi \left(x \cos \frac{3\pi}{9} + y \sin \frac{3\pi}{9} \right) + \sin \pi \left(x \cos \frac{4\pi}{9} + y \sin \frac{4\pi}{9} \right) \\
 & - \sin \pi \left(x \cos \frac{5\pi}{9} + y \sin \frac{5\pi}{9} \right) + \sin \pi \left(x \cos \frac{6\pi}{9} + y \sin \frac{6\pi}{9} \right) \\
 & \left. - \sin \pi \left(x \cos \frac{7\pi}{9} + y \sin \frac{7\pi}{9} \right) + \sin \pi \left(x \cos \frac{8\pi}{9} + y \sin \frac{8\pi}{9} \right) - 0.5 \right] \tag{10.3.8} \\
 & + e^{\frac{1}{10}(x^2+y^2)} = 3.2
 \end{aligned}$$

$$\begin{aligned}
 & e^{-\frac{1}{10}(x^2+y^2)} \left[\sin \pi x - \sin \pi \left(x \cos \frac{\pi}{9} + y \sin \frac{\pi}{9} \right) + \sin \pi \left(x \cos \frac{2\pi}{9} + y \sin \frac{2\pi}{9} \right) \right. \\
 & - \sin \pi \left(x \cos \frac{3\pi}{9} + y \sin \frac{3\pi}{9} \right) + \sin \pi \left(x \cos \frac{4\pi}{9} + y \sin \frac{4\pi}{9} \right) \\
 & - \sin \pi \left(x \cos \frac{5\pi}{9} + y \sin \frac{5\pi}{9} \right) + \sin \pi \left(x \cos \frac{6\pi}{9} + y \sin \frac{6\pi}{9} \right) \\
 & \left. - \sin \pi \left(x \cos \frac{7\pi}{9} + y \sin \frac{7\pi}{9} \right) + \sin \pi \left(x \cos \frac{8\pi}{9} + y \sin \frac{8\pi}{9} \right) - 0.5 \right] \tag{10.3.9} \\
 & + e^{\frac{1}{10}(x^2+y^2)} = 3.2
 \end{aligned}$$

The eccentric cog-wheel is obtained by making the circular boundary elliptic, as in equation 10.3.9 and shown in figure 10.3.10. Such a cog-wheel could be part of a shape for a dynein head, with a pitch fitting the cog fold of the wheel. The ATP motion of such an eccentric wheel could mechanically trigger the power stroke, and the release in the sliding mechanism that gives curvature to flagella.

10.4 Motor Proteins and the Power Stroke

The motor proteins must belong to the most spectacular of all chemicals. They are the executives for most of the motions in the animal kingdom. There are two motor proteins that seem to be most important; myosin, which with actin filament does the muscle work, and dynein which moves the doublets of tubulin rods (along the axes) in the 9+2 axoneme and makes the flagella whip.

We have already in chapter 9 considered the coordination of this motion in skeletal muscle cells. Here we will discuss the basic element of this motion.

The myosin molecule consists of a head and a helical tail. The crystal structure of the head has been determined with X-rays and with electron microscopy, and has given a molecular mechanism for the motor. First the myosin is bound to actin, involving calcium binding. ATP is bound to the back of the head in a large cleft. The cleft closes around the ATP-molecule and causes a large shape change which makes the head move along the filament, a distance of 50-100 Å. The release of inorganic phosphate during the ATP hydrolysis, provides the energy of the movement, when ADP is released, and the head goes back to the initial position. To illustrate, we do this with mathematics.

First we make the molecule of myosin I, and start with the tail. We construct a helicoid after equation 10.4.1, and the surface is in figure 10.4.1.

$$z \cos \pi x - y \sin \pi x = 0 \quad 10.4.1$$

We do the Hermite damping to make a screw with equation 10.4.2.

$$e^{-(0.2x^2 + y^2 + z^2)} [z \cos \pi x - y \sin \pi x] - 0.3 = 0 \quad 10.4.2$$

The Hermite damping is ellipsoidal to give extension along x, and the screw is shown in figure 10.4.2.

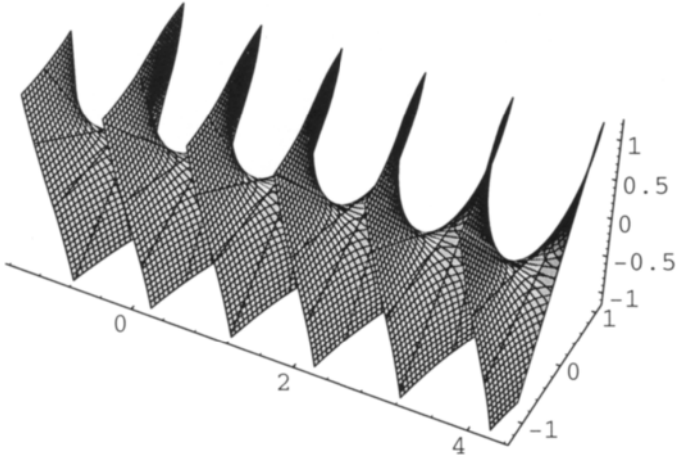


Figure 10.4.1 A helicoid.

We also make two spheres to the head after equation 10.4.3, which is shown in figure 10.4.3. One of the spheres will make the joint to the tail.

$$e^{-[(x-3.5)^2+(y+0.7)^2+z^2]} + e^{-[(x-2)^2+y^2+z^2]} - 0.75 = 0 \tag{10.4.3}$$

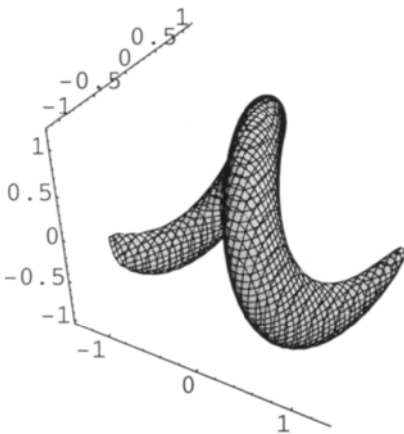


Figure 10.4.2 Hermite damping to the helicoid gives a screw.

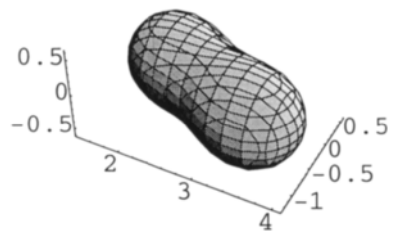


Figure 10.4.3 Two spheres.

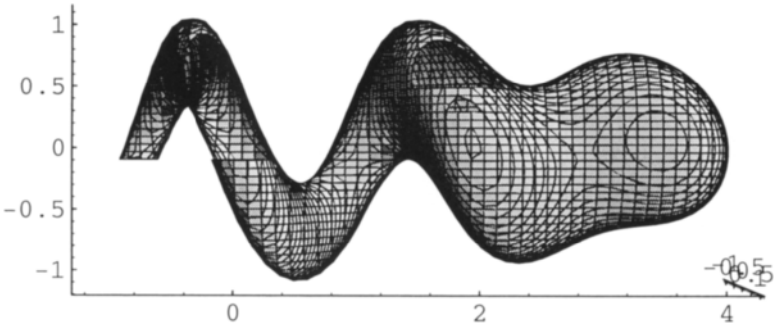


Figure 10.4.4 Myosin molecule and the power stroke after equation 10.4.5, $\Delta y=0$.

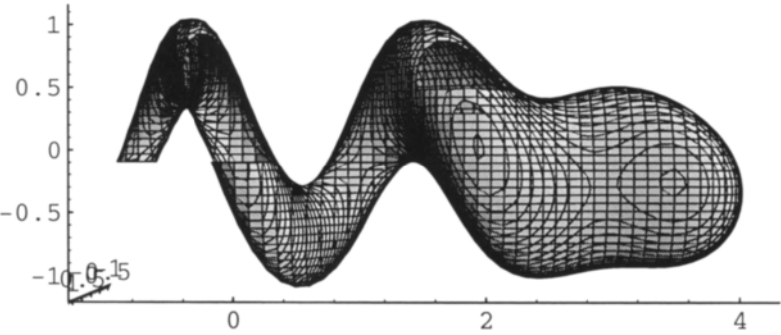


Figure 10.4.5 $\Delta y = 0.35$.

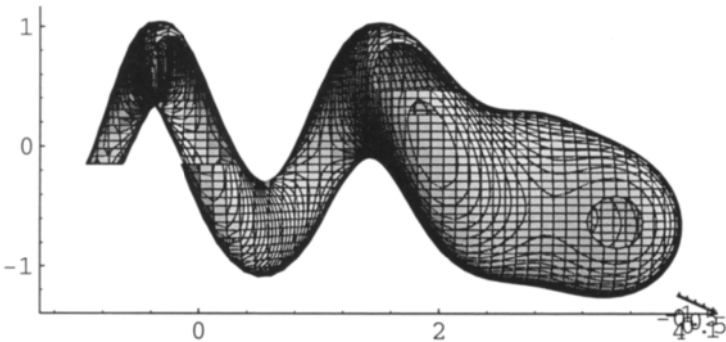


Figure 10.4.6 $\Delta y = 0.7$.

We now make these equations fuse together to the equation 10.4.4 for the myosin I molecule shown in projection. We have protected the damped tail by going up one step on the exponential scale.

$$e^{-(0.2x^2+y^2+z^2)} z \cos \pi x - y \sin \pi x - 0.3 \tag{10.4.4}$$

$$+ 0.4 [e^{-[(x-3.5)^2+(y)^2+z^2]} + e^{-[(x-2)^2+y^2+z^2]}] - 1 = 0$$

We now mimic the power stroke with biological motion, and show that in equation 10.4.5. Changes in Δy result in a move of the outer sphere, and takes the values 0, 0.35 and 0.7 in the figures 10.4.4-6.

$$e^{-(0.2x^2+y^2+z^2)} z \cos \pi x - y \sin \pi x - 0.3 \tag{10.4.5}$$

$$+ 0.4 [e^{-[(x-3.5)^2+(y+\Delta y)^2+z^2]} + e^{-[(x-2)^2+y^2+z^2]}] - 1 = 0$$

10.5 Algebraic Roots Give Curvature to Flagella

In chapter 6 the biological motion with the Hermite operator was introduced and applied in general terms to the two kinds of flagella. We shall now, in the light of more experience, analyse the flagella motion of the sperm. This motion must be of utmost importance for the evolution.

It is well understood that the flagella sperm motion is periodic, and we proposed in chapter 6 that it was damped like the harmonic oscillator.

As said above, all motion may be described by counting, here we shall first count to one, and later to two. With other words, the first root to use is $x-1/2$, and the second is $x-1$. We show the first root with equation 10.5.1 in figure 10.5.1.

$$y = x - 0.5 \tag{10.5.1}$$

We apply the Hermite operator as in equation 10.5.2, and we have a beautiful periodic-like shape which we can use for the first flagella, as shown in figure 10.5.2.

$$y + e^{-0.15x^2} (x - 0.5) = 0 \tag{10.5.2}$$

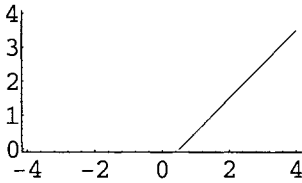


Figure 10.5.1 One root.

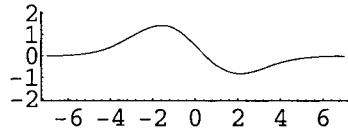


Figure 10.5.2 Hermite operator on the root.

In order to make a 'real' flagella we need to square as in equation 10.5.3, which means going explicit. The constant, here 0.01, determines the thickness of the tail. The picture is shown in figure 10.5.3.

$$[y + e^{-0.15x^2} (x - 0.5)]^2 - 0.01 = 0 \tag{10.5.3}$$

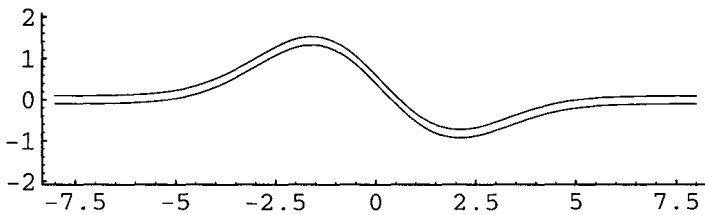


Figure 10.5.3 Going explicit with equation 10.5.3 gives thickness to the flagella tail.

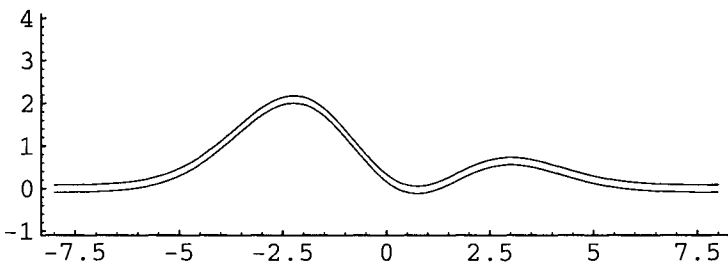


Figure 10.5.4 The tail of the mammalian sperm.

In the mammalian sperm, the tail is longer [8], so we count to two in equation 10.5.4. Due to symmetry reasons we have altered signs. A change of constants is also needed, as this is the beginning of an infinite product. The tail is shown in figure 10.5.4.

$$[-2y + e^{-0.15x^2} (x-0.5)(x-1)]^2 - 0.03 = 0 \tag{10.5.4}$$

We can now make the complete sperms by adding heads in form of spheres, and put stop to the infinite tails. We give the two equations in 10.5.5 and 10.5.6, and the sperms are shown in figure 10.5.5 and 6.

$$e^{[y + e^{-0.15x^2} (x-0.5)]^2 - 0.01} - e^{-[(x+5)^2 + (y-1)^2]} + e^{-(x+10)} + e^{(x-10)} - 1 = 0 \tag{10.5.5}$$

$$e^{[-2y + e^{-0.15x^2} (x-0.5)(x-1)]^2 - 0.02} - e^{-[(x+6)^2 + (y)^2]} + e^{-(x+10)} + e^{(x-10)} - 1 = 0 \tag{10.5.6}$$

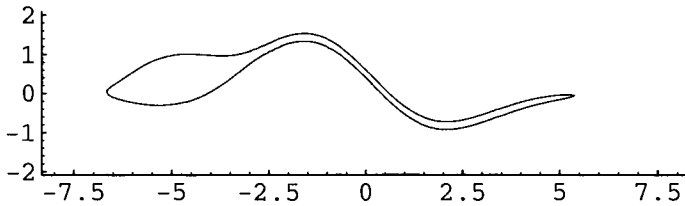


Figure 10.5.5 Head is added to the sperm of one root.

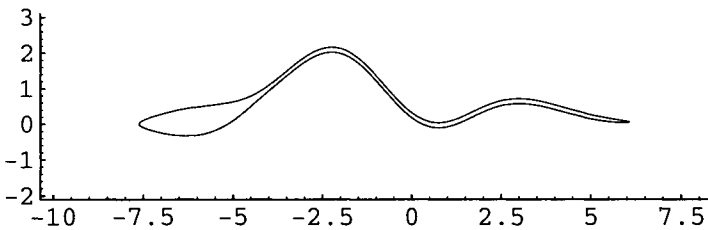


Figure 10.5.6 Head is added to the sperm of two roots.

We have shown that flagella gets its curvature from the roots, or the counting. When we now shall move the flagella, using the concept of curvature, we need many more roots, and for practical reasons it is better to use cosine. So we formulate the equations 10.5.7-9, which give the figures 10.5.7-9. With increased periodicity we get longer tails.

$$e^{[y+e^{-0.15x^2} \cos(0.25\pi x)]^2 - 0.01} - e^{-[(x+4)^2 + (y-1)^2]} + e^{-(x+10)} + e^{(x-10)} - 1 = 0 \tag{10.5.7}$$

$$e^{[y+e^{-0.15x^2} \cos(0.5\pi x)]^2 - 0.01} - e^{-[(x+4)^2 + (y-1)^2]} + e^{-(x+10)} + e^{(x-10)} - 1 = 0 \tag{10.5.8}$$

$$e^{[y+e^{-0.15x^2} \cos(0.75\pi x)]^2 - 0.01} - e^{-[(x+4)^2 + (y-1)^2]} + e^{-(x+10)} + e^{(x-10)} - 1 = 0 \tag{10.5.9}$$

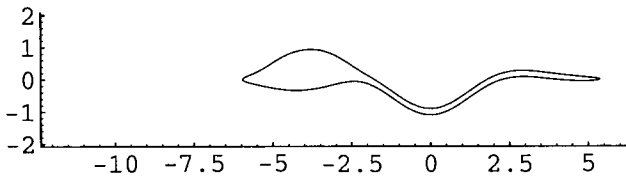


Figure 10.5.7 Flagella with cosine.

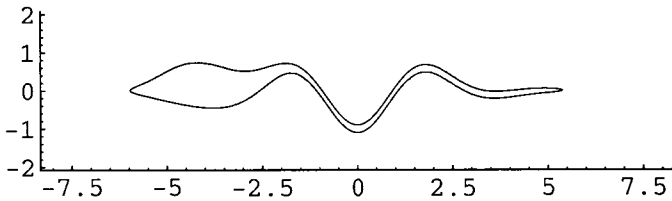


Figure 10.5.8 With double periodicity.

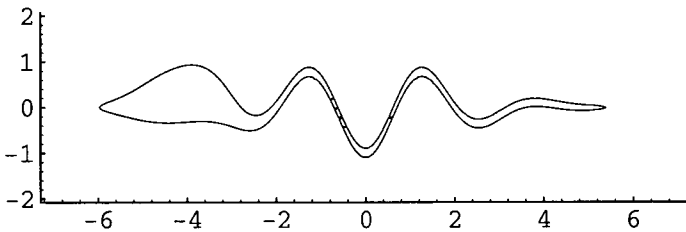


Figure 10.5.9 With triple periodicity.

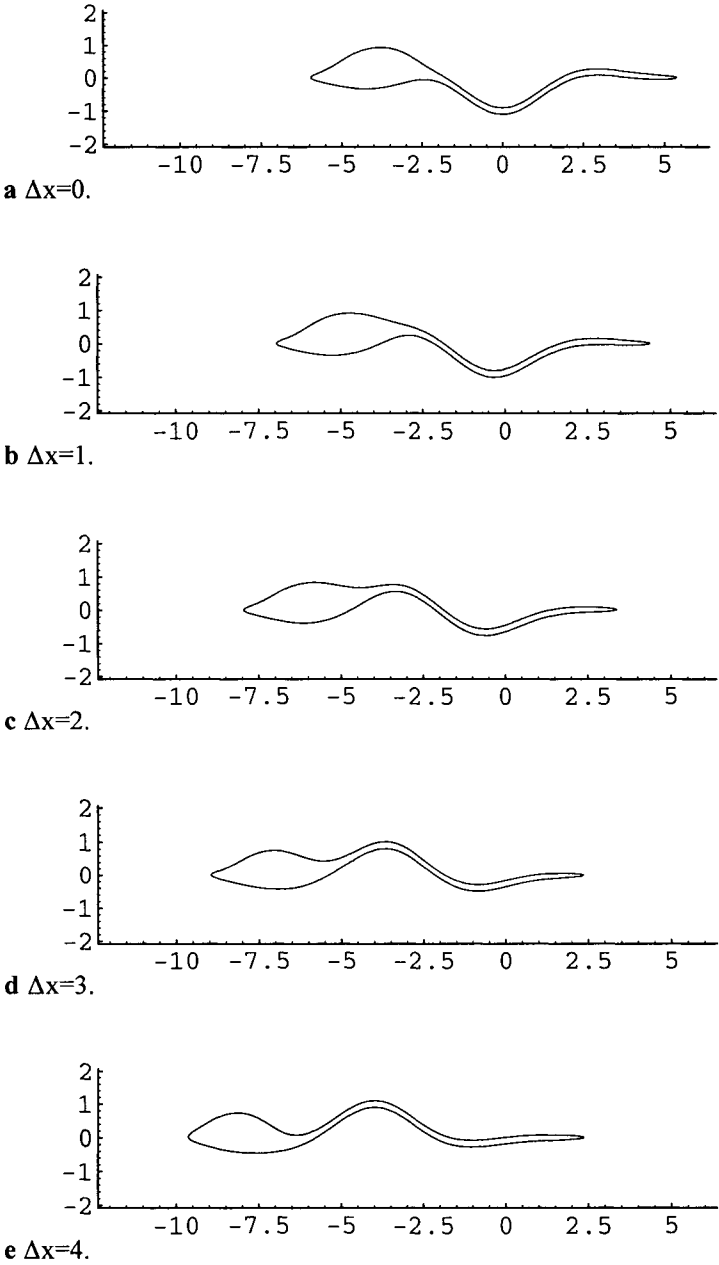


Figure 10.5.10 The flagella swims after equation 10.5.10.

We now formulate the equation that makes the sperm swim in 10.5.10. Δx varies 0, 1, 2, 3 and 4 in figures 10.5.10a-e.

$$e^{[y+e^{-0.15(x+\Delta x)} \cos(0.25\pi x)]^2 - 0.01} - e^{-[(x+4+\Delta x)^2 + (y-1)^2]} \quad 10.5.10$$

$$+ e^{-(x+10+\Delta x)} + e^{(x-10+\Delta x)} - 1 = 0$$

Chlamydomona cilia has two flagella which beat in a breast stroke swim motion. Again, this is a remarkable use of symmetry in nature, if you put a mirror plane through the axis of symmetry of the *Chlamydomona*, you will see that each of the two flagellas make the motion of the single flagella, as shown in figure 10.5.11. The motion of the arms of a breast stroke swimmer is the motion of cilia, while the motion of the legs of a crawl swimmer is the motion of flagella. The motion oscillates over $\pm 45^\circ$, cf. [9], just like in figures 10.5.10a-e here.

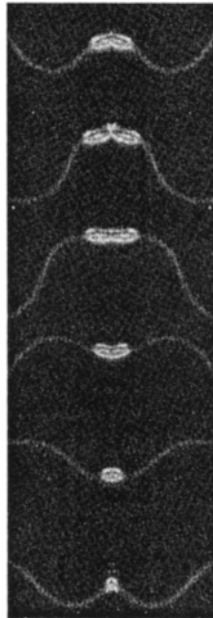


Figure 10.5.11 A crystallographic twin operation is demonstrated, which describes the relation between the motion of flagella and cilia. Mirror symmetry has been applied to the motion of cilia, modified after [9], resulting in the swim motion of flagella. If only the asymmetric part is viewed, the sequence shows flagella motion.

We do this with mathematics. We show a typical twin picture with a mirror operation in figure 10.5.12 after equation 10.5.11. The twin legs are perpendicular, just as in Chlamydomona in figure 23-29 in ref. [9].

$$\begin{aligned}
 & e^{-[x^2+e^{y-2}+e^{-y}]} + 0.2e^{-[(x+y-3)^2+e^x+e^{x+5}]} \\
 & + 0.2e^{-[(-x+y-3)^2+e^{-x}+e^{x-5}]} - 0.1 = 0
 \end{aligned}
 \tag{10.5.11}$$

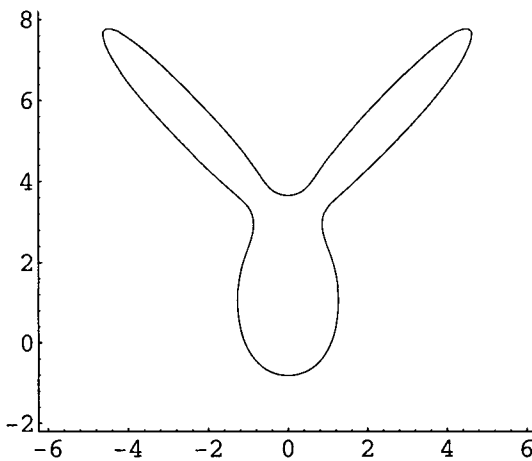


Figure 10.5.12 Mathematical twin operation gives the cilia topology.

We do the twin operation on the sperm with the equations 10.5.7 (again) and 10.5.12. The figures are in 10.5.13-14.

$$\begin{aligned}
 & e^{[y+e^{-0.15x^2} \cos(0.25\pi x)]^2-0.01} - e^{-[(x+4)^2+(y-1)^2]} \\
 & + e^{-(x+10)} + e^{(x-10)} - 1 = 0
 \end{aligned}
 \tag{10.5.7}$$

$$\begin{aligned}
 & e^{[x+e^{-0.15y^2} \cos(0.25\pi y)]^2-0.01} - e^{-[(y+4)^2+(x-1)^2]} \\
 & + e^{-(y+10)} + e^{(y-10)} - 1 = 0
 \end{aligned}
 \tag{10.5.12}$$

Now we are ready for the complete twin operation to give the Chlamydomona. We add the two equations 10.5.7 and 10.5.12 to obtain equation 10.5.13, and in figure 10.5.14 the result is shown.

$$\begin{aligned}
& e(-e^{[x+e^{-0.15y^2} \cos(0.5\pi y)]^2 - 0.01} - e^{-[(y+4)^2 + (x-1)^2]} + e^{-(y+4)} + e^{(y-8)} - 1) \\
& + e(-e^{[y+e^{-0.15x^2} \cos(0.5\pi x)]^2 - 0.01} - e^{-[(x+4)^2 + (y-1)^2]} + e^{-(x+4)} + e^{(x-8)} - 1) \\
& = 0.97
\end{aligned}$$

10.5.13

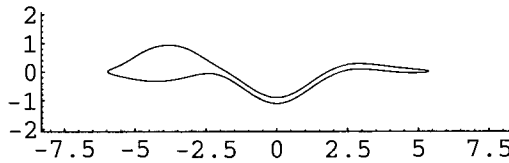


Figure 10.5.13 Flagella after equation 10.5.7.

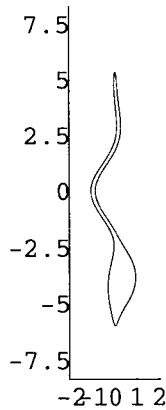


Figure 10.5.14 Flagella after equation 10.5.12.

The variable separation we have done is probably not reflecting the reality of motion, which is diagonal in the Cartesian system, we can only demonstrate a bit of the motion, but enough to see that the greatest curvature change is close to the roots of the two flagella. Just like in the movie pictures of ref. [9]. Like when you whip. Or the use of the kick for butterfly swimming. This indicates that the main part of the motion is due to the triggering of motor proteins that are operating close to the fundaments of the two flagella. So we propose that the sliding mechanism with the dynein protein and the microtubulus occurs in the very beginning of the axoneme.

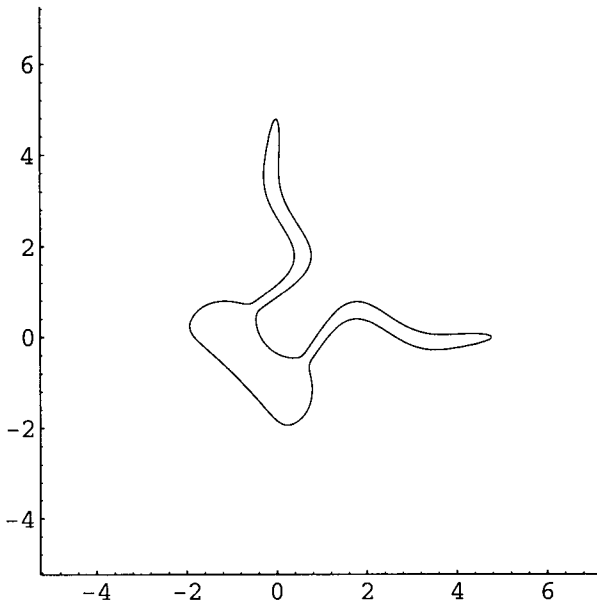


Figure 10.5.15 Mathematical twin operation to give cilia.

References 10

- 1 Enrico Fermi, *Thermodynamics*, Dover 1956
- 2 S. Andersson and M. Jacob, *THE MATHEMATICS OF STRUCTURES, THE EXPONENTIAL SCALE*, page 237, Oldenbourg, München, 1997.

- 3 S. Andersson and M. Jacob, *THE MATHEMATICS OF STRUCTURES, THE EXPONENTIAL SCALE*, page 180, Oldenbourg, München, 1997.
- 4 S. Andersson and M. Jacob, *THE MATHEMATICS OF STRUCTURES, THE EXPONENTIAL SCALE*, page 45, Oldenbourg, München, 1997.
- 5 M. Jacob, *Order, disorder and new order in the solid state*. Thesis, Lund, 1994.
- 6 M. Jacob, A routine for generating the structure of an icosahedral quasicrystal, *Z. Kristallogr.* **209** 925 (1994).
- 7 M. Jacob, S. Lidin, S. Andersson, On the Icosahedral Quasicrystal Structure, *Z. anorg. allg. Chem.* **619** (1993) 1721.
- 8 B. Alberts, D. Bray, J. Lewis, M. Raff, K. Roberts, and J.D. Watson, *Molecular Biology of THE CELL*, Garland Publishing, Third Edition, 1994, page 1026.
- 9 H. Lodish, D. Baltimore, A. Berk, S.L. Zipursky, P. Matsudaria, J. Darnell. *Molecular Cell Biology*, Scientific American Books, Third Edition, 1997, page 1080.

11 Transportation

...to resolve the puzzling question 'what is charge?' by answering 'charge is topology'... [Schutz,1]

Vesicle traffic through single and double membranes, and the Golgi machine is described.

We also describe motion through curved layers using polynomial algebra.

We describe how to make holes in double membranes - plane or curved.

Finally the nuclear pore complex, and its location in a double membrane, is described with exponential mathematics.

11.1 Background - Examples of Docking and Budding with Single Plane Layers, and Other Simple Examples

Cells and cell organelles exhibit both single and double membranes. We want to transport things through these layers. We will therefore make holes or dough-nuts in layers, using the earlier described membrane mathematics.

We start with transport through a single layer.

Budding off and fusion of vesicles are processes for transport of molecules and particles within a cell or in and out from cells. Changes of curvature is needed and one way of doing this is to organise skeletal coats of proteins, such as clathrin, which can bend the membrane and form polyhedral-shaped vesicles. There are other ways to curve a membrane that are shown below. Examples of the fusion and budding mechanisms are shown in chapter 13. Below we will below develop the mathematics needed.

A vesicle is approaching a membrane and docking - mathematically a sphere is approaching a plane as in figure 11.1.1a-e after equation 11.1.1 with Δz 1.7, 1.45, 1.4, and 0.

$$e^{-[x^2+y^2+(z-\Delta z)^2]} + e^{-z} - 1 = 0$$

11.1.1

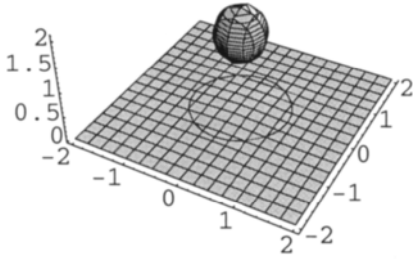


Figure 11.1.1a A vesicle is docking a membrane after equation 11.1.1. $\Delta z = 1.7$.

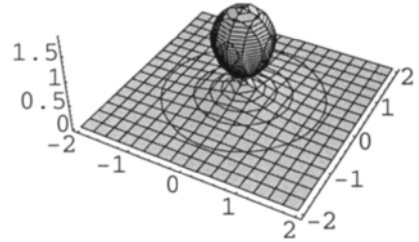


Figure 11.1.1b $\Delta z = 1.45$.

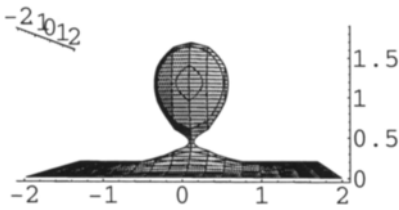


Figure 11.1.1c Different projection of b.

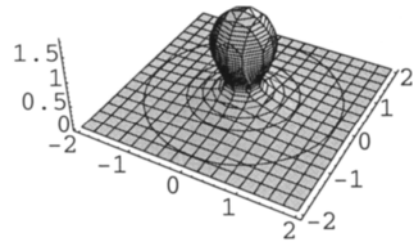


Figure 11.1.1d $\Delta z = 1.4$.

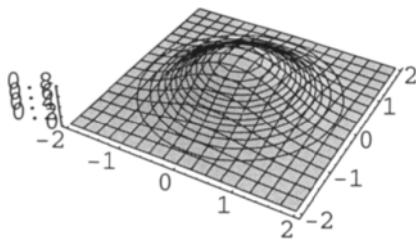


Figure 11.1.1.e $\Delta z = 0$.

The vesicle has now left its cargo to the inside of the membrane. Now we change the sign of the membrane plane to get a curvature we can use for

the budding, as in equation 11.1.2. A vesicle is now leaving the membrane as shown in figures 11.1.2a-d. $\Delta z = 0, -1, -1.3,$ and -2.5 .

$$e^{-[x^2+y^2+(z-\Delta z)^2]} + e^z - 1 = 0 \tag{11.1.2}$$

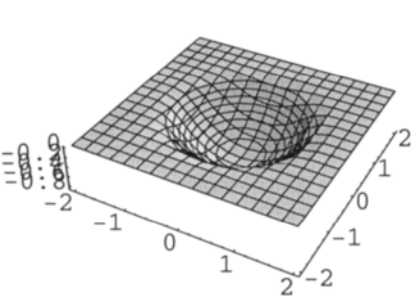


Figure 11.1.2a A vesicle is leaving the membrane. $\Delta z=0$.

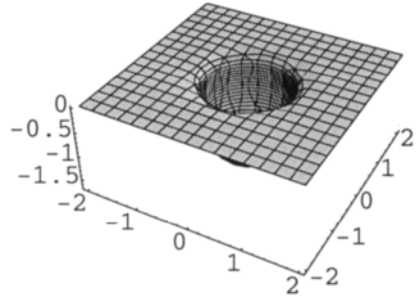


Figure 11.1.2b $\Delta z = -1$.

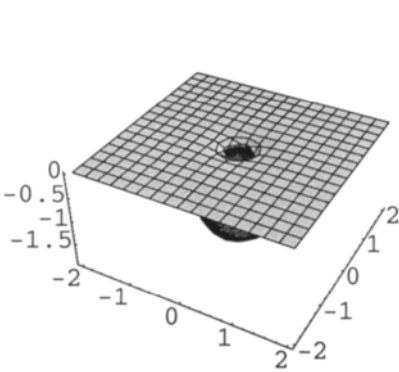


Figure 11.1.2c $\Delta z = -1.3$.

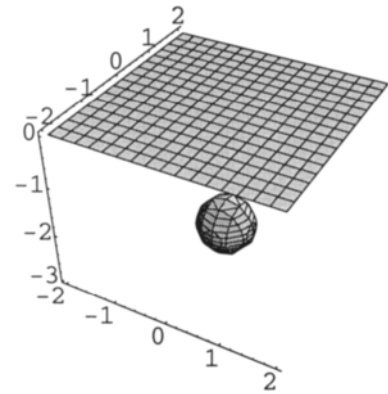


Figure 11.1.2d $\Delta z = -2.5$.

There is a steady traffic of vesicles in the cell, for example through the Golgi machine that carries cargo which needs to be processed and transported further. We demonstrate this first in two dimensions with the equation 11.1.3.

$$\begin{aligned}
&10^{-[(x-2)^2+10^{(y-8)}+10^{-(y+9)}]} + 10^{-[(x-7)^2+10^{(y-9)}+10^{-(y+8)}]} + \\
&+ 10^{-[(x-11)^2+10^{(y-7)}+10^{-(y+9)}]} + 10^{-[(x-17)^2+10^{(y-9)}+10^{-(y+7)}]} + \\
&+ 10^{-[(x-3.5)^2+y^2]} + 10^{-[(x)^2+(y-2)^2]} + 10^{-[(x-5)^2+(y+3)^2]} + \\
&+ 10^{-[(x-8)^2+(y)^2]} + 10^{-[(x-9)^2+(y-2)^2]} + 10^{-[(x-12)^2+(y+3)^2]} + \\
&+ 10^{-[(x-13.5)^2+(y)^2]} + 10^{-[(x-16)^2+(y-2)^2]} + 10^{-[(x-15)^2+(y+3)^2]} + \\
&+ 10^{-[(x-23.5)^2+(y)^2]} + 10^{-[(x-19)^2+(y-2)^2]} + 10^{-[(x-20)^2+(y+3)^2]} = 0.5
\end{aligned}
\tag{11.1.3}$$

In figure 11.1.3a the movement starts with vesicles going through the membranes, and in figure 11.1.3b all the vesicles have moved one unit in x.

The membrane system in Golgi has a low degree of order, which we will call parallel order.

We have described this and before in equation 7.5.7, and figure 7.5.9. Physically this resembles mitochondria, where parallel order as well is most common.

We have earlier seen the occurrence of lamellar membrane organisation in ER (chapter 8) and in mitochondria (chapter 9). The predominating lamellar arrangement of Golgi membranes is shown in figure 11.1.4.

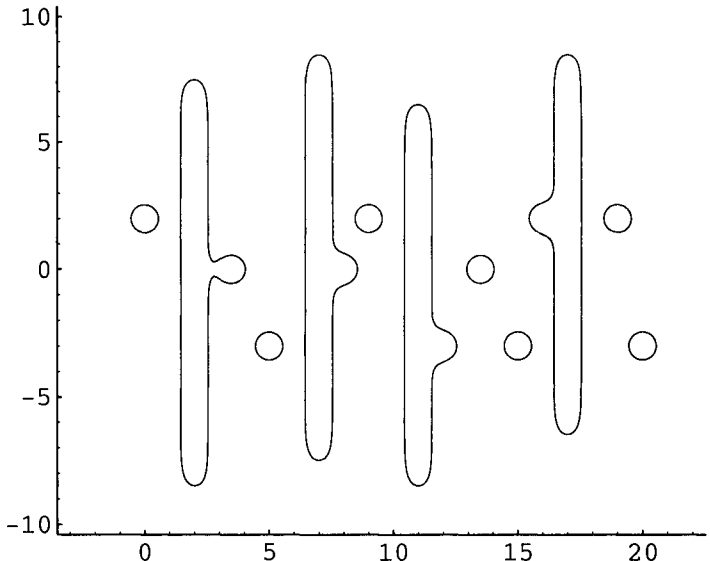


Figure 11.1.3a Golgi machine after equation 11.1.3.

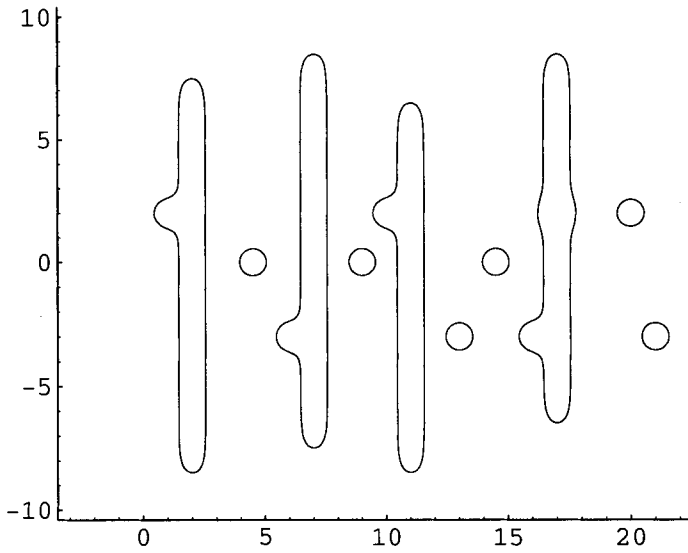


Figure 11.1.3b All vesicles have moved one unit in x.

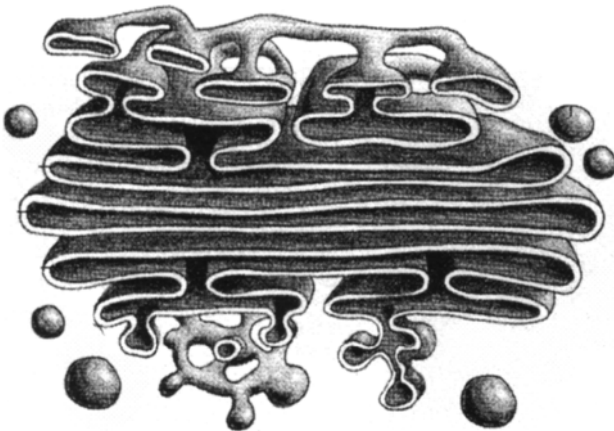


Figure 11.1.4 Reconstruction from electron micrographs of the Golgi machine. Modified after [3].

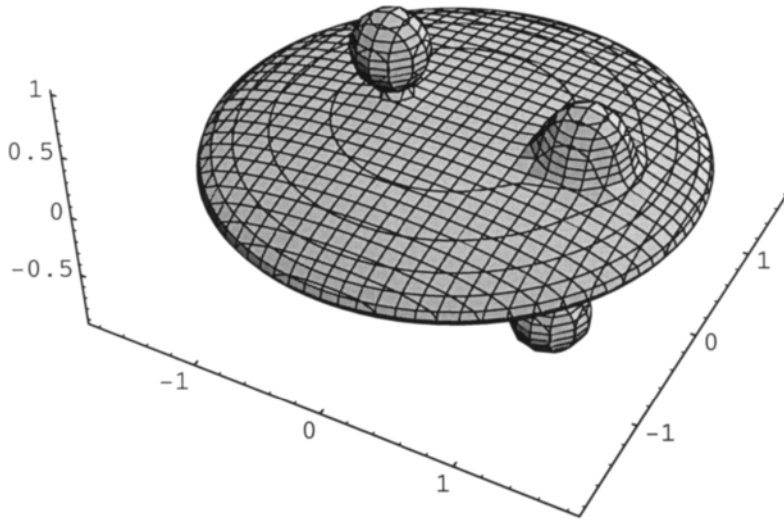


Figure 11.1.4c Cistern of Golgi machine.

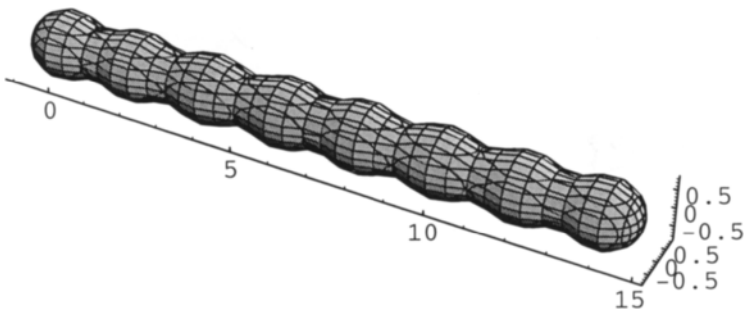


Figure 11.1.5 Vesicle production after equation 11.1.5. **a** $\Delta x=0$.

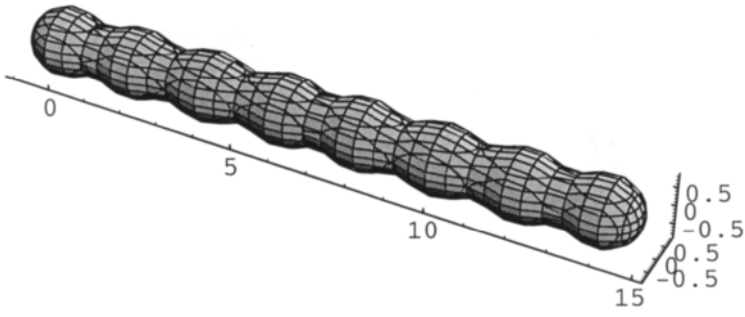


Figure 11.1.5b $\Delta x=0.3$.

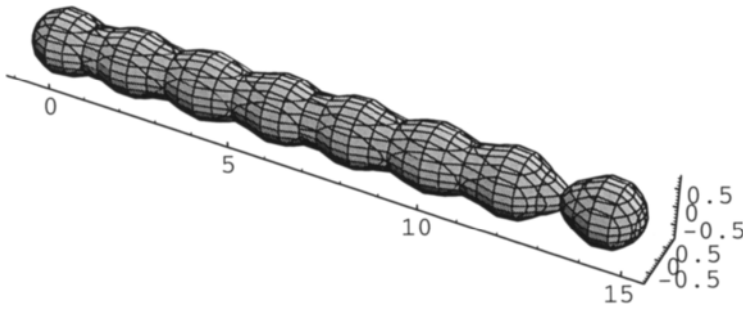


Figure 11.1.5c $\Delta x=0.5$.

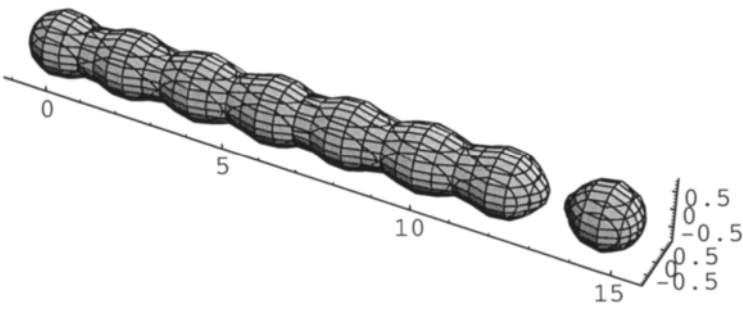


Figure 11.1.5d $\Delta x=1$.

We have also made a cistern from the Golgi machine in three dimensions as shown in figure 11.1.4c. The equation is in 11.1.4. The first term is a flattened sphere and the following three are spheres weighted to be small.

$$e^{-\frac{1}{2}[x^2+y^2+30z^2]} + e^{-20[(x+0.5)^2+y^2+(z-0.7)^2]} + \tag{11.1.4}$$

$$+ e^{-20[(x-1)^2+y^2+(z-0.4)^2]} + e^{-20[(x-1)^2+(y+0.5)^2+(z+0.7)^2]} = 0.2$$

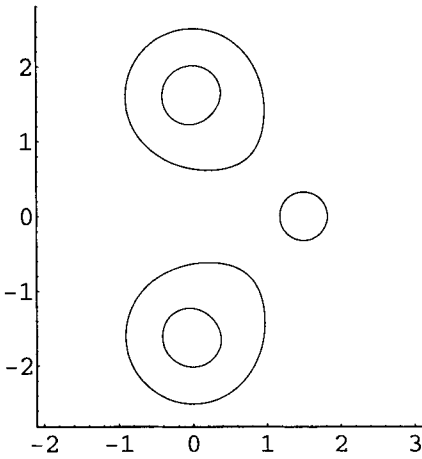


Figure 11.1.6a Sendai virus approaching two cells.

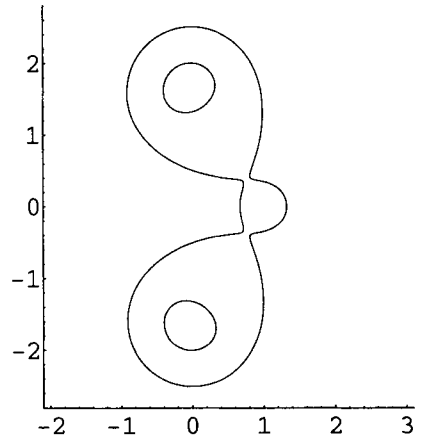


Figure 11.1.6b

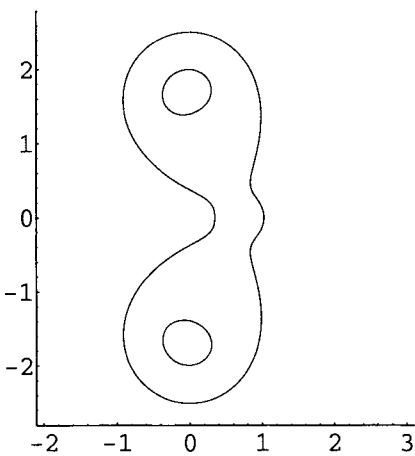


Figure 11.1.6c Fusion.

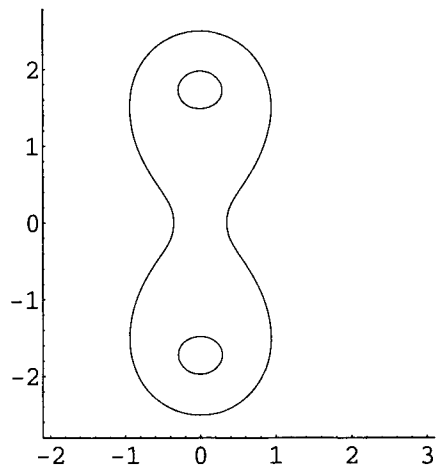


Figure 11.1.6d The cell hybrid.

Next we build a machine for producing vesicles, which corresponds to the tubular network in Golgi (also occurring in ER). This is done in equation 11.1.5. The machine is formed by a row of overlapping spheres.

$$\begin{aligned}
 & e^{-(x^2+y^2+z^2)} + e^{-((x-2)^2+y^2+z^2)} + e^{-((x-4)^2+y^2+z^2)} \\
 & + e^{-((x-6)^2+y^2+z^2)} + e^{-((x-8)^2+y^2+z^2)} + e^{-((x-10)^2+y^2+z^2)} \quad 11.1.5 \\
 & + e^{-((x-12)^2+y^2+z^2)} + e^{-((x-14-\Delta x)^2+y^2+z^2)} = 0.5
 \end{aligned}$$

Δx is 0, 0.3, 0.5 and 1 in figures 11.1.5a-d respectively, which shows how one vesicle is budded of as Δx approaches unity.

One small vesicle may of course fuse with a big one, or with two. A spectacular example is the behaviour of the Sendai virus, which may try to fuse into two cells simultaneously, resulting in a fused cell pair as modelled in figure 11.1.6a-d. This is a tool for achieving a cell hybrid [4].

11.2 Docking and Budding with Curved Single Layers

We shall now make a small vesicle approach a curved layer, which in this case will be a sphere. We use equation 11.2.1, and in figure 11.2.1a there is a vesicle with its cargo coming from the outside, and in b it has fused and delivered its cargo. We use equation 11.2.2 which has a changed sign in the exponent compared to equation 11.2.1, and which also was the case when the vesicle interacted with the plane. And the vesicle goes from inside out as shown in figure 11.2.2a and b.

$$e^{-(x^2+y^2+z^2-20)} + e^{-((x-6)^2+y^2+z^2+2)} = 0.1 \quad 11.2.1$$

$$e^{(x^2+y^2+z^2-20)} + e^{-((x+3)^2+y^2+z^2+2)} = 0.1 \quad 11.2.2$$

We will now do budding and local curvature. We return to algebra just to show that this is possible to do with some extremely simple principles and start with a single plane as the plasma membrane.

A cell membrane is characterised by its curvature. So we go to the algebra and use the general equation for a plane and transform that to equation 11.2.4.

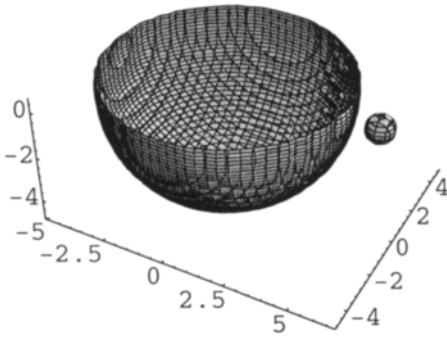


Figure 11.2.1a Docking with a curved membrane after equation 11.2.1. $x=6$.

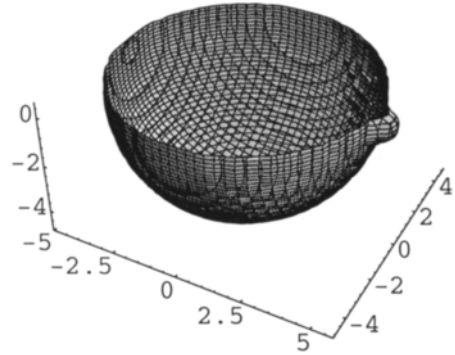


Figure 11.2.1b $x=5$.

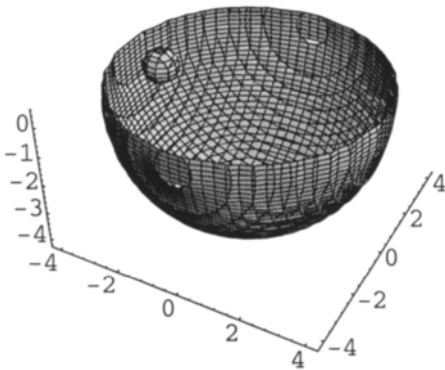


Figure 11.2.2a A vesicle goes from inside out. $x=-3$.

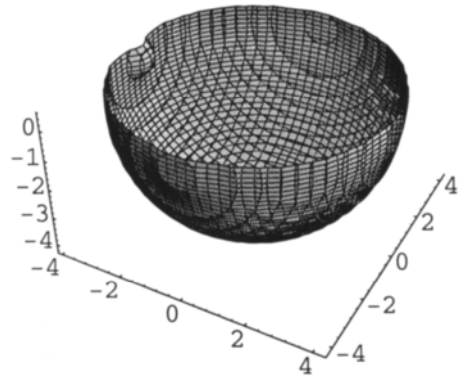


Figure 11.2.2b $x=-4$.

$$x + y + z = C \quad 11.2.3$$

$$x^n + y^n + z^n = C \quad 11.2.4$$

With n even in 11.2.4 we have described the 3D topology as built of planes in chapter 2. For the case of $n=4$ the equations for such planes are in 11.2.5.

$$x^4 = C$$

$$y^4 = C$$

$$z^4 = C$$

11.2.5

If $C=100$, $x = \sqrt[4]{100} = \pm 3.1622$ which are two of the six planes in the cube in figure 2.2.1. With n even and higher, the cube gets sharper and sharper. As there must be a constant for n even there are double roots which are the faces of polyhedra. With n odd there are only single roots, and this is analysed below.

$n=1$ and $C=0$ in equation 11.2.4, and this plane is shown in figure 11.2.3. In figures 11.2.4a-b we have the function for $n=3$ and $C=0$ shown in two different projections. Out of the total of six planes we now have three, and since the constant is 0, they have to go through the origin. If we exponentially make them meet without intersecting, curvature is given to the plane. This may now be regarded as a monkey saddle [5], and it is even more pronounced increasing the exponent to 7, as in figures 11.2.5a-b.

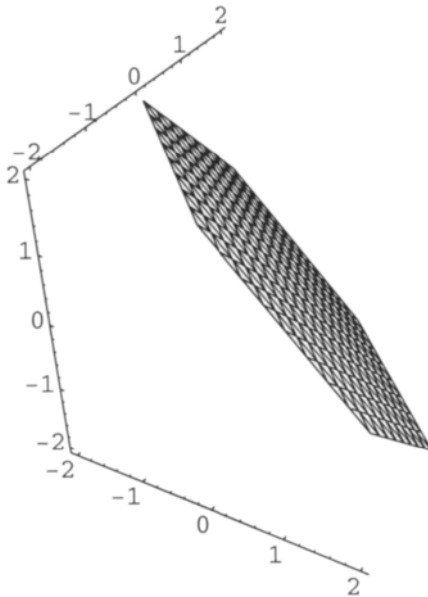


Figure 11.2.3 A plane perpendicular to the space diagonal.

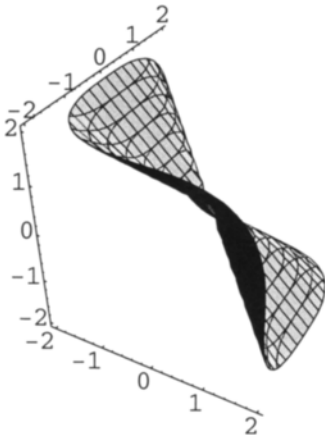


Figure 11.2.4a After equation 11.2.4, $n=3$, $C=0$.

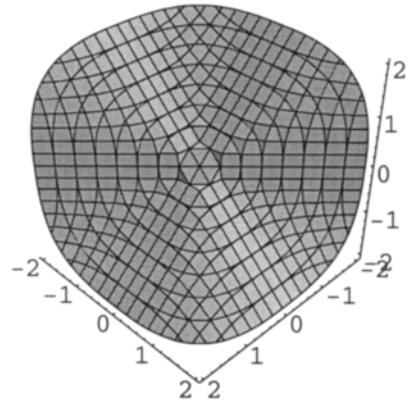


Figure 11.2.4b Different projection.

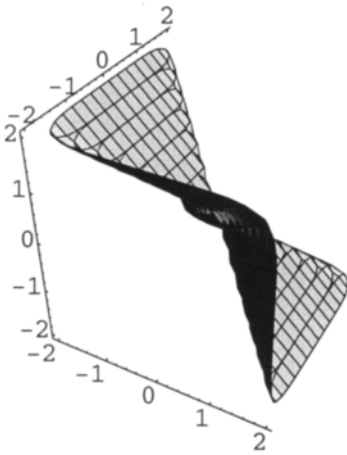


Figure 11.2.5a After equation 11.2.4, $n=7$, $C=0$.

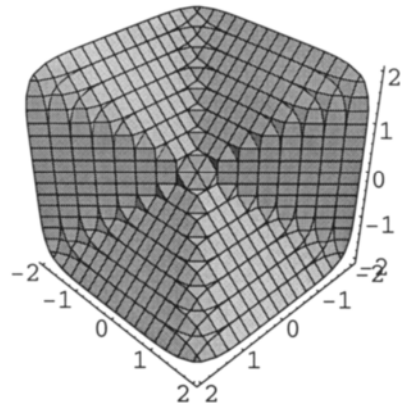


Figure 11.2.5b Different projection.

Adding a constant when n is odd means that planes will not meet in the origin. Polyhedral corners are formed as described earlier [5].

We must do the same thing with the famous Diophante or Fermat equation 11.2.6.

$$x^n + y^n - z^n = 0$$

11.2.6

So we study the equations 11.2.7 and 11.2.8, and we find the same thing, but with different orientation of the planes in figures 11.2.6a-b.

$$x + y - z = 0 \tag{11.2.7}$$

$$x^3 + y^3 - z^3 = 0 \tag{11.2.8}$$

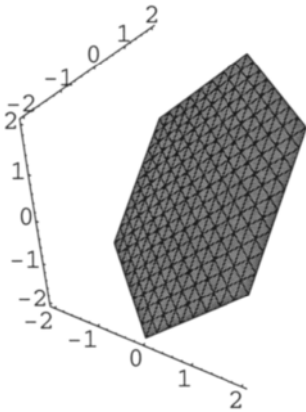


Figure 11.2.6a After equation 11.2.7.

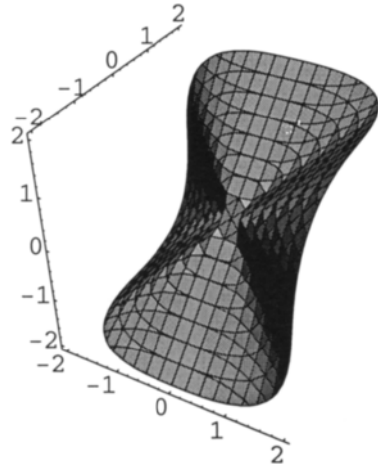


Figure 11.2.6b After equation 11.2.8.

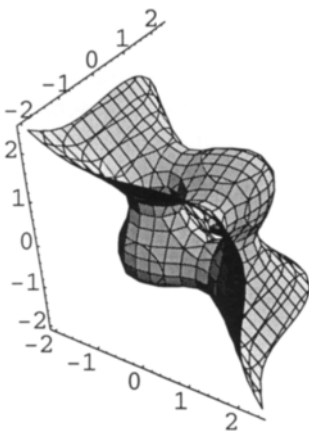


Figure 11.2.7a A small piece of the P-surface in a plane. C=0.

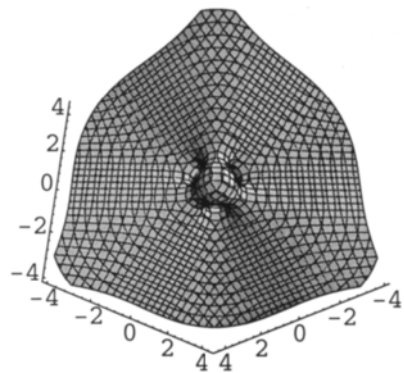


Figure 11.2.7b Different projection.

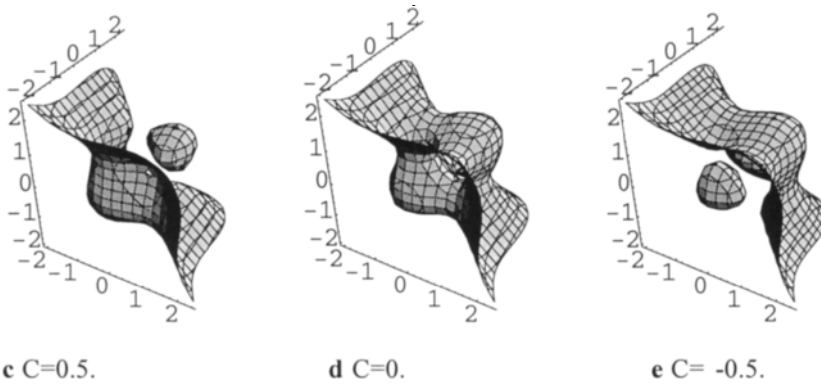


Figure 11.2.7c-e Transport of a vesicle through a plane by changing constant in equation 11.2.9.

We count or add planes to the equation for $n=3$, which means making polynomials with roots as in 11.2.9.

$$x(x-1)(x+1)+y(y-1)(y+1)+z(z-1)(z+1)=C \quad 11.2.9$$

This simple equation of 11.2.9 gives a number of beautiful pictures in figures 11.2.7a-e.

By using roots, more curvature is given to the plane in form of a small piece of the P-surface, as shown in figure 11.2.7a. This is also shown with larger boundaries in 11.2.7b. Changing the constant from 0 in a and b to 0.5 in c and -0.5 in e gives a beautiful mechanism for the transport of material through a membrane via vesicles (note that a is repeated as d). Interesting is that the approach of a vesicle to a point of a curved surface with zero mean curvature (monkey saddle) means opening three catenoids to points where there is curvature. It should be pointed out, however, that we don't know whether or not these membrane geometries have biological relevance.

An analogous lock mechanism for transport is obtained using the Diophante equation. This is interesting as equations of this type would be needed if we wanted to transform a plane to a curved and closed surface of cell type, using the monkey cell approach. Such a surface could be covered with locks which would give curvature to the surface as well as serving as places or locks of transport. This means going exponential as done in equation 11.2.10 and shown in figure 11.2.8.

$$e^{-x(x-1)(x+1)+y(y-1)(y+1)+z(z-1)(z+1)} = 1 \quad 11.2.10$$

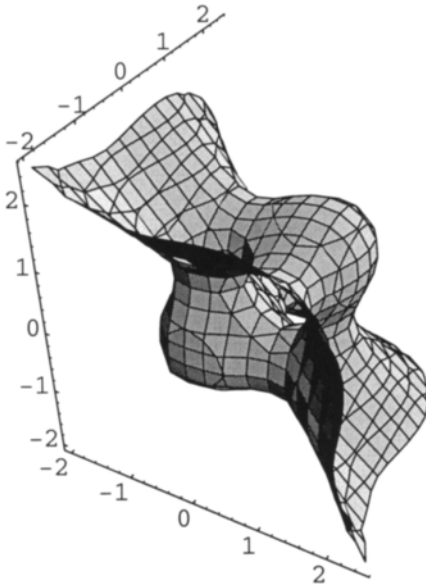


Figure 11.2.8 The exponential Diophante equation.

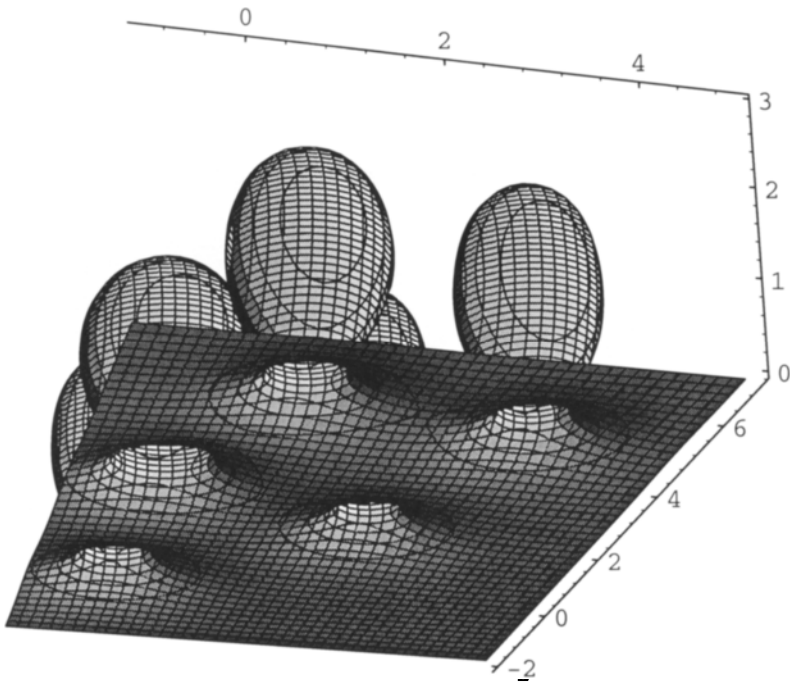


Figure 11.2.9 Invaginations.

Invaginations in a cell membrane is exemplified in figure 11.2.9. with vesicles attached at random to a cell membrane. The equation is in 11.2.11.

$$\begin{aligned}
 & e^{-(x^2+y^2+(z-1.4)^2)} + e^{-(x^2+y^2+(z-2.4)^2)} + e^{-((x-3)^2+y^2+(z-1.4)^2)} \\
 & + e^{-((x-3)^2+y^2+(z-2)^2)} + e^{-((x-2)^2+(y-2.5)^2+(z-1.4)^2)} \\
 & + e^{-((x-2)^2+(y-2.5)^2+(z-2.6)^2)} + e^{-((x-5)^2+(y-3.5)^2+(z-1.4)^2)} \\
 & + e^{-((x-5)^2+(y-3.5)^2+(z-2.5)^2)} + e^{-((x-5.5)^2+(y-1)^2+(z-1.4)^2)} \\
 & + e^{-((x-5.5)^2+(y-1)^2+(z-2.3)^2)} + e^{-z} = 1
 \end{aligned} \tag{11.2.11}$$

An attachment with three openings to a cell membrane is shown in figure 11.2.10. The equation is in 11.2.12.

$$\begin{aligned}
 & e^{-x(x-1)(x+1)+y(y-1)(y+1)+z(z-1)(z+1)} + \\
 & + e^{-((x-1.7)^2+(y-1.7)^2+(z-1.7)^2-1)} + e^{-((x-3)^2+(y-3)^2+(z-3)^2-1)} = 1
 \end{aligned}$$

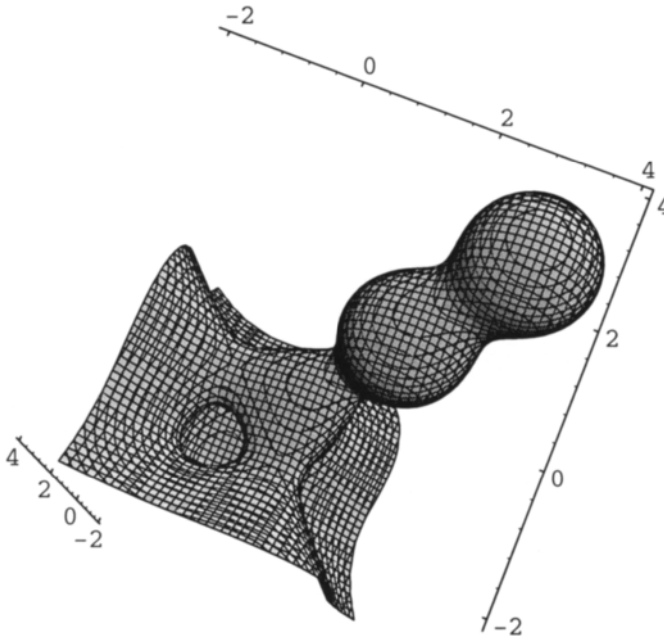


Figure 11.2.10 An attachment with three openings to a cell membrane.

11.3 Transport Through Double Layers

Double membranes surround the nucleus. As the Golgi machine and rough ER consist of thin spaces, they may also be regarded as double membranes.

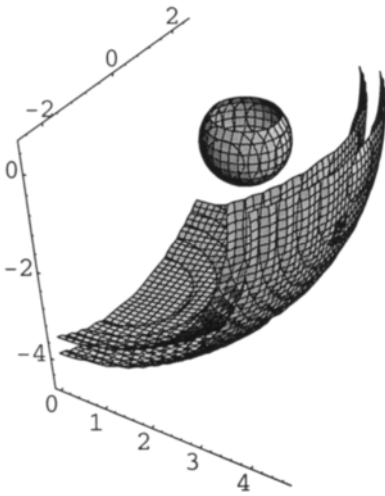


Figure 11.3.1a A vesicle is sent through a membrane after equation 11.3.1. $\Delta x = 3.5$.

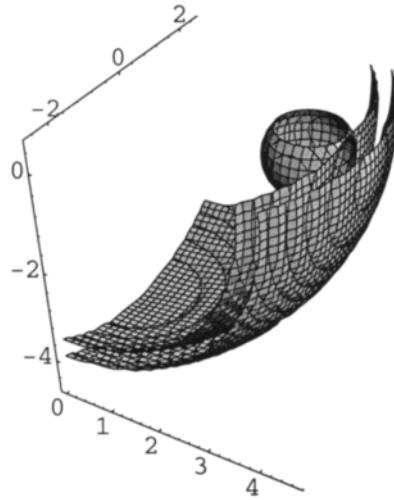


Figure 11.3.1b $\Delta x = 4.5$.

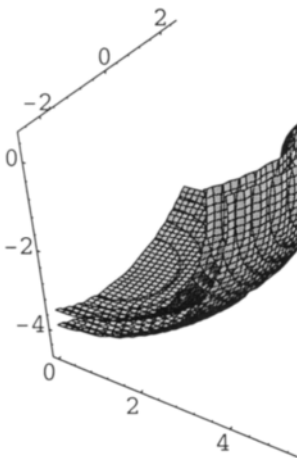


Figure 11.3.1c $\Delta x = 5.5$.

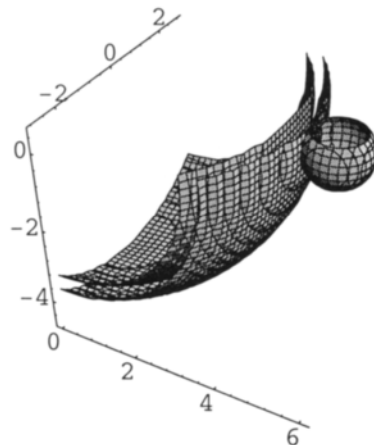


Figure 11.3.1d $\Delta x = 5.3$.

In figure 5.4.1 we made a simple experiment with a double plane. We shall now use a curved double membrane, a part of a sphere. We only need one equation, given in 11.3.1, for sending a vesicle through - and the cargo is free between the layers. If the distance between the layers is not too large, the vesicle keeps its identity and the cargo is carried through the double membrane.

$$e^{-(x^2+y^2+z^2-20)^2} + e^{-((x-\Delta x)^2+y^2+z^2+1)} = 0.2 \tag{11.3.1}$$

The Δx :s are 2.5, 3.5, 4.5, and 5.3 for figures 11.3.1a-d.

Going to the nucleus, transport seems to occur through permanent holes in the double membrane. Below, we will show how to make holes in a double membrane.

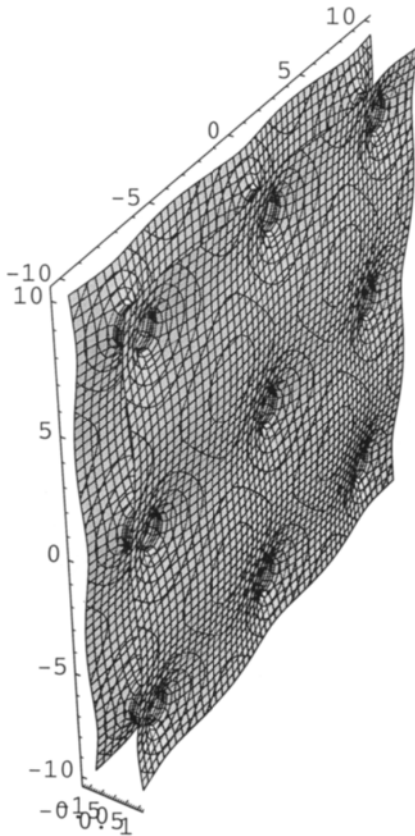


Figure 11.3.2 Plane borders give a periodic double membrane.

We start with the circular functions, and with the squared x-term we give two borders to the P-surface. We then vary the periodicity after equation 11.3.2 and obtain a beautiful periodic double membrane in figure 11.3.2.

$$\cos \pi x + \cos \frac{1}{4} \pi y + \cos \frac{1}{4} \pi z + 4x^2 = 2.8 \quad 11.3.2$$

We really need to distribute the holes individually on any membrane. We go exponential in equation 11.3.3, where we have a double plane with the z-term, the two GD-spheres make the holes as shown in figure 11.3.3.

$$e^{-(x^2+(y+2)^2+z^2)} + e^{-(x^2+(y-3)^2+z^2)} + e^{z^2} = 1.5 \quad 11.3.3$$

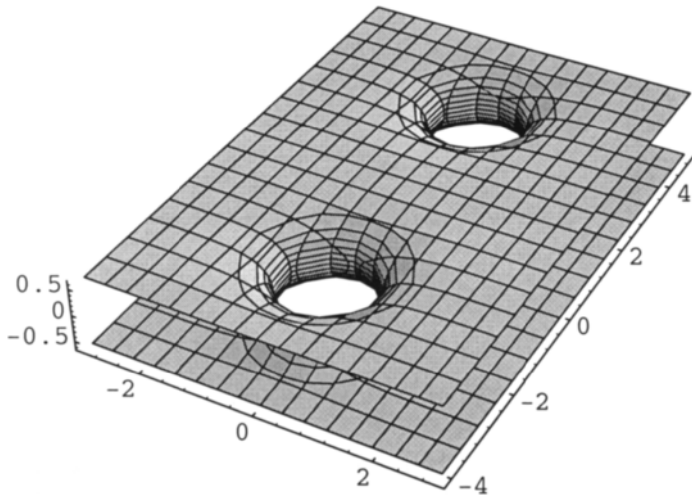


Figure 11.3.3 Two GD-spheres give holes in a double membrane.

Similarly we make holes in a sphere, and start with the circle. The equation is in 11.3.4 and the plot in figure 11.3.4.

$$e^{(x^2+y^2-8)^2} + e^{-[(x-2\sqrt{2})^2+(y)^2]} + e^{-[(x-2)^2+(y-2)^2]} + e^{-[(x)^2+(y-2\sqrt{2})^2]} + e^{-[(x-2)^2+(y+2)^2]} = 2 \quad 11.3.4$$

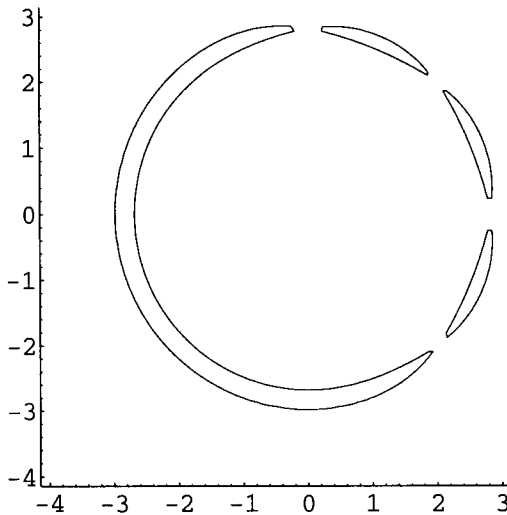


Figure 11.3.4 Small circular holes through concentric circles.

These holes resemble the nuclear pores as seen in electron micrographs of the nucleus, cf. [6].

We will now go to 3D with the equation 11.3.5 and make just one hole, as shown in figure 11.3.5.

$$e^{(x^2+y^2+z^2-8)^2} + e^{-[(x-2\sqrt{2})^2+y^2+z^2]} = 1.9 \quad 11.3.5$$

There is a regular traffic of RNA's and proteins through a nucleus pore complex that sits in the holes of the double membrane of the nucleus. Such a nuclear pore complex is a very large structure - about 1000 Å - and electron microscopy with three dimensional computer reconstruction has given detailed structural information [7,8]. It is possible to describe the complex as built of the hole in the double membrane combined with a) a system of doughnuts or b) a system of bodies. In both cases the symmetry is eight-fold and we shall here build mathematical models that well agree with the pictures obtained from the experimental observations of electron microscopy.

We shall start and use the obvious eight-fold symmetry and build a dilatation, or quasi structure like we did with the nine-fold case for the microtubulus.

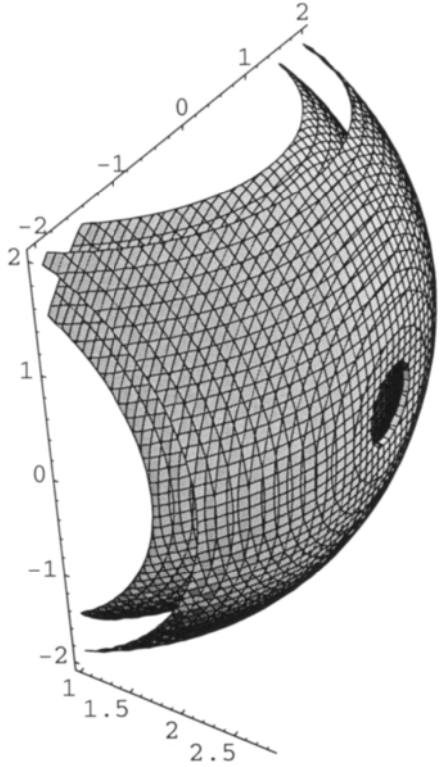


Figure 11.3.5 Nuclear pore in 3D.

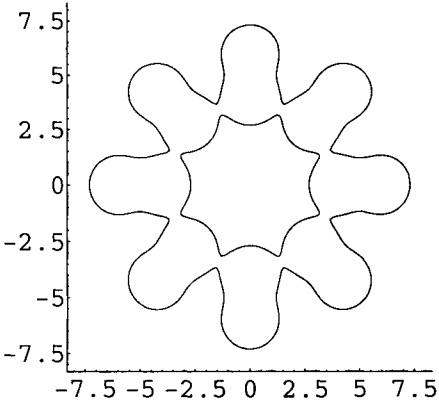


Figure 11.3.6 Double spheres in eight-fold symmetry.

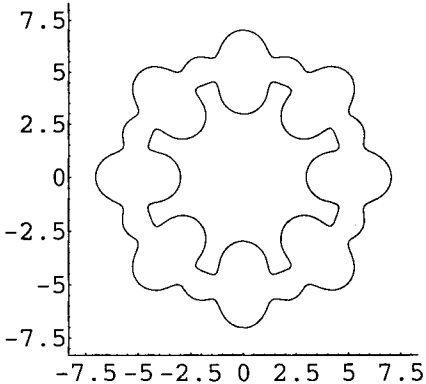


Figure 11.3.7 Small spheres connect the bigger.

$$\begin{aligned}
& e^{-[(x-2\sqrt{2})^2+(y-2\sqrt{2})^2]} + e^{-[(x-4)^2+y^2]} + \\
& + e^{-[x^2+(y-4)^2]} + e^{-[(x-2\sqrt{2})^2+(y+2\sqrt{2})^2]} + \\
& + e^{-[x^2+(y+4)^2]} + e^{-[(x+2\sqrt{2})^2+(y+2\sqrt{2})^2]} + \\
& + e^{-[(x+4)^2+y^2]} + e^{-[(x+2\sqrt{2})^2+(y-2\sqrt{2})^2]} + \\
& + e^{-[(x-3\sqrt{2})^2+(y-3\sqrt{2})^2]} + e^{-[(x-6)^2+y^2]} + \\
& + e^{-[x^2+(y-6)^2]} + e^{-[(x-3\sqrt{2})^2+(y+3\sqrt{2})^2]} + \\
& + e^{-[x^2+(y+6)^2]} + e^{-[(x+3\sqrt{2})^2+(y+3\sqrt{2})^2]} + \\
& + e^{-[(x+6)^2+y^2]} + e^{-[(x+3\sqrt{2})^2+(y-3\sqrt{2})^2]} = 0.18
\end{aligned}$$

11.3.6

$$\begin{aligned}
& e^{-[(x-2\sqrt{2})^2+(y-2\sqrt{2})^2+(z)^2]} + e^{-[(x-4)^2+y^2]} + \\
& + e^{-[x^2+(y-4)^2+z^2]} + e^{-[(x-2\sqrt{2})^2+(y+2\sqrt{2})^2]} + \\
& + e^{-[x^2+(y+4)^2+z^2]} + e^{-[(x+2\sqrt{2})^2+(y+2\sqrt{2})^2]} + \\
& + e^{-[(x+4)^2+y^2+z^2]} + e^{-[(x+2\sqrt{2})^2+(y-2\sqrt{2})^2]} + \\
& + e^{-[(x-3\sqrt{2})^2+(y-3\sqrt{2})^2+z^2]} + e^{-[(x-6)^2+y^2]} + \\
& + e^{-[x^2+(y-6)^2+z^2]} + e^{-[(x-3\sqrt{2})^2+(y+3\sqrt{2})^2]} + \\
& + e^{-[x^2+(y+6)^2+z^2]} + e^{-[(x+3\sqrt{2})^2+(y+3\sqrt{2})^2]} + \\
& + e^{-[(x+6)^2+y^2+z^2]} + e^{-[(x+3\sqrt{2})^2+(y-3\sqrt{2})^2]} + \\
& + \frac{1}{2} [e^{-[(x-7\frac{\sqrt{2}}{2})^2+(y-3\frac{\sqrt{2}}{2})^2]} + e^{-[(x-3\frac{\sqrt{2}}{2})^2+(y-7\frac{\sqrt{2}}{2})^2]} + \\
& + e^{-[(x+3\frac{\sqrt{2}}{2})^2+(y-7\frac{\sqrt{2}}{2})^2]} + e^{-[(x+7\frac{\sqrt{2}}{2})^2+(y-3\frac{\sqrt{2}}{2})^2]} + \\
& + e^{-[(x+7\frac{\sqrt{2}}{2})^2+(y+3\frac{\sqrt{2}}{2})^2]} + e^{-[(x+3\frac{\sqrt{2}}{2})^2+(y+7\frac{\sqrt{2}}{2})^2]} + \\
& + e^{-[(x-7\frac{\sqrt{2}}{2})^2+(y+3\frac{\sqrt{2}}{2})^2]} + e^{-[(x-3\frac{\sqrt{2}}{2})^2+(y+7\frac{\sqrt{2}}{2})^2]}] = 0.17
\end{aligned}$$

11.3.7

We start in two dimensions laying out double spheres that form elongated bodies as shown in figure 11.3.6. The equation is in 11.3.6. Next we add smaller bodies between the elongated ones in equation 11.3.7. This is shown in figure 11.3.7.

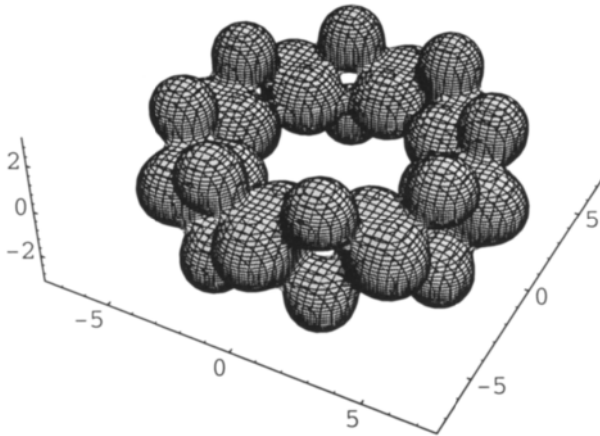


Figure 11.3.8a Nuclear pore complex after equation 11.3.8.

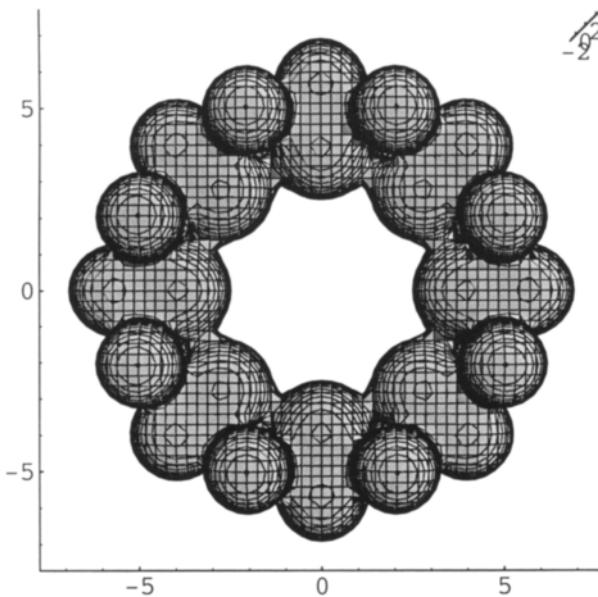


Figure 11.3.8b Different projection.

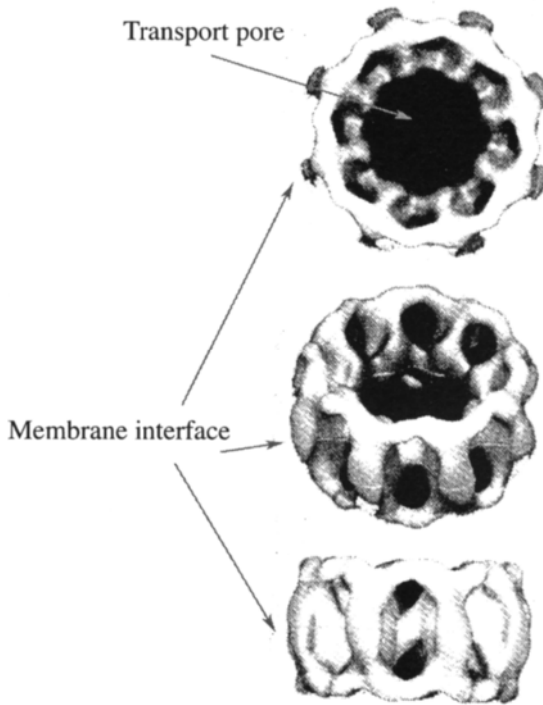


Figure 11.3.8c Computer reconstruction of nuclear pore structure, modified after [7].

Finally in *11.3.8* we have gone 3D and the result is found in figures **11.3.8a-b**. The similarity to a computer reconstruction in ref. [7] is shown in figure **11.3.8c** and this can be refined by adding more bodies of different sizes, or changes in the equation.

We have changed the constant to 0.12 in equation *11.3.8* and the z-parameter for the smaller bodies to 1.5 instead of 1.8 to produce figure **11.3.9**.

$$\begin{aligned}
 & e^{-[(x-2\sqrt{2})^2+(y-2\sqrt{2})^2+z^2]} + e^{-[(x-4)^2+y^2+z^2]} + \\
 & + e^{-[x^2+(y-4)^2+z^2]} + e^{-[(x-2\sqrt{2})^2+(y+2\sqrt{2})^2+z^2]} + \\
 & + e^{-[x^2+(y+4)^2+z^2]} + e^{-[(x+2\sqrt{2})^2+(y+2\sqrt{2})^2+z^2]} + \\
 & + e^{-[(x+4)^2+y^2+z^2]} + e^{-[(x+2\sqrt{2})^2+(y-2\sqrt{2})^2+z^2]} + \\
 & + e^{-[(x-3\sqrt{2})^2+(y-3\sqrt{2})^2+z^2]} + e^{-[(x-6)^2+y^2+z^2]} + \\
 & + e^{-[x^2+(y-6)^2+z^2]} + e^{-[(x-3\sqrt{2})^2+(y+3\sqrt{2})^2+z^2]} + \\
 & + e^{-[x^2+(y+6)^2+z^2]} + e^{-[(x+3\sqrt{2})^2+(y+3\sqrt{2})^2+z^2]} + \\
 & + e^{-[(x+6)^2+y^2+z^2]} + e^{-[(x+3\sqrt{2})^2+(y-3\sqrt{2})^2+z^2]} + \\
 & + \frac{3}{4} [e^{-[(x-7\frac{\sqrt{2}}{2})^2+(y-3\frac{\sqrt{2}}{2})^2+(z-1.8)^2]} + e^{-[(x-3\frac{\sqrt{2}}{2})^2+(y-7\frac{\sqrt{2}}{2})^2+(z-1.8)^2]} + \\
 & + e^{-[(x+3\frac{\sqrt{2}}{2})^2+(y-7\frac{\sqrt{2}}{2})^2+(z-1.8)^2]} + e^{-[(x+7\frac{\sqrt{2}}{2})^2+(y-3\frac{\sqrt{2}}{2})^2+(z-1.8)^2]} + \\
 & + e^{-[(x+7\frac{\sqrt{2}}{2})^2+(y+3\frac{\sqrt{2}}{2})^2+(z-1.8)^2]} + e^{-[(x+3\frac{\sqrt{2}}{2})^2+(y+7\frac{\sqrt{2}}{2})^2+(z-1.8)^2]} + \\
 & + e^{-[(x-7\frac{\sqrt{2}}{2})^2+(y+3\frac{\sqrt{2}}{2})^2+(z-1.8)^2]} + e^{-[(x-3\frac{\sqrt{2}}{2})^2+(y+7\frac{\sqrt{2}}{2})^2+(z-1.8)^2}] + \\
 & + \frac{3}{4} [e^{-[(x-7\frac{\sqrt{2}}{2})^2+(y-3\frac{\sqrt{2}}{2})^2+(z+1.8)^2]} + e^{-[(x-3\frac{\sqrt{2}}{2})^2+(y-7\frac{\sqrt{2}}{2})^2+(z+1.8)^2]} + \\
 & + e^{-[(x+3\frac{\sqrt{2}}{2})^2+(y-7\frac{\sqrt{2}}{2})^2+(z+1.8)^2]} + e^{-[(x+7\frac{\sqrt{2}}{2})^2+(y-3\frac{\sqrt{2}}{2})^2+(z+1.8)^2]} + \\
 & + e^{-[(x+7\frac{\sqrt{2}}{2})^2+(y+3\frac{\sqrt{2}}{2})^2+(z+1.8)^2]} + e^{-[(x+3\frac{\sqrt{2}}{2})^2+(y+7\frac{\sqrt{2}}{2})^2+(z+1.8)^2]} + \\
 & + e^{-[(x-7\frac{\sqrt{2}}{2})^2+(y+3\frac{\sqrt{2}}{2})^2+(z+1.8)^2]} + e^{-[(x-3\frac{\sqrt{2}}{2})^2+(y+7\frac{\sqrt{2}}{2})^2+(z+1.8)^2}]] = 0.17
 \end{aligned}$$

11.3.8

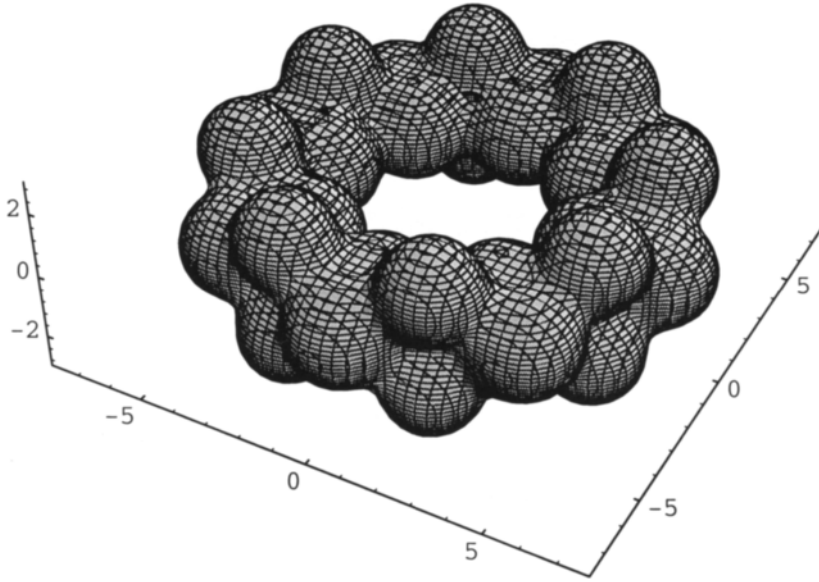


Figure 11.3.9 Nuclear pore complex after slight changes in equation 11.3.8 as described in the text.

The nuclear pore complex is a gated channel through which ribonucleo proteins are transported to the cytoplasm. Electron micrographs have been recorded during such transport, cf. [8]. We will model this with a plug within the pore in accordance with electron microscopy data. In equation 11.3.9 the first term is a double cell membrane hole, and the following three terms are torus equations. The result is shown in figure 11.3.10.

$$\begin{aligned}
 & e^{-(e^{-(x^2+(y)^2+z^2-5)}+e^{z^2-1.5})} \\
 & +2e^{-[((x^2+y^2)^{0.5}-2)^2+(z+2)^2+0.5]} \\
 & +2e^{-[((x^2+y^2)^{0.5}-2)^2+(z-2)^2+0.5]} \\
 & +2e^{-[((x^2+y^2)^{0.5}-1.2)^2+z^2+0.6]} = 1
 \end{aligned}
 \tag{11.3.9}$$

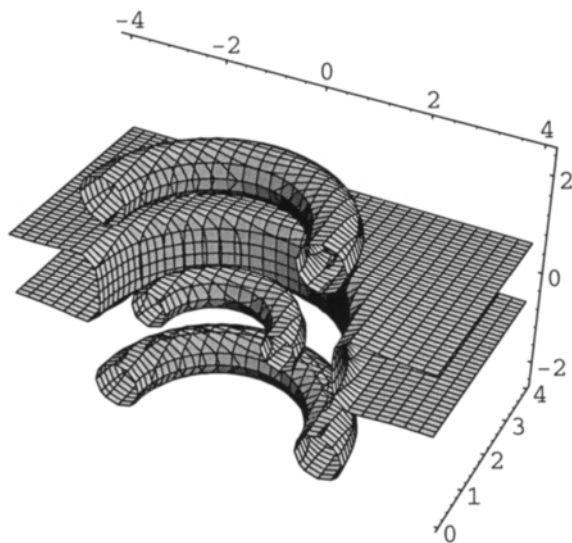


Figure 11.3.10 Different mathematics from equation 11.3.9 to describe the nuclear pore complex of ref. [8].

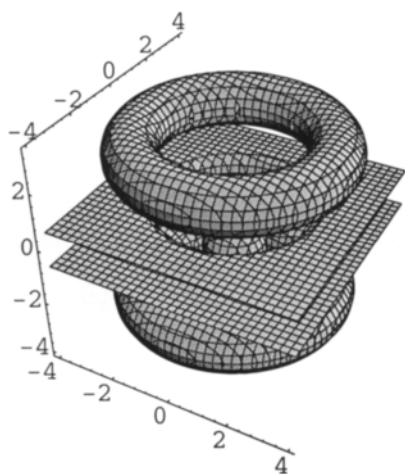


Figure 11.3.11a A plug is added.

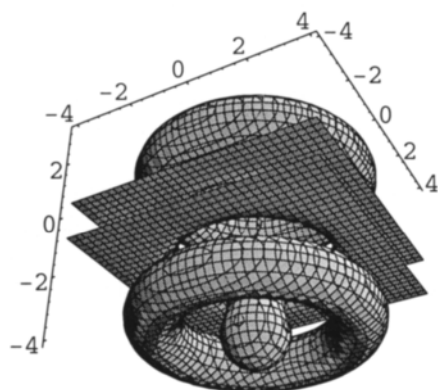


Figure 11.3.11b Different projection.

Next we make a large molecule in form of two spheres fused together to a plug consisting of the two last terms in equation 11.3.10. We see in figures 11.3.11a-b that the plug is on its way out.

$$\begin{aligned}
& e^{-(e^{-(x^2+(y)^2+z^2-5)}+e^{z^2-1.5})} \\
& +2e^{-[((x^2+y^2)^{0.5}-3)^2+(z+2.5)^2]} + \\
& +2e^{-[((x^2+y^2)^{0.5}-3)^2+(z-2.5)^2]} \\
& +e^{-(x^2+y^2+(z+3)^2-1)} + e^{-(x^2+y^2+(z-3)^2-1)} = 1
\end{aligned}
\tag{11.3.10}$$

References 11

- 1 B. Schutz. *Geometrical methods of mathematical physics*. Cambridge University Press. 1980, page 179
- 2 B. Alberts, D. Bray, J. Lewis, M. Raff, K. Roberts, and J.D. Watson, *Molecular Biology of THE CELL*, Garland Publishing, Third Edition, 1994, page 578.
- 3 B. Alberts, D. Bray, J. Lewis, M. Raff, K. Roberts, and J.D. Watson, *Molecular Biology of THE CELL*, Garland Publishing, Third Edition, 1994, page 601.
- 4 J. Darnell, H. Lodish, D. Baltimore. *Molecular Cell Biology*. Scientific American Books 1986, page 662.
- 5 M. Jacob and S. Andersson, *THE NATURE OF MATHEMATICS AND THE MATHEMATICS OF NATURE*, Elsevier, 1998.
- 6 H. Lodish, D. Baltimore, A. Berk, S.L. Zipursky, P. Matsudaria, J. Darnell., *Molecular Cell Biology*, Scientific American Books, Third Edition, 1997, page 168.
- 7 B. Alberts, D. Bray, J. Lewis, M. Raff, K. Roberts, and J.D. Watson, *Molecular Biology of THE CELL*, Garland Publishing, Third Edition, 1994, page 562.
- 8 G.M. Cooper, *THE CELL A Molecular Approach*, ASM Press, 1997, page 319-20.

12 Icosahedral Symmetry, Clathrin Structures, Spikes, Axons, the Tree, and Solitary Waves

...no law of nature indicates an intrinsic difference between left and right...
 [Weyl,1]

There is a common dividend between the headings above - the mathematics.

The icosahedron and the dodecahedron are described, and the symmetry relations to virus and clathrin is given.

The hyperbolic polyhedra and the mathematics to describe them are useful for the description of spikes and axons.

The division of cylinders or branches is described in analogy with cell division. And the growth of the tree is described.

An alternative to the common soliton mathematics is given.

12.1 The icosahedral symmetry

Many virus-structures have icosahedral symmetry, so we shall give the mathematics for this symmetry. The icosahedron is described in equation 12.1.1, and shown in figure 12.1.1. The permutations in space contain the constant τ of the golden mean, since the planes used to derive the equations have interceptions containing this constant. The icosahedron has five-fold symmetry, which we will study more in detail later on using the pentagonal dodecahedron.

$$\begin{aligned} &\tau^4(x+y+z)^4 + e\tau^4(-x+y+z)^4 + e\tau^4(x+y-z)^4 + e\tau^4(x-y+z)^4 + e(x+\tau^2y)^4 \\ &+ e(-x+\tau^2y)^4 + e(z+\tau^2x)^4 + e(z-\tau^2x)^4 + e(y+\tau^2z)^4 + e(y-\tau^2z)^4 = 10^8 \end{aligned} \quad 12.1.1$$

An icosahedral virus may have spikes, that can be made by making a hyperbolic icosahedron. In doing that we need to go over its dual which is the pentagonal dodecahedron. This is then subtracted from a sphere in equation 12.1.2, and in figure 12.1.2 we see the beautiful result.

$$\begin{aligned} &e(\tau^2+1)(x^2+y^2+z^2) - e(\tau x+y)^2 - e(-\tau x+y)^2 \\ &- e(\tau y+z)^2 - e(-\tau y+z)^2 - e(\tau z+x)^2 - e(-\tau z+x)^2 = 0 \end{aligned} \quad 12.1.2$$

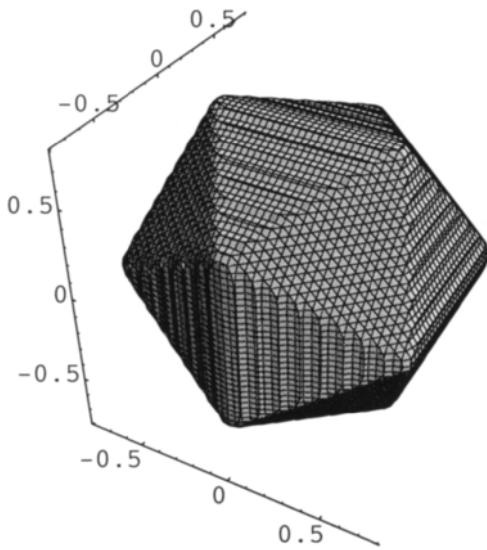


Figure 12.1.1 The icosahedron after equation 12.1.1.

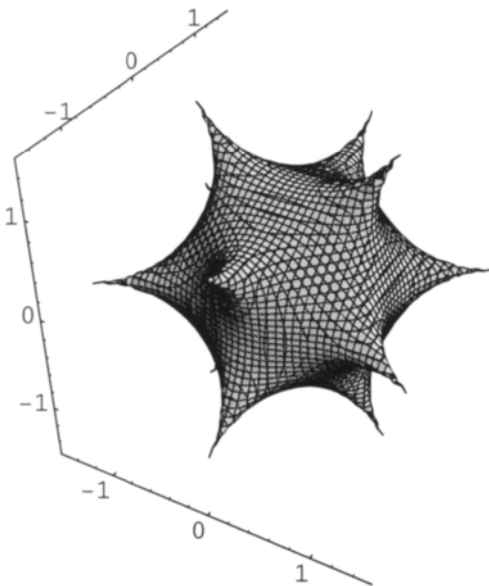


Figure 12.1.2 The hyperbolic icosahedron after equation 12.1.2.

Using the icosahedral equation we get the beautiful hyperbolic pentagonal dodecahedron in **12.1.3**.

$$\begin{aligned}
 &e^{(\tau^3+\tau^2+1)(x^2+y^2+z^2)} - e^{\tau^2(x+y+z)^2} - e^{\tau^2(-x+y+z)^2} \\
 &- e^{\tau^2(x+y-z)^2} - e^{\tau^2(x-y+z)^2} - e^{(x+\tau^2y)^2} - e^{(-x+\tau^2y)^2} \\
 &- e^{(z+\tau^2x)^2} - e^{(z-\tau^2x)^2} - e^{(y+\tau^2z)^2} - e^{(y-\tau^2z)^2} = 0
 \end{aligned}
 \tag{12.1.3}$$

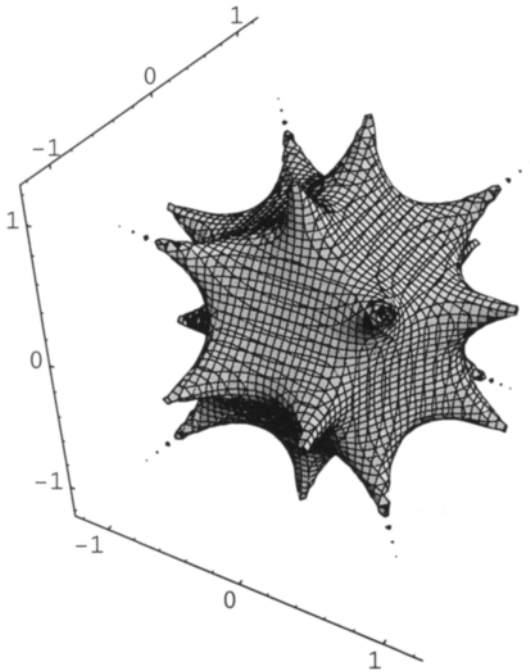


Figure 12.1.3 The hyperbolic pentagonal dodecahedron after equation 12.1.3.

There is another very simple way to derive the mathematics for this important symmetry and these polyhedra. We use the equation of dilatation [2] as in 12.1.4, which is shown in a plot in figure **12.1.4**.

$$y = x \sin \pi x
 \tag{12.1.4}$$

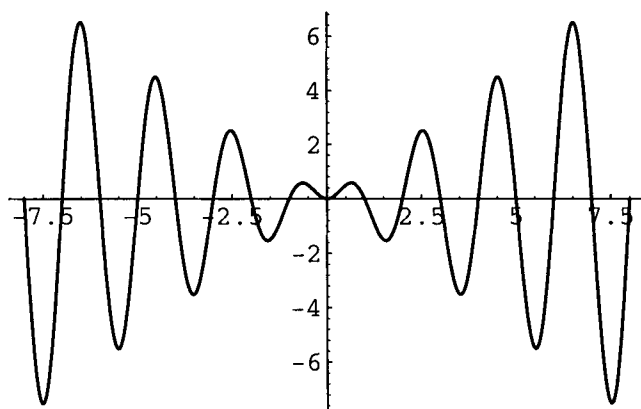


Figure 12.1.4

The function repeats itself under heavy expansion, and the symmetry in 3D is very similar with a repetition of concentric structures in space, as reported in ref. [2].

We just plot the inner geometry of the equation 12.1.5 after boundaries in figure 12.1.5, and realise there is the electron structure of B_6H_6 again.

$$x \sin \pi x + y \sin \pi y + z \sin \pi z = 1$$

12.1.5

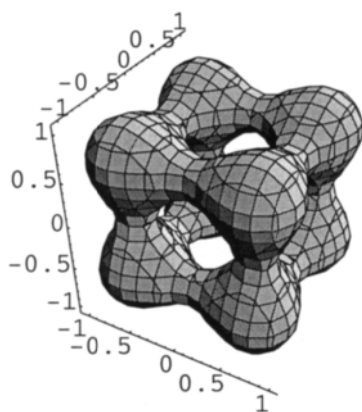


Figure 12.1.5 The electron structure of B_6H_6 after equation 12.1.5.

We can, in a similar way, make the other boron hydrides and we shall here show the two geometries of icosahedral symmetry, one of which is the $B_{12}H_{12}^{2-}$ molecule (figure 12.1.7). We start with the icosahedron itself in equation 12.1.6 and plot it in figure 12.1.6.

$$\begin{aligned}
 &\tau(x+y+z)\sin\pi\tau(x+y+z)+\tau(x-y-z)\sin\pi\tau(x-y-z) \\
 &+\tau(-x-y+z)\sin\pi\tau(-x-y+z)+\tau(-x+y-z)\sin\pi\tau(-x+y-z) \\
 &+(x+\tau^2y)\sin\pi(x+\tau^2y)+(-x+\tau^2y)\sin\pi(-x+\tau^2y) \\
 &+(y+\tau^2z)\sin\pi(y+\tau^2z)+(-y+\tau^2z)\sin\pi(-y+\tau^2z) \\
 &+(z+\tau^2x)\sin\pi(z+\tau^2x)+(-z+\tau^2x)\sin\pi(-z+\tau^2x)+2=0
 \end{aligned}
 \tag{12.1.6}$$

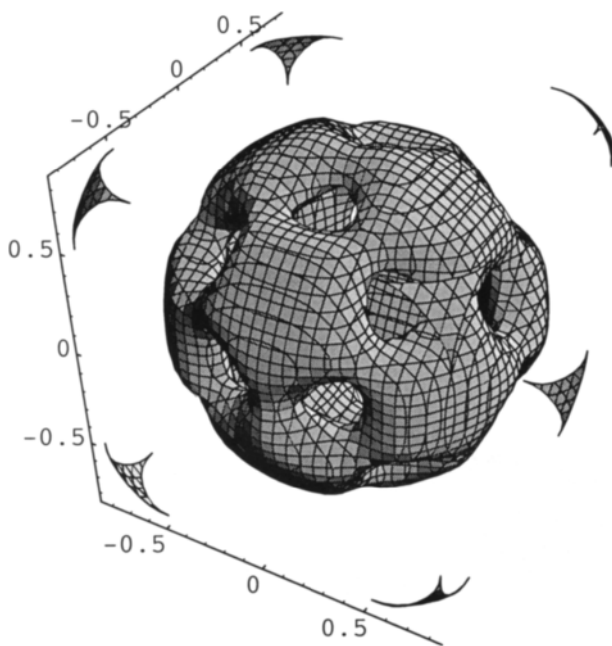


Figure 12.1.6 Icosahedral symmetry and dilatation after equation 12.1.6.

The dodecahedron has the equation in 12.1.7 and this structure is plotted in various projections, revealing the icosahedral symmetry in detail, in figure 12.1.7a-d.

$$\begin{aligned}
 &(x+\tau z)\sin\pi(x+\tau z)+(-x+\tau z)\sin\pi(-x+\tau z) \\
 &+(y+\tau x)\sin\pi(y+\tau x)+(-y+\tau x)\sin\pi(-y+\tau x) \\
 &+(z+\tau y)\sin\pi(z+\tau y)+(-z+\tau y)\sin\pi(-z+\tau y)+2.7=0
 \end{aligned}
 \tag{12.1.7}$$

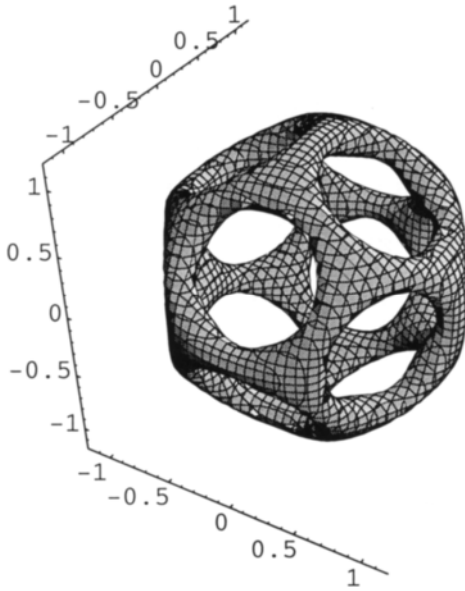


Figure 12.1.7a The dodecahedron after equation 12.1.7.

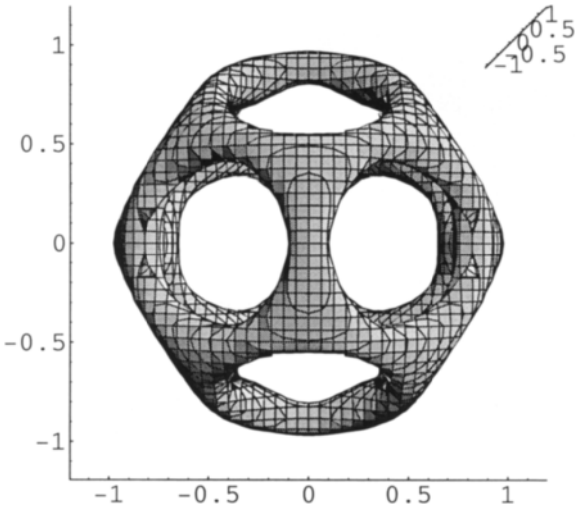


Figure 12.1.7b The dodecahedron along the 2-fold axis.

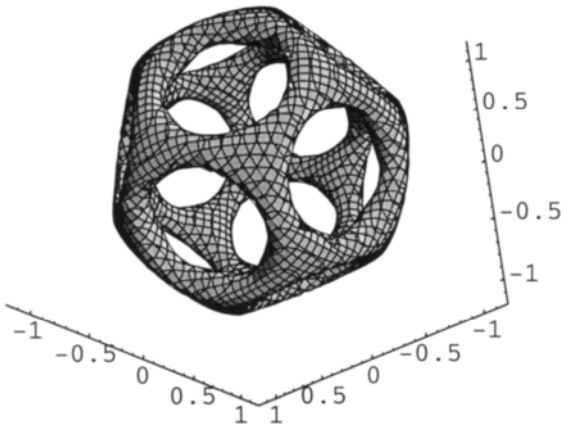


Figure 12.1.7c The dodecahedron after the 3-fold axis.

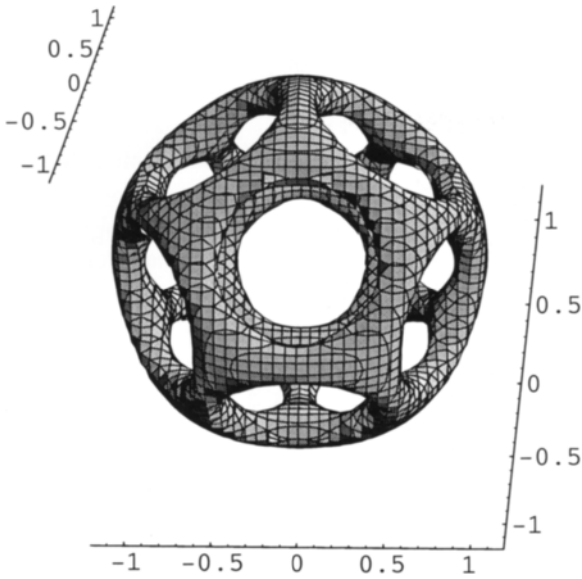


Figure 12.1.7d The dodecahedron after the 5-fold axis.

The reason we show these two models is partly due to the icosahedral virus structures, but also because the dodecahedral structure in figure 12.1.7a-d may serve as model for the clathrin structures as they occur around vesicles. The plane can be described with six-rings as in figure 12.1.8a, and with equation 12.1.8. Combining five- and six-rings creates curvature, and we get the clathrin coating structures as shown with an electron microscope graph in figure 12.1.8b after ref. [3]. The extreme is to have only five-rings, which results in the dodecahedron in figure 12.1.7a-d.

$$\cos \pi x \cos \pi \left(\frac{x}{2} + \frac{\sqrt{3}}{2} y \right) \cos \pi \left(-\frac{x}{2} + \frac{\sqrt{3}}{2} y \right) = -0.1 \quad 12.1.8$$

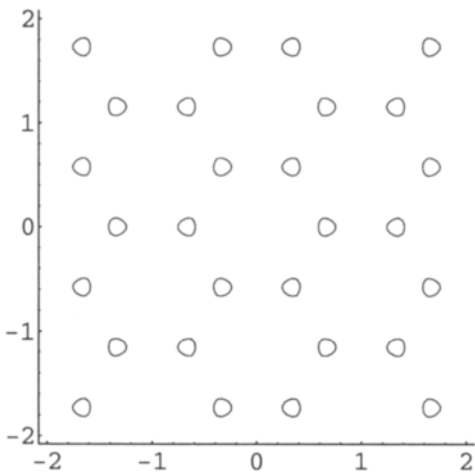


Figure 12.1.8a Plane built of six-rings.

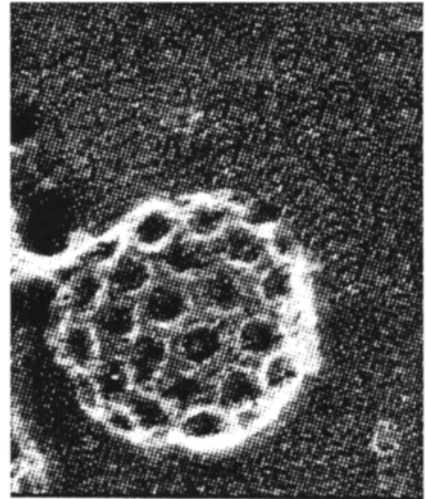


Figure 12.1.8b Single clathrin coated vesicle, modified from [3].

The dodecahedron and the icosahedron above can serve as good models for how the joining of vesicles via catenoids gives a double membrane with holes. We have first membrane units that join to the structure shown in figure 12.1.9. The equation is 12.1.7 but with a constant of 3.2. If we go exponential as in equation 12.1.9, the result is shown in figure 12.1.10 which is a good picture of how to make holes in a polyhedron. The holes go in and meet corners of the dual icosahedron and a double membrane is formed.

$$\begin{aligned}
 & e^{x+\tau z} \cos \pi(x+\tau z) + e^{-x+\tau z} \cos \pi(-x+\tau z) + e^{y+\tau x} \cos \pi(y+\tau x) \\
 & + e^{-y+\tau x} \cos \pi(-y+\tau x) + e^{z+\tau y} \cos \pi(z+\tau y) + e^{-z+\tau y} \cos \pi(-z+\tau y) \quad 12.1.9 \\
 & + 5.3 = 0
 \end{aligned}$$

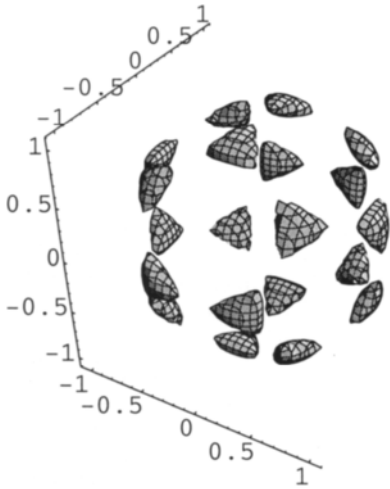


Figure 12.1.9 Membrane units (“vesicles”) approach to form a dodecahedron.

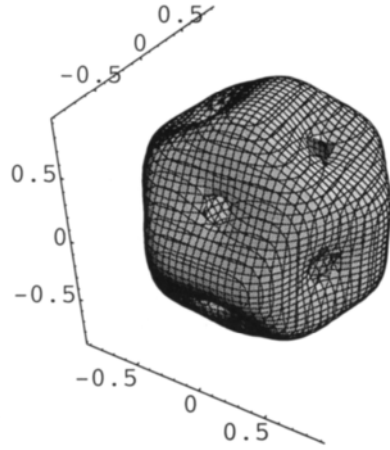


Figure 12.1.10 Double membrane of a dodecahedron. The holes go in and meet the dual, the icosahedron.

Such a double membrane can of course be made analogously by adding spheres or vesicles in a plane. The equation is in 12.1.10 and the plot is in figure 12.1.11a. In order to make the model more membrane-like we made the spheres or vesicles to ellipsoids as in equation 12.1.11. The plot in figure 12.1.11b shows the membrane.

$$\begin{aligned}
 & e^{-(x^2+y^2+z^2)} + e^{-((x-2)^2+y^2+z^2)} + e^{-(x^2+(y-2)^2+z^2)} \\
 & + e^{-((x-2)^2+(y-2)^2+z^2)} + e^{-((x-4)^2+y^2+z^2)} \\
 & + e^{-(x^2+(y-4)^2+z^2)} + e^{-((x-4)^2+(y-2)^2+z^2)} \\
 & + e^{-((x-2)^2+(y-4)^2+z^2)} + e^{-((x-4)^2+(y-4)^2+z^2)} = 0.8 \quad 12.1.10
 \end{aligned}$$

$$\begin{aligned}
 & e^{-(x^2+y^2+10z^2)} + e^{-((x-2)^2+y^2+10z^2)} + e^{-(x^2+(y-2)^2+10z^2)} \\
 & + e^{-((x-2)^2+(y-2)^2+10z^2)} + e^{-((x-4)^2+y^2+10z^2)} \\
 & + e^{-(x^2+(y-4)^2+10z^2)} + e^{-((x-4)^2+(y-2)^2+10z^2)} \\
 & + e^{-((x-2)^2+(y-4)^2+10z^2)} + e^{-((x-4)^2+(y-4)^2+10z^2)} = 0.56
 \end{aligned}
 \tag{12.1.11}$$

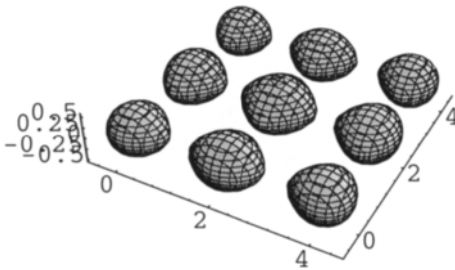


Figure 12.1.11a Ordered arrangement of vesicles.

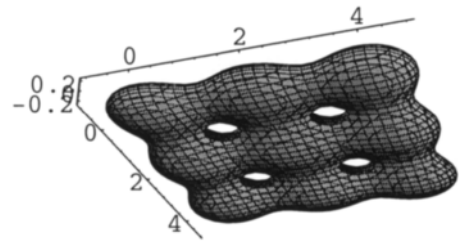


Figure 12.1.11b Vesicles are made to meet as ellipsoids and form a double membrane.

12.2 Hyperbolic Polyhedra, Long Cones, Cylinders and Catenoids

The first function we select to study is the addition of GD-terms as in equation 12.2.1.

$$e^{-x^2} + e^{-y^2} + e^{-z^2} = C
 \tag{12.2.1}$$

For a constant of $C=2$ there is the hyperbolic octahedron shown in figure 12.2.1.

We shall now do the simple mathematics behind this function which we have partly done before. As this is important for the things to come we do it in some further detail here. The GD-functions in 12.2.2 represent pairwise double planes that become closer when C approaches unity.

$$e^{-x^2} = C$$

$$e^{-y^2} = C$$

$$e^{-z^2} = C$$

12.2.2

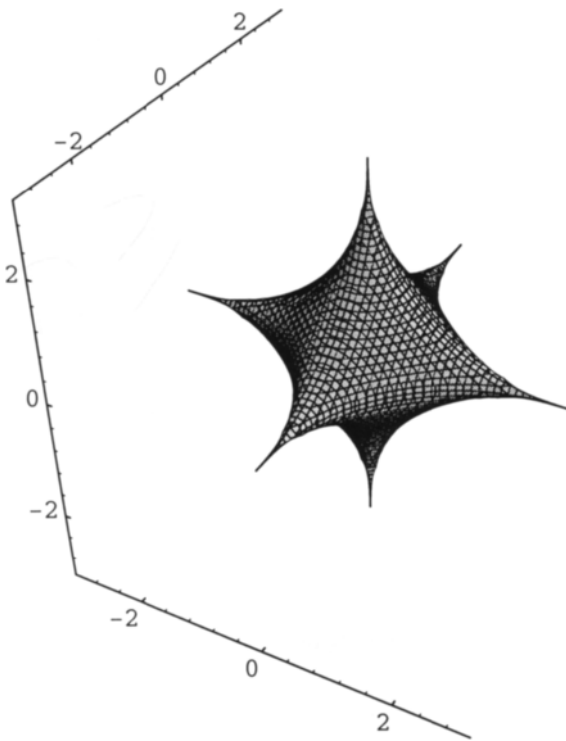


Figure 12.2.1 The beautiful hyperbolic octahedron.

In 12.2.3 the planes from these functions collaborate pair-wise, and give cylinders as shown in figure 12.2.2a-c.

$$e^{-x^2} + e^{-y^2} = 1.9$$

$$e^{-x^2} + e^{-z^2} = 1.9$$

$$e^{-y^2} + e^{-z^2} = 1.9$$

12.2.3

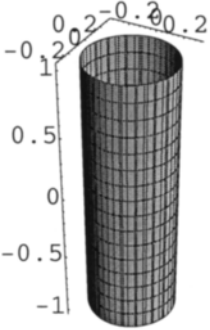


Figure 12.2.2a GD-cylinder.

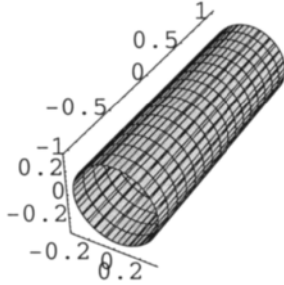


Figure 12.2.2b GD-cylinder.

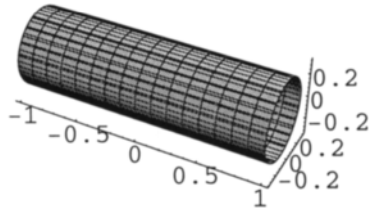


Figure 12.2.2c GD-cylinder.

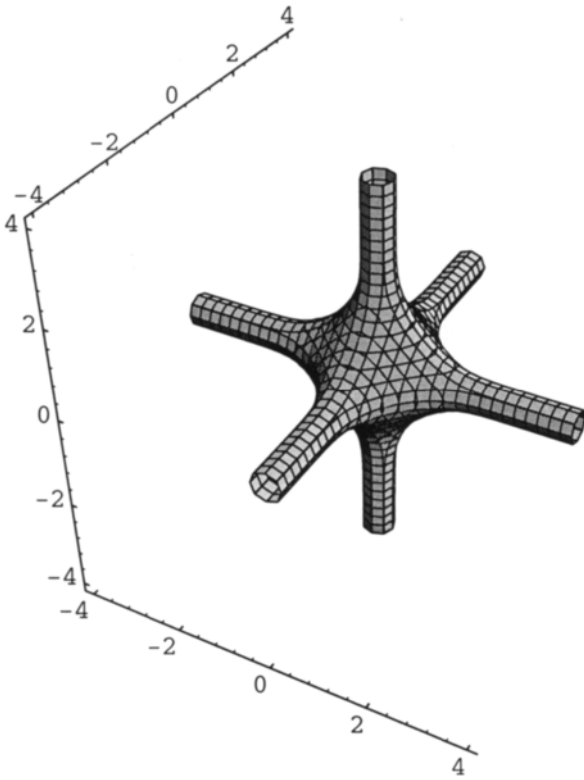


Figure 12.2.3 GD-polyhedron after equation 12.2.1 for a constant of C=2.

We now add these three rods after equation 12.2.1 with $C=1.9$ and obtain figure 12.2.3. We realise that if we for example make $z=4$ the term e^{-z^2} is about 10^{-9} and this is the reason that the function well outside origin consists of cylinders as in figure 12.2.3. And for a constant of 2 the cylinders become infinitely thin as in figure 12.2.1.

We may create a variety of structures with these mathematics. First we may put two of these hyperbolic octahedra together and get four, because of the periodicity, always with spikes as in figure 12.2.4 and equation 12.2.4.

$$e^{-x^2} + e^{-y^2} + e^{-z^2} + e^{-(x-2.5)^2} + e^{-(y-2.5)^2} + e^{-(z-2.5)^2} = 1.98 \quad 12.2.4$$

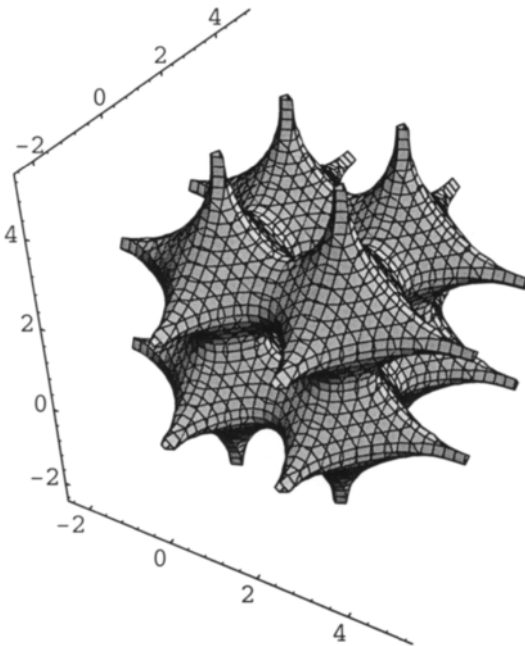


Figure 12.2.4 Two GD-polyhedra develop periodicity and multiply to eight.

We can also take these polyhedra apart after equation 12.2.5.

$$e^{-x^2} + e^{-y^2} + e^{-z^2} + e^{-(x-8)^2} + e^{-(y-8)^2} + e^{-(z-8)^2} = 1.98 \quad 12.2.5$$

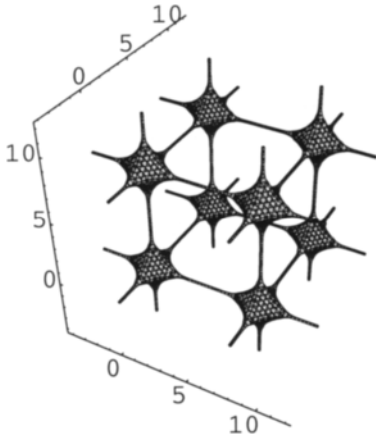


Figure 12.2.5 Periodic GD-polyhedra after equation 12.2.5.

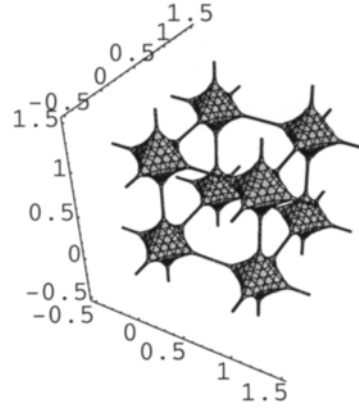


Figure 12.2.6 Periodic cosine polyhedra after equation 12.2.6.

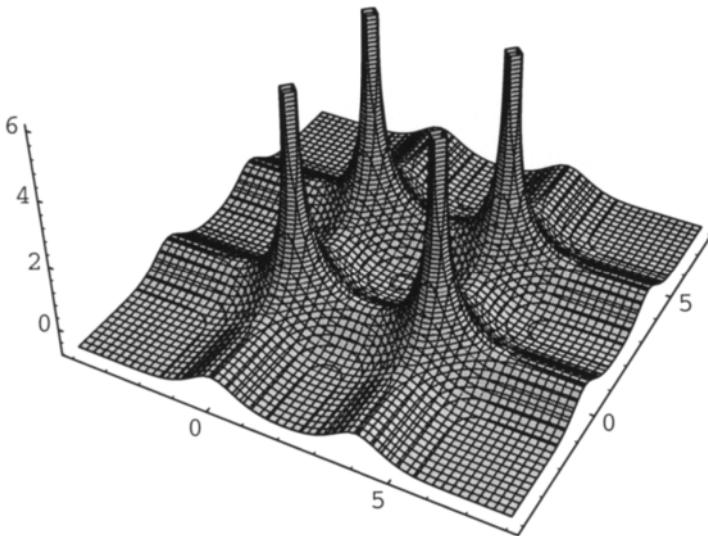


Figure 12.2.7 Spikes from a plane after equation 12.2.7.

$$(\cos \pi x)^8 + (\cos \pi y)^8 + (\cos \pi z)^8 = 1.98 \tag{12.2.6}$$

We get very similar results using cosine as in equation 12.2.6 which is due to the link between the GD-function and the circular functions we have discussed before. The two functions are shown in figures 12.2.5 (GD) and 12.2.6 (cos).

It is also possible to pull out spikes from a plane, and we do so with 12.2.7, which is shown in figure 12.2.7. An example of this is the type of structure found in lamellipodia where the micro-spikes engage in a movement called *ruffling*, cf. [3].

$$e^{-x^2} + e^{-y^2} + e^{-(x-4)^2} + e^{-(y-4)^2} + e^{-z} = 1.95 \tag{12.2.7}$$

12.3 Cylinder Division and Cylinder Fusion - Cylinder Growth

Branching structures, such as growth of trees and the pattern of rivers, represent irregular repetition of three connectors, and are common. They have been described in our time as fractal patterns.

We shall describe branching here as a phenomenon much related to cell division or cell fusion.

So far we have produced one type of geometry for making axons, in the form of cones, cylinders, or catenoids, with the periodic GD-function. When we now continue, we switch to a related type of geometry using 'handmade' cylinders of finite extension. This means that we control the length, and we can also move them. These are exactly the same mathematics we used for making filaments in section 10.2.

Our first equation is 12.3.1.

$$e^{-10(y^2+z^2)} + e^{-2x} + e^{2(x-11)} = 0.9 \tag{12.3.1}$$

In equation 12.3.1, the factor 10 in the term $10(y^2+z^2)$ helps to make the cylinder thin. With $e^{-2x} + e^{2(x-11)}$ the length of the cylinder is decided, and the factor 2 makes the ends less sharp. The rod is plotted in figure 12.3.1a-b, in b just the tip of the rod is shown.

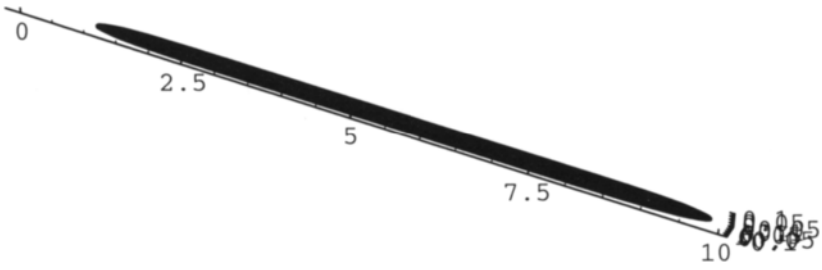


Figure 12.3.1a A cylinder of finite length after equation 12.3.1.

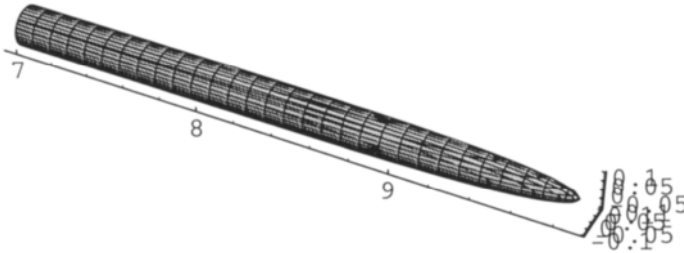


Figure 12.3.1b The tip.

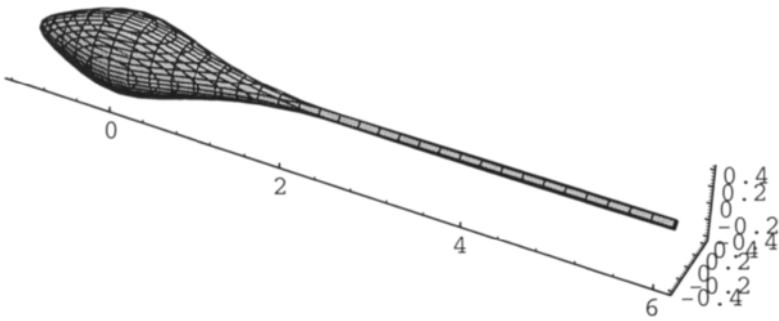


Figure 12.3.2 A model of a cell with an axon.

We shall now put a sphere at the end of the rod, like an axon coming out from a cell. This is done in equation 12.3.2 and plotted in figure 12.3.2. Of course we can put any number of axons in any direction from the cell. And we can make each one of them go to another cell, establishing communication between cells.

$$e^{-10(y^2+z^2)+e^{-(x+2)}+e^{(x-11)}} + e^{-(x^2+y^2+z^2)} = 0.9 \tag{12.3.2}$$

The cylinder has a central role in forming structures in biology. In what may be called the hierarchy of growth - the cylinder is on the top of the organisation. For example the trunk between the roots and the branches of a tree. Or the joining of chirality, the left and the right. For the last case we give the function in 12.3.3 which gives the remarkable figure in 12.3.3 where a left-handed screw is joined to a right-handed screw via a cylinder, serving as the mirror. This is also a picture from biology, the left arm is to the left and the right arm to the right, with the shoulders in between.

$$e^{x \cos \pi z^2 + y \sin \pi z^2} + e^{x^2 + y^2} = 1.95 \tag{12.3.3}$$

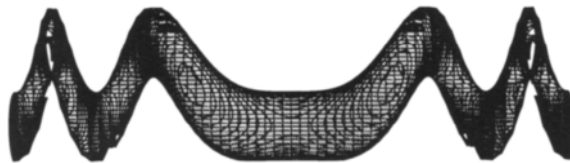


Figure 12.3.3 Left joined to right via a cylinder.

We will now return to the tree, which we will describe as a mathematical operation analogous to cell division. The branches stem from the trunk, which we regard as the arch branch. This means that after a number, n , divisions, there are 2^n individs, for $n=0$ there is just the trunk, for $n=1$ there has been a division so there are two branches of which one may still look like the trunk. However, this resemblance will disappear with increasing n . We call this connectivity three, the same as we had for the gyroid surface. Connectivity four or higher is of course possible, but does not seem to be common, and will therefore not be discussed here.

So we proceed with the branch division (grafting corresponds to fusion) and design an equation in analogy with cell division in 12.3.4. The first term is a cylinder, the trunk, to which we have added two identical pieces of

cylinders. The structure is shown in figure 12.3.4a. In equation 12.3.5 we have made the two cylinders unequal by giving them opposite slopes. We have also given the trunk a terminal. We give now biological motion to the structure by making a running through the values 1, 4, 6, and 10 in figures 12.3.4b-e. In f, one of the branches has been on the sunny side and grown, an effect obtained by changing the value of y from 15 to 20, as shown in equation 12.3.6.

$$10^{-x^2} + 2 \cdot 10^{-(x^2 + 10^{y-15} + 10^{-(y-10)})} = 0.1 \quad 12.3.4$$

$$10^{-(x^2 + 10^{(y-11)})} + 10^{-[(x + \frac{a}{10}y - a)^2 + 10^{y-15} + 10^{-(y-10)}]} \\ + 10^{-[(-x + \frac{a}{10}y - a)^2 + 10^{y-15} + 10^{-(y-10)}]} = 0.1 \quad 12.3.5$$

$$10^{-(x^2 + 10^{(y-11)})} + 10^{-[(x + \frac{a}{10}y - a)^2 + 10^{y-15} + 10^{-(y-10)}]} \\ + 10^{-[(-x + \frac{a}{10}y - a)^2 + 10^{y-20} + 10^{-(y-10)}]} = 0.1 \quad 12.3.6$$

This might be applied as a mathematical description of a nerve cell with synapses. In equation 12.3.7 we have reinforced the two extra cylinders and added two small vesicles, one has left the terminal axon, the other is about to, as shown in figure 12.3.5. In the equation a has the value of 2. One can say that instead of continuing growing with new branches, the axon stops and uses the branch division mechanism to form the synapse.

$$10^{-(x^2 + 10^{(y-11)})} + 2 \cdot 10^{-[(x + \frac{a}{10}y - a)^2 + 10^{y-15} + 10^{-(y-10)}]} \\ + 2 \cdot 10^{-[(-x + \frac{a}{10}y - a)^2 + 10^{y-15} + 10^{-(y-10)}]} \\ + 0.12 \cdot 10^{-[x^2 + (y-15.7)^2]} + 0.12 \cdot 10^{-[(x+2)^2 + (y-15.4)^2]} = 0.1 \quad 12.3.7$$

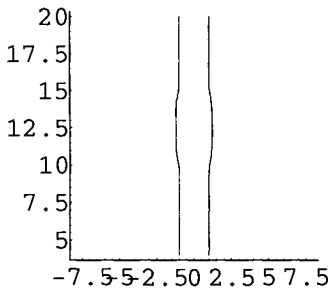


Figure 12.3.4a Two identical pieces of cylinders of identical length.

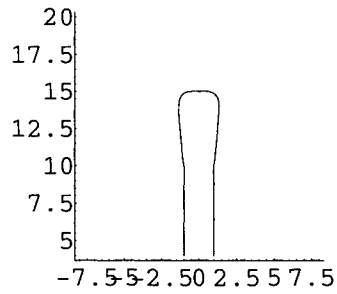


Figure 12.3.4b The two cylinders are unequal by having opposite slopes.

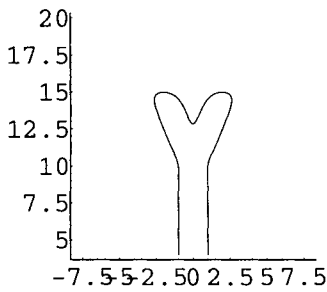


Figure 12.3.4c After equation 12.3.5 with $\alpha=4$.

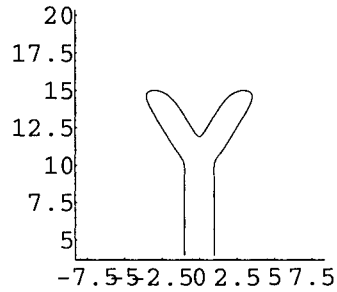


Figure 12.3.4d $\alpha=6$.

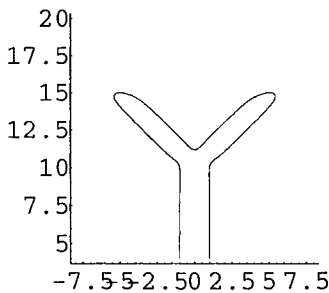


Figure 12.3.4e $\alpha=10$.

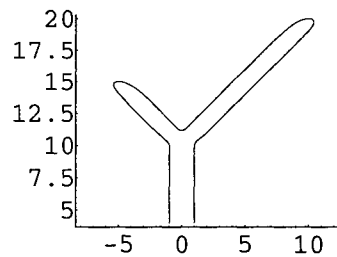


Figure 12.3.4f One branch has been on the sunny side.

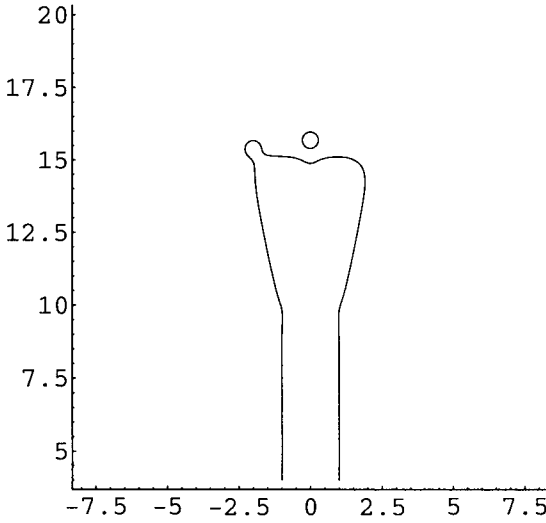


Figure 12.3.5 The branch division mechanism for modelling a synapse.

$$\begin{aligned}
 &10^{-(x^2+10^{y-6}+10^{-(y+6)})} \\
 &+0.2 \cdot 10^{-[(-x-0.9y-5)^2+10^{-(y+15)}+10^{(y+4)}]} \\
 &+0.2 \cdot 10^{-[(x-0.4y-2)^2+10^{-(y+15)}+10^{(y+4)}]} \\
 &+0.2 \cdot 10^{-[(0.1x-y-4)^2+10^{-x}+10^{(x-10)}]} \\
 &+0.12 \cdot 10^{-[(x-0.2y-7.5)^2+10^{-(y+20)}+10^{(y+10)}]} \\
 &+0.15 \cdot 10^{-[(-0.1x-y-10)^2+10^{-(x+12)}+10^{(x+2)}]} \\
 &+10^{-[(x+0.4y-2)^2+10^{-(y-5)}+10^{(y-19)}]} \\
 &+10^{-[(-x+0.4y-2)^2+10^{-(y-5)}+10^{(y-17)}]} \\
 &+10^{-[(x+2y-25)^2+10^{-(y-15)}+10^{(y-21)}]} \\
 &+10^{-[(-x+y-8)^2+10^{-(y-12)}+10^{(y-22)}]} \\
 &+10^{-[(x+1.5y-27)^2+10^{-(y-17)}+10^{(y-21)}]} \\
 &+10^{-[(-x+y-16)^2+10^{-(y-13)}+10^{(y-24)}]} = 0.1
 \end{aligned}$$

12.3.8

From this it is now easy to continue with the tree. We build further on with equations to 12.3.8 and notice that we have made roots at the lower part of figure 12.3.6, as well as branches.

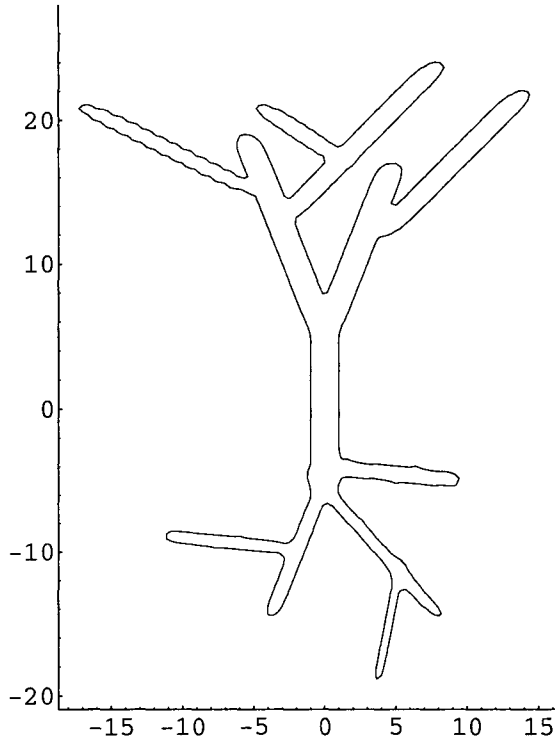


Figure 12.3.6 The tree after equation 12.3.8.

12.4 Solitary Waves, Solitons and Finite Periodicity

The nerve axon transmission of nerve pulses involves motion, which we will describe in chapter 13 with mathematics similar to what we use for solitary waves, or solitons. The commonly used, complicated, soliton mathematics will first be shortly reviewed.

A travelling wave, a running wave or a solitary wave, may for example originate from an earthquake at the bottom of the ocean that gives a giant surface wave. A solitary wave is described as a single wave that propagates continuously with symmetric shape and uniform speed. The term soliton

has been used for a solitary wave when it can interact with other solitons and retain form, and is then said to be 'particle like' [5]. The profile of a wave is given by equation 12.4.1.

$$u = f(x)$$

$$u = f(x - vt) \quad 12.4.1$$

at $t=0$ at time t

$$u = f(x) \quad u = f(x - vt)$$

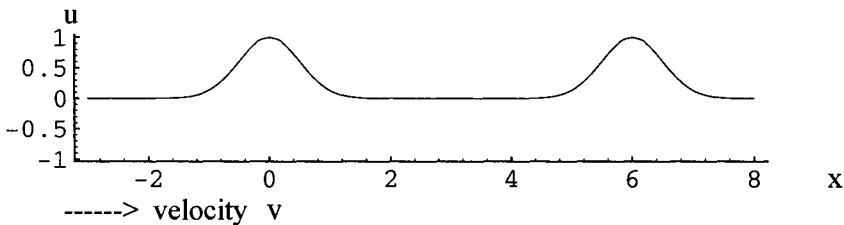


Figure 12.4.1 A solitary wave.

The classic wave equation that gives a solitary wave is the Korteweg-de Vries (KdV) equation:

$$\frac{\partial u}{\partial t} = 6u \frac{\partial u}{\partial x} - \frac{\partial^3 u}{\partial x^3} \quad 12.4.2$$

The equation is a description of running water waves - cnoidal periodic waves [4], which tend to a solitary wave in the limiting case of long wave lengths, and a solution for a moving solitary wave is found in equation 12.4.3. U is a constant, and the wave moves in the $+x$ direction with a speed of v .

$$u(x, t) = -U \operatorname{sech}^2(x - vt) \quad 12.4.3$$

Not long ago an initial solution of the KdV was set as potential in the time-independent Schrödinger equation [2], which we show below in equation 12.4.4.

$$-\frac{d^2 \psi}{dx^2} + u\psi = \lambda\psi \quad 12.4.4$$

We choose an initial solution

$$u(x) = -U \operatorname{sech}^2 x \tag{12.4.5}$$

and transform the Schrödinger equation

$$-\frac{d^2 \psi}{dx^2} + (\lambda - U \operatorname{sech}^2 x) \psi = 0 \tag{12.4.6}$$

with initial values of the form

$$u(x) = -N(N + 1) \operatorname{sech}^2 x \tag{12.4.7}$$

12.4.7 may be called a Schrödinger potential with N bound states. To some surprise, $N=2$ showed up to correspond to two solitons (for which we give the solution below) and $N=3$ gives three solitons. The N -soliton solution found, is given in equation 12.4.8 for two solitons, or $N=2$. And the equations quickly get more complicated with increasing N . After ref. [5].

$$y = 12 \frac{3 + 4 \cosh(2x - 8t) + \cosh(4x - 64t)}{[3 \cosh(x - 28t) + \cosh(3x - 36t)]^2} \tag{12.4.8}$$

$$\cosh = \frac{e^x + e^{-x}}{2}, \text{ and } \operatorname{sech} x = 1/\cosh x$$

For $t=0.5$ there is figure 12.4.2a and for $t=0.2$ figure 12.4.2b. The solitons are moving, the bigger faster than the smaller.

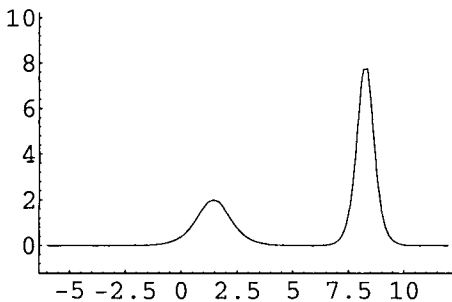


Figure 12.4.2a Two solitons.

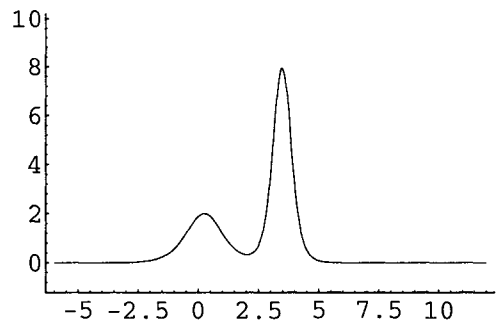


Figure 12.4.2b The two solitons have moved with different speeds.

With N , a cascade of solitons may be constructed but the mathematics turn very complicated.

This remarkable soliton theory is difficult. The possibility for varying amplitudes and speeds for a chain of solitons is not present, for example if you want to model the dynamics created when a stone is dropped into water. Such a pulse train we can instead obtain by damping a cosine function with the GD-function.

We find that the GD-function has the properties we need. And it is a much shorter way than the Korteweg-de Vries (KdV) approach.

The function $\text{sech}^2 x$ looks like a GD-function, e^{-x^2} , in figure 12.1.3a, and we can move it as a GD-function as shown in 12.1.3b. The equations are found in 12.4.9-11.

$$y = 6 \text{sech}^2 x \quad 12.4.9$$

$$y = 6 \text{sech}^2(x + \Delta x) \quad 12.4.10$$

Δx corresponds to time and is set to 8.

$$y = 6 \text{sech}^2(x - 8) \quad 12.4.11$$

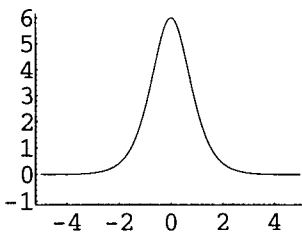


Figure 12.4.3a The solitary wave from KdV.

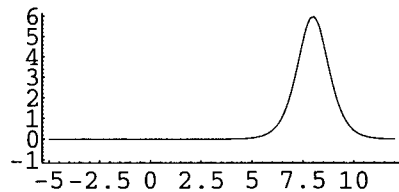


Figure 12.4.3b Motion of the KdV wave like a soliton.

We can add two solitons to one mathematical function, and one of them with double amplitude, as in figure 12.4.4a and equation 12.4.12.

$$y = 4 \text{sech}^2 x + 8 \text{sech}^2(x - 8) \quad 12.4.12$$

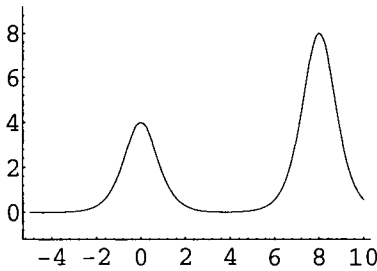


Figure 12.4.4a Two solitons in one function after equation 12.4.12.

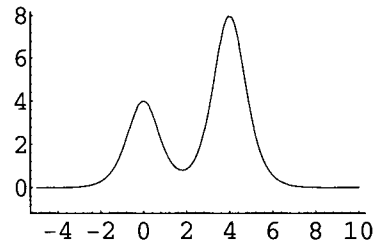


Figure 12.4.4b The two solitons move independently after 12.4.13.

We can of course also move them independently of each other as seen in figure 12.4.4b-d. The equations are in 12.4.13-15, and the solitons move through each other at the end.

$$y = 4 \operatorname{sech}^2 x + 8 \operatorname{sech}^2(x - 4) \tag{12.4.13}$$

$$y = 4 \operatorname{sech}^2 x + 8 \operatorname{sech}^2 x \tag{12.4.14}$$

$$y = 4 \operatorname{sech}^2(x - 1) + 8 \operatorname{sech}^2(x + 4) \tag{12.4.15}$$

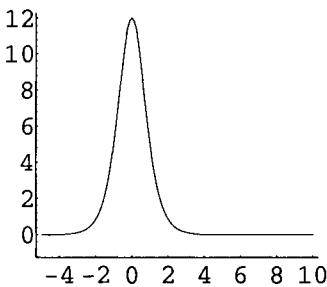


Figure 12.4.4c The two solitons move independently after 12.4.14.

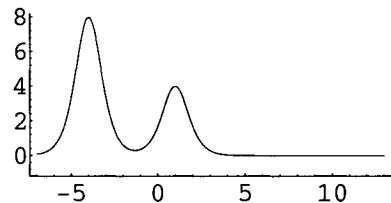


Figure 12.4.4d The two solitons move independently after 12.4.15.

This is in analogy with what was done above, solving the Schrödinger-KdV-equation. And we can easily add more solitons and change speed and amplitudes.

Thus we can use this soliton function to make many things - the periodicity, the nodal surfaces, the cubosomes, the hyperbolic polyhedra or

DNA. Just like we did with the GD-function. We demonstrate the similarity with the GD-function below.

$$\operatorname{sech} x = 1/\cosh x$$

and

$$\cosh x = \frac{1}{2}(e^x + e^{-x})$$

which means

$$\operatorname{sech}^2 x = \frac{4}{(e^x + e^{-x})^2} \quad 12.4.16$$

We plot the two functions, on top of each others, after the equations 12.4.17-18, and this is shown in figure 12.4.5. The GD function is the one with the deepest valleys.

$$y = \operatorname{sech}^2 x + \operatorname{sech}^2(x-3) + \operatorname{sech}^2(x-6) + \operatorname{sech}^2(x-9) \quad 12.4.17$$

$$y = e^{-x^2} + e^{-(x-3)^2} + e^{-(x-6)^2} + e^{-(x-9)^2} \quad 12.4.18$$



Figure 12.4.5 The sech and GD-functions compared.

What we see is a surprising similarity, this is a wave train of solitons, and the train from equation 12.4.17 may be regarded as a number of consecutive solutions to the KdV-equation, and put together to one mathematical function. We see that the KdV-solution is very close to the GD-function.

In their original work Korteweg-de Vries obtained periodic waves - called cnoidal by them - which they made to a solitary wave by the limiting case of long wavelength. We have earlier described the connection between cosine and the GD-function. Equation 12.4.19 gives a cosine function which becomes identical with the GD-function when n goes to infinity. It behaves like the cnoidal waves, which is shown in figure 12.4.6 for $n=50$ in the equation 12.4.19.

$$\cos^{2n} \frac{x}{\sqrt{n}} \Rightarrow e^{-x^2}, n \rightarrow \infty \quad 12.4.19$$



Figure 12.4.6

Bloch walls are examples in solid state physics which are described as stationary solitary waves or solitons, and which continuously separate magnetic domains in a crystal, as shown in figure 12.4.7.

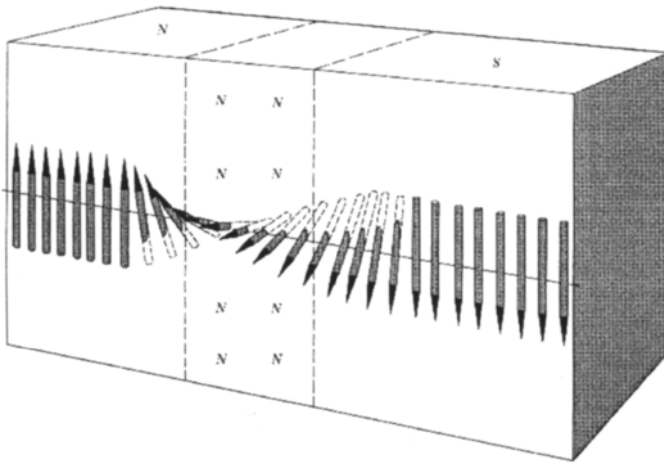


Figure 12.4.7 The structure of a Bloch wall separating domains. In metals the thickness of the region is about 1000 Å. Reproduced with permission from [6].

References

- 1 H. Weyl, *Symmetry*, Princeton University Press 1952, page 129.
- 2 M. Jacob and S. Andersson, *THE NATURE OF MATHEMATICS AND THE MATHEMATICS OF NATURE*, Elsevier, 1998, page 300.

- 3 B. Alberts, D. Bray, J. Lewis, M. Raff, K. Roberts, and J.D. Watson, *Molecular Biology of THE CELL*, Garland Publishing, Co., Third Edition, 1994, page 636.
- 4 J.J. Stoker, *Water waves, The mathematical theory with applications*. Wiley, 1958, reprinted 1992.
- 5 D. Vvdensky, *Partial differential equations*. Addison-Wesley 1992.
- 6 C. Kittel, *Introduction to solid state physics*, Wiley, Seventh Edition, 1996, page 473.

13 Axon Membranes and Synapses - A Role of Lipid Bilayer Structure in Nerve Signals

In a lecture in 1932 on limitations of physical measurements on living organisms, Niels Bohr said [1]: *"...the thought is close at hand that the least freedom we in this respect can give the organism is still big enough to let it hide its last secret."*

A puzzling feature observed to accompany the action potential conduction along the axon membrane is a phase transition in the bilayer. We provide evidence for a two-dimensional analogue to a three-dimensional transition lamellar \leftrightarrow periodically curved bilayer. It is demonstrated how such a transition can be induced by changes in the hydrocarbon chain packing pressure, determining the elastic properties of the bilayer. We argue that such an electro/mechanical coupling makes the action-potential more robust towards interference. The co-operative vesicle fusion at the synaptic signal transmission seems to involve a similar bilayer phase transition. Finally, some neuro-biological phenomena, which might be related to this model, such as effects of mechanical waves on neurons are considered.

13.1 The Nerve Impulse

The electrical nature of nerve signal conduction was revealed more than two hundred years ago through the famous experiments on frog legs by Galvani in Bologna. All living cells are characterised by a potential across the membranes, but the nerve cells are also able to change this potential and generate electrical signals. The nerve cell, the neuron, is usually elongated into a so-called axon. An axon can conduct signals over long distances; it can for example start in the brain and end in a foot. The axon ends with a synapse where the signal is transferred by transmitter molecules to another neuron or to an effector cell, such as a muscle cell.

The membrane potential is due to concentration differences between inside and outside of sodium ions and potassium ions. Sodium and potassium ion concentration gradients determines the trans-membrane potential. The sodium concentration is ten times higher outside the nerve cells, and the potassium concentration is higher inside the cells by a factor of about 35. In some nerve cells calcium has an important role in the signalling events. The potential difference is due to potassium sodium leak-channels and the

sodium-potassium pump. When there is no signal activity (resting potential), the potential measured over the cell membrane in a human neuron is about -90 mV from outside to inside surface.

The signal in a nerve cell starts with an excitation, which can be induced at a synaptic contact with another neuron or by stimulation of the neuron itself (e.g. a sensory cell), results in opening (or "activation") of voltage-gated sodium channels. Within a tenth of a millisecond the influx of sodium ions have depolarised the membrane, and the potential shifts to +35 mV (cell interior surface transiently becomes positive). The activation of these channels is induced by a reduction in potential to about -50 mV. A few tenths of a millisecond after depolarisation, the sodium-channels are closed (or "inactivated"). The membrane then returns to the resting potential, and this repolarisation takes another tenth of a ms.

The voltage-sensitive sodium channels are considered to consist of four sub-units, which together form the pore. Each sub-unit consists of six (or in one model eight) transmembrane helices. There is one transmembrane helix in these sub-units which is considered to have a major role in channel opening and closing. That is the helix termed S4, with every third amino acid residue positively charged (arginine or lysine). Increase of the positive potential at the inside of the axon membrane, which takes place via the sodium ion influx at depolarisation, means that the S4 helix will tend to move inwards (by translation and rotation within the membrane). Such motion must also have some influence on the lipid bilayer structure, something we will consider later in this chapter.

Activation and inactivation of the voltage-gated sodium channels represent the increase and the decrease respectively of the probability that a channel will open a short time (0.7 ms.). The gating current is the sum of these events. The charge movement precedes the opening, which means that first there is a conformational change in the channel protein associated with ion movement, then there is a conformation change resulting in opening. There are at least three conformational states of the channel leading to activation. These can be regarded as stepwise structural changes in the subunits due to ion movement, with one or two alternative steps resulting in inactivation. It is known that the final steps in the opening and closing need not to be voltage dependent. It therefore seems reasonable to assume that the lipid bilayer structure can be involved in these conformational steps. The model proposed below includes the experimentally known dynamic changes of the lipid bilayer at the depolarisation region, which earlier have been neglected.

The voltage-gated potassium channels primarily play a role in the repolarisation, when the transmembrane potential approaches zero, these

slow channels start to open, and when the sodium channels are inactivated, the potassium channels are fully open. As the potassium ions move out along their gradient in concert with the action of the sodium-potassium pump, repolarisation to the resting potential is achieved. Voltage-gated calcium channels mainly plays a part in the synaptic region of neurons. Also, in certain types of muscle there are almost no sodium channels and the action potential is caused mainly by the action of calcium ions.

The potential differences we have described correspond to changes at a particular point at an axon membrane. Signal propagation is a result of lateral movement of the excess of sodium ions from the site of the action potential along the inside membrane surface. The laterally situated voltage-gated sodium channels will therefore become activated. The lateral part of the membrane will become depolarised, and as this process continues along the whole membrane; we get a nerve impulse. After excitation the sodium channels have a so-called refractory period, a couple of milliseconds, during which the neuron cannot be triggered again. This refractory period makes the nerve impulse travel in only one direction along the neuron.

The propagation speed is proportional to the axon diameter. The fastest conduction, about 100 m/s, is reached in nerve-fibres that are thick and covered by a myelin sheath (myelinated). The myelin sheath is formed by multilayers of lipid bilayers from Schwann-cells and Oligodendrocytes (in the peripheral nervous system and the central nervous system respectively). This provides electrical isolation for the ion currents involved in the action potential. The myelin sheath covers the axon membrane in bands about 1-2 mm wide. Between these bands the axon membrane is "naked" (nodes of Ranvier). The signal passively spans the myelin isolation as no voltage-gated channels can be activated. There is a reduction in signal amplitude, but at the end of the myelin sheath (at a Ranvier node), the signal is strong enough to induce an new action potential. This means that the signal will "jump" along the nodes between the regularly distributed bands of myelin isolation, increasing the speed of the nerve impulse significantly.

13.2 At the Action Potential Region of the Membrane there is a Phase Transition in the Lipid Bilayer

Numerous studies have demonstrated changes in the physical properties of the axon membrane at depolarisation which have been interpreted as a phase transition in the bilayer. Orientation measurements of fluorescent probes indicated early that there is a more rigid orientation of the probe at depolarisation [2]. Kinnunen have reported that there is "conclusive

evidence for a depolarisation-induced phospholipid phase transition" based on enthalpy changes, ANS-fluorescence, IR-spectroscopy, fluidity, light scattering and birefringence [3].

There are really only two alternative phase transitions that can occur in the bilayer of the nerve membrane. The first involves crystallisation of the hydrocarbon chains, and corresponds to transitions between a lamellar liquid-crystalline phase and a gel-phase in three-dimensional lipid-water systems. This transition is proposed by Kinnunen [3] to take place at depolarisation. Considering the diversity of lipids and the large proportion of very long and polyunsaturated acyl chains in the nerve membrane lipid bilayer, however, crystallisation into the gel state of the chains seems unlikely to us. Furthermore it would be very slow in such a complex hydrocarbon chain mixture in relation to the kinetics required at depolarisation. The transition between a liquid-crystalline phase and a gel phase in all known lipid-water phase diagrams takes place at a specific temperature, and the nerve signal can be conducted at varying temperatures.

The other alternative of a phase transition along a separate bilayer corresponds to cubic \rightarrow lamellar liquid-crystalline phase in three-dimensional systems. Physical properties (such as enthalpy, fluidity and birefringence) at the transition cubic lipid bilayer to lamellar change in the same direction as those at the transition liquid crystalline (lamellar) \rightarrow gel. phase. This transition, contrary to the transition between a liquid-crystalline phase and a gel phase, according to known phase diagrams can be induced by changes in the water medium and can take place at various temperatures. We therefore propose here that this is the transition that takes place at depolarisation.

Periodically curved membrane bilayers were described in chapter 8. We can term this bilayer conformation C(2d), and the bilayer conformation corresponding to that of the $L\alpha$ -phase in a similar way $L\alpha(2d)$. The kinetics of this transition is discussed below.

The inner monolayer of the axon membrane is dominated by phosphatidylethanolamine and by the C22:6 acyl chains. Such a lipid mixture will tend to form reverse structures, such as cubic types, due to the high inner packing pressure of the bilayer. The outer monolayer is dominated by sphingomyelin and phosphatidylcholine, favouring the $L\alpha$ -type of structure. The periodic curvature is related to a high packing pressure in the hydrocarbon chain core contrary to the situation in the $L\alpha$ -conformation. The axon membrane like membranes in general, as demonstrated in chapter 8, is assumed to exist on a borderline between the C(2d) and the $L\alpha(2d)$ conformations. An $L\alpha(2d)$ conformation is related

to a hydrocarbon chain inner packing pressure, which is about equal to that of the outside. This situation is characteristic for a bilayer that lacks elasticity (neglecting influence from the polar heads). When the inside packing pressure of the bilayer is higher than that of the outside, however, there is also an elastic rigidity of the bilayer. A high inner pressure and asymmetry over the mid-surface should therefore be expected to result in curvature variation along the bilayer surface. Periodicity of curvature variations is a consequence of the general structure properties of bilayers described in chapter 8.

We would like to summarise these structural principles in the following way:

- *High inner bilayer packing pressure -> elastic rigidity -> periodically curved bilayer*
- *Inside packing pressure about equal to that of the outside -> lack of elastic rigidity of the bilayer -> planar (lamellar) type of bilayer.*

An important effect of periodicity is the coupling of thermal vibrations in time, generating standing waves.

Experimental evidence of the involvement of different bilayer conformations in the signal transmission is provided by the effect of general anaesthetic agents, see section 13.6.

We will now consider a $C(2d) \rightarrow L\alpha(2d)$ phase transition in the axon membrane coupled to the depolarisation.

13.3 A Model of a Phase-Transition/Electric Signal Coupling at Depolarisation and its Physiological Significance

The action potential propagating *along* the axon membrane is based on ionic transport *through* the bilayer, and there is a phase transition at the depolarised region of the axon membrane. Any transition within a lipid bilayer at constant temperature and pressure must be due to conformational changes of the lipid molecules and/or embedded proteins. Phase transitions induced by changes in local pH or in counter ions are common in lipid-water systems. Conformational changes of membrane embedded proteins is an alternative mechanism which can cause a bilayer transition. We will consider both alternatives, beginning with the membrane proteins. It seems reasonable to focus on the voltage-gated sodium channels, as they in some myelinated neurons alone are responsible for the depolarisation process. Let us assume that the transition into the open activation gate

conformation of the voltage-gated sodium channels and the transition from the C(2d) bilayer into the $L\alpha(2d)$ bilayer phase are results of a co-operative process, involving the S4 helix movements as described above. After a certain time delay, the channel will adapt the closed inactivation gate conformation, which might initiate reversal of the bilayer transition.

The other alternative which could induce the bilayer phase transition at depolarisation might be some threshold value in counter ion concentration at the bilayer surface (and the reversal of the transition in a similar way during repolarisation). Calcium ion concentration changes at a very low concentration range can induce such transitions. The fact that some action potentials propagate with almost no involvement of calcium ions, does however indicate that the sodium channel conformational transitions is the mechanism behind the bilayer transition.

The phase transition is illustrated schematically in figure 13.3.2. Knowing the speed of the action potential, the time of depolarisation and the wavelength being about 1000 Å (cf. chapter 8) means that the $L\alpha(2d)$ structure will have a real length corresponding to about 1000 periods of the C(2d) bilayer structure.

We have earlier shown the link between the GD-function and the circular functions, and as we need finite periodicity we design the equation 13.3.1 below. The addition of a cylinder gives figure 13.3.1 which may be described as a periodically curved cylinder, or membrane.

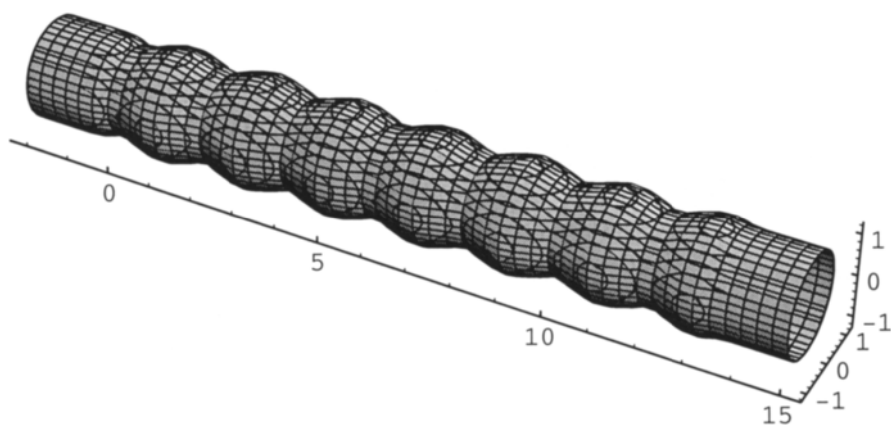


Figure 13.3.1 Periodically curved cylinder membrane.

$$\begin{aligned}
 & e^{-8x^2} - e^{-8(x-1)^2} + e^{-8(x-2)^2} - e^{-8(x-3)^2} + e^{-8(x-4)^2} - e^{-8(x-5)^2} \\
 & + e^{-8(x-6)^2} - e^{-8(x-7)^2} + e^{-8(x-8)^2} - e^{-8(x-9)^2} + e^{-8(x-10)^2} \\
 & - e^{-8(x-11)^2} + e^{-8(x-12)^2} - e^{-8(x-13)^2} + e^{x^2+y^2} - 3.5 = 0
 \end{aligned} \tag{13.3.1}$$

In this curved cylindrical surface of a membrane we want to introduce a flat region which we do by weighting after equation 13.3.2.

$$\begin{aligned}
 & e^{-8x^2} - e^{-8(x-1)^2} + e^{-8(x-2)^2} - e^{-8(x-3)^2} \\
 & + A[e^{-8(x-4)^2} - e^{-8(x-5)^2} + e^{-8(x-6)^2}] \\
 & - B[e^{-8(x-7)^2} + e^{-8(x-8)^2} - e^{-8(x-9)^2}] \\
 & + C[e^{-8(x-10)^2} - e^{-8(x-11)^2} + e^{-8(x-12)^2}] \\
 & - e^{-8(x-13)^2} + e^{x^2+y^2} - 3.5 = 0
 \end{aligned} \tag{13.3.2}$$

For $A = 0.1$, $B = 1$, and $C = 1$ the shape shown in figure 13.3.2 is obtained. As we use finite periodicity it is possible to operate locally as we have done by reducing the amplitude with A , B or C . We have thus a flat extended structure that can propagate along the cylinder *via* a bilayer phase transition. In figure 13.3.3 $A = 1$, $B = 0.1$, and $C = 1$ and in figure 13.3.4 $A = 1$, $B = 1$, and $C = 0.1$. The flat region (it is cylindrical so the Gaussian curvature is zero) has moved a distance corresponding to three terms in the complete equation.

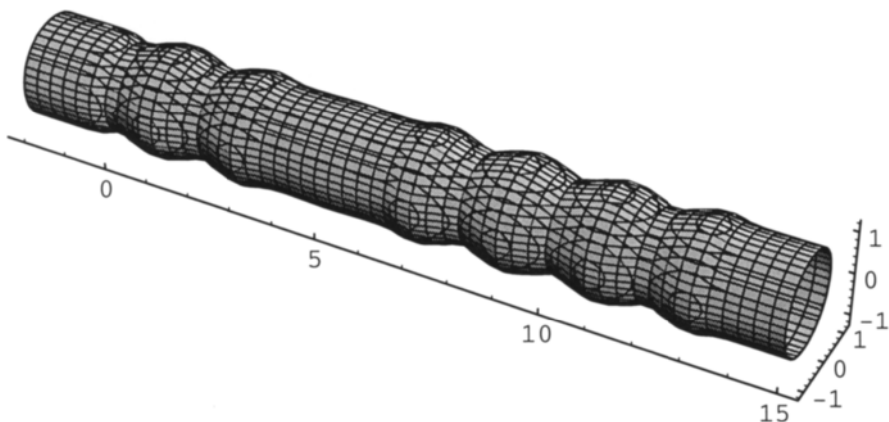


Figure 13.3.2 $A = 0.1$, $B = 1$, and $C = 1$ after equation 13.3.2.

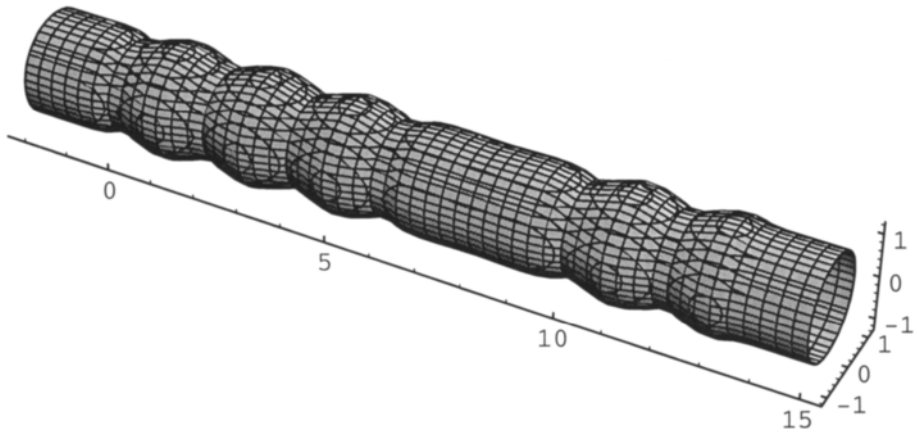


Figure 13.3.3 $A = 1$, $B = 0.1$, and $C = 1$ after equation 13.3.2.

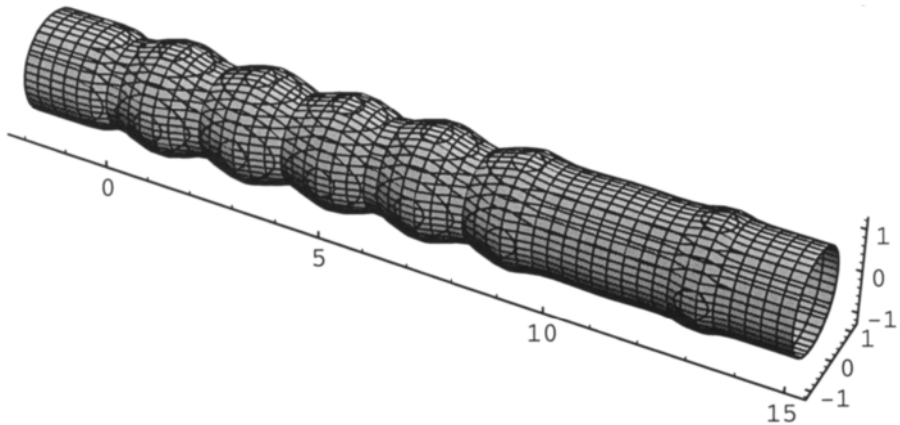


Figure 13.3.4 $A = 1$, $B = 1$, and $C = 0.1$ after equation 13.3.2.

This motion may equally well be described as a propagating phase transition as the flat region has an extension of its own. In chapter 8 we introduced oscillating wave conformations along a membrane due to bilayer elasticity. Loss of elasticity will result in a phase transition towards a flat membrane. When such a transition occur locally along an axon membrane, it will appear as a flat wave travelling in a curved membrane space.

There is another possibility of a bilayer transition in the axon membrane at depolarisation; a transition between different conformations of the periodic curvature of the bilayer. This alternative seems less likely, but is still shown below. It can be regarded as a martensitic transition along a cylindrical membrane.

We take the P-surface and add it to a cylinder, and do also put a stop to the infinite function so it only exists for values below x as in 13.3.3.

$$\cos \pi x + \cos \pi y + \cos \pi z + e^x + e^{(y^2+z^2)} \tag{13.3.3}$$

We do the same for the gyroid surface, so it only exists for values above x.

$$\cos \pi x \sin \pi y + \cos \pi z \sin \pi x + \cos \pi y \sin \pi z + e^{-x} + e^{(y^2+z^2)} \tag{13.3.4}$$

We lift both surfaces, separately, up on the exponential scale to protect them as in 13.3.5 and 13.3.6.

$$e^{-[\frac{1}{2}e^x + \frac{1}{2}(\cos \pi x + \cos \pi y + \cos \pi z) + e^{y^2+z^2}]} = \frac{1}{20} \tag{13.3.5}$$

$$e^{-[\frac{1}{2}e^{-x} + \frac{1}{2}(\cos \pi x \sin \pi y + \cos \pi z \sin \pi x + \cos \pi y \sin \pi z) + e^{y^2+z^2}]} = \frac{1}{20} \tag{13.3.6}$$

We do each of the surfaces and show this in figures 13.3.5 and 13.3.6.

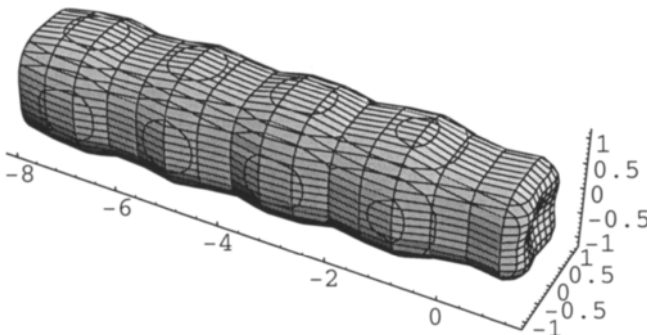


Figure 13.3.5 Cylindrical membrane with a P-type of surface curvature.

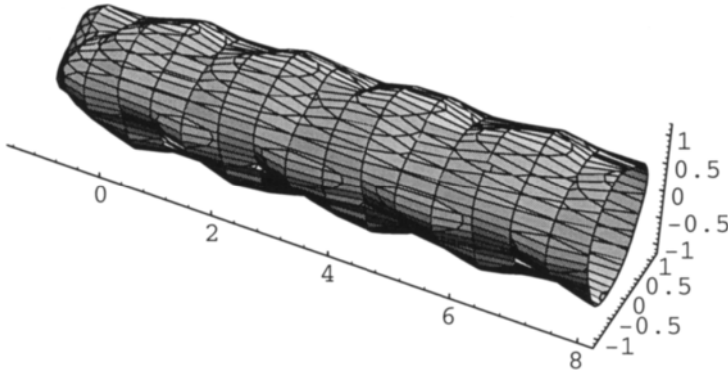


Figure 13.3.6 Cylindrical membrane with curvature according to the Gyroid surface.

We then add the two to get a transition phase boundary between the P- and the G-surfaces as in 13.3.7.

$$\begin{aligned}
 & e^{-\left[\frac{1}{2}e^{x-\Delta} + \frac{1}{2}(\cos \pi x + \cos \pi y + \cos \pi z) + e^{y^2+z^2}\right]} + \\
 & e^{-\left[\frac{1}{2}e^{-(x-\Delta)} + \frac{1}{2}(\cos \pi x \sin \pi y + \cos \pi z \sin \pi x + \cos \pi y \sin \pi z) + e^{y^2+z^2}\right]} = \frac{1}{20}
 \end{aligned}
 \tag{13.3.7}$$

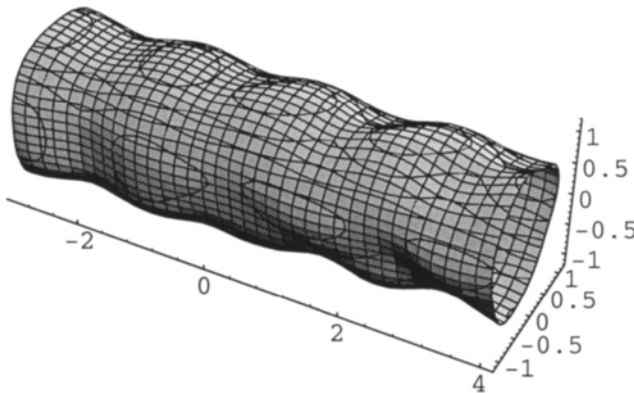


Figure 13.3.7 Phase transition in a cylindrical membrane between curvature according to the P- and the G-surfaces at $x=0$.

For $\Delta=0$ the boundary is at $x=0$, as in figure 13.3.7.

We have earlier proposed that phase transitions of lipid bilayers can be martensitic, which means that there is no nucleation, and therefore the transition speed can approach that of sound [5]. The transition between the $L\alpha$ -phase and the gel phase (crystalline chains) in phosphatidylethanolamine bilayers have been analysed and assumed to be martensitic with a rate of transition less than 1 ms [6]. The transition proposed should be even faster, as it does not involve chain crystallisation. The propagation of the signal will, due to cooperativity, be driven by both the electrical conduction with activation of adjacent ion channels and by the phase transition.

Any phase transition in a membrane is related to the mechanical properties of the bilayer. We repeat that thermal excitations will result in standing wave oscillations in a periodically curved elastic membrane, and an $L\alpha$ -type of bilayer is formed when the elasticity becomes very small. It is important in this connection to realise that the resistance against deformations *within* such a bilayer is much smaller than in periodically curved bilayers (due to the high inner packing pressure). The phase transition we have shown above into an $L\alpha$ -bilayer structure might therefore be needed in order to allow the conformational changes of the voltage-gated sodium channels. Sodium channels opened by some kind of excitation may even reduce the inner packing pressure enough to induce a bilayer transition into an $L\alpha$ -conformation. This in turn may simplify the opening of adjacent channels. Such parallel functions of voltage-gating and a bilayer transition is further developed below.

In considering the conformation of the C(2d)-bilayer, the axon diameter should also be taken into account. This diameter can vary from about 1000 Å up to extremes in the cm range. Undulations in the erythrocyte membrane have a wave-length of about 1000 Å (and an amplitude of about 100 Å) [7], and it seems reasonable to assume similar dimensions of the curvature periodicity in neuronal membranes. Therefore the curvature of a very thin axon will probably only show periodicity in the length direction. An example of such a bilayer is shown in figure 13.3.8a. It was obtained by equation 13.3.8.

$$x^2 + y^2 + 0.5\cos z = 12$$

13.3.8

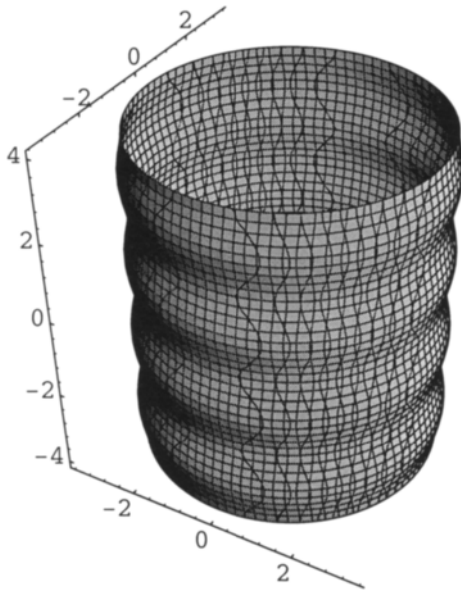


Figure 13.3.8a A periodically curved cylindrical surface according to 13.3.8.

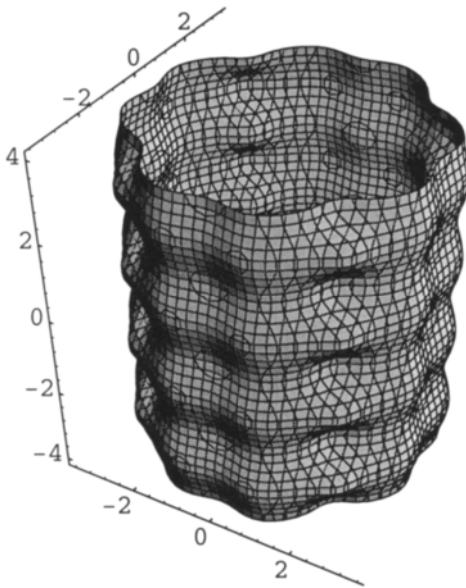


Figure 13.3.8b Cylindrical surface curved according to 13.3.9 applying a P-type of function.

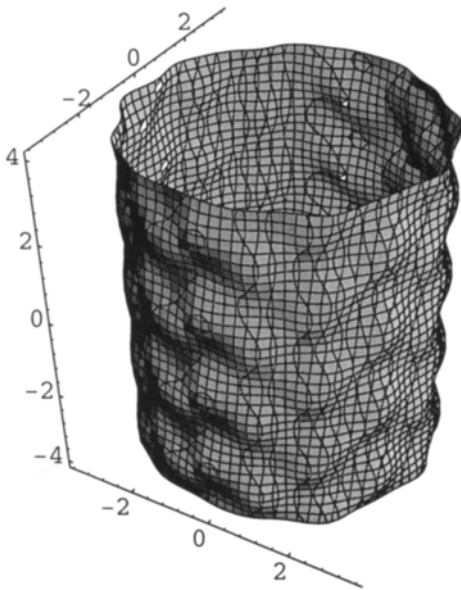


Figure 13.3.8c Cylindrical surface curved according to 13.3.10 applying a G-type of function.

Thicker axons should be expected to show periodicity, also perpendicular to the axon direction. Such conformations can be calculated by adding the D-, G- or P-surface curvature with some weight factor to a cylinder. Examples involving the P- and G-surface are shown in figures 13.3.8b and 13.3.8c respectively using equations 13.3.9 and 13.3.10.

$$x^2 + y^2 + \cos \pi x + \cos \pi y + \cos \pi z = 12 \quad 13.3.9$$

$$x^2 + y^2 + \frac{6}{10} [\cos \pi x \sin \pi z + \cos \pi y \sin \pi x + \cos \pi z \sin \pi y] = 12 \quad 13.3.10$$

A nerve of a higher animal usually consists of numerous nerve cells in a close-packed arrangement. An example is illustrated in figure 13.3.9. The inter-neuronal distances are even shorter in the brain.

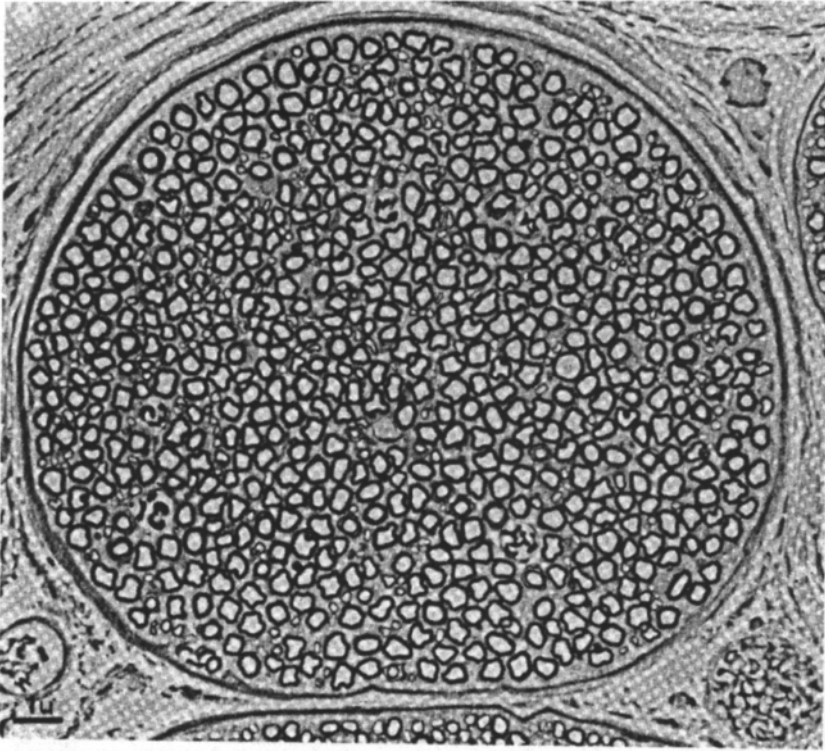


Figure 13.3.9 A section through a nerve trunk showing both myelinated (thick envelope) and unmyelinated axons, reproduced with permission from [4].

It seems likely that the electrical fields involved in the signal conduction along one axon membrane could cause disturbances in the signalling of an adjacent nerve cell, for example by inducing a false signal by triggering some voltage sensitive sodium channels. A dual mechanism, the proposed coupling between electrical and mechanical signal, would reduce the risk of conductance interference significantly.

Evidence for a phase transition occurring concomitantly with the action potential at depolarisation is given in the paragraphs 13.5 and 13.6 above. The conformation of a membrane protein, such as a voltage-gated channel, might be influenced by the conformation of the surrounding bilayer. This can lead to an increased excitability of the sodium channels during the phase transition from the C(2d)-bilayer into the L α (2d)-bilayer phase (e.g. a synergistic effect between bilayer transition and channel conformational change). If so, nature would have devised a system in which the nerve signal itself would be fool-proof. The electrical interference from neighbouring

neurons would not have any major effect, whereas an electrical pulse initiated by the neuron itself would be propagated as the phase-transition and the action potential will be coupled in time and space. Other physiological consequences of a mechanical wave component of the action potential is further discussed in the last paragraph of this chapter.

13.4 Transmission of the Nerve Signal at the Terminal Membrane of the Neurons - Synaptic Transmission

When the nerve impulse reaches the terminal region of the axon membrane, it is transmitted chemically to another neuron or to an effector cell, such as a muscle cell. This chemical coupling region is a *chemical synapse*. Transmitter molecules are released through the presynaptic region into the synaptic cleft. These molecules will diffuse over this narrow space and reach receptors specific to the transmitter at the postsynaptic membrane (of another neuron or an effector cell). The activation of the postsynaptic receptors by the chemical signal will change the ion permeability at the postsynaptic membrane which can lead to excitation or inhibition of the postsynaptic neuron or effector cell.

There are also *electrical synapses*, where the ions conducting the electrical signal can pass from one cell to another through *gap junctions*. In this way the signal is conducted by ions from one cell to another, *e.g.* in cardiac muscle cells. Sometimes electrical and chemical synaptic transmission can take place in the same synapse.

Gap junctions couple adjacent cells electrically or biochemically and have a wide range of applications. The channels are formed by hexameric proteins called connexons. Two connexons join across the intercellular gap and form the channel. The connexons tend to form a hexagonal pattern in each of the opposing membranes. The opening and closing of gap junctions is in general gated, but transitions between closed and open conformations occur less frequent than in other ion channels, and the regulation is not well understood.

An interesting feature of gap junction is the clustering of the connexons, which links the apposing membranes. This results in formation of two-dimensional crystalline order in the membranes, as is evident from the morphology of these clusters. An example of hexagon shape and truncated triangular shape is shown in figure 13.4.1.

The consequence of this crystallographical organisation is that also the lipid bilayer is a part of the two-dimensional crystal. Therefore like in

“ordinary” crystals, the motions should be coupled and follow the rules of standing waves. Thus the bilayer must move accordingly. A direct consequence of this is cooperativity in motions. Thus the opening or closing of one ion channel in a crystallographically perfect gap junction will be coupled with the same transition in neighbouring channels.

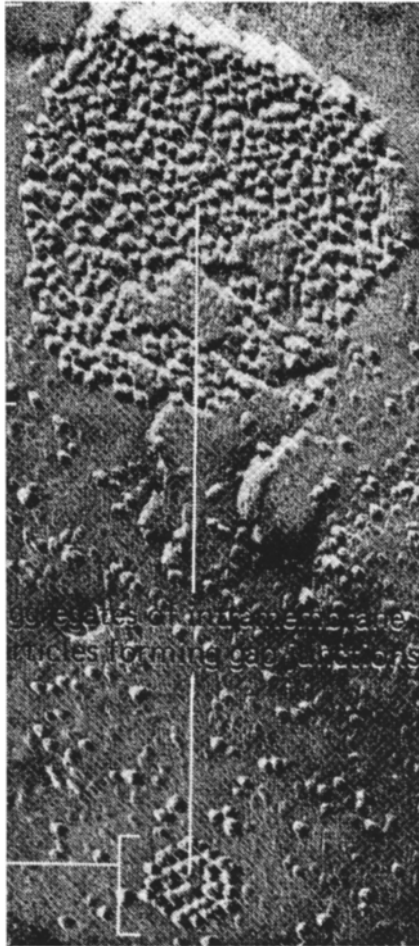


Figure 13.4.1 Gap junctions between cultured fibroblasts. Each intramembrane particle is a connexon, reproduced with permission from [16]. The text within the electron micrograph is “aggregates of intramembrane particles forming gap junctions”.

An example of a chemical synapse is the neuromuscular junction shown in figure 13.4.2. It is characterised by an extended systems of terminals at the

end of the axon, and each terminal presynaptic membrane is exposed towards a strongly expanded postsynaptic membrane.

The transmitter molecules, acetylcholine in this case, are stored in vesicles located near the presynaptic membrane. Each vesicle contains thousands of molecules. Influx of calcium ions at the synaptic terminal triggers the exocytosis of the vesicles loaded with transmitter molecules at the presynaptic membrane. The release takes place at certain “release sites”. The whole transfer process of chemical signals at the synapse is very efficient. Hundreds of signals can be transmitted within a second.

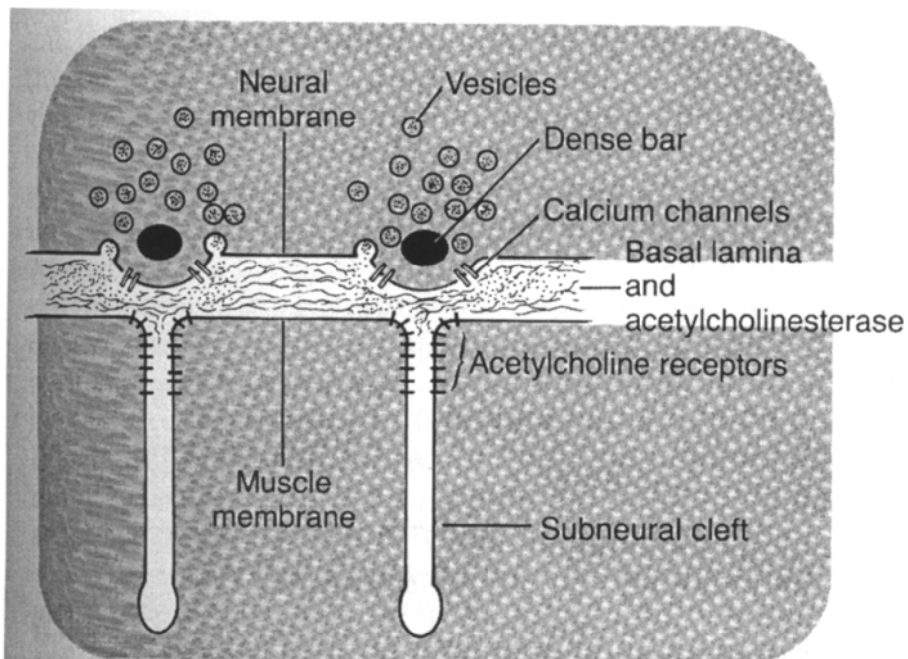


Figure 13.4.2 Illustration of the extended synaptic region at a human muscle end plate, reproduced by permission from [4]. Good electron micrographs showing the same texture can be found in [8].

The *central nervous systems* (CNS) use many different types of molecules in the synaptic transmission, although one neuron normally releases only one type of transmitter beside neuropeptides. Neuropeptides are a special group of transmitters in the brain. They are much more potent than small-molecule transmitters, and often they give long-term effects, such as prolonged closing of calcium channels. They are transported very slowly by streaming along the axon from the ribosomes where they are synthesised.

Ordinary transmitter molecules are synthesised in the cytosol at the synapse.

Signal transmission in the CNS also involves inhibitory synapses. These synapses open potassium and/or chloride channels, and cause an increase in potential negativity so that the signal amplitude needed to reach the threshold value for excitation is increased. Brain signalling involves many complex features but the main principles of synaptic transmission are the same in the whole nervous system.

Textbooks discussing the synaptic transmission usually ignore the lipid bilayer structure of the vesicles and the presynaptic membrane, and mechanisms controlling their fusion. In the well-known book FROM NEURON TO BRAIN, [19], it is stated that "... how the fusion occurs and the role played by calcium is not known". We propose here that the mass-co-operative fusion of vesicles is a local bilayer phase transition induced by calcium ions. It is well known that membrane lipid curvature is sensitive to variations in calcium ion concentration, and the bilayer curvature tend to change towards the reverse type of structure (cf. chapter 8) by addition of calcium ions. Experimental evidence for the involvement of a phase transition is also given here, based on the effect on membrane lipid phase behaviour by general anaesthetic agents. It is therefore natural to model the fusion process in the way as follows.

We will consider 12 vesicles regularly arranged at the presynaptic membrane (with somewhat different weighting to give to them the same size). The following equation gives the synaptic structure as shown in cross-section in figure 13.4.3a.

$$\begin{aligned}
 & e^{-[e^{2(x+2)} + 0.2(y^2 + z^2)]} + e^{-[e^{-2(x-2)} + 0.2(y^2 + z^2)]} \\
 & -e^{-2[(y-1)^2 + (x+3)^2 + (z)^2 - 0.5]} - e^{-6[(y-1)^2 + (x+3)^2 + (z-2)^2 - 0.5]} \\
 & -e^{-6[(y-1)^2 + (x+3)^2 + (z+2)^2 - 0.5]} - e^{-2[(y+1)^2 + (x+3)^2 + (z)^2 - 0.5]} \\
 & -e^{-6[(y+1)^2 + (x+3)^2 + (z-2)^2 - 0.5]} - e^{-6[(y+1)^2 + (x+3)^2 + (z+2)^2 - 0.5]} \quad 13.4.1 \\
 & -e^{-2[(y-1)^2 + (x+5)^2 + (z)^2 - 0.5]} - e^{-6[(y-1)^2 + (x+5)^2 + (z-2)^2 - 0.5]} \\
 & -e^{-6[(y-1)^2 + (x+5)^2 + (z+2)^2 - 0.5]} - e^{-2[(y+1)^2 + (x+5)^2 + (z)^2 - 0.5]} \\
 & -e^{-6[(y+1)^2 + (x+5)^2 + (z-2)^2 - 0.5]} - e^{-6[(y+1)^2 + (x+5)^2 + (z+2)^2 - 0.5]} \\
 & -0.4 = 0
 \end{aligned}$$

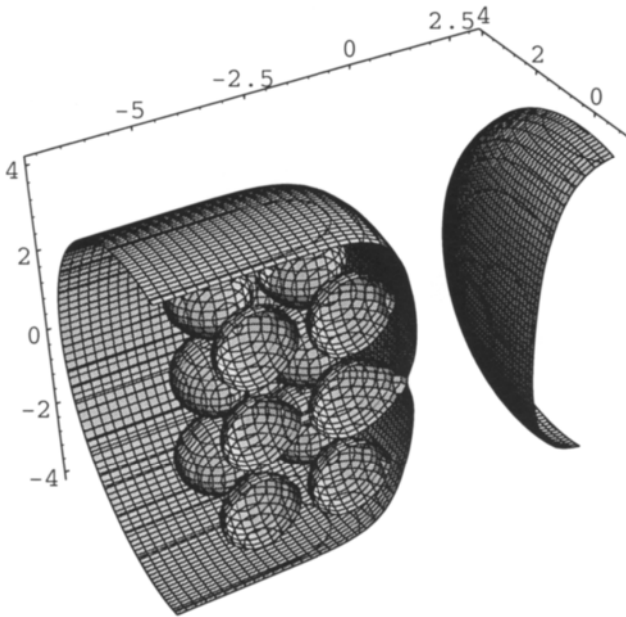


Figure 13.4.3a Vesicles at the presynaptic membrane according to 13.4.1.

From a mathematical point of view, vesicle-vesicle fusion as well as vesicle-synaptic membrane fusion may be obtained with change of constants, or with collective motion of the vesicles (mathematically similar). In the equation below we have moved the synaptic vesicles in this way. The result is a bilayer transition which leads to exocytosis of transmitter molecules into the synaptic cleft, see figure 13.4.2b.

$$\begin{aligned}
 & e^{-[e^{2(x+2)} + 0.2(y^2 + z^2)]} + e^{-[e^{-2(x-2)} + 0.2(y^2 + z^2)]} \\
 & -e^{-2[(y-1)^2 + (x+2.75)^2 + (z)^2 - 0.5]} - e^{-6[(y-1)^2 + (x+2.75)^2 + (z-2)^2 - 0.5]} \\
 & -e^{-6[(y-1)^2 + (x+2.75)^2 + (z+2)^2 - 0.5]} - e^{-2[(y+1)^2 + (x+2.75)^2 + (z)^2 - 0.5]} \\
 & -e^{-6[(y+1)^2 + (x+2.75)^2 + (z-2)^2 - 0.5]} - e^{-6[(y+1)^2 + (x+2.75)^2 + (z+2)^2 - 0.5]} \quad 13.4.2 \\
 & -e^{-2[(y-1)^2 + (x+4.5)^2 + (z)^2 - 0.5]} - e^{-6[(y-1)^2 + (x+4.5)^2 + (z-2)^2 - 0.5]} \\
 & -e^{-6[(y-1)^2 + (x+4.5)^2 + (z+2)^2 - 0.5]} - e^{-2[(y+1)^2 + (x+4.5)^2 + (z)^2 - 0.5]} \\
 & -e^{-6[(y+1)^2 + (x+4.5)^2 + (z-2)^2 - 0.5]} - e^{-6[(y+1)^2 + (x+4.5)^2 + (z+2)^2 - 0.5]} \\
 & -0.4 = 0
 \end{aligned}$$

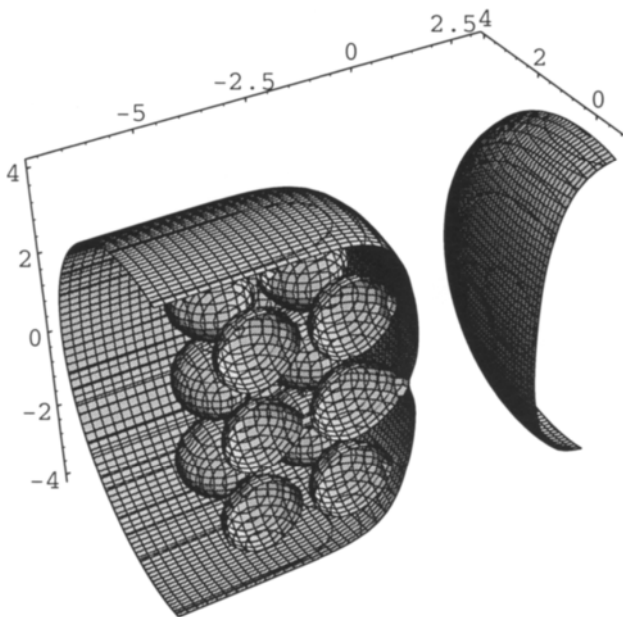


Figure 13.4.3b Illustration of co-operative fusion of synaptic vesicles with the presynaptic membrane according to 13.4.2.

Evidence for such a phase transition mechanism is provided by the effects of general anaesthetic agents, described below. In low concentrations they induce fusion of membrane lipid vesicles in model systems into a cubic phase, see paragraph 13.6. This transition can be reversed by pressure, just like the anaesthetic effect.

The vesicles are recycled in the presynaptic membrane. These cycles may also involve a bilayer phase transition. In principle this transition is the reversal of the transition shown in figure 13.4.3.

An additional feature of a phase transition wave, propagating with the electrical pulse along the axon, is the possibility of a direct coupling of events involved in the synaptic transmission. In chemical synapses an arriving action potential may *via* its adjoining bilayer transition induce the influx of calcium ions and vesicle fusion. In electrical synapses it may link the action potential to opening of connexons at gap junctions.

Release of transmitter molecules also involves proteins coating the vesicles (clathrins) controlling vesicle dynamics. Syntaxins are proteins with a

general function as receptors to provide specificity at docking and fusion of vesicles. One of them, syntaxin 5, controls transport between ER and Golgi [9]. Another, Syntaxin 1, is present at the synapse, both in the vesicles and the presynaptic membrane [10]. The specific traffic-controlling proteins and the bilayer transition might be mechanisms working in parallel, providing redundancy for control and safety, analogously to the wave transition coupled to the electrical signal in the action potential.

13.5 Synchronisation of Muscle Cell Activation

The functional unit of skeletal muscles is a motor neuron linked to the muscle cell *via* the muscle end plate, see figure 13.4.1. Acetylcholine molecules are transmitted to the muscle cell membrane (the sarcolemma), where an action potential is fired. The contraction mechanism is activated by calcium ion flux from the endoplasmatic reticulum of the muscle cell (termed sarcoplasmatic reticulum (SR)) to the T-tubuli system. This membrane system penetrates the muscle cell. It was shown in chapter 8 how it under pathological conditions can form cubosomes.

For control of movement of a skeletal muscle, the contraction of each individual muscle cell must take place simultaneously. This requires synchronisation of both action potentials and contraction. We discuss this question also in chapter 11, in relation to the crystallographic order within the actin-myosin complex.

The calcium release channels in the SR-membrane consist of a complex of four ryanodine receptor channels (RyR-1). This complex is stabilised by four molecules of a small protein molecule FKBP12, which also co-ordinates the opening and closing of the RyR-1-units of the tetrameric calcium channel. The channels are arranged in rows, separated by a short distance or in contact. Every second of these channels are associated to receptors termed DHPR in the T-tubuli membrane.

It has been assumed that surface membrane depolarisation, sensed by DHPR, triggers calcium ion release through the RyR-1-channels due to a mechanical coupling between the channel proteins and DHPR. Adjacent channels (that means every second channel which is not linked to DHPR) are assumed to open by the released calcium ions.

An interesting study has recently proposed that all the calcium channels release calcium simultaneously [11] due to a lateral mechanical link. Such co-ordinated channel opening contrary to stochastic opening would provide a fast calcium release.

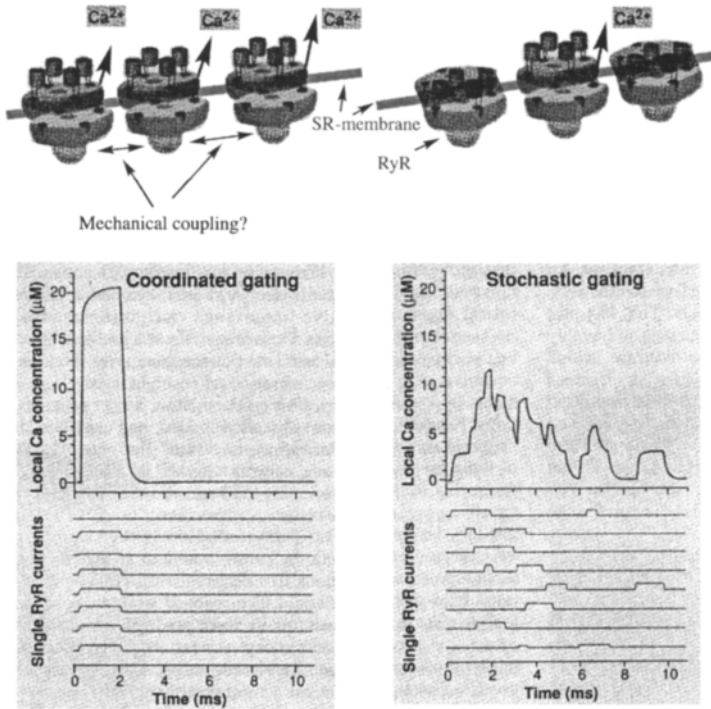


Figure 13.5.1 The coordinated (left) and the stochastic gating mechanisms (right) of calcium ion release into the T-tubuli system, modified after [12].

It also provides a mechanism for opening of the channels not associated to DHPR. The coupled opening is proposed to provide a “safety margin for excitation-contraction coupling” [12]. The two mechanisms are illustrated in figure 13.5.1.

A phase transition in the lipid bilayer, as described in connection with the action potential and synaptic signal conduction, can achieve the proposed mechanical coupling between the RyR-1 channels. The driving force for a phase transition switching all channels to open can be provided by the bilayer curvature changes at one channel. We therefore propose that the co-ordinating mechanism of the RyR-1 channel opening, like that of the voltage-gated sodium channel opening at the action potential propagation, involves a membrane bilayer phase transition.

13.6 The General Anaesthetic Effect

Ethyl ether was used by William Mortimer to reduce pain in tooth extraction, and he suggested to the surgeon Warren at Massachusetts General hospital to try it in surgery. The first operation seen by a large audience took place in October 1846, and it was a success. A year later, James Simpson in Glasgow started to use chloroform in childbirth.

General anaesthetic agents have their main effect on the central nervous system and block the sensory nerve impulses coming from peripheral nerves. These molecules inhibit the transmission of the nerve signal at the synapses. At higher concentrations (not used clinically though), they also block conduction of the electrical signal along axons.

A wide range of small molecules exhibit anaesthetic effects. Even the atomic state can block the nerve signal transmission; the noble gas xenon has been used clinically. Ethyl ether and chloroform have been used for a long time. Today methoxyflurane and halothane dominate. Other anaesthetic agents are nitrous oxide and fluroxene. A common feature is their lipophilic character.

The first theory of the effect was presented about a hundred years ago by Overton and Meyer. They demonstrated a direct relation between the anaesthetic potency (the critical concentration in order to reach an anaesthetic state) and the partition coefficient between olive oil and water.

In the 60's Pauling and Miller proposed that the anaesthetic agent formed hydrates which immobilised water at the membrane surface as a mechanism behind their physiological effect. Later it has been found that there are compounds with good anaesthetic effect which do not form hydrates, for example sulphur hexafluoride.

A third theory based on conformational changes of protein molecules was presented by Frank and Lieb in 1982 [13]. A protein used as a model for neuron membrane proteins, the enzyme luciferase, is inhibited by anaesthetic agents with no lipids present.

In connection with our work on curvature and periodicity in lipid-water systems and in membranes, it was natural to examine the effect of general anaesthetic agents on aqueous phase behaviour of lipids, cf. [13]. When chloroform, ethyl ether or halothane were added to an aqueous dispersion of a phospholipid L α -phase (forming liposomes or vesicles), the bilayers fused and formed a cubic phase. Concentrations of chloroform below 0.1 %

(w/w) in the water medium were enough to induce a transition of a dispersion of 5 % phospholipids in water.

Based on this work it was proposed that the anaesthetic effect is due to a favouring of a periodically curved conformation in the nerve membrane bilayer where the conformation is balancing between an $L\alpha(2d)$ and a $C(2d)$ state. Such conformational effects would block the phase transition proposed above to be involved in the synaptic transmission and in the action potential propagation. A simple model for the influence of membrane curvature on the conformation of an ion channel is shown in figure 13.6.1.

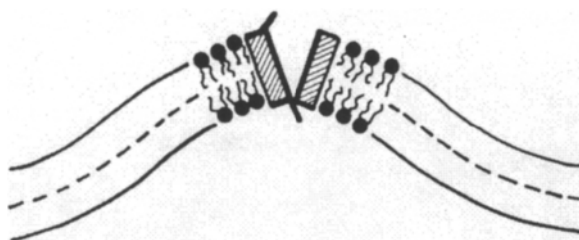


Figure 13.6.1 Schematic illustration of the axon membrane conformation favoured by general anaesthetic agents, and the proposed blocking effect of the state of ion channels, reproduced with permission from [18].

The well known pressure reversal of the anaesthetic effect can be explained by favouring of the planar ($L\alpha$ -type) conformation on behalf of the periodically curved bilayer. Pressure can be applied to achieve a phase transition from a lamellar ($L\alpha$) phase into a cubic phase (C). Analogously in two dimensions, pressure should be expected to favour a $C(2d)$ conformation in relation to the $L\alpha(2d)$ conformation.

As mentioned initially, the clinical application of anaesthetic agents use concentrations that only block the signal at the synaptic transmission, whereas the action potential conduction is not influenced. The change of the $L\alpha(2d)/C(2d)$ balance at the presynaptic region will tend to block the transition shown in figure 13.4.2 by stabilising the fused “cubic” related conformation of the bilayer.

It was explained in chapter 8 how the formation of a periodically curved bilayer is related to the existence of a high inner packing pressure in the hydrocarbon chain core. A mechanism of general anaesthesia has been proposed recently based on “lateral pressure profile in membranes” [15].

Needless to say this is just another way of describing the favouring of periodic curvature or $L\alpha$ -type of conformation.

Local anaesthetic activity is provided by a group of molecules which are weak bases (thus cationic) and contain an aromatic group. Lidocain was the first agent, which became widely used in clinical practice. They work by specific blocking of the sodium channels, and they have also some non-specific effect on the lipid bilayer. Their effect can thus be reversed by hydrostatic pressure (although only partly) like effects of general anaesthetic agents, indicating some influence on phase transitions in the neuron bilayer. Local anaesthetic agents are all amphiphilic and will therefore be solubilised in the lipid bilayers.

13.7 Physiological Significance of Involvement of a Lipid Bilayer Phase Transition in Nerve Signal Conduction

It may seem obvious that if a mechanical wave is involved in the conduction of nerve signals, as proposed above, a mechanical disturbance in the surrounding tissue can influence the signal. We believe that there is one such phenomenon, which we call *mechanical anaesthesia*.

The possibility to transfer mechanical energy over distances in a controlled way exists in animals living under water. Whales and dolphins have developed an advanced sonar system with high output-levels (over 200 dB) and a broad frequency range (40 to 140 kHz). There are increasing evidence that many whales and dolphins use the sonar system as an offensive weapon to paralyse its prey [20]. Applying our proposed model involving a mechanical component of the nervous signal, the mechanism where the high intensity mechanical pulses disturbs the nervous system may be understood. It is debated whether the “debilitation” of the prey is achieved by one acoustic pulse or by a train of sound waves. In both alternatives, such influence on the nerve system by mechanical waves seems natural if there is a mechanical component involved in the nerve impulse conduction.

A mechanical/electrical coupling may also extend the sensitivity of sensory neurons, as indicated by the following observation. A shark is able to detect a fish hidden in the sand from the gill movement, even though the electrical field from these nerve signals and muscle movements are much weaker than the electrical background noise [17]. A resonance amplification in the shark’s electrical sensors might be obtained by tuning their bilayer oscillations in phase with the neuron pulse train controlling the gill motion in the prey.

Experiments on the effects of ultrasound on the CNS of mammals have shown that pulse-trains of ultrasound administered at a rate of 4 to 10 pulses/second induce reversible effects on brain function and nerve conduction [21]. The energy intensities applied were considered to be non-thermal (10-50 mW/cm²). The frequencies of the administered signals is in the same range as we consider the “standing waves” of neuronal membranes to be in (see chapter 8), as based on the oscillation frequency of erythrocyte membrane undulations.

Another interesting phenomenon is the effects of magnetic fields on brain functions. It has been documented that extremely weak oscillating magnetic fields can influence the human brain [22]. Alternating fields with complex waveforms with a frequency of 4Hz and a strength of about 1 microtesla were used. As currents pass through the ion channels in the neuronal cell membrane, an applied magnetic field will result in a mechanical force perpendicular to the applied field and to the current passing through the ion channels. If there are wave motions at the neuronal membranes one should therefore expect that the resulting mechanical force will affect these motions, especially if the signal is administered at a resonant frequency in phase or out of phase with the neuronal membrane oscillations. The net result would be a disturbance of the “mechanical” component of the nerve signal thus affecting neuron function.

References 13

- 1 N. Bohr, *Atomfysik og menneskelig erkendelse*, Bonniers, Stockholm (1958).
- 2 I. Tasaki, M. Hallet and E. Carbone, *J. Membrane Biol.* **11**, 353 (1973).
- 3 P. Kinnunen, *Chem. Phys. Lipids* **57**, 375 (1991).
- 4 A. C. Guyton, *TEXTBOOK OF MEDICAL PHYSIOLOGY*, 8th ed, W. B. Saunders Co., Philadelphia (1991).
- 5 S. Andersson, S. Hyde, K. Larsson and S. Lidin, *Chem. Rev.* **88**, 2212 (1988).
- 6 P. Laggner and M. Kriechbaum, *Chem. Phys. Lipids* **57**, 121 (1991).

-
- 7 K. Zeeman, H. Engelhart and E. Sackmann, *Eur. Biophys. J.* **18**, 203 (1990).
 - 8 R. D Adams, M. Victor, and A. H. Ropper, *PRINCIPLES OF NEUROBIOLOGY*, Sixth Ed., McGraw-Hill, New York (1997).
 - 9 T. Rowe, C. Dascher, S. Bannykh. H. Plutner and W. E. Balch, *Science* **279**, 696 (1998).
 - 10 C. Walch-Solimena et al., *J. Cell Biol.* **128**, 637 (1995).
 - 11 S. O. Marx, K. Ondrias, and A. Marks, *Science* **281**, 818 (1998).
 - 12 D. M. Bers and M. Fill, *Science* **281**, 790 (1998).
 - 13 N. P. Frank and W. R. Lieb, *Nature* **300**, 487 (1982).
 - 14 K. Larsson, *Langmuir* **4**, 215 (1988).
 - 15 R. S. Cantor, *Biochemistry* **36**, 2339 (1997).
 - 16 N. B. Gilula, *CELL COMMUNICATION*, Ed. R. P. Cox, John Wiley & Sons, Inc., (1974).
 - 17 Research news comment, *Science* **272**, 646 (1996).
 - 18 S. Hyde, S. Andersson, K. Larsson, Z. Blum, T. Landh, S. Lidin and B. Ninham; *THE LANGUAGE OF SHAPE*, Elsevier, Amsterdam, 1997.
 - 19 J. G. Nichols, A. R. Martin and B. G. Wallace, *FROM NEURON TO BRAIN*, THIRD ED., Sinauer Ass. Publishers, Mass, US (1992).
 - 20 K. S. Norris and B. Möhl, *The American Naturalist* **122**, 85 (1983).
 - 21 V.A. Velling and S.P. Shklyaruk, *Neurosci Behav Physiol.* **5**, 369 (1988).
 - 22 P.M. Richards, M.A. Persinger and S.A.Koren, *Intern. J. Neuroscience* **71**, 71 (1993).

This Page Intentionally Left Blank

14 The Lung Surface Structure and Respiration

Dum spiro spero (as long as I breathe I hope).

An interpretation of Cicero's *Epistolae ad Atticum*.

There is a highly organised structure at the alveolar surface called tubular myelin, which has been considered to provide a depot for a lipid-protein monolayer towards air. Tubular myelin was earlier assumed to consist of intersecting bilayers. We give evidence for a quite different structure of tubular myelin, with the bilayer forming an intersection-free classical minimal surface, the tetragonal CLP-surface. It is demonstrated how this CLP-structure forms a coherent surface phase, which rules out the generally accepted monolayer model of the alveolar surface. The CLP-bilayer of this surface phase forms the interface towards air simply by opening up along the methyl end group planes of the bilayer. The mathematics introduced in this book have been a prerequisite for describing the dynamics of this alveolar surface structure during respiration.

14.1 The Alveolar Surface

Terrestrial organisms, birds and insects exchange gases needed in their metabolism with surrounding air. Plants consume carbon dioxide and expire oxygen whereas land-living animals and whales survive through the reverse gas exchange. The gas transport at the surface takes place by diffusion. Larger animals need *ventilation* to increase the gas transport; they breathe. The lungs take care of this gas exchange, the *respiration*, involving both convection and diffusion.

The lungfish is considered to be the first animal breathing air. Next in the evolution came amphibia with better developed lungs but still they needed an additional gas exchange through their wet skin.

Our lungs expose the surface of a tennis court towards air, with millions of mm. size vesicles, the alveoli, forming the endings of the bronchial tree. The alveoli are located at the pulmonary capillaries, where oxygen-deficient blood from peripheral tissues takes up oxygen and leaves its load of carbon dioxide.

The oxygen consumption at rest is about 0.3 litre/minute, whereas the carbon dioxide excess is about 0.25 litre/minute. The air that reaches the alveoli has reached body temperature and is fully saturated by water after the transport through the respiratory system.

To fill air into the lungs it is necessary to overcome the surface tension in each alveolus. The pressure difference across the interface is proportional to the surface tension, and it is also related to the curvature (for spheres like alveoli defined by their radius r) according to Laplace's law;

$$\delta p = 2\gamma / r$$

where δp is the pressure gradient over the surface and γ is the interfacial tension.

We will describe how the dynamic interfacial tension of the alveolar surface is controlled by a lipid-protein, liquid-crystalline "surface phase", cf. [1].

14.2 Lung Surfactant

The term lung surfactant is used for the lipid-protein complex excreted from type II epithelial cells. The pathway for the surfactant to the alveolar surface is illustrated in figure 14.2.1. The surfactant complex form liposome-like structures called lamellar bodies (LB), which are rearranged into so-called tubular myelin (TM). TM is highly organised, and is considered to serve as a precursor for a surfactant monolayer at the interface towards air. This has been the generally accepted model of the surface of pulmonary alveoli for a long time.

There are, however, experimental observations which contradict the monolayer theory although they seldom are discussed (probably due to lack of an alternative model). One example is a study where a rabbit lung was filled with hexadecane in order to better preserve the surface film. A multilayer lining of the alveolar surface was then observed [3] as shown in figure 14.2.2.

The surfactant in its native form is a lipid bilayer containing about 10% (w/w) proteins. The lipids are dominated by dipalmitoyl-phosphatidylcholine (DPPC) (about 80%), and the second most abundant lipid (about 10%) is phosphatidylglycerol (PG). In premature mammals, most of the phosphatidylglycerol is replaced by phosphatidylinositol. This lipid is also anionic and should be expected to exhibit similar structural behaviour.

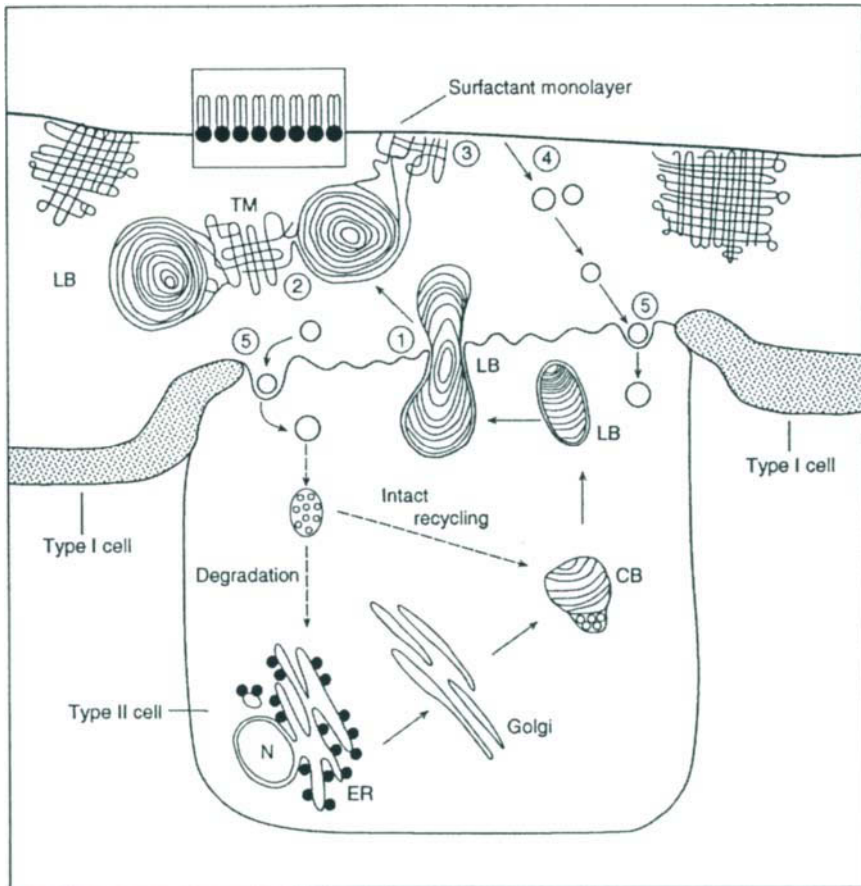


Figure 14.2.1 Diagram illustrating the traditional monolayer model of the alveolar surface and the pathways of lung surfactant, reproduced with permission from [2]. The aggregate structures are explained in the text. The numbers 1-3 indicate surfactant transport to the surface and 4,5 illustrate circulation back.

The proteins are dominated by the four surfactant proteins A-D (SP-A, SP-B, SP-C, SP-D). SP-A and SP-D are hydrophilic, and form well-defined micelle-like oligomers [4]. Thus six trimers of the SP-A monomer (28-36 kD depending on degree of glycosylation) form a funnel-shaped aggregate, whereas four trimers of SP-D associate into a symmetric oligomer. The proteins SP-B and SP-C are extremely hydrophobic.

The surfactant proteins determines the structure of the surfactant bilayer. The addition of SP-B to DPPC/PG mixtures yield structures similar to TM. The morphological changes of the bilayer into TM, as shown in figure

14.2.1, are induced by calcium ions. It can also be mentioned that the surfactant proteins have immunological functions, such as stimulating macrophage chemotaxis.

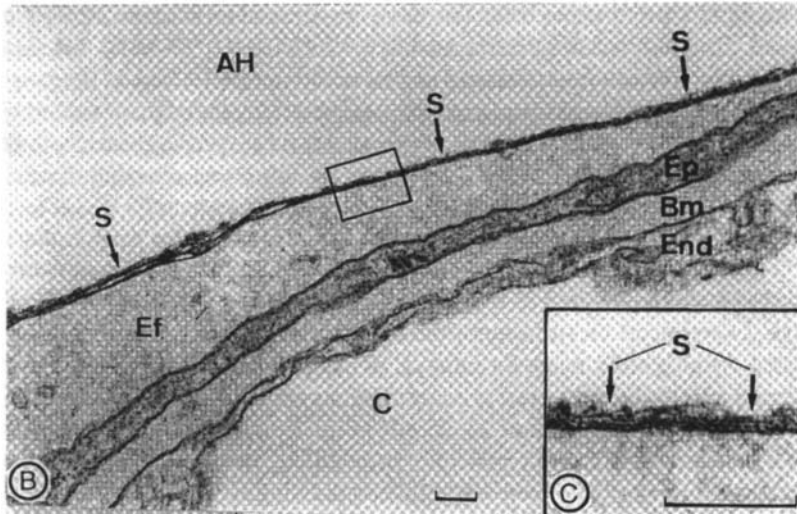


Figure 14.2.2 Rabbit lung fixed by vascular perfusion after filling the lung with hexane, reproduced with permission from [3]. Scale marker 1 micron. AH alveoli after contact with hexane, S multilayer of surfactant lining the surface, Ef edema fluid, Ep epithelial cell layer, Bm basement membrane, C capillary lumen and End endothelial cell layer.

Hills [5] has in his book described the fascinating history behind the discovery of surfactant at the surface of alveoli. The most important step was measurements of the surface tension of water when samples from lung washings were added, proving the existence of a surface-active material. Even today, however, the exact value of the surface tension reduction is under debate (cf. [5]) ranging from values close to zero up to about 20 mN/m.

14.3 Structure of Tubular Myelin - A Bilayer arranged as the Classical CLP-Surface

The schematic structure of TM indicated in figure 14.2.1 is based on numerous electron microscopy studies. The name was chosen due to some resemblance with the so-called myelin figures, a term used to describe the

texture in the polarising microscope of myelin and later used for similar optical textures of phospholipid samples dispersed in water. The optical birefringence in such samples, however, has no direct relation to electron microscopy textures.

Typical electron microscopy textures of TM are shown in figures **14.3.1** and **14.3.2**.

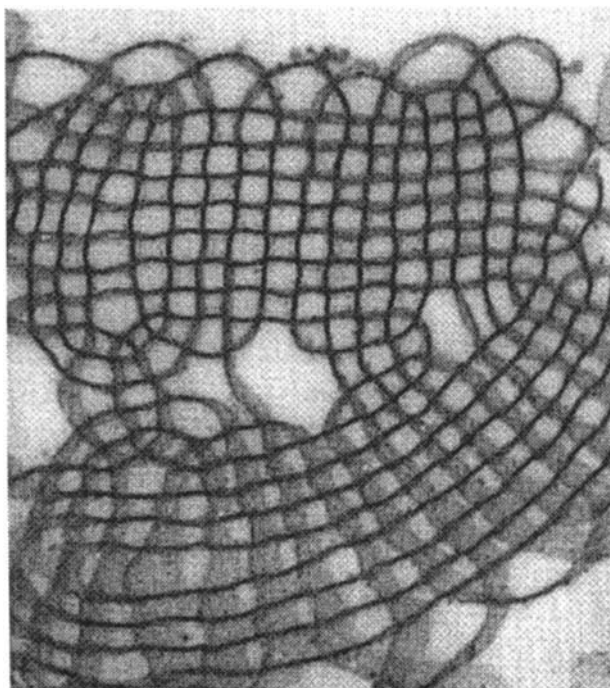


Figure 14.3.1 A transmission electron micrograph of an ultrathin section of tubular myelin from a fetal rat lung, reproduced by permission from [7].

The diameters of the TM aggregates are 2-3 microns. The closing of the bilayer towards an outside water phase seen in figure **14.3.1** is also a characteristic feature, which has been observed in many other studies.

Interpretations of the observed TM texture assumes that the lipid bilayers are parallel to two perpendicular planes, which intersect so that the cross-section form a square pattern. Deviations from that, as seen for example in figure **14.3.2**, have been interpreted as deformations of the square pattern.

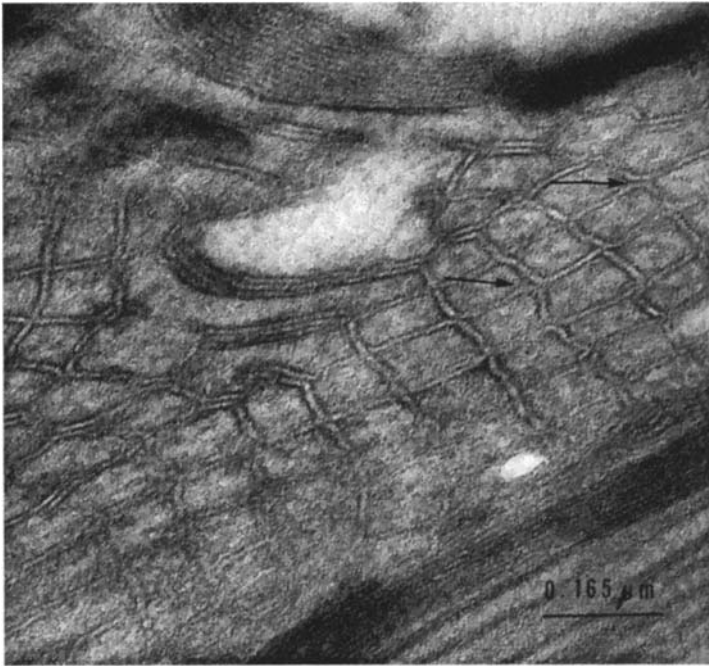


Figure 14.3.2 Tubular myelin near a dissociating lamellar body. Electron micrograph of a rat lung sample, after [6]. The two sides of the bilayer are seen, and at some locations (arrows) it can be observed how the bilayers appear to cross each other but there is no intersection.

A different structure was recently proposed based on a cryo transmission electron microscopy study [1]. Furthermore the surface lining was observed to consist of a uniform and coherent phase. This *surface phase model* was derived by the mathematics we describe in this book, and we will therefore describe it in detail in order to illustrate the potential of our approach.

First it was concluded from the EM data that TM consists of a lipid-protein bilayer according to the classic CLP-surface. Weierstrass parametrisation of this minimal surface was first derived by Lidin and Hyde [8]. Characteristic features of this structure are:

- The bilayers can cross each other without intersection. Intersecting bilayers, as in the earlier structure interpretation, have never been observed in any lipid-water system.

- This structure is a minimal surface, which we know is a common structure principle of lipid bilayers.
- This structure is able to explain several physiological phenomena previously not understood, such as:
 - Hysteresis during tidal breathing.
 - Ultra low surface tension.
 - The dry/wet alveolus debate.
 - Release kinetics of pulmonary administered pharmaceuticals.

Applying a nodal surface approach, we derived the following simple mathematical function of the CLP-surface [1]:

$$\cos \frac{\pi}{4}(x-y)e^{\frac{1}{40} \cos \pi z} - \cos \frac{\pi}{4}(x+y) = 0 \quad 14.3.1$$

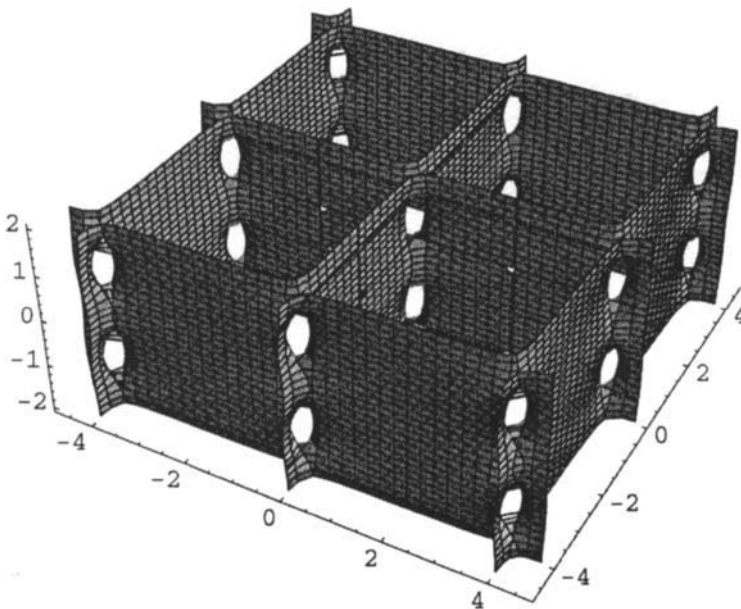


Figure 14.3.3. A part of the CLP-surface calculated according to formula 14.3.1, defining the structure of TM.

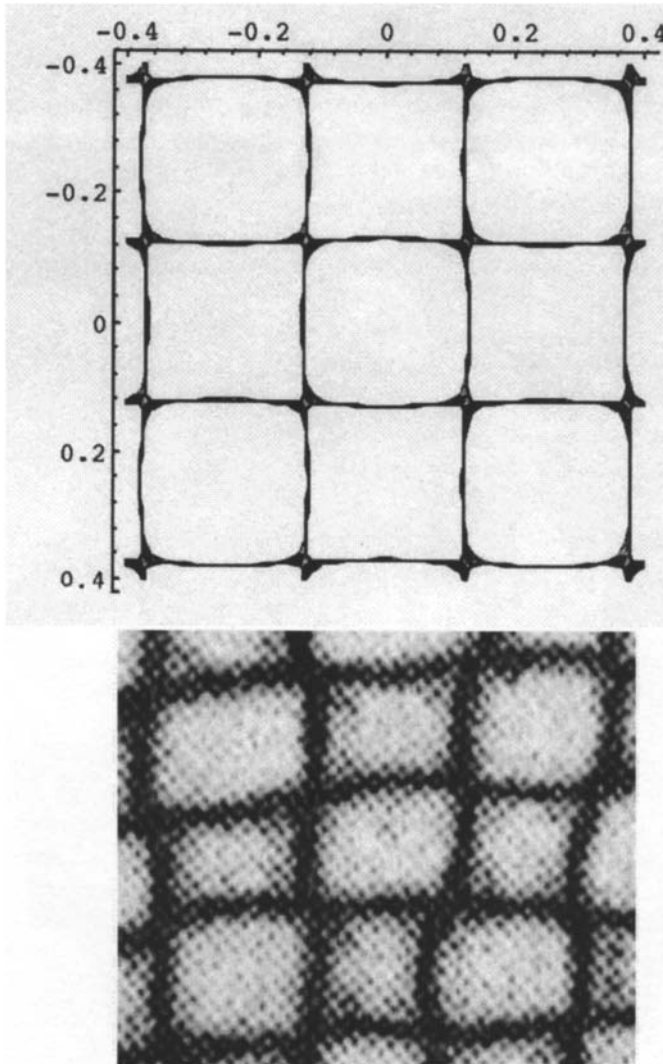


Figure 14.3.4 The characteristic electron microscopy square net texture reproduced from Young et al. [7] is shown (lower fig.) together with a cross-section of a thin slice of the calculated surface shown in figure 14.3.3.

The CLP-surface is shown in figure 14.3.3. A slice of the structure projected along the c -axis forms the characteristic square pattern. The size and the shape of the openings between the tubular units can be varied by variation of a constant in the equation. The value 40 was used in equation

14.3.1 in order to obtain circular openings. A tendency to favour a circular shape compared to an elliptic one under relaxed conditions seems likely with regard to the liquid character of the bilayer. As usual, the surface represents the centre of the bilayer. Obviously it is one single bilayer free from self-intersections and curved to form a tetragonal structure. Two sets of planes can go through each other via saddles. The average curvature is zero everywhere whereas the Gaussian curvature varies between near zero at the dominating planar (or almost planar) regions to maxima (of the absolute values) at the openings between the tubular structure units.

The relation between the calculated structure according to our CLP-bilayer model and an observed cross-section of TM is shown in figure 14.3.4.

The possibility of intersection-free crossing of the bilayers is also confirmed in certain electron micrographs. One such crossing can be observed in figure 14.3.2, showing both surfaces of the bilayer (marked by arrows).

14.4 The Existence of a Coherent *Surface Phase* Lining the Alveoli

By depositing the surface layer of freshly opened and blood free rabbit lung directly on the electron microscopy grid, it was shown that the TM structure forms a coherent *phase* lining the lung alveoli [1]. In order to reduce the risk of artefact formation we used cryo transmission electron microscopy (cryo-TEM). The grid with the deposited surface film is plunged into liquid ethane and frozen so rapidly that the water does not crystallise but forms amorphous ice, also called vitrification. The microscopy sample is kept at a temperature below -160°C and the water is present during the recording of the micrographs. The natural contrast of the sample is utilised, thus no staining of the samples is required, cf. [10].

A deposited alveolar surface sample is shown in figure 14.4.1. The distance between the layers is in good agreement with earlier reported values of about 40-60 nm.

Important independent evidence comes from another technique with reduced risks for artefacts; freeze-fracture electron microscopy, cf. [9]. The occurrence of some pattern at the surface is characteristic for a phase with a certain organisation, like a liquid crystal, contrary to a true liquid (water covered by a monolayer). Such patterns were observed.

An *en face* freeze fracture replica of the alveolar surface from a rat lung is shown in figure 14.4.2a.

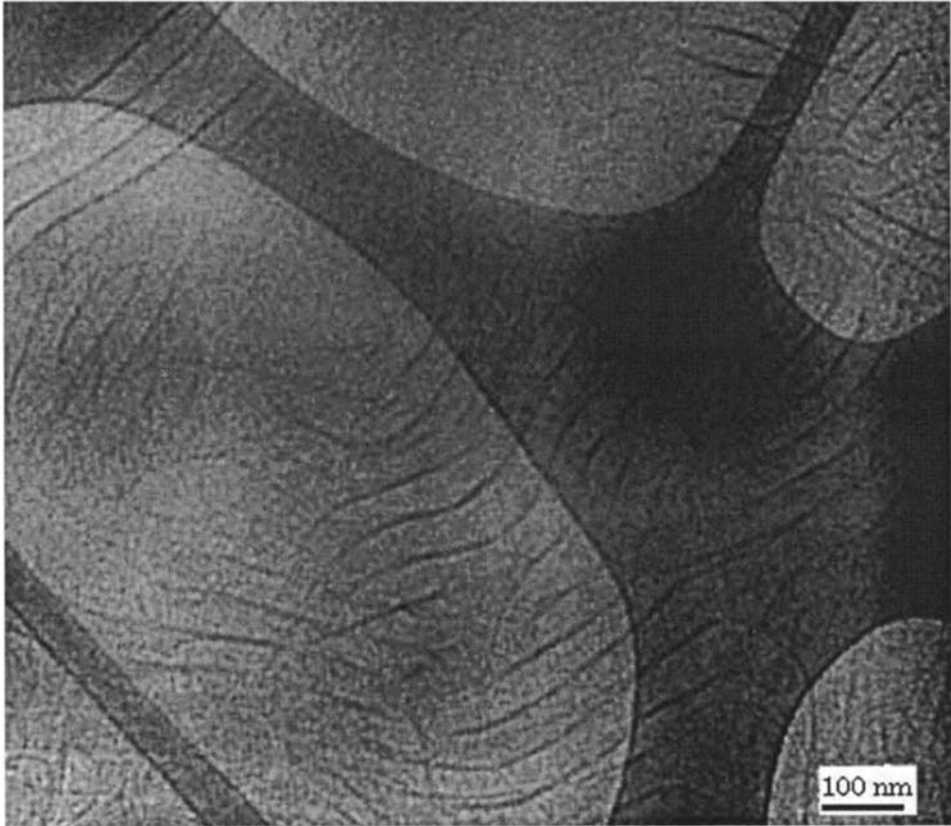


Figure 14.4.1 The cryo-TEM texture of the deposited alveolar surface layer observed to form a coherent phase. The tubuli are mainly oriented in parallel with the surface plane, after[1].

The linear grooves are 60 to 100 nm apart. This texture is also consistent with the ordered array of bilayers seen in figure 14.4.1, although the bilayers appear to be somewhat more disordered here (maybe a consequence of the replication technique). The important feature of the observed texture is that the surface is not smooth, but shows hills and valleys, with distances related to the periodicity seen in figure 14.4.1. Thus also this work supports the proposed existence of a surface phase. A “free” monolayer on an aqueous phase would be expected to show a smooth surface texture.

It should be mentioned that the author behind this study [9] even states “the walls of tubular myelin seem to constitute the surface film” in the comments to a micrograph of a fracture through the alveolar lining, which is shown in figure 14.4.2b.



Figure 14.4.2a Electron micrograph of a replica of the alveolar surface, reproduced with permission from [9].

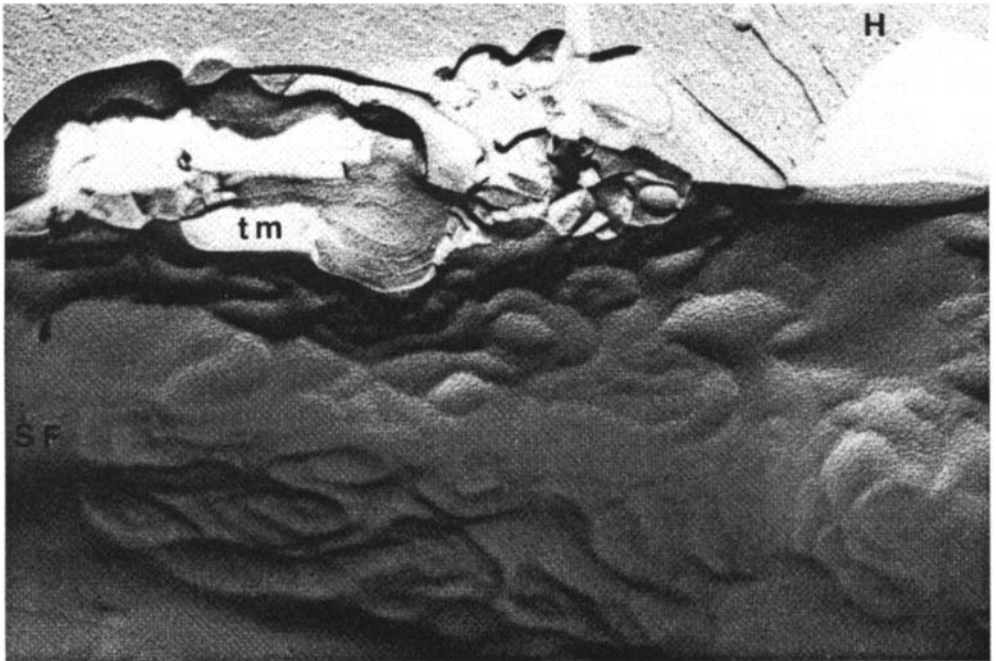


Figure 14.4.2b Fracture through the alveolar surface layer (freeze-fracture)Hypophase (H), Surface film (SF) Tubular myelin (tm), reproduced with permission from [9].

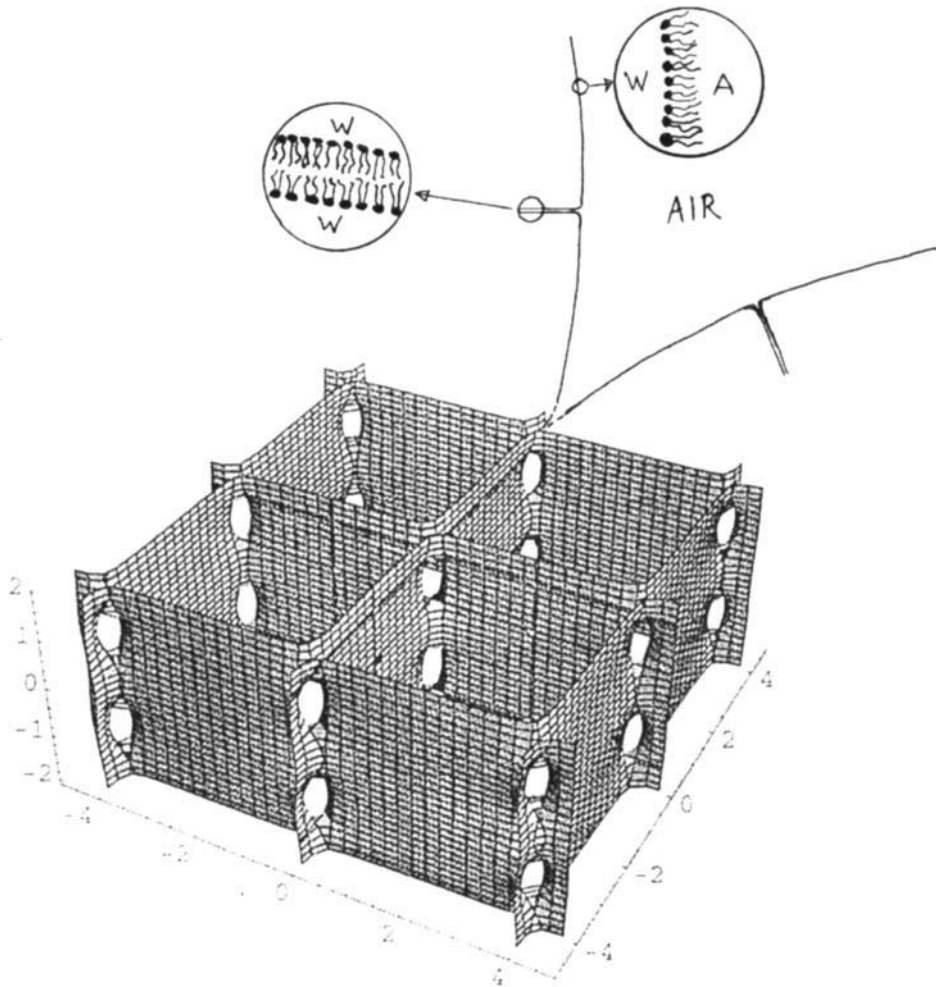


Figure 14.4.3 An alternative of interface structure formation by opening of the CLP-bilayer structure at the methyl end group surface when it becomes exposed to air (the polar head groups of the lipid molecules are indicated by circles and the two attached hydrocarbon chains are shown by their chain axes).

There are many ultrastructural studies in the literature on TM demonstrating the square pattern formed by the bilayers. Most samples have been prepared from lung washings, which means that a surface phase has been dispersed. Still, some of the samples show structurally homogeneous regions extending up to several microns (see for example figure 14.3.1). Available data are thus consistent with a uniform *phase* lining the alveolar surface which has a *CLP-bilayer structure*.

The surface phase is a liquid-crystalline type of lipid bilayer phase with water on each side of the bilayer. The bilayer, curved as a CLP-surface, has a general resemblance with the cubosome-types of structure we have seen earlier in this book. This phase can easily and fast open up an interface towards air. It can also form a closed bilayer towards a water phase underneath. We will see below that this structure is ideal for forming such interfaces.

The general occurrence of phases at interfaces in lipid-water systems is a neglected phenomenon. Emulsion stability is often due to a lamellar liquid-crystalline phase between oil droplets and outside water. The cubosomes also illustrates this. “Synthetic“ cubosomes of high kinetic stability can be prepared in systems of pure lipids provided that three phases exist in equilibrium; a cubic phase, a lamellar phase and water. Mechanically it is possible to prepare colloidal particles from such a three-phase mixture, with the lamellar phase forming an envelope on a cubic phase core.

We will now demonstrate how the CLP-bilayer structure can form an interface towards air outwards and an aqueous phase inwards. We will describe two alternatives of interface formation towards air. The driving force for reorganisation of the lipid bilayer into a monolayer towards air is the reduction in free surface energy. The CLP-bilayer may open up along the mid-surface, to give an interface towards air consisting of the methyl end groups of the lipid acyl chains.

Figure 14.4.3 shows one possibility of how an interface towards air can be formed by opening up the lipid bilayer at the gap between the methyl end groups. Let us assume that the phase flows up through the water medium surrounding the lamellar bodies, from which the structure is formed, and reaches the surface towards air. The two regions on each side of the air medium (see figure 14.4.3) can spread laterally along the alveolar surface.

Whether or not there exists “free” water together with the surface phase in the alveolus is further considered below. If free water is present it must correspond to water which can not be accommodated into the bilayer-water structure. The surface phase with the lipid bilayer CLP-surface swells to a maximum water content of about 90% (w/w), and if more water is present it will coexist in equilibrium with the surface phase. The structure formed in the case that there is a water phase underneath must consist of a closed bilayer. Figure 14.4.4 illustrates how the surface phase can form the complete lining of the alveolar surface. This surface structure towards an outside water phase is consistent with results from experimental ultrastructural studies of lung washings, cf. figure 14.3.1.

The “flat” interface towards air in figure 14.4.4 is one of two principal possibilities. The second alternative of surface phase interface towards air involves the formation of a curved surface, like the surface towards an outside water phase shown in figure 14.4.4. This surface structure alternative is shown in figure 14.4.5. We consider the occurrence of “hills and valleys” as seen in freeze fracture images of the alveolar surface (cf. figure 14.4.2) as evidence supporting this surface structure alternative.

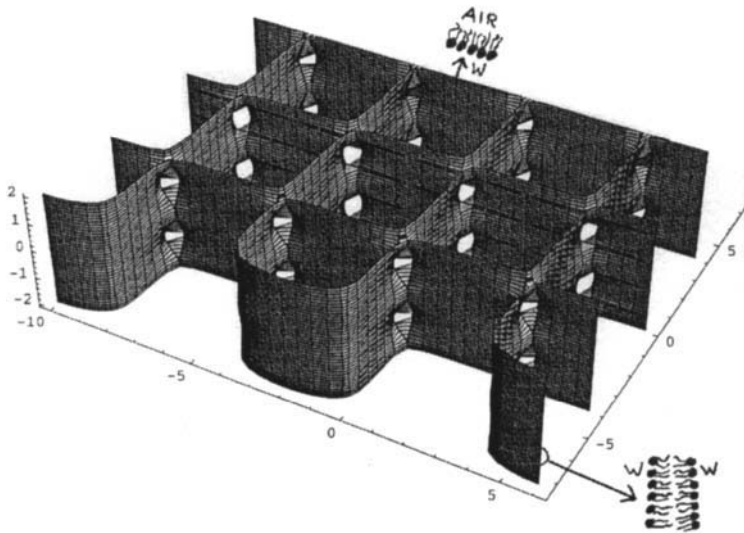


Figure 14.4.4 The alveolar surface phase and its structure towards air above (one of two alternatives, cf. figure 14.4.5) and water or a hydrophilic medium underneath.

A dynamic model indicating how the produced TM from lamellar bodies (LB) is condensed to form the surface phase is illustrated in figure 14.4.6. An important aspect is the occurrence or not of “free” water. We believe that a normal lung has very small (thin) regions where a water phase exists between the epithelial cells and the CLP-surface phase (tubular myelin). Lamellar bodies, macrophages and cell residues occurring in this zone require an aqueous environment. These regions are of course hydrophilic.

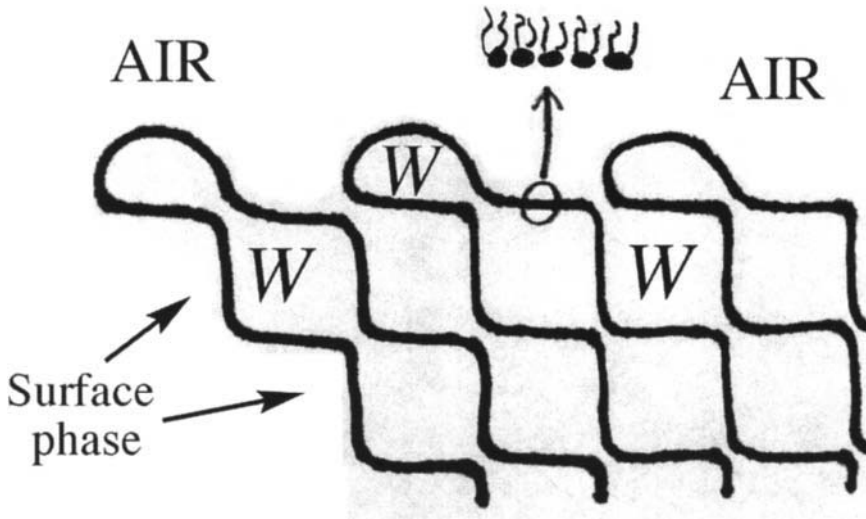


Figure 14.4.5 Schematic illustration of an alternative organisation compared to that in figure 14.4.4 towards air. A cross-section through the surface phase is shown at a fixed z-value of the CLP-structure, where the surface structure towards air is closed in the similar way as the surface towards an outside water phase (as shown in figure 14.4.4). Sections above or below in the z-direction will show the bilayer tilted in the opposite direction, and when these two orientations overlap we get the TM square pattern.

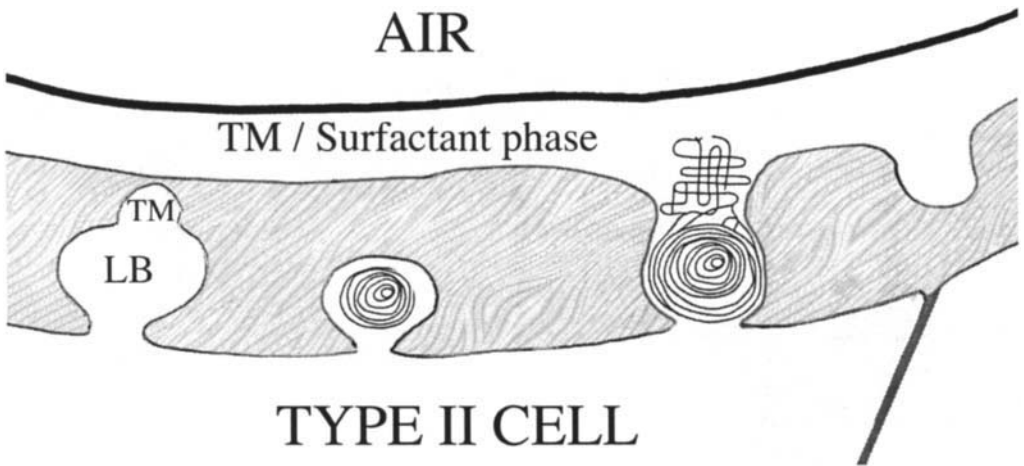


Figure 14.4.6 Illustration of flow of TM from type II cells *via* lamellar bodies (LB) to form a coherent surface phase. The shaded regions show the localisation of a hydrophilic medium, which in the case of edema (cf. figure 14.4.2) is a “free” water phase (coexisting in equilibrium with a maximally swollen surface phase).

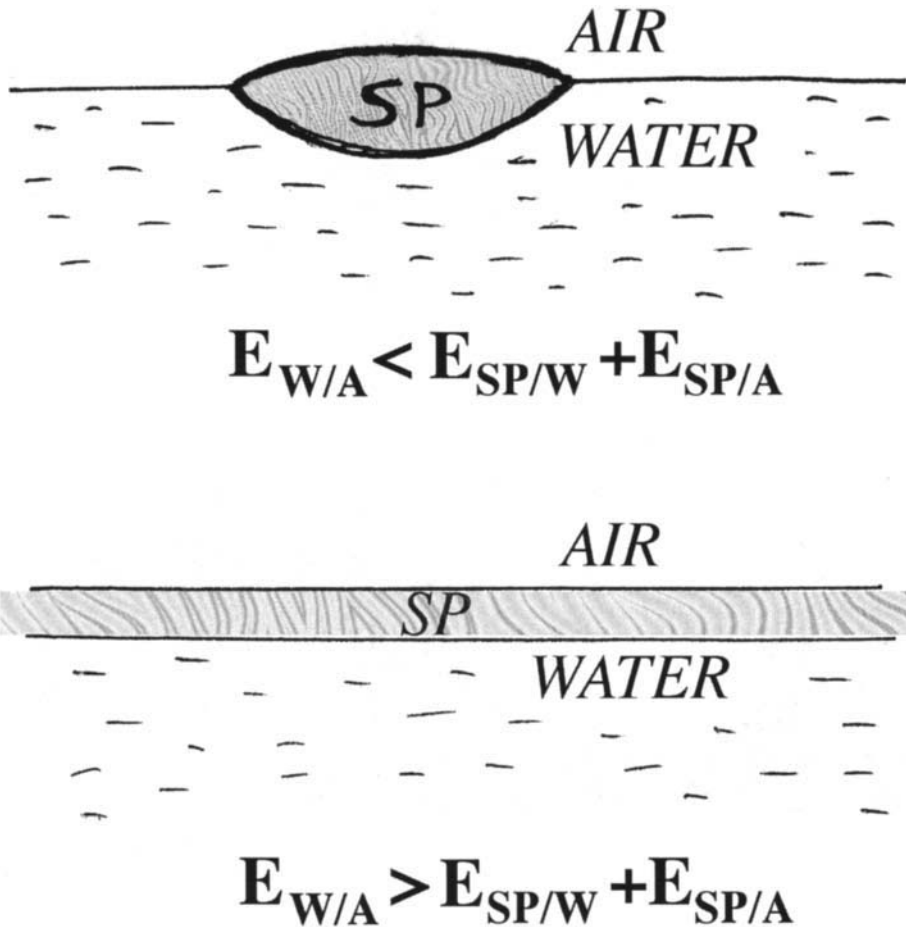


Figure 14.4.7 The alternatives of free surface energy (E) relations at the air/water interface (A/W) the surface phase/air (SP/A) interface and the surface phase/water (SP/W) interface, which determine if spreading takes place (below) or lens-shaped droplets are formed (above). At the alveolar surface the conditions for spreading are fulfilled.

The controversy in the literature whether the surface in the lungs are “dry” or “wet”, cf. [5], is resolved by our present structure model. A water droplet deposited on a fully swollen surface phase will not be taken up but stay outside; the surface will therefore appear dry. If the alveolar surface phase is not fully swollen, a deposited water droplet will just be absorbed.

One of us (M.L.) has observed in rabbit lung experiments how the surface phase is drawn up in a glass capillary which is brought in contact with the alveolar surface. The surface phase forms a well-defined layer above and in equilibrium with a water phase, which originates from an edema (obtained under such traumatic conditions). It was also seen that the surface phase is birefringent, which proves that it is a liquid-crystalline phase (with lower symmetry than cubic).

Whether or not one liquid phase will spread on the surface of another liquid or float as lens-shaped droplets (if its density is lower) is determined by the tendency to reduce the free surface (interfacial) energy. The two alternatives are shown in figure 14.4.7 applied on the alveolar surface phase and water.

A controversial question for a long time has been if the alveolar surface is wet or dry, cf. [5]. This question is the same as asking whether or not there is a free water phase at the alveolar surface. It should be pointed out that a water phase at the surface is required in the traditional structure models involving a lipid monolayer on water, see figure 14.2.2. According to our model the alveolar surface is dry under normal conditions. It might even be possible that the production and secretion of surfactant is controlled by some physical factor, for example by the occurrence of “free” water. If there is free water, more LB will be secreted, and induced by calcium ions they will *via* TM produce more surface phase. The water content of TM and the surface phase (about 90% (w/w)) is several times higher than that of LB, which is reported to contain about 20%(w/w) [11]. Therefore a transition from LB to TM means that any “free” water can immediately be taken up. If an excess of water enters the alveolus, the surface phase will foam, and expand through the lung lumen. This is a well known characteristic of lung edema.

14.5 Respiration

We will now show the dynamics of the surface phase structure involved in breathing.

In order to calculate the structure of a thin layer of the surface phase, the exponential description can be applied. Applying planar boundaries along the *y*-direction as indicated by EM data we obtain the equation 14.5.1.

$$e^{\left[\cos\frac{\pi}{4}(x-y)e^{\frac{1}{20}\cos\pi z} - \cos\frac{\pi}{4}(x+y)\right]} + e^{-(y-8)^2} + e^{-(y+8)^2} - 1 = 0 \quad 14.5.1$$

A section of this closed structure is shown in figure 14.5.1. A part of the same structure was shown in figure 14.4.3 and 14.4.4. It should be mentioned that the size of the “holes” between the tubular units shown here is twice the size of those shown in figure 14.3.3 (the corresponding constant in the equation was changed from 40 to 20).

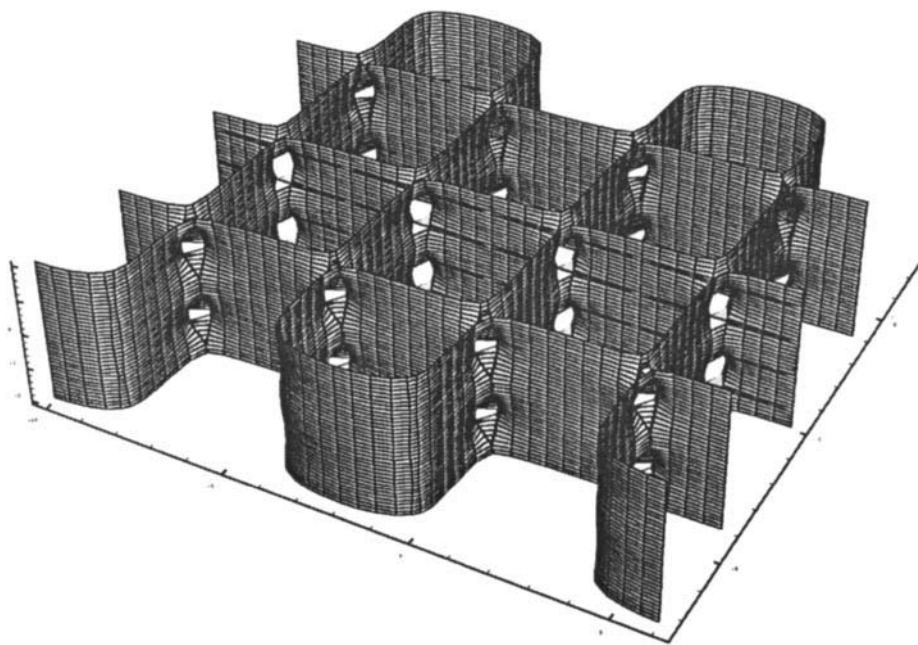


Figure 14.5.1 A thin layer of a closed CLP-structure proposed to form the surface phase of the alveoli, calculated according to the equation 14.5.1.

How fast is the spreading process at the surface towards air of this surface phase? We know from surface balance that spreading of an amphiphilic solvent over a water surface (e.g. *n*-butanol) takes place within fractions of a second. The CLP-surface phase, however, will spread slower due to its high viscosity. Our observations of the physical properties of the alveolar surface phase obtained from the glass capillary showed that the viscosity is comparable to that of lamellar liquid-crystalline phases with a similar water content. Spreading of the surface phase, involving “opening” of the surface

as indicated in figures 14.4.4 and 14.4.5, is proposed to account for expansions during the respiration cycle. In addition to that, there will certainly be transitory deformations, which we show below. The surface transformation processes during the compression phase of the respiration is just the reversal of these structural changes.

14.6 Physiological Significance of the Existence of an Organised Surface Phase at the Alveolar Surface

The existence of an organised surface phase has important implications. Most important is that there is no separate monolayer lining the surface. The surface towards air is just an inner surface of this organised phase (exposing the lipid methyl end groups as indicated in figures 14.3.3 and 14.3.4). Such a surface structure is mechanically very robust as being part of a phase, contrary to a separate monolayer on water. Extensive studies of lipid monolayers on water in the surface balance have demonstrated the fragile character of such surface films. The highly ordered surface structure and the mechanical properties of the surface phase explain the ultra-low surface tension, even under rapid variations in surface area.

The surface phase structure also allows variations in water content; the surface phase swells according to the amount of water available. Above its limit of swelling a water phase can coexist in thermodynamic equilibrium. Furthermore the occurrence of "free" water may control surface phase formation as pointed out above.

A characteristic feature of the CLP-surface phase structure is the possibility of free flow of the bilayer within the phase with a minor need of mechanical energy. Such flow can rapidly account for changes of outer shape, such as increasing the surface area inducing thinning of a layer of this phase. During the respiration cycle there is a need for expansion and compression of the surface phase, which require changes in surface area. This can thus be obtained by flow of bilayer material. It can also be achieved, however, by a rectangular deformation of the square cross-section of the tubular units. By replacing $(x-y)$ in (2) by $(3/4x-y)$ and $(x+y)$ by $(3/4x+y)$ the surface area is increased, and by replacing $(x-y)$ by $(x-3/4y)$ and $(x+y)$ by $(x+3/4y)$ the surface area is reduced. The calculated changes are demonstrated in figure 14.6.1. Thus the structure of this surface phase provides a mechanism for surface area changes similar to that of a concertina. This property of the structure is consistent with the low energy requirement for tidal breathing. The orthogonal bilayer cross-section pattern and its outer closed conformation are consistent with numerous ultrastructure textures.

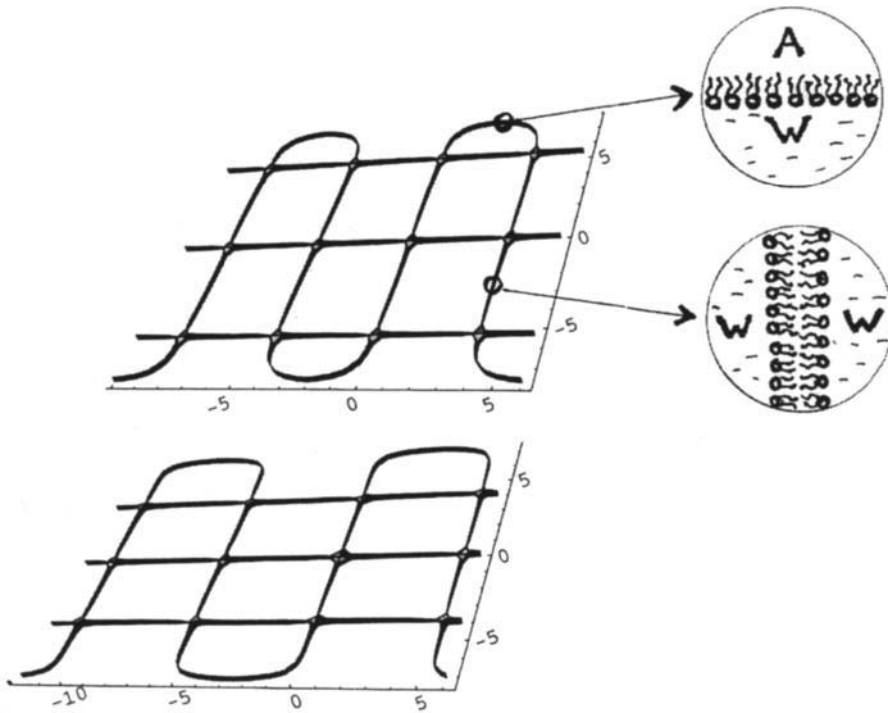


Figure 14.6.1 Calculated thin slices of cross-sections of the CLP-surface seen along the c-axis; deformed so as to give a compression and expansion of the surface area required by the respiratory cycle. The surface towards air (A) formed by the methyl end groups, and the lipid bilayer exposed to water (W) on each side are also illustrated. The bilayer also has junctions downwards to the liposome-like structures from which tubular myelin is formed.

We have pointed out two mechanisms for surface area changes here. How are they related? It seems likely that only deformation is fast enough to account for surface area changes at a fast breathe. Then comes the flow of lipid bilayer through the surface phase with a slower kinetic, which allows relaxation of the deformed structure towards the ideal CLP-conformation of the bilayer.

Oxygen and carbon dioxide have much higher solubilities in hydrocarbon chain regions of lipid bilayers than in water. Therefore the existence of a lipid bilayer continuum from the epithelial cells to the air surface of the alveoli means that there is an additional transportation route of the respiration gases beside the aqueous medium. Also this feature demonstrates

the major difference between this surface phase model of the alveolar lining and the earlier model with a separate monolayer outside a water phase.

Knowledge on the lung surfactant system and its structure is fundamental in order to understand normal lung function as well as pathological conditions. Functional aspects were discussed above. The surface phase model also provides a basis for development of new therapies. A well known lung dysfunction condition, hyaline membrane disease (respiratory distress syndrome), is caused by a lack of surfactant. Synthetic surfactant systems for pulmonary administration in order to cure this condition should take the CLP-bilayer structure into account, and ideally an artificial surfactant should result in a tetragonal structure at the alveolar surface.

A successful new principle for pulmonary drug delivery of proteins is under clinical evaluation at present. If the protein is delivered as particles about 20 microns in size, they are too large to immediately be consumed by the alveolar macrophages. Insulin for example can be administered in this way. The kinetics is very slow; absorption takes a couple of days. This is probably a consequence of the location of the insulin particles within the surface phase, which in effect becomes a controlled-release system.

The resistance of the lungs against pollution of dust particles and microbes is impressive. Alveolar macrophage activity can partly account for this, but much is due to the efficient ciliary transport system removing contaminants up along the bronchial tree, the Pater Noster apparatus. There seems to be a flow of surface phase up along the bronchial tree (surfactant has been identified there, [5]). The existence of a surface phase in the alveolus means that particles can be trapped in this phase, keeping e.g. a virus particle well away from the alveolar cell surface until the phase domain containing the particle is ingested by a macrophage. Or the phase may "flow" outside the alveoli, and the phase as a whole will be transported by ciliary movement up through the bronchial tree.

References 14

- 1 M. Larsson, K. Larsson, S. Andersson, J. Kakhar, T. Nylander and B. Ninham, *J. Dispersion Sci. Techn.* in press (1999).
- 2 J. J. Batenburg, *Lung Biology in Health and Disease* (Robertson & Tausch eds.) **84**, 47 (1995).
- 3 S. Schurch and H. Bachhofen, *Lung Biology in Health and Disease* (Robertson & Tausch eds.) **84**, 3 (1995).

- 4 J. F. van Iwaarden and L. M. G. van Golde, *Lung Biology in Health and Disease* (Robertson & Taeusch eds.) **84**, 47 (1995).
- 5 B. A. Hills, *THE BIOLOGY OF SURFACTANT*, Cambridge University Press, Cambridge, 1988.
- 6 R. J. Sanderson and A. E. Vatter, *J. Cell Biol.* **74**, 1027 (1977).
- 7 S. L. Young, E. K. Fram, and E. W. Larson. *Exp. Lung Res.* **18**, 497 (1992).
- 8 S. Lidin, and S. T. Hyde, *J. Phys. France* **48**, 15 (1987).
- 9 T. Manabe, *J. Ultrastruct. Res.* **69**, 86 (1979).
- 10 J. R. Bellare, H. T. Davis, L. E. Scriven and Y. Talmon, *J. Electron Microsc. Tech.* **10**, 87 (1988).
- 11 C. Grathwohl, G. E. Newman, P. J. R. Phizackerly and M.-H. Town, *Biochim. Biophys. Acta* **552**, 509 (1979).

15 Epilogue

For the harmony of the world is made manifest in Form and Number, and the heart and soul of all the poetry of Natural Philosophy are embodied in the concept of mathematic beauty [D'Arcy Thompson, 1].

Some general aspects of shape in biology is discussed here on the basis of the material presented earlier in this book. The role of biomembranes and transformations of lipid bilayer structures has been a major theme, and the significance in the evolution of lipid-like molecules self-assembled into bilayers is considered. Finally we speculate on application possibilities of the biomathematical approach introduced here.

The universality of biological shapes is demonstrated in D'Arcy Thompson's classical work from 1917 "On Growth and Form" [1]. Morphologies such as the logarithmic spiral and the honeycomb pattern occur in a wide diversity of organisms. The common *phylum* (i.e. body plan) through the animal kingdom is an elongated body with a head and a tail. The same organisation can be found in unicellular organisms. The sperm is one example and we calculated its shape and dynamics in chapter 10. The same shape can be recognised in individual biomolecules, for example in myelin which also was considered in chapter 10.

The mathematics we have introduced can thus be applied at quite different scales, but it is obviously most fruitful when the shape is described with a resolution of atomic distances. Shape and motion can then be related to known atomic, molecular and colloidal forces. This approach may under such conditions reveal new functional mechanisms. The lipid bilayer dynamics of cell membranes (chapter 8), the wave conformation model in order to explain the axon membrane phase transition involved in nerve signal conduction (chapter 13), and the surface phase proposed to line lung alveoli (chapter 14) are examples of new structural descriptions made possible by this new mathematics. Conformation and dynamics of cell membranes provide universal functions in biology. We will briefly consider a lipid-controlled structure in order to illustrate this universality of membrane conformations.

The back of the eye is lined with photoreceptor cells; neurons specialised to become excited by light. Each neuron can produce an electrical signal by the excitation induced by a single quantum of light; by one photon. The signals from different photoreceptor cells are then added in the retina and

processed in the brain. Vertebrates have two kinds of photoreceptor cells - rods and cones. Both are dominated by a lipid membrane system that forms a pile of membrane discs (cf. figure 15.1). The distribution of ions and the membrane potential of these neurons follow the general properties of neurons described in chapter 13. In darkness the sodium pores are kept open by cyclic guanosine monophosphate (cGMP). The flow of sodium ions inwards keeps an "equilibrium" value of the membrane potential of -40 mV (the sodium pumps keep transporting these ions out). When such a receptor is exposed to light, 11-*cis* retinal activates pigment molecules in the membrane, and *via* a complex reaction chain cGMP is cleaved. The reduction in cGMP concentration results in closing of sodium pores, and the negative value of the potential increases therefore. When it reaches about -65 mV, the cell becomes hyperpolarised and an electrical signal is conducted to the synaptic terminal.

The photoreceptor membrane systems must be organised perfectly from a crystallographic point of view, in order to reach the optical efficiency level of individual photons. A part of the outer segment of the rod membranes is modelled in figure 15.1. The equation for calculation of membrane discs and the surface membrane is given in equation 15.1.

$$\begin{aligned}
 & e^{-[e^{x^{10}} + e^{-(y-1)-2.8}]} \cdot e^{-[10(x^4 + (5(y+0.5))^4 - 0.1)]} \\
 & \cdot e^{-[10(x^4 + (5(y+0.1))^4 - 0.5)]} \cdot e^{-[10(x^4 + (5(y-0.3))^4 - 0.7)]} \\
 & \cdot e^{-[10(x^4 + (5(y-0.7))^4 - 0.8)]} \cdot e^{-[10(x^4 + (5(y-1.1))^4 - 0.8)]} \\
 & \cdot e^{-[10(x^4 + (5(y-1.5))^4 - 0.8)]} \cdot e^{-[10(x^4 + (5(y-1.9))^4 - 0.8)]} = 0.02
 \end{aligned}
 \tag{15.1}$$

These discs are located inside a surface membrane. The cones have similar piles of membrane discs but there they are part of the same membrane.

A quite similar membrane system is found in the chloroplasts of plants, the organelles specialised for harvesting light in order to drive the photosynthesis. The thylacoid membrane system in chloroplasts form piles of membrane discs, which are very similar to those in the photoreceptor cells. Like the membrane discs in cones they consist of a single lipid membrane. Both these two types of membrane systems have evolved in order to utilise light efficiently. The similarity in *shapes* reflect this functional relation. It is remarkable, however, that the *chemical* compositions are quite different. Not only the light harvesting lipids and the pigment molecules are different but also the membrane lipids. The photoreceptor cell membranes are dominated by phospholipids, whereas the thylacoid membranes consist mainly of galactolipids. The fact that

closely related physical structures are formed in systems with so different chemical compositions indicates that enzyme systems for synthesis/modification of these lipid species are controlled by some physical property related to shape, as discussed in chapter 8.

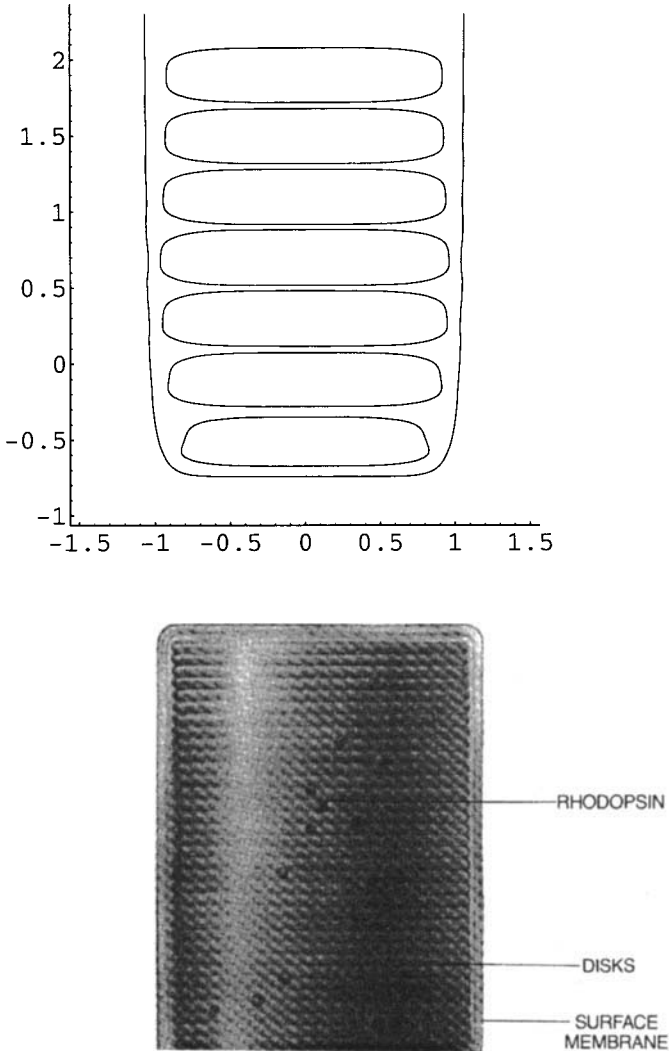


Figure 15.1 The calculated pile of membrane discs forming the outer segment of a rod photoreceptor cell. A schematic illustration according to ultrastructural studies of this part of a cone is shown below, reconstructed after [2].

The general mechanisms behind shapes in the plant, and the animal kingdom are still unknown. D'Arcy Thompson questioned natural selection according to Darwin in this respect. Based on numerous examples he concluded that shape can be determined in a *direct* way by laws of physics without having to be *selected*. Even with our present knowledge of the genetic mechanisms, many questions on biologic shape remain open. Philip Ball has recently published a beautiful book [3], extending ideas from D'Arcy Thompson towards the knowledge of biological pattern formation and morphology of today.

We would like to cite what he writes on the origin of shape:

“I don't think we know very much yet about whether natural selection has the power to modify or suppress certain pattern-forming principles that occur in nature. But I would suggest that, in the here and now, such principles undoubtedly exist - and do so in sharp distinction from the idea that genes are like a *deus ex machina* that holds all biological processes in thrall, building organisms in a laborious, brick-by-brick manner.”

Another very interesting book on the same theme was published by Ian Stewart [4] almost simultaneously as Philip Ball's book. The title of Stewart's book: “Life's other secret” refers to DNA as being the first secret. In his preface he writes:

“The mathematical control of the growing organism is the *other* secret - the second secret, if you will - of life. Without it we will never solve the secrets of the living world - for life is a partnership between genes and mathematics, and we must take proper account of the role of *both* partners.”

Needless to say we have also been inspired by the thinking of D'Arcy Thompson; in “Language of Shape”, [5], as well as in the present book.

In the introduction to this book we mentioned the obvious significance in the first form of life of a lipid membrane. Archaeobacteria existing today represent a very primitive form of life. Their membrane lipids are quite different from those of other living organisms. A most interesting property of these lipids is that they under a wide variety of physiological conditions exhibit a cubic structure which exist in equilibrium with excess of water [5]. We have earlier speculated on the advantages of cubosomes in early forms of life [6]. In the introduction we discussed the fundamental need early in the evolution to encapsulate and protect the genetic material. Lipid-like molecules which were able to self-assemble into bilayer structures were certainly around, cf. [5]. We will just illustrate here how molecular interaction might lead to such encapsulation.

In figure 15.2a we show how a cubosome-like membrane may form an envelope to protect genetic/catalytic molecules like RNA. The bilayer can be formed from the different types of the lipid structures we have become acquainted with in this book. Here we use a chiral unit of a D-surface “cubosome”; uniaxially compressed, according to equation 15.2.

$$\begin{aligned}
 & e^{-[(x+1)^2+(y+1)^2+(z-0.6)^2]} + e^{-[(x-1)^2+(y+1)^2+(z-1.2)^2]} \\
 & + e^{-[(x-1)^2+(y-1)^2+(z-1.8)^2]} + e^{-[(x+1)^2+(y-1)^2+(z-2.4)^2]} \\
 & + e^{-[(x+1)^2+(y+1)^2+(z-3)^2]} + e^{-[(x-1)^2+(y+1)^2+(z-3.6)^2]} \\
 & + e^{-[(x-1)^2+(y-1)^2+(z-4.2)^2]} - 0.4 = 0
 \end{aligned}
 \tag{15.2}$$

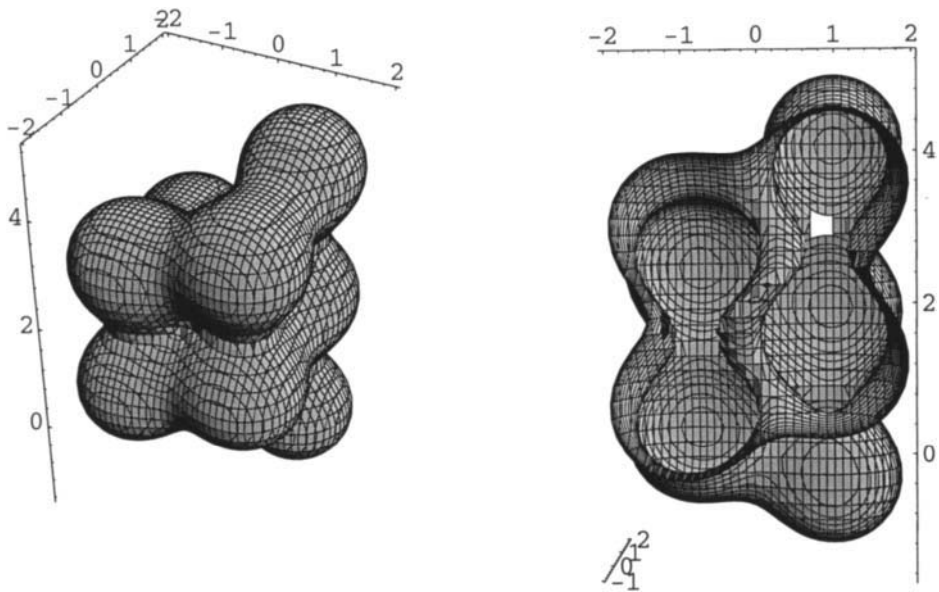


Figure 15.2a Helical arrangement of vesicles according to the D-surface.

This structure after fusion of the vesicles forms a spiral tube as shown in figure 15.2b. It can have any periodicity allowed by the shape of the lipid molecules, and it will end with half-spheres.

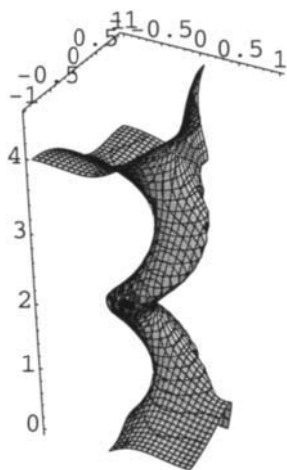


Figure 15.2b Helical membrane structure formed from figure 15.2a by vesicle fusion.

Primitive lipid-like molecules can be assumed to build the vesicles that condense to this chiral membrane (as usual only the mid-surface is shown in figure 15.2b). Parts of the inside surface along every pitch can have a curvature that fit an RNA-helix. Interaction between “content” and “container” may have had a profound effect on the choice and structure of the material used for the genetic code.

In this context it should also be mentioned that membrane lipids in mammalian cells are involved in control of gene expression. Enzymatically produced fatty acids from membrane phospholipids can up-regulate or suppress gene expression via the so-called peroxisome proliferator activated receptor in the nucleus.

The breaking of symmetry in dividing cells, and the principles behind pattern formation were proposed to originate from competition between diffusion and autocatalytic processes by Alan Turing in the fifties. This field is very well described in the two recent books by Philip Ball [3] and Ian Stewart [4] mentioned earlier. The colour patterns of living organisms, for example, can be explained by Turing’s diffusion-reaction equations.

Simple organisms have a low degree of differentiation and therefore high symmetry. Many genes behind differentiation have now been mapped. The formation of limbs, such as our arms or the wings of a bird, is an illustrative example. Certain proteins have been identified - called *Sonic hedgehog*

proteins [7] - that are secreted from the cells in the embryo just where the limb will grow out. The growth process is related to the concentration of these proteins (morphogens). It is most interesting that the same proteins also are responsible for other patterns in the differentiation. Thus these proteins determines whether a neuron will develop into a sensory or a motor nerve cell. They are also involved in the bilateral organisation of the brain [6].

Going backwards in evolution we reduce the degree of differentiation. Our earliest ancestors, the first animals, lived in the precambrian sea. During the first stage of the precambrian period, 700 to 570 million years ago, only a few species seemed to have existed [8]. They were soft-bodied creatures, and one called *Pteridinium* is shown in figure 15.3.

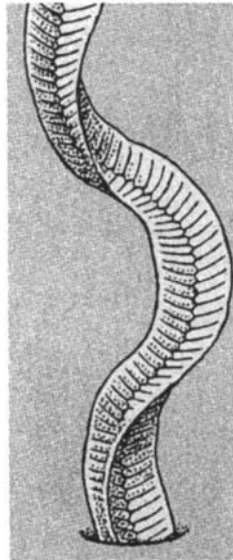


Figure 15.3 A fossil of *Pteridinium*, mid-part of the body reconstructed after [8].

These animals were filter-feeding, and they had to be flat due to the limitations of diffusion of nutrients. There is a clear resemblance between the body shape in figure 15.3, and planes crossing one another without intersections. The alternatives of two and three such crossing planes are shown in our earlier book [9]. Two planes corresponds to Scherk's classical minimal surface, shown in figure 15.4. Such a shape can be determined by a simple frame network, the rest will be the result of physical forces (e.g. surface tension).

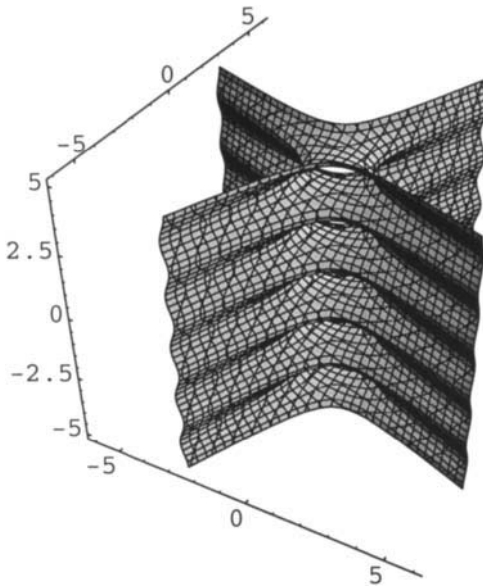


Figure 15.4 An illustration of a minimal surface formed by two planes crossing one another without intersections. This tower surface is derived in appendix 6.

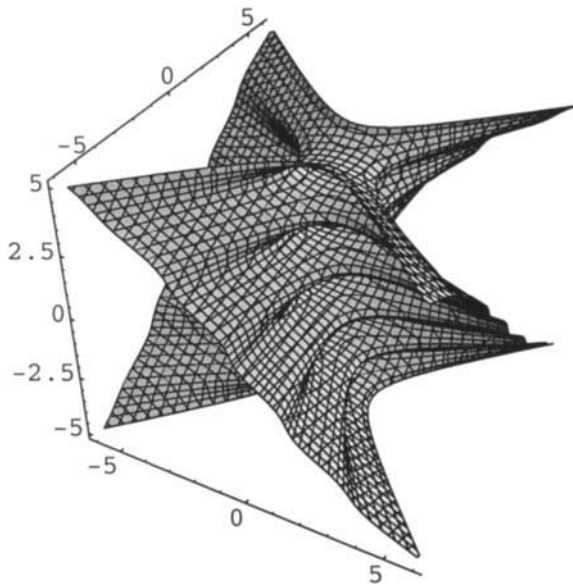


Figure 15.5 Helical deformation of the minimal surface shown in figure 15.4.

If the angles between the quadrants are allowed to vary, for example by some oscillation around 90°, water will be forced to move through the openings. In a filter-feeding animal this might be an ideal mechanism for uptake of nutrients.

There is also a possibility for helical deformation of this surface as demonstrated in appendix 5, and shown in figure 15.5.

This deformation and its reversal, done under varying speed, can provide a propelling function for swimming.

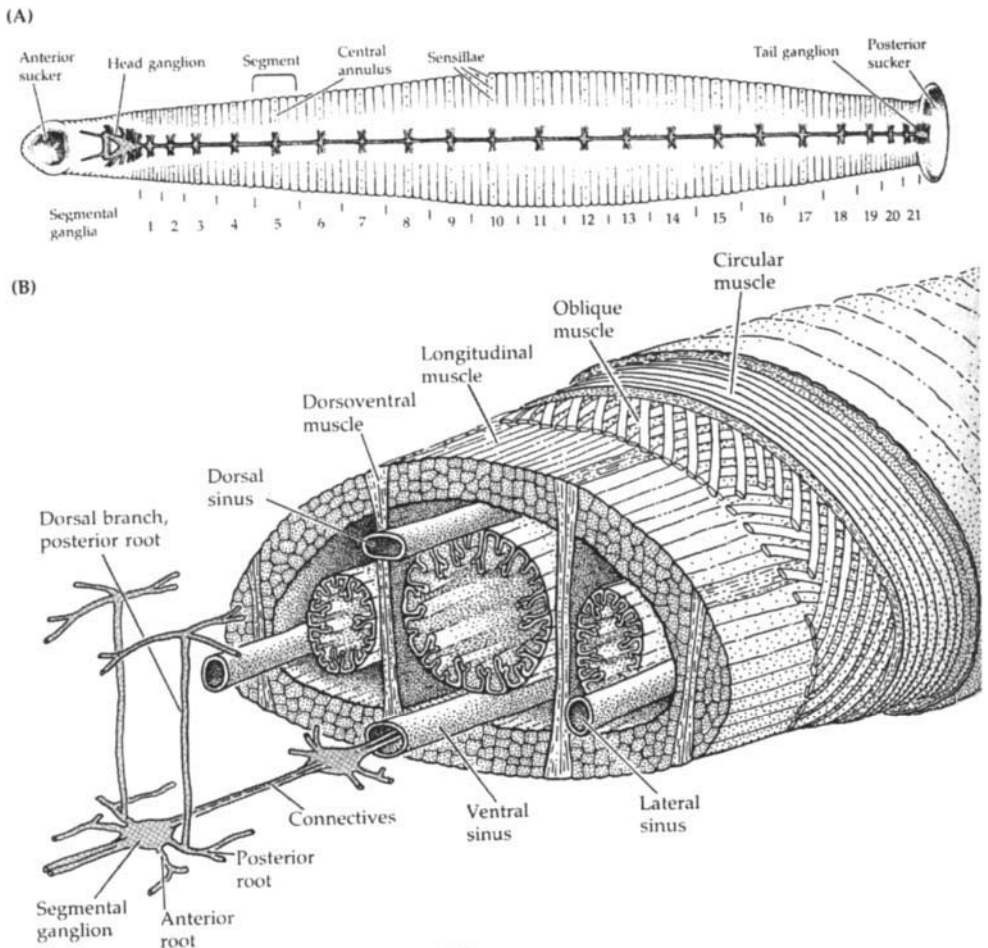


Figure 15.6 Anatomic description of a leech with special attention to the neurons, reproduced with permission from [10].

We will finally consider another primitive animal. The anatomy of the leech has been known for a long time as they have been used in medical practice for many hundred years. They are even used today in connection with advanced hand surgery. An illustration is given in figure 15.6. Each segment is controlled by a ganglion; an aggregate of neurons. These ganglia, also those in the head and the tail each consist of only about 400 neurons [10]. Their geometry is well defined with axons - “connectives” - along the body direction, and perpendicular to them a set of “roots” - axons going out to the body wall. We would like to cite a comment on these ganglia from the book “From Neurons to Brain” [10]: “As one looks at these limited aggregates of cells laid out in an orderly pattern, one cannot but marvel at how they, on their own, being the brain of the creature, are responsible for all its movements, hesitations, avoidance, mating, feeding, and sensations.” The general mechanisms governing the geometry of the neural projections and the synaptic connections are probably significant features in order to understand brain function. Maybe a simple neuron organisation as this would be fruitful to describe, using the biomathematical approach we have introduced in this book.

Acknowledgement

We sincerely thank Johanna Jakobsson for valuable discussions.

References 15

- 1 D’Arcy Wentworth Thompson, ON GROWTH AND FORM, Cambridge University Press, Cambridge (1942).
- 2 J. L. Schnapf and D. A. Bailor, Sci. Am. **256**, 32 (1987).
- 3 P. Ball, THE SELF-MADE TAPESTRY: PATTERN FORMATION IN NATURE, Oxford University Press (1998).
- 4 I. Stewart, LIFE’S OTHER SECRET, THE NEW MATHEMATICS OF THE LIVING WORLD, John Wiley & Sons, Inc., New York (1998).
- 5 A. Gulik, V. Luzzati, M. DeRosa and A. Gambacorta, J. Mol. Biol. **201**, 429 (1988).

-
- 6 S. T. Hyde, S. Andersson, K. Larsson, Z. Blum, T. Landh, S. Lidin and B. Ninham, *THE LANGUAGE OF SHAPE*. Elsevier, Amsterdam (1997).
 - 7 R. D. Riddle and C. J. Tabin, *Sci. Am.* **280**, 74 (1999).
 - 8 M. A. S. McMenamin, *Sci. Am.* **256**, 84 (1987).
 - 9 M. Jacob and S. Andersson; *THE NATURE OF MATHEMATICS AND THE MATHEMATICS OF NATURE*, Elsevier, Amsterdam, 1998.
 - 10 J. G. Nicholls, A. R. Martin and B. Wallace, *FROM NEURON TO BRAIN*, 3rd ed., Sinauer ass. inc. Publishers, Sunderland, Mass. (1992).

This Page Intentionally Left Blank

Appendix 1 - The Plane, the Cylinder and the Sphere

The geometry for the plane, the cylinder, and the sphere is fundamental in the mathematics we develop in this book. We here give the equations and show the relationships, and different orientations in space.

In chemistry we need to do experiments - to "cook" and see what happens. Every biological phenomenon is also chemistry, as it can be traced back to certain molecules. But most of this chemistry has a complexity beyond what can be defined by traditional mathematics. As mentioned earlier, the theme of this book is new mathematics which are able to describe structures in biology and changes of these structures. In the hurdle of understanding we do experimental mathematics.

For readers lacking a mathematical background, we will in the different appendix present some basic concepts needed to apply this analytical description of structure and dynamics. The reader is recommended to perform some of these calculations, using Mathematica as shown in appendix 9.

The realisation that the laws of Nature could be described with differential equations has dominated the scene for very long. We use such mathematics to model motion, and have commonly accepted the notion of force and acceleration.

Calculus was a tremendous achievement in the history of science. One example is the minimal surface, which describes a very simple physical phenomenon which is believed to be important for such diverse structures as lipid membranes in biology and surface chemistry based industrial application. The problem with the minimal surface mathematics is that you immediately run into deep difficulties. Take a copper wire, bend it arbitrarily and join the ends. Then dip it in soap water and when bringing it up there is a beautiful surface formed in fractions of a second, which is the true minimal surface. The tragedy is that you cannot do these mathematics with calculus. It is too difficult.

We cannot do these mathematics either. But we can calculate related surfaces that appear to be more relevant, both to biomembranes and technology; nodal surfaces of standing wave oscillating surfaces. And we can construct other surfaces which we know are important. So we leave the soap problem for now, but return to it later in the appendix.

Mathematics was invented by man to describe subtle ways of thinking, and this is still why we use mathematics. It is used to give models for how space is curved and what time really is, and to describe what electrons are doing in superconductors. It is used to give models for what things look like with our eyes and with our way of thinking. There exists 'a language of shape' or 'an aesthetic measure'.

We believe biology can be described with another, entirely different, branch of mathematics, which is called topology. Topology is difficult to define or describe, but it has been said that it is mathematics without equations. We have developed a type of mathematics which gives topology with equations. Of course it is then obvious to apply calculus to these methods, but we are not going to do that. We shall just do the mathematics, because we think that great parts of these mathematics can be applied directly to biology.

We have found that all the mathematics we shall use may be described by planes, cylinders and spheres. And that cylinders and spheres may also be described by planes.

We begin by formulating simple equations, and see what they mean in space. The equations in 1.1a-d represent different planes, and are plotted in the corresponding figures 1.1a-d.

$$x = 0$$

1.1a

$$x = 1$$

1.1b

$$y = 0$$

1.1c

$$z = 0$$

1.1d

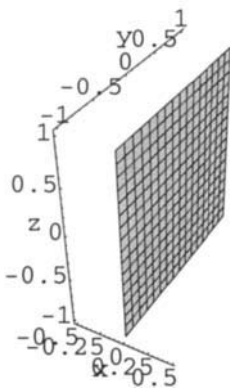


Figure 1.1a The plane $x=0$.

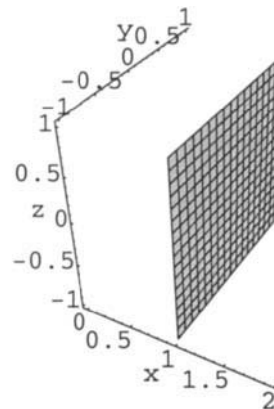


Figure 1.1b The plane has been shifted and is now $x=1$.

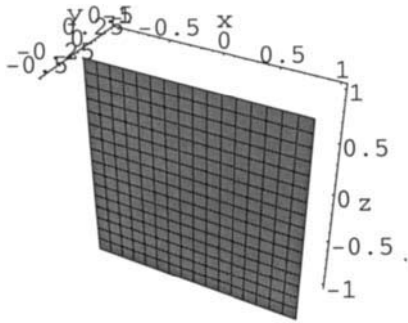


Figure 1.1c The plane $y=0$.

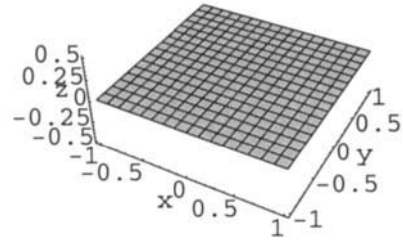


Figure 1.1d The plane $z=0$.

These planes are of course infinite, and we show only a part of them in these figures by restricting the values of x,y,z to the range from -1 to 1 .

Planes may be tilted by adding different planes together, as is done in equations 1.2a-d, and illustrated in figures 1.2a-d.

- $x + y = 0$ 1.2a
- $x + 0.8y = 0$ 1.2b
- $x + z = 0$ 1.2c
- $y + z = 0$ 1.2d

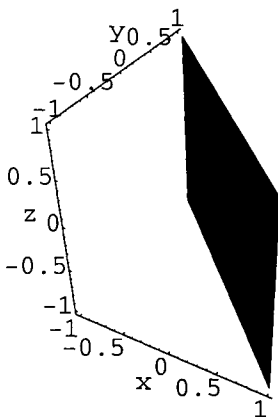


Figure 1.2a The plane $x+y=0$.

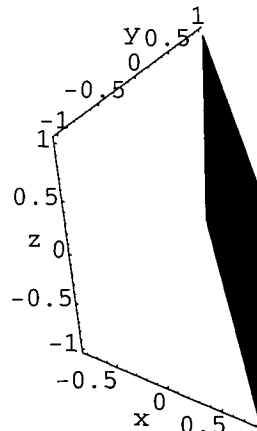


Figure 1.2b The plane $x+0.8y=0$.

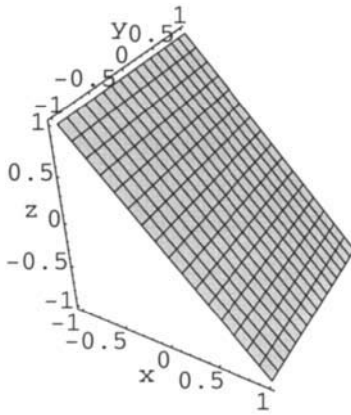


Figure 1.2c The plane $x+z=0$.

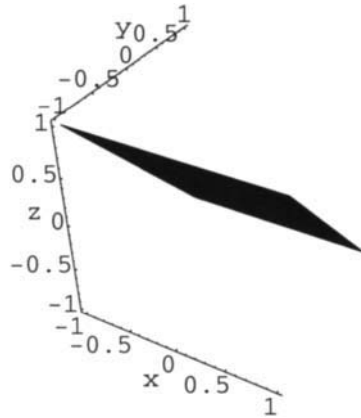


Figure 1.2d The plane $y+z=0$.

The general case with addition of all three variables is given in equation 1.3, and creates a plane perpendicular to the space diagonal axis, as shown in figure 1.3.

$$x+y+z=0$$

1.3

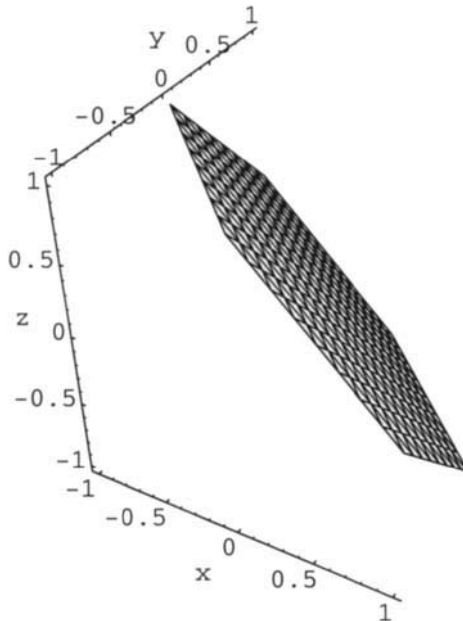


Figure 1.3 The plane $x+y+z=0$.

So far we have been studying addition of planes. Next is to study the simple products given in equation 1.4a-d, which each generate two planes, one on each side of the origin. We see that we again have infinite planes, and with the boundaries chosen, the square products are shown in figures 1.4a-d.

$$x^2 = 1 \tag{1.4a}$$

$$(x - 0.2y)^2 = 1 \tag{1.4b}$$

$$y^2 = 1 \tag{1.4c}$$

$$z^2 = 1 \tag{1.4d}$$

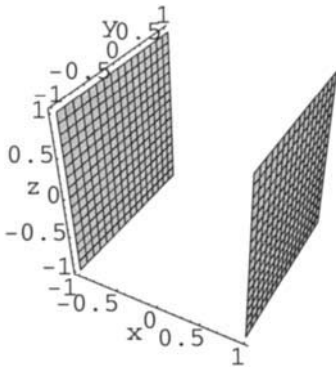


Figure 1.4a The planes are $x+1=0$ and $x-1=0$, or $x^2 - 1 = 0$.

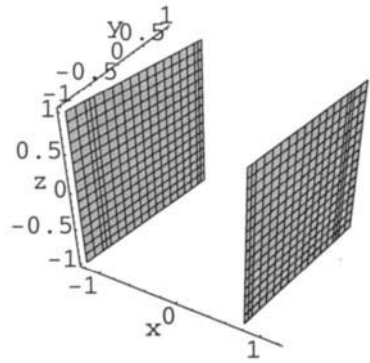


Figure 1.4b The planes are $(x - 0.2y)^2 = 1$.

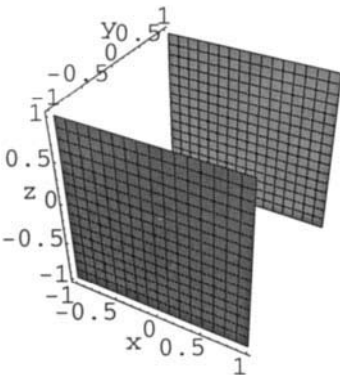


Figure 1.4c The planes are $y^2 - 1 = 0$.

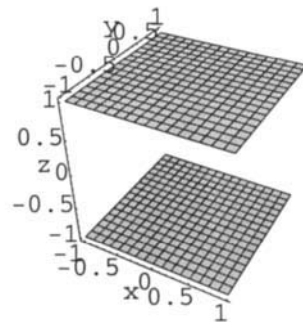


Figure 1.4d The planes are $z^2 - 1 = 0$.

Three sets of squared planes added together as in equation 1.5a, gives a sphere as shown in figure 1.5a, which is plotted for the constant C=1. Changing the constant as in equation 1.5b, changes the size of the sphere, as in figure 1.5b.

$$x^2 + y^2 + z^2 = 1 \tag{1.5a}$$

$$x^2 + y^2 + z^2 = 1/5 \tag{1.5b}$$

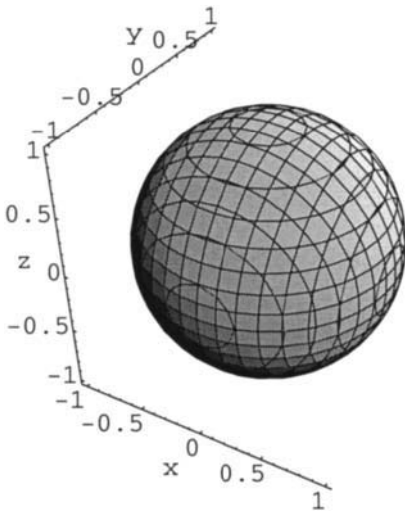


Figure 1.5a Three pairs of perpendicular planes give a sphere.

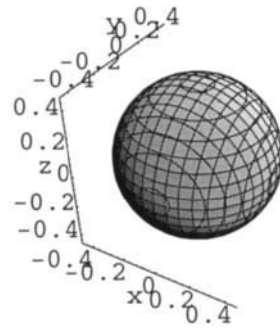


Figure 1.5b Lower constant.

If we add the squares pairwise as in the equations 1.6a-d, the planes collaborate to form infinite cylinders as illustrated in figure 1.6a-d.

$$x^2 + y^2 = 1 \tag{1.6a}$$

$$x^2 + z^2 = 1 \tag{1.6b}$$

$$z^2 + y^2 = 1 \tag{1.6c}$$

$$(x + 0.2z)^2 + (y + 0.2z)^2 = 1 \tag{1.6d}$$

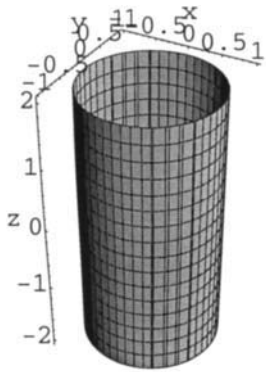


Figure 1.6a Two pairs of planes after equation $x^2 + y^2 = 1$.

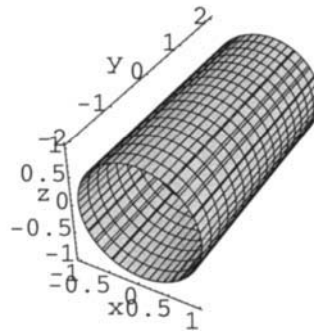


Figure 1.6b Two pairs of planes after equation $x^2 + z^2 = 1$.

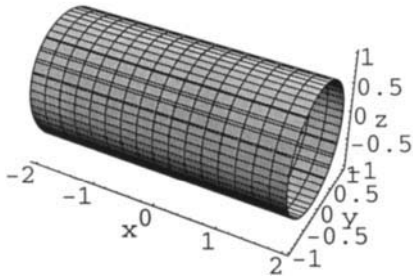


Figure 1.6c Two pairs of planes after equation $z^2 + y^2 = 1$.

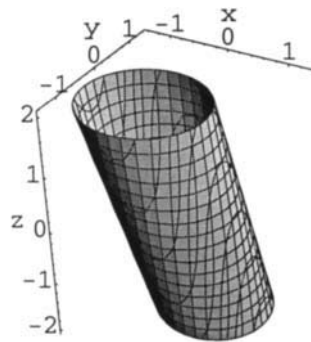


Figure 1.6d Cylinder tilted after equation $(x + 0.2z)^2 + (y + 0.2z)^2 = 1$.

We shall now make cylinders parallel with the cubic space diagonals. The equations for these four cylinders are built up by tilted planes, and have been derived in ref. [1]. The equations are given in 1.7a-d.

$$(x - z)^2 + (y - z)^2 + (x - y)^2 = 1 \tag{1.7a}$$

$$(x + z)^2 + (y + z)^2 + (x - y)^2 = 1 \tag{1.7b}$$

$$(x - z)^2 + (y + z)^2 + (x + y)^2 = 1 \tag{1.7c}$$

$$(x + z)^2 + (y - z)^2 + (x + y)^2 = 1 \tag{1.7d}$$

If we in equation 17 above, plot each term, like for example $(x-z)^2 = 1$, we will find a pair of planes again, and all three terms build six planes, which together build a cylinder, as in figure 1.7a-h. The planes are from equation 1.2. Each figure to the right is a projection of the figure to the left.

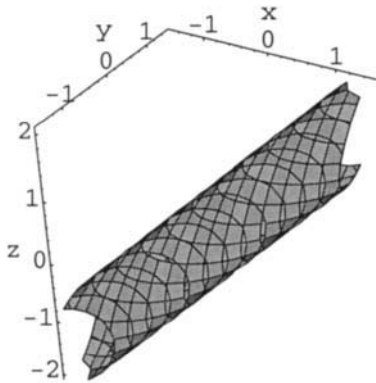


Figure 1.7a Cylinder after equation 1.7a.

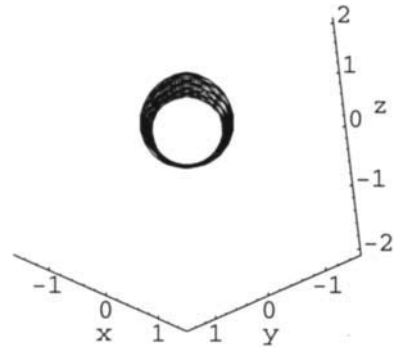


Figure 1.7b Different orientation.

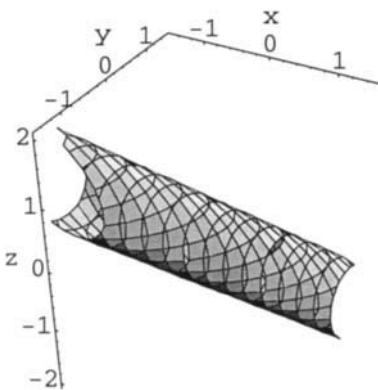


Figure 1.7c Cylinder after equation 1.7b.

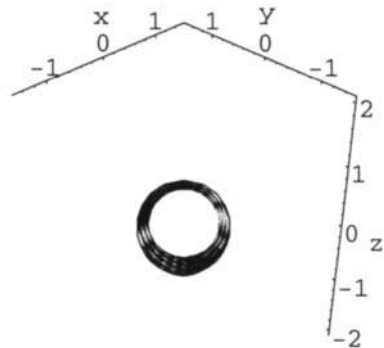


Figure 1.7d Different orientation.

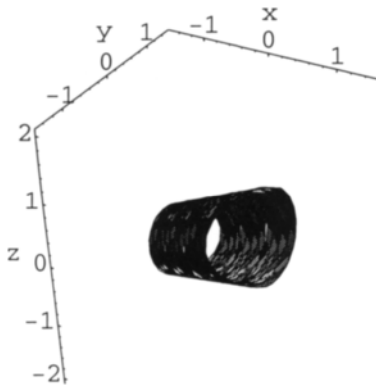


Figure 1.7e Cylinder after equation 1.7c.

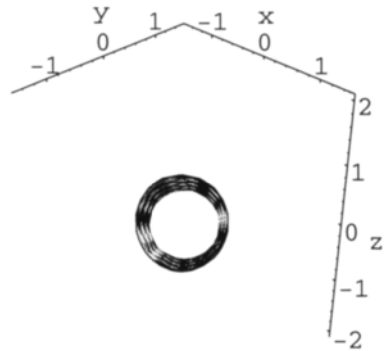


Figure 1.7f Different orientation.

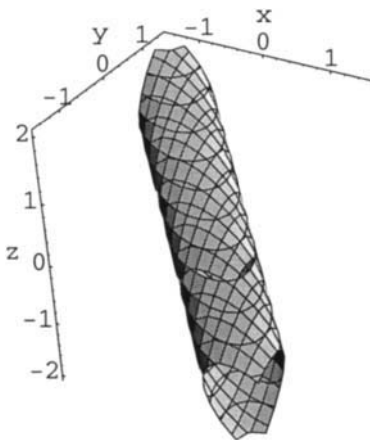


Figure 1.7g Cylinder after equation 1.7d.

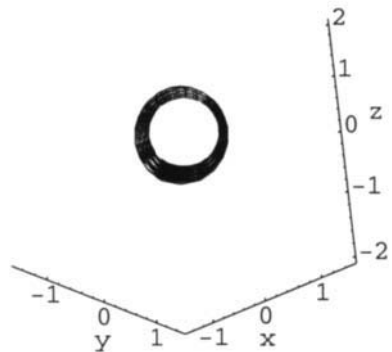


Figure 1.7h Different orientation.

References Appendix 1

- 1 M. Jacob and S. Andersson, *THE NATURE OF MATHEMATICS AND THE MATHEMATICS OF NATURE*, page 242, Elsevier, 1998.

This Page Intentionally Left Blank

Appendix 2 - Periodicity

The roots of periodicity in the algebra is described. The infinite repetition of planes, cylinders and spheres using the circular functions is shown to give the surface structures.

Many things in biology are periodic, both in structure and in motion, as we can see in this book. So here we will study the fundamentals of periodicity.

What we do is a part of algebra that is of interest in geometry. We begin with the simplest of roots and come to the equation of products below.

The function $x^2 = 1$ can be written $x^2 - 1 = 0$, or

$$(x - 1)(x + 1) = 0$$

We continue with an important equation (2.1), which is a part of the fundamental theorem of algebra, and contains more roots.

$$x(x - 1)(x - 2)(x - 3)(x - 4)(x - 5) = 0 \tag{2.1}$$

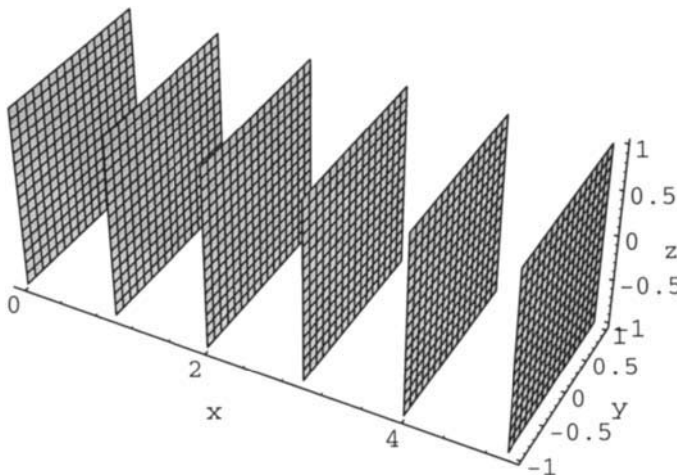


Figure 2.1 Finite algebraic periodicity.

We plot this algebraic equation in figure 2.1 and see that roots in 3D are infinite planes, and that the periodicity is finite. This is very important and we shall return to it later. If we make this product to have an *infinite* number of roots, we have the definition of a circular function (like cosine) as discussed in chapter 2.

We plot $\sin\pi x=0$ in figure 2.2. The function of course consists of an infinite number of planes along x, but is for comparison here plotted with the same borders as used in figure 2.1.

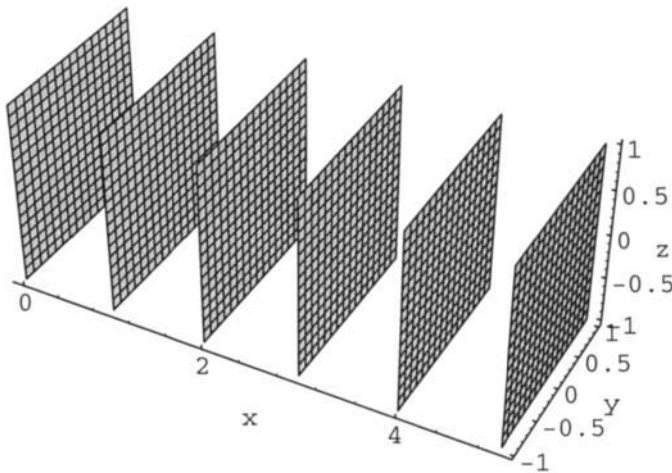


Figure 2.2 Periodicity after sine.

Now we know how cosine describes periodicity, and we can add planes periodically, similar to what we did earlier. We shall get cylinders and spheres again, but since we now use periodical functions, bundles of them are created, and they will therefore form periodic structures.

We have the bundles of planes in equations in 2.2a-c, and the plots in figures 2.3a-c.

$$\cos \pi x = 0 \quad 2.2a$$

$$\cos \pi y = 0 \quad 2.2b$$

$$\cos \pi z = 0 \quad 2.2c$$

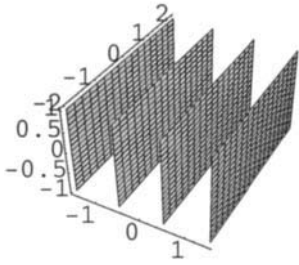


Figure 2.3a Planes after $\cos \pi x = 0$.

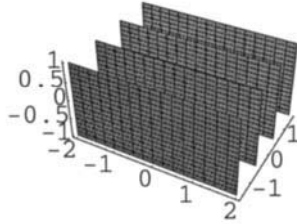


Figure 2.3b Planes after $\cos \pi y = 0$.

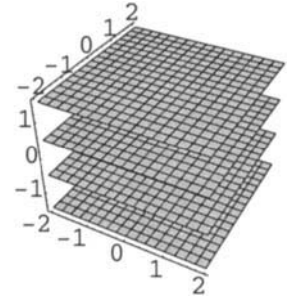


Figure 2.3c Planes after $\cos \pi z = 0$.

First we use the cylinder equations 1.6 and 1.7 to get the circular equations for periodic packing of cylinders in 2.3 and 2.4. The plots are in figure 2.4 and 2.5a-b.

$$\cos \pi x + \cos \pi y - 1 = 0 \tag{2.3}$$

$$\cos \pi(x - y) + \cos \pi(x - z) + \cos \pi(y - z) - 2 = 0 \tag{2.4}$$

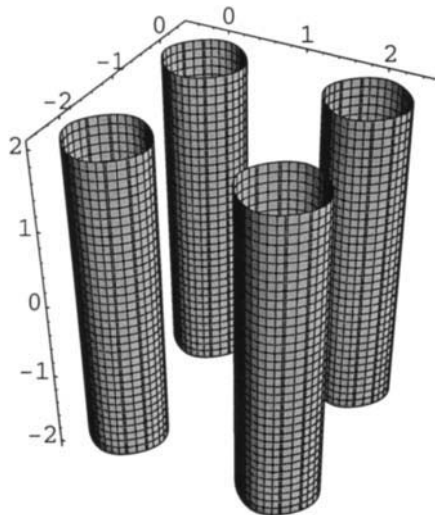


Figure 2.4 The pairwise adding of planes after equation 2.3 give cylinders.

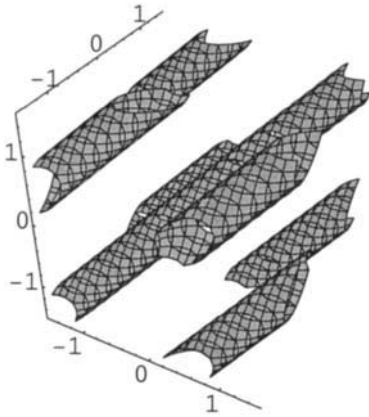


Figure 2.5a The adding of planes after equation 2.4 give cylinders.

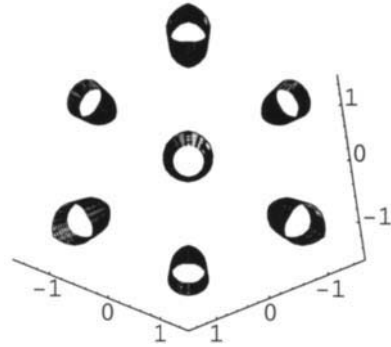


Figure 2.5b Different projection.

Many phenomena in molecular biology involve periodic surfaces which can be seen as the result of vesicle fusion, and we shall derive some of them accordingly (a vesicle is a spherical shell formed by a biological membrane).

We make vesicles or spheres by combining planes, and since we need many vesicles for the periodic aggregations, we use the circular functions. The functions $\cos x$, $\cos y$ and $\cos z$ are three sets of infinite planes, shown in figures 2.3a-c. If we add them together with the isovalue constant $C=1.25$ in equation 2.5, spheres are formed as in figure 2.6. We see that each sphere is surrounded by six others, which means that seven vesicles have to meet in fixed geometry to form a surface. The connectivity is said to be six.

$$\cos \pi x + \cos \pi y + \cos \pi z = C \quad 2.5$$

Changing the constant to $C=0.8$ makes the vesicles meet and form catenoids, as shown in figure 2.7.

At zero constant after equation 2.6 there is the famous P-surface in figure 2.8.

$$\cos \pi x + \cos \pi y + \cos \pi z = 0 \quad 2.6$$

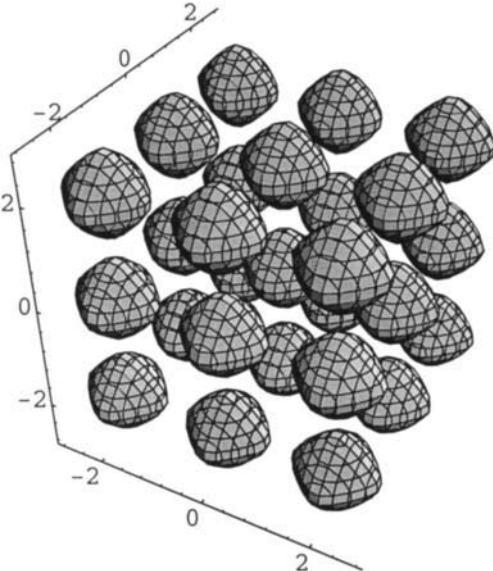


Figure 2.6 Planes from a circular function make vesicles.

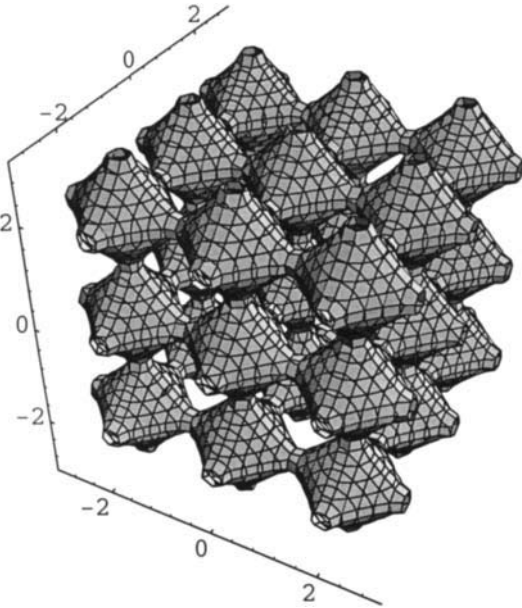


Figure 2.7 Vesicles are made to meet.

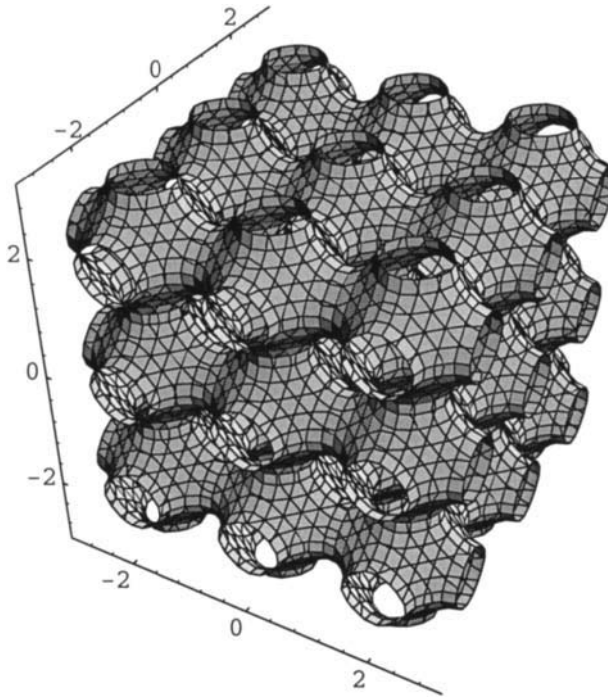


Figure 2.8 The nodal P-surface.

Next is the permutation of planes in space, taken from equation 1.2 in appendix 1, and shown here in equation 2.7 for $C=2$.

$$\begin{aligned} &\cos \pi(x+y) + \cos \pi(x-y) + \cos \pi(x+z) \\ &+ \cos \pi(z-x) + \cos \pi(y+z) + \cos \pi(y-z) = 2 \end{aligned} \quad 2.7$$

The plot is shown in figure 2.9 and shows spheres or vesicles in a packing called a body centred arrangement (see appendix 6). The same packing is found in the atomic arrangements in many metals, and in stainless steel. Eight atoms here surround a ninth, and the connectivity is therefore eight. The structure is, however, not of great importance in biology. Still, we have it here to complete the picture of the symmetry that is derived from these permutation in space. We make the spheres approach each other, and at a constant of -0.2 there are catenoids between the bodies, which now have become cubic as shown in figure 2.10. Finally there is figure 2.11 for a constant of -0.5 and with smaller boundaries.

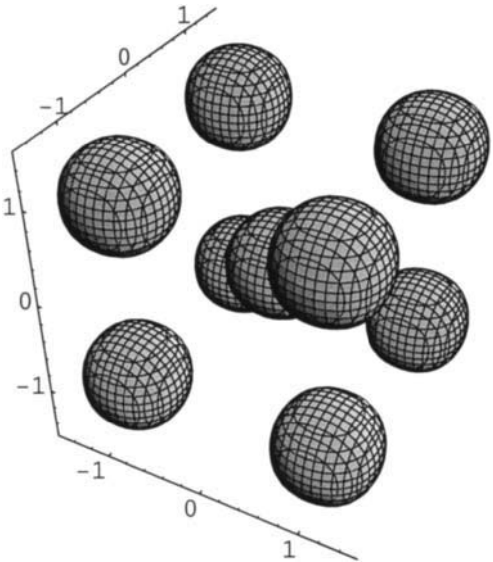


Figure 2.9 Permutations in space of equations for planes give a body centred structure of vesicles.

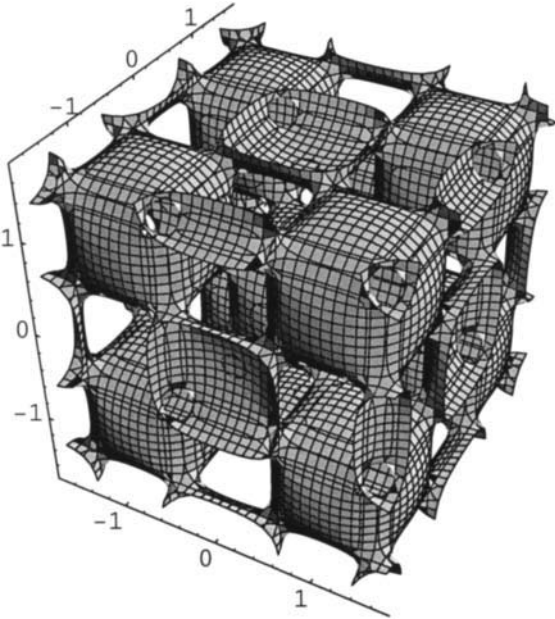


Figure 2.10 Spheres meet and form catenoids.

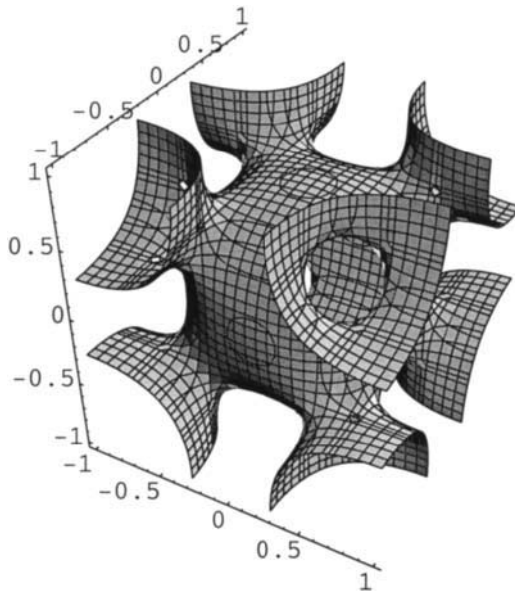


Figure 2.11 The connectivity is eight.

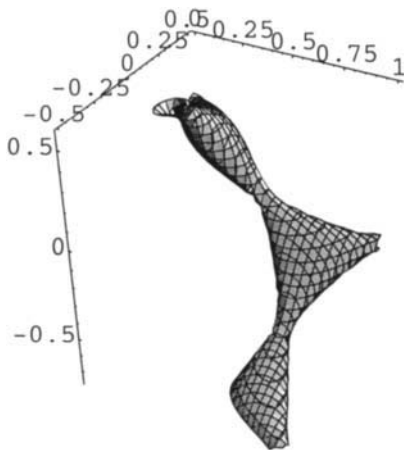


Figure 2.12a The connectivity is three.

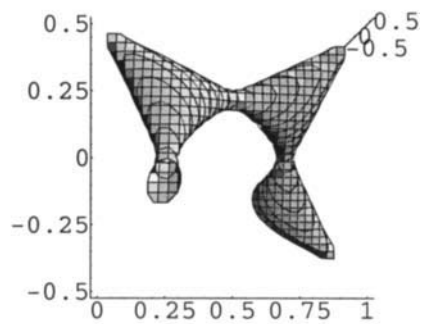


Figure 2.12b Different projection

The same plane permutation as above, put together with a phase shift (sine in stead of cosine) after equation 2.8, gives bodies of a shape considerably

different from spherical. This is because only three bodies surround a fourth, as shown in the plot in figure 2.12a and the projection in b. The connectivity is said to be three.

$$\begin{aligned} \sin \pi(x + y) + \sin \pi(x - y) + \sin \pi(x + z) \\ + \sin \pi(z - x) + \sin \pi(y + z) + \sin \pi(y - z) = 2.8 \end{aligned} \tag{2.8}$$

And for a constant of 2.7 there is figure 2.13, which is a part of the famous gyroid surface (after gyrate, which means moving around in circles or spirals), which was described in figures 4.1.2, 5, 6.

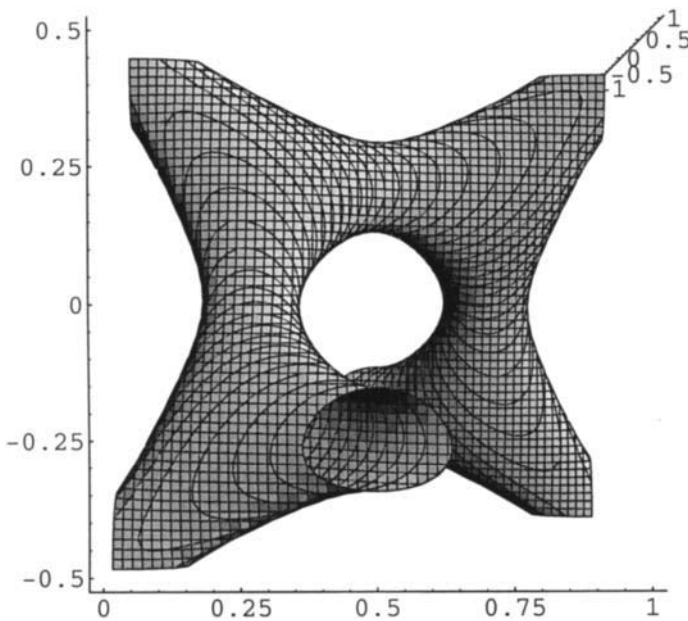


Figure 2.13 Part of the gyroid surface showing repeated three-connectivity.

The general case in 3D with $x+y+z$ has four planes, of which one was shown with a phase shift in figures 1.3a-b. The permutations are in equation 2.9, and the plot is shown for $C=1$ in figure 2.14a. The phase shift from cosine to sine in 2.14b, after equation 2.10 with $C=1$, which shifts the structure.

$$\begin{aligned} \cos \pi(x + y + z) + \cos \pi(x - y - z) \\ + \cos \pi(-x - y + z) + \cos \pi(-x + y - z) = C \end{aligned} \tag{2.9}$$

$$\begin{aligned} &\cos \pi(x + y + z - \frac{1}{2}) + \cos \pi(x - y - z - \frac{1}{2}) \\ &+ \cos \pi(-x - y + z - \frac{1}{2}) + \cos \pi(-x + y - z - \frac{1}{2}) = C \end{aligned} \quad 2.10$$

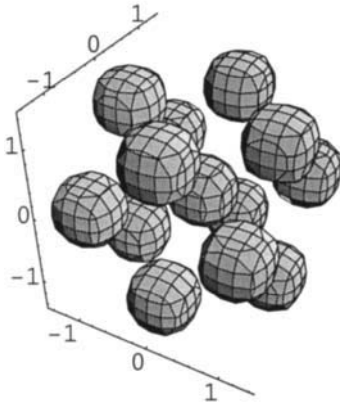


Figure 2.14a Cubeoctahedron of spheres in cubic close packing.

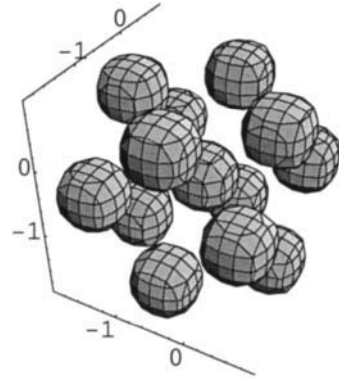


Figure 2.14b Phase shift.

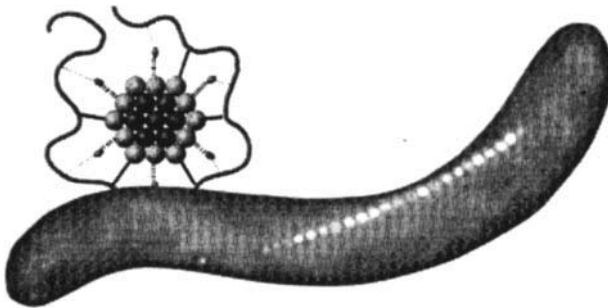


Figure 2.15 *Magnetospirillum magnetotacticum* with a string of Fe_3O_4 magnetite crystals [3].

The spheres are located at the vertices of a cubeoctahedron, which gives cubic close packing. Such packing of atoms is not common in biology but occurs for example for the Fe_3O_4 magnetite crystals in the bacterium *Magnetospirillum magnetotacticum*. The morphology of the particles is cube octahedral as here, with the space diagonal [111] axes oriented along the linear chain as shown in figure 2.15, ref. [3].

A smaller constant makes the spheres approach each other, and finally the perpendicular planes intersect.

Adding equations 2.9 and 2.10 gives the well known formula for the D surface as shown in chapter 2 and 8.

In chapter 2 we also carried out a discussion from the foundations of our biomathematics, where we showed that these fundamental surfaces grew out from infinite products of planes, or roots. The position of the individual planes determine the roots in the algebraic products, and the phase in the circular equations determines the positions of the infinitely repeated roots. The simplest formula for the D-surface seems to be the one given in equation 2.11, which is the one that will be used in the description of the structure of the D-surface below.

$$\begin{aligned} &\cos\pi\left(x+y+z+\frac{1}{4}\right)+\cos\pi\left(x-y-z+\frac{1}{4}\right) \\ &+\cos\pi\left(-x-y+z+\frac{1}{4}\right)+\cos\pi\left(-x+y-z+\frac{1}{4}\right)=C \end{aligned} \tag{2.11}$$

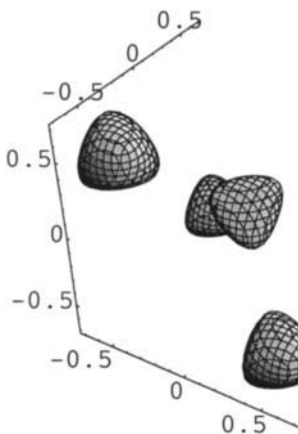


Figure 2.16a Vesicles in a diamond arrangement.

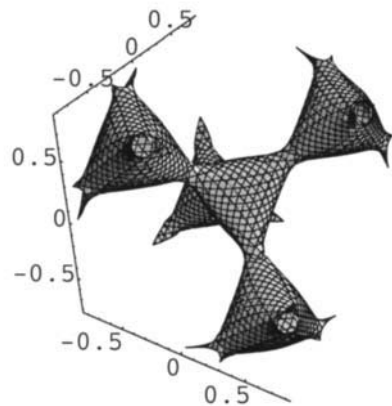


Figure 2.16b Vesicles meet to show the connectivity that is four.

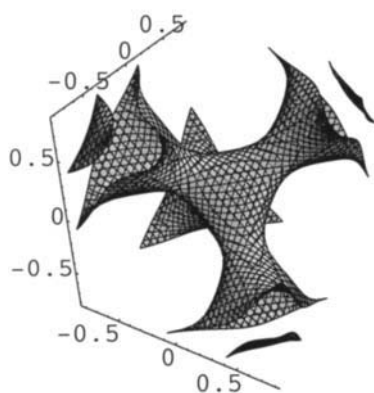


Figure 2.16c The D-surface.

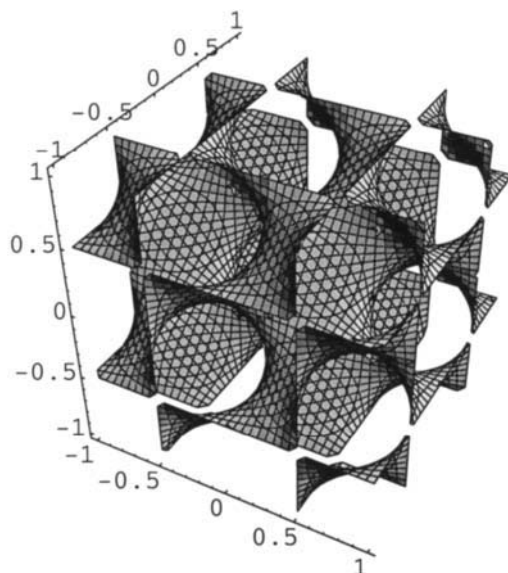


Figure 2.17 Bigger part of the D-surface.

We select a constant of 2.3 to show the sphere-like tetrahedra in space in figure 2.16a. The ordered structure of these bodies is that of the carbon atoms in diamond, and by changing the constant to 1.9 and 1.5 there are figures 2.16b-c, which show the development of catenoids between vesicles. There are four bodies around a fifth, and the connectivity is said to be four. Finally there is the complete structure of the D-surface at a constant of 0 in figure 2.17.

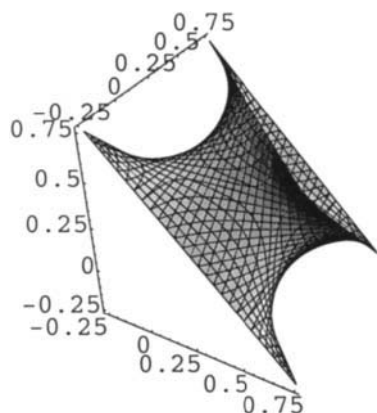


Figure 2.18a Boundaries to give the characteristic catenoid in the D-surface.

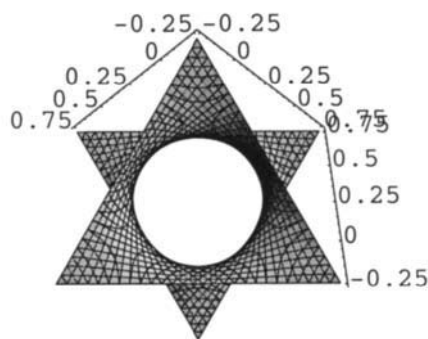


Figure 2.18b Different projection.

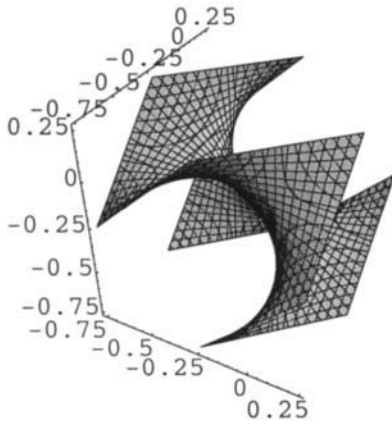


Figure 2.18c Monkey saddle in the D-surface.

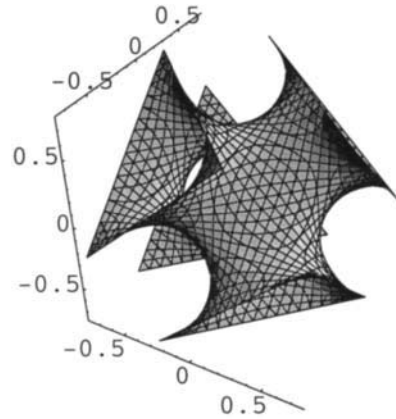


Figure 2.18d Typical part of the D-surface.

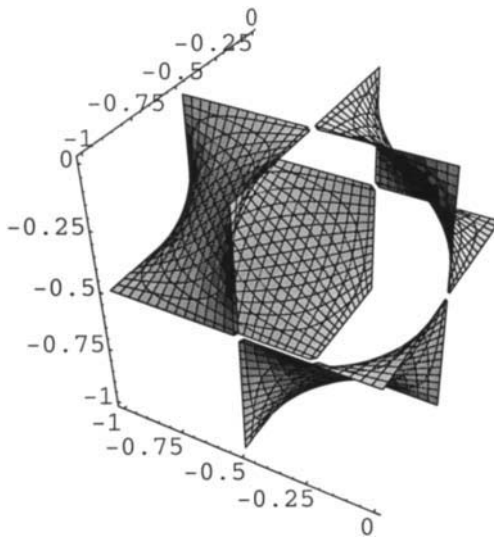


Figure 2.18e Different kinds of monkey saddles in the D-surface.

We have selected certain important parts of this surface by using appropriate boundaries, and show them in figure 2.18a-e. They clearly show the relationship to the D-minimal surface. Metal wires following the

boundaries of these surfaces will, when dipped into soap water and lifted out again, generate the D-minimal surface, which is topologically identical to the nodal D-surface. The nodal surfaces are very similar to the minimal surface analogues.

Of the surfaces discussed above, the ones with the lowest connectivity are of importance in biology. This means the G-, the D- and the P-surfaces. The nodal surfaces are the three dimensional correspondences to the two dimensional nodal lines, which are the curves along which a membrane remains at rest during eigenvibrations [2]. We have kept the original names of the minimal surfaces to describe the nodal surfaces, as these names reflect the symmetries common to the two types of surfaces. P stands for primitive, D stands for diamond, and G for gyroid.

We have used these surfaces to describe finite crystal shapes, or giant molecular phenomena like cubosomes (colloidal particles of bilayers with periodicity according to the D-, G-, or P-surfaces). As these have boundaries as ordinary molecules, a minimal surface description is impossible. An obvious description is of course the nodal description of standing wave character.

Some of the minimal surfaces represent, as special cases, groups of important surfaces or functions. We have done the most important ones in form of some periodic examples related to the nodal surfaces. When we later review differential geometry and curvature in appendix 8, some other minimal surfaces appear for mainly historical reasons, as type representatives. Their chemical or physical importance is very limited.

References Appendix 2

- 1 M. Jacob and S. Andersson, *THE NATURE OF MATHEMATICS AND THE MATHEMATICS OF NATURE*, Elsevier, 1998.
- 2 Courant & Hilbert, *Methods of Mathematical Physics*, Volume 1, Wiley, New York, 1953, p 300.
- 3 R.B. Frankel, D.A. Bazylinski, and D. Schüler, Eleventh Toyota Conference (cover picture), *Supramolecular Science* Vol. 5, No 3-4, 1998 p. 383.

Appendix 3 - The Exponential Scale, the GD function, Cylinder and Sphere Fusion

The GD function is used to demonstrate the properties of the exponential scale. Via the formation of catenoids, cylinders and spheres are brought together into structures.

We have shown how to make a plane, a cylinder, or a sphere, and we have made bundles of them by going periodic. We have seen how planes interact and collaborate in space to form spheres, which collaborate to build some very fundamental surfaces.

We shall now learn how to find a function that makes it possible to put two spheres next to each other in space. We will then bring them together, so they interact or react. The same can also be performed with planes, cylinders, or virtually any function. To do this we need *the exponential scale*.

The Gauss distribution (GD) function is famous for describing all kind of variations of properties in biology (see chapter 15). It is also known as the error function, and as the initial solution to the diffusion equation. We give the function in 3.1.

$$y = e^{-x^2} \tag{3.1}$$

In three dimensions, this function is built of infinite planes as shown in the equations 3.2a-c. The constant, $-1/2$, controls the distance between the planes.

$$e^{-x^2} - \frac{1}{2} = 0 \tag{3.2a}$$

$$e^{-y^2} - \frac{1}{2} = 0 \tag{3.2b}$$

$$e^{-z^2} - \frac{1}{2} = 0 \tag{3.2c}$$

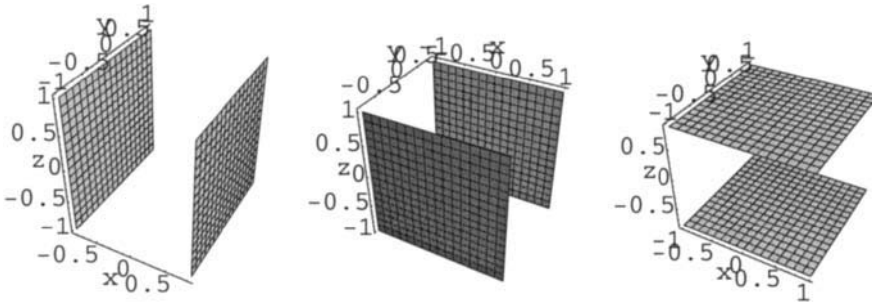


Figure 3.1a-c From the equations in 3.2 respectively.

If we add these equations pairwise, as in equation 3.3, we get cylinders as shown in figures 3.2a-c.

$$e^{-(x^2+y^2)} - \frac{1}{2} = 0 \tag{3.3a}$$

$$e^{-(x^2+z^2)} - \frac{1}{2} = 0 \tag{3.3b}$$

$$e^{-(z^2+y^2)} - \frac{1}{2} = 0 \tag{3.3c}$$

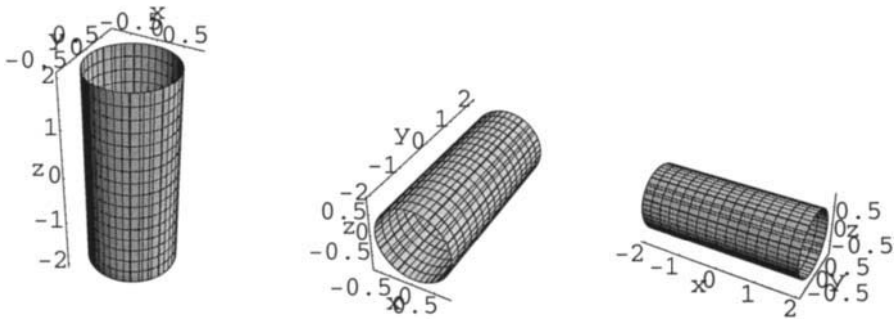


Figure 3.2a-c From the equations in 3.3.

We make an experiment. From above, we know that the each of the two individual equations in 3.4 gives a cylinder. If we add the two cylinders, we have equation 3.5, in which they fuse together to an ellipsoid, as in figure 3.3.

$$x^2 + y^2 = 1 \tag{3.4a}$$

$$x^2 + z^2 = 1 \tag{3.4b}$$

$$2x^2 + y^2 + z^2 = 2 \tag{3.5}$$

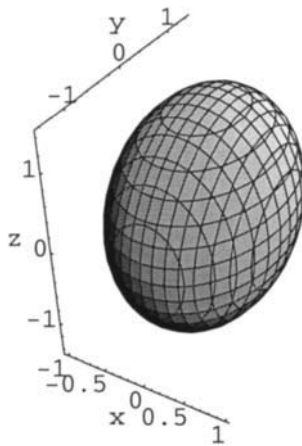


Figure 3.3 Ellipsoid after equation 3.5.

We know from earlier that we can move and tilt planes and cylinders. We add the two cylinders on an exponential scale, and give one of them a shift, as in equation 3.6, and figure 3.4.

$$e^{-(x^2+y^2)} + e^{-((x-4.5)^2+z^2)} - 0.5 = 0 \tag{3.6}$$

We see that the two cylinders are perfectly separated after equation 3.6. As we will learn, the exponential scale represents a wonderful method to extend mathematics of structures far beyond what earlier was possible. In equation 3.7 we let Δx take the values 2.5, 2 and 0, and find the corresponding figures in 3.5a-c.

$$e^{-(x^2+y^2)} + e^{-((x-\Delta x)^2+z^2)} - 0.5 = 0 \tag{3.7}$$

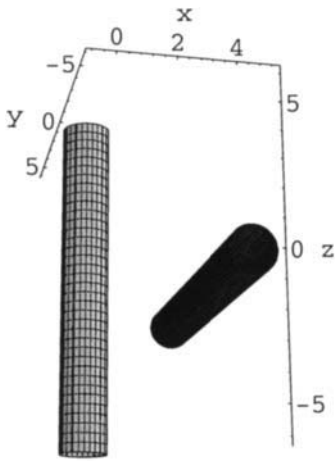


Figure 3.4 Two cylinders in space after exponential scale.

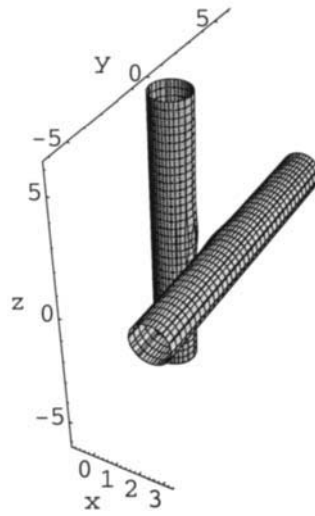


Figure 3.5a Rods are moved after equation 3.7. $\Delta x=2.5$.

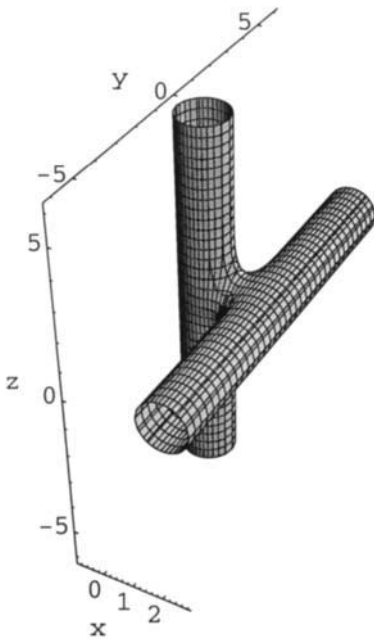


Figure 3.5b $\Delta x=2$.

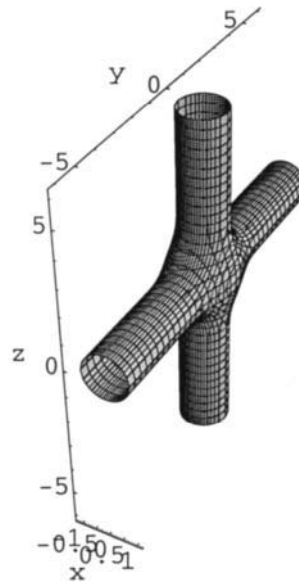


Figure 3.5c $\Delta x=0$.

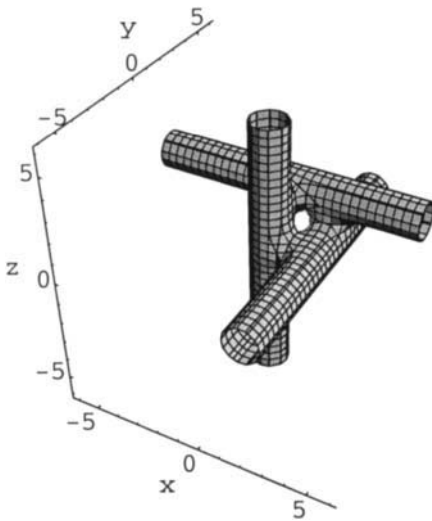


Figure 3.6 Three non-intersecting rods after equation 3.8.

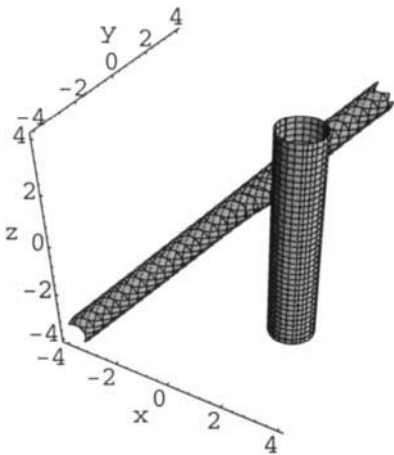


Figure 3.7a Two different kinds of rods.

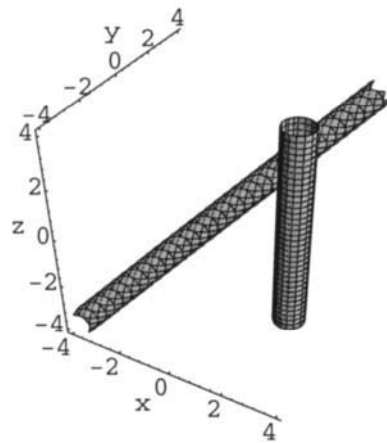


Figure 3.7b One rod is made smaller after equation 3.10.

Finally, in equation 3.8 we have three rods in space as shown in figure 3.6.

$$e^{-(x^2+y^2)} + e^{-((x-2)^2+z^2)} + e^{-((z-2)^2+(y-2)^2)} - 0.5 = 0 \quad 3.8$$

We may add one of the rods from above to a rod parallel to a cubic space diagonal (after 1.7), as in equation 3.9 and figure 3.7a.

$$e^{-((x-2.5)^2+y^2)} + e^{-((x-z)^2+(y-z)^2)+(x-y)^2} - 0.5 = 0 \quad 3.9$$

We change the size of the first rod in figure 3.7b after equation 3.10.

$$e^{-2((x-2.5)^2+y^2)} + e^{-((x-z)^2+(y-z)^2)+(x-y)^2} - 0.5 = 0 \quad 3.10$$

We move the first rod so the two intersect in figure 3.8 after equation 3.11.

$$e^{-2((x)^2+y^2)} + e^{-((x-z)^2+(y-z)^2)+(x-y)^2} - 0.5 = 0 \quad 3.11$$

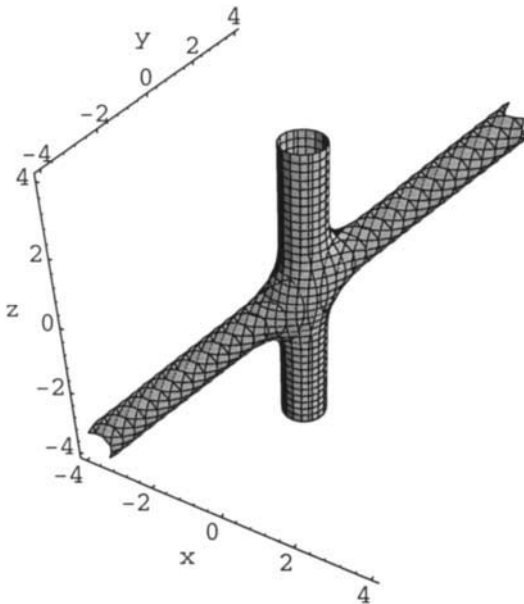


Figure 3.8 The two rods intersect.

Minimal surfaces are common in Nature, but we have learnt that the general minimal surfaces were difficult to handle mathematically.

As many shapes are determined by surface tension (cf. chapter 14), the implicit functions here are excellent for many things, and we will show a

couple of simple examples. We have studied the cylinders, and will now move on to look at the spheres.

We will show mathematically based “attraction” which agrees with our experimental knowledge of vesicle fusion.

We start by putting two spheres well apart by using the exponential scale in equation 3.12. We make the equation symmetric to be able to analyse it, and plot it for C=0.95 in figure 3.9.

$$e^{-((x-1.5)^2+y^2+z^2)} + e^{-((x+1.5)^2+y^2+z^2)} - C = 0 \tag{3.12}$$

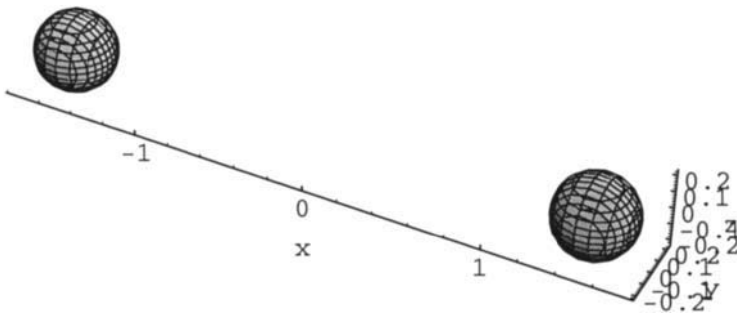


Figure 3.9 Two spheres well apart after equation 3.12.

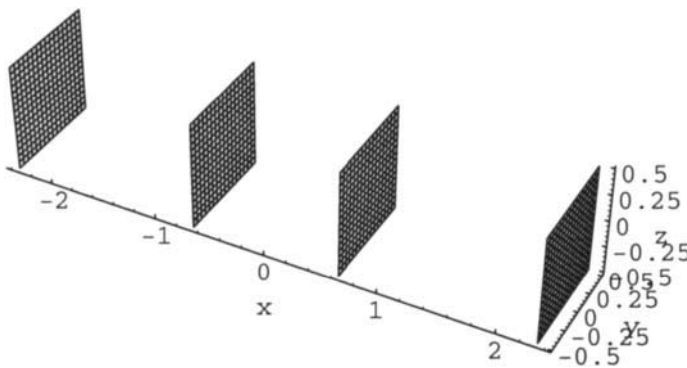


Figure 3.10 The planes instead of the spheres, to show the roots.

We then study the function along x by making $y=z=0$, which simplifies the equation, as in 3.13.

$$e^{-(x-1.5)^2} + e^{-(x+1.5)^2} - C = 0 \quad 3.13$$

This is plotted in figure 3.10 for $C=0.5$, and we see that it has four roots where the planes (earlier spheres) cut the x -axis. We come to an important property of these exponential functions, and show this by getting the roots out explicitly. It is easily realised from equation 3.13, that for x values close to 1.5, the second term is much smaller than the first term;

$$e^{-(1.5+1.5)^2} = e^{-(3)^2} \approx 10^{-4}$$

This means we put

$$e^{-(x-1.5)^2} = C$$

$$-(x-1.5)^2 = \ln C$$

$$x = 1.5 \pm \sqrt{-\ln C},$$

and the other pair of roots

$$x = -1.5 \pm \sqrt{-\ln C}.$$

For $C=0.5$ the roots are ± 0.67 and ± 2.33 , which was shown in figure 3.10.

Changing x^2 in the exponent back to $x^2+y^2+z^2$, we get spheres which become infinitely small when C approaches unity, since $e^0=1$ and $\ln C < 0$.

With C becoming smaller, the spheres become larger.

We plot the function for $C=0.5$ in equation 3.12 in figure 3.11.

The spheres approach each other as they grow in size. They meet at $x=y=z=0$, and the constant is determined by the calculation below, which is used in equation 3.12 to give figure 3.12a-b.

$$C = e^{(-1.5)^2} + e^{(1.5)^2} = 2e^{-2.25}$$

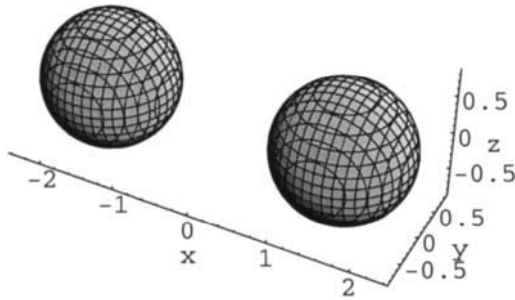


Figure 3.11 The spheres are closer because they are bigger.

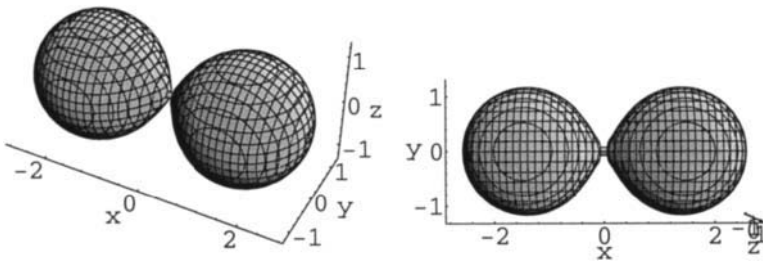


Figure 3.12 A constant of $2e^{-225}$ in equation 3.12 makes the spheres just meet.

The catenoid between the two spheres is developed for a constant of 0.15 in figure 3.13.

We changed the size of the spheres to make them meet in a combined function on the exponential scale. We now move the spheres towards each other by changing their coordinates, which is done with the equation 3.14, which is very similar to 3.12.

$$e^{-((x-\Delta x)^2+y^2+z^2)} + e^{-((x+\Delta x)^2+y^2+z^2)} - 0.5 = 0 \tag{3.14}$$

We go along x again and make $x=0$, and obtain a simple expression when the spheres meet;

$$e^{-(\Delta x)^2} + e^{-(\Delta x)^2} - 0.5 = 0$$

$$\Delta x = \sqrt{\ln 4}$$

Δx takes the values 1.8, 1.2, $\sqrt{\ln 4}$, and 1.1 below in figures 3.14a-d.

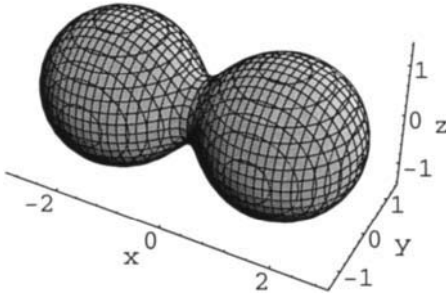


Figure 3.13 Still smaller constant, and a catenoid is developed.

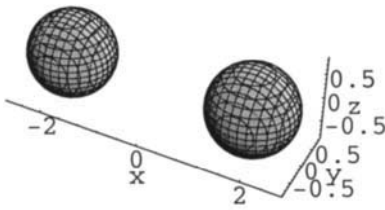


Figure 3.14a Spheres are moved after equation 3.13. $\Delta x = 1.8$.

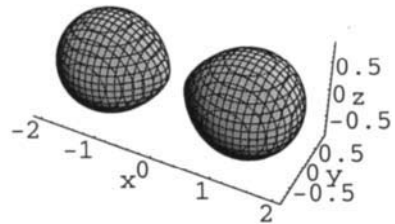


Figure 3.14b $\Delta x = 1.2$.

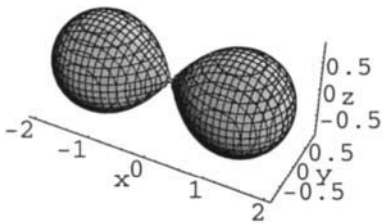


Figure 3.14c $\Delta x = \sqrt{\ln 4}$.

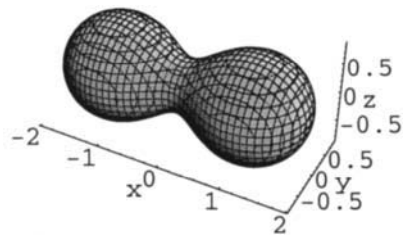


Figure 3.14d $\Delta x = 1.1$.

Appendix 4 - The Exponential Scale, the Planes and the Natural Function, Addition and Subtraction

The natural exponential is used to develop the exponential scale to make a polyhedron like the cube, or to make closed cylinders by using lids, or catenoids between planes, or spikes coming out from a plane.

The method of putting lids on cylinders and joining them in 2D- or 3D-space is used frequently in this book. We refer especially to the description of a mitochondrion and its division, and to the description of a muscle sarcomere and its motion of contraction, which both are in 2D. We also refer to the description of the dynamics of filaments and the Golgi machine in 3D. And to the flagella and the tree, in 2D.

We will now start to make planes on the exponential scale. We use the natural function, which is also called the Euler function after its inventor.

$$y = e^x \tag{4.1}$$

In one or two dimensions, this explicit function is very important for the fundamentals of mathematics. One application is the exponential growth.

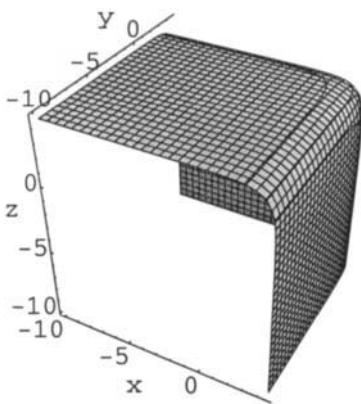


Figure 4.1a Exponential corner after equation 4.2.

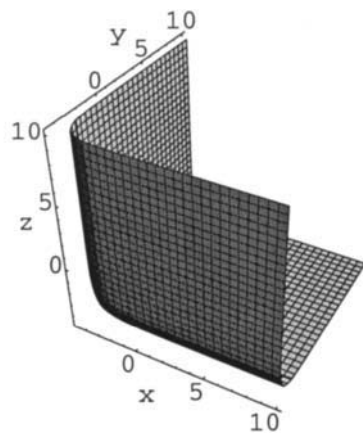


Figure 4.1b Exponential corner after equation 4.3.

The three dimensional implicit form is of great importance in geometry, as we have shown in section 5.2, which also is shown in refs. [1,2,3,4,5,6,7]. Here we show the geometry of equation 4.2 in figure 4.1a. In figures 4.1-3, the constant for equations 4.2-7 is set to $C=100$.

$$e^x + e^y + e^z = C \quad 4.2$$

And we show the geometry for equation 4.3 in figure 4.1b, which is a symmetrically equivalent version of 4.2.

$$e^{-x} + e^{-y} + e^{-z} = C \quad 4.3$$

We construct a cube by putting all these planes together in equation 4.4 and figure 4.2a.

$$e^x + e^y + e^z + e^{-x} + e^{-y} + e^{-z} = C \quad 4.4$$

We can move one of the cube-planes to elongate the cube, as shown in equation 4.5, and figure 4.2b.

$$e^{x-4} + e^y + e^z + e^{-x} + e^{-y} + e^{-z} = C \quad 4.5$$

The position of the moved plane is now around eight in x.

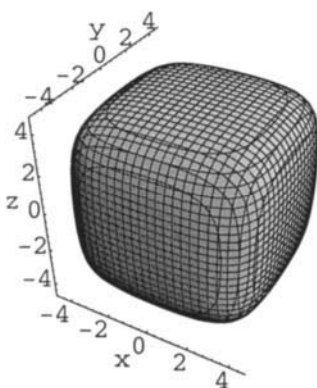


Figure 4.2a Cube after equation 4.4.

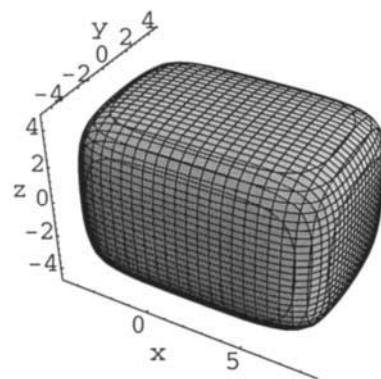


Figure 4.2b A plane moved in the cube after 4.5, creating a tetragonal polyhedron.

If we take away the cube-face, or plane, which is given by the term e^{-y} in equation 4.6, and shown in figure 4.3a, we get a square cylinder with one end closed.

$$e^x + e^y + e^z + e^{-x} + e^{-z} = C \tag{4.6}$$

By removing two of the planes from equation 4.4, we obtain the square cylinder in equation 4.7 and figure 4.3b.

$$e^x + e^z + e^{-x} + e^{-z} = C \tag{4.7}$$

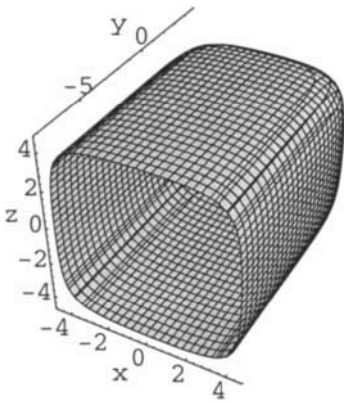


Figure 4.3a One plane missing from the cube, after equation 4.6.

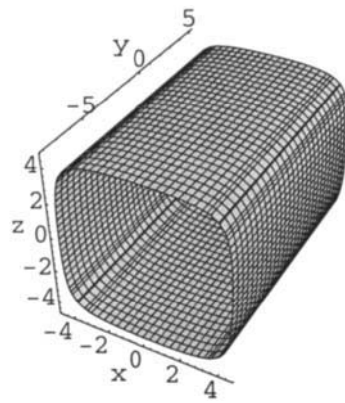


Figure 4.3b Two planes missing from the cube, after equation 4.7.

We now want to use this knowledge to put an end or two to a cylinder. We do that in line with above with the equations 4.8 and 4.9. The signs in the exponents are in accordance with the signs of the planes in the cube above. All is shown in figures 4.4a-b.

$$x^2 + y^2 + e^{(z-4)} = 10 \tag{4.8}$$

$$x^2 + y^2 + e^{(z-4)} + e^{-(z+6)} = 10 \tag{4.9}$$

Next, we wish to join different cylinders in space, which may correspond to a peptide chain. We then need to go to the GD-related functions of the exponential scale.

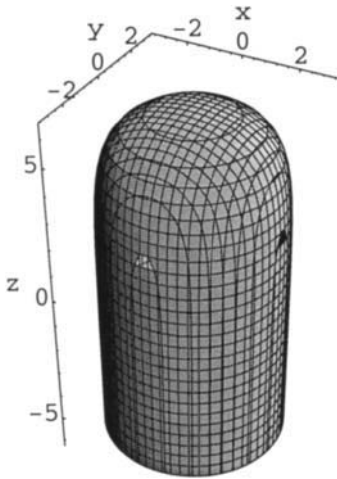


Figure 4.4a An end to a cylinder after 4.8.

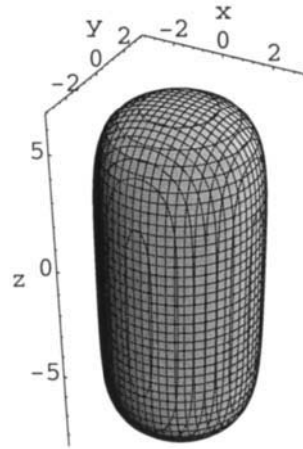


Figure 4.4b Two ends to a cylinder after 4.9.

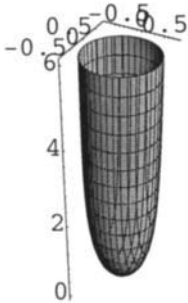


Figure 4.5a Single closed cylinder after equation 4.10.

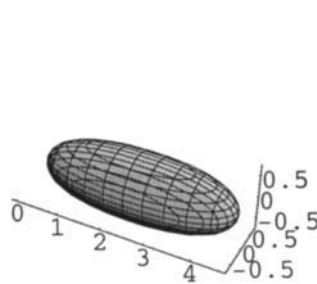


Figure 4.5b Double closed cylinder after equation 4.11.

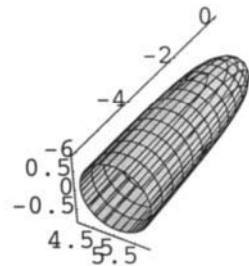


Figure 4.5c Single closed cylinder after equation 4.12.

We make three cylinders of different orientations in space. To do this we design the equations 4.10-12.

$$e^{-(x^2+y^2+e^{-z})} = 0.5 \tag{4.10}$$

$$e^{-(z^2+y^2+e^{-x}+e^{x-5})} = 0.5 \tag{4.11}$$

$$e^{-((x-5)^2+z^2+e^y)} = 0.5 \tag{4.12}$$

These cylinders are shown in figures 4.5a-c. We add them together in the equation 4.13, and the result is given in two different projections in figure 4.6a-b.

$$e^{-(x^2+y^2+e^{-z})} + e^{-(z^2+y^2+e^{-x}+e^{x-5})} + e^{-((x-5)^2+z^2+e^y)} = 0.6 \tag{4.13}$$

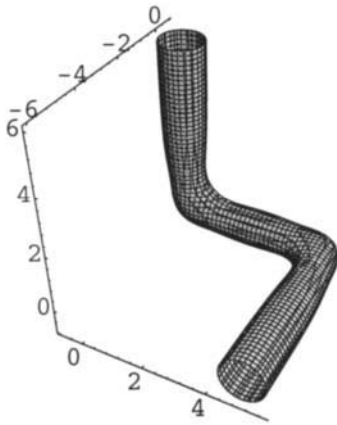


Figure 4.6a The three cylinders added together at the closed ends, after equation 4.13.

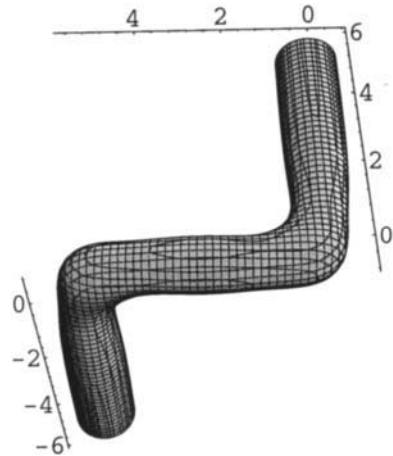


Figure 4.6b Different projection of a.

Here we have seen various effects of omitting planes, for example opening one face of a cube. Next we will see what happens when a plane is subtracted from this cube. We make a cube where we have changed the sign for one of the terms, *i.e.* the e^z plane is subtracted, in equation 4.14. The result is dramatic as shown in figure 4.7.

$$e^x + e^y - e^z + e^{-x} + e^{-y} + e^{-z} = 100 \tag{4.14}$$

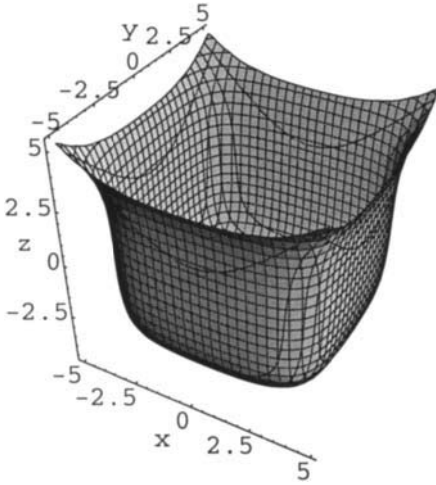


Figure 4.7 A plane is subtracted from a cube after 4.14.

We do the same with the closed cylinder of equation 4.9 and figure 4.4b, and get equation 4.15.

$$x^2 + y^2 - e^z - e^{-z} = 0 \tag{4.15}$$

This is shown in figure 4.8 which is the famous catenoid, which is a minimal surface.

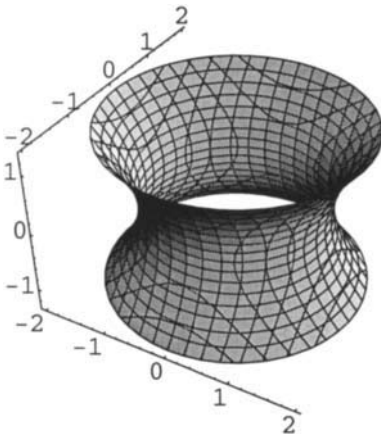


Figure 4.8 Two planes subtracted from a cylinder after 4.15.

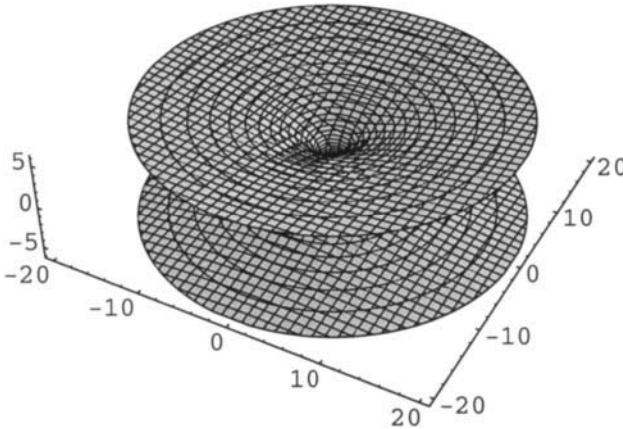


Figure 4.9 Extended borders to show the catenoid minimal surface of figure 4.8.

Extended borders in figure 4.9 show where the planes are.

There are several ways to make catenoids, and our favourite is the one with the GD-function, since it can be moved around, and multiples can be made. We show this with the equations 4.16-18 and figures 4.10-12.

In these equations, e^{z^2} represents two parallel planes, and the GD-type $e^{-(x^2+y^2)}$ -function is the cylinder.

$$e^{-(x^2+y^2)} + e^{z^2} = 1.5 \tag{4.16}$$

With equation 4.17 we can change the distance between the planes, by moving the first z-term.

$$e^{-(x^2+y^2)} + e^{z-2} + e^{-z} = 1.5 \tag{4.17}$$

In equation 4.18 there are two catenoids, which are shown in figure 4.12, and of course these can also be moved around.

$$e^{-(x^2+y^2)} + e^{-(x^2+(y-4)^2)} + e^z + e^{-z} = 2.5 \tag{4.18}$$

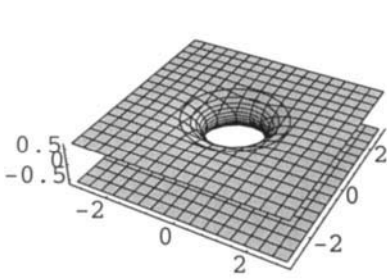


Figure 4.10 This is the structure of holes in a lamellar liquid crystalline phase, or the pore structure of cell nuclear membranes (the surfaces shown corresponds to the polar head groups of the lipid bilayer). After equation 4.16.

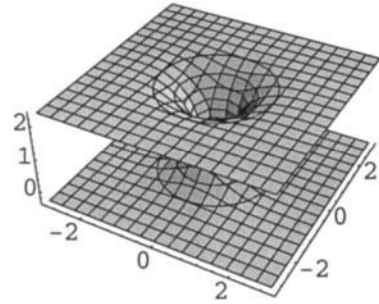


Figure 4.11 With a GD-description it is possible to change the distance between planes.

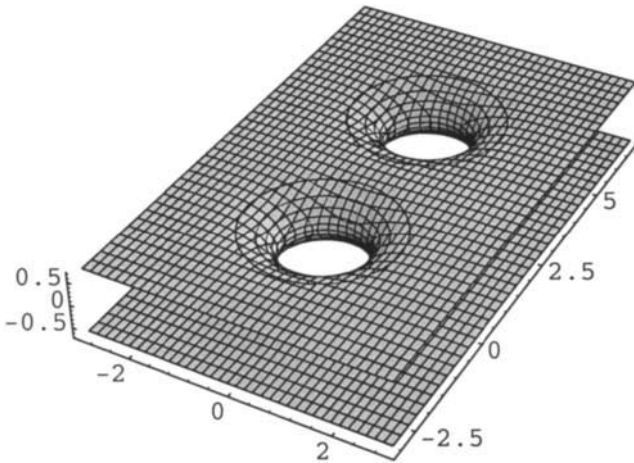


Figure 4.12 With a GD-description it is possible to make two, or more catenoids between planes.

With just one plane in 4.19 we get a spike. This structure can however be changed with the constant. The topology in figure 4.13 is very similar to the structure of half the pseudo-sphere, which is famous for having constant negative Gaussian curvature.

$$e^{-(x^2+y^2)} + e^{-z} = 1$$

4.19

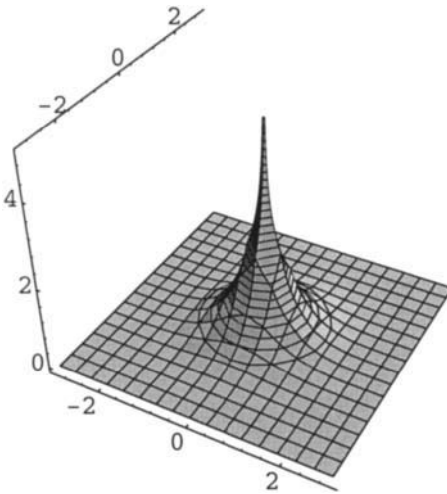


Figure 4.13 With one plane after 4.19 there is a spike.

References Appendix 4

- 1 M. Jacob and S. Andersson, *THE NATURE OF MATHEMATICS AND THE MATHEMATICS OF NATURE*, Elsevier, 1998.
- 2 S. Andersson and M. Jacob, *The exponential Scale*, Supplement No. 13 of *Zeitschrift für Kristallographie*, R. Oldenbourg Verlag, München, 1997.
- 3 S. Andersson, M. Jacob, S. Lidin, On the shapes of crystals, *Z. Kristallogr.* **210**, 3-4 (1995).
- 4 S. Andersson, M. Jacob, K. Larsson, S. Lidin, Structure of the Cubosome - a closed Lipid Bilayer Aggregate, *Z. Kristallogr.* **210** (1995) 315-318.
- 5 K. Larsson, M. Jacob, S. Andersson, Lipid bilayer standing waves in cell membranes, *Z. Kristallogr.* **211** (1996) 875-878.

- 6 S. Andersson, M. Jacob, On the structure of mathematics and crystals, *Z. Kristallogr.* **212** (1997) 334-346.
- 7 M. Jacob, Saddle, Tower and Helicoidal surfaces, *J.Phys. II France* **7** (1997) 1035-1044.

Appendix 5 - Multiplication of Planes, Saddles and Spirals

Saddles are derived from planes and used to derive important surfaces. Helicoids are derived from saddles, and via the exponential scale multiple spirals are described. Finally, the surface for the DNA-molecule is derived, also with the saddle-approach using the exponential scale.

Multiplication of planes gives saddles as we will show in this appendix. The simple product xy in equation 5.1a is two intersecting planes, as shown in figure 5.1a.

$$xy = 0$$

5.1a

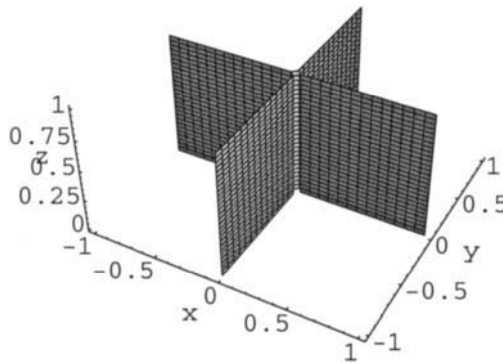


Figure 5.1.a Two intersecting planes.

Adding a z -plane gives equation 5.1b, which gives the saddle in figure 5.1b.

$$xy = z$$

5.1b

Rotating the saddle 45° after equation 5.2, gives figure 5.1b.

$$(x + y)(x - y) = z$$

5.2

In figures 5.2a-b, the borders are extended, and it becomes clear that these saddles are derived from planes.

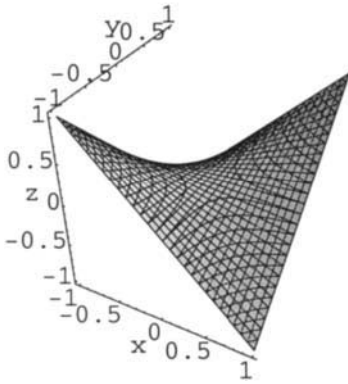


Figure 5.1b A saddle after 5.1.

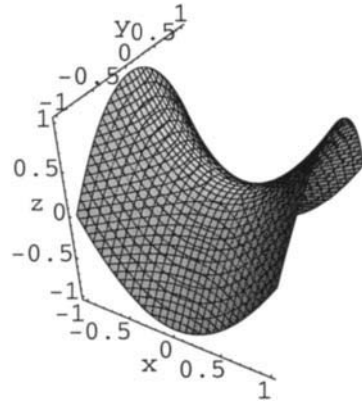


Figure 5.1c The saddle is rotated 45° after equation 5.2.

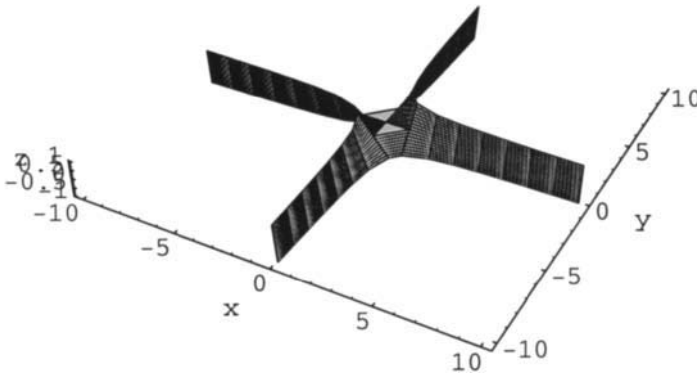


Figure 5.2a Extending the borders shows that the saddles are derived from planes.

Using a circular function as in equation 5.3, the saddles are repeated along z to a beautiful tower surface in figure 5.3. This is the fundamental structure unit of the lipid-protein bilayer at the alveolar surface of lungs (see chapter 14).

$$xy + \cos \pi z = 0$$

5.3

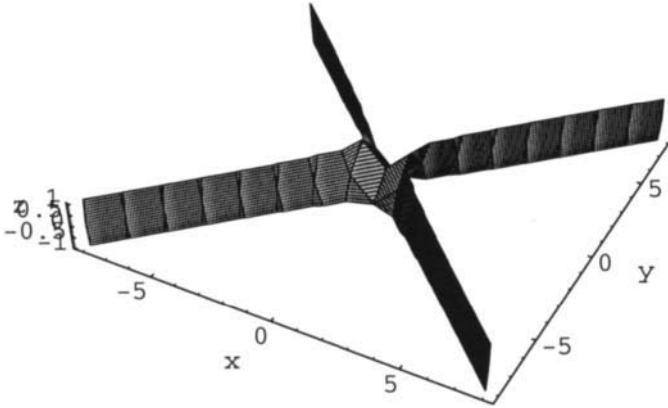


Figure 5.2b The saddle is rotated 45°.

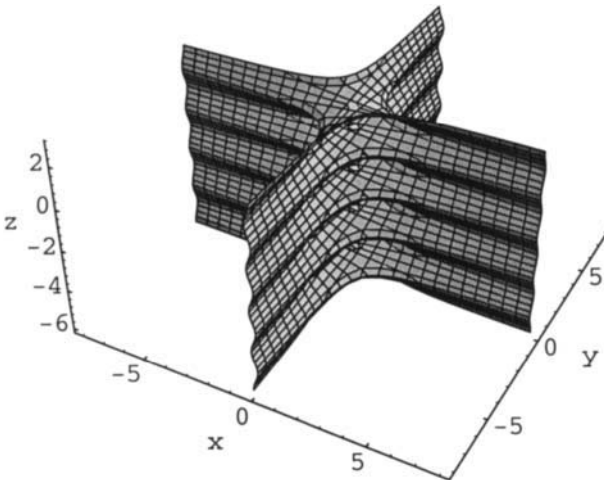


Figure 5.3 Saddles repeat along z to a beautiful tower surface after equation 5.3.

We also make three planes meet after 5.4, and the intersecting planes are shown in figure 5.4.

$$y\left(\frac{\sqrt{3}}{2}x + \frac{1}{2}y\right)\left(\frac{\sqrt{3}}{2}x - \frac{1}{2}y\right) = 0 \quad 5.4$$

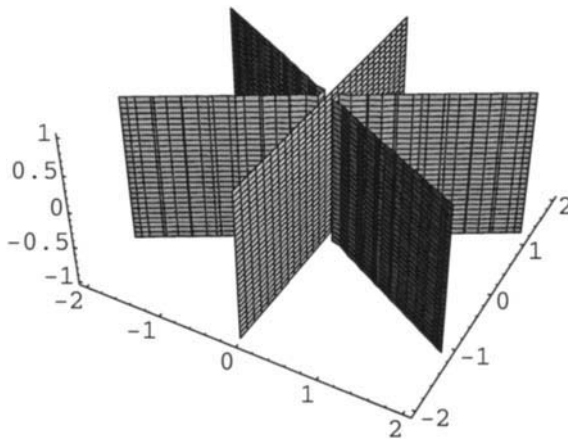


Figure 5.4 Three intersecting planes.

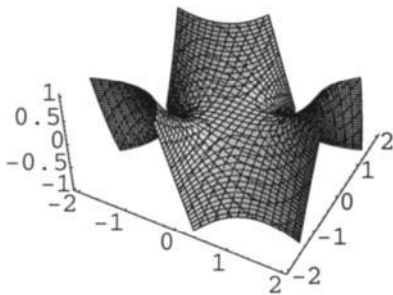


Figure 5.5a Bringing in z gives a monkey saddle after equation 5.5.

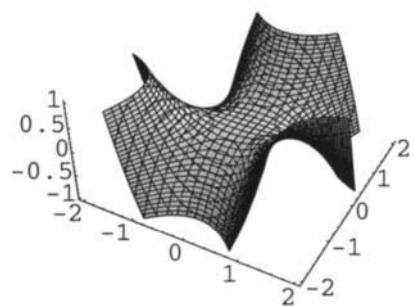


Figure 5.5b Rotated after equation 5.6.

Bringing in a z-plane gives a saddle as in equation 5.5, and the saddle is then rotated with equation 5.6.

$$x\left(\frac{1}{2}x + \frac{\sqrt{3}}{2}y\right)\left(-\frac{1}{2}x + \frac{\sqrt{3}}{2}y\right) + z = 0 \tag{5.5}$$

$$y\left(\frac{\sqrt{3}}{2}x + \frac{1}{2}y\right)\left(\frac{\sqrt{3}}{2}x - \frac{1}{2}y\right) + z = 0 \tag{5.6}$$

We see the two saddles next to each other in figures 5.5a-b.

Extending the borders as in figure 5.5c shows how the monkey saddle really is built up by planes.

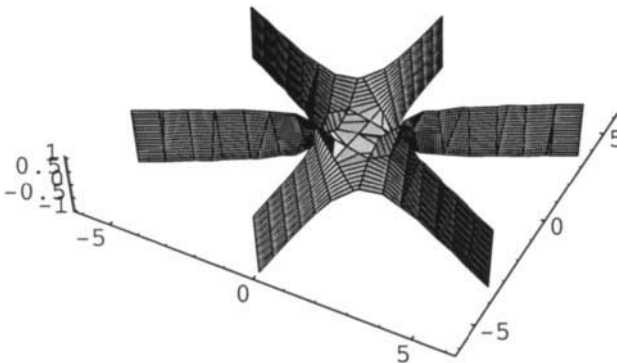


Figure 5.5c Extended borders show that the monkey saddle is also built of planes.

Finally, using a circular function as in equation 5.7, the saddles are repeated along z to a beautiful tower surface in figure 5.6.

$$x\left(\frac{1}{2}x + \frac{\sqrt{3}}{2}y\right)\left(-\frac{1}{2}x + \frac{\sqrt{3}}{2}y\right) + \cos \pi z = 0 \tag{5.7}$$

These tower surfaces in figures 5.3 and 5.6 are of course beautiful demonstrations of how planes can go through each other continuously without intersections.

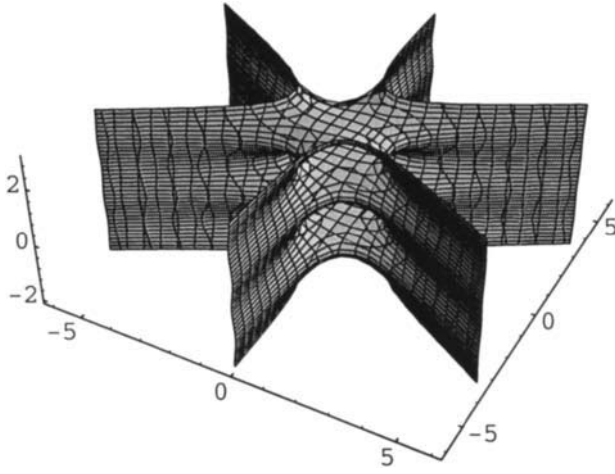


Figure 5.6 The monkey saddle also builds a tower surface.

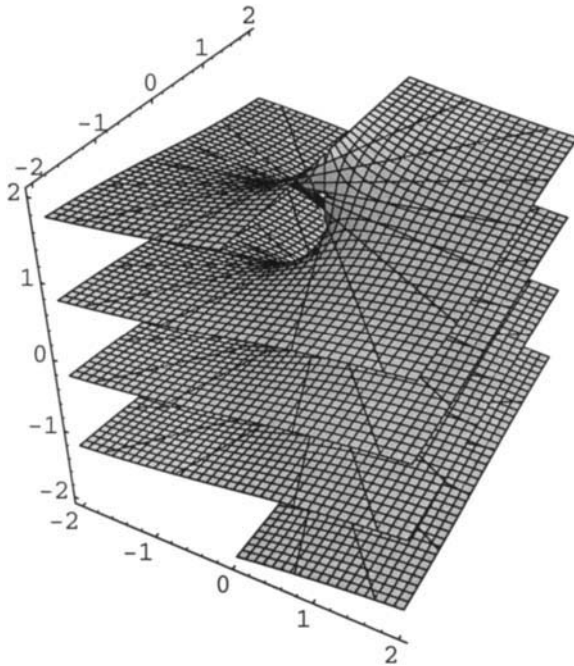


Figure 5.7 Helicoid.

The chiral helicoid, or screw, or spiral surface, is a very important surface in chemistry, physics and mathematics. We start by giving its beautiful and simple equation in 5.8.

$$x \sin \pi z + y \cos \pi z = 0 \tag{5.8}$$

We have shown how to derive this surface from planes using the fundamentals of mathematics, *i.e.* the algebra in chapter 2. We refer to that and just here say that we make the x and the y planes rotate by using the circular functions on the z terms. This helicoid surface is given in figure 5.7.

What was done above, can with the exponential scale be made finite or partly finite. We show beautiful applications of this below.

The helicoid is made finite in its extension in the xy plane by adding a cylinder as in equation 5.9, which results in the spiral in figure 5.8.

$$x \cos \pi z + y \sin \pi z + x^2 + y^2 = 0 \tag{5.9}$$

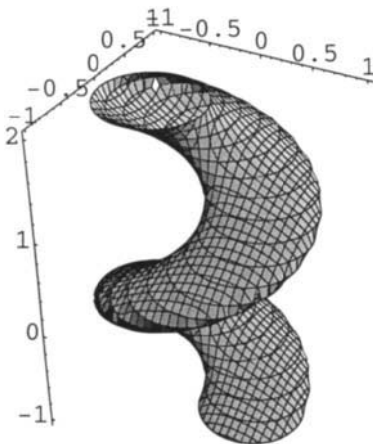


Figure 5.8 A helicoid and a cylinder makes a spiral.

To create a double spiral, we bring in more planes, which we naturally get from the saddles above, as shown in equation 5.10.

$$xy \cos \pi z + \frac{(x^2 - y^2) \sin \pi z}{2} + \frac{e^{x^2 + y^2}}{10} = 0 \quad 5.10$$

Bringing in even more planes from the saddle equations in 5.5-6 we get a triple spiral in equation 5.11.

$$\begin{aligned} & x\left(\frac{1}{2}x + \frac{\sqrt{3}}{2}y\right)\left(-\frac{1}{2}x + \frac{\sqrt{3}}{2}y\right)\cos \pi z \\ & + y\left(\frac{\sqrt{3}}{2}x + \frac{1}{2}y\right)\left(\frac{\sqrt{3}}{2}x - \frac{1}{2}y\right)\sin \pi z + \frac{1}{20e^{x^2 + y^2}} = 0 \end{aligned} \quad 5.11$$

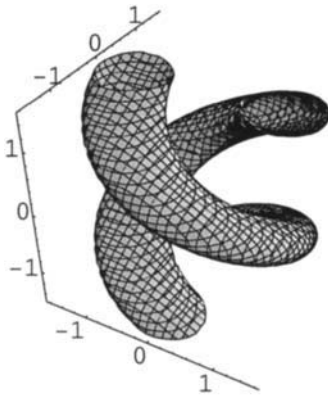


Figure 5.9a Equation with a saddle gives the double spiral.

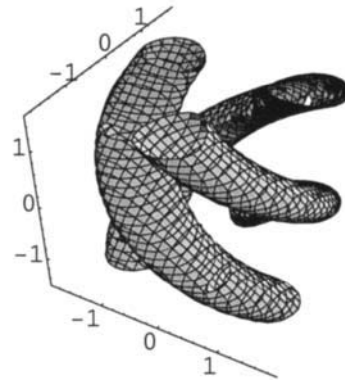


Figure 5.9b Equation with a monkey saddle gives the triple spiral.

This was a couple of cases from the general spiral equation, as given by two of us in ref. [1].

The general equation for the multi-spiral of the DNA-type was derived by one of us via the so called helicoidal saddle tower surfaces [2]. Here we shall demonstrate this by showing the derivation of the DNA-surface itself.

We start by deriving a tower surface, which is a hybrid of the two saddle orientations above, and is plotted below in figure 5.10 after equation 5.12.

$$\frac{1}{2(x^2 - y^2)} + xy - \cos \pi z = 0 \quad 5.12$$

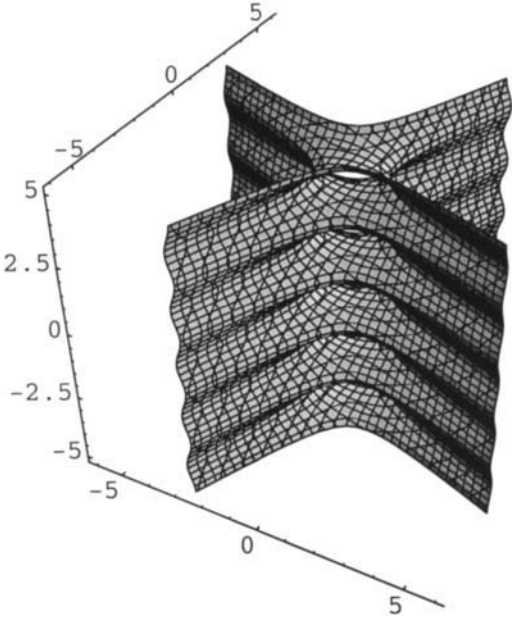


Figure 5.10 A tower surface after equation 5.12.

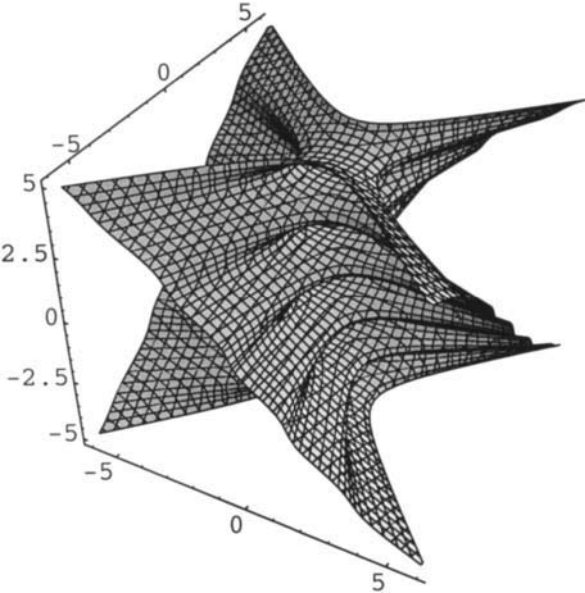


Figure 5.11 A helicoidal tower surface after 5.13.

This tower surface is transformed in equation 5.13 to a helicoidal tower surface by applying the helicoid equation 5.8, which is illustrated in figure 5.11.

$$xy \cos\left(\frac{\pi z}{10}\right) + \frac{1}{2}(x^2 - y^2)\sin\left(\frac{\pi z}{10}\right) - \cos \pi z = 0 \tag{5.13}$$

The tower surface has now become a formidable screw.

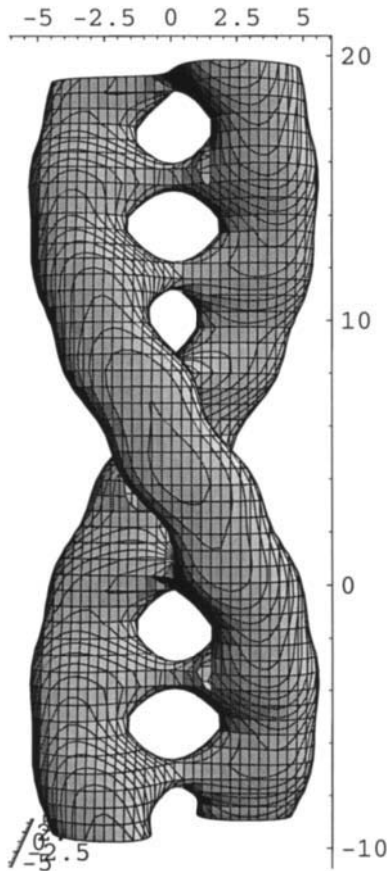


Figure 5.12 A part of an idealised DNA double helix (the DNA molecule) after equation 5.14, identical with the original in ref. [2].

We then add the damping in form of an exponential cylinder, and change the saddle period to get the right number of hydrogen bond bridges in the pitch of the DNA. The equation for this saddle description of a part of an idealised DNA double helix (the DNA-molecule) is now identical to the original in ref. [2]. The equation is given in 5.14 and the formidable structure is shown in figure 5.12.

$$xy \cos\left(\frac{\pi z}{10}\right) + \frac{1}{2}(x^2 - y^2) \sin\left(\frac{\pi z}{10}\right) - \cos\left(\frac{\pi z}{2}\right) + \frac{3}{5}e^{(x^2 + y^2)/10} = 0 \quad 5.14$$

References Appendix 5

- 1 M. Jacob and S. Andersson, *THE NATURE OF MATHEMATICS AND THE MATHEMATICS OF NATURE*, Elsevier, 1998.
- 2 Jacob, M., *J. Phys. II France*, 7 (1997) 1035-1044.

This Page Intentionally Left Blank

Appendix 6 - Symmetry

The concepts of group, translation, unit cell and crystal classes are described. Two-fold, six-fold, and four-fold axes of symmetry are defined. Unit cells are described as parallelepipeds, made of planes. These planes are repeated with circular functions to give crystal structures.

By studying the interaction between vesicles, cylinders, and planes, we could in the earlier appendices show that structures of proper symmetry stemmed from a fundamental theorem of algebra. We have found that the implicit permutation of the variables in space give functions which seem to be synonyms with symmetry, ref. [1]. Below we give the traditional way of describing symmetries and simpler structures.

As geometry can be described as 'earth measurement' (what we can measure with a ruler), symmetry may be explained as 'form measurement'. In the geometry of a triangle with equal sides there is a 3-fold axis of rotation, in a square there is a 4-fold axis, in a regular pentagon there is a 5-fold axis, and in a hexagon there is a 6-fold axis. And between your hands there is a mirror plane (bilateral symmetry) when they are oriented next to each other. Now you know the fundamentals of symmetry, and we go directly to 3D space.

Structures in 3D can have all different types of order, ranging from completely disordered to completely ordered in all three directions. Structures that are periodic in one direction are for instance the actin filament and the DNA. There are also structures that are periodic in two directions, and one example is the structure of the surface lining in the alveolus, as discussed in chapter 14. Structures that are periodic in three dimensions are very common in biology, for example apatite in bone, cubosomes in cell membrane aggregates, and crystalline proteins in muscles.

In all these cases a smallest unit of the structure is repeated in the x-, y-, and/or z-directions in a parallel manner. This *unit cell* is in three dimensions a parallelepiped, and it can have different symmetry ranging from triclinic to cubic, as shown below. The unit cell repetition is called *translation*. Periodic translation of a unit cell and its contents forms an infinite structure, and such a structure will also have a symmetry, which

depends on the form or symmetry of unit cell that is repeated. This is what we will discuss.

In crystallography words like group, symmetry group and symmetry operations are frequently used. If we say a figure is symmetric, it means we can do symmetry operations which leave the whole figure unchanged while permuting its parts. The symmetry operations of any figure form a group, which is called the symmetry groups of the figure. If a figure is completely irregular, like the letter **F**, its symmetry group is of the order one, consisting of the identity only. The letter **E** has bilateral symmetry, the mirror plane being horizontal, and its symmetry group is of order two. The letter **N** is symmetrical by a half turn, which is a rotation of π , a reflection in a point, or a central inversion. The symmetry group is still of order two, and the group is said to be cyclic.

It was not until 1924 the famous mathematician George Pólya managed to show that there are only 17 plane groups in 2D - no more and no less. In 3D there are 230 space groups.

On the other hand, in the thirteenth century Spain, the Moors used all these seventeen plane groups in the art of filling a plane with a repeating pattern for their decoration of Alhambra. By trial and error of course. Another famous use of these seventeen groups is found in the work of Dutch artist M. C. Escher, who instead of the abstract patterns of the Moors, used animal shapes.

There is much more to say about the theory of symmetry, space groups and the reciprocal lattice. We stop for the moment and concentrate on examples of structures and symmetry.

The structures to come will all contain the periodic translation operation, which is of immense importance. Molecules order up after the translation to a crystal, and its structure may be studied with single crystal x-ray diffraction methods. Almost all our knowledge of protein structure, lipid self-assembly and DNA came through such studies. Some molecules can be studied in a high resolution electron microscope, and information is obtained via three dimensional reconstruction of the 2D images recorded. This is another important tool in modern molecular biology.

There are seven coordinate systems used by crystallographers, which are called the crystal systems. There are the axes a , b , c and the angles between them are α , β , γ (these are the lengths of the sides, and the angles between them, in the unit cell). Corresponding to x , y , z in our graphics here, these ' a , b , c ' are all unity, and they are all perpendicular to each other. We shall

not use the vector or tensor notation, we just use everyday crystallographic terminology.

The seven crystallographic coordinate systems are listed below;

Triclinic $a \neq b \neq c$ and $\alpha \neq \beta \neq \gamma$

Monoclinic $a \neq b \neq c$ and $\beta \neq 90^\circ$

Orthorhombic $a \neq b \neq c$ and $\alpha = \beta = \gamma = 90^\circ$

Tetragonal $a = b \neq c$ and $\alpha = \beta = \gamma = 90^\circ$

Hexagonal $a = b \neq c$ and $\alpha = \beta = 90^\circ$; $\gamma = 120^\circ$

Trigonal (can be treated as hexagonal)

Cubic $a = b = c$ and $\alpha = \beta = \gamma = 90^\circ$

It must be said that the metric rules above do not describe the true symmetry, but are rather conditions necessary, but not sufficient. Equalities may only be there within the experimental error. When a complete crystal structure determination has been carried out on a crystal, the symmetry is determined, and with this the coordinate system is also determined.

So we determine the symmetry for a crystal and its structure, by making a structure analysis at lowest possible resolution.

The simplest possible box is a cube, since all axes are of equal size and perpendicular to each other. Cubes with rounded edges and vertices are shown in figure 6.1, and we have taken the opportunity to use the exponential scale and included one of the three mutually perpendicular 4-fold axes in figure 6.1a, and one of the six 2-fold axes in figure 6.1b. The equations are in 6.1 and 6.2.

$$e^{-2.4e^{x^2+y^2}} + e^{-(e^{x^2} + e^{y^2} + e^{z^2} - 10)} = 0.08 \quad 6.1$$

$$e^{-1.2(e^{(-x-y+z)^2} + e^{(-x+y-z)^2})} + e^{-(e^{x^2} + e^{y^2} + e^{z^2} - 10)} = 0.08 \quad 6.2$$

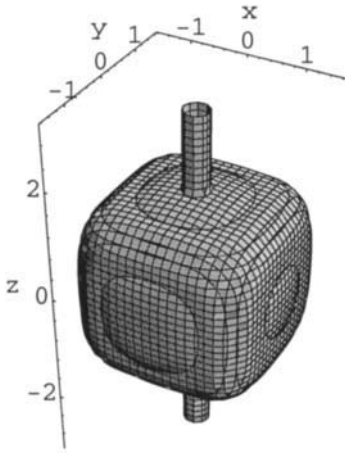


Figure 6.1a 4-fold axis in cubic symmetry.

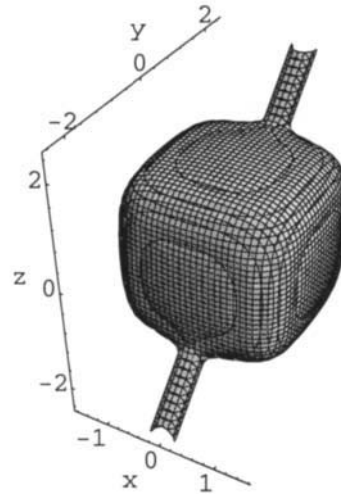


Figure 6.1b 2-fold axis in cubic symmetry.

In a cubic crystal structure there is no requirement to have a 4-fold axis, but it is necessary to have the four 3-fold axes, for cubic symmetry, which are shown as cylinders in figure 6.2 after equation 6.3.

$$\begin{aligned}
 &e^{-0.8(e^{(x+y)^2} + e^{(y+z)^2} + e^{(x-z)^2})} \\
 &+ e^{-0.8(e^{(x-y)^2} + e^{(y+z)^2} + e^{(x+z)^2})} \\
 &+ e^{-0.8(e^{(x-y)^2} + e^{(y-z)^2} + e^{(x-z)^2})} \\
 &+ e^{-0.8(e^{(x+y)^2} + e^{(y-z)^2} + e^{(x+z)^2})} \\
 &+ e^{-(e^{x^2} + e^{y^2} + e^{z^2} - 20)} = 0.08
 \end{aligned}
 \tag{6.3}$$

There are also plenty of mirror planes in the cube, as seen in for example figure 6.6.

Next, we turn to the hexagonal class, and we demonstrate the important 6-fold axis with a hexagonal prism in figure 6.3a after equation 6.4.

$$e^{(2y\sqrt{3}/3)^4} + e^{(x+y\sqrt{3}/3)^4} + e^{(-x+y\sqrt{3}/3)^4} + e^{z^4} - 10^6 = 0 \tag{6.4}$$

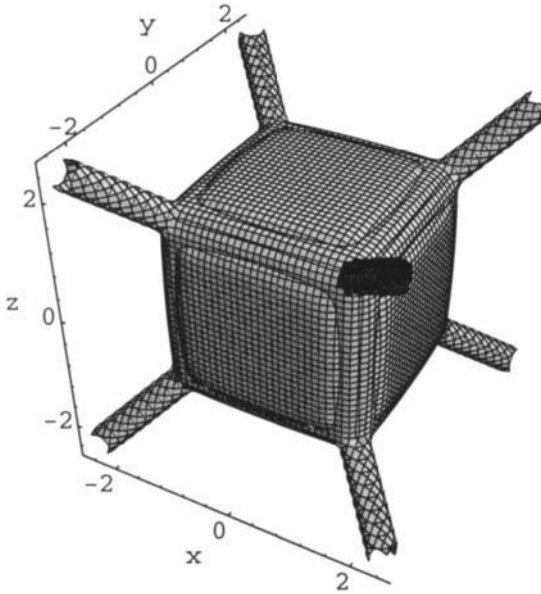


Figure 6.2 Four 3-fold axes in cubic symmetry.

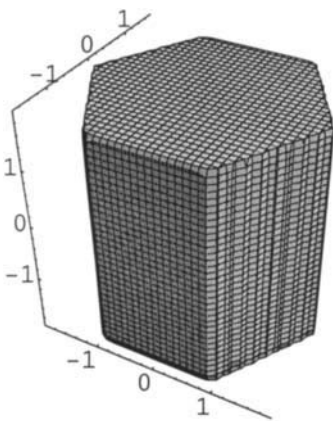


Figure 6.3a 6-fold axis with a hexagonal prism.

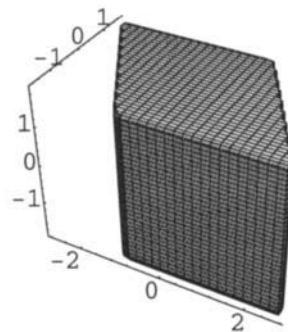


Figure 6.3b A third of the hexagonal prism.

The asymmetrical unit (smallest possible unit to repeat with symmetry) is a third of the hexagonal prism. This is also a picture of the hexagonal coordinate system with origin in an obtuse corner shown in figure 6.3b.

$$e^{(2y\sqrt{3}/3)^4} + e^{(x+y\sqrt{3}/3)^4} + e^{z^4} - 10^6 = 0 \quad 6.5$$

Going tetragonal we loose the 3-fold axes, and three of the four 4-fold axes from the cubic system. The picture is in 6.4 and the equation is 6.6.

$$e^{-2.4e^{x^2+y^2}} + e^{-(e^{x^4} + e^{y^4} + 6e^{z^4} - 20)} = 0.08 \quad 6.6$$

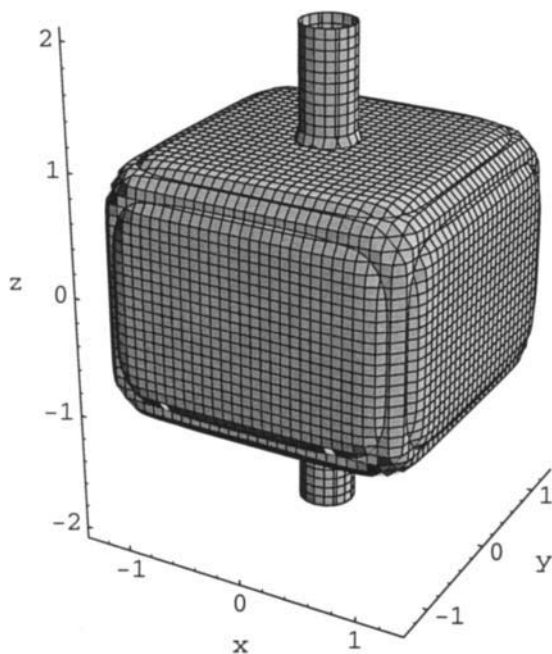


Figure 6.4 The 4-fold axis in tetragonal symmetry.

Next is the orthorhombic class, which only has 2-fold axes, as shown in figure 6.5. It also has mirror planes, which are not indicated.

$$\begin{aligned}
 & e^{-2.5e^{x^2+y^2}} + e^{-2.5e^{x^2+z^2}} + e^{-2.5e^{y^2+z^2}} \\
 & + e^{-(e^{x^6} + 4e^{y^6} + 16e^{z^6} - 20)} = 0.08
 \end{aligned}
 \tag{6.7}$$

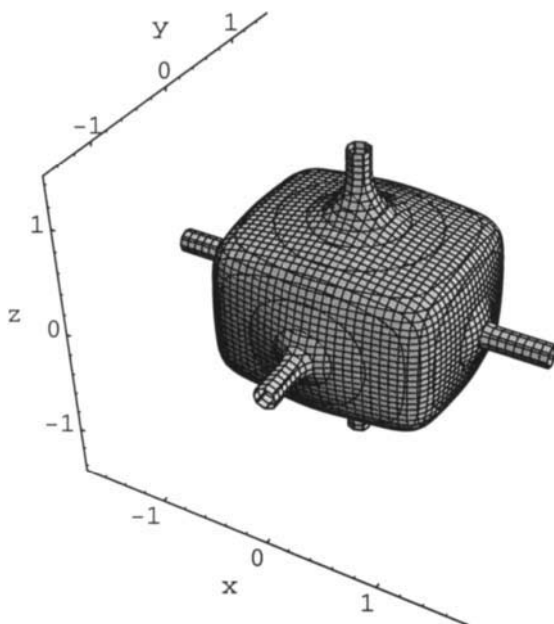


Figure 6.5 Three 2-fold axes in orthorhombic symmetry.

We do not show the monoclinic or triclinic systems here.

We have studied the symmetry of the crystal classes in form of the parallelepipeds of the coordinate systems, and will now give the structures when these aggregates are repeated with translation. We have earlier described translation as the roots of the polynom of counting, cf. equation 6.8.

$$(x-1)(x-2)(x-3)(x-4)\dots \tag{6.8}$$

Making the product infinite, we have the circular functions (cf. chapter 3), and the repetition of the cube with translation is in equation 6.9. This is a solution to the wave equation. The surface consists of three sets of planes that intersect, and the periodicity with cubes are shown in figure 6.6a, where we clearly can see the symmetry elements.

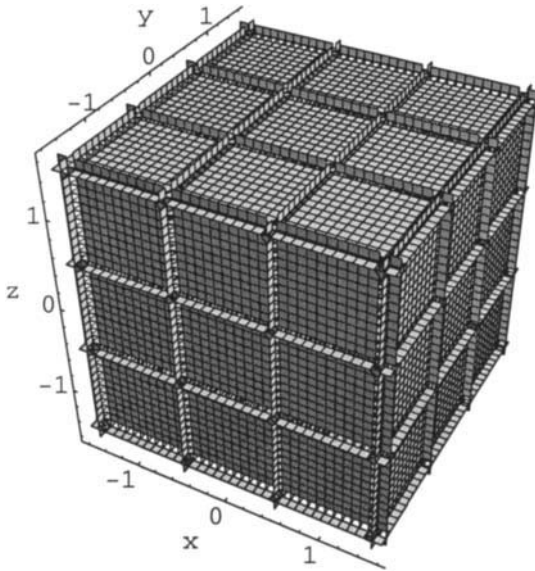


Figure 6.6a Periodicity with cubes.

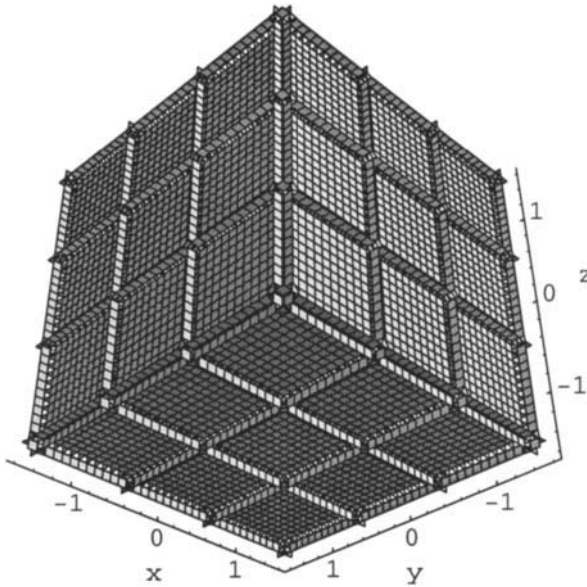


Figure 6.6b Different projection of a.

$$\cos \pi x \cos \pi y \cos \pi z = 0 \quad 6.9$$

The hexagonal repetition of hexagons is described by equation 6.10 and is shown in figure 6.7. There are here four sets of planes that intersect.

$$\sin\left(\pi \frac{2\sqrt{3}}{3} y\right) \sin\left(\pi\left(x + y \frac{\sqrt{3}}{3}\right)\right) \sin\left(\pi\left(-x + y \frac{\sqrt{3}}{3}\right)\right) \sin(\pi z) = 0 \quad 6.10$$

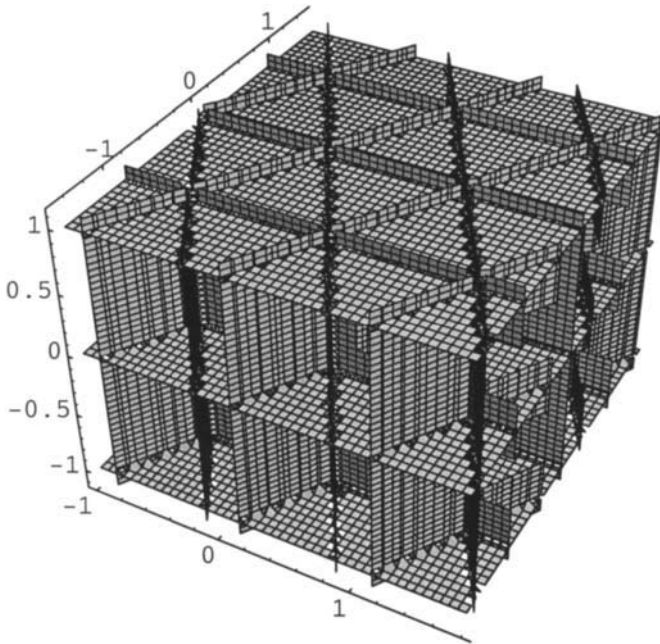


Figure 6.7 Hexagonal repetition.

The equations for the tetragonal and orthorhombic structures of infinite extensions of boxes are shown in figures 6.8-9 from equations 6.11-12.

$$\cos(\pi x) \cos(\pi y) \cos\left(\frac{3\pi z}{2}\right) = 0 \quad 6.11$$

$$\cos(\pi x) \cos\left(\frac{\pi y}{2}\right) \cos\left(\frac{3\pi z}{2}\right) = 0 \quad 6.12$$

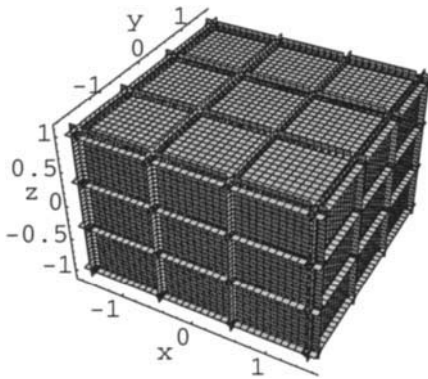


Figure 6.8 Tetragonal structure.

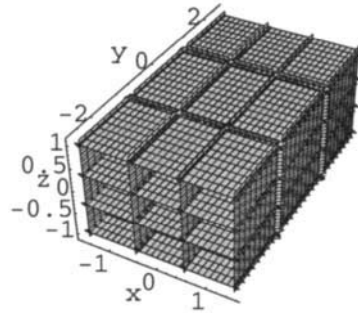


Figure 6.9 Orthorhombic structure.

In order to make complete atomic structures, the boxes are filled with atoms. In the case of the cube, we begin with one atom in each box, which results in the structure in figure 6.10. This structure is called primitive cubic packing.

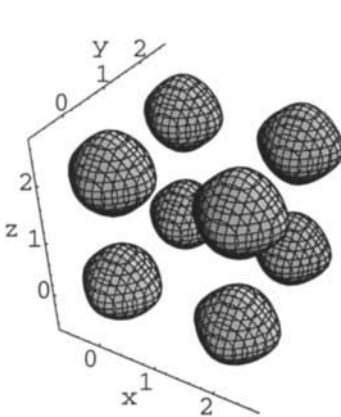


Figure 6.10 Primitive structure.

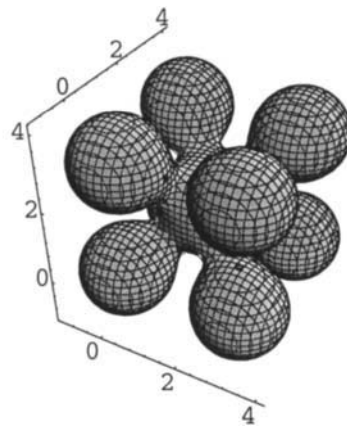


Figure 6.11 Body centred structure.

If the cube in figure 6.10 is filled with an atom in the centre, we get figure 6.11, which is called a body centred structure (*bcc* = body centred cubic). We also fill the neighbouring cubes, and show a larger part of this structure in figure 6.12. The centre of the atoms are at the corners of a polyhedron called the rhombic dodecahedron. This structure is found in many metals and also in stainless steel.

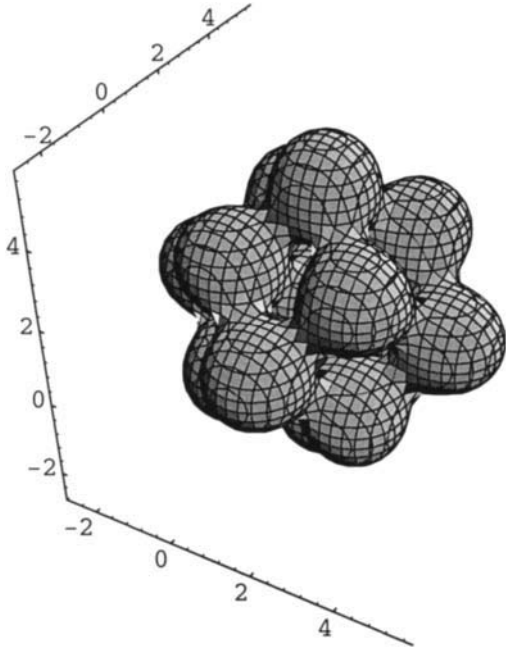


Figure 6.12 Atoms sit at the corners of a rhombic dodecahedron.

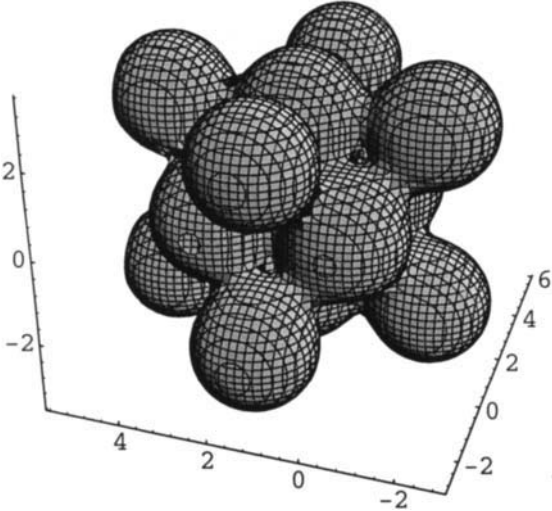


Figure 6.13 Cubic closest packing of atoms.

In the next structure, we fill the box in figure 6.10 with one atom at the centre of each face, as shown in figure 6.13. As each such atom is shared with another box (the face is common to two boxes) there are three atoms added to the box. This is called a face centred cubic arrangement of atoms (*fcc*), and as this is the closest packing of atoms in a cubic structure it is also called cubic close packing (*ccp*). Many metals adopt this structure.

This geometrical picture in 6.13 as described in a way where the atoms represent the vertices of eight tetrahedra surrounding one octahedron, was first described by Kepler and is called *stella octangula*.

Another piece of cubic close packing is shown in figure 6.14. The centre of each atom around the central is a corner of the polyhedron called the cube octahedron, which is the morphology of the Fe_3O_4 magnetite crystals in the bacterium *Magnetospirillum magnetotacticum*, which was shown in figure 2.15 in appendix 2.

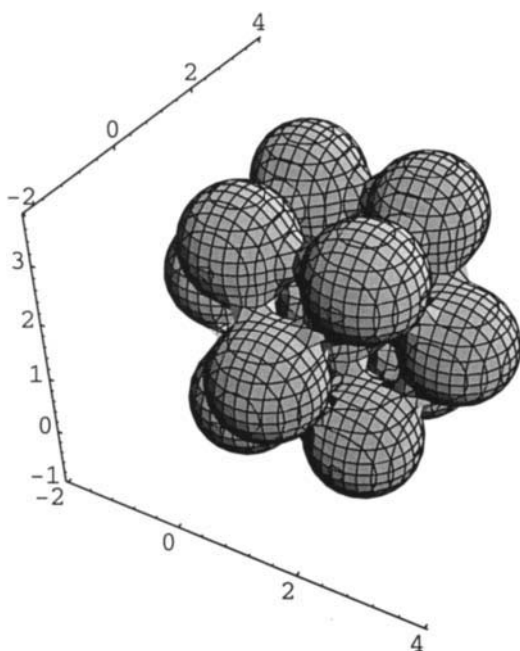


Figure 6.14 Another piece of cubic close packing - the cube octahedron.

We also give a hexagonally close packed (*hcp*) arrangement of atoms in figure 6.15. As this is not a polyhedron, mathematically it has been given the name "isomer form of cube octahedron", or by chemists just the

"hexagonal form of a cube octahedron". Hcp is also a common structure for metals, titanium being one of them.

The figures 6.10-15 are all from ref. [1].

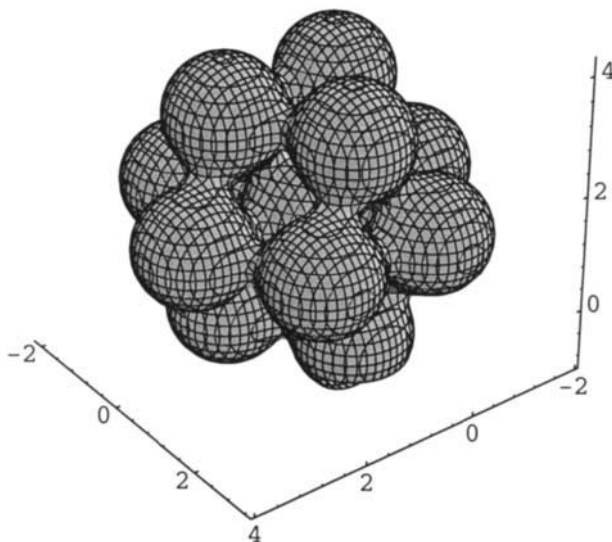


Figure 6.15 Hexagonally close packed (*hcp*) arrangement of atoms.

The structures above are simple, and are described with atomic positions and symmetry elements, where the symmetry elements create copies of the original atom in new positions. This means that if you have an atom in a general position (x, y, z) , it can be repeated by a body centred operation to $(x + 1/2, y + 1/2, z + 1/2)$. Then we may have a centre of symmetry with (x, y, z) repeated to $(-x, -y, -z)$. We can also have a mirror plane with (x, y, z) going to $(x, -y, z)$. Then this atom may be repeated by a 3-fold rotation axis to two more positions. Or by a 4-fold axis to three more positions, or by a 2-fold rotation to one more. And there can also be a chiral structure having a screw. We give this as another example below.

A general point defining an atomic position is (x, y, z) . The first screw operation we call 4_1 and it takes us to the point $(-y, x, 1/4 + z)$. The second screw operation is 4_1^2 and its point is $(-x, -y, 1/2 + z)$, and the third is 4_1^3

and the point is $(y, -x, 3/4+z)$. All possible combinations of these symmetry operations in the seven crystal classes give the 230 groups in space. A general point in the cubic system may be repeated in various places in the unit cell up to 192 times, with only the three variables x, y, z for the general position. Hence, we can describe the position of 192 atoms only with the three variables x, y, z . If we had the lowest case possible, which is the triclinic without a centre of symmetry, 192 atoms in the unit cell would need 576 $(3 \cdot 192)$ variables or parameters to be determined in a crystal structure determination. This is a very difficult task indeed, so symmetry is very important for information reduction.

The icosahedron and symmetrically related polyhedra have 2-fold, 3-fold, and 5-fold axes of symmetry (as shown in chapter 12), and several virus molecules have this symmetry. Molecules of any symmetry which crystallise to form a crystal may be studied with great detail with diffraction methods. The structure of giant particles such as virus (molecules) have been determined (except for the genome inside which is disordered relative to the surrounding protein molecules). The genome, as said, has no 3D translational periodic symmetry [2], and the immense amount of information collected from the complicated structure determination of such structures, only gives a part of the structure.

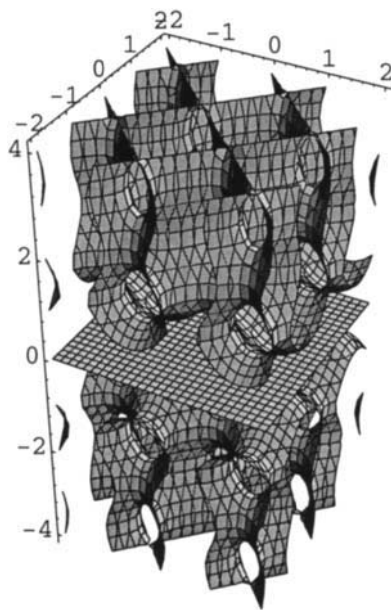


Figure 6.16 A mathematical mirror plane.

Five-fold symmetry cannot be repeated with periodic translation - the so-called quasi crystals of certain alloys have dilatation symmetry [3]. In Nautilus and Turitella there is a characteristic piece which is repeated under dilatation (congruent), as the animal grows. The liposomes and Schwann cell are other another examples of dilatation. A more difficult one is the formidable two dimensional organisation of logarithmic spirals into Phyllotaxis in botany.

The most famous symmetry operation is the mirror, which may be called the reflection or the bilateral operation. In crystals we often discuss the *mirror plane* although the actual plane is never there. But we have made it visible in a mathematical crystal with the equation 6.13, shown in figure 6.16.

$$\sin \pi z + z \sin \pi x + z \sin \pi y = 0 \quad 6.13$$

References Appendix 6

- 1 M. Jacob and S. Andersson, *THE NATURE OF MATHEMATICS AND THE MATHEMATICS OF NATURE*, Elsevier, 1998.
- 2 C. Brändén and John Tooze, *INTRODUCTION TO PROTEIN STRUCTURE*, Garland, NewYork, 1991, page 162.
- 3 Jacob M., A routine for generating the structure of an icosahedral quasicrystal, *Z. Kristallogr.* **209**, 925 (1994).

This Page Intentionally Left Blank

Appendix 7 - The Complex Exponential, the Natural Exponential and the GD-Exponential - General Examples and Finite Periodicity

The complex exponential and its relation to cosine is described. More examples of the exponential scale is shown using higher exponentials. The GD function is used to build finite periodicity with several examples.

In physics and also in chemistry it is very common to use the complex exponential, e^{ix} .

We shall shortly explain and use complex numbers. The number i is an imaginary number, it does not physically exist. The number i is $\sqrt{-1}$.

From the expansions of the circular functions, shown in equations 7.1-2 and the expansion of the natural exponential in 7.3,

$$\sin x = x - \frac{x^3}{3!} + \frac{x^5}{5!} - \dots \tag{7.1}$$

$$\cos x = 1 - \frac{x^2}{2!} + \frac{x^4}{4!} - \dots \tag{7.2}$$

$$e^x = 1 + \frac{x}{1!} + \frac{x^2}{2!} + \frac{x^3}{3!} + \frac{x^4}{4!} + \frac{x^5}{5!} \dots \tag{7.3}$$

$$e^{ix} = 1 + \frac{ix}{1!} - \frac{x^2}{2!} - \frac{ix^3}{3!} + \frac{x^4}{4!} + \frac{ix^5}{5!} \dots$$

it is clear that e^{ix} can be written

$$e^{ix} = \cos x + i \sin x. \tag{7.5}$$

And it is easy to show that

$$\sin x = \frac{1}{2}i(e^{ix} - e^{-ix}) \quad 7.6$$

and

$$\cos x = \frac{1}{2}(e^{ix} + e^{-ix}). \quad 7.7$$

These are the miracles in mathematics: The derivative of \cos is sine and vice versa, the derivative of e^x is e^x , which is the natural function. The complex exponential is e^{ix} , and its remarkable and strange relations with the circular functions are given in equations 7.6-7. We conclude by giving the most beautiful formula of all, as discovered by de Moivre in 7.8.

$$e^{\pi i} = -1 \quad 7.8$$

Using e^{ix} means that the real part is $\cos x$ and the imaginary part is $\sin x$ from 7.5. Or,

$$\operatorname{Re}[e^{ix}] = \cos x$$

and

$$\operatorname{Im}[e^{ix}] = \sin x.$$

But the general function to use is the complex exponential:

$$e^{\pi i x} + e^{\pi i y} + e^{\pi i z} \quad 7.9$$

We write

$$e^{ix} = \cos x + i \sin x$$

and the real part of the complex exponential is

$$\operatorname{Re}[e^{\pi i x} + e^{\pi i y} + e^{\pi i z}] = \cos \pi x + \cos \pi y + \cos \pi z. \quad 7.10$$

So when you see e^{ix} , it is often understood that it is just $\cos x$. And the complex exponential in 3D is an alternative for description of a cubosome structure in biology, or a primitive cubic structure in crystallography.

We may do a generalisation in 7.11, and come back to the natural exponential.

$$e^{x^n} + e^{y^n} + e^{z^n} = C \tag{7.11}$$

For n odd we have the cube corner, which is shown in figure 7.1a for n=5. With increasing n there are sharper edges and corners. For n even there is the cube, which is shown in figure 7.1b for n=6.

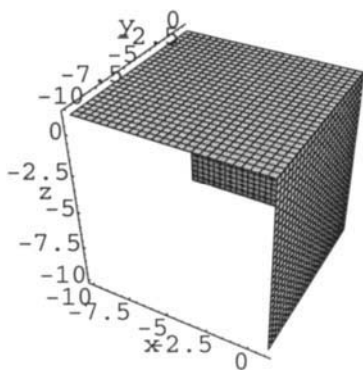


Figure 7.1a n odd in 7.11 is the cube corner.

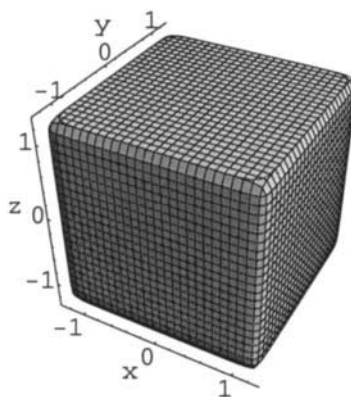


Figure 7.1b n even in 7.11 generates the cube.

We do the same generalisation with the complex exponential in equation 7.12.

$$e^{(ix)^n} + e^{(iy)^n} + e^{(iz)^n} = C \tag{7.12}$$

With n=1 we have the circular functions, and with n=2 the GD-function, since $i^2 = -1$.

A beautiful example of emerging periodicity is the double planes from the GD-function, which automatically create eight identical cube corners through cubic symmetry operations, from equation 7.13, and this is shown in figure 7.2. The sharp edges and corners come from the high exponent.

$$e^{-x^6} + e^{-y^6} + e^{-z^6} = 0.01 \tag{7.13}$$

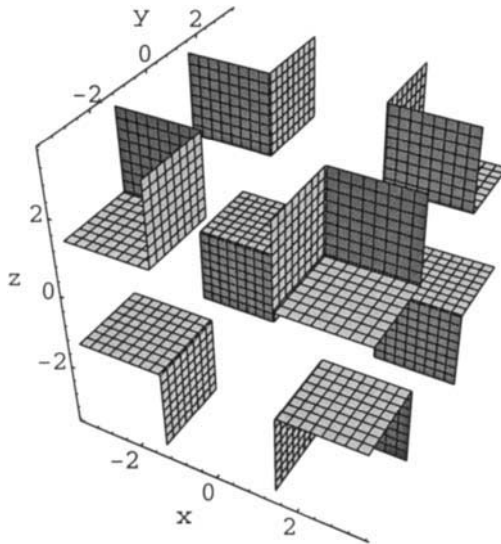


Figure 7.2 Finite periodicity after equation 7.13.

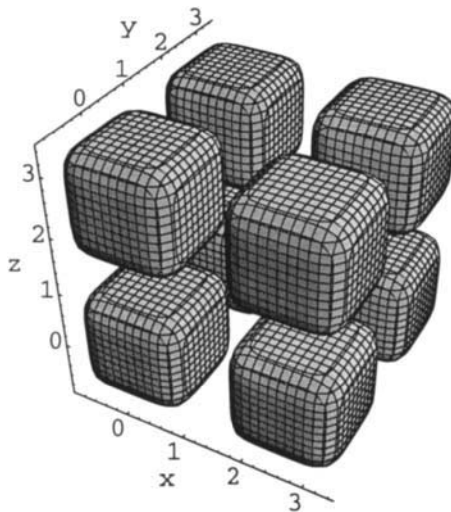


Figure 7.3 More finite periodicity after equation 7.14.

Adding three more terms containing translation as in equation 7.14, gives the full cubes in figure 7.3.

$$e^{-x^6} + e^{-y^6} + e^{-z^6} + e^{-(x-2)^6} + e^{-(y-2)^6} + e^{-(z-2)^6} = 2.9 \tag{7.14}$$

Three terms in space after 7.15 give the 27 cubes in figure 7.4.

$$e^{-x^6} + e^{-y^6} + e^{-z^6} + e^{-(x-2)^6} + e^{-(y-2)^6} + e^{-(z-2)^6} + e^{-(x-4)^6} + e^{-(y-4)^6} + e^{-(z-4)^6} = 2.9 \tag{7.15}$$

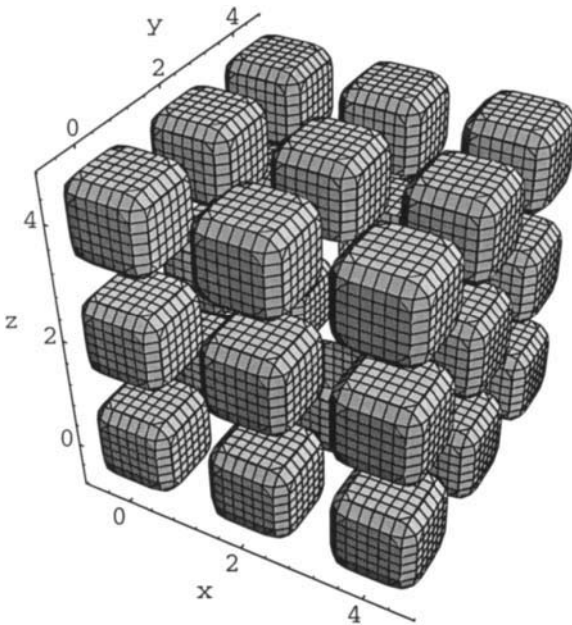


Figure 7.4 Three terms in space after 7.15 give 27 cubes.

And four terms in space after 7.16 give the formidable repetition in figure 7.5.

$$e^{-x^6} + e^{-y^6} + e^{-z^6} + e^{-(x-2)^6} + e^{-(y-2)^6} + e^{-(z-2)^6} + e^{-(x-4)^6} + e^{-(y-4)^6} + e^{-(z-4)^6} + e^{-(x-6)^6} + e^{-(y-6)^6} + e^{-(z-6)^6} = 2.9 \tag{7.16}$$

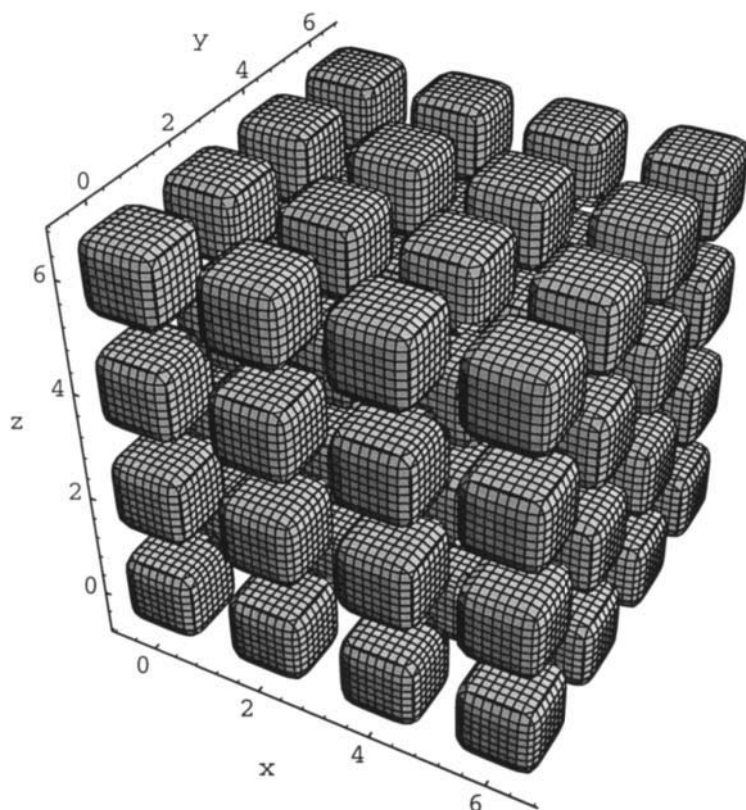


Figure 7.5 Four terms in space after 7.16 give 64 cubes.

The GD-function was used earlier to describe finite periodicity, which of course originates from the properties of the GD-function itself. This property of the GD-function has been used extensively in this book for the description of ordinary molecules, or giant molecular aggregates like the cubosomes. There is a special link between this GD-function and the square of cosine as we have shown in ref. [1].

The GD-function is very dynamic at change of constant, and in order to enlighten a comparison with a circular function, we go explicit and work at zero constant via sign shifts for every second term in equation 7.17a.

$$\begin{aligned}
 y = & e^{-x^2} - e^{-(x-2)^2} + e^{-(x-4)^2} - e^{-(x-6)^2} + e^{-(x-8)^2} - e^{-(x-10)^2} \\
 & + e^{-(x-12)^2} - e^{-(x-14)^2} + e^{-(x-16)^2} - e^{-(x-18)^2} + e^{-(x-20)^2} - e^{-(x-22)^2}
 \end{aligned}
 \tag{7.17.c}$$

We plot this together with the cosine function in 7.17.b

$$y = 0.957 \cos \frac{\pi x}{2} \tag{7.17.b}$$

The two functions seem to overlap completely in figure 7.6. Changing base to make the factor unity instead of 0.957 would make the two functions very similar within the boundaries used, but they would still not be completely identical.

In this way we have made a function of terms in 3D with zero constant in 7.18 and we seem to have a perfect P-surface in figure 7.6.

$$\begin{aligned} & -e^{-(x-6)^2} - e^{-(y-6)^2} - e^{-(z-6)^2} \\ & +e^{-(x-4)^2} + e^{-(y-4)^2} + e^{-(z-4)^2} \\ & -e^{-(x-2)^2} - e^{-(y-2)^2} - e^{-(z-2)^2} \\ & +e^{-x^2} + e^{-y^2} + e^{-z^2} \\ & -e^{-(x+2)^2} - e^{-(y+2)^2} - e^{-(z+2)^2} \\ & +e^{-(x+4)^2} + e^{-(y+4)^2} + e^{-(z+4)^2} \\ & -e^{-(x+6)^2} - e^{-(y+6)^2} - e^{-(z+6)^2} = 0 \end{aligned} \tag{7.18}$$

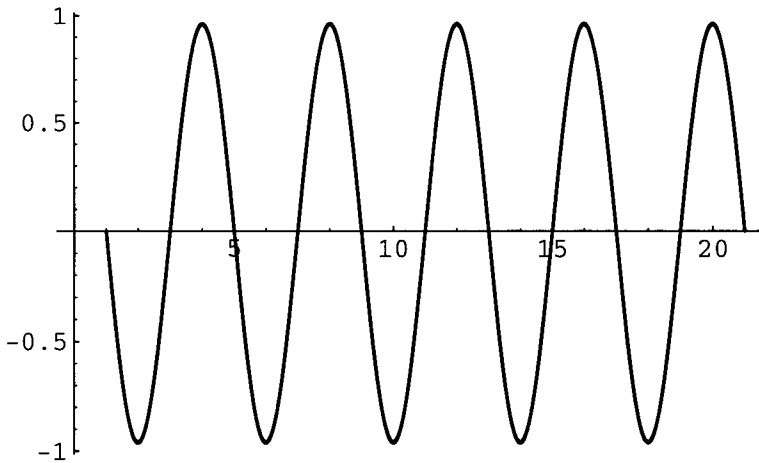


Figure 7.6 Two functions after equations 7.17.a and 7.17.b plotted together to show how similar they are.

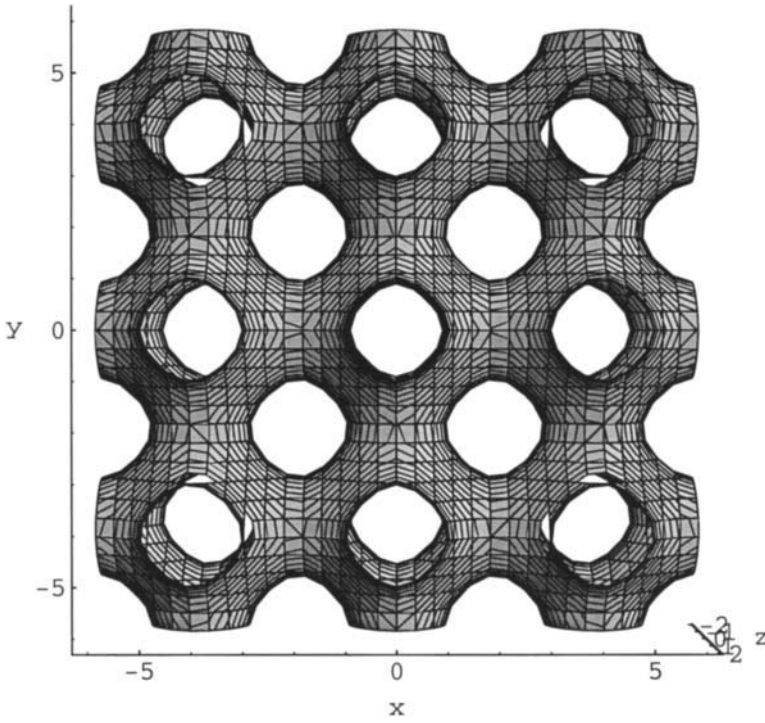


Figure 7.7 P-surface after equation 7.18.

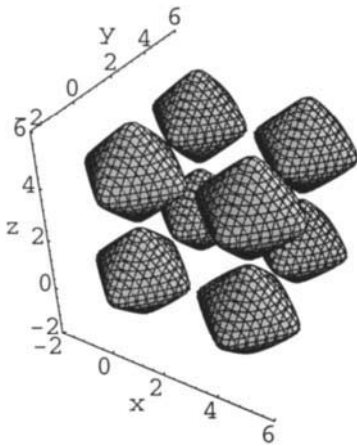


Figure 7.8a C=1 in equation 7.18.

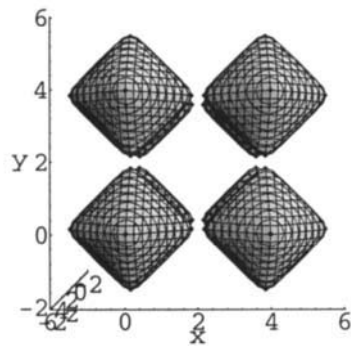


Figure 7.8b Different projection.

Using a constant of unity instead of zero in equation 7.18, we get figure 7.8a-b. Despite the change of constant, the function is still very similar to a circular function [1].

We shall do one more example of this remarkable periodicity, and use the screw equation in 7.19.

$$z \cos\left(\frac{\pi x}{2}\right) + y \sin\left(\frac{\pi x}{2}\right) = 0 \tag{7.19}$$

In constructing the analogous GD-equation, we make a simple translation which corresponds to the phase shift as in equation 7.20. Figure 7.9 is calculated with the GD-function, and figure 7.10 with the circular functions.

$$\begin{aligned} & y[e^{-(x-7)^2} - e^{-(x-5)^2} + e^{-(x-3)^2} - e^{-(x-1)^2} + e^{-(x+1)^2} \\ & - e^{-(x+3)^2} + e^{-(x+5)^2} - e^{-(x+7)^2}] \\ & - z[-e^{-(x-8)^2} + e^{-(x-6)^2} - e^{-(x-4)^2} + e^{-(x-2)^2} - e^{-(x)^2} \\ & + e^{-(x+2)^2} - e^{-(x+4)^2} + e^{-(x+6)^2} - e^{-(x+8)^2}] = 0 \end{aligned} \tag{7.20}$$

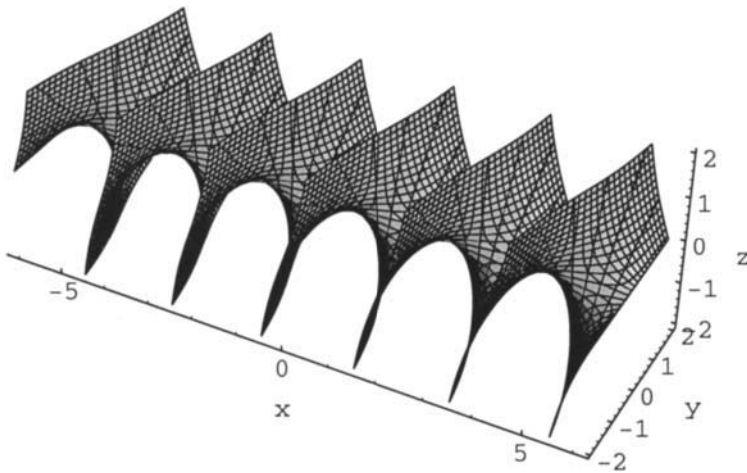


Figure 7.9 Helicoid calculated with GD-function.

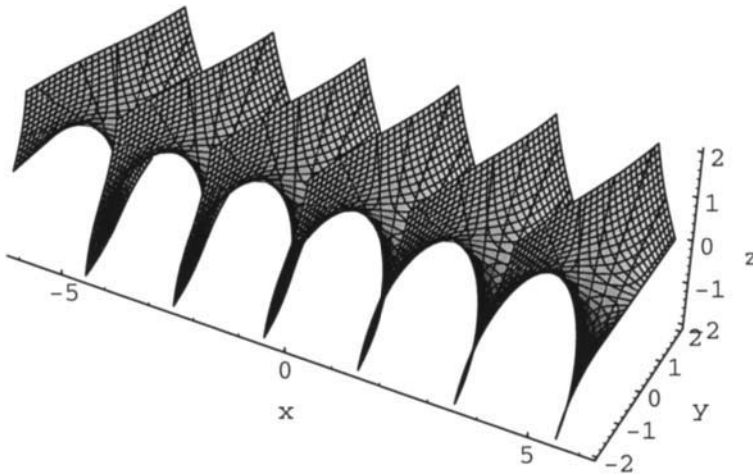


Figure 7.10 Helicoid calculated with circular functions.

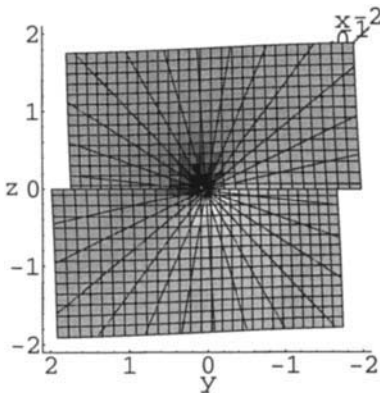


Figure 7.11a Helicoid after circular functions plotted to show the ruling (straight lines).

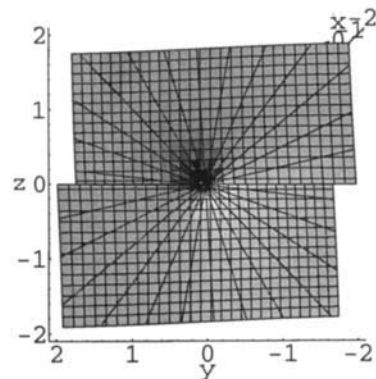


Figure 7.11b Helicoid after GD, plotted to show the ruling.

The helicoid minimal surface is built of straight lines as shown in the Mathematica plot in 7.11a, and the same seems to be the case for the GD-helicoid in 7.11b. The similarity is extraordinary, but still they are not identical. A calculation of curvature after ref. [1] shows that the GD-helicoid has non-zero mean curvature, while the other of course has not.

We shall give more examples of how to use the exponential scale. In equation 7.21 a tetrahedron is described in the ordinary way, and in

equation 7.22 another tetrahedron of reverse orientation is given. The two tetrahedra are shown in figures 7.12a-b. A tetrahedron may be said to be built of every second plane in an octahedron, and if these equations are added in 7.21 and 7.22 there is the octahedron in equation 7.23, which is shown in figure 7.12c.

$$e^{(x+y+z)^3} + e^{(x-y-z)^3} + e^{(-x-y+z)^3} + e^{(-x+y-z)^3} - 200 = 0 \tag{7.21}$$

$$e^{(-x-y-z)^3} + e^{(-x+y+z)^3} + e^{(x+y-z)^3} + e^{(x-y+z)^3} - 200 = 0 \tag{7.22}$$

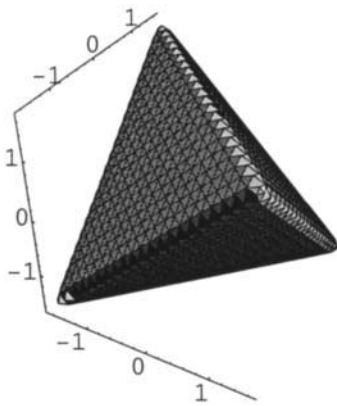


Figure 7.12a Tetrahedron built of planes after equation 7.21.

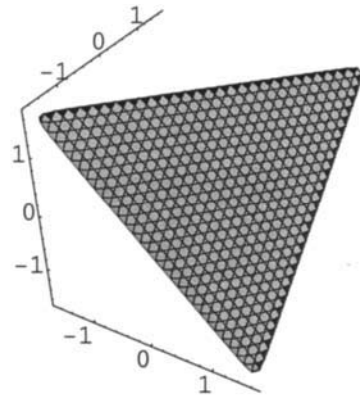


Figure 7.12b Tetrahedron of reverse orientation built of planes after equation 7.22.

$$e^{(x+y+z)^3} + e^{(x-y-z)^3} + e^{(-x-y+z)^3} + e^{(-x+y-z)^3} + e^{(-x-y-z)^3} + e^{(-x+y+z)^3} + e^{(x+y-z)^3} + e^{(x-y+z)^3} - 400 = 0 \tag{7.23}$$

If we now add the tetrahedra and want to keep their shapes, we must go up in scale to a GD-similar function as in 7.24. This is shown in figure 7.12d.

$$e^{-(e^{(x+y+z)^3} + e^{(x-y-z)^3} + e^{(-x-y+z)^3} + e^{(-x+y-z)^3} - 200)} + e^{-(e^{(-x-y-z)^3} + e^{(-x+y+z)^3} + e^{(x+y-z)^3} + e^{(x-y+z)^3} - 200)} = 0.2 \tag{7.24}$$

We recognise this beautiful geometry as Kepler's *stella octangula*. Or as a combination of two interpenetrating tetrahedra.

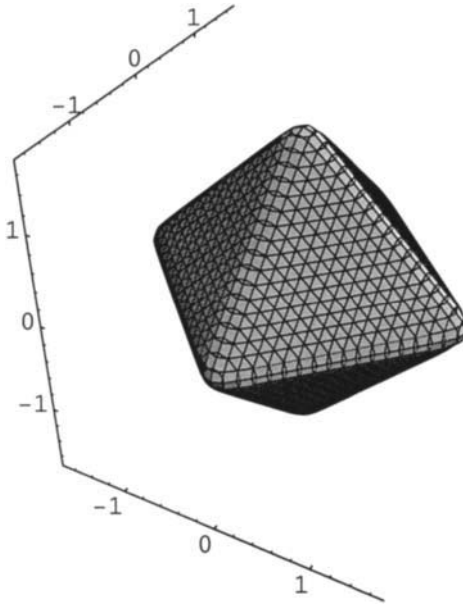


Figure 7.12c The planes of 7.21 and 7.22 collaborate in equation 7.23 to form an octahedron.

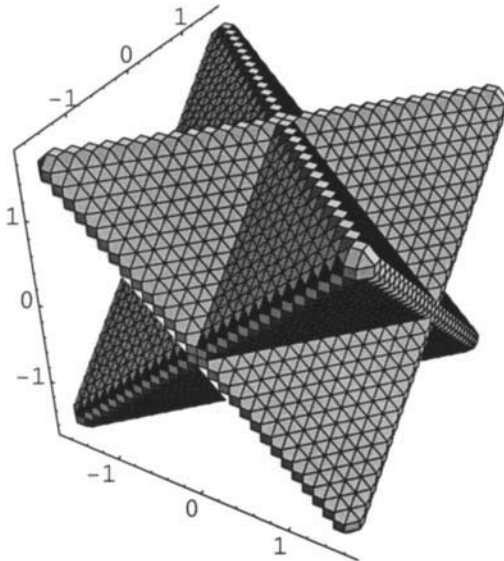


Figure 7.12d Going up in scale with a GD-function after 7.24 means that the orientations of the tetrahedra are kept in this *stella octangula*.

The simple topological relation between the icosahedron and the cube-octahedron has been rediscovered ever since Euclid. We use the icosahedral equation in 7.25 and turn it into 7.26, which means making the second set of terms cubic. By themselves these terms form a polyhedron which in structure is related to the rhombic dodecahedron, the pentagonal dodecahedron and the cube. The first set of terms are those of an octahedron.

$$e^{\tau^4(x+y+z)^4} + e^{\tau^4(-x+y+z)^4} + e^{\tau^4(x+y-z)^4} + e^{\tau^4(x-y+z)^4} + e^{(x+\tau^2y)^4} + e^{(-x+\tau^2y)^4} + e^{(z+\tau^2x)^4} + e^{(z-\tau^2x)^4} + e^{(y+\tau^2z)^4} + e^{(y-\tau^2z)^4} = C \tag{7.25}$$

$$\tau = \frac{\sqrt{5}+1}{2} \approx 1.618$$

$$\tau^2 = \tau + 1 \approx 2.618$$

$$\frac{1}{\tau} = \tau - 1 \approx 0.618$$

$$e^{\tau^4(x+y+z)^4} + e^{\tau^4(-x+y+z)^4} + e^{\tau^4(x+y-z)^4} + e^{\tau^4(x-y+z)^4} + e^{(\tau^2y)^4} + e^{(\tau^2y)^4} + e^{(\tau^2x)^4} + e^{(\tau^2x)^4} + e^{(\tau^2z)^4} + e^{(\tau^2z)^4} = 400 \tag{7.26}$$

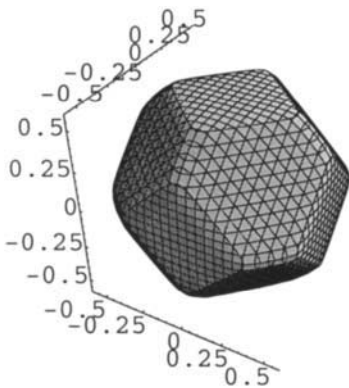


Figure 7.13a Truncated octahedron as obtained from an icosahedral equation topologically transformed into 7.26 which gives this figure.

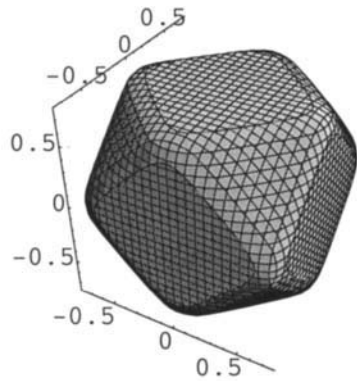


Figure 7.13b The transformation is continued to give equation 7.27 which is the cube octahedron.

This gives the truncated octahedron (truncated by the cube) in figure 7.13a. The topological path from the icosahedron is clear and could of course be done continuously by a stepwise change of the variable constants.

$$\begin{aligned}
 & e^{(x+y+z)^4} + e^{(-x+y+z)^4} + e^{(x+y-z)^4} + e^{(x-y+z)^4} \\
 & + e^{(2y)^4} + e^{(2y)^4} + e^{(2x)^4} + e^{(2x)^4} + e^{(2z)^4} + e^{(2z)^4} = 400
 \end{aligned}
 \tag{7.27}$$

In 7.26 we change τ^4 to 1 for the octahedral terms, and τ^2 to 2 for the cubic terms, and have equation 7.27. The cube-octahedron is shown in figure 7.13b.

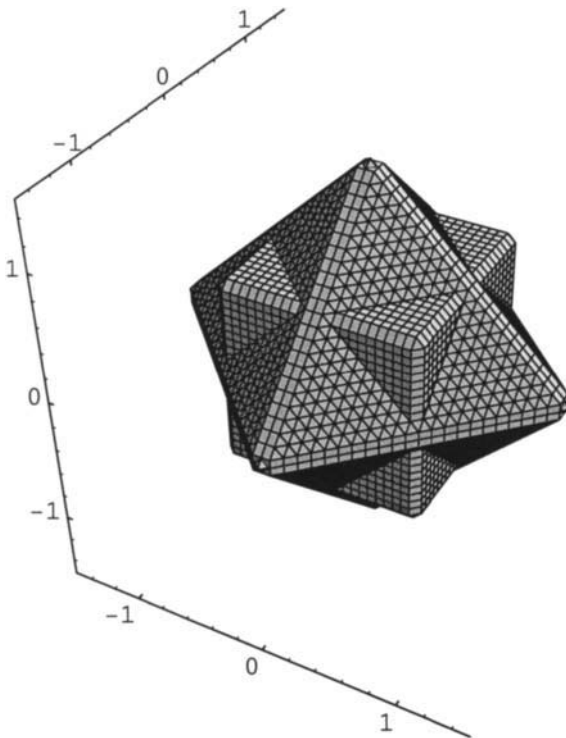


Figure 7.14 A compound of the octahedron and the cube after equation 7.28.

Finally, we make a compound which is between the octahedron and the cube by adding the equations from 7.27 higher up on the exponential scale, as in equation 7.28. We have the formidable polyhedron in figure 7.14.

$$e^{-[e^{(x+y+z)^4} + e^{(-x+y+z)^4} + e^{(x+y-z)^4} + e^{(x-y+z)^4} - 200]} \tag{7.28}$$

$$+ e^{-[e^{(2y)^4} + e^{(2y)^4} + e^{(2x)^4} + e^{(2x)^4} + e^{(2z)^4} + e^{(2z)^4} - 200]} - 1 = 0$$

We conclude with a rule of thumb when working with the exponential scale. Using the natural exponential means that you often work with very large numbers and also with very small. The sum of the terms is the iso-surface constant, which often is very large. When subtracting exponential terms, the constant may be set to zero, but you still handle very large numbers.

With GD-similar expressions you still handle very small or very large numbers. But the constant is small, or zero, due to the nature of the function.

So you should keep in mind that you are using very large and very small numbers, and that there is a limit for what your graphic program can handle.

It is well worth to remember that Nature uses billions and billions of atoms or molecules when making the shape of things to a scale or size. Like a cell. And the size of an atom is a fraction of billions and billions of the size of a thing the atoms or molecules are predestined to make. Nature uses very large numbers. And very small.

References Appendix 7

1 M. Jacob and S. Andersson, *THE NATURE OF MATHEMATICS AND THE MATHEMATICS OF NATURE*, Elsevier, 1998.

This Page Intentionally Left Blank

Appendix 8 - Classical Differential Geometry and the Exponential Scale

Important concepts like curvature, points, and the Bonnet transformation are discussed. Simple minimal surfaces are compared with nodal surfaces. Pretzels of different genus, including a wheel, are described.

Differential geometry means parametrisation and the use of curvilinear coordinates (coordinate system in the surface), curvature and non-Euclidean geometry. The language is the tensor analysis, and the tool is the complex analysis with Riemann surfaces. In 4D the applications are in the description of the amalgamation of space and time, and the general theory of relativity. Curvature is essential, and especially the Gaussian curvature which is independent of the space dimension.

An application for calculus is the study of minimal surfaces, and in the calculus the Weierstrass machine of elliptic integrals was a tremendous achievement. Today it is very much used for the numerical solution of coordinates to many beautiful minimal surfaces.

An important goal in the history of differential geometry was to transform a general implicit function $f(x,y,z)=0$ into an explicit Monge-form $z=f(x,y)$, for practical reasons in the parametrisation and in the Riemann space.

We have been doing a great deal of differential geometry using the exponential scale. And naturally we must work with implicit functions then. We have invented surfaces that can be used to describe phenomena in biology. We have found that the surfaces we want are obtained by the addition, subtraction or multiplication of planes. Most of it possible through the use of the exponential scale.

This will only deal with the part of differential geometry that is useful for us, which naturally will be a great part of the elementary mathematics of that geometry. In 3D we deal with surfaces, their description in shape and form, their properties like the mean and gaussian curvatures, and the relationships between surfaces and transformations to other surfaces. We

have introduced saddles, monkey saddles, nodal surfaces or minimal surfaces, and we will now continue with the concept of curvature.

Take a surface and let a plane rotate through a surface point P in its normal \mathbf{n} as shown in figure 8.1 from Hyde [4]. The section of this normal plane and the surface is a curve of curvature, k . During the rotation, k must attain one maximum and one minimum value, k_1 and k_2 . These are called principal curvatures, and the corresponding planar curves principal lines of curvature. These two curvatures are very useful in the description of the properties of surfaces. Their product is the *Gaussian curvature* (K), in 8.1, and the *mean curvature* ($2H$) describes the sum as in 8.2.

$$k_1 k_2 = K \quad 8.1$$

$$\frac{k_1 + k_2}{2} = H \quad 8.2$$

Figure 8.2 from Hyde [4] shows three surfaces with principal curvatures. The top picture has an *elliptic point* with positive Gaussian curvature, below there is a *parabolic point* with one principal curvature equal to zero. Which means that $K=0$. And in the bottom picture the principal curvatures are of opposite sign in the *saddle point* and the Gaussian curvature is negative. The plane has of course $H=K=0$.

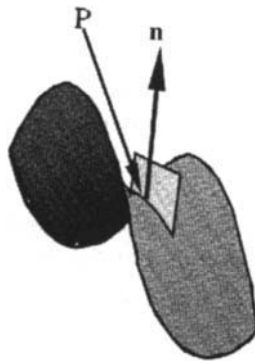


Figure 8.1 Normal vector and normal plane through a point P of a surface.

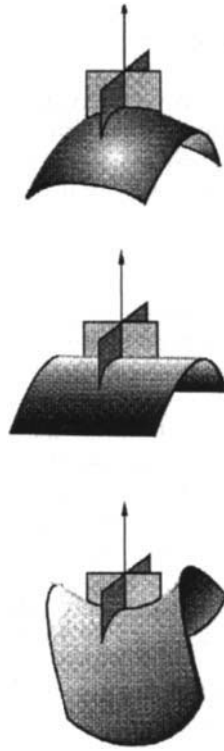


Figure 8.2 From top and down there is an elliptic, a parabolic and a saddle point.

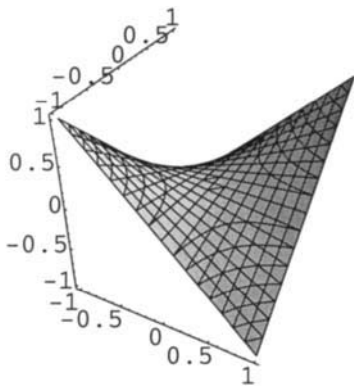


Figure 8.3 A saddle.

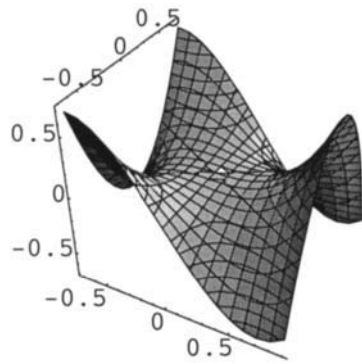


Figure 8.4 A monkey saddle.

A simple example of a surface of negative Gaussian curvature is the saddle. One example of this is shown in figure 8.3, according to equation 8.3.

$$xy - z = 0 \quad 8.3$$

A point on such a surface is called hyperbolic and the saddle point itself has maximum curvature.

The monkey saddle in figure 8.4 is a very remarkable surface. Hilbert gave it the name since a monkey beside its two legs also has a tail. The monkey saddle has negative Gaussian curvature everywhere, except in the centre where it is zero. Such a point is called a *flat point*. We have used an equation (8.4) from the literature to show the monkey saddle in figure 8.4.

$$x(x^2 - 3y^2) - z = 0 \quad 8.4$$

Next follows some important surfaces analysed and compared with the GD or nodal surfaces. Examples of surfaces built of saddles are the catenoid and the helicoid in equations 8.5 and 8.6.

$$x^2 + y^2 - \cosh^2 z = 0 \quad (\text{catenoid}) \quad 8.5$$

$$x \cos \pi z + y \sin \pi z = 0 \quad (\text{helicoid}) \quad 8.6$$

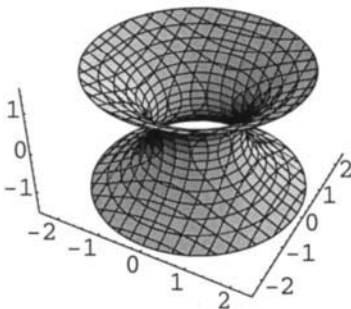


Figure 8.5 Catenoid minimal surface.

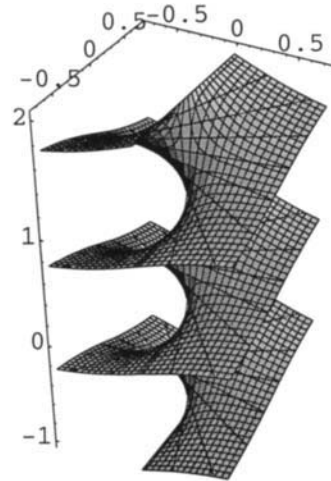


Figure 8.6 Helicoid minimal surface.

As

$$\cosh^2 z = \frac{1}{2}[\cosh 2z + 1]$$

and

$$\cosh 2z = \frac{1}{2}[e^{2z} + e^{-2z}]$$

we realise that the catenoid is built of two planes and a cylinder. We have earlier shown how the helicoid is described by planes.

Both are minimal surfaces, or soap-water film surfaces. The minimal surfaces are well characterised, having $H=0$ everywhere and $K \leq 0$. These two surfaces are very special, they have the same Gaussian curvature on corresponding points. This means they are isometric and can be bent into each other without stretching, like a paper can be rolled into a cylinder. It is called the Bonnet transition and we show it in figure 8.7, after Hyde [4]. The helicoid is ruled, which means it is built of straight lines, some of which are easily seen in the plot of figure 8.6. During the Bonnet transition these straight lines become principle lines of curvature in the catenoid.

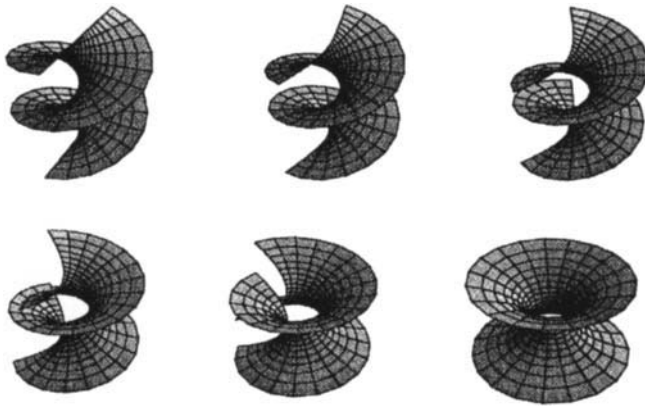


Figure 8.7 The isometric Bonnet transition.

Mathematically we have made a similar transformation on the nodal periodic surfaces in chapter 4, section 4.4 in this book.

We will continue and show how some classic surfaces may be described using our methods. Two famous minimal surfaces are the first and the fifth of the Scherk surfaces.

Remembering that

$$2 \sinh x = e^x - e^{-x}, \quad 8.7$$

we do our analysis of the fifth Scherk surface and start with

$$\sinh x \sinh y = 0, \quad 8.8$$

which is two intersecting planes in figure 8.8. We continue with the equation 8.9 and obtain a saddle in figure 8.9.

$$\sinh x \sinh y - z = 0 \quad 8.9$$

In figure 8.10 we have the minimal surface called Scherk's fifth surface after equation 8.10. With the equation $xy = \cos \pi z$ there is what we call the 'nodal' correspondent for this tower surface.

$$\sinh x \sinh y - \sin \pi z = 0 \quad 8.10$$

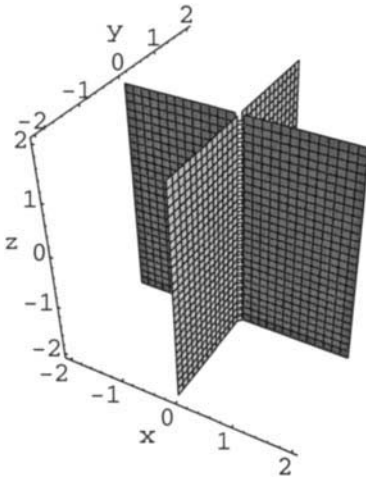


Figure 8.8 Two intersecting planes after 8.8.

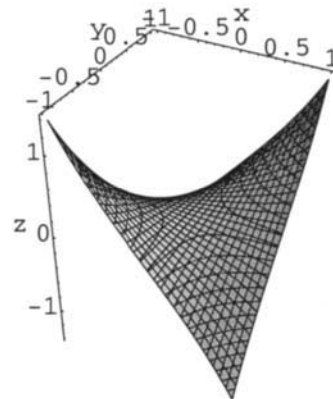


Figure 8.9 Saddle after 8.9 which builds Scherk's fifth minimal surface.

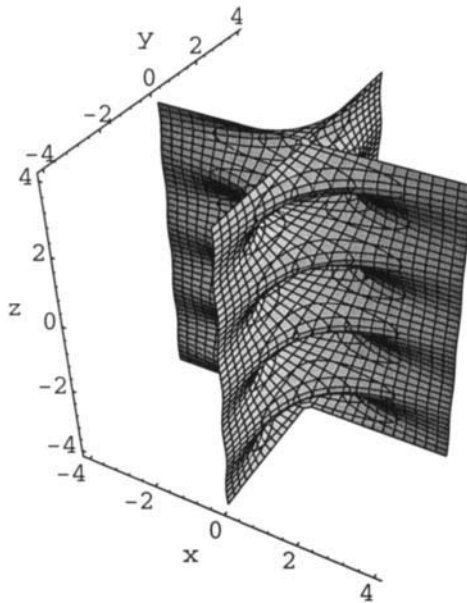


Figure 8.10 Scherk's fifth surface after equation 8.10, which also is a minimal surface.

Scherk's first surface is given in equation 8.11.

$$e^z \cos \pi x - \cos \pi y = 0 \tag{8.11}$$

We start the analysis with equation 8.12, which is a saddle like in figure 8.3, but with different orientation. We show it in figure 8.11.

$$zx - y = 0 \tag{8.12}$$

The saddle is repeated along y after equation 8.13 which is the tower surface, or nodal surface, variant of the minimal surface shown in figure 8.10. They have different orientations, but are otherwise almost identical.

$$zx - \cos \pi y = 0 \tag{8.13}$$

In figure 8.13 we show the surface that corresponds to the further development in equation 8.14.

$$z \cos \pi x - \cos \pi y = 0 \tag{8.14}$$

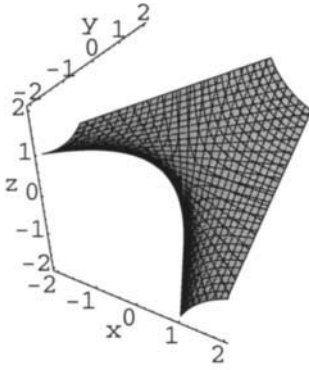


Figure 8.11 Saddle after 8.12.

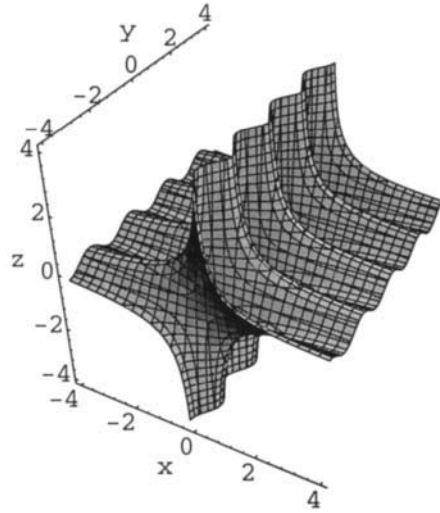


Figure 8.12 Tower surface, topologically the same as Scherk's fifth surface.

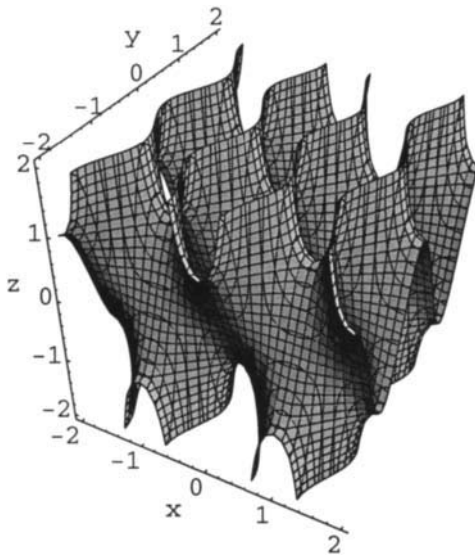


Figure 8.13 Surface after equation 8.14.

Finally, in the equation for the minimal surface we see that instead of z there is e^z , which means that the term containing z is always positive. The resulting Scherk's first minimal surface is very simple and beautiful. A bundle of an infinite number of planes meet a bundle of perpendicular planes in a manner that occurs without intersections.

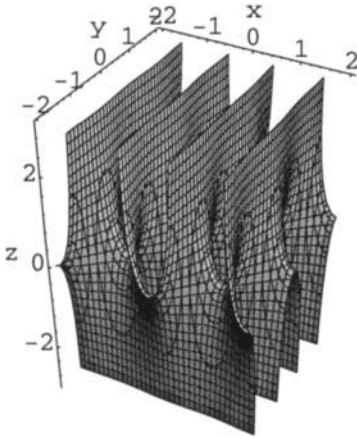


Figure 8.14a. Scherk's first minimal surface with equation 8.11.

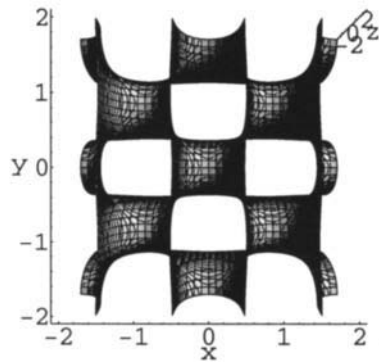


Figure 8.14b Different projection.

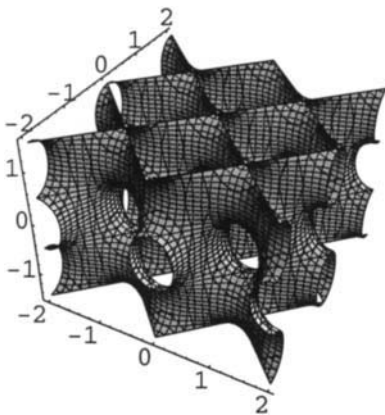


Figure 8.15a The nodal CLP-surface which builds the alveolar structure described in chapter 14.

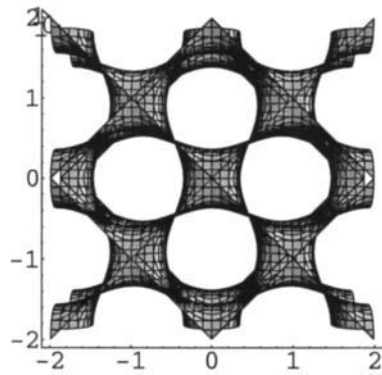


Figure 8.15b Different projection of a.

We continue and go circular also in the last direction, z , with equation 8.15. Saddles now repeat along z , and we have the nodal correspondence to the CLP minimal surface, cf. 8.15ab. This tetragonal surface is built of two sets of planes that meet in a perpendicular manner without self intersections. This surface builds the alveolar structure as described in chapter 14. The Weierstrass parametrisation of this minimal surface was first derived by Lidin and Hyde [3].

$$e^{\cos\pi z} \cos\pi x - \cos\pi y = 0 \quad 8.15$$

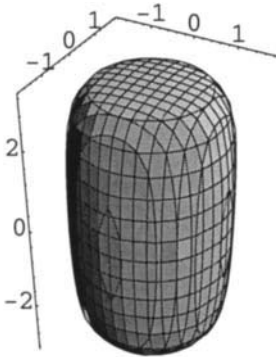


Figure 8.16a After equation 8.17.

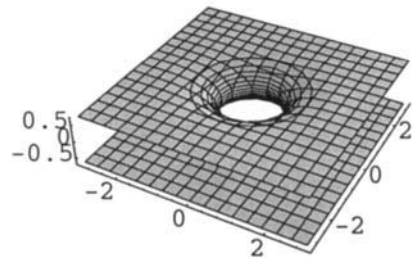


Figure 8.16b After equation 8.18.

A classic surface in differential geometry is the torus. Its equation is in 8.16.

$$((x^2 + y^2)^{0.5} - 2)^2 + z^2 = 1 \quad 8.16$$

We have designed various ways to make a torus before [1]. In order to make the famous pretzels (the name is given by Hilbert [2]) we need a flexible way that also demonstrates the use of the exponential scale. We showed in equation 4.16-18 of this appendix how to make catenoids going through two parallel planes. We shall proceed accordingly. In equation 8.17 we have added one cylinder with two planes, and obtain a closing of the cylinder as shown in figure 8.16a. Introducing a negative sign in the exponent opens up the structure, and with equation 8.18 there is the catenoid in figure 8.16b.

$$e^{(x^2+y^2)} + e^z + e^{-z} = 25 \tag{8.17}$$

$$e^{-(x^2+y^2)} + e^z + e^{-z} = 2.5 \tag{8.18}$$

In order to make a catenoid we need to close the planes, which we do by adding an exponential cylinder in equation 8.19, and the result is shown in figure 8.17.

$$e^{-(x^2+y^2)} + e^z + e^{-z} + e^{\frac{1}{10}[x^2+y^2]} = 3.7 \tag{8.19}$$

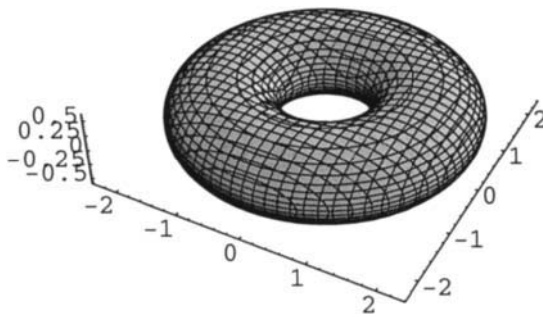


Figure 8.17 A torus after 8.19.

The catenoid in figure 8.16b is made with a GD-type cylinder, which means it can be moved or multiplied. We do the latter with equation 8.20 and in figure 8.18 there is the first pretzel.

$$e^{-(x^2+(y-2)^2)} + e^{-(x^2+(y+2)^2)} + e^z + e^{-z} + e^{\frac{1}{10}[x^2+(\frac{1}{2}y)^2]} = 3.7 \tag{8.20}$$

We continue with equation 8.21 to make a pretzel of genus three as shown in figure 8.19.

$$e^{-(x^2+(y-2)^2)} + e^{-((x-2)^2+(y)^2)} + e^{-(x^2+(y+2)^2)} + e^z + e^{-z} + e^{\frac{1}{25}[x^2+y^2]} = 3.9 \tag{8.21}$$

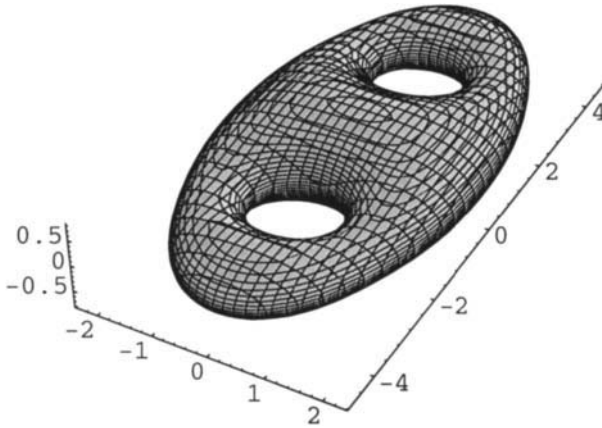


Figure 8.18 A pretzel after 8.20.

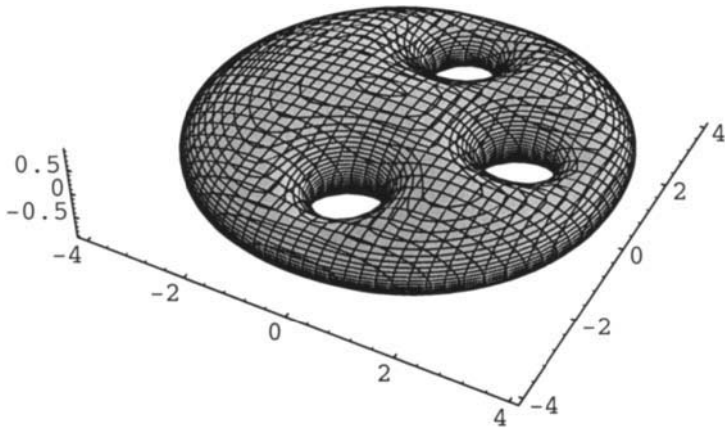


Figure 8.19 Another pretzel after 8.21.

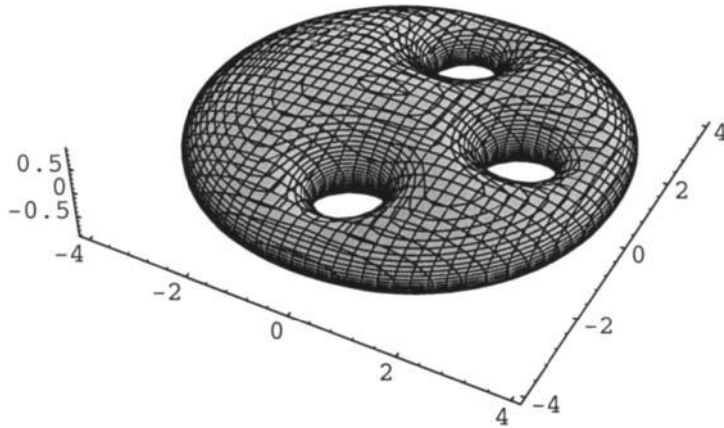


Figure 8.20a The wheel after 8.22.

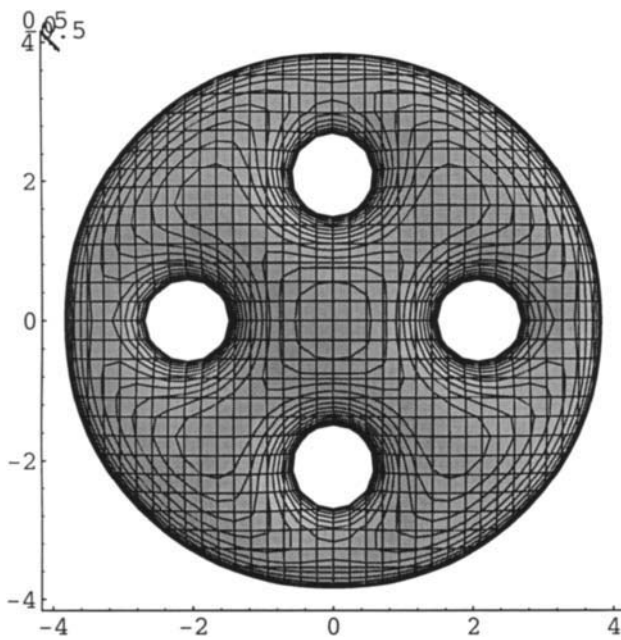


Figure 8.20b Different projection.

And finally we make the wheel with equation 8.22 as shown in two projections in figure 8.20a-b.

$$\begin{aligned}
 & e^{-(x^2+(y-2)^2)} + e^{-(x^2+(y+2)^2)} + e^{-((x-2)^2+(y)^2)} \\
 & + e^{-((x+2)^2+(y)^2)} + e^z + e^{-z} + e^{\frac{1}{25}[x^2+y^2]} = 3.9
 \end{aligned}
 \tag{8.22}$$

References Appendix 8

- 1 M. Jacob and S. Andersson, *THE NATURE OF MATHEMATICS AND THE MATHEMATICS OF NATURE*, Elsevier, 1998.
- 2 D. Hilbert and S. Cohn-Vossen, *GEOMETRY and the IMAGINATION*, Chelsea, New York, 1952, page 82.
- 3 S. Lidin, and S. T. Hyde, *J. Phys. France* **48**, 15 (1987).
- 4 S. Hyde, S. Andersson, K. Larsson, Z. Blum, T. Landh, S. Lidin and B. Ninham; *THE LANGUAGE OF SHAPE*, Elsevier, Amsterdam, 1997, pages 4-5 and 28.

Appendix 9 - Mathematica

We have been using *Mathematica*, and give here some examples. The subroutines `ContourPlot3D` and `ImplicitPlot` are for the implicit functions we use.

```
ImplicitPlot[E^y^4+E^x^4==200000,{x,-2,2},{y,-2,2},PlotPoints->200,  
Axes->False]
```

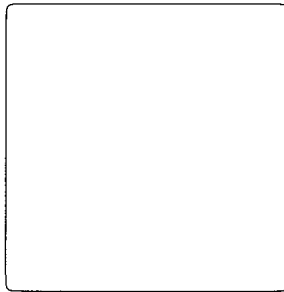


Figure 9.1 Square after the plot above.

```
ContourPlot3D[x^10+y^10+z^10-100,{x,2,-2},{y,2,-2},{z,2,-2},  
MaxRecursion>2,PlotPoints->{{4,4},{4,4},{4,4}},Boxed->False,  
Axes->True]
```

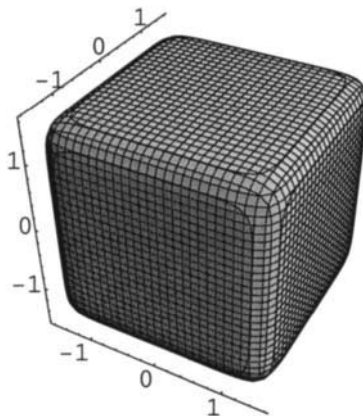


Figure 9.2 Cube after the plot above.

Another useful program is Plot, which is one-dimensional.

First is plot a Gauss error function and compare it with an ordinary cosine function.

```
Plot[{10^(-(x^2))+10^-((x-2)^2)+10^-((x-4)^2)+
10^-((x-6)^2)-.6,.4Cos[Pi x]},{x,-4,10},
PlotPoints->200,Axes->False]
```

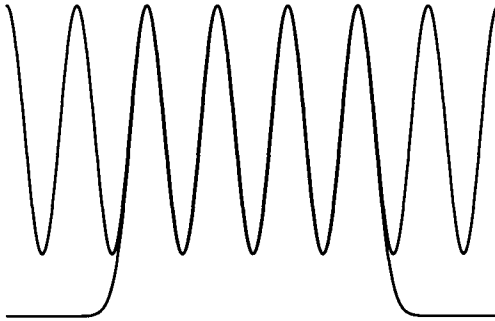


Figure 9.3 GD function and cosine after plot above.

Mathematica Scripts Used

The following is a compilation of the Mathematica scripts used to construct the surfaces illustrated in the figures in this book.

Chapter 2

Fig. 2.1.1: ContourPlot3D[(x-1)(x-2)(x-3)(x-4),{x,0,5},{y,-1,1},{z,-1,1},MaxRecursion->2,PlotPoints->{{5,3},{5,3},{5,3}},Boxed->False,Axes->True]

Fig. 2.1.2: ContourPlot3D[Sin[Pi x],{x,0,5},{y,-1,1},{z,-1,1},MaxRecursion->2,PlotPoints->{{5,3},{5,3},{5,3}},Boxed->False,Axes->True]

Fig. 2.2.1: ContourPlot3D[(x^2-1),{x,-2,2},{y,-1,1},{z,-1,1},MaxRecursion->2,PlotPoints->{{5,3},{5,3},{5,3}},Boxed->False,Axes->True]

Fig. 2.2.2: ContourPlot3D[(y^2-1),{x,-1,1},{y,-2,2},{z,-1,1},MaxRecursion->2,PlotPoints->{{5,3},{5,3},{5,3}},Boxed->False,Axes->True]

Fig. 2.2.3: ContourPlot3D[(z^2-1),{x,-1,1},{y,-1,1},{z,-2,2},MaxRecursion->2,PlotPoints->{{5,3},{5,3},{5,3}},Boxed->False,Axes->True]

Fig. 2.2.4: ContourPlot3D[(x²+y²-1),{x,-2,2},{y,-1,1},{z,-1,1},MaxRecursion->2,PlotPoints->{{5,3},{5,3},{5,3}},Boxed->False,Axes->True]

Fig. 2.2.5: ContourPlot3D[(x²+y²+z²-1),{x,-2,2},{y,-1,1},{z,-1,1},MaxRecursion->2,PlotPoints->{{5,3},{5,3},{5,3}},Boxed->False,Axes->True]

Fig. 2.2.6: ContourPlot3D[(x⁴+y⁴-1),{x,-1,1},{y,-1,1},{z,-1,1},MaxRecursion->2,PlotPoints->{{5,3},{5,3},{5,3}},Boxed->False,Axes->True]

Fig. 2.2.7: ContourPlot3D[(x⁴+y⁴+z⁴-1),{x,-2,2},{y,-1,1},{z,-1,1},MaxRecursion->2,PlotPoints->{{5,3},{5,3},{5,3}},Boxed->False,Axes->True]

Fig. 2.2.8: ContourPlot3D[(x y)+ z ,{x,2,-2},{y,2,-2},{z,1,-1},MaxRecursion->2,PlotPoints->{{4,4},{4,4},{4,4}},Boxed->False,Axes->True]

Fig. 2.2.9: ContourPlot3D[(x y)+ z ,{x,30,-30},{y,30,-30},{z,30,-30},MaxRecursion->2,PlotPoints->{{4,4},{4,4},{4,4}},Boxed->False,Axes->True]Show[%,ViewPoint->{-0.000,0.000,3.384}]

Fig. 2.2.10: ContourPlot3D[(x y)+ z (z-.5),{x,1,-1},{y,1,-1},{z,1,-.5},MaxRecursion->2,PlotPoints->{{4,4},{4,4},{4,4}},Boxed->False,Axes->True]

Fig. 2.2.11: ContourPlot3D[(x y)+ z (z-.5)(z-1),{x,1,-1},{y,1,-1},{z,2,-1},MaxRecursion->2,PlotPoints->{{4,4},{4,4},{4,4}},Boxed->False,Axes->True]

Fig. 2.2.12: ContourPlot3D[(x y)+ z (z-.5)(z-1)(z-1.5),{x,1,-1},{y,1,-1},{z,2,-1},MaxRecursion->2,PlotPoints->{{4,4},{4,4},{4,4}},Boxed->False,Axes->True]

Fig. 2.2.13: ContourPlot3D[(x y)+ z(z-.5)(z-1)(z-1.5)(z-2)(z-2.5)(z-3),{x,2,-2},{y,2,-2},{z,2.5,0.5},MaxRecursion->2,PlotPoints->{{4,4},{4,4},{4,4}},Boxed->False,Axes->True]

Fig. 2.2.14: ContourPlot3D[x z+z y,{x,-1,1},{y,-1,1},{z,-1,1},MaxRecursion->2,PlotPoints->{{5,3},{5,3},{5,3}},Boxed->False,Axes->True]

Fig. 2.2.15: ContourPlot3D[(x z)+y (z-.5),{x,-1,1},{y,-1,1},{z,-3,3},MaxRecursion->2,PlotPoints->{{5,3},{5,3},{5,3}},Boxed->False,Axes->True]

Fig. 2.2.16: ContourPlot3D[x z(z-1)+y (z-.5),{x,-1,1},{y,-1,1},{z,-3,3},MaxRecursion->2,PlotPoints->{{4,4},{4,4},{4,4}},Boxed->False,Axes->True]

Fig. 2.2.17: ContourPlot3D[x z(z-1)+y (z-.5) (z-1.5),{x,-1,1},{y,-1,1},{z,3,-2},MaxRecursion->2,PlotPoints->{{5,3},{5,3},{5,4}},Boxed->False,Axes->True]

Fig. 2.2.18: ContourPlot3D[x z(z-1) (z-2) (z-3) (z-4) (z-5) (z-6) (z-7) + y (z-.5) (z-1.5) (z-2.5) (z-3.5) (z-4.5) (z-5.5) (z-6.5),{x,-1,1},{y,-1,1},{z,2,6},MaxRecursion->2,PlotPoints->{{4,4},{4,4},{6,4}},Boxed->False,Axes->True]

Fig. 2.2.19: Show[%, ViewPoint->{-0.012, -3.384, 0.042}]

Fig. 2.2.20: ContourPlot3D[(x-4) (z-1) (z-2) (z-3) (z-4) (z-5) (z-6) + (y-4) (z-.5) (z-1.5) (z-2.5) (z-3.5) (z-4.5) (z-5.5),{x,4.6,3.4},{y,4.6,3.4},{z,2,4},MaxRecursion->2,PlotPoints->{{4,4},{4,4},{4,4}},Boxed->False,Axes->True]

Fig. 2.2.21: ContourPlot3D[(x-4) (z-5) (z-6) (z-7) (z-8) (z-9) (z-10) + (y-4) (z-4.5) (z-5.5)

(z-6.5) (z-7.5) (z-8.5) (z-9.5),{x,4.6,3.4},{y,4.6,3.4},{z,6,8},MaxRecursion->2,PlotPoints->{{4,4},{4,4},{4,4}},Boxed->False,Axes->True]

Fig. 2.3.1: ContourPlot3D[x(x-1)(x-2)(x-3),{x,-1,4},{y,-1,4},{z,-1,4},MaxRecursion->2,PlotPoints->{{5,3},{5,3},{5,3}},Boxed->False,Axes->True]

Fig. 2.3.2: ContourPlot3D[y(y-1)(y-2)(y-3),{x,-1,4},{y,-1,4},{z,-1,4},MaxRecursion->2,PlotPoints->{{5,3},{5,3},{5,3}},Boxed->False,Axes->True]

Fig. 2.3.3: ContourPlot3D[z(z-1)(z-2)(z-3),{x,-1,4},{y,-1,4},{z,-1,4},MaxRecursion->2,PlotPoints->{{5,3},{5,3},{5,3}},Boxed->False,Axes->True]

Fig. 2.3.4: ContourPlot3D[x(x-1)(x-2)(x-3)+y(y-1)(y-2)(y-3)+z(z-1)(z-2)(z-3)+1,{x,-1,4},{y,-1,4},{z,-1,4},MaxRecursion->2,PlotPoints->{{4,4},{4,4},{4,4}},Boxed->False,Axes->True]

Fig. 2.3.5: ContourPlot3D[(x-6)(x-7)(x-8)(x-9)+(y-6)(y-7)(y-8)(y-9)+(z-6)(z-7)(z-8)(z-9)+1,{x,5,10},{y,5,10},{z,5,10},MaxRecursion->2,PlotPoints->{{4,4},{4,4},{4,4}},Boxed->False,Axes->True]

Fig. 2.3.6: ContourPlot3D[x(x-1)(x-2)(x-3)+y(y-1)(y-2)(y-3)+z(z-1)(z-2)(z-3),{x,-1,3.3},{y,-1,3.3},{z,-1,2.75},MaxRecursion->2,PlotPoints->{{4,4},{4,4},{4,4}},Boxed->False,Axes->True]
Show[%, ViewPoint->{0.742, -1.370, 3.004}]

Fig. 2.3.7: ContourPlot3D[
z(z-1)(z+1)(z+2)(z-2)(z+3)(z-3)(z+4)(z-4)(z+5)(z-5)(z+6)+
x(x-1)(x-2)(x+1)(x+2)(x-3)(x-3)(x+4)(x-4)(x+5)(x-5)(x+6)+
y(y-1)(y-2)(y+1)(y+2)(y-3)(y-3)(y+4)(y-4)(y+5)(y-5)(y+6)-20000,
{x,-3.8,2.6},{y,-3.8,2.6},{z,-3.8,2.6},MaxRecursion->2,PlotPoints->{{3,5},{3,5},{3,5}},
Boxed->False,Axes->True]

Fig. 2.3.8: ContourPlot3D[x y+x z+z y+1,{x,-5,5},{y,-5,5},{z,5,-5},MaxRecursion->2,PlotPoints->{{5,3},{5,3},{5,3}},Boxed->False,Axes->True]

Fig. 2.3.9: Show[%, ViewPoint->{-1.930, -1.994, -1.937}]

Fig. 2.3.10: ContourPlot3D[x y z ,{x,.25,-.25},{y,.25,-.25},{z,.25,-.25},MaxRecursion->2,PlotPoints->{{4,4},{4,4},{4,4}},Boxed->False,Axes->True]

Fig. 2.3.11: ContourPlot3D[x y z + (z-.5)(y-.5)(x-.5),{x,-.25,.75},{y,-.25,.75},{z,-.25,.75},MaxRecursion->2,PlotPoints->{{4,4},{4,4},{4,4}},Boxed->False,Axes->True]

Fig. 2.3.12: ContourPlot3D[x y z(z-1)(y-1)(x-1) + (z-.5)(y-.5)(x-.5),{x,-.25,1.25},{y,-.25,1.25},{z,-.25,1.25},MaxRecursion->2,PlotPoints->{{4,4},{4,4},{4,4}},Boxed->False,Axes->True]

Fig. 2.3.13: ContourPlot3D[x y z(z-1)(y-1)(x-1) + (z-.5)(y-.5)(x-.5)(z-1.5)(y-1.5)(x-1.5),{x,-.25,1.75},{y,-.25,1.75},{z,-.25,1.75},MaxRecursion->2,PlotPoints->{{4,4},{4,4},{4,4}},Boxed->False,Axes->True]

Fig. 2.3.14: ContourPlot3D[x y z(z-1)(y-1)(x-1) + (z-.5)(y-.5)(x-.5)(z-1.5)(y-1.5)(x-1.5),{x,-2,4},{y,-2,4},{z,-2,4},MaxRecursion->2,PlotPoints->{{5,4},{5,4},{5,4}},Boxed->False,Axes->True]

Fig. 2.3.15: ContourPlot3D[x y z(z-.5)(y-.5)(x-.5),{x,-1,1.5},{y,-1,1.5},{z,-1,1.5},MaxRecursion->2,PlotPoints->{{3,5},{3,5},{3,5}},Boxed->False,Axes->True]

Fig. 2.3.16: ContourPlot3D[x y z -1,{x,10,-10},{y,10,-10},{z,10,-10},MaxRecursion->2,PlotPoints->{{4,4},{4,4},{4,4}},Boxed->False,Axes->True]

Fig. 2.3.17: ContourPlot3D[Cos[Pi(y)]Cos[Pi(x)]Cos[Pi(z)]+Sin[Pi(z)]Sin[Pi(y)]Sin[Pi(x)],{x,1.05,-1.05},{y,1.05,-1.05},{z,1.05,-1.05},MaxRecursion->2,PlotPoints->{{4,4},{4,4},{4,4}},Boxed->False,Axes->True]

Fig. 2.3.18: ContourPlot3D[Sin[Pi(x)]Cos[Pi(y)]+Cos[Pi(x)]Sin[Pi(z)]+Cos[Pi(z)]Sin[Pi(y)],{x,1,-1},{y,1,-1},{z,1,-1},MaxRecursion->2,PlotPoints->{{5,3},{5,3},{5,3}},Boxed->False,Axes->True]

Fig. 2.3.19: ContourPlot3D[Cos[Pi(x)]Cos[Pi(y)]+Cos[Pi(x)]Cos[Pi(z)]+Cos[Pi(z)]Cos[Pi(y)],{x,1,-1},{y,1,-1},{z,1,-1},MaxRecursion->2,PlotPoints->{{5,3},{5,3},{5,3}},Boxed->False,Axes->True]

Fig. 2.3.20: ContourPlot3D[x y z + z+y+x,{x,1.5,-1.5},{y,1.5,-1.5},{z,1.5,-1.5},MaxRecursion->2,PlotPoints->{{4,4},{4,4},{4,4}},Boxed->False,Axes->True]

Fig. 2.3.21: ContourPlot3D[x y z + z+y+x,{x,10,-10},{y,10,-10},{z,10,-10},MaxRecursion->2,PlotPoints->{{4,4},{4,4},{4,4}},Boxed->False,Axes->True]

Fig. 2.3.22: ContourPlot3D[2Cos[Pi x] Cos[Pi y] Cos[Pi z] + Cos[Pi x]+ Cos[Pi y]+ Cos[Pi z],{x,-1.5,1.5},{y,-1.5,1.5},{z,1.5,-1.5},MaxRecursion->2,PlotPoints->{{5,4},{5,4},{5,4}},Boxed->False,Axes->True]

Chapter 3

Fig. 3.2.1: ContourPlot3D[Cos[Pi x] Cos[Pi y] -2,{x,-1.5,1.5},{y,-1.5,1.5},{z,1,-1},MaxRecursion->2,PlotPoints->{{5,3},{5,3},{5,3}},Boxed->False,Axes->True]

Fig. 3.2.2: ContourPlot3D[Cos[Pi x] Cos[Pi y],{x,-1,1},{y,-1,1},{z,1,-1},MaxRecursion->2,PlotPoints->{{4,4},{4,4},{5,3}},Boxed->False,Axes->True]

Fig. 3.2.3: ContourPlot3D[Cos[Pi x] Cos[Pi y]-1 Cos[2 Pi z]-.05,{x,-1.6,1.6},{y,-1.6,1.6},{z,1,-1},MaxRecursion->2,PlotPoints->{{5,4},{5,4},{5,4}},Boxed->False,Axes->True]

Fig. 3.2.4: ContourPlot3D[Cos[Pi x] Cos[Pi y]-5 Cos[2 Pi z],{x,-1.5,1.5},{y,-1.5,1.5},{z,1,-1},MaxRecursion->2,PlotPoints->{{5,3},{5,3},{5,3}},Boxed->False,Axes->True]

Fig. 3.2.5: Show[%, ViewPoint->{0.000, 0.000, 3.384}]

Fig. 3.2.6: ContourPlot3D[Cos[Pi x] Cos[Pi y]- Cos[2 Pi z],{x,-1,1},{y,-1,1},{z,1,-1},MaxRecursion->2,PlotPoints->{{4,4},{4,4},{4,4}},Boxed->False,Axes->True]

Fig. 3.2.7: ContourPlot3D[x-y+x z,{x,-3,3},{y,-3,3},{z,5,-5},MaxRecursion->2,PlotPoints->{{5,3},{5,3},{5,3}},Boxed->False,Axes->True]

Fig. 3.2.8: Show[%, ViewPoint->{-0.012, -3.382, -0.093}]

Fig. 3.2.9: ContourPlot3D[Cos[Pi x]- Cos[Pi y]+ Cos[Pi x] Cos[Pi z],{x,-2,2},{y,-2,2},{z,1.5,-1.5},MaxRecursion->2,PlotPoints->{{5,4},{5,4},{5,4}},Boxed->False,Axes->True]

Fig. 3.2.10: ContourPlot3D[Cos[Pi x]- Cos[Pi y]+ .1 Cos[Pi x] Cos[Pi z],{x,-2,2},{y,-2,2},{z,1.5,-1.5},MaxRecursion->2,PlotPoints->{{5,4},{5,4},{5,4}},Boxed->False,Axes->True]

Fig. 3.2.11: ContourPlot3D[Cos[Pi x]-Cos[Pi y]+.1 Cos[Pi x] Cos[Pi z]+.5,{x,-2,2},{y,-2,2},{z,1.5,-1.5},MaxRecursion->2,PlotPoints->{{5,3},{5,3},{5,3}},Boxed->False,Axes-> True]

Fig. 3.2.12: ContourPlot3D[y x (x-y)(y+x),{x,-2,2},{y,-2,2},{z,1,-1},MaxRecursion->2,PlotPoints->{{4,4},{4,4},{5,3}},Boxed->False,Axes->True]

Fig. 3.2.13: ContourPlot3D[6(Sin[Pi y] Sin[Pi x]) (Sin[Pi(x-y)] Sin[Pi(y+x)]),{x,-9,9},{y,-9,9},{z,1,0},MaxRecursion->2,PlotPoints->{{4,4},{4,4},{5,3}},Boxed->False,Axes-> True]

Fig. 3.2.14: ContourPlot3D[y x (x-y)(y+x)-z,{x,-2,2},{y,-2,2},{z,1,-1},MaxRecursion->2,PlotPoints->{{4,4},{4,4},{5,3}},Boxed->False,Axes->True]

Fig. 3.2.15: ContourPlot3D[6(Sin[Pi y] Sin[Pi x]) (Sin[Pi(x-y)] Sin[Pi(y+x)]) + .1 (Sin[2 Pi z]), {x,-9,9},{y,-9,9},{z,1.2,0},MaxRecursion->2,PlotPoints->{{4,4},{4,4},{4,4}},Boxed->False,Axes->True]

Fig. 3.2.16: ContourPlot3D[6(Sin[Pi y] Sin[Pi x]) (Sin[Pi(x-y)] Sin[Pi(y+x)]) + (Sin[2 Pi z]),{x,-9,9},{y,-9,9},{z,1.2,0},MaxRecursion->2,PlotPoints->{{4,4},{4,4},{4,4}},Boxed->False,Axes->True]

Fig. 3.2.17: Show[%, ViewPoint->{-0.000, -0.000, 3.384}]

Fig. 3.3.1: ContourPlot3D[x(x+1.732 y)-(x+1.732 y),{x,-.5,.5},{y,-.6,.6},{z,.375,-.375},MaxRecursion->2,PlotPoints->{{5,3},{5,3},{5,3}},Boxed->False,Axes->True]

Fig. 3.3.2: ContourPlot3D[x(x+1.732 y)-(x+1.732 y)-z,{x,-1,1},{y,-1,1},{z,.375,-.375},MaxRecursion->2,PlotPoints->{{5,3},{5,3},{5,3}},Boxed->False,Axes->True]

Fig. 3.3.3: ContourPlot3D[x(x+1.732 y)-(x+1.732 y)-z,{x,-10,10},{y,-10,10},{z,10,-10},MaxRecursion->2,PlotPoints->{{5,3},{5,3},{5,3}},Boxed->False,Axes->True]

Fig. 3.3.4: Show[%, ViewPoint->{0.000, -0.000, 3.384}]

Fig. 3.3.5: ContourPlot3D[Cos[2 Pi x] Cos[Pi (x+1.732 y)] Cos[Pi (-x+1.732 y)]-0.000001,{x,-.5,.5},{y,-.5,.5},{z,.25,-.25},MaxRecursion->2,PlotPoints->{{5,4},{5,4},{5,3}},Boxed->False,Axes->True]

Fig. 3.3.6: ContourPlot3D[Cos[2 Pi x] Cos[Pi (x+1.732 y)] Cos[Pi (-x+1.732 y)]-1,{x,-.75,.75},{y,-.85,.85},{z,.375,-.375},MaxRecursion->2,PlotPoints->{{5,4},{5,4},{5,3}},Boxed->False,Axes->True]

Fig. 3.3.7: ContourPlot3D[Cos[2 Pi x] Cos[Pi (x+1.732 y)] Cos[Pi (-x+1.732 y)]+.03,{x,-.45,.45},{y,-.46,.46},{z,.375,-.375},MaxRecursion->2,PlotPoints->{{5,4},{5,4},{5,3}},Boxed->False,Axes->True]

Fig. 3.3.8: ContourPlot3D[Cos[2 Pi x] Cos[Pi (x+1.732 y)] Cos[Pi (-x+1.732 y)]

```
+ .02 Cos[4 Pi z], {x, -.5, .5}, {y, -.45, .45}, {z, .5, -.5}, MaxRecursion->2, PlotPoints->
{{5, 4}, {5, 4}, {5, 4}}, Boxed->False, Axes->True]
```

Fig. 3.3.9: ContourPlot3D[Cos[2 Pi x] Cos[Pi (x+1.732 y)] Cos[Pi (-x+1.732 y)] +.1 Cos[4 Pi z], {x, -.5, .5}, {y, -.45, .45}, {z, .5, -.5}, MaxRecursion->2, PlotPoints->{{5, 4}, {5, 4}, {5, 4}}, Boxed->False, Axes->True]

Fig. 3.3.10: ContourPlot3D[Sin[2 Pi x] Sin[Pi (x+1.732 y)] Sin[Pi (-x+1.732 y)], {x, -.5, .45}, {y, -.6, .6}, {z, .375, -.375}, MaxRecursion->2, PlotPoints->{{4, 4}, {4, 4}, {4, 4}}, Boxed->False, Axes->True]

Fig. 3.3.11: ContourPlot3D[Sin[2 Pi x] Sin[Pi (x+1.732 y)] Sin[Pi (-x+1.732 y)]-.1, {x, -.1, .4}, {y, -.8, .8}, {z, .375, -.375}, MaxRecursion->2, PlotPoints->{{3, 5}, {3, 5}, {3, 5}}, Boxed->False, Axes->True]

Fig. 3.3.12a: ContourPlot3D[Sin[2 Pi x] Sin[Pi (x+1.732 y)] Sin[Pi (-x+1.732 y)]+.025 Sin[4 Pi z], {x, -1.05, .45}, {y, -.85, .85}, {z, .375, -.375}, MaxRecursion->2, PlotPoints->{{3, 5}, {3, 5}, {3, 5}}, Boxed->False, Axes->True]

Fig. 3.3.12b: Show[%, ViewPoint->{0.000, 0.000, 3.384}]

Fig. 3.3.13: ContourPlot3D[Sin[2 Pi x] Sin[Pi (x+1.732 y)] Sin[Pi (-x+1.732 y)]+.25 Sin[4 Pi z], {x, -1.05, .45}, {y, -.85, .85}, {z, .375, -.375}, MaxRecursion->2, PlotPoints->{{3, 5}, {3, 5}, {3, 5}}, Boxed->False, Axes->True]

Fig. 3.3.14: Show[%, ViewPoint->{0.000, 0.000, 3.384}]

Fig. 3.3.15: ContourPlot3D[6 Sin[2 Pi x] Sin[Pi (x+1.732 y)] Sin[Pi (-x+1.732 y)]+Sin[Pi z], {x, -1.05, .45}, {y, -.85, .85}, {z, 1.8, -.8}, MaxRecursion->2, PlotPoints->{{3, 5}, {3, 5}, {3, 5}}, Boxed->False, Axes->True]

Fig. 3.3.16: Show[%, ViewPoint->{0.000, -0.000, 3.384}]

Chapter 4

Fig. 4.1.1: ContourPlot3D[Cos[Pi z]+Cos[Pi y]+Cos[Pi x], {x, 2, -2}, {y, 2, -2}, {z, 2, -2}, MaxRecursion->2, PlotPoints->{{5, 4}, {5, 4}, {5, 4}}, Boxed->False, Axes->True]

Fig. 4.1.2 ContourPlot3D[Sin[Pi(x+y)]+Sin[Pi(x-y)]+Sin[Pi(x+z)]+Sin[Pi(-x+z)]+Sin[Pi(y+z)]+Sin[Pi(y-z)], {x, 1, -1}, {y, 1, -1}, {z, 1, -1}, MaxRecursion->2, PlotPoints->{{5, 4}, {5, 4}, {5, 4}}, Boxed->False, Axes->True]

Fig. 4.1.3: ContourPlot3D[Cos[Pi(x+y)]+Cos[Pi(x-y)]+Cos[Pi(x+z)]+Cos[Pi(-x+z)]+Cos[Pi(y+z)]+Cos[Pi(y-z)], {x, 1, -1}, {y, 1, -1}, {z, 1, -1}, MaxRecursion->2, PlotPoints->{{4, 4}, {4, 4}, {4, 4}}, Boxed->False, Axes->True]

Fig. 4.1.4: ContourPlot3D[(Cos[Pi(x+y+z)]+Cos[Pi(x-y-z)]+Cos[Pi(-x-y+z)]+Cos[Pi(-x+y-z)]+Sin[Pi(x+y+z)]+Sin[Pi(x-y-z)]+Sin[Pi(-x-y+z)]+Sin[Pi(-x+y-z)]), {x, 1.05, -1.05}, {y, 1.05, -1.05}, {z, 1.05, -1.05}, MaxRecursion->2, PlotPoints->{{5, 4}, {5, 4}, {5, 4}}, Boxed->False, Axes->True]

Fig. 4.1.5: ContourPlot3D[Sin[Pi(x+y)]+Sin[Pi(x-y)]+Sin[Pi(x+z)]+Sin[Pi(-x+z)]+Sin[Pi(y+z)]+Sin[Pi(y-z)],{x,1,-1},{y,1,-1},{z,1,-1},MaxRecursion->2,PlotPoints->{{5,4},{5,4},{5,4}},Boxed->False,Axes->True] Show[%, ViewPoint->{3.383, -0.000, 0.000}]

Fig. 4.1.6: Show[%, ViewPoint->{-1.954, -1.940, -1.966}]

Fig. 4.1.7: ContourPlot3D[(Cos[Pi(x+y+z)]+Cos[Pi(x-y-z)]+Cos[Pi(-x-y+z)]+Cos[Pi(-x+y-z)]+Sin[Pi(x+y+z)]+Sin[Pi(x-y-z)]+Sin[Pi(-x-y+z)]+Sin[Pi(-x+y-z)]),{x,1.05,-1.05},{y,1.05,-1.05},{z,1.05,-1.05},MaxRecursion->2,PlotPoints->{{5,4},{5,4},{5,4}},Boxed->False,Axes->True] Show[%, ViewPoint->{1.957, 1.958, 1.945}]

Fig. 4.1.8: Show[%, ViewPoint->{-2.388, -2.397, 0.042}]

Fig. 4.1.9: ContourPlot3D[Cos[Pi(x+y)]+Cos[Pi(x-y)]+Cos[Pi(x+z)]+Cos[Pi(-x+z)]+Cos[Pi(y+z)]+Cos[Pi(y-z)]+1,{x,1,-1},{y,1,-1},{z,1,-1},MaxRecursion->2,PlotPoints->{{4,4},{4,4},{4,4}},Boxed->False,Axes->True]

Fig. 4.1.10: ContourPlot3D[Cos[Pi(x+y)]+Cos[Pi(x-y)]+Cos[Pi(x+z)]+Cos[Pi(-x+z)]+Cos[Pi(y+z)]+Cos[Pi(y-z)]+1,{x,1.4,-1.4},{y,1.4,-1.4},{z,1.4,-1.4},MaxRecursion->2,PlotPoints->{{5,4},{5,4},{5,4}},Boxed->False,Axes->True]

Fig. 4.2.1: ContourPlot3D[Cos[Pi(x)],{x,1.6,-1.6},{y,1.6,-1.6},{z,1,-1},MaxRecursion->2,PlotPoints->{{5,3},{5,3},{5,3}},Boxed->False,Axes->True]

Fig. 4.2.2: ContourPlot3D[Cos[Pi(x)]+1(Cos[Pi(y)]+Cos[Pi(z)]),{x,1.7,-1.7},{y,1.7,-1.7},{z,1,-1},MaxRecursion->2,PlotPoints->{{5,3},{5,3},{5,3}},Boxed->False,Axes->True]

Fig. 4.2.3: ContourPlot3D[Cos[Pi(x)]+2(Cos[Pi(y)]+Cos[Pi(z)]),{x,1.7,-1.7},{y,1.7,-1.7},{z,0,2},MaxRecursion->2,PlotPoints->{{5,3},{5,3},{5,3}},Boxed->False,Axes->True]

Fig. 4.2.4: ContourPlot3D[Cos[Pi(x)]+5 (Cos[Pi(y)]+Cos[Pi(z)]),{x,1.7,-1.7},{y,1.7,-1.7},{z,0,2},MaxRecursion->2,PlotPoints->{{5,3},{5,3},{5,3}},Boxed->False,Axes->True]

Fig. 4.2.5: ContourPlot3D[Cos[Pi(x)]+8(Cos[Pi(y)]+Cos[Pi(z)]),{x,2,-2},{y,2,-2},{z,0,2},MaxRecursion->2,PlotPoints->{{5,3},{5,3},{5,3}},Boxed->False,Axes->True]

Fig. 4.2.6: ContourPlot3D[Cos[Pi(x)]+Cos[Pi(y)]+Cos[Pi(z)],{x,2,-2},{y,2,-2},{z,0,2},MaxRecursion->2,PlotPoints->{{5,3},{5,3},{5,3}},Boxed->False,Axes->True]

Fig. 4.2.7: ContourPlot3D[Sin[Pi(x+y)],{x,1,-1},{y,1,-1},{z,1,-1},MaxRecursion->2,PlotPoints->{{5,3},{5,3},{5,3}},Boxed->False,Axes->True]

Fig. 4.2.8: ContourPlot3D[Sin[Pi(x+y)]+1(Sin[Pi(x-y)]+Sin[Pi(x+z)]+Sin[Pi(-x+z)]+Sin[Pi(y+z)]+Sin[Pi(y-z)]),{x,1,-1},{y,1,-1},{z,1,-1},MaxRecursion->2,PlotPoints->{{5,3},{5,3},{5,3}},Boxed->False,Axes->True]

Fig. 4.2.9: ContourPlot3D[Sin[Pi(x+y)]+3(Sin[Pi(x-y)]+Sin[Pi(x+z)]+Sin[Pi(-x+z)]+Sin[Pi(y+z)]+Sin[Pi(y-z)]),{x,1,-1},{y,1,-1},{z,1,-1},MaxRecursion->2,PlotPoints->{{5,3},{5,3},{5,3}},Boxed->False,Axes->True]

Fig. 4.2.10: ContourPlot3D[Sin[Pi(x+y)]+8(Sin[Pi(x-y)]+Sin[Pi(x+z)]+Sin[Pi(-x+z)]+Sin[Pi(y+z)]+Sin[Pi(y-z)]),{x,1,-1},{y,1,-1},{z,1,-1},MaxRecursion->2,PlotPoints->{{4,4},{4,4},{4,4}},Boxed->False,Axes->True]

Fig. 4.2.11: ContourPlot3D[Sin[Pi(x)]+.1(Sin[Pi(x+y)]+Sin[Pi(xy)]+Sin[Pi(x+z)]+Sin[Pi(x+z)]+Sin[Pi(y+z)]+Sin[Pi(y-z)]),{x,1.2,-1.2},{y,1,1},{z,1,1},MaxRecursion->2,PlotPoints->{{5,3},{5,3},{5,3}},Boxed->False,Axes->True]

Fig. 4.2.12 ContourPlot3D[Sin[Pi(x)]+.3(Sin[Pi(x+y)]+Sin[Pi(x-y)]+Sin[Pi(x+z)]+Sin[Pi(-x+z)]+Sin[Pi(y+z)]+Sin[Pi(y-z)]),{x,1.2,-1.2},{y,1,1},{z,1,-1},MaxRecursion->2,PlotPoints->{{5,3},{5,3},{5,3}},Boxed->False,Axes->True] Show[%,ViewPoint->{0.056,3.383,-0.026}]

Fig. 4.2.13: ContourPlot3D[Sin[Pi(x)]+.37(Sin[Pi(x+y)]+Sin[Pi(x-y)]+Sin[Pi(x+z)]+Sin[Pi(-x+z)]+Sin[Pi(y+z)]+Sin[Pi(y-z)]),{x,1.2,-1.2},{y,1,1},{z,1,-1},MaxRecursion->2,PlotPoints->{{4,4},{4,4},{4,4}},Boxed->False,Axes->True] Show[%,ViewPoint->{0.056,-3.383,-0.026}]

Fig. 4.2.14: ContourPlot3D[Sin[Pi(x)]+.6(Sin[Pi(x+y)]+Sin[Pi(x-y)]+Sin[Pi(x+z)]+Sin[Pi(-x+z)]+Sin[Pi(y+z)]+Sin[Pi(y-z)]),{x,1.2,-1.2},{y,1,-1},{z,1,-1},MaxRecursion->2,PlotPoints->{{4,4},{4,4},{4,4}},Boxed->False,Axes->True]

Fig. 4.2.15: ContourPlot3D[Cos[Pi(x+y+z)],{x,1,-1},{y,1,-1},{z,1,-1},MaxRecursion->2,PlotPoints->{{5,3},{5,3},{5,3}},Boxed->False,Axes->True]

Fig. 4.2.16: ContourPlot3D[Cos[Pi(x+y+z)]+.2(Cos[Pi(x-y-z)]+Cos[Pi(-x-y+z)]+Cos[Pi(-x+y-z)]+Sin[Pi(x+y+z)]+Sin[Pi(x-y-z)]+Sin[Pi(-x-y+z)]+Sin[Pi(-x+y-z)]),{x,1,-1},{y,1,-1},{z,1,-1},MaxRecursion->2,PlotPoints->{{4,4},{4,4},{4,4}},Boxed->False,Axes->True]

Fig. 4.2.17: ContourPlot3D[Cos[Pi(x+y+z)]+.3(Cos[Pi(x-y-z)]+Cos[Pi(-x-y+z)]+Cos[Pi(-x+y-z)]+Sin[Pi(x+y+z)]+Sin[Pi(x-y-z)]+Sin[Pi(-x-y+z)]),{x,1,-1},{y,1,-1},{z,1,-1},MaxRecursion->2,PlotPoints->{{4,4},{4,4},{4,4}},Boxed->False,Axes->True]

Fig. 4.2.18: ContourPlot3D[Cos[Pi(x+y+z)]+.5(Cos[Pi(x-y-z)]+Cos[Pi(-x-y+z)]+Cos[Pi(-x+y-z)]+Sin[Pi(x+y+z)]+Sin[Pi(x-y-z)]+Sin[Pi(-x-y+z)]+Sin[Pi(-x+y-z)]),{x,1,-1},{y,1,-1},{z,1,-1},MaxRecursion->2,PlotPoints->{{4,4},{4,4},{4,4}},Boxed->False,Axes->True]

Fig. 4.2.19: ContourPlot3D[Cos[Pi(x+y+z)]+(Cos[Pi(x-y-z)]+Cos[Pi(-x-y+z)]+Cos[Pi(-x+y-z)]+Sin[Pi(x+y+z)]+Sin[Pi(x-y-z)]+Sin[Pi(-x-y+z)]+Sin[Pi(-x+y-z)]),{x,1,-1},{y,1,-1},{z,1,-1},MaxRecursion->2,PlotPoints->{{4,4},{4,4},{4,4}},Boxed->False,Axes->True]

Fig. 4.3.1: ContourPlot3D[Cos[Pi(x-y)]+Cos[Pi(-x+z)]+Cos[Pi(y-z)],{x,1.5,-1.5},{y,1.5,-1.5},{z,1.5,-1.5},MaxRecursion->2,PlotPoints->{{5,3},{5,3},{5,3}},Boxed->False,Axes->True]

Fig. 4.3.2: Show[%,ViewPoint->{-1.961,-1.968,-1.932}]

Fig. 4.3.3: ContourPlot3D[Cos[Pi(x-y)]+Cos[Pi(-x+z)]+Cos[Pi(y-z)]+.8(Cos[Pi(x)]+Cos[Pi(z)]+Cos[Pi(y)]),{x,1.5,-1.5},{y,1.5,-1.5},{z,1.5,-1.5},MaxRecursion->2,PlotPoints->{{5,3},{5,3},{5,3}},Boxed->False,Axes->True] Show[%,ViewPoint->{-1.961,-1.968,-1.932}]

Fig. 4.3.4: ContourPlot3D[Cos[Pi(x-y)]+Cos[Pi(-x+z)]+Cos[Pi(y-z)]+1.2
(Cos[Pi(x)]+Cos[Pi(z)]+Cos[Pi(y)]),{x,1.5,-1.5},{y,1.5,-1.5},{z,1.5,-1.5},MaxRecursion->2,
PlotPoints->{{5,3},{5,3},{5,3}},Boxed->False,Axes->True]
Show[%,ViewPoint->{-1.961,-1.968,-1.932}]

Fig. 4.3.5: ContourPlot3D[Cos[Pi(x-y)]+Cos[Pi(-x+z)]+Cos[Pi(y-z)]+1.8 (Cos[Pi(x)]+
Cos[Pi(z)]+Cos[Pi(y)]),{x,1.5,-1.5},{y,1.5,-1.5},{z,1.5,-1.5},MaxRecursion->2,
PlotPoints->{{5,3},{5,3},{5,3}},Boxed->False,Axes->True]
Show[%,ViewPoint->{-1.961,-1.968,-1.932}]

Fig. 4.3.6: ContourPlot3D[Cos[Pi(x-y)]+Cos[Pi(-x+z)]+Cos[Pi(y-z)]+2.4
(Cos[Pi(x)]+Cos[Pi(z)]+Cos[Pi(y)]),{x,2,-2},{y,2,-2},{z,2,-2},MaxRecursion->2,
PlotPoints->{{5,3},{5,3},{5,3}},Boxed->False,Axes->True]

Fig. 4.3.7: ContourPlot3D[Sin[Pi(x-y)]+Sin[Pi(-x+z)]+Sin[Pi(y-z)]-.5,
{x,1.5,-1.5},{y,1.5,-1.5},{z,1.5,-1.5},MaxRecursion->2,PlotPoints->
{{5,3},{5,3},{5,3}},Boxed->False,Axes->True]

Fig. 4.3.8: Show[%,ViewPoint->{-1.961,-1.968,-1.932}]

Fig. 4.3.9: ContourPlot3D[.15(Sin[Pi(x+y)]+Sin[Pi(x+z)]+Sin[Pi(y+z)]+
Sin[Pi(x-y)]+Sin[Pi(-x+z)]+Sin[Pi(y-z)]-.5,{x,1.5,-1.5},{y,1.5,-1.5},{z,1.5,-1.5},
MaxRecursion->2,PlotPoints->{{5,4},{5,4},{5,4}},Boxed->False,Axes->True]

Fig. 4.3.10: Show[%,ViewPoint->{-1.961,-1.968,-1.932}]

Fig. 4.3.11: ContourPlot3D[.2(Sin[Pi(x+y)]+Sin[Pi(x+z)]+Sin[Pi(y+z)]+
Sin[Pi(x-y)]+Sin[Pi(-x+z)]+Sin[Pi(y-z)]-.5,{x,1.5,-1.5},{y,1.5,-1.5},{z,1.5,-1.5},
MaxRecursion->2,PlotPoints->{{5,4},{5,4},{5,4}},Boxed->False,Axes->True]

Fig. 4.3.12: ContourPlot3D[.3(Sin[Pi(x+y)]+Sin[Pi(x+z)]+Sin[Pi(y+z)]+
Sin[Pi(x-y)]+Sin[Pi(-x+z)]+Sin[Pi(y-z)]-.5,{x,1.5,-1.5},{y,1.5,-1.5},{z,1.5,-1.5},
MaxRecursion->2,PlotPoints->{{5,4},{5,4},{5,4}},Boxed->False,Axes->True]

Fig. 4.3.13: Show[%,ViewPoint->{-1.967,-1.962,-1.932}]

Fig. 4.3.14: ContourPlot3D[.6(Sin[Pi(x+y)]+Sin[Pi(x+z)]+Sin[Pi(y+z)]+
Sin[Pi(x-y)]+Sin[Pi(-x+z)]+Sin[Pi(y-z)]-.5,{x,1.5,-1.5},{y,1.5,-1.5},{z,1.5,-1.5},
MaxRecursion->2,PlotPoints->{{5,4},{5,4},{5,4}},
Boxed->False,Axes->True]

Fig. 4.3.15: ContourPlot3D[Sin[Pi(x-y)]+Sin[Pi(-x+z)]+Sin[Pi(y-z)]+.2(Cos[Pi(x+y+z)]+
Cos[Pi(x-y-z)]+Cos[Pi(-x-y+z)]+Cos[Pi(-x+y-z)]+Sin[Pi(x+y+z)]+Sin[Pi(x-y-z)]+
Sin[Pi(-x-y+z)]+Sin[Pi(-x+y-z)]-.5,{x,1,-1},{y,1,-1},{z,1,-1},MaxRecursion->2,
PlotPoints->{{5,3},{5,3},{5,3}},Boxed->False,Axes->True]

Fig. 4.3.16: Show[%,ViewPoint->{-1.961,-1.968,-1.932}]

Fig. 4.3.17: ContourPlot3D[Sin[Pi(x-y)]+Sin[Pi(-x+z)]+Sin[Pi(y-z)]+
.6(Cos[Pi(x+y+z)]+Cos[Pi(x-y-z)]+Cos[Pi(-x-y+z)]+Cos[Pi(-x+y-z)]+
Sin[Pi(x+y+z)]+Sin[Pi(x-y-z)]+Sin[Pi(-x-y+z)]+Sin[Pi(-x+y-z)]-.5,
{x,1,-1},{y,1,-1},{z,1,-1},MaxRecursion->2,PlotPoints->{{5,3},
{5,3},{5,3}},Boxed->False,Axes->True]

Fig. 4.3.18: Show[%,ViewPoint->{1.957,1.958,1.945}]

Fig. 4.3.19: ContourPlot3D[Sin[Pi(x-y)]+Sin[Pi(-x+z)]+Sin[Pi(y-z)]+
2(Cos[Pi(x+y+z)]+Cos[Pi(x-y-z)]+Cos[Pi(-x-y+z)]+Cos[Pi(-x+y-z)]+
Sin[Pi(x+y+z)]+Sin[Pi(x-y-z)]+Sin[Pi(-x-y+z)]+Sin[Pi(-x+y-z)])-.5,
{x,1,-1},{y,1,-1},{z,1,-1},MaxRecursion->2,PlotPoints->{{5,3},
{5,3},{5,3}},Boxed->False,Axes->True]

Fig. 4.3.20: Show[%,ViewPoint->{1.957,1.958,1.945}]

Fig. 4.3.21: ContourPlot3D[Cos[Pi x]+ Cos[Pi y]-.4,{x,3,-1},{y,3,-1},{z,1,-1},
MaxRecursion->2,PlotPoints->{{5,3},{5,3},{5,3}},Boxed->False,Axes->True]

Fig. 4.3.22: ContourPlot3D[Cos[Pi(x+y)]+Cos[Pi(x-y)]-.4,{x,1.5,-1.5},{y,1.5,-1.5},{z,1,-1},
MaxRecursion->2,PlotPoints->{{5,3},{5,3},{5,3}},Boxed->False,Axes->True]

Fig. 4.3.23: ContourPlot3D[Cos[2 Pi x]+ Cos[2 Pi y]+.2 Cos[2 Pi z]+.5,{x,1,-1},{y,1,-1},
{z,1,-1},MaxRecursion->2,PlotPoints->{{5,3},{5,3},{5,3}},Boxed->False,Axes->True]

Fig. 4.3.24: ContourPlot3D[Cos[2 Pi x]+ Cos[2 Pi y]+.4 Cos[2 Pi z]+.5,{x,1,-1},{y,1,-1},
{z,1,-1},MaxRecursion->2,PlotPoints->{{5,3},{5,3},{5,3}},Boxed->False,Axes->True]

Fig. 4.3.25: ContourPlot3D[Cos[2 Pi x]+ Cos[2 Pi y]+.6 Cos[2 Pi z]+.5,{x,1,-1},{y,1,-1},
{z,1,-1},MaxRecursion->2,PlotPoints->{{5,3},{5,3},{5,3}},Boxed->False,Axes->True]

Fig. 4.3.26: ContourPlot3D[Cos[2 Pi x]+ Cos[2 Pi y]+.8 Cos[2 Pi z]+.5,{x,1,-1},{y,1,-1},
{z,1,-1},MaxRecursion->2,PlotPoints->{{5,3},{5,3},{5,3}},Boxed->False,Axes->True]

Fig. 4.3.27: ContourPlot3D[Sin[Pi(x+y)]+Sin[Pi(x-y)]-.2,{x,2.1,-1.1},{y,1.6,-1.6},{z,1,-1},
MaxRecursion->2,PlotPoints->{{5,3},{5,3},{5,3}},Boxed->False,Axes->True]

Fig. 4.3.28: ContourPlot3D[Sin[Pi(x+y)]+Sin[Pi(x-y)]+.1(Sin[Pi(x+z)]+
Sin[Pi(-x+z)]+Sin[Pi(y+z)]+Sin[Pi(y-z)])-.2,{x,1.2,-1.2},{y,1,-1},{z,1.2,-1.2},
MaxRecursion->2,PlotPoints->{{5,4},{5,4},{5,3}},Boxed->False,Axes->True]

Fig. 4.3.29: ContourPlot3D[Sin[Pi(x+y)]+Sin[Pi(x-y)]+.2(Sin[Pi(x+z)]+
Sin[Pi(-x+z)]+Sin[Pi(y+z)]+Sin[Pi(y-z)])-.2,{x,1,-1},{y,1,-1},{z,1,-1},MaxRecursion->
2,PlotPoints->{{5,3},{5,3},{5,3}},Boxed->False,Axes->True]

Fig. 4.3.30: ContourPlot3D[Sin[Pi(x+y)]+Sin[Pi(x-y)]+.4(Sin[Pi(x+z)]+
Sin[Pi(-x+z)]+Sin[Pi(y+z)]+Sin[Pi(y-z)]),{x,1,-1},{y,1,-1},{z,1,-1},MaxRecursion->
2,PlotPoints->{{5,3},{5,3},{5,3}},Boxed->False,Axes->True]

Fig. 4.3.31: ContourPlot3D[.02(Sin[Pi(x+y)]+Sin[Pi(x-y)]+Sin[Pi(x+z)]+
Sin[Pi(-x+z)]+Sin[Pi(y+z)]+Sin[Pi(y-z)]+Cos[Pi(x)]+Cos[Pi(y)]),{x,2,-2},{y,2,-2},
{z,1,-1},MaxRecursion->2,PlotPoints->{{5,4},{5,4},{5,3}},Boxed->False,Axes->True]

Fig. 4.3.32: ContourPlot3D[.08(Sin[Pi(x+y)]+Sin[Pi(x-y)]+Sin[Pi(x+z)]+
Sin[Pi(-x+z)]+Sin[Pi(y+z)]+Sin[Pi(y-z)]+Cos[Pi(x)]+Cos[Pi(y)]),{x,2,-2},{y,2,-2},
{z,1,-1},MaxRecursion->2,PlotPoints->{{5,4},{5,4},{5,3}},Boxed->False,Axes->True]

Fig. 4.3.33: ContourPlot3D[.4(Sin[Pi(x+y)]+Sin[Pi(x-y)]+Sin[Pi(x+z)]+Sin[Pi(-x+z)]+
Sin[Pi(y+z)]+Sin[Pi(y-z)]+Cos[Pi(x)]+Cos[Pi(y)]),{x,2,-2},{y,2,-2},{z,1,-1},
MaxRecursion->2,PlotPoints->{{5,4},{5,4},{5,3}},Boxed->False,Axes->True]

Fig. 4.3.34: ContourPlot3D[.8(Sin[Pi(x+y)]+Sin[Pi(x-y)]+Sin[Pi(x+z)]+Sin[Pi(-x+z)]+Sin[Pi(y+z)]+Sin[Pi(y-z)]+Cos[Pi(x)]+Cos[Pi(y)],{x,2,-2},{y,2,-2},{z,1,-1},MaxRecursion->2,PlotPoints->{{5,4},{5,4},{5,3}},Boxed->False,Axes->True]

Fig. 4.3.35: ContourPlot3D[2(Sin[Pi(x+y)]+Sin[Pi(x-y)]+Sin[Pi(x+z)]+Sin[Pi(-x+z)]+Sin[Pi(y+z)]+Sin[Pi(y-z)]+Cos[Pi(x)]+Cos[Pi(y)],{x,2,-2},{y,2,-2},{z,1,-1},MaxRecursion->2,PlotPoints->{{5,4},{5,4},{5,3}},Boxed->False,Axes->True]

Fig. 4.3.36: Show[%,ViewPoint->{0.000,0.000,3.384}]

Fig. 4.3.37: ContourPlot3D[Cos[Pi(x+y)]+Cos[Pi(x-y)].02(Cos[Pi(x+y+z)]+Cos[Pi(x-y-z)]+Cos[Pi(-x-y+z)]+Cos[Pi(-x+y-z)]+Sin[Pi(x+y+z)]+Sin[Pi(x-y-z)]+Sin[Pi(-x-y+z)]+Sin[Pi(-x+y-z)]),{x,1.6,-1.6},{y,1.6,-1.6},{z,1,-1},MaxRecursion->2,PlotPoints->{{5,4},{5,4},{5,3}},Boxed->False,Axes->True]

Fig. 4.3.38: ContourPlot3D[Cos[Pi(x+y)]+Cos[Pi(x-y)].2 (Cos[Pi(x+y+z)]+Cos[Pi(x-y-z)]+Cos[Pi(-x-y+z)]+Cos[Pi(-x+y-z)]+Sin[Pi(x+y+z)]+Sin[Pi(x-y-z)]+Sin[Pi(-x-y+z)]+Sin[Pi(-x+y-z)]),{x,1.6,-1.6},{y,1.6,-1.6},{z,1,-1},MaxRecursion->2,PlotPoints->{{5,4},{5,4},{5,3}},Boxed->False,Axes->True]

Fig. 4.3.39: ContourPlot3D[Cos[Pi(x+y+z)]+Sin[Pi(x-y-z)].2,{x,1,-1},{y,1,-1},{z,1,-1},MaxRecursion->2,PlotPoints->{{5,3},{5,3},{5,3}},Boxed->False,Axes->True]

Fig. 4.3.40: ContourPlot3D[Cos[Pi(x+y+z)]+Sin[Pi(x-y-z)].1(Cos[Pi(x-y-z)]+Cos[Pi(-x-y+z)]+Cos[Pi(-x+y-z)]+Sin[Pi(x+y+z)]+Sin[Pi(-x-y-z)]+Sin[Pi(-x-y-z)]+.2,{x,1,-1},{y,1,-1},{z,1,-1},MaxRecursion->2,PlotPoints->{{5,4},{5,4},{5,4}},Boxed->False,Axes->True]

Fig. 4.3.41: ContourPlot3D[Cos[Pi(x+y+z)]+Sin[Pi(x-y-z)].3(Cos[Pi(x-y-z)]+Cos[Pi(-x-y+z)]+Cos[Pi(-x+y-z)]+Sin[Pi(x+y+z)]+Sin[Pi(-x-y-z)]+Sin[Pi(-x-y-z)]+.2,{x,1,-1},{y,1,-1},{z,1,-1},MaxRecursion->2,PlotPoints->{{5,3},{5,3},{5,3}},Boxed->False,Axes->True]

Fig. 4.3.42: ContourPlot3D[Cos[Pi(x+y+z)]+Sin[Pi(x-y-z)].5(Cos[Pi(x-y-z)]+Cos[Pi(-x-y+z)]+Cos[Pi(-x+y-z)]+Sin[Pi(x+y+z)]+Sin[Pi(-x-y-z)]+Sin[Pi(-x-y-z)]+.5,{x,1,-1},{y,1,-1},{z,1,-1},MaxRecursion->2,PlotPoints->{{5,3},{5,3},{5,3}},Boxed->False,Axes->True]

Fig. 4.4.1: ContourPlot3D[Sin[Pi(x+y)]+Sin[Pi(x-y)]+(Sin[Pi(x+z)]+Sin[Pi(-x+z)]+Sin[Pi(y+z)]+Sin[Pi(y-z)]),{x,.85,-.85},{y,.85,-.85},{z,.85,-.85},MaxRecursion->2,PlotPoints->{{5,3},{5,3},{5,3}},Boxed->False,Axes->True]

Fig. 4.4.2: ContourPlot3D[.5 (Cos[Pi(x+y+z)]+Cos[Pi(x-y-z)]+Cos[Pi(-x-y+z)]+Cos[Pi(-x+y-z)]+Sin[Pi(x+y+z)]+Sin[Pi(x-y-z)]+Sin[Pi(-x-y+z)]+Sin[Pi(-x+y-z)]+Sin[Pi(x+y)]+Sin[Pi(x-y)]+(Sin[Pi(x+z)]+Sin[Pi(-x+z)]+Sin[Pi(y+z)]+Sin[Pi(y-z)]),{x,.85,-.85},{y,.85,-.85},{z,.85,-.85},MaxRecursion->2,PlotPoints->{{5,3},{5,3},{5,3}},Boxed->False,Axes->True]

Fig. 4.4.3: ContourPlot3D[(Cos[Pi(x+y+z)]+Cos[Pi(x-y-z)]+Cos[Pi(-x-y+z)]+Cos[Pi(-x+y-z)]+Sin[Pi(x+y+z)]+Sin[Pi(x-y-z)]+Sin[Pi(-x-y+z)]+Sin[Pi(-x+y-z)]+Sin[Pi(x+y)]+Sin[Pi(x-y)]+(Sin[Pi(x+z)]+Sin[Pi(-x+z)]+Sin[Pi(y+z)]+Sin[Pi(y-z)]),{x,.85,-.85},{y,.85,-.85},{z,.85,-.85},MaxRecursion->2,PlotPoints->{{5,3},{5,3},{5,3}},Boxed->False,Axes->True]

Fig. 4.4.4: ContourPlot3D[(Cos[Pi(x+y+z)]+Cos[Pi(x-y-z)]+Cos[Pi(-x-y+z)]+)

```
Cos[Pi(-x+y-z)]+Sin[Pi(x+y+z)]+Sin[Pi(x-y-z)]+Sin[Pi(-x-y+z)]+Sin[Pi(-x+y-z)]+
.75(Sin[Pi(x+y)]+Sin[Pi(x-y)]+Sin[Pi(x+z)]+Sin[Pi(-x+z)]+Sin[Pi(y+z)]+Sin[Pi(y-z)]),
{x,.85,-.85},{y,.85,-.85},{z,.85,-.85},MaxRecursion->2,PlotPoints->{{5,3},{5,3},{5,3}},
Boxed->False,Axes->True]
```

Fig. 4.4.5: ContourPlot3D[(Cos[Pi(x+y+z)]+Cos[Pi(x-y-z)]+Cos[Pi(-x-y+z)]+
Cos[Pi(-x+y-z)]+Sin[Pi(x+y+z)]+Sin[Pi(x-y-z)]+Sin[Pi(-x-y+z)]+Sin[Pi(-x+y-z)]+
.5(Sin[Pi(x+y)]+Sin[Pi(x-y)]+Sin[Pi(x+z)]+Sin[Pi(-x+z)]+Sin[Pi(y+z)]+Sin[Pi(yz)]),
{x,.85,.85},{y,.85,.85},{z,.85,.85},MaxRecursion->2,PlotPoints->{{5,3},{5,3},{5,3}},
Boxed->False,Axes->True]

Fig. 4.4.6: ContourPlot3D[(Cos[Pi(x+y+z)]+Cos[Pi(x-y-z)]+Cos[Pi(-x-y+z)]+
Cos[Pi(-x+y-z)]+Sin[Pi(x+y+z)]+Sin[Pi(x-y-z)]+Sin[Pi(-x-y+z)]+Sin[Pi(-x+y-z)]+
.25(Sin[Pi(x+y)]+Sin[Pi(x-y)]+Sin[Pi(x+z)]+Sin[Pi(-x+z)]+Sin[Pi(y+z)]+Sin[Pi(y-z)]),
{x,.85,-.85},{y,.85,-.85},{z,.85,-.85},MaxRecursion->2,PlotPoints->{{5,3},{5,3},{5,3}},
Boxed->False,Axes->True]

Fig. 4.4.7: ContourPlot3D[(Sin[Pi(x+y)]+Sin[Pi(x-y)]+Sin[Pi(x+z)]+Sin[Pi(-x+z)]+
Sin[Pi(y+z)]+Sin[Pi(y-z)]),{x,1.2,-1.2},{y,1.2,-1.2},{z,1.2,-1.2},MaxRecursion->2,
PlotPoints->{{5,4},{5,4},{5,4}},Boxed->False,Axes->True]

Fig. 4.4.8: Show[%,ViewPoint->{0.056,-3.382,-0.093}]

Fig. 4.4.9: ContourPlot3D[(Sin[Pi(x+y)]+Sin[Pi(x-y)]+Sin[Pi(x+z)]+Sin[Pi(-x+z)]+
Sin[Pi(y+z)]+Sin[Pi(y-z)]+(Cos[Pi(x)]+Cos[Pi(y)]+Cos[Pi(z)]),{x,1.2,-1.2},{y,1.2,-1.2},
{z,1.2,-1.2},MaxRecursion->2,PlotPoints->{{5,4},{5,4},{5,4}},Boxed->False,Axes->True]
Show[%,ViewPoint->{-0.012,-3.384,0.042}]

Fig. 4.4.10: ContourPlot3D[(Sin[Pi(x+y)]+Sin[Pi(x-y)]+Sin[Pi(x+z)]+Sin[Pi(-x+z)]+
Sin[Pi(y+z)]+Sin[Pi(y-z)]+1.7(Cos[Pi(x)]+Cos[Pi(y)]+Cos[Pi(z)]),{x,1.2,-1.2},{y,1.2,-1.2},
{z,1.2,-1.2},MaxRecursion->2,PlotPoints->{{5,4},{5,4},{5,4}},Boxed->False,Axes->True]
Show[%,ViewPoint->{0.056,-3.382,-0.093}]

Fig. 4.4.11: ContourPlot3D[(Sin[Pi(x+y)]+Sin[Pi(x-y)]+Sin[Pi(x+z)]+Sin[Pi(-x+z)]+
Sin[Pi(y+z)]+Sin[Pi(y-z)]+2.2(Cos[Pi(x)]+Cos[Pi(y)]+Cos[Pi(z)]),{x,1.2,-1.2},{y,1.2,-1.2},
{z,1.2,-1.2},MaxRecursion->2,PlotPoints->{{5,4},{5,4},{5,4}},Boxed->False,Axes->True]
Show[%,ViewPoint->{0.056,-3.382,-0.093}]

Fig. 4.4.12: ContourPlot3D[(Sin[Pi(x+y)]+Sin[Pi(x-y)]+Sin[Pi(x+z)]+Sin[Pi(-x+z)]+
Sin[Pi(y+z)]+Sin[Pi(y-z)]+3(Cos[Pi(x)]+Cos[Pi(y)]+Cos[Pi(z)]),{x,1.2,-1.2},{y,1.2,-1.2},
{z,1.2,-1.2},MaxRecursion->2,PlotPoints->{{5,4},{5,4},{5,4}},Boxed->False,Axes->True]
Show[%,ViewPoint->{0.056,-3.382,-0.093}]

Chapter 5

Fig. 5.2.1: ContourPlot3D[E^x-100,{x,5,-5},{y,5,-5},{z,5,-5},MaxRecursion->2,
PlotPoints->{{5,3},{5,3},{5,3}},Boxed->False,Axes->True]

Fig. 5.2.2: ContourPlot3D[E^x+E^-x-100,{x,5,-5},{y,5,-5},{z,5,-5},MaxRecursion->2,
PlotPoints->{{5,3},{5,3},{5,3}},Boxed->False,Axes->True]

Fig. 5.2.3: ContourPlot3D[E^x+E^y-100,{x,5,-5},{y,5,-5},{z,5,-5},
MaxRecursion->2,PlotPoints->{{5,3},{5,3},{5,3}},Boxed->False,Axes->True]

Fig. 5.2.4: ContourPlot3D[E^x+E^y-1000,{x,7,-7},{y,7,-7},{z,7,-7},
MaxRecursion->2,PlotPoints->{{5,3},{5,3},{5,3}},Boxed->False,Axes->True]

Fig. 5.2.5: ContourPlot3D[E^x+E^y+E^z-100,{x,5,-5},{y,5,-5},{z,5,-5},
MaxRecursion->2,PlotPoints->{{5,3},{5,3},{5,3}},Boxed->False,Axes->True]

Fig. 5.2.6: ContourPlot3D[E^x+E^y+E^z+E^-x+E^-y+E^-z-100,{x,5,-5},{y,5,-5},{z,5,-5},
MaxRecursion->2,PlotPoints->{{5,3},{5,3},{5,3}},Boxed->False,Axes->True]

Fig. 5.2.7: ContourPlot3D[E^(x-6)+E^(y)+E^(z)+E^-(x-6)+E^-(y)+E^-(z)-100,
{x,11,1},{y,5,-5},{z,5,-5},MaxRecursion->2,PlotPoints->{{5,3},
{5,3},{5,3}},Boxed->False,Axes->True]

Fig. 5.2.8: ContourPlot3D[E^x+E^y+E^z+E^-x+E^-y+E^-z-1000,{x,7,-7},{y,7,-7},{z,7,-7},
MaxRecursion->2,PlotPoints->{{5,3},{5,3},{5,3}},Boxed->False,Axes->True]

Fig. 5.2.9: ContourPlot3D[E^x+E^y+E^z+E^-x+E^-y+E^-z-1000,{x,7,-7},{y,7,-7},{z,7,-7},
MaxRecursion->2,PlotPoints->{{5,3},{5,3},{5,3}},Boxed->False,Axes->True]

Fig. 5.2.10: ContourPlot3D[E^x^6+E^y^6+E^z^6-1000,{x,1.4,-1.4},{y,1.4,-1.4},{z,1.4,-1.4},
MaxRecursion->2,PlotPoints->{{4,4},{4,4},{4,4}},Boxed->False,Axes->True]

Fig. 5.2.11: ContourPlot3D[E^(x+y+z)^3+E^(x-y-z)^3+ E^(-x-y+z)^3+E^(y-z-x)^3-40000,
{x,2.5,-2.5},{y,2.5,-2.5},{z,2.5,-2.5},MaxRecursion->2,PlotPoints->{{5,3},{5,3},{5,3}},
Boxed->False,Axes->True]

Fig. 5.2.12: ContourPlot3D[E^(x+y+z)^4+E^(x-y-z)^4+ E^(-x-y+z)^4+E^(x+y-z)^4-40000,
{x,1.7,-1.7},{y,1.7,-1.7},{z,1.7,-1.7},MaxRecursion->2,PlotPoints->{{4,4},{4,4},{4,4}},
Boxed->False,Axes->True]

Fig. 5.3.1: ContourPlot3D[E^-x^2-1,{x,2,-2},{y,3,-3},{z,3,-3},MaxRecursion->2,
PlotPoints->{{5,3},{5,3},{5,3}},Boxed->False,Axes->True]

Fig. 5.3.2: ContourPlot3D[E^-x^2-9,{x,1,-1},{y,3,-3},{z,3,-3},MaxRecursion->2,
PlotPoints->{{5,3},{5,3},{5,3}},Boxed->False,Axes->True]

Fig. 5.3.3: ImplicitPlot[E^-((x)^2)+E^-((x-8)^2)-y==0,{x,2,-2},{y,2.2,-2},PlotPoints->200,
Axes->True]

Fig. 5.3.4: ImplicitPlot[E^-((x)^2)+2E^-((x-8)^2)-y==0,{x,10,-3},{y,3,-2},PlotPoints->200,
Axes->True]

Fig. 5.3.5: ContourPlot3D[E^-((x)^2+(y)^2+(z-3)^2)+E^-((x)^2+(y)^2+(z)^2)-.25,{x,1.5,-1.5},
{y,1.5,-1.6},{z,4.3,-1.7},MaxRecursion->2,PlotPoints->{{5,3},{5,3},{5,4}},Boxed->
False,Axes->True]

Fig. 5.3.6: Show[%,ViewPoint->{3.381,0.144,-0.03}]

Fig. 5.3.7: ContourPlot3D[E^-((x)^2+(y)^2+(z-3)^2)+E^-((x)^2+(y)^2+(z)^2)-.2108,
{x,1.5,-1.5},{y,1.5,-1.6},{z,4.3,-1.7},MaxRecursion->2,PlotPoints->{{5,3},{5,3},{5,4}},
Boxed->False,Axes->True]
Show[%,ViewPoint->{3.381,0.144,-0.031}]

Fig. 5.3.8: ContourPlot3D[E^-((x)^2+(y)^2+(z-3)^2)+E^-((x)^2+(y)^2+(z)^2)

`-18, {x, 1.5, -1.5}, {y, 1.5, -1.6}, {z, 4.3, -1.7}, MaxRecursion->2, PlotPoints->{{5, 3}, {5, 3}, {5, 4}}, Boxed->False, Axes->True] Show[%, ViewPoint->{3.381, 0.144, -0.031}]`

Fig. 5.3.9: `ContourPlot3D[.2 E^-((x)^2+(y)^2+(z-2.6)^2)+E^-((x)^2+(y)^2+(z)^2)-.18, {x, 1.5, -1.5}, {y, 1.5, -1.6}, {z, 3.5, -1.5}, MaxRecursion->2, PlotPoints->{{5, 4}, {5, 4}, {5, 4}}, Boxed->False, Axes->True]`

Fig. 5.3.10: `ContourPlot3D[.2 E^-((x)^2+(y)^2+(z-2.4)^2)+E^-((x)^2+(y)^2+(z)^2)-.18, {x, 1.5, -1.5}, {y, 1.5, -1.6}, {z, 3.5, -1.5}, MaxRecursion->2, PlotPoints->{{5, 4}, {5, 4}, {5, 4}}, Boxed->False, Axes->True]`

Fig. 5.3.11: `ContourPlot3D[.2 E^-((x)^2+(y)^2+(z-2.36)^2)+E^-((x)^2+(y)^2+(z)^2)-.18, {x, 1.5, -1.5}, {y, 1.5, -1.6}, {z, 3.5, -1.5}, MaxRecursion->2, PlotPoints->{{5, 4}, {5, 4}, {5, 4}}, Boxed->False, Axes->True]`

Fig. 5.3.12: `ContourPlot3D[E^-((x)^2+(y)^2+(z-3)^2)+E^-((x)^2+(y)^2+(z)^2)+.1 E^-((x)^2+(y)^2+(z-1.5)^2)-.2108, {x, 1.5, -1.5}, {y, 1.5, -1.6}, {z, 4.3, -1.7}, MaxRecursion->2, PlotPoints->{{5, 3}, {5, 3}, {5, 4}}, Boxed->False, Axes->True]`

Fig. 5.3.13: `ContourPlot3D[E^-((x)^2+(y)^2+(z-3)^2)+E^-((x)^2+(y)^2+(z)^2)-.1 E^-((x)^2+(y)^2+(z-1.5)^2)-.2108, {x, 1.5, -1.5}, {y, 1.5, -1.6}, {z, 4.3, -1.7}, MaxRecursion->2, PlotPoints->{{5, 3}, {5, 3}, {5, 4}}, Boxed->False, Axes->True] Show[%, ViewPoint->{3.381, 0.144, -0.031}]`

Fig. 5.3.14: `ImplicitPlot[E^-((y-1.7)^2+x^2)+.4 E^-(((y)^2+(x-2)^2))+E^-((y+1.7)^2+x^2)===.4, {x, 2.4, -1.5}, {y, -3, 3}, PlotPoints->200]`

Fig. 5.3.15a: `ImplicitPlot[E^-((y-1.25)^2+x^2)+E^-((y+1.25)^2+x^2)===.4, {x, 2.4, -1.5}, {y, -3, 3}, PlotPoints->200]`

Fig. 5.3.15b: `ImplicitPlot[E^-((y-1.25)^2+x^2)-.4 E^-(((y)^2+(x)^2))+E^-((y+1.25)^2+x^2)===.4, {x, 2.4, -1.5}, {y, -3, 3}, PlotPoints->200]`

Fig. 5.3.16: `ImplicitPlot[E^-((y^2+x^2-14)^2)+E^-((y-7)^2+(x+1)^2-.5)^2===.6, {x, -5, 7}, {y, -5, 8}, PlotPoints->100]`

Fig. 5.4.1: `ContourPlot3D[.25 E^-((x-3.5)^2+y^2+z^2-.25)+.25 E^-((x-3)^2+(y+2.3)^2+z^2-.25)+.25 E^-((x-5)^2+y^2+(z+2.5)^2-.25)+E^-((x^2-1))+E^-((x-8)^2)-.2, {x, 9.5, -3}, {y, 3, -3.2}, {z, 3, -3}, MaxRecursion->2, PlotPoints->{{7, 4}, {5, 3}, {5, 3}}, Boxed->False, Axes->True]`

Fig. 5.4.2: `ContourPlot3D[x^2+ y^2-2 z^2, {x, 4, -4}, {y, 4, -4}, {z, 2.8, -2.8}, MaxRecursion->2, PlotPoints->{{5, 3}, {5, 3}, {5, 3}}, Boxed->False, Axes->True]`

Fig. 5.4.3: `ContourPlot3D[x^2+ y^2-2 z^2-4, {x, 4, -4}, {y, 4, -4}, {z, 2.5, -2.5}, MaxRecursion->2, PlotPoints->{{5, 3}, {5, 3}, {5, 3}}, Boxed->False, Axes->True]`

Fig. 5.4.4: `ContourPlot3D[E^(x^2+ y^2-2 z^2-4)+E^-((3((x)^2+y^2+(z-3.5)^2))-15, {x, 3, -3}, {y, 3, -3}, {z, 4.3, -4.3}, MaxRecursion->2, PlotPoints->{{3, 5}, {3, 5}, {3, 5}}, Boxed->False, Axes->True]`

Fig. 5.4.5: `ContourPlot3D[E^(x^2+ y^2-2 z^2-4)+E^-((1.6((x)^2+y^2+(z)^2))-15, {x, 2, -2}, {y, 2, -2}, {z, 1.5, -1.5}, MaxRecursion->2, PlotPoints->{{5, 4}, {5, 4}, {5, 4}}, Boxed->False, Axes->True]`

Fig. 5.4.6: ContourPlot3D[E^(x^2+ y^2-2 z^2-4)+E^-(2((x)^6+y^6+(z)^6))-15, {x,3,-3},{y,3,-3},{z,3,-3},MaxRecursion->2,PlotPoints->{{3,5},{3,5},{3,5}}, Boxed->False,Axes->True]

Fig. 5.4.7: ContourPlot3D[E^(x^2+ y^2-2 z^2-4)+E^-(.4(E^(x+y+z)+E^(x-y-z)) +E^(-x-y+z)+E^(y-z+3-x)))-15,{x,3,-3},{y,3,-3},{z,4,-4},MaxRecursion->2,PlotPoints->{{3,5},{3,5},{3,5}},Boxed->False,Axes->True]

Fig. 5.4.8: ContourPlot3D[E^(x^2+ y^2-2 z^2-4)+E^-(.362(E^(x+y+z)+E^(x-y-z)+ E^(-x-y+z)+E^(y-z-x)))-15{x,2,-2},{y,2,-2},{z,2,-2},MaxRecursion->2,PlotPoints->{{3,5},{3,5},{3,5}},Boxed->False,Axes->True] Show[%, ViewPoint->{0.000,-0.000,3.384}]

Fig. 5.4.9: ContourPlot3D[E^-(x^2+ y^2+(z-4)^2)+E^-(((x^2+y^2)^.5-4)^2+z^2)-.2, {x,5.5,-5.5},{y,5.5,-5.5},{z,5.3,-1.3},MaxRecursion->2,PlotPoints->{{5,3},{5,3},{4,4}}, Boxed->False,Axes->True]

Fig. 5.4.11: ContourPlot3D[E^(.2(x^2+y^2))+E^(y Cos[.5 Pi(z)]+x Sin[.5 Pi(z)]+.5 E^(y Cos[.5 Pi(z+2)]+x Sin[.5 Pi(z+2)]))-3.5,{x,1.9,-1.9},{y,1.9,-1.9},{z,4,-4}, MaxRecursion->2,PlotPoints->{{5,3},{5,3},{6,4}},Boxed->False,Axes->True] Show[%,ViewPoint->{-2.4,-2.4,0.0211}]

Fig. 5.4.12: ContourPlot3D[E^-(.5(E^(.2(x^2+y^2))+E^(y Cos[.5 Pi(z)]+x Sin[.5 Pi(z)]+.5 E^(y Cos[.5 Pi(z+2)]+x Sin[.5 Pi(z+2)])))+.25 E^-(((x^2+y^2)^.5-5)^2+z^2))-1,{x,6,-6}, {y,6,-6},{z,4,-4},MaxRecursion->2,PlotPoints->{{3,5},{3,5},{3,5}},Boxed->False,Axes-> True] Show[%, ViewPoint->{1.318,-2.981,0.910}]

Fig. 5.4.13: ContourPlot3D[E^-(.5(E^(.2(x^2+y^2))+ E^(y Cos[.5 Pi(z)]+x Sin[.5 Pi(z)]+.5 E^(y Cos[.5 Pi(z+2)]+x Sin[.5 Pi(z+2)])))+.25 E^-(((x^2+y^2)^.5-5)^2+(z+4)^2)-.1,{x,6,-6},{y,6,-6},{z,5,-5},MaxRecursion->2,PlotPoints->{{3,5},{3,5},{4,5}},Boxed-> False,Axes->True]

Chapter 6

Fig. 6.1.1: ContourPlot3D[x^4-3x^2+2.25+y^4-3y^2+z^4-3z^2,{x,2,-2},{y,2,-2},{z,0,-2}, MaxRecursion->2,PlotPoints->{{5,3},{5,3},{5,3}},Boxed->False,Axes->True]

Fig. 6.1.2: ContourPlot3D[z (z-1)(z+1)(z-2)+ x(x-1)(x+1)(x-2)+ y(y-1)(y+1)(y-2), {x,-1.4,2.4},{y,-1.4,2.4},{z,5,-2.2},MaxRecursion->2,PlotPoints->{{5,3},{5,3},{5,3}}, Boxed->False,Axes->True]

Fig. 6.1.3: ContourPlot3D[x^4-3x^2+3.5+y^4-3y^2+z^4-3z^2,{x,2,-2},{y,2,-2},{z,2,-2}, MaxRecursion->2,PlotPoints->{{5,3},{5,3},{5,3}},Boxed->False,Axes->True]

Fig. 6.1.4: Plot[{E^-x^2(1680-13440*x^2+13440*x^4-3584*x^6+256*x^8), 3000 Cos[1 Pi (x)]},{x,-3,3},PlotPoints->200,Axes->True]

Fig. 6.1.5: HermiteH[10,x] Plot[{E^-(.5 x^2) (-30240 + 302400*x^2 -403200*x^4 +161280*x^6 - 23040*x^8+1024*x^10),-30000 Cos [1.5 Pi (x)]},{x,0,2},PlotPoints->200, Axes->True]

Fig. 6.1.6: HermiteH[20,x] Plot[{E^-(.5 x^2)(670442572800 - 13408851456000*x^2+40226554368000*x^4-42908324659200*x^6 +

```
21454162329600*x^8-5721109954560*x^10+866834841600*x^12 -
76205260800*x^14+3810263040*x^16-99614720*x^18 + 1048576*x^20),
670000000000 Cos [2 Pi (x)],{x,0,2},PlotPoints->200,Axes->True]
```

Fig. 6.1.9: Plot[{E^{-(x²)}, Cos [2 Pi (x)]}, {x,-3,3}, PlotPoints->200, Axes->False]

Fig. 6.1.10: Plot[E^{-(x²)} Cos [2 Pi (x)], {x,-3,3}, PlotPoints->200, Axes->False]

Fig. 6.2.1: Plot[E^{-(x²)} Cos [2 Pi (x)], {x,-3,3}, PlotPoints->200, Axes->True]

Fig. 6.2.2: ImplicitPlot[-E^{-(.5(x)²)} (Cos [Pi x]) - y == 0, {x,-4.2,5}, {y,1.5,-1}, PlotPoints->200, Axes->True]

Fig. 6.2.3: ContourPlot3D[(z Cos[2 Pi x] - y Sin[2 Pi x]), {x,1,-1}, {y,.5,-.5}, {z,.5,-.5}, MaxRecursion->2, PlotPoints->{{5,3}, {5,3}, {5,3}}, Boxed->False, Axes->True]

Fig. 6.2.4: ContourPlot3D[(z Cos[2 Pi x] - y Sin[2 Pi x]) - 4(z²+y²), {x,1,-1}, {y,.3,-.3}, {z,.3,-.3}, MaxRecursion->2, PlotPoints->{{5,4}, {4,4}, {4,4}}, Boxed->False, Axes->True]

Fig. 6.2.5: ContourPlot3D[E^{-(x²)} (z Cos[2 Pi x] - y Sin[2 Pi x]) - 4(z²+y²), {x,1.8,-1.8}, {y,.3,-.3}, {z,.3,-.3}, MaxRecursion->2, PlotPoints->{{3,5}, {3,5}, {3,5}}, Boxed->False, Axes->True]

Fig. 6.2.6: Show[%, ViewPoint->{0.123,-3.381,-0.031}]

Fig. 6.3.1: ContourPlot3D[E^{-((x)²+(y)²+(z)²)} (Cos [Pi x] + Cos [Pi y] + Cos [Pi z]) - .5, {x,1.3,-1}, {y,1,-1}, {z,1,-1}, MaxRecursion->2, PlotPoints->{{5,3}, {5,3}, {5,3}}, Boxed->False, Axes->True]

Fig. 6.3.2: ContourPlot3D[E^{-((x)²+(y)²+5(z)²)} (Cos [.5 Pi x] + Cos [Pi y] + Cos [Pi z]) - .5, {x,1.3,-1}, {y,9,-9}, {z,6,-6}, MaxRecursion->2, PlotPoints->{{5,3}, {5,3}, {5,3}}, Boxed->False, Axes->True]

Fig. 6.3.3: ImplicitPlot[(Cos [Pi x] + Cos [Pi y]) == .1, {x,3,-3}, {y,3,-3}, PlotPoints->100]

Fig. 6.3.4 a: ImplicitPlot[E^{-(.5((x+4)²+(y)²)} (Cos [Pi x] + Cos [Pi y]) == .1, {x,7,-7}, {y,3,-3}, PlotPoints->200]

Fig. 6.3.4 b: ImplicitPlot[E^{-(.25((x-4)²+(y)²)} (Cos [Pi x] + Cos [Pi y]) == .1, {x,7,-7}, {y,3,-3}, PlotPoints->200]

Fig. 6.3.5: ImplicitPlot[E^{-(.5((x+4)²+(y)²)} (Cos [Pi x] + Cos [Pi y]) + E^{-(.25((x-4)²+(y)²)} (Cos [Pi x] + Cos [Pi y]) == .1, {x,7,-7}, {y,3,-3}, PlotPoints->100]

Fig. 6.3.6: ContourPlot3D[E^{-(.5((x+4)²+(y)²+(z)²)} (Cos [Pi x] + Cos [Pi y] + Cos [Pi z]) + E^{-(.25((x-4)²+(y)²+(z)²)} (Cos [Pi x] + Cos [Pi y] + Cos [Pi z]) - .1, {x,7,-7}, {y,3.5,-3.5}, {z,3.5,-3.5}, MaxRecursion->2, PlotPoints->{{4,5}, {3,5}, {3,5}}, Boxed->False, Axes->True]

Fig. 6.3.7: ContourPlot3D[E^{-2((x)²+(y)²+(z)²)} (Sin [Pi (-x+y-z)] + Sin [Pi (-x-y+z)] + Sin [Pi (x-y-z)] + Sin [Pi (+x+y+z)] + Cos [Pi (-x+y-z)] + Cos [Pi (-x-y+z)] + Cos [Pi (x-y-z)] + Cos [Pi (+x+y+z)]) - .4, {x,1,-1}, {y,1,-1}, {z,1,-1}, MaxRecursion->2, PlotPoints->{{5,3}, {5,3}, {5,3}}, Boxed->False, Axes->True]

Fig. 6.4.1: `ImplicitPlot[(((x+y)^4+(x-y)^4==1,((.8 x)+y)^4+(x-(.8 y))^4==1,((.6 x)+y)^4+(x-(.6 y))^4==1,((.4x)+y)^4+(x-(.4 y))^4==1,((.2 x)+y)^4+(x-(.2 y))^4==1,(y)^4+(x)^4==1},{x,1.2,-1.2},{y,1.2,-1.2},PlotPoints->100]`

Fig. 6.4.2: `ImplicitPlot[{{(x-1)^2+(y)^2==.005,(x-.707)^2+(y-.707)^2==.005,(x)^2+(y-1)^2==.005,(x-.6)^2+(y-.8)^2==.005,(x-.2)^2+(y-.98)^2==.005,(x-.8)^2+(y-.6)^2==.005,(x-.4)^2+(y-.916)^2==.005,(x-.9)^2+(y-.436)^2==.005,(x-.97)^2+(y-.24)^2==.005},{x,1.2,-.2},{y,1.2,-.2},PlotPoints->100]`

Fig. 6.4.3: `ImplicitPlot[{{(x-1)^2+(2y)^2==.005,(x-.707)^2+(2y-.707)^2==.005,(x)^2+(2y-1)^2==.005,(x-.6)^2+(2y-.8)^2==.005,(x-.2)^2+(2y-.98)^2==.005,(x-.8)^2+(2y-.6)^2==.005,(x-.4)^2+(2y-.916)^2==.005,(x-.9)^2+(2y-.436)^2==.005,(x-.97)^2+(2y-.24)^2==.005},{x,1.2,-.2},{y,1.2,-.2},PlotPoints->100]`

Fig. 6.4.4: `ImplicitPlot[{4(x-1)^2+(2y)^2==.005,4(x-.707)^2+(2y-.707)^2==.005,4(x)^2+(2y-1)^2==.005,4(x-.6)^2+(2y-.8)^2==.005,4(x-.2)^2+(2y-.98)^2==.005,4(x-.8)^2+(2y-.6)^2==.005,4(x-.4)^2+(2y-.916)^2==.005,4(x-.9)^2+(2y-.436)^2==.005,4(x-.97)^2+(2y-.24)^2==.005},{x,1.2,-.2},{y,1.2,-.2},PlotPoints->100]`

Chapter 7

Fig. 7.1.1: `ContourPlot3D[E^(-x^2)Cos[Pi x]E^(-y^2)Cos[Pi y]E^(-z^2)Cos[Pi z]-.05,{x,1.7,-1.7},{y,1.7,-1.7},{z,1.7,-1.7},MaxRecursion->2,PlotPoints->{{3,5},{3,5},{3,5}},Boxed->False,Axes->True]`

Fig. 7.1.2: `ContourPlot3D[E^(-x^2)Cos[2 Pi x]E^(-y^2)Cos[2 Pi y]E^(-z^2)Cos[2 Pi z]-.05,{x,1.7,-1.7},{y,1.7,-1.7},{z,1.7,-1.7},MaxRecursion->2,PlotPoints->{{3,5},{3,5},{3,5}},Boxed->False,Axes->True]`

Fig. 7.2.1 a: `ContourPlot3D[Cos[Pi x],{x,2,-2},{y,2,-2},{z,1,-1},MaxRecursion->2,PlotPoints->{{5,3},{5,3},{5,3}},Boxed->False,Axes->True]`

Fig. 7.2.1 b: `ContourPlot3D[Cos[Pi y],{x,2,-2},{y,2,-2},{z,1,-1},MaxRecursion->2,PlotPoints->{{5,3},{5,3},{5,3}},Boxed->False,Axes->True]`

Fig. 7.2.1 c: `ContourPlot3D[Cos[Pi z],{x,2,-2},{y,2,-2},{z,2,-2},MaxRecursion->2,PlotPoints->{{5,3},{5,3},{5,3}},Boxed->False,Axes->True]`

Fig. 7.2.2a: `ContourPlot3D[Cos[Pi x]+Cos[Pi y]-1,{x,2.5,-.5},{y,2.5,-.5},{z,2,-2},MaxRecursion->2,PlotPoints->{{5,3},{5,3},{5,3}},Boxed->False,Axes->True]`

Fig. 7.2.2b: `ContourPlot3D[Cos[Pi x]+Cos[Pi z]-1,{x,2.5,-.5},{y,2,-2},{z,2.5,-.5},MaxRecursion->2,PlotPoints->{{5,3},{5,3},{5,3}},Boxed->False,Axes->True]`

Fig. 7.2.2c: `ContourPlot3D[Cos[Pi y]+Cos[Pi z]-1,{x,2,-2},{y,2.5,-.5},{z,2.5,-.5},MaxRecursion->2,PlotPoints->{{5,3},{5,3},{5,3}},Boxed->False,Axes->True]`

Fig. 7.2.3: `ContourPlot3D[Cos[Pi y]+Cos[Pi z]+Cos[Pi x],{x,2,-2},{y,2,-2},{z,2,-2},MaxRecursion->2,PlotPoints->{{4,4},{4,4},{4,4}},Boxed->False,Axes->True]`

Fig. 7.2.4: `ContourPlot3D[Cos[Pi y]Cos[Pi z]Cos[Pi x]-.001,{x,2,-2},{y,2,-2},{z,2,-2},MaxRecursion->2,PlotPoints->{{4,4},{4,4},{4,4}},Boxed->False,Axes->True]`

Fig. 7.2.5: ContourPlot3D[Cos[Pi y]Cos[Pi z]Cos[Pi x]-2,{x,2.5,-2},{y,2,-2.5},{z,2.5,-2},MaxRecursion->2,PlotPoints->{{3,5},{3,5},{3,5}},Boxed->False,Axes->True]

Fig. 7.2.6: ContourPlot3D[Cos[2 Pi x]+Cos[2 Pi y]+Cos[2 Pi z]+(x^2+y^2+z^2)-2,{x,2,-2},{y,2,-2},{z,2,-2},MaxRecursion->2,PlotPoints->{{4,4},{4,4},{4,4}},Boxed->False,Axes->True]

Fig. 7.2.7: ContourPlot3D[Cos[Pi x]+Cos[Pi y]+Cos[Pi z]+(x^2+y^2)-1,{x,2,-2},{y,2,-2},{z,3,-3},MaxRecursion->2,PlotPoints->{{4,4},{4,4},{4,4}},Boxed->False,Axes->True]

Fig. 7.2.8: ContourPlot3D[Cos[Pi x]+Cos[Pi y]+Cos[Pi z]+(x^2)-.5,{x,2,-2},{y,3,-3},{z,3,-3},MaxRecursion->2,PlotPoints->{{5,4},{5,4},{5,4}},Boxed->False,Axes->True]

Fig. 7.2.9: ContourPlot3D[E^(Cos[3 Pi x]+Cos[3 Pi y]+Cos[3 Pi z])+(E^x^2+E^y^2+E^z^2)-8.5,{x,1.4,-1.4},{y,1.4,-1.4},{z,1.4,-1.4},MaxRecursion->2,PlotPoints->{{4,4},{4,4},{4,4}},Boxed->False,Axes->True]

Fig. 7.2.10: ContourPlot3D[E^(Cos[Pi(x+y+z)]+Cos[Pi(x-y-z)]+Cos[Pi(-x-y+z)]+Cos[Pi(y-z-x)])+E^(Sin[Pi(x+y+z)]+Sin[Pi(x-y-z)]+Sin[Pi(-x-y+z)]+Sin[Pi(y-z-x)])+E^(x+y+z)+E^(x-y-z)+E^((-x-y+z))+E^(y-z-x))-11,{x,1.8,-1.8},{y,1.8,-1.8},{z,1.8,-1.8},MaxRecursion->2,PlotPoints->{{5,4},{5,4},{5,4}},Boxed->False,Axes->True]

Fig. 7.2.11: ContourPlot3D[E^(Sin[4 Pi (x+y)]+Sin[4 Pi (x-y)]+Sin[4 Pi (x+z)]+Sin[4 Pi (z-x)]+Sin[4 Pi (y+z)]+Sin[4 Pi (y-z)])+(E^x^2+E^y^2+E^z^2)-5.5,{x,1.3,-1.3},{y,1.3,-1.3},{z,1.3,-1.3},MaxRecursion->2,PlotPoints->{{5,5},{5,5},{5,5}},Boxed->False,Axes->True,AxesLabel->{x,y,z}]

Fig. 7.3.1a: ContourPlot3D[(E^-(x)^2)-.5,{x,-4,4},{y,-4,4},{z,-4,4},MaxRecursion->2,PlotPoints->{{5,3},{5,3},{5,3}},Boxed->False,Axes->True]

Fig. 7.3.1b: ContourPlot3D[(E^-(y)^2)-.5,{x,-4,4},{y,-4,4},{z,-4,4},MaxRecursion->2,PlotPoints->{{5,3},{5,3},{5,3}},Boxed->False,Axes->True]

Fig. 7.3.1c: ContourPlot3D[(E^-(z)^2)-.5,{x,-4,4},{y,-4,4},{z,-4,4},MaxRecursion->2,PlotPoints->{{5,3},{5,3},{5,3}},Boxed->False,Axes->True]

Fig. 7.3.2: ContourPlot3D[(E^-(x)^2)+(E^-(y)^2)+(E^-(z)^2)+.5,{x,-4,4},{y,-4,4},{z,-4,4},MaxRecursion->2,PlotPoints->{{5,3},{5,3},{5,3}},Boxed->False,Axes->True]

Fig. 7.3.3: ContourPlot3D[(E^-(x)^2)+(E^-(y)^2)+(E^-(z)^2)+1.8,{x,-3,3},{y,-3,3},{z,-3,3},MaxRecursion->2,PlotPoints->{{5,4},{5,4},{5,4}},Boxed->False,Axes->True]

Fig. 7.3.4: ContourPlot3D[(E^-(x)^2)+(E^-(y)^2)+(E^-(z)^2)+2.5,{x,-1,1},{y,-1,1},{z,-1,1},MaxRecursion->2,PlotPoints->{{5,3},{5,3},{5,3}},Boxed->False,Axes->True]

Fig. 7.3.5: ContourPlot3D[(E^-(x)^2)+(E^-(y)^2)+(E^-(z)^2)+(E^-(x-2)^2)+(E^-(y-2)^2)+(E^-(z-2)^2)-2.7,{x,-1,3},{y,-1,3},{z,-1,3},MaxRecursion->2,PlotPoints->{{5,3},{5,3},{5,3}},Boxed->False,Axes->True]

Fig. 7.3.6: ContourPlot3D[(E^-(x)^2)+(E^-(y)^2)+(E^-(z)^2)+(E^-(x-2)^2)+(E^-(y-2)^2)+(E^-(z-2)^2)-2.9,{x,-6,2.5},{y,-6,2.5},{z,-6,2.5},MaxRecursion->2,PlotPoints->{{5,3},{5,3},{5,3}},Boxed->False,Axes->True]

Fig. 7.3.7: ContourPlot3D[(E⁻(x²)+(E⁻(y²)+(E⁻(z²)+(E⁻(x-2)²)+(E⁻(y-2)²)+(E⁻(z-2)²)+(E⁻(x-4)²)+(E⁻(y-4)²)+(E⁻(z-4)²)-2.85,{x,-1,5.5},{y,-1,5.5},{z,-1,5.5},MaxRecursion->2,PlotPoints->{{3,5},{3,5},{3,5}},Boxed->False,Axes->True]

Fig. 7.3.8: ContourPlot3D[(E⁻(x²)+E⁻((x-2)²)+E⁻((x-4)²)+E⁻((x-6)²)+E⁻((x-8)²)+E⁻((x-10)²)+(E⁻(y²)+E⁻((y-2)²)+E⁻((y-4)²)+E⁻((y-6)²)+E⁻((y-8)²)+E⁻((y-10)²)+(E⁻(z²)+E⁻((z-2)²)+E⁻((z-4)²)+E⁻((z-6)²)+E⁻((z-8)²)+E⁻((z-10)²)-2.65,{x,-2,12},{y,-2,12},{z,-2,12},MaxRecursion->2,PlotPoints->{{5,5},{5,5},{5,5}},Boxed->False,Axes->True]

Fig. 7.4.1 : ContourPlot3D[E⁻((x+y)²)-.8,{x,-1,1},{y,-1,1},{z,-1,1},MaxRecursion->2,PlotPoints->{{5,3},{5,3},{5,3}},Boxed->False,Axes->True]

Fig. 7.4.2: ContourPlot3D[E⁻((x+y-.5)²)+E⁻((x-y-.5)²)+E⁻((x+z-.5)²)+E⁻((y+z-.5)²)+E⁻((-x+z-.5)²)+E⁻((y-z-.5)²)+E⁻((x+y+1.5)²)+E⁻((x-y+1.5)²)+E⁻((x+z+1.5)²)+E⁻((y+z+1.5)²)+E⁻((-x+z+1.5)²)+E⁻((y-z+1.5)²)+E⁻((x+y+2.5)²)+E⁻((x-y-2.5)²)+E⁻((x+z-2.5)²)+E⁻((y+z-2.5)²)+E⁻((-x+z-2.5)²)+E⁻((y-z-2.5)²)+-5.3,{x,-2.5,3},{y,-2.5,3},{z,-2.5,3},MaxRecursion->2,PlotPoints->{{6,4},{6,4},{6,4}},Boxed->False,Axes->True]

Fig. 7.4.3: ContourPlot3D[E⁻((x+y-.5)²)+E⁻((x-y-.5)²)+E⁻((x+z-.5)²)+E⁻((y+z-.5)²)+E⁻((-x+z-.5)²)+E⁻((y-z-.5)²)+E⁻((x+y-2.5)²)+E⁻((x-y-2.5)²)+E⁻((x+z-2.5)²)+E⁻((y+z-2.5)²)+E⁻((-x+z-2.5)²)+E⁻((y-z-2.5)²)+E⁻((x+y+1.5)²)+E⁻((x-y+1.5)²)+E⁻((x+z+1.5)²)+E⁻((y+z+1.5)²)+E⁻((-x+z+1.5)²)+E⁻((y-z+1.5)²)+E⁻((x+y-4.5)²)+E⁻((x-y-4.5)²)+E⁻((x+z-4.5)²)+E⁻((y+z-4.5)²)+E⁻((-x+z-4.5)²)+E⁻((y-z-4.5)²)+E⁻((x+y+3.5)²)+E⁻((x-y+3.5)²)+E⁻((x+z+3.5)²)+E⁻((y+z+3.5)²)+E⁻((-x+z+3.5)²)+E⁻((y-z+3.5)²)+E⁻((x+y+5.5)²)+E⁻((x-y+5.5)²)+E⁻((x+z+5.5)²)+E⁻((y+z+5.5)²)+E⁻((-x+z+5.5)²)+E⁻((y-z+5.5)²)-5.3,{x,-6,5.6},{y,-6,5.6},{z,-6,5.6},MaxRecursion->2,PlotPoints->{{5,5},{5,5},{5,5}},Boxed->False,Axes->True] Show[%,ViewPoint->{1.957, 1.945,1.959}]

Fig. 7.5.1 : ContourPlot3D[E⁻((x+y+z)²)-.8,{x,-1,1},{y,-1,1},{z,-1,1},MaxRecursion->2,PlotPoints->{{5,3},{5,3},{5,3}},Boxed->False,Axes->True]

Fig. 7.5.2: ContourPlot3D[E⁻((x+y+z+.5)²)+E⁻((x-y+z+.5)²)+E⁻((x+y-z+.5)²)+E⁻((-x+y+z+.5)²)+-2.3,{x,7,-1.5},{y,7,-1.5},{z,7,-1.5},MaxRecursion->2,PlotPoints->{{5,3},{5,3},{5,3}},Boxed->False,Axes->True]

Fig. 7.5.3: ContourPlot3D[E⁻((x+y+z+.5)²)+E⁻((x-y+z+.5)²)+E⁻((x+y-z+.5)²)+E⁻((-x+y+z+.5)²)+E⁻((x+y+z-1.5)²)+E⁻((x-y+z-1.5)²)+E⁻((x+y-z-1.5)²)+E⁻((-x+y+z-1.5)²)-3.7,{x,2,-1.5},{y,2,-1.5},{z,2,1.5},MaxRecursion->2,PlotPoints->{{5,4},{5,4},{5,4}},Boxed->False,Axes->True]

Fig. 7.5.4: ContourPlot3D[E⁻((x+y+z+.5)²)+E⁻((x-y+z+.5)²)+E⁻((x+y-z+.5)²)+E⁻((-x+y+z+.5)²)+E⁻((x+y+z+2.5)²)+E⁻((x-y+z+2.5)²)+E⁻((x+y-z+2.5)²)+E⁻((-x+y+z+2.5)²)+E⁻((x+y+z-1.5)²)+E⁻((x-y+z-1.5)²)+E⁻((x+y-z-1.5)²)+E⁻((-x+y+z-1.5)²)-3.7,{x,-2.4,2},{y,-2.4,2},{z,-2.4,2},MaxRecursion->2,PlotPoints->{{5,4},{5,4},{5,4}},Boxed->False,Axes->True]

Fig. 7.5.5: ContourPlot3D[E⁻((x+y+z+.5)²)+E⁻((x-y+z+.5)²)+E⁻((x+y-z+.5)²)+E⁻((-x+y+z+.5)²)+E⁻((x+y+z+2.5)²)+E⁻((x-y+z+2.5)²)+E⁻((x+y-z+2.5)²)+E⁻((-x+y+z+2.5)²)+E⁻((x+y+z-1.5)²)+E⁻((x-y+z-1.5)²)+E⁻((x+y-z-1.5)²)+E⁻((-x+y+z-1.5)²)+E⁻((x+y+z+4.5)²)+E⁻((x-y+z+4.5)²)+E⁻((x+y-z+4.5)²)+E⁻((-x+y+z+4.5)²)+E⁻((x+y+z-3.5)²)+E⁻((x-y+z-3.5)²)+E⁻((x+y-z-3.5)²)+E⁻((-x+y+z-3.5)²)+

$E^{-((x+y+z-3.5)^2)-3.5}$, {x,-5,4.2}, {y,-5,4.2}, {z,-5,4.2}, MaxRecursion->2, PlotPoints->{{5,5}, {5,5}, {5,5}}, Boxed->False, Axes->True]

Fig. 7.5.7: ContourPlot3D[E^{-(x-3)²+E^{-(x-5)²+E^{-(x-8)²+E^{-(x-13)²+E^{-(x-21)²+E^{-(x-34)²+E^{-(y-3)²+E^{-(y-5)²+E^{-(y-8)²+E^{-(y-13)²+E^{-(y-21)²+E^{-(y-34)²+E^{-(z-3)²+E^{-(z-5)²+E^{-(z-8)²+E^{-(z-13)²+E^{-(z-21)²+E^{-(z-34)²-2.5}, {x,9,2}, {y,9,2}, {z,9,2}, MaxRecursion->2, PlotPoints->{{6,4}, {6,4}, {6,4}}, Boxed->False, Axes->True]}}}}}}}}}}}}}}}}}

Fig. 7.5.8: ImplicitPlot[E^{-(y-3)²+E^{-(y-5)²+E^{-(y-8)²+E^{-(y-13)²+E^{-(y-21)²+E^{-(y-34)²+E^{-(x-3)²+E^{-(x-5)²+E^{-(x-8)²+E^{-(x-13)²+E^{-(x-21)²+E^{-(x-34)²}==1.9}, {x,0,35}, {y,0,35}, PlotPoints->200]}}}}}}}}}}

Fig. 7.5.9: ImplicitPlot[E^{-(y-3)²+E^{-(y-5)²+E^{-(y-9)²+E^{-(y-12)²+E^{-(y-15)²+E^{-(x-2)²+E^{-(x-4)²+E^{-(x-7)²+E^{-(x-10)²+E^{-(x-12)²}==1.85}, {x,0,16}, {y,0,16}, PlotPoints->200]}}}}}}}}

Fig. 7.6.1a: ContourPlot3D[E^{-(x²+y²+(z-2)²)+E^{-((x-2)²+y²+z²)+E^{-(x²+y²+z²)+E^{-((x)²+(y)²+(z+2)²)+E^{-(x²+(y+2)²+(z)²)+E^{-((x+2)²+(y)²+z²)+E^{-(x²+(y-2)²+z²)-.85}, {x,2.5,-2.5}, {y,2.5,-2.5}, {z,2.5,-2.5}, MaxRecursion->2, PlotPoints->{{3,5}, {3,5}, {3,5}}, Boxed->False, Axes->True]}}}}}}

Fig. 7.6.1b: ContourPlot3D[E^{-(x²+y²+(z-2)²)+E^{-((x-2)²+y²+z²)+E^{-(x²+y²+z²)+E^{-((x)²+(y)²+(z+2)²)+E^{-(x²+(y+2)²+(z)²)+E^{-((x+2)²+(y)²+z²)+E^{-(x²+(y-2)²+z²)-.7}, {x,3,-3}, {y,3,-3}, {z,3,3}, MaxRecursion->2, PlotPoints->{{5,4}, {5,4}, {5,4}}, Boxed->False, Axes->True]}}}}}}

Fig. 7.6.2: ContourPlot3D[E^{-((x-2)²+y²+(z-2)²)+E^{-(x²+y²+(z-2)²)+E^{-((x-2)²+y²+z²)+E^{-(x²+y²+z²)+E^{-((x-2)²+(y-2)²+(z-2)²)+E^{-(x²+(y-2)²+(z-2)²)+E^{-((x-2)²+(y-2)²+z²)+E^{-((x-4)²+y²+z²)+E^{-((x-4)²+(y-2)²+z²)+E^{-((x-4)²+y²+z²)+E^{-((x-4)²+(y-2)²+(z-2)²)+E^{-((x-4)²+y²+(z-2)²)+E^{-((x-4)²+(y-2)²+(z-4)²)+E^{-((x-4)²+y²+(z-4)²)+E^{-((x-2)²+y²+(z-4)²)+E^{-((x-2)²+y²+(z-4)²)+E^{-((x-2)²+y²+(z-4)²)+E^{-((x-2)²+(y-4)²+(z-2)²)+E^{-((x-2)²+(y-4)²+(z-2)²)+E^{-((x-2)²+(y-4)²+(z-2)²)+E^{-((x-2)²+(y-4)²+z²)+E^{-((x-4)²+(y-4)²+z²)+E^{-((x-4)²+(y-4)²+z²)+E^{-((x-4)²+(y-4)²+(z-2)²)+E^{-((x-4)²+(y-4)²+(z-4)²)+E^{-((x-2)²+(y-4)²+(z-4)²)+E^{-((x-2)²+(y-4)²+(z-4)²-.68}, {x,5.5,-1.5}, {y,5.5,-1.5}, {z,2.5,-1.5}, MaxRecursion->2, PlotPoints->{{3,5}, {3,5}, {3,5}}, Boxed->False, Axes->True]}}}}}}}}}}}}}}}}}}}}}}}}}}

Fig. 7.6.3a: ContourPlot3D[E^{-((x-1)²+(y-1)²+(z-1)²)+E^{-((x+1)²+(y+1)²+(z+1)²)+E^{-((x+1)²+(y-3)²+(z-3)²)+E^{-((x-3)²+(y+1)²+(z-3)²)+E^{-((x-3)²+(y-3)²+(z+1)²)-.12}, {x,5,-2.7}, {y,5,-2.7}, {z,5,-2.7}, MaxRecursion->2, PlotPoints->{{5,4}, {5,4}, {5,4}}, Boxed->False, Axes->True]}}}}

Fig. 7.6.3b: ContourPlot3D[E^{-((x-1)²+(y-1)²+(z-1)²)+E^{-((x+1)²+(y+1)²+(z+1)²)+E^{-((x+1)²+(y-3)²+(z-3)²)+E^{-((x-3)²+(y+1)²+(z-3)²)+E^{-((x-3)²+(y-3)²+(z+1)²)-.08}, {x,5,-2.7}, {y,5,-2.7}, {z,5,-2.7}, MaxRecursion->2, PlotPoints->{{5,4}, {5,4}, {5,4}}, Boxed->False, Axes->True]}}}}

Fig. 7.6.4: ContourPlot3D[E^{-((x-1)²+(y-1)²+(z-1)²)+E^{-((x+1)²+(y+1)²+(z+1)²)+E^{-((x+1)²+(y-3)²+(z-3)²)+E^{-((x-3)²+(y+1)²+(z-3)²)+E^{-((x-3)²+(y-3)²+(z+1)²)+E^{-((x-1)²+(y-5)²+(z-5)²)+E^{-((x-5)²+(y-1)²+(z-5)²)+E^{-((x+3)²+(y-1)²+(z-5)²)+E^{-((x-1)²+(y+3)²+(z-5)²)-.08}, {x,7,-4.7}, {y,7,-4.7}, {z,7,-4.7}, MaxRecursion->2, PlotPoints->{{3,5}, {3,5}, {3,5}}, Boxed->False, Axes->True]}}}}}}}}

Fig. 7.6.5: ContourPlot3D[E^-E^((x-2)^2+y^2+z^2)+E^-E^((x-1)^2+(y-1.732)^2+z^2)+E^-E^((x^2+y^2+z^2)+E^-E^((x-1)^2+(y-5.77)^2+(z-1.633)^2)+E^-E^((x-2)^2+y^2+(z-3.27)^2)+E^-E^((x-1)^2+(y-1.732)^2+(z-3.27)^2)+E^-E^((x^2+y^2+(z-3.27)^2)+E^-E^((x-4)^2+y^2+z^2)+E^-E^((x-5)^2+(y-1.732)^2+z^2)+E^-E^((x-2)^2+(y-3.464)^2+z^2)+E^-E^((x-4)^2+(y-3.464)^2+z^2)+E^-E^((x-4)^2+(y-3.464)^2+z^2)+E^-E^((x-4)^2+(y-3.464)^2+(z-3.27)^2)+E^-E^((x-5)^2+(y-3.464)^2+(z-3.27)^2)+E^-E^((x-3)^2+(y-5.2)^2+(z-3.27)^2)+E^-E^((x-3)^2+(y-5.2)^2+(z)^2)+E^-E^((x-3)^2+(y-4.041)^2+(z-1.633)^2)+E^-E^((x-6)^2+y^2+(z-3.27)^2)+E^-E^((x-6)^2+y^2+(z)^2)+E^-E^((x-5)^2+(y-5.77)^2+(z-1.633)^2)+E^-E^((x-6)^2+(y-3.46)^2+(z-3.27)^2)+E^-E^((x)^2+(y-3.464)^2+(z-3.27)^2)+E^-E^((x-3)^2+(y+1.732)^2+(z-3.27)^2)+E^-E^((x-6)^2+(y-3.46)^2+(z)^2)+E^-E^((x)^2+(y-3.464)^2+(z)^2)+E^-E^((x-3)^2+(y+1.732)^2+(z)^2)+E^-E^((x-3)^2+(y+1.732)^2+(z)^2)+E^-E^((x-5)^2+(y-2.883)^2+(z-4.9)^2)+E^-E^((x-1)^2+(y-2.883)^2+(z+4.9)^2)+E^-E^((x-3)^2+(y+5.77)^2+(z-4.9)^2)+E^-E^((x-5)^2+(y-2.883)^2+(z+1.633)^2)+E^-E^((x-1)^2+(y-2.883)^2+(z+1.633)^2)+E^-E^((x-3)^2+(y+5.77)^2+(z+1.633)^2)-.05,{x,7,-1},{y,6.5,-3},{z,6,-3},MaxRecursion->2,PlotPoints->{{4,5},{4,5},{4,5}},Boxed->False,Axes->True]

Fig. 7.6.6: ContourPlot3D[E^-((x+1)^2+(y-1)^2+(z-1)^2)+E^-((x-1)^2+(y-1)^2+(z-3)^2)+E^-((x-3)^2+(y-3)^2+(z-3)^2)+E^-((x-1)^2+(y+1)^2+(z-5)^2)+E^-((x-3)^2+(y-5)^2+(z-5)^2)+E^-((x-5)^2+(y-3)^2+(z-1)^2)-.25,{x,-3,7},{y,-3,7},{z,-1,7},MaxRecursion->2,lotPoints->{{3,5},{3,5},{3,5}},Boxed->False,Axes->True]

Fig. 7.6.7: ContourPlot3D[E^-((x+.5)^2+(y-.5)^2+(z-.5)^2)+E^-((x-.5)^2+(y-.5)^2+(z-1.5)^2)+E^-((x-.5)^2+(y+.5)^2+(z-2.5)^2)+E^-((x+.5)^2+(y+.5)^2+(z-3.5)^2)+E^-((x+.5)^2+(y-4.5)^2+(z-5)^2)+E^-((x+.5)^2+(y-3.5)^2+(z-3.5)^2)+E^-((x-.5)^2+(y-3.5)^2+(z-5)^2)+E^-((x-.5)^2+(y-4.5)^2+(z-1.5)^2)+E^-((x-3.5)^2+(y-3.5)^2+(z-3.5)^2)+E^-((x-3.5)^2+(y-4.5)^2+(z-5)^2)+E^-((x-4.5)^2+(y-4.5)^2+(z-1.5)^2)+E^-((x-1.5)^2+(y-1.5)^2+(z-1.5)^2)+E^-((x-1.5)^2+(y-2.5)^2+(z-2.5)^2)+E^-((x-2.5)^2+(y-2.5)^2+(z-3.5)^2)+E^-((x-2.5)^2+(y-1.5)^2+(z-.5)^2)+E^-((x-4.5)^2+(y-3.5)^2+(z-2.5)^2)+E^-((x-3.5)^2+(y-.5)^2+(z-.5)^2)+E^-((x-4.5)^2+(y-.5)^2+(z-1.5)^2)+E^-((x-3.5)^2+(y+.5)^2+(z-3.5)^2)+E^-((x-4.5)^2+(y+.5)^2+(z-2.5)^2)+E^-((x+.5)^2+(y-.5)^2+(z-4.5)^2)+E^-((x-.5)^2+(y-.5)^2+(z-5.5)^2)+E^-((x-.5)^2+(y+.5)^2+(z-6.5)^2)+E^-((x+.5)^2+(y+.5)^2+(z-7.5)^2)+E^-((x+.5)^2+(y-4.5)^2+(z-4.5)^2)+E^-((x+.5)^2+(y-3.5)^2+(z-7.5)^2)+E^-((x-.5)^2+(y-3.5)^2+(z-6.5)^2)+E^-((x-.5)^2+(y-4.5)^2+(z-5.5)^2)+E^-((x-1.5)^2+(y-1.5)^2+(z-5.5)^2)+E^-((x-1.5)^2+(y-2.5)^2+(z-6.5)^2)+E^-((x-2.5)^2+(y-2.5)^2+(z-7.5)^2)+E^-((x-2.5)^2+(y-1.5)^2+(z-4.5)^2)+E^-((x-3.5)^2+(y-4.5)^2+(z-4.5)^2)+E^-((x-4.5)^2+(y-4.5)^2+(z-5.5)^2)+E^-((x-3.5)^2+(y-3.5)^2+(z-7.5)^2)+E^-((x-4.5)^2+(y-3.5)^2+(z-6.5)^2)+E^-((x-3.5)^2+(y-.5)^2+(z-4.5)^2)+E^-((x-4.5)^2+(y-.5)^2+(z-6.5)^2)+E^-((x-3.5)^2+(y+.5)^2+(z-7.5)^2)+E^-((x-4.5)^2+(y+.5)^2+(z-6.5)^2)-.9,{x,-1,6},{y,-2,6},{z,-1,9},MaxRecursion->2,PlotPoints->{{5,4},{5,4},{5,4}},Boxed->False,Axes->True]

Fig. 7.6.8a: ContourPlot3D[E^-((x^2+y^2+(z)^2)+E^-((x-2)^2+y^2+z^2)+E^-((x-4)^2+(y)^2+(z)^2)+E^-((x-6)^2+(y)^2+(z)^2)-.5,{x,7,-1},{y,1,-1},{z,1,-1},MaxRecursion->2,PlotPoints->{{5,3},{5,3},{5,4}},Boxed->False,Axes->True]

Fig. 7.6.8b: ContourPlot3D[E^-((x^2+y^2+(z)^2)+E^-((x-2)^2+y^2+z^2)+E^-((x-2)^2+(y)^2+(z-2)^2)+E^-((x-4)^2+(y)^2+(z-2)^2)+E^-((x-4)^2+(y)^2+(z-4)^2)+E^-((x-6)^2+(y)^2+(z-4)^2)-.5,{x,7,-1},{y,2,-2},{z,6,-1},MaxRecursion->2,PlotPoints->{{7,4},{7,4},{7,4}},Boxed->False,Axes->True]

Fig. 7.6.9a: ContourPlot3D[E^-((x^2+y^2+(z-2)^2)+E^-((x-2)^2+y^2+z^2)+E^-((x^2+y^2+z^2)+E^-((x+2)^2+(y)^2+(z-2)^2)+E^-((x-2)^2+(y)^2+(z+2)^2)+E^-((x+2)^2+(y-2)^2+(z+2)^2)+E^-((x+2)^2+(y-2)^2+(z)^2)+E^-((x+2)^2+(y-4)^2+(z)^2)+E^-((x+2)^2+(y-4)^2+(z-2)^2)+E^-((x+2)^2+(y-6)^2+(z-2)^2)+

```
E^-((x)^2+(y-6)^2+(z+2)^2)+E^-((x)^2+(y-6)^2+(z)^2)+E^-((x-2)^2+(y-6)^2+(z)^2)+
E^-((x-2)^2+(y-6)^2+(z-2)^2)+E^-((x-4)^2+(y-6)^2+(z-2)^2)+E^-((x-4)^2+(y-4)^2+
(z+2)^2)+E^-((x-4)^2+(y-4)^2+(z)^2)+E^-((x-4)^2+(y-2)^2+(z)^2)+E^-((x-4)^2+(y-2)^2+
(z-2)^2)+E^-((x-4)^2+(y)^2+(z-2)^2)-.5,{x,5,-3},{y,7,-1},{z,5,-3},MaxRecursion->2,
PlotPoints->{{7,4},{7,4},{7,4}},Boxed->False,Axes->True]
```

Fig. 7.6.9b: Show[%, ViewPoint->{-0.000, 0.000, 3.384}]

Chapter 8

Fig. 8.2.2: ContourPlot3D[E^-((E^(Cos[Pi x] Sin[Pi z]+ Cos[Pi y] Sin[Pi x]+ Sin[Pi y] Cos[Pi z]))+E^-(Cos[Pi x] Sin[Pi z]+ Cos[Pi y] Sin[Pi x]+Sin[Pi y] Cos[Pi z]))-1+ .2(x^2+y^2+z^2)))+ .2 E^-E^(Cos[Pi x])-1,{x,4,-4},{y,4,-4},{z,4,-4},MaxRecursion->2, PlotPoints->{{3,5},{3,5},{3,5}},Boxed->False,Axes->True]

Fig. 8.2.3: Show[%, ViewPoint->{0.000, -0.000, 3.384}]

Fig. 8.2.4: ContourPlot3D[E^-((E^(Cos[Pi x] Sin[Pi z]+ Cos[Pi y] Sin[Pi x]+ Sin[Pi y] Cos[Pi z]))+E^-(Cos[Pi x] Sin[Pi z]+ Cos[Pi y] Sin[Pi x]+ Sin[Pi y] Cos[Pi z]))-1+2(x^2+y^2+z^2)))+ .2 E^-E^(Cos[Pi x])-1,{x,4,-4},{y,4,0},{z,4,-4}, MaxRecursion->2,PlotPoints->{{3,5},{3,5},{3,5}},Boxed->False,Axes->True]

Fig. 8.2.5: ContourPlot3D[E^-((E^(Cos[Pi x] Sin[Pi z]+ Cos[Pi y] Sin[Pi x]+Sin[Pi y] Cos[Pi z]))+E^-(Cos[Pi x] Sin[Pi z]+ Cos[Pi y] Sin[Pi x]+Sin[Pi y] Cos[Pi z]))-1+ .2(x^2+y^2+z^2)))+.2 E^-E^(Cos[Pi x])-1,{x,3.5,-3.5},{y,4,0},{z,2,-2},MaxRecursion->2, PlotPoints->{{3,5},{3,5},{3,5}},Boxed->False,Axes->True] Show[%,ViewPoint->{0.000,-0.000,3.384}]

Fig. 8.2.6: ContourPlot3D[E^-((E^(Cos[Pi x] Sin[Pi z]+ Cos[Pi y] Sin[Pi x]+ Sin[Pi y] Cos[Pi z]))+E^-(Cos[Pi x] Sin[Pi z]+ Cos[Pi y] Sin[Pi x]+Sin[Pi y] Cos[Pi z]))-1+ .2(x^2+y^2+z^2)))+ .2 E^-E^(Cos[Pi x])-1,{x,2,-2},{y,4,0},{z,2,-2},MaxRecursion->2, PlotPoints->{{3,5},{3,5},{3,5}},Boxed->False,Axes->True] Show[%, ViewPoint->{3.384, 0.019, -0.026}]

Fig. 8.2.7: ContourPlot3D[E^-((E^(Cos[Pi x] Sin[Pi z]+ Cos[Pi y] Sin[Pi x]+Sin[Pi y] Cos[Pi z]))+E^-(Cos[Pi x] Sin[Pi z]+ Cos[Pi y] Sin[Pi x]+Sin[Pi y] Cos[Pi z]))-1+ .2(x^2+y^2+z^2)))+.2 E^-E^(Cos[Pi x])-1,{x,65,-.65},{y,3,-3},{z,3,-3},MaxRecursion->2, PlotPoints->{{3,5},{6,4},{6,4}},Boxed->False,Axes->True] Show[%, ViewPoint->{3.384, 0.019, -0.026}]

Fig. 8.5.2a: ContourPlot3D[.02 (Cos[2 Pi x]+Cos[2 Pi y]+Cos[2 Pi z])+(x^2+y^2+z^2)-1, {x,1,-1},{y,1,-1},{z,1,-1},MaxRecursion->2,PlotPoints->{{4,4},{4,4},{4,4}},Boxed->False, Axes->True]

Fig. 8.5.2b: ContourPlot3D[-.02 (Cos[2 Pi x]+Cos[2 Pi y]+Cos[2 Pi z])+(x^2+y^2+z^2)-1, {x,1.2,-1.2},{y,1.2,-1.2},{z,1.2,-1.2},MaxRecursion->2,PlotPoints->{{4,4},{4,4},{4,4}}, Boxed->False,Axes->True]

Fig. 8.5.3a: ContourPlot3D[.4 (Cos[2 Pi x] Sin[2 Pi z]+ Cos[2 Pi y] Sin[2 Pi x]+ Cos[2 Pi z] Sin[2 Pi y])+(x^2+y^2+z^2)-12,{x,4,-0},{y,0,-4},{z,4,-0},MaxRecursion->2, PlotPoints->{{4,4},{4,4},{4,4}},Boxed->False,Axes->True]

Fig. 8.5.3b: ContourPlot3D[-.4 (Cos[2 Pi x] Sin[2 Pi z]+ Cos[2 Pi y] Sin[2 Pi x]+

`Cos[2 Pi z] Sin[2 Pi y]]+(x^2+y^2+z^2)-12,{x,4,-0},{y,0,-4},{z,4,-0},MaxRecursion->2,PlotPoints->{{4,4},{4,4},{4,4}},Boxed->False,Axes->True]`

Fig. 8.5.3c: `ContourPlot3D[.25 (Cos[2 Pi x] Sin[2 Pi z]+ Cos[2 Pi y] Sin[2 Pi x]+ Cos[2 Pi z] Sin[2 Pi y]]+(x^2+y^2+z^2)-12,{x,4,-0},{y,0,-4},{z,4,-0},MaxRecursion->2,PlotPoints->{{4,4},{4,4},{4,4}},Boxed->False,Axes->True]`

Fig. 8.5.3d: `ContourPlot3D[.6 (Cos[2 Pi x] Sin[2 Pi z]+ Cos[2 Pi y] Sin[2 Pi x]+ Cos[2 Pi z] Sin[2 Pi y]]+(x^2+y^2+z^2)-12,{x,4,-0},{y,0,-4},{z,4,-0},MaxRecursion->2,PlotPoints->{{4,4},{4,4},{4,4}},Boxed->False,Axes->True]`

Fig. 8.5.3e: `ContourPlot3D[.3 (Cos[2 Pi x] Sin[2 Pi z]+ Cos[2 Pi y] Sin[2 Pi x]+ Cos[2 Pi z] Sin[2 Pi y]]+(x^2+y^2+z^2)-12,{x,4,-0},{y,0,-4},{z,4,-0},MaxRecursion->2,PlotPoints->{{4,4},{4,4},{4,4}},Boxed->False,Axes->True]`

Fig. 8.5.4: `ContourPlot3D[.4 (Cos[2 Pi x] Sin[2 Pi z]+ Cos[2 Pi y] Sin[2 Pi x]+ Cos[2 Pi z] Sin[2 Pi y]]+(x^2+y^2+z^2)-12,{x,4,-4},{y,4,-4},{z,4,-4},MaxRecursion->2,PlotPoints->{{5,5},{5,5},{5,5}},Boxed->False,Axes->True]`

Fig. 8.5.5: `ContourPlot3D[.4 (Cos[2 Pi x] Sin[2 Pi z]+ Cos[2 Pi y] Sin[2 Pi x]+ Cos[2 Pi z] Sin[2 Pi y]]+(x^2+y^2+z^2)-12,{x,4,-4},{y,4,-4},{z,4,-4},MaxRecursion->2,PlotPoints->{{5,5},{5,5},{5,5}},Boxed->False,Axes->True]`

Chapter 9

Fig. 9.1.1a: `ImplicitPlot[(x)^-2==4,{x,6,-3},{y,4,-4},PlotPoints->100]`

Fig. 9.1.1b: `ImplicitPlot[(x)^-2+(x-4)^-2==4,{x,6,-3},{y,4,-4},PlotPoints->100]`

Fig. 9.1.1c: `ImplicitPlot[E^-(x)^2+E^-(x-4)^2==.8,{x,6,-3},{y,4,-4},PlotPoints->100]`

Fig. 9.1.1d: `ImplicitPlot[E^-((x)^2+(y)^2-1)==.5,{x,3,-3},{y,3,-3},PlotPoints->100]`

Fig. 9.1.1e: `ImplicitPlot[E^-((x)^2+(y)^2-5)==.5,{x,3,-3},{y,3,-3},PlotPoints->100]`

Fig. 9.1.1f: `ImplicitPlot[E^-((x)^2+(y)^2-5)^2==.5,{x,3,-3},{y,3,-3},PlotPoints->100]`

Fig. 9.1.2a: `ImplicitPlot[E^-((x)^2+(y)^2-5)+E^-((x)^2+(y)^2-5)==.5,{x,7.5,-3},{y,3,-3},PlotPoints->100]`

Fig. 9.1.2b: `ImplicitPlot[E^-((x-2)^2+(y)^2-5)+E^-((x)^2+(y)^2-5)==.5,{x,7.5,-3},{y,3,-3},PlotPoints->100]`

Fig. 9.1.2c: `ImplicitPlot[E^-((x-3)^2+(y)^2-5)+E^-((x)^2+(y)^2-5)==.5,{x,7.5,-3},{y,3,-3},PlotPoints->100]`

Fig. 9.1.2d: `ImplicitPlot[E^-((x-4)^2+(y)^2-5)+E^-((x)^2+(y)^2-5)==.5,`

`ImplicitPlot[E^-((x-4)^2+(y)^2-5)+E^-((x)^2+(y)^2-5)+E^-((x-4)^2+(y-3)^2-5)+E^-((x)^2+(y-3)^2-5)==.5,{x,7.5,-3},{y,7,-3},PlotPoints->100]`

Fig. 9.1.2f: `ImplicitPlot[E^-((x-4)^2+(y)^2-5)+E^-((x)^2+(y)^2-5)+E^-((x-4)^2+(y-4)^2-5)+E^-((x)^2+(y-4)^2-5)==.5,{x,7.5,-3},{y,7,-3},PlotPoints->100]`

Fig. 9.1.3 a: `ImplicitPlot[E^-((x)^4+(y)^4-5)+E^-((x)^4+(y)^4-5)===.5,{x,5,-2},{y,2,-2},PlotPoints->100]`

Fig. 9.1.3 b: `ImplicitPlot[E^-((x-2)^4+(y)^4-5)+E^-((x)^4+(y)^4-5)===.5,{x,5,-2},{y,2,-2},PlotPoints->100]`

Fig. 9.1.3 c: `ImplicitPlot[E^-((x-3.1)^4+(y)^4-5)+E^-((x)^4+(y)^4-5)===.5,{x,5,-2},{y,2,-2},PlotPoints->100]`

Fig. 9.1.3 d: `ImplicitPlot[E^-((x-3.2)^4+(y)^4-5)+E^-((x)^4+(y)^4-5)===.5,{x,5,-2},{y,2,-2},PlotPoints->100]`

Fig. 9.1.3 e: `ImplicitPlot[E^-((x-3.2)^4+(y)^4-5)+E^-((x)^4+(y)^4-5)+E^-((x)^4+(y-3.2)^4-5)+E^-((x-3.2)^4+(y-3.2)^4-5)===.5,{x,5,-2},{y,5,-2},PlotPoints->100]`

Fig. 9.1.4 a: `ContourPlot3D[E^-((x)^2+(y)^2+z^2-5)+E^-((x)^2+(y)^2+z^2-5)-.5,{x,-2.9,3},{y,-2.9,2.9},{z,2.9,-2.9},MaxRecursion->2,PlotPoints->{{4,4},{4,4},{4,4}},Boxed->False,Axes->True]`

Fig. 9.1.4 b: `ContourPlot3D[E^-((x-1)^2+(y)^2+z^2-5)+E^-((x)^2+(y)^2+z^2-5)-.5,{x,-2.9,4},{y,-2.9,2.9},{z,2.9,-2.9},MaxRecursion->2,PlotPoints->{{4,4},{4,4},{4,4}},Boxed->False,Axes->True]`

Fig. 9.1.4 c: `ContourPlot3D[E^-((x-2)^2+(y)^2+z^2-5)+E^-((x)^2+(y)^2+z^2-5)-.5,{x,-2.9,5},{y,-2.9,2.9},{z,2.9,-2.9},MaxRecursion->2,PlotPoints->{{4,4},{4,4},{4,4}},Boxed->False,Axes->True]`

Fig. 9.1.4 d: `ContourPlot3D[E^-((x-4)^2+(y)^2+z^2-5)+E^-((x)^2+(y)^2+z^2-5)-.5,{x,-2.9,7},{y,-2.9,2.9},{z,2.9,-2.9},MaxRecursion->2,PlotPoints->{{4,4},{4,4},{4,4}},Boxed->False,Axes->True]`

Fig. 9.1.4 e: `ContourPlot3D[E^-((x-5)^2+(y)^2+z^2-5)+E^-((x)^2+(y)^2+z^2-5)-.5,{x,-2.9,8},{y,-2.9,2.9},{z,2.9,-2.9},MaxRecursion->2,PlotPoints->{{4,4},{4,4},{4,4}},Boxed->False,Axes->True]`

Fig. 9.1.5 a: `ContourPlot3D[E^-((x)^2+(y)^2+z^2-5)+E^-((x-5)^2+(y)^2+z^2-5)+E^-((x)^2+(y)^2+z^2-5)+E^-((x-5)^2+(y)^2+z^2-5)-.5,{x,-2.6,8},{y,-2.6,3},{z,2.9,-2.9},MaxRecursion->2,PlotPoints->{{4,4},{4,4},{4,4}},Boxed->False,Axes->True]`

Fig. 9.1.5 b: `ContourPlot3D[E^-((x)^2+(y)^2+z^2-5)+E^-((x-5)^2+(y)^2+z^2-5)+E^-((x)^2+(y-2)^2+z^2-5)+E^-((x-5)^2+(y-2)^2+z^2-5)-.5,{x,-2.6,8},{y,-2.6,4},{z,2.9,-2.9},MaxRecursion->2,PlotPoints->{{4,4},{4,4},{4,4}},Boxed->False,Axes->True]`

Fig. 9.1.5 c: `ContourPlot3D[E^-((x)^2+(y)^2+z^2-5)+E^-((x-5)^2+(y)^2+z^2-5)+E^-((x)^2+(y-3)^2+z^2-5)+E^-((x-5)^2+(y-3)^2+z^2-5)-.5,{x,-2.6,8},{y,-2.6,6},{z,2.9,-2.9},MaxRecursion->2,PlotPoints->{{4,4},{4,4},{4,4}},Boxed->False,Axes->True]`

Fig. 9.1.5 d: `ContourPlot3D[E^-((x)^2+(y)^2+z^2-5)+E^-((x-5)^2+(y)^2+z^2-5)+E^-((x)^2+(y-5)^2+z^2-5)+E^-((x-5)^2+(y-5)^2+z^2-5)-.5,{x,-2.7,7.6},{y,-2.7,7.6},{z,2.8,-2.8},MaxRecursion->2,PlotPoints->{{4,4},{4,4},{4,4}},Boxed->False,Axes->True]`

Fig. 9.1.6 a: `ContourPlot3D[E^-((x)^2+(y)^2+z^2-5)+E^-((x-5)^2+(y)^2+z^2-5)+E^-((x)^2+(y-5)^2+z^2-5)+E^-((x-5)^2+(y-5)^2+z^2-5)+E^-((x)^2+(y)^2+z^2-5)+`

$E^{-((x-5)^2+(y)^2+(z)^2-5)}+E^{-((x)^2+(y-5)^2+z^2-5)}+E^{-((x-5)^2+(y-5)^2+(z)^2-5)}-.5,$
 $\{x,-2.6,8\},\{y,-2.6,8\},\{z,2.9,-2.9\},\text{MaxRecursion}\rightarrow 2,\text{PlotPoints}\rightarrow\{\{4,4\},\{4,4\},\{4,4\}\},\text{Boxed}\rightarrow$
 $\text{False},\text{Axes}\rightarrow\text{True}]$

Fig. 9.1.6 b: ContourPlot3D[E^{−((x)²+(y)²+z²−5)}+E^{−((x−5)²+(y)²+z²−5)}+E^{−((x)²+(y−5)²+z²−5)}+E^{−((x−5)²+(y−5)²+z²−5)}+E^{−((x)²+(y)²+(z−1)²−5)}+E^{−((x−5)²+(y)²+(z−1)²−5)}+E^{−((x)²+(y−5)²+(z−1)²−5)}+E^{−((x−5)²+(y−5)²+(z−1)²−5)}−.5,{x,-2.6,8},{y,-2.6,8},{z,3.9,-2.9},MaxRecursion→2,PlotPoints→{{4,4},{4,4},{4,4}},Boxed→False,Axes→True]

Fig. 9.1.6 c: ContourPlot3D[E^{−((x)²+(y)²+z²−5)}+E^{−((x−5)²+(y)²+z²−5)}+E^{−((x)²+(y−5)²+z²−5)}+E^{−((x−5)²+(y−5)²+z²−5)}+E^{−((x)²+(y)²+(z−3.5)²−5)}+E^{−((x−5)²+(y)²+(z−3.5)²−5)}+E^{−((x)²+(y−5)²+(z−3.5)²−5)}+E^{−((x−5)²+(y−5)²+(z−3.5)²−5)}−.5,{x,-2.6,8},{y,-2.6,8},{z,6,-2.9},MaxRecursion→2,PlotPoints→{{4,4},{4,4},{4,4}},Boxed→False,Axes→True]

Fig. 9.1.6 d: ContourPlot3D[E^{−((x)²+(y)²+z²−5)}+E^{−((x−5)²+(y)²+z²−5)}+E^{−((x)²+(y−5)²+z²−5)}+E^{−((x−5)²+(y−5)²+z²−5)}+E^{−((x)²+(y)²+(z−5)²−5)}+E^{−((x−5)²+(y)²+(z−5)²−5)}+E^{−((x)²+(y−5)²+(z−5)²−5)}+E^{−((x−5)²+(y−5)²+(z−5)²−5)}−.5,{x,-2.6,8},{y,-2.6,8},{z,8,-2.9},MaxRecursion→2,PlotPoints→{{4,4},{4,4},{4,4}},Boxed→False,Axes→True]

Fig. 9.2.1 a: ImplicitPlot[E^{−((x)²+(y)²−5)²==.5,{x,8,-3},{y,3,-3},PlotPoints→100]}

Fig. 9.2.1 b: ImplicitPlot[E^{−((x)²+(y)²−5)²+E^{−((x−1)²+(y)²−5)²==.5,{x,8,-3},{y,3,-3},PlotPoints→100]}}

Fig. 9.2.1 c: ImplicitPlot[(E^{−((x)²+(y)²−5)}+E^{−((x−1)²+(y)²−5)}−1)²==.5,{x,8,-3},{y,3,-3},PlotPoints→100]

Fig. 9.2.1 d: ImplicitPlot[(E^{−((x)²+(y)²−5)}+E^{−((x−3)²+(y)²−5)}−1)²==.5,{x,8,-3},{y,3,-3},PlotPoints→100]

Fig. 9.2.1 e: ImplicitPlot[(E^{−((x)²+(y)²−5)}+E^{−((x−4)²+(y)²−5)}−1)²==.5,{x,8,-3},{y,3,-3},PlotPoints→100]

Fig. 9.2.1 f: ImplicitPlot[(E^{−((x)²+(y)²−5)}+E^{−((x−4.7)²+(y)²−5)}−1)²==.5,{x,8,-3},{y,3,-3},PlotPoints→100]

Fig. 9.2.1 g: ImplicitPlot[(E^{−((x)²+(y)²−5)}+E^{−((x−5)²+(y)²−5)}−1)²==.5,{x,8,-3},{y,3,-3},PlotPoints→100]

Fig. 9.2.1 h: ImplicitPlot[(E^{−((x)²+(y)²−5)}+E^{−((x−5.4)²+(y)²−5)}−1)²==.5,{x,8,-3},{y,3,-3},PlotPoints→100]

Fig. 9.2.2 a: ImplicitPlot[E^{−(((x)²+(y)²)−6)}(Cos[2 Pi x]+Cos[2Pi y])+E^{−((x)⁴+(y)⁴−6)}+E^{−(((x)²+(y)²)−6)}(Cos[2 Pi x]+ Cos[2Pi y])+ E^{−((x)⁴+(y)⁴−6)}==44,{x,4.5,-2},{y,2,-2},PlotPoints→100]

Fig. 9.2.2 b: ImplicitPlot[E^{−(((x)²+(y)²)−6)}(Cos[2 Pi x]+ Cos[2Pi y])+E^{−((x)⁴+(y)⁴−6)}+E^{−(((x−1)²+(y)²)−6)}(Cos[2 Pi x]+ Cos[2Pi y])+ E^{−((x−1)⁴+(y)⁴−6)}==44,{x,4.5,-2},{y,2,-2},PlotPoints→100]

Fig. 9.2.2 c: ImplicitPlot[E^{−(((x)²+(y)²)−6)}(Cos[2 Pi x]+ Cos[2Pi y])+

$$E^{-(x^4+y^4-6)}+E^{-((x-2)^2+(y^2)-6)} (\text{Cos}[2 \text{ Pi } x]+ \text{Cos}[2\text{Pi } y])+ E^{-(x-2)^4+(y)^4-6} \\ =44,\{x,4.5,-2\},\{y,2,-2\},\text{PlotPoints}\rightarrow 100]$$

Fig. 9.2.2 d: `ImplicitPlot[E^-(((x)^2+(y)^2)-6) (Cos[2 Pi x]+ Cos[2Pi y])+ E^{-(x)^4+(y)^4-6}+E^{-((x-2.5)^2+(y)^2)-6) (Cos[2 Pi x]+ Cos[2Pi y])+ E^{-(x-2.5)^4+(y)^4-6}=44,\{x,4.5,-2\},\{y,2,-2\},PlotPoints->100]`

Fig. 9.2.2 e: `ImplicitPlot[E^-(((x)^2+(y)^2)-6) (Cos[2 Pi x]+ Cos[2Pi y])+ E^{-(x)^4+(y)^4-6}+E^{-((x-2.7)^2+(y)^2)-6) (Cos[2 Pi x]+ Cos[2Pi y])+ E^{-(x-2.7)^4+(y)^4-6}=44,\{x,4.5,-2\},\{y,2,-2\},PlotPoints->100]`

Fig. 9.2.2 f: `ImplicitPlot[E^-(((x)^2+(y)^2)-6) (Cos[2 Pi x]+ Cos[2Pi y])+ E^{-(x)^4+(y)^4-6}+E^{-((x-3)^2+(y)^2)-6) (Cos[2 Pi x]+ Cos[2Pi y])+ E^{-(x-3)^4+(y)^4-6} =44,\{x,4.5,-2\},\{y,2,-2\},PlotPoints->100]`

Fig. 9.2.2 g: `ImplicitPlot[E^-(((x)^2+(y)^2)-6) (Cos[2 Pi x]+ Cos[2Pi y])+ E^{-(x)^4+(y)^4-6}+E^{-(((x-3)^2+(y)^2)-6) (Cos[2 Pi x]+ Cos[2Pi y])+ E^{-(x-3)^4+(y)^4-6}+E^{-(((x)^2+(y-3)^2)-6) (Cos[2 Pi x]+ Cos[2Pi y])+ E^{-(x)^4+(y-3)^4-6}+E^{-(((x-3)^2+(y-3)^2)-6) (Cos[2 Pi x]+ Cos[2Pi y])+ E^{-(x-3)^4+(y-3)^4-6}=88,\{x,4.5,-2\},\{y,4.5,-2\},PlotPoints->100]`

Fig. 9.2.5 a: `ImplicitPlot[10^-((x-3)^2+10^-(y-10)+10^(y-33)) +10^-((x-8)^2+10^-(y-10)+10^(y-33))+10^-((x+3)^2+10^(y-33)+10^-(y+15))+10^-((x)^2+10^(y-8)+10^-(y+15))+10^-((x-5)^2+10^(y-8)+10^-(y+15))+10^-((x-15)^2+10^(y-8)+10^-(y+15))+10^-((x-17)^2+10^(y-28)+10^-(y-15))+10^-((x-11)^2+10^(y-18)+10^-(y+10))+10^-((x-20)^2+10^(y+15)+10^(y-33))+10^-((y-33)^2+10^(x-21)+10^-(x+4))+10^-((y+15)^2+10^(x-21)+10^-(x+4)) =0.6,\{x,-7,23\},\{y,-16,38\},PlotPoints->100]`

Fig. 9.2.5 b: `ImplicitPlot[10^-((x-3)^2+10^-(y-10)+10^(y-33)) +10^-((x-8)^2+10^-(y-10)+10^(y-33)) +10^-((x+3)^2+10^(y-33)+10^-(y+15))+10^-((x)^2+10^(y-8)+10^-(y+15))+10^-((x-5)^2+10^(y-8)+10^-(y+15))+10^-((x-15)^2+10^(y-8)+10^-(y+15))+10^-((x-17)^2+10^(y-28)+10^-(y-15))+10^-((x-11)^2+10^(y-18)+10^-(y+10))+10^-((x-20)^2+10^-(y+15)+10^(y-33))+10^-((y-33)^2+10^(x-21)+10^-(x+4))+10^-((y+15)^2+10^(x-21)+10^-(x+4))+10^-((x-13)^2+10^-(y-10)+10^(y-33))+10^-((x-18)^2+10^-(y-10)+10^(y-33)) +10^-((x-7)^2+10^(y-33)+10^-(y+15))+10^-((x-10)^2+10^(y-8)+10^-(y+15))+10^-((x-15)^2+10^(y-8)+10^-(y+15))+10^-((x-25)^2+10^(y-8)+10^-(y+15))+10^-((x-27)^2+10^(y-28)+10^-(y-15))+10^-((x-21)^2+10^(y-18)+10^-(y+10))+10^-((x-30)^2+10^-(y+15)+10^(y-33))+10^-((y-33)^2+10^(x-31)+10^-(x-6))+10^-((y+15)^2+10^(x-31)+10^-(x-6))=0.6,\{x,-7,33\},\{y,-16,38\},PlotPoints->100]`

Fig. 9.2.5 c: `ImplicitPlot[10^-((x-3)^2+10^-(y-10)+10^(y-33)) +10^-((x-8)^2+10^-(y-10)+10^(y-33)) +10^-((x+3)^2+10^(y-33)+10^-(y+15))+10^-((x)^2+10^(y-8)+10^-(y+15))+10^-((x-5)^2+10^(y-8)+10^-(y+15))+10^-((x-15)^2+10^(y-8)+10^-(y+15))+10^-((x-17)^2+10^(y-28)+10^-(y-15))+10^-((x-11)^2+10^(y-18)+10^-(y+10))+10^-((x-20)^2+10^-(y+15)+10^(y-33))+10^-((y-33)^2+10^(x-21)+10^-(x+4))+10^-((y+15)^2+10^(x-21)+10^-(x+4))+10^-((x-26)^2+10^-(y-10)+10^(y-33)) +10^-((x-31)^2+10^-(y-10)+10^(y-33))+10^-((x-20)^2+10^(y-33)+10^-(y+15))+10^-((x-23)^2+10^(y-8)+10^-(y+15))+10^-((x-28)^2+10^(y-8)+10^-(y+15))+10^-((x-38)^2+10^(y-8)+10^-(y+15))+10^-((x-40)^2+10^(y-28)+10^-(y-15))+10^-((x-34)^2+10^(y-18)+10^-(y+10))+10^-((x-43)^2+10^-(y+15)+10^(y-33))+10^-((y-33)^2+10^(x-44)+10^-(x-19))+10^-((y+15)^2+10^(x-44)+10^-(x-19)) =0.6,\{x,-7,45\},\{y,-16,38\},PlotPoints->100]`

Fig. 9.2.5 d: `ImplicitPlot[10^-((x-3)^2+10^-(y-10)+10^(y-33)) +10^-((x-8)^2+10^-(y-10)+10^(y-33))+10^-((x+3)^2+10^(y-33)+10^-(y+15))+10^-((x)^2+10^(y-8)+10^-(y+15))+`

```

10^-((x-5)^2+10^(y-8)+10^-(y+15))+10^-((x-15)^2+10^(y-8)+10^-(y+15))+10^-((x-17)^2+
10^(y-28)+10^-(y-15))+10^-((x-11)^2+10^(y-18)+10^-(y+10))+10^-((x-20)^2+10^-(y+15)+
10^(y-33))+10^-((y-33)^2+10^(x-21)+10^-(x+4))+10^-((y+15)^2+10^(x-21)+10^-(x+4))+
10^-((x-28)^2+10^-(y-10)+10^(y-33))+10^-((x-33)^2+10^-(y-10)+10^(y-33))+
10^-((x-22)^2+10^(y-33)+10^-(y+15))+10^-((x-25)^2+10^(y-8)+10^-(y+15))+
10^-((x-30)^2+10^(y-8)+10^-(y+15))+10^-((x-40)^2+10^(y-8)+10^-(y+15))+
10^-((x-42)^2+10^(y-28)+10^-(y-15))+10^-((x-36)^2+10^(y-18)+10^-(y+10))+
10^-((x-45)^2+10^-(y+15)+10^(y-33))+10^-((y-33)^2+10^(x-46)+10^-(x-21))+
10^-(y+15)^2+10^(x-46)+10^-(x-21))=0.6,{x,-7,48},{y,-16,38},PlotPoints->100]

```

Fig. 9.3.2: `ImplicitPlot[Cos[Pi x] Cos[Pi (.5 x+.866 y)] Cos[Pi (-.5 x+.866 y)]+Cos[2 Pi x] Cos[2 Pi (.5 x+.866 y)] Cos[2 Pi (-.5 x+.866 y)]=.7,{x,-4,4},{y,-4,4},PlotPoints->200]`

```

Fig. 9.3.3: ImplicitPlot[.00012(E^(y Sin[Pi/3]+x Cos[Pi/3])+E^(y Sin[Pi 2/3]+
x Cos[Pi 2/3])+E^(y Sin[Pi 3/3]+x Cos[Pi 3/3])+E^-(y Sin[Pi/3]+x Cos[Pi/3])+
E^-(y Sin[Pi 2/3]+x Cos[Pi 2/3])+E^-(y Sin[Pi 3/3]+x Cos[Pi 3/3]))+
E^-(Cos[Pi x] Cos[Pi (.5 x+.866 y)] Cos[Pi (-.5 x+.866 y)] +Cos[2 Pi x]
Cos[2 Pi (.5 x+.866 y)] Cos[2 Pi (-.5 x+.866 y)])=.5,{x,-9,9},{y,-9,9},PlotPoints->300]

```

Fig. 9.3.4: `ContourPlot3D[Cos[Pi x] Cos[Pi (.5 x+.866 y)] Cos[Pi (-.5 x+.866 y)] + Cos[2 Pi x] Cos[2 Pi (.5 x+.866 y)] Cos[2 Pi (-.5 x+.866 y)]-.7,{x,1,-1},{y,1,-1},{z,6,-6}, MaxRecursion->2,PlotPoints->{{3,5},{3,5},{4,4}},Boxed->False,Axes->True]`

Fig. 9.3.5: `ContourPlot3D[Cos[Pi x] Cos[Pi (.5 x+.866 y)] Cos[Pi (-.5 x+.866 y)] + Cos[2 Pi x] Cos[2 Pi (.5 x+.866 y)] Cos[2 Pi (-.5 x+.866 y)]+.075 Cos[4 Pi z]-.5,{x,-6,-6},{y,-6,-6},{z,-6,-6},MaxRecursion->2,PlotPoints->{{5,4},{5,4},{5,3}},Boxed->False,Axes->True]`

Fig. 9.3.6: `Show[%,ViewPoint->{-0.000,-0.000,3.384}]`

```

Fig. 9.3.7: ImplicitPlot[10^-((x-4)^2+10^(y-22)+10^-(y+4))+10^-((x)^2+10^(y-22)+
10^-(y+4))+10^-((x-8)^2+10^(y-22)+10^-(y+4)) +.15 10^-((x-2)^2+10^-(y-15)) +
.15 10^-((x-6)^2+10^-(y-15)) +.15 10^-((x+2)^2+10^-(y-15)) +.15 10^-((x-10)^2+
10^-(y-15)) +.15 10^-((x-2)^2+10^(y-3))+.15 10^-((x-6)^2+10^(y-3))+.15 10^-((x+2)^2+
10^(y-3))+.15 10^-((x-10)^2+10^(y-3))+.2 10^-((y-38)^2+10^(x-11)+10^-(x+2))+
.2 10^-(y+19)^2+10^(x-11)+10^-(x+2))=0.1,{x,-10,12},{y,-22,41},PlotPoints->200]

```

```

Fig. 9.3.8: ImplicitPlot[10^-((x-4)^2+10^(y-22)+10^-(y+4))+10^-((x)^2+10^(y-22)+
10^-(y+4))+10^-((x-8)^2+10^(y-22)+10^-(y+4)) +.15 10^-((x-2)^2+10^-(y-10)) +
.15 10^-((x-6)^2+10^-(y-10)) +.15 10^-((x+2)^2+10^-(y-10)) +.15 10^-((x-10)^2+
10^-(y-10)) +.15 10^-((x-2)^2+10^(y-8))+.15 10^-((x-6)^2+10^(y-8))+.15 10^-((x+2)^2+
10^(y-8))+.15 10^-((x-10)^2+10^(y-8))+.2 10^-((y-33)^2+10^(x-11)+10^-(x+2))+
.2 10^-(y+15)^2+10^(x-11)+10^-(x+2))=0.1,{x,-10,12},{y,-22,41},PlotPoints->200]

```

Fig. 9.4.1 a: `ContourPlot3D[E^-(E^((x^2+y^2))+ E^(y Cos[Pi(z)]+x Sin[Pi(z)]))-1.25]+ E^-(E^(((x)^2+(y)^2))+ E^(y Cos[Pi(z)]+(x) Sin[Pi(z)]))-1.25]-.125,{x,1.5,-1},{y,1.5,-1},{z,2,-4},MaxRecursion->2,PlotPoints->{{4,4},{4,4},{5,4}},Boxed->False,Axes->True]`

Fig. 9.4.1 b: `ContourPlot3D[E^-(E^((x^2+y^2))+ E^(y Cos[Pi(z)]+x Sin[Pi(z)]))-1.25]+ E^-(E^(((x-1)^2+(y-1)^2))+ E^(y-1) Cos[Pi(z)]+(x-1) Sin[Pi(z)]))-1.25]-.125,{x,1.8,-.8},{y,1.8,-.8},{z,2,-4},MaxRecursion->2,PlotPoints->{{5,4},{5,4},{6,4}},Boxed->False,Axes->True]`

Fig. 9.4.1 c: `ContourPlot3D[E^-(E^((x^2+y^2))+ E^(y Cos[Pi(z)]+x Sin[Pi(z)]))-1.25]+`

```
E^-(E^(((x-1.1)^2+(y-1.1)^2))+ E^((y-1.1) Cos[ Pi( z)]+(x-1.1) Sin[ Pi( z)])-.125)-.125,
{x,1.9,-.8},{y,1.9,-.8},{z,2,-4},MaxRecursion->2,PlotPoints->{{5,4},{5,4},{6,4}},Boxed->
False,Axes->True] Show[%, ViewPoint->{2.371, -2.414, 0.042}]
```

Fig. 9.4.1 d: ContourPlot3D[E^-(E^(x^2+y^2))+E^(y Cos[Pi(z)]+x Sin[Pi(z)])-.125)+ E^-(E^(((x-1.25)^2+(y-1.25)^2))+ E^((y-1.25) Cos[Pi(z)]+(x-1.25) Sin[Pi(z)])-.125)-.125, {x,2.5,-1},{y,2.5,-1},{z,2,-4},MaxRecursion->2,PlotPoints->{{5,4},{5,4},{6,4}},Boxed->False,Axes->True]

Fig. 9.4.2 a: ContourPlot3D[E^-(E^(x^2+y^2))+ E^(y Cos[Pi(z)]+x Sin[Pi(z)])-.125)+ E^-(E^(((x-1.5)^2+(y-1.5)^2))+ E^((y-1.5) Cos[Pi(z+1)]+(x-1.5) Sin[Pi(z+1)])-.125)-.125, {x,2.5,-1},{y,2.5,-1},{z,2,-4},MaxRecursion->2,PlotPoints->{{5,4},{5,4},{5,4}},Boxed->False,Axes->True]

Fig. 9.4.2 b: ContourPlot3D[E^-(E^(x^2+y^2))+ E^(y Cos[Pi(z)]+x Sin[Pi(z)])-.125)+ E^-(E^(((x-1.25)^2+(y-1.25)^2))+ E^((y-1.25) Cos[Pi(z+1)]+(x-1.25) Sin[Pi(z+1)])-.125)-.125, {x,2.1,-1},{y,2.1,-1},{z,2,-4},MaxRecursion->2,PlotPoints->{{5,4},{5,4},{6,4}},Boxed->False,Axes->True]

Fig. 9.4.2 c: ContourPlot3D[E^-(E^(x^2+y^2))+ E^(y Cos[Pi(z)]+x Sin[Pi(z)])-.125)+E^-(E^(((x-1)^2+(y-1)^2))+ E^((y-1) Cos[Pi(z+1)]+(x-1) Sin[Pi(z+1)])-.125)-.125, {x,1.9,-1},{y,1.9,-1},{z,2,-4},MaxRecursion->2,PlotPoints->{{5,4},{5,4},{6,4}},Boxed->False,Axes->True]

Fig. 9.4.2 d: ContourPlot3D[E^-(E^(x^2+y^2))+ E^(y Cos[Pi(z)]+x Sin[Pi(z)])-.125)+ E^-(E^(((x-.8)^2+(y-.8)^2))+ E^((y-.8) Cos[Pi(z+1)]+(x-.8) Sin[Pi(z+1)])-.125)-.125, {x,1.7,-.7},{y,1.7,-.7},{z,2,-4},MaxRecursion->2,PlotPoints->{{5,4},{5,4},{6,4}},Boxed->False,Axes->True]

Fig. 9.4.3 a: ContourPlot3D[E^-(.2E^(x^2+(y-3)^2))+2 x (y-3) Cos[Pi z]-(x^2-(y-3)^2) Sin[Pi z]) +E^-(.2E^(((z)^2+(y)^2))+2 (z) (y) Cos[Pi (x)]+(z)^2-(y)^2)Sin[Pi (x)]-1, {x,2,-2}, {y,4.5,-1.7},{z,2,-2},MaxRecursion->2,PlotPoints->{{7,4},{7,4},{7,4}},Boxed->False, Axes->True]

Fig. 9.4.3 b: Show[%,ViewPoint->{0.000,-0.000,3.384}]

Fig. 9.4.4 a: ContourPlot3D[E^-(.2E^(x^2+(y-1.5)^2))+2 x (y-1.5) Cos[Pi z]-(x^2-(y-1.5)^2)Sin[Pi z])+E^-(.2E^(((z)^2+(y)^2))+2 (z) (y) Cos[Pi (x)]+(z)^2-(y)^2)Sin[Pi (x)]-1, {x,4.5,-4.5},{y,3,-2},{z,4.5,-4.5},MaxRecursion->2,PlotPoints->{{4,5},{4,5},{4,5}},Boxed->False,Axes->True] Show[%, ViewPoint->{-0.061, 3.383, 0.042}]

Fig. 9.4.4 b: Show[%, ViewPoint->{0.000, -0.000, 3.384}]

Chapter 10

Fig. 10.1.1: ImplicitPlot[E^-(x^2)+E^-(x-8)^2-y==0,{x,2,-2},{y,2.2,2},PlotPoints->200,Axes->True]

Fig. 10.1.2: ImplicitPlot[E^-(x^2)+2E^-(x-3)^2-y==0, {x,10,-3},{y,3,-2},PlotPoints->200,Axes->True]

Fig. 10.1.3: ImplicitPlot[E^-(x^2)+E^-(x-2.5)^2-y==0, {x,6,-4},{y,1.2,-1.2},PlotPoints->200,Axes->True]

Fig. 10.1.4 a: ContourPlot3D[E^{-(x)²+(z)²+(y)²}+E^{-((x)²+(z)²+(y)²)-.25},{x,2,-2},{y,2,-2},{z,2,-2},MaxRecursion->2,PlotPoints->{{5,3},{5,3},{5,3}},Boxed->False,Axes->True]

Fig. 10.2.1: ContourPlot3D[E^{-((x-1)²+(y-1)²+(z)²}+E^{-((x+1)²+(y+1)²+(z)²}+E^{-((x-1)²+(y+1)²+(z-2)²}+E^{-((x+1)²+(y-1)²+(z-2)²}+E^{-((x-1)²+(y-1)²+(z-4)²}+E^{-((x+1)²+(y+1)²+(z-4)²}+E^{-((x-1)²+(y+1)²+(z-6)²}+E^{-((x+1)²+(y-1)²+(z-6)²}+E^{-((x-1)²+(y-1)²+(z-8)²}+E^{-((x+1)²+(y+1)²+(z-8)²}+E^{-((x+1)²+(y-1)²+(z-10.5)²}+E^{-((x+1)²+(y+1)²+(z-12.5)²}-0.25,{x,2.7,-2.3},{y,2.3,-2.3},{z,14,-1.5},MaxRecursion->2,PlotPoints->{{5,4},{5,4},{7,4}},Boxed->False,Axes->True]

Fig. 10.2.2: ContourPlot3D[E[^](Cos[.5 Pi x]+Cos[.5 Pi (z+2)])+E[^](Cos[.5 Pi z]+Cos[.5 Pi (y+2)])+E[^](Cos[.5 Pi y]+Cos[.5 Pi (x+2)])-6,{x,3,-3},{y,3,-3},{z,3,-3},MaxRecursion->2,PlotPoints->{{5,4},{5,4},{5,4}},Boxed->False,Axes->True,AxesLabel->{x,y,z}]

Fig. 10.2.3: ContourPlot3D[E^{-((x)²+(y+2)²)²}+E^{-(y²+(z+2)²)²}+E^{-(z²+(x+2)²)²}+E^{-((x)²+(y-2)²)²}+E^{-(y²+(z-2)²)²}+E^{-(z²+(x-2)²)²}-0.65,{x,3,-3},{y,3,-3},{z,3,-3},MaxRecursion->2,PlotPoints->{{5,3},{5,3},{5,3}},Boxed->False,Axes->True]

Fig. 10.2.4: ContourPlot3D[E[^](Cos[.5 Pi (x-y)]+Cos[.5 Pi ((y+z)]+Cos[.5 Pi ((x+z)]))+E[^](Cos[.5 Pi (x+y+2)]+Cos[.5 Pi ((y-z)]+Cos[.5 Pi ((x+z+2)]))+E[^](Cos[.5 Pi (x-y)]+Cos[.5 Pi ((y+z+2)]+Cos[.5 Pi ((x-z-2)]))+E[^](Cos[.5 Pi (x-y+2)]+Cos[.5 Pi ((y-z-2)]+Cos[.5 Pi ((x-z)]))-15,{x,2.7,-2.7},{y,2.7,-2.7},{z,2.7,-2.7},MaxRecursion->2,PlotPoints->{{6,4},{6,4},{6,4}},Boxed->False,Axes->True]

Fig. 10.2.5: ContourPlot3D[E^{-(((x-y)²)+((y+z)²)+((x+z)²)}+E^{-(((x+y)²)+((y+z+4)²)+((x-z-4)²)}+E^{-(((x-y+4)²)+((y-z-4)²)+((x-z)²)}+E^{-(((x+y-4)²)+((y-z)²)+((x+z-4)²)}-95,{x,4,-4},{y,4,-4},{z,4,-4},MaxRecursion->2,PlotPoints->{{7,5},{7,5},{7,5}},Boxed->False,Axes->True]

Fig. 10.2.6: ContourPlot3D[E^{-(10(y²+(z)²)+E^{^(x-6)}+E^{-(x+6)})-.5},{x,6,-6},{y,3,-3},{z,3,-3},MaxRecursion->2,PlotPoints->{{5,3},{5,3},{5,3}},Boxed->False,Axes->True]

Fig. 10.2.7: ContourPlot3D[E^{-(100(y²+(z)²)+E^{^(x-10)}+E^{-(x+10)})-.5},{x,10,-10},{y,1,-1},{z,1,-1},MaxRecursion->2,PlotPoints->{{5,4},{5,4},{5,4}},Boxed->False,Axes->False]

Fig. 10.2.8: ContourPlot3D[E^{-(100(y²+(z)²)+E^{^(x-10)}+E^{-(x+10)})-.5},{x,10,-10},{y,1,-1},{z,1,-1},MaxRecursion->2,PlotPoints->{{5,4},{5,4},{5,4}},Boxed->False,Axes->True]

Fig. 10.2.9: ContourPlot3D[E^{-(100(y²+(z)²)+E^{^(x-8)}+E^{-(x+14)})-.5},{x,8,-14},{y,1,-1},{z,1,-1},MaxRecursion->2,PlotPoints->{{5,4},{5,4},{5,4}},Boxed->False,Axes->True]

Fig. 10.2.10: ContourPlot3D[E^{-(100(y²+(z)²)+E^{^(x-15)}+E^{-(x+15)})-.5},{x,15,-15},{y,1,-1},{z,1,-1},MaxRecursion->2,PlotPoints->{{5,4},{5,4},{5,4}},Boxed->False,Axes->True]

Fig. 10.2.11: ContourPlot3D[E^{-(100(y²+(z)²)+E^{^(x-15)}+E^{-(x+15)})-.5},{x,15,-15},{y,1,-1},{z,1,-1},MaxRecursion->2,PlotPoints->{{5,4},{5,4},{5,4}},Boxed->False,Axes->True]

Boxed->False, Axes->False]

Fig. 10.2.12: ContourPlot3D[E^{-(5 (x²+(y+2)²))+E^{-(5 (x²+(y-3)²))+E^{-(5 ((x-.5)²+(z)²))+E^{-(z-12))+E^{-(z+12)}-.5,{x,3,-3},{y,5,-4},{z,12.5,-12.5}, MaxRecursion->2, PlotPoints->{{5,4},{5,4},{5,4}}, Boxed->False, Axes->True]}}}}

Fig. 10.3.1: ImplicitPlot[E^{(y Sin[Pi/9]+x Cos[Pi/9])³+E^{(-y Sin[Pi 2/9]-x Cos[Pi 2/9])³+E^{(y Sin[Pi 3/9]+x Cos[Pi 3/9])³+E^{(-y Sin[Pi 4/9]-x Cos[Pi 4/9])³+E^{(y Sin[Pi 5/9]+x Cos[Pi 5/9])³+E^{(-y Sin[Pi 6/9]-x Cos[Pi 6/9])³+E^{(y Sin[Pi 7/9]+x Cos[Pi 7/9])³+E^{(-y Sin[Pi 8/9]-x Cos[Pi 8/9])³+E^{(y Sin[Pi 9/9]+x Cos[Pi 9/9])³=20000000,{x,-4,2.9},{y,-4,2.7}, PlotPoints->200]}}}}}}}}}

Fig. 10.3.2: ImplicitPlot[Sin[Pi x]- Sin[Pi (x Cos[Pi/5] + y Sin[Pi/5])] + Sin[Pi (x Cos[2 Pi/5] + y Sin[2 Pi/5])]-Sin[Pi (x Cos[3 Pi/5] + y Sin[3 Pi/5])] + Sin[Pi (x Cos[4 Pi/5] + y Sin[4 Pi/5])]=2,{x,-10,10},{y,-10,10}, PlotPoints->200]

Fig. 10.3.3: ImplicitPlot[(Sin[Pi x] -Sin[Pi (x Cos[Pi/9] + y Sin[Pi/9])] + Sin[Pi (x Cos[2 Pi/9] + y Sin[2 Pi/9])]-Sin[Pi (x Cos[3 Pi/9] + y Sin[3 Pi/9])]+ Sin[Pi (x Cos[4 Pi/9] + y Sin[4 Pi/9])]-Sin[Pi (x Cos[5 Pi/9] + y Sin[5Pi/9])] + Sin[Pi (x Cos[6 Pi/9] + y Sin[6Pi/9])] -Sin[Pi (x Cos[7 Pi/9] + y Sin[7Pi/9])]+ Sin[Pi (x Cos[8 Pi/9] + y Sin[8Pi/9])])=3,{x,-10,10},{y,-10,10}, PlotPoints->100]

Fig. 10.3.4: ImplicitPlot[E^{-(.25((x)²+y²))((Sin[Pi x] -Sin[Pi (x Cos[Pi/9] + y Sin[Pi/9])] +Sin[Pi (x Cos[2 Pi/9] + y Sin[2 Pi/9])]-Sin[Pi (x Cos[3 Pi/9] + y Sin[3 Pi/9])]+Sin[Pi (x Cos[4 Pi/9] + y Sin[4 Pi/9])]-Sin[Pi (x Cos[5 Pi/9] + y Sin[5Pi/9])] +Sin[Pi (x Cos[6 Pi/9] + y Sin[6Pi/9])] -Sin[Pi (x Cos[7 Pi/9] + y Sin[7Pi/9])]+Sin[Pi (x Cos[8 Pi/9] + y Sin[8Pi/9])])-.5)² ==1,{x,-6,6},{y,-6,6}, PlotPoints->100]}

Fig. 10.3.5: ImplicitPlot[E^{-(.25((x)²+y²))((Sin[Pi x] -Sin[Pi (x Cos[Pi/9] + y Sin[Pi/9])] +Sin[Pi (x Cos[2 Pi/9] + y Sin[2 Pi/9])]- Sin[Pi (x Cos[3 Pi/9] + y Sin[3 Pi/9])]+Sin[Pi (x Cos[4 Pi/9] + y Sin[4 Pi/9])]-Sin[Pi (x Cos[5 Pi/9] + y Sin[5Pi/9])] +Sin[Pi (x Cos[6 Pi/9] + y Sin[6Pi/9])] -Sin[Pi (x Cos[7 Pi/9] + y Sin[7Pi/9])]+Sin[Pi (x Cos[8 Pi/9] + y Sin[8Pi/9])])-.5)² ==.175,{x,-6,6},{y,-6,6}, PlotPoints->100]}

Fig. 10.3.6: ImplicitPlot[E^{-(.1(x²+y²))((Sin[Pi x] -Sin[Pi (x Cos[Pi/9] + y Sin[Pi/9])]+ Sin[Pi (x Cos[2 Pi/9] + y Sin[2 Pi/9])]- Sin[Pi (x Cos[3 Pi/9] + y Sin[3 Pi/9])]+ Sin[Pi (x Cos[4 Pi/9] + y Sin[4 Pi/9])]-Sin[Pi (x Cos[5 Pi/9] + y Sin[5Pi/9])]+ Sin[Pi (x Cos[6 Pi/9] + y Sin[6Pi/9])] -Sin[Pi (x Cos[7 Pi/9] + y Sin[7Pi/9])]+ Sin[Pi (x Cos[8 Pi/9] + y Sin[8Pi/9])])-.5)² +.1E^{(.1(x²+y²))}=3.2,{x,-8,8},{y,-8,8}, PlotPoints->200]}

Fig. 10.3.7: ImplicitPlot[E^{-(.1(x²+y²))((Sin[Pi x] -Sin[Pi (x Cos[Pi/9] + y Sin[Pi/9])]+ Sin[Pi (x Cos[2 Pi/9] + y Sin[2 Pi/9])]-Sin[Pi (x Cos[3 Pi/9] + y Sin[3 Pi/9])]+ Sin[Pi (x Cos[4 Pi/9] + y Sin[4 Pi/9])]-Sin[Pi (x Cos[5 Pi/9] + y Sin[5Pi/9])]+ Sin[Pi (x Cos[6 Pi/9] + y Sin[6Pi/9])]-Sin[Pi (x Cos[7 Pi/9] + y Sin[7Pi/9])]+ Sin[Pi (x Cos[8 Pi/9] + y Sin[8Pi/9])])-1)² +.1 E^{(.1(x²+y²-1))}=2,{x,-6,6},{y,-6,6}, PlotPoints->100]}

Fig. 10.3.8: ContourPlot3D[E^{-(.25((x)²+y²))((Sin[Pi x] -Sin[Pi (x Cos[Pi/9] + ySin[Pi/9])]+Sin[Pi (x Cos[2 Pi/9] + y Sin[2 Pi/9])]- Sin[Pi (x Cos[3 Pi/9] + y Sin[3 Pi/9])]+Sin[Pi (x Cos[4 Pi/9] + y Sin[4 Pi/9])]-Sin[Pi (x Cos[5 Pi/9] + y Sin[5Pi/9])] +Sin[Pi (x Cos[6 Pi/9] + y Sin[6Pi/9])] -Sin[Pi (x Cos[7 Pi/9] + y Sin[7Pi/9])]+Sin[Pi (x Cos[8 Pi/9] + y Sin[8Pi/9])])-.5)² ==1,{x,-6,6},{y,-6,6}, PlotPoints->100]}

$y \sin[7\pi/9]] + \sin[\pi (x \cos[8\pi/9] + y \sin[8\pi/9])] - .5)^2 - 1, \{x, -4.5, 4.5\}, \{y, -4.5, 4.5\},$
 $\{z, -2, 2\}, \text{MaxRecursion} \rightarrow 2, \text{PlotPoints} \rightarrow \{\{7, 4\}, \{7, 4\}, \{7, 4\}\}, \text{Boxed} \rightarrow \text{False}, \text{Axes} \rightarrow \text{True}$

Fig. 10.3.9: $\text{ImplicitPlot}[E^{-(.1(x^2+y^2))}(\sin[\pi x] - \sin[\pi (x \cos[\pi/9] + y \sin[\pi/9])] + \sin[\pi (x \cos[2\pi/9] + y \sin[2\pi/9])] - \sin[\pi (x \cos[3\pi/9] + y \sin[3\pi/9])] + \sin[\pi (x \cos[4\pi/9] + y \sin[4\pi/9])] - \sin[\pi (x \cos[5\pi/9] + y \sin[5\pi/9])] + \sin[\pi (x \cos[6\pi/9] + y \sin[6\pi/9])] - \sin[\pi (x \cos[7\pi/9] + y \sin[7\pi/9])] + \sin[\pi (x \cos[8\pi/9] + y \sin[8\pi/9])] - .5) + E^{(.1(x^2+y^2))} = 3.2, \{x, -5, 4\}, \{y, -5, 4\},$
 $\text{PlotPoints} \rightarrow 100]$

Fig. 10.3.10: $\text{ImplicitPlot}[E^{-(.1(x^2+y^2))}(\sin[\pi x] - \sin[\pi (x \cos[\pi/9] + y \sin[\pi/9])] + \sin[\pi (x \cos[2\pi/9] + y \sin[2\pi/9])] - \sin[\pi (x \cos[3\pi/9] + y \sin[3\pi/9])] + \sin[\pi (x \cos[4\pi/9] + y \sin[4\pi/9])] - \sin[\pi (x \cos[5\pi/9] + y \sin[5\pi/9])] + \sin[\pi (x \cos[6\pi/9] + y \sin[6\pi/9])] - \sin[\pi (x \cos[7\pi/9] + y \sin[7\pi/9])] + \sin[\pi (x \cos[8\pi/9] + y \sin[8\pi/9])] - .5) + E^{(.1(x^2+2y^2))} = 3.2, \{x, -5, 4\}, \{y, -4, 4\},$
 $\text{PlotPoints} \rightarrow 100]$

Fig. 10.4.1: $\text{ContourPlot3D}[\{z \cos[\pi x] - y \sin[\pi x]\}, \{x, 4.3, -1.5\}, \{y, 1.1, -1.3\},$
 $\{z, 1.2, -1.1\}, \text{MaxRecursion} \rightarrow 2, \text{PlotPoints} \rightarrow \{\{3, 5\}, \{3, 5\}, \{3, 5\}\}, \text{Boxed} \rightarrow \text{False}, \text{Axes} \rightarrow \text{True}]$

Fig. 10.4.2: $\text{ContourPlot3D}[(E^{-(.2(x)^2+y^2+z^2)}) (z \cos[\pi x] - y \sin[\pi x] - .3),$
 $\{x, 1.4, -1.4\}, \{y, 1.2, -1.2\}, \{z, 1.2, -1.2\}, \text{MaxRecursion} \rightarrow 2, \text{PlotPoints} \rightarrow \{\{6, 4\}, \{5, 4\}, \{5, 4\}\},$
 $\text{Boxed} \rightarrow \text{False}, \text{Axes} \rightarrow \text{True}]$

Fig. 10.4.3: $\text{ContourPlot3D}[E^{-(.2(x-3.5)^2+(y+.7)^2+z^2)} + E^{-(.2(x-2)^2+y^2+z^2)} - .75,$
 $\{x, 4.3, .5\}, \{y, .8, -1.3\}, \{z, 1, -1\}, \text{MaxRecursion} \rightarrow 2, \text{PlotPoints} \rightarrow \{\{5, 3\}, \{5, 3\}, \{5, 3\}\},$
 $\text{Boxed} \rightarrow \text{False}, \text{Axes} \rightarrow \text{True}]$

Fig. 10.4.4: $\text{ContourPlot3D}[E^{-(.2(x)^2+y^2+z^2)} (z \cos[\pi x] - y \sin[\pi x] - .3) + .4 E^{-(.2(x-3.5)^2+(y)^2+z^2)} + .4 E^{-(.2(x-2)^2+y^2+z^2)} - 1, \{x, 4.3, -1.5\}, \{y, 1.1, -1.3\},$
 $\{z, 1.2, -1.1\}, \text{MaxRecursion} \rightarrow 2, \text{PlotPoints} \rightarrow \{\{7, 4\}, \{5, 4\}, \{5, 4\}\}, \text{Boxed} \rightarrow \text{False}, \text{Axes} \rightarrow \text{True}]$
 $\text{Show}[\%, \text{ViewPoint} \rightarrow \{0.000, -0.000, 3.384\}]$

Fig. 10.4.5: $\text{ContourPlot3D}[E^{-(.2(x)^2+y^2+z^2)} (z \cos[\pi x] - y \sin[\pi x] - .3) + .4 E^{-(.2(x-3.5)^2+(y+.35)^2+z^2)} + .4 E^{-(.2(x-2)^2+y^2+z^2)} - 1, \{x, 4.3, -1.5\}, \{y, 1.1, -1.3\},$
 $\{z, 1.2, -1.1\}, \text{MaxRecursion} \rightarrow 2, \text{PlotPoints} \rightarrow \{\{7, 4\}, \{5, 4\}, \{5, 4\}\}, \text{Boxed} \rightarrow \text{False}, \text{Axes} \rightarrow \text{True}]$
 $\text{Show}[\%, \text{ViewPoint} \rightarrow \{0.000, -0.000, 3.384\}]$

Fig. 10.4.6: $\text{ContourPlot3D}[E^{-(.2(x)^2+y^2+z^2)} (z \cos[\pi x] - y \sin[\pi x] - .3) + .4 E^{-(.2(x-3.5)^2+(y+.7)^2+z^2)} + .4 E^{-(.2(x-2)^2+y^2+z^2)} - 1, \{x, 4.3, -1.5\}, \{y, 1.1, -1.4\},$
 $\{z, 1.2, -1.1\}, \text{MaxRecursion} \rightarrow 2, \text{PlotPoints} \rightarrow \{\{7, 4\}, \{5, 4\}, \{5, 4\}\}, \text{Boxed} \rightarrow \text{False}, \text{Axes} \rightarrow \text{True}]$
 $\text{Show}[\%, \text{ViewPoint} \rightarrow \{0.000, -0.000, 3.384\}]$

Fig. 10.5.1: $\text{ImplicitPlot}[y - x + .5 = 0, \{x, 4, -4\}, \{y, 4, 0\}, \text{PlotPoints} \rightarrow 100]$

Fig. 10.5.2: $\text{ImplicitPlot}[y + E^{-.15x^2}(x-.5) = 0, \{x, 7, -7\}, \{y, 2, -2\}, \text{PlotPoints} \rightarrow 100]$

Fig. 10.5.3: $\text{ImplicitPlot}[(E^{-(.15(x)^2)}(x-.5) - y)^2 - .01 = 0, \{x, 8, -8\}, \{y, 2, -2\},$
 $\text{PlotPoints} \rightarrow 100]$

Fig. 10.5.4: $\text{ImplicitPlot}[(E^{-(.15(x)^2)}(x-.5)(x-1) - 2y)^2 - .03 = 0,$
 $\{x, 8, -8\}, \{y, 4, -1\}, \text{PlotPoints} \rightarrow 200]$

Fig. 10.5.5: $\text{ImplicitPlot}[E^{-(.15(x)^2)}(x-.5) + y^2 - .01 - E^{-(x+5)^2+(y-1)^2} - 1 + E^{-(x+10) + E^{-(x-10)} = 0, \{x, 8, -8\}, \{y, 2, -2\}, \text{PlotPoints} \rightarrow 100]$

Fig. 10.5.6: `ImplicitPlot[E^((E^(-.15(x)^2)(x-.5)(x-1)-2y)^2-.02)-E^-((x+6)^2+(y)^2)-1+E^-(x+10)+E^(x-10)=0,{x,8,-10},{y,3,-2},PlotPoints->200]`

Fig. 10.5.7: `ImplicitPlot[E^((-E^(-.15(x)^2)Cos[.25Pi x]-y)^2-.01)-E^-((x+4)^2+(y-1)^2)-1+E^-(x+10)+E^(x-10)=0,{x,6,-12},{y,2,-2},PlotPoints->100]`

Fig. 10.5.8: `ImplicitPlot[E^((-E^(-.15(x)^2)Cos[.5Pi x]-y)^2-.01)-E^-((x+4)^2+(y-1)^2)-1+E^-(x+10)+E^(x-10)=0,{x,8,-8},{y,2,-2},PlotPoints->150]`

Fig. 10.5.9: `ImplicitPlot[E^((-E^(-.15(x)^2)Cos[.75Pi x]-y)^2-.01)-E^-((x+4)^2+(y-1)^2)-1+E^-(x+10)+E^(x-10)=0,{x,7,-7},{y,2,-2},PlotPoints->150]`

Fig. 10.5.10: `ImplicitPlot[E^((-E^(-.15(x)^2)Cos[.25Pi x]-y)^2-.01)-E^-((x+4)^2+(y-1)^2)-1+E^-(x+10)+E^(x-10)=0,{x,6,-12},{y,2,-2},PlotPoints->100]`

Fig. 10.5.12: `In[37]:=ImplicitPlot[E^-(x^2+E^(y-2)+E^-(y))+.2 E^-((x+y-3)^2+E^(x)+E^-(x+5))+.2 E^-((-x+y-3)^2+E^(x-5)+E^-(x))-1=0,{x,6,-6},{y,8,-2},PlotPoints->100]`

Fig. 10.5.13: `ImplicitPlot[E^((E^(-.15(x)^2)Cos[.25 Pi x]+y)^2-.01)-E^-((x+4)^2+(y-1)^2)-1+E^-(x+10)+E^(x-10)=0,{x,8,-8},{y,2,-2},PlotPoints->100]`

Fig. 10.5.14: `ImplicitPlot[E^((E^(-.15(y)^2)Cos[.25 Pi y]+x)^2-.01)-E^-((y+4)^2+(x-1)^2)-1+E^-(y+10)+E^(y-10)=0,{x,2,-2},{y,8,-8},PlotPoints->100]`

Fig. 10.5.15: `ImplicitPlot[E^-(E^((E^(-.15(y)^2)Cos[.5 Pi y]+x)^2-.01)-E^-((y+4)^2+(x-1)^2)-1+E^-(y+3)+E^(y-8))+E^-(E^((E^(-.15(x)^2)Cos[.5 Pi x]+y)^2-.01)-E^-((x+4)^2+(y-1)^2)-1+E^-(x+3)+E^(x-8))-1=0,{x,10,-5},{y,10,-5},PlotPoints->100]`

Chapter 10

Fig. 10.1.1: `ImplicitPlot[E^-((x)^2)+E^-((x-8)^2)-y=0,{x,2,-2},{y,2.2,-2},PlotPoints->200,Axes->True]`

Fig. 10.1.2: `ImplicitPlot[E^-((x)^2)+2E^-((x-3)^2)-y=0,{x,10,-3},{y,3,-2},PlotPoints->200,Axes->True]`

Fig. 10.1.3: `ImplicitPlot[E^-((x)^2)+E^-((x-2.5)^2)-y=0,{x,6,-4},{y,1.2,-1.2},PlotPoints->200,Axes->True]`

Fig. 10.1.4 a: `ContourPlot3D[E^-((x)^2+(z)^2+(y)^2)+E^-((x)^2+(z)^2+(y)^2)-.25,{x,2,-2},{y,2,-2},{z,2,-2},MaxRecursion->2,PlotPoints->{{5,3},{5,3},{5,3}},Boxed->False,Axes->True]`

Fig. 10.2.1: `ContourPlot3D[E^-((x-1)^2+(y-1)^2+(z)^2)+E^-((x+1)^2+(y+1)^2+(z)^2)+E^-((x-1)^2+(y+1)^2+(z-2)^2)+E^-((x+1)^2+(y-1)^2+(z-2)^2)+E^-((x-1)^2+(y-1)^2+(z-4)^2)+E^-((x+1)^2+(y+1)^2+(z-4)^2)+E^-((x-1)^2+(y+1)^2+(z-6)^2)+E^-((x+1)^2+(y-1)^2+(z-6)^2)+E^-((x-1)^2+(y-1)^2+(z-8)^2)+E^-((x+1)^2+(y+1)^2+(z-8)^2)+E^-((x+1)^2+(y-1)^2+(z-10.5)^2)+E^-((x+1)^2+(y+1)^2+(z-12.5)^2)-.25,{x,2.7,-2.3},{y,2.3,-2.3},{z,14,-1.5},MaxRecursion->2,PlotPoints->{{5,4},{5,4},{7,4}},Boxed->False,Axes->True]`

Fig. 10.2.2: ContourPlot3D[E^(Cos[.5 Pi x]+Cos[.5 Pi (z+2)])+E^(Cos[.5 Pi z]+Cos[.5 Pi (y+2)])+E^(Cos[.5 Pi y]+Cos[.5 Pi (x+2)])-6,{x,3,-3},{y,3,-3},{z,3,-3},MaxRecursion->2,PlotPoints->{{5,4},{5,4},{5,4}},Boxed->False,Axes->True,AxesLabel->{x,y,z}]

Fig. 10.2.3: ContourPlot3D[E^-((x)^2+(y+2)^2)^2+ E^-(y^2+(z+2)^2)^2+E^-(z^2+(x+2)^2)^2+E^-((x)^2+(y-2)^2)^2+ E^-(y^2+(z-2)^2)^2+E^-(z^2+(x-2)^2)^2-.65,{x,3,-3},{y,3,-3},{z,3,-3},MaxRecursion->2,PlotPoints->{{5,3},{5,3},{5,3}},Boxed->False,Axes->True]

Fig. 10.2.4: ContourPlot3D[E^(Cos[.5 Pi (x-y)]+Cos[.5 Pi ((y+z)]+Cos[.5 Pi ((x+z)]))+E^(Cos[.5 Pi (x+y+2)]+Cos[.5 Pi ((y-z)]+Cos[.5 Pi ((x+z+2)]))+E^(Cos[.5 Pi (x+y)]+Cos[.5 Pi ((y+z+2)]+Cos[.5 Pi ((x-z-2)]))+E^(Cos[.5 Pi (x-y+2)]+Cos[.5 Pi ((y-z-2)]+Cos[.5 Pi ((x-z)]))-15,{x,2.7,-2.7},{y,2.7,-2.7},{z,2.7,-2.7},MaxRecursion->2,PlotPoints->{{6,4},{6,4},{6,4}},Boxed->False,Axes->True]

Fig. 10.2.5: ContourPlot3D[E^-(((x-y)^2)+((y+z)^2)+((x+z)^2))+E^-(((x+y)^2)+((y+z+4)^2)+((x-z-4)^2))+E^-(((x-y+4)^2)+((y-z-4)^2)+((x-z)^2))+E^-(((x+y-4)^2)+((y-z)^2)+((x+z-4)^2))+.95,{x,4,-4},{y,4,-4},{z,4,-4},MaxRecursion->2,PlotPoints->{{7,5},{7,5},{7,5}},Boxed->False,Axes->True]

Fig. 10.2.6: ContourPlot3D[E^-(10(y^2+(z)^2)+E^(x-6)+ E^-(x+6))-5,{x,6,-6},{y,3,-3},{z,3,-3},MaxRecursion->2,PlotPoints->{{5,3},{5,3},{5,3}},Boxed->False,Axes->True]

Fig. 10.2.7: ContourPlot3D[E^-(100(y^2+(z)^2)+E^(x-10)+E^-(x+10))-5,{x,10,-10},{y,1,-1},{z,1,-1},MaxRecursion->2,PlotPoints->{{5,4},{5,4},{5,4}},Boxed->False,Axes->False]

Fig. 10.2.8: ContourPlot3D[E^-(100(y^2+(z)^2)+E^(x-10)+ E^-(x+10))-5,{x,10,-10},{y,1,-1},{z,1,-1},MaxRecursion->2,PlotPoints->{{5,4},{5,4},{5,4}},Boxed->False,Axes->True]

Fig. 10.2.9: ContourPlot3D[E^-(100(y^2+(z)^2)+E^(x-8)+E^-(x+14))-5,{x,8,-14},{y,1,-1},{z,1,-1},MaxRecursion->2,PlotPoints->{{5,4},{5,4},{5,4}},Boxed->False,Axes->True]

Fig. 10.2.10: ContourPlot3D[E^-(100(y^2+(z)^2)+E^(x-15)+E^-(x+15))-5,{x,15,-15},{y,1,-1},{z,1,-1},MaxRecursion->2,PlotPoints->{{5,4},{5,4},{5,4}},Boxed->False,Axes->True]

Fig. 10.2.11: ContourPlot3D[E^-(100(y^2+(z)^2)+E^(x-15)+E^-(x+15))-5,{x,15,-15},{y,1,-1},{z,1,-1},MaxRecursion->2,PlotPoints->{{5,4},{5,4},{5,4}},Boxed->False,Axes->False]

Fig. 10.2.12: ContourPlot3D[E^-(5 (x^2+(y+2)^2))+E^-(5 (x^2+(y-3)^2))+E^-(5 ((x-5)^2+(z)^2))+E^(z-12)+E^-(z+12) -.5,{x,3,-3},{y,5,-4},{z,12.5,-12.5},MaxRecursion->2,PlotPoints->{{5,4},{5,4},{5,4}},Boxed->False,Axes->True]

Fig. 10.3.1: ImplicitPlot[E^(y Sin[Pi/9]+x Cos[Pi/9])^3+E^(-y Sin[Pi 2/9]-x Cos[Pi 2/9])^3+E^(y Sin[Pi 3/9]+x Cos[Pi 3/9])^3+E^(-y Sin[Pi 4/9]-x Cos[Pi 4/9])^3+E^(y Sin[Pi 5/9]+x Cos[Pi 5/9])^3+E^(-y Sin[Pi 6/9]-x Cos[Pi 6/9])^3+E^(y Sin[Pi 7/9]+x Cos[Pi 7/9])^3+E^(-y Sin[Pi 8/9]-x Cos[Pi 8/9])^3+E^(y Sin[Pi 9/9]+x Cos[Pi 9/9])^3=20000000,{x,-4,2.9},{y,-4,2.7},PlotPoints->200]

Fig. 10.3.2: ImplicitPlot[Sin[Pi x]- Sin[Pi (x Cos[Pi/5] + y Sin[Pi/5])]+ Sin[Pi (x Cos[2 Pi/5] + y Sin[2 Pi/5])]-Sin[Pi (x Cos[3 Pi/5] + y Sin[3 Pi/5])] +

$\text{Sin}[\text{Pi} (x \text{Cos}[8 \text{Pi}/9] + y \text{Sin}[8\text{Pi}/9])] - .5) + \text{E}^{.1(x^2+2y^2)} = 3.2, \{x, -5.4\}, \{y, -4.4\},$
 $\text{PlotPoints} \rightarrow 100]$

Fig. 10.4.1: $\text{ContourPlot3D}[(z \text{Cos}[\text{Pi} x] - y \text{Sin}[\text{Pi} x]), \{x, 4.3, -1.5\}, \{y, 1.1, -1.3\}, \{z, 1.2, -1.1\},$
 $\text{MaxRecursion} \rightarrow 2, \text{PlotPoints} \rightarrow \{\{3, 5\}, \{3, 5\}, \{3, 5\}\}, \text{Boxed} \rightarrow \text{False}, \text{Axes} \rightarrow \text{True}]$

Fig. 10.4.2: $\text{ContourPlot3D}[\text{E}^{-((.2(x)^2+y^2+z^2))} (z \text{Cos}[\text{Pi} x] - y \text{Sin}[\text{Pi} x]) - .3),$
 $\{x, 1.4, -1.4\}, \{y, 1.2, -1.2\}, \{z, 1.2, -1.2\}, \text{MaxRecursion} \rightarrow 2, \text{PlotPoints} \rightarrow \{\{6, 4\}, \{5, 4\}, \{5, 4\}\},$
 $\text{Boxed} \rightarrow \text{False}, \text{Axes} \rightarrow \text{True}]$

Fig. 10.4.3: $\text{ContourPlot3D}[\text{E}^{-((x-3.5)^2+(y+.7)^2+z^2)} + \text{E}^{-((x-2)^2+y^2+z^2)} - .75,$
 $\{x, 4.3, .5\}, \{y, .8, -1.3\}, \{z, 1, -1\}, \text{MaxRecursion} \rightarrow 2, \text{PlotPoints} \rightarrow \{\{5, 3\}, \{5, 3\}, \{5, 3\}\},$
 $\text{Boxed} \rightarrow \text{False}, \text{Axes} \rightarrow \text{True}]$

Fig. 10.4.4: $\text{ContourPlot3D}[\text{E}^{-((.2(x)^2+y^2+z^2))} (z \text{Cos}[\text{Pi} x] - y \text{Sin}[\text{Pi} x]) - .3) +$
 $.4 \text{E}^{-((x-3.5)^2+(y)^2+z^2)} + .4 \text{E}^{-((x-2)^2+y^2+z^2)} - 1, \{x, 4.3, -1.5\}, \{y, 1.1, -1.3\},$
 $\{z, 1.2, -1.1\}, \text{MaxRecursion} \rightarrow 2, \text{PlotPoints} \rightarrow \{\{7, 4\}, \{5, 4\}, \{5, 4\}\}, \text{Boxed} \rightarrow \text{False}, \text{Axes} \rightarrow \text{True}]$
 $\text{Show}[\%, \text{ViewPoint} \rightarrow \{0.000, -0.000, 3.384\}]$

Fig. 10.4.5: $\text{ContourPlot3D}[\text{E}^{-((.2(x)^2+y^2+z^2))} (z \text{Cos}[\text{Pi} x] - y \text{Sin}[\text{Pi} x]) - .3) + .4$
 $\text{E}^{-((x-3.5)^2+(y+.35)^2+z^2)} + .4 \text{E}^{-((x-2)^2+y^2+z^2)} - 1, \{x, 4.3, -1.5\}, \{y, 1.1, -1.3\},$
 $\{z, 1.2, -1.1\}, \text{MaxRecursion} \rightarrow 2, \text{PlotPoints} \rightarrow \{\{7, 4\}, \{5, 4\}, \{5, 4\}\}, \text{Boxed} \rightarrow \text{False}, \text{Axes} \rightarrow \text{True}]$
 $\text{Show}[\%, \text{ViewPoint} \rightarrow \{0.000, -0.000, 3.384\}]$

Fig. 10.4.6: $\text{ContourPlot3D}[\text{E}^{-((.2(x)^2+y^2+z^2))} (z \text{Cos}[\text{Pi} x] -$
 $y \text{Sin}[\text{Pi} x]) - .3) + .4 \text{E}^{-((x-3.5)^2+(y+.7)^2+z^2)} + .4 \text{E}^{-((x-2)^2+y^2+z^2)} - 1, \{x, 4.3, -1.5\},$
 $\{y, 1.1, -1.4\}, \{z, 1.2, -1.1\}, \text{MaxRecursion} \rightarrow 2, \text{PlotPoints} \rightarrow \{\{7, 4\}, \{5, 4\}, \{5, 4\}\}, \text{Boxed} \rightarrow \text{False},$
 $\text{Axes} \rightarrow \text{True}]$
 $\text{Show}[\%, \text{ViewPoint} \rightarrow \{0.000, -0.000, 3.384\}]$

Fig. 10.5.1: $\text{ImplicitPlot}[y - x + .5 = 0, \{x, 4, -4\}, \{y, 4, 0\}, \text{PlotPoints} \rightarrow 100]$

Fig. 10.5.2: $\text{ImplicitPlot}[y + \text{E}^{-.15x^2}(x-.5) = 0, \{x, 7, -7\}, \{y, 2, -2\}, \text{PlotPoints} \rightarrow 100]$

Fig. 10.5.3: $\text{ImplicitPlot}[(-\text{E}^{-.15(x)^2}(x-.5) - y)^2 - .01 = 0, \{x, 8, -8\}, \{y, 2, -2\},$
 $\text{PlotPoints} \rightarrow 100]$

Fig. 10.5.4: $\text{ImplicitPlot}[(\text{E}^{-.15(x)^2}(x-.5)(x-1) - 2y)^2 - .03 = 0, \{x, 8, -8\}, \{y, 4, -1\},$
 $\text{PlotPoints} \rightarrow 200]$

Fig. 10.5.5: $\text{ImplicitPlot}[\text{E}^{-(\text{E}^{-.15(x)^2}(x-.5) + y)^2 - .01} - \text{E}^{-((x+5)^2+(y-1)^2)} - 1 +$
 $\text{E}^{-(x+10)} + \text{E}^{(x-10)} = 0, \{x, 8, -8\}, \{y, 2, -2\}, \text{PlotPoints} \rightarrow 100]$

Fig. 10.5.6: $\text{ImplicitPlot}[\text{E}^{-(\text{E}^{-.15(x)^2}(x-.5)(x-1) - 2y)^2 - .02} - \text{E}^{-((x+6)^2+(y)^2)} - 1 +$
 $\text{E}^{-(x+10)} + \text{E}^{(x-10)} = 0, \{x, 8, -10\}, \{y, 3, -2\}, \text{PlotPoints} \rightarrow 200]$

Fig. 10.5.7: $\text{ImplicitPlot}[\text{E}^{-(\text{E}^{-.15(x)^2} \text{Cos}[.25\text{Pi} x] - y)^2 - .01} - \text{E}^{-((x+4)^2+(y-1)^2)} - 1 +$
 $\text{E}^{-(x+10)} + \text{E}^{(x-10)} = 0, \{x, 6, -12\}, \{y, 2, -2\}, \text{PlotPoints} \rightarrow 100]$

Fig. 10.5.8: $\text{ImplicitPlot}[\text{E}^{-(\text{E}^{-.15(x)^2} \text{Cos}[.5\text{Pi} x] - y)^2 - .01} - \text{E}^{-((x+4)^2+(y-1)^2)} - 1 +$
 $\text{E}^{-(x+10)} + \text{E}^{(x-10)} = 0, \{x, 8, -8\}, \{y, 2, -2\}, \text{PlotPoints} \rightarrow 150]$

Fig. 10.5.9: $\text{ImplicitPlot}[\text{E}^{-(\text{E}^{-.15(x)^2} \text{Cos}[.75\text{Pi} x] - y)^2 - .01} - \text{E}^{-((x+4)^2+(y-1)^2)} - 1 +$
 $\text{E}^{-(x+10)} + \text{E}^{(x-10)} = 0, \{x, 7, -7\}, \{y, 2, -2\}, \text{PlotPoints} \rightarrow 150]$

Fig. 10.5.10: `ImplicitPlot[E^(-(E^(-.15(x)^2)Cos[.25Pi x]-y)^2-.01)-E^-((x+4)^2+(y-1)^2)-1+E^-(x+10)+E^(x-10)==0,{x,6,-12},{y,2,-2},PlotPoints->100]`

Fig. 10.5.12: `In[37]:=ImplicitPlot[E^-(x^2+E^(y-2)+E^-(y))+.2 E^-((x+y-3)^2+E^(x)+E^-(x+5))+.2 E^-((-x+y-3)^2+E^(x-5)+E^-(x))-1==0,{x,6,-6},{y,8,-2},PlotPoints->100]`

Fig. 10.5.13: `ImplicitPlot[E^((E^(-.15(x)^2)Cos[.25 Pi x]+y)^2-.01)-E^-((x+4)^2+(y-1)^2)-1+E^-(x+10)+E^(x-10)==0,{x,8,-8},{y,2,-2},PlotPoints->100]`

Fig. 10.5.14: `ImplicitPlot[E^((E^(-.15(y)^2)Cos[.25 Pi y]+x)^2-.01)-E^-((y+4)^2+(x-1)^2)-1+E^-(y+10)+E^(y-10)==0,{x,2,-2},{y,8,-8},PlotPoints->100]`

Fig. 10.5.15: `ImplicitPlot[E^-(E^((E^(-.15(y)^2)Cos[.5 Pi y]+x)^2-.01)-E^-((y+4)^2+(x-1)^2)-1+E^-(y+3)+E^(y-8))+E^-(E^((E^(-.15(x)^2)Cos[.5 Pi x]+y)^2-.01)-E^-((x+4)^2+(y-1)^2)-1+E^-(x+3)+E^(x-8))-.97==0,{x,10,-5},{y,10,-5},PlotPoints->100]`

Chapter 11

Fig. 11.1.1: `ContourPlot3D[E^-(x^2+y^2+(z-1.7)^2)+ E^-z-1 ,{x,2,-2},{y,2,-2},{z,2.2,-1},MaxRecursion->2,PlotPoints->{{5,3},{5,3},{5,4}},Boxed->False,Axes->True]`

Fig. 11.1.2: `ContourPlot3D[E^-(x^2+y^2+(z)^2)^2+ E^-z-1 ,{x,2,-2},{y,2,-2},{z,.5,-3},MaxRecursion->2,PlotPoints->{{5,3},{5,3},{5,4}},Boxed->False,Axes->True]`

Fig. 11.1.3: `ImplicitPlot[10^-((x-2)^2+10^(y-8)+10^-(y+9))+10^-((x-7)^2+10^(y-9))+10^-(y+8)+10^-((x-11)^2+10^(y-7)+10^-(y+9))+10^-((x-17)^2+10^(y-9)+10^-(y+7))+10^-((x-3.5)^2+y^2)+10^-((x)^2+(y-2)^2)+10^-((x-5)^2+(y+3)^2)+10^-((x-8)^2+y^2)+10^-((x-9)^2+(y-2)^2)+10^-((x-12)^2+(y+3)^2)+10^-((x-13.5)^2+y^2)+10^-((x-16)^2+(y-2)^2)+10^-((x-15)^2+(y+3)^2)+10^-((x-23.5)^2+y^2)+10^-((x-19)^2+(y-2)^2)+10^-((x-20)^2+(y+3)^2)==.5,{x,-3,22},{y,10,-10},PlotPoints->200]`

Fig. 11.1.4: `ContourPlot3D[E^-(.5(x^2+y^2+30 (z)^2))+E^-(20((x+5)^2+y^2+(z-.7)^2))+E^-(20((x-1)^2+y^2+(z-.4)^2))+E^-(20((x-1)^2+(y+.5)^2+(z+.7)^2))-2,{x,2,-2},{y,2,-2},{z,1,-.9},MaxRecursion->2,PlotPoints->{{3,5},{3,5},{3,5}},Boxed->False,Axes->True]`

Fig. 11.1.5 b: `ContourPlot3D[E^-((x)^2+(y)^2+(z)^2)+E^-((x-2)^2+(y)^2+(z)^2)+E^-((x-4)^2+(y)^2+(z)^2)+E^-((x-6)^2+(y)^2+(z)^2)+E^-((x-8)^2+(y)^2+(z)^2)+E^-((x-10)^2+(y)^2+(z)^2)+E^-((x-12)^2+(y)^2+(z)^2)+E^-((x-14.3)^2+(y)^2+(z)^2))-5,{x,15.5,-1},{y,1.7,-1.7},{z,1.7,-1.7},MaxRecursion->2,PlotPoints->{{5,4},{5,3},{5,3}},Boxed->False,Axes->True]`

Fig. 11.1.6: `ImplicitPlot[.5E^-((x)^2+(y-1.6)^2-.5)^2+.5E^-((x-1.5)^2+(y)^2)+E^-((x)^2+(y+1.6)^2-.5)^2==.45,{x,3,-2},{y,2.7,-2.7},PlotPoints->100]`

Fig. 11.2.1: `ContourPlot3D[E^-((x)^2+(z)^2+(y)^2-20)+E^-((x-6)^2+(z)^2+(y)^2+2)-1,{x,7,-5},{y,5,-5},{z,.5,-.5},MaxRecursion->2,PlotPoints->{{5,4},{5,4},{5,4}},Boxed->False,Axes->True]`

Fig. 11.2.2: `ContourPlot3D[E^-((x)^2+(z)^2+(y)^2-20)+E^-((x+3)^2+(z)^2+(y)^2+2)-1,{x,6,-5},{y,5,-5},{z,.5,-.5},MaxRecursion->2,PlotPoints->{{5,4},{5,4},{5,4}},Boxed->False,Axes->True]`

Fig. 11.2.3: ContourPlot3D[(x)+(z)+(y),{x,2,-2},{y,2,-2},{z,2,-2},MaxRecursion->2,PlotPoints->{{5,3},{5,3},{5,3}},Boxed->False,Axes->True]

Fig. 11.2.4 b: ContourPlot3D[(x)^3+(z)^3+(y)^3,{x,2,-2},{y,2,-2},{z,2,-2},MaxRecursion->2,PlotPoints->{{5,3},{5,3},{5,3}},Boxed->False,Axes->True]Show[%,ViewPoint->{1.957,1.958,1.945}]

Fig. 11.2.5 b: ContourPlot3D[(x)^7+(z)^7+(y)^7,{x,2,-2},{y,2,-2},{z,2,-2},MaxRecursion->2,PlotPoints->{{5,3},{5,3},{5,3}},Boxed->False,Axes->True]Show[%,ViewPoint->{1.957,1.958,1.945}]

Fig. 11.2.6 a: ContourPlot3D[(x)-(z)+(y),{x,2,-2},{y,2,-2},{z,2,-2},MaxRecursion->2,PlotPoints->{{5,3},{5,3},{5,3}},Boxed->False,Axes->True]

Fig. 11.2.6 b: ContourPlot3D[(x)^3-(z)^3+(y)^3,{x,2,-2},{y,2,-2},{z,2,-2},MaxRecursion->2,PlotPoints->{{5,3},{5,3},{5,3}},Boxed->False,Axes->True]

Fig. 11.2.7: ContourPlot3D[z (z-1) (z+1)+ x (x-1) (x+1)+ y (y-1) (y+1),{x,-2,2.5},{y,-2,2.5},{z,-2,2.5},MaxRecursion->2,PlotPoints->{{5,3},{5,3},{5,3}},Boxed->False,Axes->True]

Fig. 11.2.8: ContourPlot3D[E^-(z (z-1) (z+1)+ x (x-1) (x+1)+ y (y-1) (y+1))-1,{x,-2,2.5},{y,-2,2.5},{z,-2,2.5},MaxRecursion->2,PlotPoints->{{5,3},{5,3},{5,3}},Boxed->False,Axes->True]

Fig. 11.2.9: ContourPlot3D[E^-(x^2+y^2+(z-1.4)^2)+E^-(x^2+y^2+(z-2.4)^2)+E^-((x-3)^2+y^2+(z-1.4)^2)+E^-((x-3)^2+y^2+(z-2)^2)+E^-((x-2)^2+(y-2.5)^2+(z-1.4)^2)+E^-((x-2)^2+(y-2.5)^2+(z-2.6)^2)+E^-((x-5)^2+(y-3.5)^2+(z-1.4)^2)+E^-((x-5)^2+(y-3.5)^2+(z-2.5)^2)+E^-((x-5.5)^2+(y-1)^2+(z-1.4)^2)+E^-((x-5.5)^2+(y-1)^2+(z-2.3)^2)+E^-z-1,{x,7,-2},{y,5,-1},{z,3,0},MaxRecursion->2,PlotPoints->{{6,4},{6,4},{6,4}},Boxed->False,Axes->True]

Fig. 11.2.10: ContourPlot3D[E^-(z (z-1) (z+1)+ x (x-1) (x+1)+ y (y-1) (y+1))+E^-(((x-1.7)^2)+((y-1.7)^2)+((z-1.7)^2)-1)+E^-(((x-3)^2)+((y-3)^2)+((z-3)^2)-1)-1,{x,-2,4.5},{y,-2,4.5},{z,-2,4.5},MaxRecursion->2,PlotPoints->{{7,4},{7,4},{7,4}},Boxed->False,Axes->True]Show[%,ViewPoint->{0.359,-0.858,3.253}]

Fig. 11.3.1: ContourPlot3D[E^-((x)^2+(z)^2+(y)^2-20)^2+E^-((x-2.5)^2+(z)^2+(y)^2+1)-2,{x,5.5,0},{y,2.5,-2.5},{z,5,-5.5},MaxRecursion->2,PlotPoints->{{5,4},{5,4},{5,4}},Boxed->False,Axes->True]

Fig. 11.3.2: ContourPlot3D[Cos[Pi x]+Cos[.25 Pi y]+Cos[.25 Pi z]+4 (x^2)-2.8,{x,2,-2},{y,10,-10},{z,10,-10},MaxRecursion->2,PlotPoints->{{3,5},{4,5},{4,5}},Boxed->False,Axes->True]

Fig. 11.3.3: ContourPlot3D[E^-(x^2+(y+2)^2+z^2)+E^-(x^2+(y-3)^2+z^2)+E^-z^2-1.5,{x,3,-3},{y,5,-4},{z,75,-75},MaxRecursion->2,PlotPoints->{{5,3},{5,3},{5,3}},Boxed->False,Axes->True]

Fig. 11.3.4: ImplicitPlot[E^((x)^2+(y)^2-8)^2+E^-((x-2.83)^2+(y)^2)+E^-((x-2)^2+(y-2)^2)+E^-((x)^2+(y-2.83)^2)+E^-((x-2)^2+(y+2)^2)=2,{x,3,-4},{y,3,-4},PlotPoints->100]

Fig. 11.3.5: ContourPlot3D[E^((x)^2+(y)^2-8+z^2)^2+E^-((x-2.8)^2+(y)^2+z^2)-1.9,{x,1,3},{y,-2,2},{z,-2,2},MaxRecursion->2,PlotPoints->{{5,4},{5,4},{5,4}},Boxed->False,Axes->True]

Fig. 11.3.6: `ImplicitPlot[E^-(((x-2.82)^2+(y-2.82)^2))+E^-(((x-4)^2+(y)^2))+E^-(((x)^2+(y-4)^2))+E^-(((x-2.82)^2+(y+2.82)^2))+E^-(((x)^2+(y+4)^2))+E^-(((x+2.82)^2+(y+2.82)^2))+E^-(((x+4)^2+(y)^2))+E^-(((x+2.82)^2+(y-2.82)^2))+E^-(((x-4.23)^2+(y-4.23)^2))+E^-(((x-6)^2+(y)^2))+E^-(((x)^2+(y-6)^2))+E^-(((x+4.23)^2+(y+4.23)^2))+E^-(((x)^2+(y+6)^2))+E^-(((x+4.23)^2+(y+4.23)^2))+E^-(((x+6)^2+(y)^2))+E^-(((x+4.23)^2+(y-4.23)^2)]=.18,{x,-8,8},{y,-8,8},PlotPoints->100]`

Fig. 11.3.7: `ImplicitPlot[E^-(((x-2.82)^2+(y-2.82)^2))+E^-(((x-4)^2+(y)^2))+E^-(((x)^2+(y-4)^2))+E^-(((x-2.82)^2+(y+2.82)^2))+E^-(((x)^2+(y+4)^2))+E^-(((x+2.82)^2+(y+2.82)^2))+E^-(((x+4)^2+(y)^2))+E^-(((x+2.82)^2+(y-2.82)^2))+E^-(((x-4.23)^2+(y-4.23)^2))+E^-(((x-6)^2+(y)^2))+E^-(((x)^2+(y-6)^2))+E^-(((x-4.23)^2+(y+4.23)^2))+E^-(((x)^2+(y+6)^2))+E^-(((x+4.23)^2+(y+4.23)^2))+E^-(((x+6)^2+(y)^2))+E^-(((x+4.23)^2+(y-4.23)^2))+.5 E^-(((x-5.11)^2+(y-2.1)^2))+.5 E^-(((x-2.1)^2+(y-5.1)^2))+.5 E^-(((x+2.11)^2+(y-5.1)^2))+.5 E^-(((x+5.1)^2+(y-2.1)^2))+.5 E^-(((x+5.11)^2+(y+2.1)^2))+.5 E^-(((x+2.11)^2+(y+5.1)^2))+.5 E^-(((x-5.11)^2+(y+2.1)^2))+.5 E^-(((x-2.11)^2+(y+5.1)^2)]=.35,{x,-8,8},{y,-8,8},PlotPoints->100]`

Fig. 11.3.8 a: `ContourPlot3D[E^-(((x-2.82)^2+(y-2.82)^2+(z)^2))+E^-(((x-4)^2+(y)^2+(z)^2))+E^-(((x)^2+(y-4)^2+(z)^2))+E^-(((x-2.82)^2+(y+2.82)^2+(z)^2))+E^-(((x)^2+(y+4)^2+(z)^2))+E^-(((x+2.82)^2+(y+2.82)^2+(z)^2))+E^-(((x+4)^2+(y)^2+(z)^2))+E^-(((x+2.82)^2+(y-2.82)^2+(z)^2))+E^-(((x-4.23)^2+(y-4.23)^2+(z)^2))+E^-(((x-6)^2+(y)^2+(z)^2))+E^-(((x)^2+(y-6)^2+(z)^2))+E^-(((x-4.23)^2+(y+4.23)^2+(z)^2))+E^-(((x)^2+(y+6)^2+(z)^2))+E^-(((x+4.23)^2+(y+4.23)^2+(z)^2))+E^-(((x+6)^2+(y)^2+(z)^2))+E^-(((x+4.23)^2+(y-4.23)^2+(z)^2))+.75(E^-(((x-5.11)^2+(y-2.1)^2+(z-1.8)^2))+E^-(((x-2.1)^2+(y-5.1)^2+(z-1.8)^2))+E^-(((x+2.11)^2+(y-5.1)^2+(z-1.8)^2))+E^-(((x+5.1)^2+(y-2.1)^2+(z-1.8)^2))+E^-(((x+5.11)^2+(y+2.1)^2+(z-1.8)^2))+E^-(((x+2.1)^2+(y+5.1)^2+(z-1.8)^2))+E^-(((x-5.11)^2+(y+2.1)^2+(z-1.8)^2))+E^-(((x-2.1)^2+(y+5.1)^2+(z-1.8)^2))+.75(E^-(((x-5.11)^2+(y-2.1)^2+(z+1.8)^2))+E^-(((x-2.1)^2+(y-5.1)^2+(z+1.8)^2))+E^-(((x+2.11)^2+(y-5.1)^2+(z+1.8)^2))+E^-(((x+5.1)^2+(y-2.1)^2+(z+1.8)^2))+E^-(((x+5.11)^2+(y+2.1)^2+(z+1.8)^2))+E^-(((x+2.1)^2+(y+5.1)^2+(z+1.8)^2))+E^-(((x-5.11)^2+(y+2.1)^2+(z+1.8)^2))+E^-(((x-2.1)^2+(y+5.1)^2+(z+1.8)^2)))-.17 ,{x,8,-8},{y,8,-8},{z,3.25,-3.25},MaxRecursion->2,PlotPoints->{{7,4},{7,4},{7,4}},Boxed->False,Axes->True]`

Fig. 11.3.8 b: `Show[%,ViewPoint->{0.000,-0.000,3.384}]`

Fig. 11.3.9: `ContourPlot3D[E^-(((x-2.82)^2+(y-2.82)^2+(z)^2))+E^-(((x-4)^2+(y)^2+(z)^2))+E^-(((x)^2+(y-4)^2+(z)^2))+E^-(((x-2.82)^2+(y+2.82)^2+(z)^2))+E^-(((x)^2+(y+4)^2+(z)^2))+E^-(((x+2.82)^2+(y+2.82)^2+(z)^2))+E^-(((x+4)^2+(y)^2+(z)^2))+E^-(((x+2.82)^2+(y-2.82)^2+(z)^2))+E^-(((x-4.23)^2+(y-4.23)^2+(z)^2))+E^-(((x-6)^2+(y)^2+(z)^2))+E^-(((x)^2+(y-6)^2+(z)^2))+E^-(((x-4.23)^2+(y+4.23)^2+(z)^2))+E^-(((x)^2+(y+6)^2+(z)^2))+E^-(((x+4.23)^2+(y+4.23)^2+(z)^2))+E^-(((x+6)^2+(y)^2+(z)^2))+E^-(((x+4.23)^2+(y-4.23)^2+(z)^2))+.75(E^-(((x-5.11)^2+(y-2.1)^2+(z-1.5)^2))+E^-(((x-2.1)^2+(y-5.1)^2+(z-1.5)^2))+E^-(((x+2.11)^2+(y-5.1)^2+(z-1.5)^2))+E^-(((x+5.1)^2+(y-2.1)^2+(z-1.5)^2))+E^-(((x+5.11)^2+(y+2.1)^2+(z-1.5)^2))+E^-(((x+2.1)^2+(y+5.1)^2+(z-1.5)^2))+E^-(((x-5.11)^2+(y+2.1)^2+(z-1.5)^2))+E^-(((x-2.1)^2+(y+5.1)^2+(z-1.5)^2))+.75(E^-(((x-5.11)^2+(y-2.1)^2+(z+1.5)^2))+E^-(((x-2.1)^2+(y-5.1)^2+(z+1.5)^2))+E^-(((x+2.11)^2+(y-5.1)^2+(z+1.5)^2))+E^-(((x+5.1)^2+(y-2.1)^2+(z+1.5)^2))+E^-(((x+5.11)^2+(y+2.1)^2+(z+1.5)^2))+E^-(((x+2.1)^2+(y+5.1)^2+(z+1.5)^2))+E^-(((x-5.11)^2+(y+2.1)^2+(z+1.5)^2))+E^-(((x-2.1)^2+(y+5.1)^2+(z+1.5)^2)))-.12 ,{x,8,-8},{y,8,-8},{z,3.3,-3.3},MaxRecursion->2,PlotPoints->{{7,4},{7,4},{7,4}},Boxed->False,Axes->True]`

Fig. 11.3.10: ContourPlot3D[E^-(E^-(x^2+(y)^2+z^2-5)+ E^(z^2)-1.5)+ 2 E^-(((x^2+y^2)^.5-1.2)^2+(z)^2+.6)+ 2 E^-(((x^2+y^2)^.5-2)^2+(z+2)^2+.5) + 2 E^-(((x^2+y^2)^.5-2)^2+(z-2)^2+.5) -1, {x,4,-4}, {y,4,0}, {z,4,4}, MaxRecursion->2,PlotPoints->{{3,5},{3,5},{3,5}},Boxed->False,Axes->True]

Fig. 11.3.11 a: ContourPlot3D[E^-(E^-(x^2+(y)^2+z^2-5)+E^(z^2)-1.5)+(E^-(x^2+ y^2+(z+3)^2-1))+E^-(x^2+ y^2+(z+1)^2-1))+2 E^-(((x^2+y^2)^.5-3)^2+(z+2.5)^2)+ 2 E^-(((x^2+y^2)^.5-3)^2+(z-2.5)^2)-1, {x,4,-4}, {y,4,-4}, {z,-5,4},MaxRecursion->2, PlotPoints->{{3,5},{3,5},{3,5}},Boxed->False,Axes->True]

Fig. 11.3.11 b:Show[%,ViewPoint->{1.359,-2.509,-1.819}]

Chapter 12

Fig. 12.1.1:ContourPlot3D[(E^((x+2.618 y)^4)+E^((-x+2.618 y)^4)+E^((y+2.618 z)^4)+ E^((-y+2.618z)^4)+E^((-2.618x+z)^4)+E^((2.618x+z)^4))+E^(1.618 (x+y+z))^4+ E^(1.618 (x-y-z))^4+E^(1.618 (-x-y+z))^4+ E^(1.618 (-x+y-z))^4-10^8, {x,.8,-.8}, {y,.8,-.8}, {z,.8,-.8},MaxRecursion->2,PlotPoints->{{4,5},{4,5},{4,5}}, Boxed->False,Axes->True]

Fig. 12.12: ContourPlot3D[E^(3.618(x^2+y^2+z^2))-E^((1.618x+y)^2)-E^((-1.618x+y)^2)- E^((1.618y+z)^2)-E^((-1.618y+z)^2)-E^((-x+1.618z)^2)-E^(x+1.618z)^2, {x,1.5,-1.5}, {y,1.5,-1.5}, {z,1.5,-1.5},MaxRecursion->2,PlotPoints->{{4,5},{4,5},{4,5}},Boxed-> False,Axes->True]

Fig. 12.1.3: ContourPlot3D[E^(7.854(x^2+y^2+z^2))-E^((-1.618x+1.618y+1.618z)^2) +E^((1.618x+1.618y-1.618z)^2)+E^((1.618x-1.618y+1.618z)^2)+ E^((1.618x+1.618y+1.618z)^2)+E^((x+2.618y)^2)+E^((-x+2.618y)^2)+E^((2.618x+z)^2)+ E^((-2.618x+z)^2)+E^((-y+2.618z)^2)+E^((y+2.618z)^2)), {x,1.6,-1.6}, {y,1.6,-1.6}, {z,1.6,-1.6},MaxRecursion->2,PlotPoints->{{5,5},{5,5},{5,5}},Boxed->False,Axes->True]

Fig. 12.1.4: Plot[x Sin [Pi (x)},{x,-8,8},PlotPoints->200,Axes->True]

Fig. 12.1.5: ContourPlot3D[z Sin[Pi z]+ x Sin[Pi x]+y Sin[Pi y] -1, {x,1.2,-1.2}, {y,1.2,-1.2}, {z,1.2,-1.2},MaxRecursion->2,PlotPoints->{{5,3},{5,3},{5,3}}, Boxed->False,Axes->True]

Fig. 12.1.6: ContourPlot3D[Sin[Pi((x+2.618 y))]/((x+2.618 y))+ Sin[Pi((-x+2.618 y))]/((-x+2.618 y))+Sin[Pi((y+2.618 z))]/((y+2.618 z))+ Sin[Pi((-y+2.618 z))]/((-y+2.618z))+Sin[Pi((z-2.618 x))]/((-2.618x+z))+ Sin[Pi((z+2.618 x))]/((2.618x+z))+Sin[Pi(1.618(x+y+z))]/(1.618 (x+y+z))+ Sin[Pi(1.618(x-y-z))]/(1.618 (x-y-z))+Sin[Pi(1.618(-x-y+z))]/(1.618 (-x-y+z))+ Sin[Pi(1.618(-x+y-z))]/(1.618 (-x+y-z)), {x,.82,-.82}, {y,.82,-.82}, {z,.82,-.82}, MaxRecursion->2,PlotPoints->{{3,5},{3,5},{3,5}},Boxed->False,Axes->True]

Fig. 12.1.7: ContourPlot3D[Sin[Pi((1.618x+y))]/ ((1.618x+y))+Sin[Pi((-1.618x+y))]/ ((-1.618x+y))+Sin[Pi((1.618y+z))]/ ((1.618y+z))+Sin[Pi((-1.618y+z))]/ ((-1.618y+z))+ Sin[Pi((x-1.618z))]/ ((x-1.618z))+Sin[Pi((x+1.618z))]/ ((x+1.618z))+2.7, {x,1.15,-1.15}, {y,1.15,-1.15}, {z,1.15,-1.15},MaxRecursion->2,PlotPoints->{{5,4},{5,4},{5,4}}, Boxed->False,Axes->True]

Fig. 12.1.8: ImplicitPlot[Cos[Pi x] Cos[Pi (.5 x+.866 y)] Cos[Pi (-.5 x+.866 y)]=-1, {x,- 2,2}, {y,-2,2},PlotPoints->100]

Fig. 12.1.9: ContourPlot3D[Sin[Pi((1.618x+y))] ((1.618x+y))+Sin[Pi((-1.618x+y))] ((-1.618x+y))+Sin[Pi((1.618y+z))] ((1.618y+z))+Sin[Pi((-1.618y+z))] ((-1.618y+z))+Sin[Pi((-x+1.618z))] ((-x+1.618z))+Sin[Pi((x+1.618z))] ((x+1.618z))+3.2,{x,1.15,-1.15},{y,1.15,-1.15},{z,1.15,-1.15},MaxRecursion->2,PlotPoints->{{5,4},{5,4},{5,4}},Boxed->False,Axes->True]

Fig. 12.1.10: ContourPlot3D[Cos[Pi((1.618x+y))] E^((1.618x+y)^2)+Cos[Pi((-1.618x+y))] E^((-1.618x+y)^2)+Cos[Pi((1.618y+z))] E^((1.618y+z)^2)+Cos[Pi((-1.618y+z))] E^(-1.618y+z)^2)+Cos[Pi((-x+1.618z))] E^(-x+1.618z)^2)+Cos[Pi((x+1.618z))] E^(x+1.618z)^2)+5.3,{x,9,-9},{y,9,-9},{z,9,-9},MaxRecursion->2,PlotPoints->{{5,4},{5,4},{5,4}},Boxed->False,Axes->True]

Fig. 12.1.11 a: ContourPlot3D[+E^-((x-2)^2+y^2+z^2)+E^-(x^2+y^2+z^2)+E^-((x-2)^2+(y-2)^2+z^2)+E^-(x^2+(y-2)^2+z^2)+E^-((x-4)^2+(y-2)^2+z^2)+E^-((x-4)^2+y^2+z^2)+E^-((x-2)^2+(y-4)^2+z^2)+E^-(x^2+(y-4)^2+z^2)+E^-((x-4)^2+(y-4)^2+z^2)-.8,{x,4.7,-.7},{y,4.7,-.7},{z,7,-.7},MaxRecursion->2,PlotPoints->{{3,5},{3,5},{5,3}},Boxed->False,Axes->True]

Fig. 12.1.11 b: ContourPlot3D[E^-((x-2)^2+y^2+10 z^2)+E^-(x^2+y^2+10 z^2)+E^-((x-2)^2+(y-2)^2+10 z^2)+E^-(x^2+(y-2)^2+10 z^2)+E^-((x-4)^2+y^2+10 z^2)+E^-((x-2)^2+(y-4)^2+10 z^2)+E^-(x^2+(y-4)^2+10 z^2)+E^-((x-4)^2+(y-4)^2+10 z^2)-.56,{x,5,-1},{y,5,-1},{z,35,-35},MaxRecursion->2,PlotPoints->{{3,5},{3,5},{5,3}},Boxed->False,Axes->True] Show[%,ViewPoint->{0.864,-2.828,-1.645}]

Fig. 12.2.1: ContourPlot3D[E^-((x)^2)+E^-((z)^2)+E^-((y)^2)-2,{x,3,-3},{y,3,-3},{z,3,-3},MaxRecursion->2,PlotPoints->{{5,5},{5,5},{5,5}},Boxed->False,Axes->True]

Fig. 12.2.2: ContourPlot3D[E^-((x)^2)+E^-((y)^2)-1.9,{x,35,-35},{y,35,-35},{z,1,-1},MaxRecursion->2,PlotPoints->{{5,3},{5,3},{5,3}},Boxed->False,Axes->True]

Fig. 12.2.3: ContourPlot3D[E^-((x)^2)+E^-((y)^2)+E^-((z)^2)-1.9,{x,4,-4},{y,4,-4},{z,4,-4},MaxRecursion->2,PlotPoints->{{5,4},{5,4},{5,4}},Boxed->False,Axes->True]

Fig. 12.2.4: ContourPlot3D[(E^-(x)^2)+(E^-(y)^2)+(E^-(z)^2)+(E^-(x-2.5)^2)+(E^-(y-2.5)^2)+(E^-(z-2.5)^2)-1.98,{x,-4,6},{y,-4,6},{z,-4,6},MaxRecursion->2,PlotPoints->{{4,5},{4,5},{4,5}},Boxed->False,Axes->True]

Fig. 12.2.5: ContourPlot3D[(E^-(x)^2)+(E^-(y)^2)+(E^-(z)^2)+(E^-(x-8)^2)+(E^-(y-8)^2)+(E^-(z-8)^2)-1.98,{x,-4,12},{y,-4,12},{z,-4,12},MaxRecursion->2,PlotPoints->{{5,5},{5,5},{5,5}},Boxed->False,Axes->True]

Fig. 12.2.6: ContourPlot3D[(Cos[Pi x])^8+(Cos[Pi y])^8+(Cos[Pi z])^8-1.98,{x,1.5,-.5},{y,1.5,-.5},{z,1.5,-.5},MaxRecursion->2,PlotPoints->{{5,4},{5,4},{5,4}},Boxed->False,Axes->True]

Fig. 12.2.7: ContourPlot3D[E^-(z)+E^-(x)^2+E^-(y)^2+E^-(x-4)^2+E^-(y-4)^2-1.95,{x,8,-4},{y,8,-4},{z,6,-1},MaxRecursion->2,PlotPoints->{{7,4},{7,4},{7,4}},Boxed->False,Axes->True]

Fig. 12.3.1 a: ContourPlot3D[E^-(10(y^2+(z)^2)+E^-(2 x)+E^(2 (x-11)))-.9,{x,12,-1},{y,1,-1},{z,1,-1},MaxRecursion->2,PlotPoints->{{5,4},{5,3},{5,3}},Boxed->False,Axes->True]

Fig. 12.3.1 b: ContourPlot3D[E⁻(10(y²+z²))+E⁻(2 x)+E² (x-11))-9,{x,10.5,7}, {y,15,-15},{z,15,-15},MaxRecursion->2,PlotPoints->{{5,4},{5,3},{5,3}},Boxed->False, Axes->True]

Fig. 12.3.2: ContourPlot3D[E⁻(10(y²+z²)+ E²((x-11))+ E⁻(x+2))+ E⁻((y²+ (x)²+z²))-96,{x,6,-2},{y,45,-45},{z,45,-45},MaxRecursion->2, PlotPoints->{{5,4},{5,3},{5,3}},Boxed->False,Axes->True]

Fig. 12.3.3: ContourPlot3D[E²(z Cos[Pi x²]+ y Sin[Pi x²])+E²(z²+y²))-1.95, {x,2,-2},{y,55,-55},{z,55,-55},MaxRecursion->2,PlotPoints->{{5,5},{5,4},{5,4}}, Boxed->False,Axes->False]

Fig. 12.3.4 a: ImplicitPlot[10⁻((x)²)+ 2 10⁻((x)²+10²(y-15))+10⁻(y-10))=0.1, {x,-8,8},{y,4,20},PlotPoints->100]

Fig. 12.3.4 b: ImplicitPlot[10⁻((x)²+10²(y-11))+10⁻((x+1 y-1)²+10²(y-15)+ 10⁻(y-10))+10⁻((-x+1 y-1)²+10²(y-15))+10⁻(y-10))=0.1,{x,-8,8},{y,4,20}, PlotPoints->100]

Fig. 12.3.5: ImplicitPlot[10⁻((x)²+10²(y-11))+.12 10⁻((x)²+(y-15.7)²)+ .12 10⁻((x+2)²+(y-15.4)²)+2 10⁻((x+2 y-2)²+10²(y-15))+10⁻(y-10))+ 2 10⁻((-x+2 y-2)²+10²(y-15))+10⁻(y-10))=0.1,{x,-8,8},{y,4,20},PlotPoints->200]

Fig. 12.3.6: ImplicitPlot[10⁻((x)²+10²(y-6))+10⁻(y+6) +.2 10⁻((-x-9 y-5)²+ 10⁻(y+15))+10²(y+4))+.2 10⁻((x-4 y-2)²+10⁻(y+15))+10²(y+4))+.2 10⁻((-1x-y-4)²+ 10²(x-10))+10⁻(x))+.12 10⁻((x-2 y-7.5)²+10⁻(y+20))+10²(y+10))+.15 10⁻((-1x-y- 10)²+10⁻(x+12))+10²(x+2))+ 10⁻((x+4 y-2)²+10²(y-19))+10⁻(y-5))+ 10⁻((-x+4 y-2)²+10²(y-17))+10⁻(y-5))+10⁻((x+2 y-25)²+10²(y-21))+10⁻(y-15))+ 10⁻((-x+ y-8)²+10²(y-22))+10⁻(y-12))+10⁻((x+1.5 y-27)²+10²(y-21))+10⁻(y-17))+ 10⁻((-x+ y-16)²+10²(y-24))+10⁻(y-13))=0.1,{x,-18,16},{y,-20,27},PlotPoints->100]

Fig. 12.4.1: ImplicitPlot[E⁻(- 2(x-6)²)-y +E⁻(2 x²)=0,{x,8,-3},{y,-1,1}, PlotPoints->100]

Fig. 12.4.2 a: ImplicitPlot[-12(3+4Cosh[2x-8 .5])+Cosh[4x-64 .5])/(3 Cosh[x-28 .5]+ Cosh[3x-36 .5])²+y=0,{x,12,-6},{y,-1,10},PlotPoints->100]

Fig. 12.4.2 b: ImplicitPlot[-12(3+4Cosh[2x-8 .2])+Cosh[4x-64 .2])/(3 Cosh[x-28 .2]+ Cosh[3x-36 .2])²+y=0,{x,12,-6},{y,-1,10},PlotPoints->100]

Fig. 12.4.3 a: ImplicitPlot[6 (Sech[x])²-y=0,{x,5,-5},{y,6,-1},PlotPoints->100]

Fig. 12.4.3 b: ImplicitPlot[6 (Sech[x-8])²-y=0,{x,12,-5},{y,6,-1},PlotPoints->100]

Fig. 12.4.4 a: ImplicitPlot[4 (Sech[x])²+8 (Sech[x-8])²-y=0,{x,10,-5},{y,9,-1}, PlotPoints->100]

Fig. 12.4.4 b: ImplicitPlot[4 (Sech[x])²+8 (Sech[x-4])²-y=0,{x,10,-5},{y,8,-1}, PlotPoints->100]

Fig. 12.4.5: ImplicitPlot[{y- (Sech[x])²-(Sech[x-3])²-(Sech[x-6])²-(Sech[x-9])² =0,E⁻x²+E⁻(x-3)²+E⁻(x-6)²+E⁻(x-9)²-y=0},{x,-4,13},{y,-2,2},PlotPoints->200, Axes->False]

Fig. 124.6: `ImplicitPlot[Cos[(2/100)^.5 x]^100-y ==0,{x,-3,50},{y,-1,1},PlotPoints->200, Axes->False]`

Chapter 13

Fig. 13.3.1: `ContourPlot3D[E^(-8 x^2)-E^(-8 (x-1)^2)+E^(-8 (x-2)^2)-E^(-8 (x-3)^2) + 1 (E^(-8 (x-4)^2) -E^(-8 (x-5)^2)+ E^(-8 (x-6)^2)) -1(E^(-8 (x-7)^2)-E^(-8 (x-8)^2) + E^(-8 (x-9)^2)) +E^(-8 (x-10)^2) -E^(-8 (x-11)^2) +E^(-8 (x-12)^2)- E^(-8 (x-13)^2) + E^(y^2+z^2)-3.5,{x,15,-2},{y,3,-3},{z,3,-3},MaxRecursion->2, PlotPoints->{{7,4},{5,4},{5,4}},Boxed->False,Axes->True]`

Fig. 13.3.2: `ContourPlot3D[E^(-8 x^2)-E^(-8 (x-1)^2)+E^(-8 (x-2)^2)-E^(-8 (x-3)^2) + .1 (E^(-8 (x-4)^2) -E^(-8 (x-5)^2)+ E^(-8 (x-6)^2)) -1(E^(-8 (x-7)^2)-E^(-8 (x-8)^2) + E^(-8 (x-9)^2)) +E^(-8 (x-10)^2) -E^(-8 (x-11)^2)+E^(-8 (x-12)^2)- E^(-8 (x-13)^2) + E^(y^2+z^2)-3.5,{x,15,-2},{y,3,-3},{z,3,-3},MaxRecursion->2, PlotPoints->{{7,4},{5,4},{5,4}},Boxed->False,Axes->True]`

Fig. 13.3.3: `ContourPlot3D[E^(-8 x^2)-E^(-8 (x-1)^2)+E^(-8 (x-2)^2)-E^(-8 (x-3)^2) + 1 (E^(-8 (x-4)^2) -E^(-8 (x-5)^2)+E^(-8 (x-6)^2)) -1(E^(-8 (x-7)^2)-E^(-8 (x-8)^2) + E^(-8 (x-9)^2))+E^(-8 (x-10)^2) -E^(-8 (x-11)^2)+E^(-8 (x-12)^2)- E^(-8 (x-13)^2) + E^(y^2+z^2)-3.5,{x,15,-2},{y,3,-3},{z,3,-3},MaxRecursion->2,PlotPoints-> {{7,4},{5,4},{5,4}},Boxed->False,Axes->True]`

Fig. 13.3.4: `ContourPlot3D[E^(-8 x^2)-E^(-8 (x-1)^2)+E^(-8 (x-2)^2)-E^(-8 (x-3)^2) + 1 (E^(-8 (x-4)^2) -E^(-8 (x-5)^2)+ E^(-8 (x-6)^2)) -1(E^(-8 (x-7)^2)-E^(-8 (x-8)^2) + E^(-8 (x-9)^2))+E^(-8 (x-10)^2) -E^(-8 (x-11)^2) +E^(-8 (x-12)^2)- E^(-8 (x-13)^2) + E^(y^2+z^2)-3.5,{x,15,-2},{y,3,-3},{z,3,-3},MaxRecursion->2,PlotPoints-> {{7,4},{5,4},{5,4}},Boxed->False,Axes->True]`

Fig. 13.3.5: `ContourPlot3D[E^(-.5 E^x)+.5(Cos[Pi x]+Cos[Pi y]+Cos[Pi z]) + E^(y^2+z^2))-0.5,{x,-8,1.5},{y,-1.2,1.2},{z,-1.2,1.2},MaxRecursion->2,PlotPoints-> {{5,3},{5,3},{5,3}},Boxed->False,Axes->True]`

Fig. 13.3.6: `ContourPlot3D[E^(-.5 E^(-x)+.5(Cos[Pi x]Sin[Pi y]+Cos[Pi z]Sin[Pi x]+ Sin[Pi z]Cos[Pi y]) +E^(y^2+z^2))-0.5,{x,8,-1.5},{y,-1.2,1.2},{z,-1.2,1.2},MaxRecursion->2, PlotPoints->{{5,3},{5,3},{5,3}},Boxed->False,Axes->True]`

Fig. 13.3.7: `ContourPlot3D[E^(-.5 E^(-x)+.5(Cos[Pi x]Sin[Pi y]+Cos[Pi z]Sin[Pi x]+ Sin[Pi z]Cos[Pi y]) +E^(y^2+z^2))+E^(-.5 E^x)+.5(Cos[Pi x]+Cos[Pi y]+Cos[Pi z]) + E^(y^2+z^2))-0.5,{x,4,-3},{y,-1.2,1.2},{z,-1.2,1.2},MaxRecursion->2,PlotPoints-> {{5,4},{5,3},{5,3}},Boxed->False,Axes->True]`

Fig. 13.3.8 a: `ContourPlot3D[.5 Cos[Pi z]+(y^2+x^2)-12,{x,-4,4},{y,-4,4},{z,-4,4}, MaxRecursion->2,PlotPoints->{{5,4},{5,4},{5,4}},Boxed->False,Axes->True]`

Fig. 13.3.8 b: `ContourPlot3D[(Cos[Pi z]+Cos[Pi x]+Cos[Pi y])+(y^2+x^2)-12,{x,-4,4}, {y,-4,4},{z,-4,4},MaxRecursion->2,PlotPoints->{{5,4},{5,4},{5,4}},Boxed->False,Axes->True]`

Fig. 13.3.8 c: `ContourPlot3D[.6 (Cos[Pi x] Sin[Pi z]+Cos[Pi y] Sin[Pi x]+ Cos[Pi z] Sin[Pi y])+(y^2+x^2)-12,{x,-4,4},{y,-4,4},{z,-4,4},MaxRecursion->2, PlotPoints->{{5,4},{5,4},{5,4}},Boxed->False,Axes->True]`

Fig. 13.4.3 a: ContourPlot3D[E^-(E^(2(x+2))+.2 (y^2+z^2))+E^-(E^(-2(x-2))+.2 (y^2+z^2))-E^(-2((y-1)^2+z^2+(x+3)^2-.5))-E^(-6((y-1)^2+(z-2)^2+(x+3)^2-.5))-E^(-6((y-1)^2+(z+2)^2+(x+3)^2-.5))-E^(-2((y+1)^2+z^2+(x+3)^2-.5))-E^(-6((y+1)^2+(z-2)^2+(x+3)^2-.5))-E^(-6((y+1)^2+(z+2)^2+(x+3)^2-.5))-E^(-2((y-1)^2+z^2+(x+5)^2-.5))-E^(-6((y-1)^2+(z-2)^2+(x+5)^2-.5))-E^(-6((y-1)^2+(z+2)^2+(x+5)^2-.5))-E^(-2((y+1)^2+z^2+(x+5)^2-.5))-E^(-6((y+1)^2+(z-2)^2+(x+5)^2-.5))-E^(-6((y+1)^2+(z+2)^2+(x+5)^2-.5))-E^(-2((y+1)^2+z^2+(x+5)^2-.5))-.04,{x,-7,3},{y,-1,4.1},{z,-4.1,4.1},MaxRecursion->2,PlotPoints->{{6,4},{6,4},{6,4}},Boxed->False,Axes->True] Show[%, ViewPoint->{-1.344, -2.329, 2.054}]

Fig. 13.4.3 b: ContourPlot3D[E^-(E^(2(x+2))+.2 (y^2+z^2))+E^-(E^(-2(x-2))+.2 (y^2+z^2))-E^(-2((y-1)^2+z^2+(x+2.75)^2-.5))-E^(-6((y-1)^2+(z-2)^2+(x+2.75)^2-.5))-E^(-6((y-1)^2+(z+2)^2+(x+2.75)^2-.5))-E^(-2((y+1)^2+z^2+(x+2.75)^2-.5))-E^(-6((y+1)^2+(z-2)^2+(x+2.75)^2-.5))-E^(-6((y+1)^2+(z+2)^2+(x+2.75)^2-.5))-E^(-2((y-1)^2+z^2+(x+4.5)^2-.5))-E^(-6((y-1)^2+(z-2)^2+(x+4.5)^2-.5))-E^(-6((y-1)^2+(z+2)^2+(x+4.5)^2-.5))-E^(-2((y+1)^2+z^2+(x+4.5)^2-.5))-E^(-6((y+1)^2+(z-2)^2+(x+4.5)^2-.5))-E^(-6((y+1)^2+(z+2)^2+(x+4.5)^2-.5))-0.04,{x,-7,3},{y,-1,4.1},{z,-4.1,4.1},MaxRecursion->2,PlotPoints->{{3,5},{3,5},{3,5}},Boxed->False,Axes->True] Show[%, ViewPoint->{-1.344, -2.329, 2.054}]

Chapter 14

Fig. 14.3.3: ContourPlot3D[(Cos[.25 Pi (x-y)] E^(.025 Cos[Pi z])-(Cos[.25 Pi(x+ y)])), {x,4.6,-4.6},{y,4.6,-4.6},{z,2,-2},MaxRecursion->2,PlotPoints->{{5,4},{5,4},{4,4}},Boxed->False,Axes->True]

Fig. 14.5.1: ContourPlot3D[E^(Cos[.25 Pi (x-y)] E^(.05 Cos[Pi z])-(Cos[.25 Pi(x+ y)]))+E^-((y-8)^2)+E^-((y+8)^2)-1,{x,6,-10},{y,8.3,-8.3},{z,2,-2},MaxRecursion->2,PlotPoints->{{5,4},{5,4},{5,4}},Boxed->False,Axes->True]

Subject Index

A

actin · 206; 207; 208; 211; 223; 228;
229; 230; 244; 431
Alhambra · 432
alveolar surface · 341; 342; 343; 349;
350; 351; 352; 353; 354; 356; 357;
358; 361; 420
alveolar surface phase · 354; 356; 357;
358
amalgamation · 163; 463
amoeba · 168
amphiphilic · 1; 337; 358
anaesthetic agents · 2; 183; 184; 317;
330; 332; 335; 336; 337
anaesthetic effects · 335
apoptosis · 168
Archaeobacteria · 366
Archimedes · 105
axon membrane · 3; 313; 314; 315; 316;
317; 320; 321; 326; 327; 336; 363
axoneme · 223; 236; 240; 242; 244; 255

B

$B_{12}H_{12}^{2-}$ · 289
bacteriorhodopsin · 175
bilateral symmetry · 431; 432
bilayer compressibility · 181
bilayer motions · 3; 187
biological motion · 4; 76; 122; 129;
139; 212; 223; 247; 302
Bloch walls · 311
body centred structure · 391; 440
Bonnet transformation · 47; 68; 463
breast stroke · 223; 252
budding off · 188; 189
butter fly · 255

C

catenoids · 28; 34; 38; 39; 41; 52; 57;
58; 61; 62; 68; 73; 76; 97; 99; 141;
153; 181; 211; 223; 227; 229; 234;
270; 292; 299; 388; 390; 396; 399;
409; 415; 416; 472
cell division · 4; 193; 194; 196; 198;
199; 200; 201; 204; 227; 232; 285;
299; 301
cell hybrid · 264; 265
cell membrane systems · 163
cell membranes · 1; 2; 3; 4; 41; 73; 131;
162; 163; 164; 167; 169; 180; 184;
363; 364; 417
cell organelles · 1; 182; 257
chemical synapse · 327; 328; 332
chirality · 187; 301
Chlamydomona · 252; 253; 254
chloroplasts · 168; 364
cilia · 223; 236; 252; 253; 255
clathrin · 92; 189; 257; 285; 292
cnoidal waves · 311
colloidal particles · 163; 164; 176; 353;
398
colloidal state · 1
complex exponential · 447; 448; 449
complex number · 447
compound · 460
concentration gradient · 2; 83; 105; 225;
227; 229; 313
connectivity · 131; 153; 154; 155; 158;
159; 160; 161; 180; 301; 388; 390;
392; 393; 396; 398
connexons · 327; 332
cosh · 74; 76
crawling of cells · 116
cruciform · 193; 217; 219
cubic lipid bilayers · 164; 177
cubic phases · 2; 164; 180; 184
cubosomes · 4; 16; 131; 132; 133; 135;
147; 163; 164; 169; 179; 180; 182;

187; 310; 333; 353; 366; 398; 431;
452
curvature elasticity · 181
cyclic crawling · 116
cytoskeleton proteins · 1

D

D surface · 22; 23; 24; 25; 48; 65; 154;
157; 395
D'Arcy Thompson · 363; 366
de Moivre · 448
depolarisation · 314; 316; 317; 318;
321; 326; 333
Diffusion equation · 74
dilatation · 111; 151; 223; 237; 242;
276; 287; 289; 445
Diophante · 268; 270; 271
DNA · 3; 27; 100; 101; 102; 193; 213;
214; 217; 219; 220; 310; 366; 419;
426; 429; 431; 432
dodecahedron · 138; 144; 285; 287; 289;
290; 291; 292; 293; 440; 441; 459
dynein · 3; 244; 255

E

earthquake · 305
eccentric wheel · 244
eigenvibrations · 398
electrical synapses · 327; 332
ELF structure · 17
elliptic point · 464
endocytosis · 92; 116
endoplasmic reticulum · 2; 3; 4; 163;
164; 167; 169; 170; 171; 172; 174;
188; 260; 265; 273; 333
erythrocyte membranes · 187
Escher · 432
excitation · 314; 315; 323; 327; 330;
334; 363
exocytosis · 92; 116; 329; 331
exponential scale · 3; 76; 180; 212;
237; 247; 399; 401; 402; 405; 407;
409; 411; 419; 425; 433; 447; 456;
460; 461; 463; 472

F

Fermat · 268

fetal rat lung · 345
Fibonacci · 151; 152; 238
Filament construction · 235
finite periodicity · 1; 73; 83; 107; 131;
141; 151; 152; 318; 319; 447; 450;
452
flagella · 4; 105; 111; 113; 115; 116;
126; 223; 236; 244; 247; 248; 249;
251; 252; 255; 409
flagella of bacteria · 113
flagella of sperms · 111
fractal · 4; 299
fundamental theorem · 7; 8; 9; 16; 105;
106; 107; 385; 431

G

gap junctions · 327; 328; 332
garnet · 231
Gauss distribution · 75; 81; 399
gaussian curvature · 11; 166; 180; 181;
319; 349; 416; 463; 464; 466; 467
goke · 236
golden mean · 285
Golgi · 3; 4; 184; 188; 257; 259; 260;
261; 262; 264; 265; 273; 333; 409
groves · 101
gyroid surface · 47; 48; 139; 156; 165;
170; 230; 301; 321; 393

H

harmonic oscillator · 106; 132; 247
Helfrich · 5; 183; 185; 191
helicoid · 15; 16; 114; 244; 245; 425;
428; 456; 466; 467
helicoidal tower surface · 428
Hermite function · 83; 105; 106; 108;
109; 110; 111; 115; 131; 132
Hermite polynoms · 106
hexagon · 187; 209; 431
hexagonal · 2; 27; 28; 36; 38; 41; 42;
58; 62; 131; 154; 175; 182; 184;
207; 208; 209; 327; 433; 434; 435;
436; 439; 443
Hilbert · 398; 466; 472; 476
Holliday junction · 193; 214
Hyde · 5; 31; 45; 72; 162; 165; 190;
221; 338; 339; 346; 362; 373; 464;
467; 472; 476

hydrophilic · 1; 343; 354; 355
hydrophobic · 1; 343
hyperbolic polyhedra · 285; 310

I

icosahedron · 285; 286; 289; 292; 293;
444; 459; 460
infinite product · 8; 9; 18; 23; 25; 132;
248; 395
infinite products · 9; 23; 25; 395
Invaginations · 271; 272
IPMS · 2; 4
IWP surface · 24

K

kick · 255
kinesin · 3

L

lamellar bodies · 342; 353; 354; 355
Laplace equation · 74
leech · 371; 372
Lidin · 5; 31; 42; 45; 103; 162; 190;
221; 256; 338; 339; 346; 362; 373;
417; 472; 476
lipid bilayers · 3; 163; 164; 165; 177;
180; 188; 315; 323; 337; 345; 347;
360
lung surfactant · 342; 343; 361
lungs · 341; 342; 356; 361
Luzzati · 1; 372

M

magnetic domains · 311
magnetite · 394; 395; 442
mathematical mirror · 444
Max Born · 72
mean curvature · 270; 456; 464
membrane lipids · 2; 41; 164; 184; 364;
366; 368
microtubuli · 3
microtubulus · 235; 236; 239; 255
minimal surface structures · 164
mitochondria · 164; 168; 169; 193; 204;
260

mitochondrion · 193; 201; 204; 206;
409
monkey saddle · 22; 23; 25; 26; 36; 37;
58; 61; 267; 270; 397; 422; 423;
424; 426; 464; 466
motion · 4; 73; 74; 76; 87; 96; 97; 101;
105; 111; 112; 113; 114; 115; 116;
117; 118; 119; 120; 122; 125; 126;
127; 129; 139; 180; 181; 193; 194;
201; 207; 208; 212; 223; 224; 227;
232; 236; 244; 247; 252; 255; 257;
302; 305; 314; 320; 331; 337; 363;
375; 385; 409
muscle cell · 131; 166; 193; 206; 244;
313; 327; 333
myelinated · 315; 318; 326
myosin · 206; 207; 208; 211; 223; 244;
247

N

natural exponential · 76; 78; 409; 447;
449; 461
natural number · 76
Neovius surface · 25; 26
nerve signal conduction · 313; 363
nerve trunk · 326
Nesper · 45; 49; 72; 177; 178; 191
neuromuscular junction · 328
Newton · 105
nonagon · 236
nuclear pore complex · 4; 257; 276; 282;
283

O

octahedron · 18; 80; 107; 132; 149;
294; 295; 442; 457; 458; 459; 460
organelles · 1; 163; 182; 223; 225; 257;
364
orthorhombic · 436; 437; 439

P

P surface · 47; 48; 153
parabolic point · 464
pentagonal dodecahedron · 285
periodic motion · 111; 116; 118; 120;
193
photoreceptor membrane · 364

pinocytosis · 89; 189
 polymerase · 101; 214
 polynomial algebra · 257
 potassium channels · 315
 power expansion · 9; 16; 108
 power stroke · 207; 223; 244; 246; 247
 precipitation · 225; 227; 228
 presynaptic membrane · 329; 330; 331;
 332; 333
 pretzel · 473; 474
 prolamellar body · 168
 proteins · 1; 4; 92; 113; 129; 131; 160;
 163; 165; 168; 175; 188; 211; 223;
 227; 229; 234; 236; 244; 255; 257;
 276; 282; 317; 327; 332; 333; 335;
 342; 343; 361; 368; 431
 pulmonary capillaries · 341

Q

quasi symmetry · 237

R

Ranvier node · 315
 repolarisation · 314; 315; 318
 respiration · 341; 359; 360
 rhombic dodecahedron · 138; 144; 440;
 441; 459
 RNA · 213; 214; 217; 276; 367; 368
 rod packing · 27; 28; 230
 ruffling · 299

S

sacromere · 27
 saddle point · 464; 465; 466
 sarcoplasmic reticulum · 333
 Scherk · 13; 369; 468; 469; 470; 471
 Schrödinger · 106; 107; 132; 306; 307;
 310
 sech · 75; 83; 311
 Sendai virus · 264; 265
 shoulders · 301
 Signal propagation · 315
 sodium channels · 314; 315; 318; 323;
 326; 337
 solitons · 75; 305; 306; 307; 308; 309;
 310; 311
 solubility · 4; 223; 225

spikes · 285; 297; 299; 409
 standing wave conformations · 2; 180;
 184
 standing wave dynamics · 163
 stella octangula · 442; 457; 458
 Streptomyces hygroscopicus · 183
 symmetry group · 432
 synaptic transmission · 327; 329; 330;
 332; 336
 Synge · 105; 130

T

tetragonal · 27; 28; 29; 30; 31; 32; 34;
 36; 47; 61; 62; 64; 65; 160; 161;
 341; 349; 361; 410; 436; 439; 472
 tetrahedron · 80; 98; 99; 124; 126; 137;
 456
 The CLP surface · 64
 thylakoid membranes · 168
 tidal breathing · 347; 359
 topology · 2; 31; 126; 131; 160; 214;
 217; 225; 253; 257; 266; 376; 416
 torus · 99; 101; 102; 282; 472; 473
 tower surfac · 13; 15; 370; 420; 421;
 423; 424; 426; 427; 428; 468; 469
 tower surface · 13; 15; 370; 420; 421;
 423; 424; 426; 427; 428; 468; 469
 transmitter molecules · 313; 329; 330;
 331; 332
 travelling waves · 75
 tree · 4; 285; 301; 305; 341; 361; 409
 truncated octahedron · 460
 tubular myelin · 341; 342; 345; 350;
 354; 360
 Tubulin · 235
 twin operation · 34; 223; 252; 253; 254;
 255

U

unmyelinated axons · 326

V

vesicle · 3; 85; 86; 87; 88; 89; 91; 92;
 93; 96; 153; 163; 180; 184; 188;
 189; 190; 225; 257; 258; 259; 265;
 266; 270; 273; 274; 313; 329; 331;
 332; 368; 388; 405

vesicle transport · 163; 189
virus · 4; 264; 265; 285; 292; 361; 444
von Schnering · 26; 45; 49; 72; 177;
178; 191

W

Wave equation · 74

wave motions · 2; 177; 180; 182; 189;
190; 208; 338
wave packet · 109; 111
wavelet · 109
Weierstrass · 31; 42; 346; 463; 472
wheel · 111; 243; 244; 463; 475; 476

This Page Intentionally Left Blank